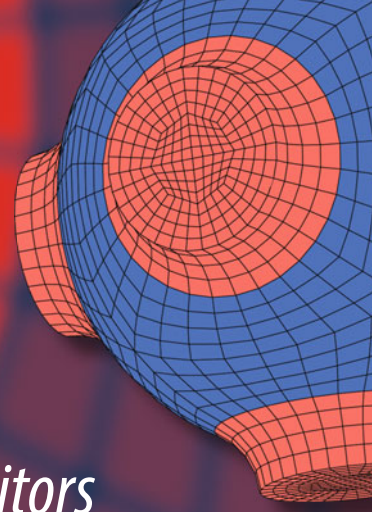


Advanced Structured Materials

Holm Altenbach
Suren Manuk Mkhitarian
Vahram Hakobyan
Avetik Varazdat Sahakyan *Editors*



Solid Mechanics, Theory of Elasticity and Creep

 Springer


Advanced Structured Materials

Volume 185

Series Editors

Andreas Öchsner, Faculty of Mechanical Engineering, Esslingen University of Applied Sciences, Esslingen, Germany

Lucas F. M. da Silva, Department of Mechanical Engineering, Faculty of Engineering, University of Porto, Porto, Portugal

Holm Altenbach , Faculty of Mechanical Engineering, Otto von Guericke University Magdeburg, Magdeburg, Sachsen-Anhalt, Germany

Common engineering materials are reaching their limits in many applications, and new developments are required to meet the increasing demands on engineering materials. The performance of materials can be improved by combining different materials to achieve better properties than with a single constituent, or by shaping the material or constituents into a specific structure. The interaction between material and structure can occur at different length scales, such as the micro, meso, or macro scale, and offers potential applications in very different fields.

This book series addresses the fundamental relationships between materials and their structure on overall properties (e.g., mechanical, thermal, chemical, electrical, or magnetic properties, etc.). Experimental data and procedures are presented, as well as methods for modeling structures and materials using numerical and analytical approaches. In addition, the series shows how these materials engineering and design processes are implemented and how new technologies can be used to optimize materials and processes.


Advanced Structured Materials is indexed in Google Scholar and Scopus.

Holm Altenbach · Suren Manuk Mkhitarian ·
Vahram Hakobyan · Avetik Varazdat Sahakyan
Editors

Solid Mechanics, Theory of Elasticity and Creep

 Springer

Editors

Holm Altenbach 
Faculty of Mechanical Engineering
Institute of Mechanics
Otto-von-Guericke-Universität Magdeburg
Magdeburg, Sachsen-Anhalt, Germany

Vahram Hakobyan
Institute of Mechanics
National Academy of Sciences of Armenia
Yerevan, Armenia

Suren Manuk Mkhitarian
National Academy of Sciences of Armenia
Yerevan, Armenia

Avetik Varazdat Sahakyan
Institute of Mechanics
National Academy of Sciences of Armenia
Yerevan, Armenia

ISSN 1869-8433

ISSN 1869-8441 (electronic)

Advanced Structured Materials

ISBN 978-3-031-18563-2

ISBN 978-3-031-18564-9 (eBook)

<https://doi.org/10.1007/978-3-031-18564-9>

© The Editor(s) (if applicable) and The Author(s), under exclusive license to Springer Nature Switzerland AG 2023

This work is subject to copyright. All rights are solely and exclusively licensed by the Publisher, whether the whole or part of the material is concerned, specifically the rights of translation, reprinting, reuse of illustrations, recitation, broadcasting, reproduction on microfilms or in any other physical way, and transmission or information storage and retrieval, electronic adaptation, computer software, or by similar or dissimilar methodology now known or hereafter developed.

The use of general descriptive names, registered names, trademarks, service marks, etc. in this publication does not imply, even in the absence of a specific statement, that such names are exempt from the relevant protective laws and regulations and therefore free for general use.

The publisher, the authors, and the editors are safe to assume that the advice and information in this book are believed to be true and accurate at the date of publication. Neither the publisher nor the authors or the editors give a warranty, expressed or implied, with respect to the material contained herein or for any errors or omissions that may have been made. The publisher remains neutral with regard to jurisdictional claims in published maps and institutional affiliations.

This Springer imprint is published by the registered company Springer Nature Switzerland AG
The registered company address is: Gewerbestrasse 11, 6330 Cham, Switzerland

Preface



N. Kh. Harutyunyan (1922–1993)

On November 23, 2022, we are celebrating the 110th anniversary of the birth of N. Kh. Harutyunyan, who was one of the founders of the Armenian school of mechanics. He was a prominent and distinguished scientist who has gained wide international recognition, one of the most energetic and skillful organizer of science and higher education in Armenia, a prominent political leader, academician of Armenian National Academy of Sciences. His name is connected with the formation and further progress of a number of scientific directions in mechanics of deformable solid bodies, among them theory of elasticity, creep, and contact mechanics. He formed several generations of scientists in both Armenia and other countries.

N. Kh. Harutyunyan was born in 1912 in Yerevan (Russian Empire, now the capital of the Republic of Armenia). For many years, he lived with his grandfather—the famous historian Leo, whose huge scientific figure instilled in the young man respect for science. In 1930, he entered the Moscow Military Engineering Academy named after V. V. Kuybyshev. After graduating from it in 1936 and being qualified as engineer-hydroconstructor, he returned to Armenia. He started his professional career as a leading engineer of the construction company Sevan-Zangustroy. At the same

time, he taught at the Yerevan Polytechnic Institute. In 1937, N. Kh. Harutyunyan entered the postgraduate courses of the Leningrad Polytechnic Institute (now Peter the Great St. Petersburg Polytechnic University). Communication with the greatest scientists in mechanics like B. G. Galerkin, E. L. Nikolai, and A. I. Lurie played a decisive role in his future scientific development. N. Kh. Harutyunyan always had special love and respect toward the Leningrad school of mechanics, and his scientific contacts with this school have never been broken. After defending his first doctoral thesis (candidate of sciences) in 1941, he went to the front. His military service during the World War II was marked with the Orders of Patriotic War of I and II degree, the Order of the Red Star and medals.

Demobilized from the army in 1945, N. Kh. Harutyunyan returned to Armenia and started again his scientific and pedagogical activities. In 1949 in Moscow, at the Institute of Mechanics of the USSR Academy of Sciences, he defended the doctoral thesis and was awarded the title of doctor of technical sciences. In 1950, he became the title of professor. In the same year, he was elected a full member of the Academy of Sciences of Armenia and a member of the Presidium of this academy.

In 1952–55, his scientific activities continued at the Academy of Sciences, where he worked as the Academician-Secretary of the Department of Engineering Sciences. In 1955, N. Kh. Harutyunyan was appointed the head of the newly created laboratory of creep and strength at the Institute of Mathematics and Mechanics. In 1959, he was elected the vice-president of the Academy of Sciences. In parallel with his scientific work, he is engaged in pedagogical activities. In 1945–51, he taught at Yerevan Polytechnic Institute, in 1951, at Yerevan State University where he was the professor of the Chair of Theoretical Mechanics, and in 1958, he became the head of newly created Chair of Theory of Elasticity and Plasticity (now Chair of Continuum Mechanics) and led it till 1978. In 1961, N. Kh. Harutyunyan was appointed the rector of Yerevan State University. Thanks to his efforts, the chair of Biophysics, Nuclear Physics, Economic Cybernetics, and the Joint Computer Center of the Academy of Sciences and YSU were established. In 1962, he was awarded the honorary title of the Honored Scientist of the Armenian SSR. For many years, he was a member of the USSR National Committee on Theoretical and Applied Mechanics and its Presidium. He was appointed the editor-in-chief of the Journal *Proceedings of the Armenian SSR Academy of Sciences, Mechanics* and a member of the Editorial Board of *Proceedings of the USSR Academy of Sciences, Mekhanika Tverdogo Tela* (English translation *Mechanics of Solids*, now published by Springer).



From the left: S. P. Timoshenko, N. Kh. Harutyunyan, and Ya. G. Panovko at the 11th IUTAM-Congress in Munich (1964)

N. Kh. Harutyunyan was actively involved in social-political and state activities. He was many times elected a deputy of the Supreme Soviet of the Republic and the Supreme Soviet of the USSR; in 1962–1975, he was the chairman of the Presidium of the Supreme Soviet of the Armenian SSR and deputy chairman of the Presidium of the Supreme Soviet of the USSR. In the Soviet Union and abroad, he adequately represented Armenia and its achievements in various fields of public life.

N. Kh. Harutyunyan's research activities developed mainly in two directions: the mathematical theory of elasticity and the theory of creep. His first works on elasticity theory were on torsion and bending of prismatic rods with polygonal cross section, where he proposed an effective method for solving these problems, based on reducing them to the solution of infinite systems of algebraic equations. The method was applied in numerous studies and became classical. It was included in monographs and textbooks. Scientific results, obtained in this direction, were generalized. Finally, they were summarized in the fundamental book: *Torsion of Elastic Bodies* (authors N. Kh. Harutyunyan and B. L. Abrahamyan), published in Moscow in 1963. N. Kh. Harutyunyan had performed extensive scientific-research work in the field of elastic contact and mixed boundary value problems and obtained exact solutions classes of these problems together with his students. He also developed the scientific approach to contact problems concerning the load transfer to elastic solid bodies by means of thin-walled stringers.

N. Kh. Harutyunyan had made the greatest scientific contribution to the theory of creep. After analyzing the results of numerous experiments, N. Kh. Harutyunyan and G. N. Maslov concluded that in problems of strength and durability of engineering structures made, for example, of concrete, plastics, soils, glass-reinforced plastics, classical approaches did not work. In addition to the usual physical and mechanical properties of materials, one should also consider the properties due to

the creep phenomenon, such as aging and heredity. This fundamental idea was a new mathematical theory of creep of aging bodies, developed by N. Kh. Harutyunyan, which later entered the science as the Maslov-Arutyunyan creep theory. Considering this theory, the existing standards for the calculation of strength and longevity of numerous construction structures and their elements have been changed. The fundamental results of N. Kh. Harutyunyan's theory of creep have been summed up in his fundamental monograph *Some Problems of Creeping Theory*, which was published in Moscow in 1952. It was translated and published in England, France, and China. Some chapters were published in Germany, Poland, and Romania. In the formulations of the linear and nonlinear theories of creep Harutyunyan constructed contact and numerous other problems of theoretical and practical importance. In the nonlinear problems, he formulated the superposition principle of generalized displacements.

In the last two decades of his scientific activity, N. Kh. Harutyunyan considerably generalized and developed his original theory of creep, having worked out the theory of creep of inhomogeneously aging bodies and created a new scientific direction: the mathematical theory of growing deformable bodies. The scientific results are summarized in numerous monographs and scientific papers. In 1975, N. Kh. Harutyunyan moved to Moscow and started to work at the Institute for Problems in Mechanics of the USSR Academy of Sciences as the head of the Department of Viscoelastic Body Mechanics. During the years of his stay in Moscow, his scientific and personal relations with Armenia did not weaken. He was also the head of the Department of Theory of Viscoelasticity at the Institute of Mechanics of the Armenian Academy of Sciences.

N. Kh. Harutyunyan died on January 18, 1993, in Moscow and remained devoted to science until the end of his life. He left a huge scientific heritage, including seven fundamental monographs, around two hundred original works, a scientific school, numerous students, and followers in Armenia and abroad. His scientific ideas and results will undoubtedly serve as a basis for new ideas and creative achievements of young scientists and a wide range of researchers.

Magdeburg, Germany
Yerevan, Armenia
Yerevan, Armenia
Yerevan, Armenia
August 2022

Holm Altenbach
Suren Manuk Mkhitaryan
Vahram Hakobyan
Avetik Varazdat Sahakyan

Monographs of N. Kh. Arutyunyan

1. Арутюнян, Н.Х.: Некоторые вопросы теории ползучести. М.-Л., Гостехиздат, 1952.
 - French translation: Arutiunian, N.Kh.: Applications de la Théorie du Fluage. Paris, 1957.
 - Chinese translation Beijing, 1961.
 - English translation: Arutyunyan, N.Kh.: Some Problems in the Theory of Creep, Oxford, Pergamon Press, 1965.
2. Арутюнян Н.Х., Абрамян Б.Л.: Кручение упругих тел. Moscow, 1963 (Arutyunyan, N.Kh., Abramyan B.L.: Torsion of elastic bodies).
3. Арутюнян Н.Х.: Теория ползучести неоднородно-стареющих тел. Moscow, 1981 (Arutyunyan N.Kh.: The theory of creep of inhomogeneously aging bodies).
4. Арутюнян Н.Х., Колмановский, В.Б.: Теория ползучести неоднородных тел. Moscow, 1983 (Arutyunyan, N.Kh., Kolmanovsky, V.B.: Theory of creep of inhomogeneous bodies).
5. Арутюнян, Н.Х., Дроздов, А.Д., Наумов, В.Э.: Механика растущих вязкоупруго-пластических тел. Moscow, 1987 (Arutyunyan, N.Kh., Drozdov, A.D., Naumov, V.E.: Mechanics of growing viscoelastic-plastic bodies).
6. Арутюнян, Н.Х., Зевин, А.А.: Расчет строительных конструкций с учетом ползучести. Moscow, 1988 (Arutyunyan, N.Kh., Zevin, A.A.: Calculation of building structures taking into account creep).
7. Арутюнян, Н.Х., Манжиров, А.В., Наумов, В.Э.: Контактные задачи механики растущих тел. Moscow, Наука, 1991 (Арутюнян, Н.Х., Манжиров, А.В., Наумов, В.Э.: Контактные задачи механики растущих тел).
8. Арутюнян, Н.Х., Манжиров, А.В.: Контактные задачи теории ползучести. Ереван, 1999 (Arutyunyan, N.Kh., Manzhirov, A.V.: Contact problems of creep theory).

Contents

1	On One Non-classical 3D Problem for a Layered Package of Isotropic Plate and the Problem of Earthquakes Prediction	1
	Lenser A. Aghalovyan and Mher L. Aghalovyan	
1.1	Introduction	1
1.2	Solution of 3D Quasistatic Problems	3
1.3	Investigation of Fast Dynamic Processes	10
1.4	Conclusions	15
	References	15
2	Diffraction of Plane Waves in an Elastic Half-Plane Enhanced Along Its Boundary by a Semi-infinite Stringer	17
	Karo L. Aghayan and Rafik A. Baghdasaryan	
2.1	Introduction	17
2.2	Statement of the Problem	18
2.3	Influence Function	19
2.4	Solution of the Contact Problem	22
2.5	Determination of the Radiated Wave Field	27
2.6	Numerical Analysis	29
2.7	Conclusion	31
	References	32
3	Analysis of Equivalence Conditions of Model of an Inhomogeneous Elastic Half-Space and Model of an Inhomogeneous Elastic Layer on the Elastic Foundation	33
	Sergei M. Aizikovich, Polina A. Lapina, and Sergei S. Volkov	
3.1	Introduction	33
3.2	Statement of the Contact Problem on the Shear of the Surface of an Inhomogeneous Half-Space	34
3.3	Models of an Inhomogeneous Half-Space	35
3.4	Integral Equations of Contact Problems and Solution Methods	36
3.5	Numerical Analysis	37

3.6	Conclusion	39
	References	40
4	Docking of Inhomogeneous Surfaces of Piezoelectric Layers in a Composite Waveguide as a Harvesters of Wave Energy	43
	Ara S. Avetisyan and Andranik A. Kamalyan	
4.1	Introduction	44
4.2	Modeling of a Two-Layer Piezoelectric Waveguide, Taking into Account the Roughness of the Surfaces of the Constituent Layers	45
4.3	Formulation of a Mathematical Boundary Value Problem in a Three-Layer Sandwich with a Thin Inhomogeneous Filling	47
4.4	Solution of the Mathematical Boundary Problem	49
4.5	Conclusion	55
	References	56
5	About One Approach in Prevention of the Emerging Dangerous Phenomena Caused by the Existence of Defect in Continuous Media	57
	Vladimir A. Babeshko, Ilya S. Telyatnikov, Alla V. Pavlova, and Maksim N. Kolesnikov	
5.1	Introduction	58
5.2	Formulation of the Problem	59
5.3	Eigenfunction Method in the Plane Problem of Vertical Vibrations for a Plate with a New Type Crack	63
5.4	Numerical Implementation Results	68
5.5	Conclusion	73
	References	74
6	Stress–Strain State of a Magnetoelastic Ferromagnetic Plane with a Crack Under the Action of a Magnetic Field	77
	Gevorg Y. Baghdasaryan	
6.1	Introduction	77
6.2	Statement of the Problem	78
6.3	Solution of the Problem in the Case of a Constant Transverse Magnetic Field	80
6.4	Solution of the Problem	82
6.5	Coefficients of Intensity of Magnetoelastic Stresses and Induced Magnetic Field	86
6.6	Occurrence of Concentrations of Magnetoelastic Stresses Due to Longitudinal Shear Due to the Orientation of the External Magnetic Field	87
	References	91

7	The Effect of Longitudinal Oscillations Resonance on Stability and Domains of Attraction in the Generalized Kapitza Problem . . .	93
	Alexander K. Belyaev, Oksana R. Polyakova, and Tatyana P. Tovstik	
7.1	Introduction	93
7.2	Model of a Compressed Pendulum. Complete Nonlinear System of Equations	94
7.3	Averaged Motion Equation of the Pendulum	96
7.4	Stability Conditions for the Upper Equilibrium Position	98
7.5	Oscillation Stability Zone	98
7.6	Conclusion	99
	References	100
8	Band Gaps of Metastructure with Periodically Attached Piezoelectric Patches and Internal Hinges	101
	Karen Ghazaryan, Samvel Jilavyan, Davit Piliposyan, and David Aznaurov	
8.1	Introduction	101
8.2	Band Gaps of a Beam with Periodically Attached Piezoelectric Patches	102
8.3	Band Gaps of a Beam with Periodically Attached Piezoelectric Patches and Internal Hinges	106
8.4	Analysis and Conclusions	109
	References	111
9	Periodic Contact Problem for a Two-level System of Punches and a Viscoelastic Half-space	115
	Irina G. Goryacheva and Anastasiya A. Yakovenko	
9.1	Introduction	115
9.2	Statement of the Contact Problem	117
9.3	Contact Problem Solution for the First Level Punches	118
9.3.1	Derivation of the Main Equations for Calculation of the First Level Contact Characteristics	118
9.3.2	Determination of the Instant of Time When the Second Level of Punches Comes into Contact with the Half-space	120
9.3.3	Analysis of the Indentation of the First Level Punches into the Half-space	122
9.4	Two-level Contact of the System of Punches and the Half-space	124
9.4.1	Asymptotic Analysis of the Contact Characteristics	124
9.4.2	Solution of the Viscoelastic Two-level Periodic Problem	126
9.4.3	Analysis of the Dependence of the Real Contact Area on Time	128

9.5	Conclusions	129
	References	130
10	On an Axisymmetric Contact Problem for a Piecewise-Homogeneous Space with Disk-Shaped Crack	133
	Vahram N. Hakobyan, Aram H. Grigoryan, and Harutyun A. Amirjanyan	
10.1	Introduction	133
10.2	Statement of the Problem and Derivation of Governing Equations	134
10.3	Solution of the Governing Singular Integral Equation	139
10.4	Numerical Analysis	143
10.5	Conclusion	145
	References	146
11	High-Temperature Creep of Cast Irons	147
	Abhijit Joshi, Konstantinos P. Baxevanakis, and Vadim V. Silberschmidt	
11.1	Introduction to Cast Iron	147
11.2	Microstructure of Cast Iron	149
11.3	Chemical Composition of Cast Iron	150
11.4	Mechanical Properties of Cast Iron	152
11.5	High-Temperature Applications of Cast Irons	154
11.6	Introduction to Creep	156
11.7	Creep Models	157
	11.7.1 Empirical Models	157
	11.7.2 Mechanism-Based Models	160
	11.7.3 Continuum-Mechanics and Micromechanical Models	162
11.8	Creep in Cast Irons	162
11.9	Experimental Results for CGI Creep	164
	References	169
12	About the Energy Dissipation Coefficient of Thin-Walled Glass-Plastic Pipes with the Initial Reinforcement Asymmetry with Respect to Axis Subjected to Pulsating Internal Hydrostatic Pressure	175
	Koryun A. Karapetyan and Sona Sh. Valesyan	
12.1	Introduction	176
12.2	Research Methodology	177
12.3	Results and Discussions	179
12.4	Conclusions	182
	References	183

13 Contact Problem for Coated Viscoelastic Tube and Rigid Inserts with Complex Profiles 185
 Kirill E. Kazakov

13.1 Introduction 185

13.2 Problem Formulation and Mathematical Model 186

13.3 Getting an Analytical Solution 190

13.4 Conclusions 193

References 193

14 Inelastic Behavior of High-Temperature Steel Under Cyclic Loading Conditions 195
 Katharina Knape and Holm Altenbach

14.1 Introduction 195

14.2 Two-Time-Scale Technique 197

14.3 Material Model 198

14.3.1 Elastic Behavior 198

14.3.2 Inelastic Behavior 199

14.3.3 Application of the Two-Time-Scale Approach 201

14.4 Simulation of the Material Behavior 201

14.4.1 Cyclic Loading Condition 202

14.4.2 Results of the Finite Element Simulation 202

14.5 Conclusion 205

References 206

15 One Case of a Lubrication Problem for a Line Contact of Elastic Solids with Soft Double Coatings 207
 Ilya I. Kudish and Sergei S. Volkov

15.1 Introduction 208

15.2 Main Simplified Relationships Used in the Problem Formulation 209

15.3 Some Results for the Lubrication Problem 215

15.4 Closure 218

References 218

16 On the Exact Solution of the First Boundary Value Problem for a Plane with a Circular Hole in the Formulation of the Nonlinear Power-Law Theory of Steady Creep Under Antiplane Deformation 221
 Suren M. Mkhitarian

16.1 Introduction 221

16.2 Representation of Stresses and Strain Rates in Terms of the Harmonic Function of Pseudostresses 223

16.3 Formulation of the Problem and Derivation of the Basic Equations 227

16.4 Solving Nonlinear Singular Integral Equation 230

16.5 Conclusion 234

References 234

17 On the Generalised Boundary Conditions in Harutyunyan’s Model of Growing Solids 237
 Evgenii V. Murashkin

17.1 Introduction 237

17.2 Governing Equations of Harutyunyan’s Model of Surface Growing Solids 238

17.3 Differential Constraints on Propagating Growing Surface 240

17.4 Pseudoscalar Geometry of Propagating Growing Surface 241

17.5 Differential Constraints on Propagating Growing Pseudoscalar Surface 243

17.6 Conclusions 244

References 245

18 Concerning Identification of Two Thermomechanical Characteristics of Functionally Graded Pipe 247
 Rostislav D. Nedin, Sergei A. Nesterov, and Alexander O. Vatulyan

18.1 Intro 248

18.2 Inverse Thermoelasticity Problem Statement 249

18.3 Solution of the Direct Thermoelasticity Problem 251

18.4 Iterative Scheme for Solving the Inverse Thermoelasticity Problem 254

18.5 Results of Two Thermomechanical Characteristics Reconstruction 257

18.6 Conclusion 261

References 262

19 Regularities of Technological Residual Stress Fields Formation in Cylindrical Products Manufactured by Additive Methods 265
 Dmitry A. Parshin

19.1 Introduction 265

19.2 Basic Relations for the Problem Under Consideration 266

19.3 Calculating Residual Stresses After Stopping Rotation 268

19.4 Conclusions 273

References 273

20 Two-Point Rotations in Geometry of Finite Deformations 275
 Yuri N. Radayev

20.1 Requisite Notions and Equations 275

20.2 Pairs of Reciprocal Deformation and Strain Tensors 277

20.3 Unconventional Orthogonality of the Two-point Rotation Tensor 279

20.4 Conventionally Orthogonal Finite Rotation Tensors. Finite Rotation Pseudovectors 281

20.5 Final Remarks and Conclusions 282

References 283

21 Quadrature Formulas for Integrals with a Weak Singularity in the Kernel and a Weight Function of Jacobi Polynomials with Complex Exponents 285
 Avetik V. Sahakyan and Harutyun A. Amirjanyan

21.1 Introduction 285

21.2 Quadrature Formula for an Integral with a Logarithmic Singularity 286

21.3 Numerical Analysis 291

21.4 Quadrature Formula for an Integral with a Signum Function 294

21.5 Quadrature Formulas for Particular Values of the Exponents α and β 295

21.6 Conclusion 297

References 297

22 Bending and Contact Problem for a Graphene Sheet Within the Framework of the Model of Bending Deformation of Elastic Thin Plates Based on Cosserat Theory 299
 Samvel H. Sargsyan

22.1 Introduction 299

22.2 Basic System of Equations, Boundary Conditions and Variational Lagrange Principle of Bending Deformation of an Elastic Plate Based on Cosserat Theory 301

22.3 Bending of a Hinged Supported Rectangular Plate Under the Action of a Distributed Normal Load 303

22.4 Elastic Constants of the Plane Stress State and Bending Deformation of Plates for the Graphene Material 305

22.5 An Example of Calculating the Bending of a Graphene Sheet ... 306

22.6 Cylindrical Bending of a Plate (Graphene Sheet) with a Rigid Stamp 306

22.7 Conclusion 309

References 310

23 Non-axisymmetric Vibration of Tuned Thin Functionally Graded Planar Structures 311
 Getachew T. Sedebo, Michael Y. Shatalov, and Stephan V. Joubert

23.1 Introduction 312

23.2 Equations of Motion 313

23.3 Implicit Boundary Conditions 314

23.4 Exact Solutions to the Boundary Value Problems 316

23.5 Explicit Boundary Conditions 319

23.6 Numerical Results 323

23.7 Conclusions and Discussions 326

Appendix A 328

References 331

24 Adhesive Contact Problems of the Theory of Viscoelasticity 333
 Nugzar Shavlakadze

24.1 Introduction 333

24.2 Formulation of the Problems and Reduction to the Integral Equations 334

24.3 The Asymptotic Investigation 336

24.4 An Approximate Solution of SIDE (3) 338

24.5 Discussion and Numerical Results 343

References 344

25 An Efficient Treatment of Sound Diffraction by Arbitrary Obstacles with Angles 347
 Mezhlum Sumbatyan and Natalia Musatova

25.1 Introduction 347

25.2 Formulation of the Problem 348

25.3 An Example of a Specific Geometry 350

25.4 Qualitative Algebraic Properties of the Basic Matrix 352

25.5 Two Methods to Improve the Structure of the Basic Matrix 354

25.6 Conclusions 358

References 359

26 Exact Solution of the Axisymmetric Problem for Poroelastic Finite Cylinder 361
 Natalya Vaysfeld and Zinaida Zhuravlova

26.1 Introduction 361

26.2 Statement of the Problem 363

26.3 Exact Solution of a One-Dimensional Problem in the Transform Domain and Its Analytical Inversion 365

26.4 Results and Discussion 366

26.5 Conclusions 370

References 372

Contributors

Lenser A. Aghalovyan Institute of Mechanics, National Academy of Sciences of Armenia, Yerevan, Republic of Armenia

Mher L. Aghalovyan Institute of Mechanics, National Academy of Sciences of Armenia, Yerevan, Republic of Armenia

Karo L. Aghayan Institute of Mechanics, National Academy of Sciences of Armenia, Yerevan, Republic of Armenia

Sergei M. Aizikovich Research and Education Center «Materials», Don State Technical University, Rostov-on-Don, Russian Federation

Holm Altenbach Engineering Mechanics, Institute of Mechanics, Otto-von-Guericke-University Magdeburg, Magdeburg, Germany

Harutyun A. Amirjanyan Institute of Mechanics, National Academy of Sciences of Armenia, Yerevan, Republic of Armenia

Ara S. Avetisyan Institute of Mechanics of National Academy of Sciences of Armenia, Yerevan, Republic of Armenia

David Aznaurov Institute of Mechanics, National Academy of Sciences, Yerevan, Republic of Armenia

Vladimir A. Babeshko Southern Scientific Center, Russian Academy of Sciences, Rostov-on-Don, Russian Federation

Gevorg Y. Baghdasaryan Institute of Mechanics, National Academy of Sciences of Armenia, Yerevan, Republic of Armenia

Rafik A. Baghdasaryan National Polytechnic University of Armenia, Yerevan, Republic of Armenia

Konstantinos P. Baxevanakis Wolfson School of Mechanical, Electrical and Manufacturing Engineering, Loughborough University, Leicestershire, UK

Alexander K. Belyaev Institute for Problems in Mechanical Engineering of the Russian Academy of Sciences, St. Petersburg, Russia

Karen Ghazaryan Institute of Mechanics, National Academy of Sciences, Yerevan, Republic of Armenia

Irina G. Goryacheva Ishlinsky Institute for Problems in Mechanics RAS, Moscow, Russian Federation

Aram H. Grigoryan Institute of Mechanics NAS RA, Yerevan, Republic of Armenia

Vahram N. Hakobyan Institute of Mechanics NAS RA, Yerevan, Republic of Armenia

Samvel Jilavyan Faculty of Mathematics and Mechanics, Yerevan State University, Yerevan, Republic of Armenia

Abhijit Joshi Wolfson School of Mechanical, Electrical and Manufacturing Engineering, Loughborough University, Leicestershire, UK

Stephan V. Joubert Department of Mathematics and Statistics, Tshwane University of Technology, Pretoria, South Africa

Andranik A. Kamalyan Institute of Mechanics of National Academy of Sciences of Armenia, Yerevan, Republic of Armenia

Koryun A. Karapetyan Experimental Investigations Laboratory, Institute of Mechanics of National Academy of Sciences of Armenia, Yerevan, Republic of Armenia

Kirill E. Kazakov Ishlinsky Institute for Problems in Mechanics of the Russian Academy of Sciences, Moscow, Russian Federation

Katharina Knape Engineering Mechanics, Institute of Mechanics, Otto-von-Guericke-University Magdeburg, Magdeburg, Germany

Maksim N. Kolesnikov Kuban State University, Krasnodar, Russian Federation

Ilya I. Kudish ILRIMA Consulting, Inc., Millersburg, MI, USA

Polina A. Lapina Research and Education Center «Materials», Don State Technical University, Rostov-on-Don, Russian Federation

Suren M. Mkhitarian Institute of Mechanics, National Academy of Sciences of RA, Yerevan, Republic of Armenia

Evgenii V. Murashkin Ishlinsky Institute for Problems in Mechanics of the Russian Academy of Sciences, Moscow, Russian Federation

Natalia Musatova Vorovich Institute of Mathematics, Mechanics and Computer Science, Southern Federal University, Rostov-on-Don, Russian Federation

Rostislav D. Nedin Institute of Mathematics, Mechanics and Computer Sciences named after I.I. Vorovich, Southern Federal University, Rostov-on-Don, Russian Federation;

Southern Mathematical Institute, Vladikavkaz Scientific Center of Russian Academy of Sciences, Vladikavkaz, Russian Federation

Sergei A. Nesterov Institute of Mathematics, Mechanics and Computer Sciences named after I.I. Vorovich, Southern Federal University, Rostov-on-Don, Russian Federation;

Southern Mathematical Institute, Vladikavkaz Scientific Center of Russian Academy of Sciences, Vladikavkaz, Russian Federation

Dmitry A. Parshin Institute for Problems in Mechanics RAS, Moscow, Russian Federation

Alla V. Pavlova Kuban State University, Krasnodar, Russian Federation

Davit Piliposyan Institute of Mechanics, National Academy of Sciences, Yerevan, Republic of Armenia

Oksana R. Polyakova Saint-Petersburg State University of Architecture and Civil Engineering, St. Petersburg, Russia

Yuri N. Radayev Institute for Problems in Mechanics of RAS, Moscow, Russian Federation

Avetik V. Sahakyan Institute of Mechanics, National Academy of Sciences of Armenia, Yerevan, Republic of Armenia

Samvel H. Sargsyan State University of Shirak, Gyumri, Armenia

Getachew T. Sedebo Department of Mathematics and Statistics, Tshwane University of Technology, Pretoria, South Africa

Michael Y. Shatalov Department of Mathematics and Statistics, Tshwane University of Technology, Pretoria, South Africa

Nugzar Shavlakadze Tbilisi State University A. Razmadze Mathematical Institute, Georgian Technical University, Tbilisi, Georgia

Vadim V. Silberschmidt Wolfson School of Mechanical, Electrical and Manufacturing Engineering, Loughborough University, Leicestershire, UK

Mezhlum Sumbatyan Vorovich Institute of Mathematics, Mechanics and Computer Science, Southern Federal University, Rostov-on-Don, Russian Federation

Ilya S. Telyatnikov Kuban State University, Krasnodar, Russian Federation

Tatyana P. Tovstik Institute for Problems in Mechanical Engineering of the Russian Academy of Sciences, St. Petersburg, Russia

Sona Sh. Valesyan Experimental Investigations Laboratory, Institute of Mechanics of National Academy of Sciences of Armenia, Yerevan, Republic of Armenia;

National University of Architecture and Construction of Armenia, Yerevan, Republic of Armenia

Alexander O. Vatulyan Institute of Mathematics, Mechanics and Computer Sciences named after I.I. Vorovich, Southern Federal University, Rostov-on-Don, Russian Federation;

Southern Mathematical Institute, Vladikavkaz Scientific Center of Russian Academy of Sciences, Vladikavkaz, Russian Federation

Natalya Vaysfeld Faculty of Mathematics, Physics and Information Technologies, Odessa I.I. Mechnikov National University, Odessa, Ukraine;

King's College, London, UK

Sergei S. Volkov Laboratory of Functionally Graded and Composite Materials, Research and Education Center «Materials», Don State Technical University, Rostov-on-Don, Russian Federation

Anastasiya A. Yakovenko Ishlinsky Institute for Problems in Mechanics RAS, Moscow, Russian Federation

Zinaida Zhuravlova Faculty of Mathematics, Physics and Information Technologies, Odessa I.I. Mechnikov National University, Odessa, Ukraine

Chapter 1

On One Non-classical 3D Problem for a Layered Package of Isotropic Plate and the Problem of Earthquakes Prediction



Lenser A. Aghalovyan and Mher L. Aghalovyan

Abstract The 3D problem of elasticity theory for a layered package of isotropic plates is solved. It is considered that the facial surface of the package is free, and values of displacements of points of the contact surface between second and third layers are known as measurement data by inclinometers or strainmeters placed there. The asymptotic solution of the problem is found, and the potential strain energy is determined. Based on regularly carried out measurements, the entire process of accumulation of critical potential energy of deformation is traced, leading to the global destruction—an earthquake. The estimation of the magnitude of the expected earthquake is given. Fleeting dynamic processes are studied.

Keywords Laminated plates · 3D problems elasticity · Asymptotic method · Earthquake prediction

1.1 Introduction

Modern seismology the occurrence of strong earthquakes associates with the tectonics of Lithospheric plates of the planet Earth. It has been established that the planet Earth ($R_E = 6378$ km) is heterogeneous and layered. It consists of Earth's Crust, Upper and Lower Mantle, Outer and Inner Cores. The distinctive feature of these layers, in particular, is significantly different velocities of propagation V_P , V_S of longitudinal (primary) P and transverse (secondary, shear) S waves in them. For example, these waves propagate in the rod with velocities

L. A. Aghalovyan (✉) · M. L. Aghalovyan
Institute of Mechanics, National Academy of Sciences of Armenia, Baghramyan 24/2 ave.,
Yerevan 0019, Republic of Armenia
e-mail: lagal@sci.am

M. L. Aghalovyan
e-mail: mheraghalovyan@yahoo.com

© The Author(s), under exclusive license to Springer Nature Switzerland AG 2023
H. Altenbach et al. (eds.), *Solid Mechanics, Theory of Elasticity and Creep*,
Advanced Structured Materials 185, https://doi.org/10.1007/978-3-031-18564-9_1

$$V_P = \sqrt{\frac{E}{\rho}}, \quad V_S = \sqrt{\frac{G}{\rho}}, \quad G = \frac{E}{2(1 + \nu)} \quad (1.1)$$

and in the plate

$$V_P = \sqrt{\frac{E}{\rho} \frac{1 - \nu}{(1 + \nu)(1 - 2\nu)}}, \quad V_S = \sqrt{\frac{G}{\rho}} \quad (1.2)$$

where E is the Young's modulus, G is the shear modulus, ν is the Poisson's ratio and ρ is the density.

The thickness of the Earth's Crust in the land is 20–70 km, and under the oceans—5–15 km. Earth's Crust is also layered with basic layers:

- sedimentary ($V_P = 2, 0 \div 5, 0$ km/s; $h_1 = 10 \div 25$ km),
- granite ($V_P = 5, 5 \div 6, 0$ km/s; $h_2 = 30 \div 40$ km) and
- basaltic ($V_P = 6, 5 \div 7, 4$ km/s; $h_3 = 15 \div 20$ km).

Within the Upper Mantle, at a depth of 100 ÷ 250 km, there is a layer (Asthenosphere), where the speed of V_S shear waves decreases significantly, but the speed V_P doesn't increase with depth ($V_P \approx \text{const}$, $V_S \approx 0$), i.e., there is a liquid-like incompressible layer. The incompressibility of the layer makes it possible to withstand very high pressures. Part of Upper Mantle to the border with the Asthenosphere, together with Earth's Crust, makes up Lithosphere. By the network of deep faults, Lithosphere is divided into several large blocks which are called plates. The great Lithospheric plates of the Earth are: Euroasian, Pacific Ocean, Indo-Australian, South-American, North-American, African, Anatolian, Arabian, etc.

It has been established that earthquake sources are located in narrow zones of Earth's Crust (seismic zones), which are zones of tectonic interaction between adjacent Lithospheric plates (95% of earthquakes) [3, 5–7].

The process of earthquakes preparation includes two main stages of tectonic movements: slow (age-old) and fast (jump-like). Age-old movements may last decades; therefore, they are quasistatic. Over the years, in Lithospheric plates and individual blocks of Earth's Crust, deformations accumulate, which when having reached the critical value of the order 10^{-4} , and according to the data of Rikitake [7]—the order $4, 7 \times 10^{-5}$, leading to the global destruction (an earthquake). The main part of the accumulated huge potential energy of deformation is released in the form of volumetric elastic longitudinal P and shear S waves, as well as Rayleigh's and Love's surface waves. Always V_P speed is greater than V_S speed.

By fixing the time of arrival of these waves at the given point (seismic station): $t_P = L/V_P$, $t_S = L/V_S$, where L —distance from the source of the earthquake to the seismic station, we find the distance L :

$$L = \frac{V_P V_S}{V_P - V_S} \Delta t, \quad \Delta t = t_S - t_P \quad (1.3)$$

In Eq. (1.3), Δt is the time of delay of the arrival of the wave S in relation to the arrival time of the wave P , in seconds. Often approximately considered that

$V_P V_S / (V_P - V_S) \approx 10$ km/s. For the territory of Armenia $V_P V_S / (V_P - V_S) \approx 7, 1$ km/s, and according to M. Okomoto data, for Japan $V_P V_S / (V_P - V_S) \approx 8$ km/s. The data of three seismic stations allow the establishment of the location of the earthquake source, as the area (point) of intersection of three spheres with radii L_1, L_2, L_3 and centers at these stations. This is what most of seismic stations are engaged, fixing an event that has already occurred. Fast movements are dynamic and arise as a result of Foreshock, Earthquake itself, and Aftershock. Thus, earthquakes are the result of accumulation over the years critical deformations, leading to the global destruction—an earthquake. This means, that for earthquakes prediction, it is necessary to determine the stress-strain states (SSS) of Lithospheric plates and blocks of Earth's Crust and follow to their changing during the time.

In the middle of twentieth century, seismologists discovered that before an earthquake, in the place of expected earthquake, noticeable deformations (displacements of points) of Earth's surface are occurred [5, 7]. At the same time, the natural problem (Rikitake's problem) arose—by knowing the structure of the terrain and its physical and mechanical parameters (layering, Young's and shear's modulus, density, etc.) to determine the SSS of the Lithospheric plate or the corresponding block of Earth's Crust and according to data of regularly carried out new measurements, monitor its changing over time. It has been proved by us, that the Rikitake's problem has the unique solution [1], which can be found by the asymptotic method of solving singularly perturbed differentiated equations [2].

In order to reduce the influence of changes of external anomalous, in particular, atmospheric factors, on data caused by the truly proceeding processes inside the layered package (Lithospheric plate, block of Earth's Crust), seismologists began to place measuring instruments—inclinometers, strainmeters, inside the package at some depth from the facial surface. In this paper, the asymptotic solution of 3D quasistatic problem has been found, when measuring instruments are placed on the surface of contact between the second and third layers. The found solution allows to carry out the wide range of special studies.

1.2 Solution of 3D Quasistatic Problems

Let Lithospheric plates and blocks of Earth's Crust consist of N isotropic layers with thickness h_j and occupied the domain

$$Z = \left\{ (x, y, z) : 0 \leq x \leq a, 0 \leq y \leq b, 0 \leq z \leq h, \right. \\ \left. h = \sum_{j=1}^N h_j, \min(a, b) = l, h \ll l \right\}.$$

As it stated above, the process of the first stage of earthquake preparation is slow; therefore, it is quasistatic (age-old). For determining the stress-strain state of the layered package, it is necessary to determine in the domain Z the solution to equilibrium equations of elasticity theory:

- equilibrium relations for the isotropic body

$$\frac{\partial \sigma_{jx}}{\partial x} + \frac{\partial \sigma_{jy}}{\partial y} + \frac{\partial \sigma_{jz}}{\partial z} + F_j(x, y, z) = 0, \quad j = x, y, z \quad (1.4)$$

- strain-displacement relations

$$\begin{aligned} \varepsilon_{xx} &= \frac{\partial u}{\partial x} = \beta_{11}\sigma_{xx} - \beta_{12}(\sigma_{yy} + \sigma_{zz}) + \alpha_{11}\theta(x, y, z) \\ \varepsilon_{yy} &= \frac{\partial v}{\partial y} = \beta_{11}\sigma_{yy} - \beta_{12}(\sigma_{xx} + \sigma_{zz}) + \alpha_{22}\theta(x, y, z) \\ \varepsilon_{zz} &= \frac{\partial w}{\partial z} = \beta_{11}\sigma_{zz} - \beta_{12}(\sigma_{xx} + \sigma_{yy}) + \alpha_{33}\theta(x, y, z) \\ \varepsilon_{xy} &= \frac{\partial u}{\partial y} + \frac{\partial v}{\partial x} = \frac{1}{G}\sigma_{xy} \\ \varepsilon_{xz} &= \frac{\partial u}{\partial z} + \frac{\partial w}{\partial x} = \frac{1}{G}\sigma_{xz} \\ \varepsilon_{yz} &= \frac{\partial v}{\partial z} + \frac{\partial w}{\partial y} = \frac{1}{G}\sigma_{yz} \end{aligned} \quad (1.5)$$

where ε_{jk} is the components of strain tensor, u, v, w are the displacements, $\theta = T(x, y, z) - T_0(x, y, z)$ is the temperature changes. In addition,

$$\beta_{11} = \frac{1}{E}, \quad \beta_{12} = \frac{\nu}{E}, \quad G = \frac{E}{2(1 + \nu)} \quad (1.6)$$

For a layered package to all quantities are assigned an index n (number of a layer: $n = 1, 2, \dots, N$). It is assumed that

- the facial surface of the package is free

$$\sigma_{xz}^{(1)}(z = 0) = 0, \quad \sigma_{yz}^{(1)}(z = 0) = 0, \quad \sigma_{zz}^{(1)}(z = 0) = 0 \quad (1.7)$$

- the values of the displacements of points of the surface of contact between second and third layers are known, as data of the measuring instruments at $t = t_*$

$$u^{(2)}(z = H_2, t_*) = u^{(3)}(z = H_2, t_*) = u^+(x, y), \quad H_2 = h_1 + h_2; \quad (u, v, w) \quad (1.8)$$

- the conditions of full contact between all adjacent layers must also be satisfied

$$\begin{aligned} \sigma_{xz}^{(n)}(z = H_n) &= \sigma_{xz}^{(n+1)}(z = H_n), \quad (x, y, z), \quad H_n = h_1 + h_2 + \dots + h_n \\ u^{(n)}(z = H_n) &= u^{(n+1)}(z = H_n), \quad (u, v, w), \quad n = 1, 2, \dots, (N - 1) \end{aligned} \quad (1.9)$$

For solving the set boundary value problem of the elasticity theory—seismology, let us move in Eqs. (1.4) and elasticity relations (1.5) to dimensionless coordinates and displacements:

$$x = l\xi, \quad y = l\eta, \quad z = h\zeta, \quad U = u/l, \quad V = v/l, \quad W = w/l \quad (1.10)$$

where

$$h = \sum_{j=1}^N h_j.$$

As a result, we will obtain the system that is singularly perturbed related to a small parameter $\varepsilon = h/l$. The solution to this system consists of solutions of the external problem (I^{out}) and the boundary layer (I_b). The solution to the external problem is sought in the form:

$$\begin{aligned} \sigma_{jz}^{\text{out}(n)} &= \varepsilon^{-1+s} \sigma_{jz}^{(n,s)}, \quad (x, y, z); \quad s = \overline{0, N} \\ U^{\text{out}(n)} &= \varepsilon^s U^{(n,s)}, \quad (U, V, W) \end{aligned} \quad (1.11)$$

where $s = \overline{0, N}$ means, summation by umbral (repeating) index s over all integer values from zero to number of approximations S .

By substituting (1.11) into mentioned above transformed system and by equaling in each equation the corresponding coefficients at ε , for determining $\sigma_{jz}^{(n,s)}$, $U^{(n,s)}$, $V^{(n,s)}$, $W^{(n,s)}$ we will obtain system of differential equations:

$$\begin{aligned} \frac{\partial \sigma_{xx}^{(n,s-1)}}{\partial \xi} + \frac{\partial \sigma_{xy}^{(n,s-1)}}{\partial \eta} + \frac{\partial \sigma_{xz}^{(n,s)}}{\partial \zeta} + F_x^{(n)} &= 0 \\ F_x^{(n,0)} = h\varepsilon F_x^{(n)}, \quad F_x^{(n,s)} &= 0, \quad s \neq 0, \quad (x, y, z) \\ \frac{\partial \sigma_{xy}^{(n,s-1)}}{\partial \xi} + \frac{\partial \sigma_{yy}^{(n,s-1)}}{\partial \eta} + \frac{\partial \sigma_{yz}^{(n,s)}}{\partial \zeta} + F_y^{(n)} &= 0 \\ \frac{\partial \sigma_{xz}^{(n,s-1)}}{\partial \xi} + \frac{\partial \sigma_{yz}^{(n,s-1)}}{\partial \eta} + \frac{\partial \sigma_{zz}^{(n,s)}}{\partial \zeta} + F_z^{(n)} &= 0 \\ \frac{\partial W^{(n,s-1)}}{\partial \xi} + \frac{\partial U^{(n,s)}}{\partial \zeta} &= \frac{1}{G^{(n)}} \sigma_{xz}^{(n,s)}, \\ \frac{\partial W^{(n,s-1)}}{\partial \eta} + \frac{\partial V^{(n,s)}}{\partial \zeta} &= \frac{1}{G^{(n)}} \sigma_{yz}^{(n,s)} \\ \sigma_{xy}^{(n,s)} &= G^{(n)} \left(\frac{\partial V^{(n,s-1)}}{\partial \xi} + \frac{\partial U^{(n,s-1)}}{\partial \eta} \right) \\ \frac{\partial U^{(n,s-1)}}{\partial \xi} &= \beta_{11}^{(n)} \sigma_{xx}^{(n,s)} - \beta_{12}^{(n)} \sigma_{yy}^{(n,s)} - \beta_{12}^{(n)} \sigma_{zz}^{(n,s)} + \alpha_{11}^{(n)} \theta^{(n,s)} \\ \frac{\partial V^{(n,s-1)}}{\partial \eta} &= \beta_{11}^{(n)} \sigma_{yy}^{(n,s)} - \beta_{12}^{(n)} \sigma_{xx}^{(n,s)} - \beta_{12}^{(n)} \sigma_{zz}^{(n,s)} + \alpha_{22}^{(n)} \theta^{(n,s)} \\ \frac{\partial W^{(n,s)}}{\partial \zeta} &= \beta_{11}^{(n)} \sigma_{zz}^{(n,s)} - \beta_{12}^{(n)} \sigma_{xx}^{(n,s)} - \beta_{12}^{(n)} \sigma_{yy}^{(n,s)} + \alpha_{33}^{(n)} \theta^{(n,s)} \\ \theta^{(n,0)} &= \varepsilon \theta^{(n)}, \quad \theta^{(n,s)} = 0, \quad s \neq 0 \end{aligned} \quad (1.12)$$

In (1.12) any value of type $Q^{(n,m)}$ when $m < 0$. From system (1.12), it follows:

$$\begin{aligned}
\sigma_{xz}^{(n,s)} &= G^{(n)} \frac{\partial U^{(n,s)}}{\partial \zeta} + G^{(n)} \frac{\partial W^{(n,s-1)}}{\partial \xi} \\
\sigma_{yz}^{(n,s)} &= G^{(n)} \frac{\partial V^{(n,s)}}{\partial \zeta} + G^{(n)} \frac{\partial W^{(n,s-1)}}{\partial \eta} \\
\sigma_{xx}^{(n,s)} &= \frac{1}{\Delta^{(n)}} \left[b_1^{(n,s)} (\beta_{11}^{(n)} - \beta_{12}^{(n)}) + b_2^{(n,s)} \beta_{12}^{(n)} - \alpha_{33}^{(n)} \beta_{12}^{(n)} \theta^{(n,s)} \right] + \frac{\beta_{12}^{(n)}}{\Delta^{(n)}} \frac{\partial W^{(n,s)}}{\partial \zeta} \\
\Delta^{(n)} &= \left(\beta_{11}^{(n)} + \beta_{12}^{(n)} \right) \left(\beta_{11}^{(n)} - 2\beta_{12}^{(n)} \right) \\
\sigma_{yy}^{(n,s)} &= \frac{1}{\Delta^{(n)}} \left[b_1^{(n,s)} \beta_{12}^{(n)} + b_2^{(n,s)} (\beta_{11}^{(n)} - \beta_{12}^{(n)}) - \alpha_{33}^{(n)} \beta_{12}^{(n)} \theta^{(n,s)} \right] + \frac{\beta_{12}^{(n)}}{\Delta^{(n)}} \frac{\partial W^{(n,s)}}{\partial \zeta} \\
\sigma_{zz}^{(n,s)} &= b_3^{(n,s)} + \frac{\beta_{11}^{(n)} - \beta_{12}^{(n)}}{\Delta^{(n)}} \frac{\partial W^{(n,s)}}{\partial \zeta} \\
b_1^{(n,s)} &= \frac{\partial U^{(n,s-1)}}{\partial \xi} - \alpha_{11}^{(n)} \theta^{(n,s)} \\
b_2^{(n,s)} &= \frac{\partial V^{(n,s-1)}}{\partial \eta} - \alpha_{22}^{(n)} \theta^{(n,s)} \\
b_3^{(n,s)} &= \frac{1}{\Delta^{(n)}} \left[\beta_{12}^{(n)} (b_1^{(n,s)} + b_2^{(n,s)}) - (\beta_{11}^{(n)} - \beta_{12}^{(n)}) \alpha_{33}^{(n)} \theta^{(n,s)} \right]
\end{aligned} \tag{1.13}$$

By substituting the values of $\sigma_{xz}^{(n,s)}$, $\sigma_{yz}^{(n,s)}$, $\sigma_{zz}^{(n,s)}$ into the first three equations of system (1.12), we will obtain equations for determining $U^{(n,s)}$, $V^{(n,s)}$, $W^{(n,s)}$:

$$\begin{aligned}
G^{(n)} \frac{\partial^2 U^{(n,s)}}{\partial \zeta^2} &= R_u^{(n,s)} \\
R_u^{(n,s)} &= -F_x^{(n,s)} - G^{(n)} \frac{\partial^2 W^{(n,s-1)}}{\partial \xi \partial \zeta} - \frac{\partial \sigma_{xx}^{(n,s-1)}}{\partial \xi} - \frac{\partial \sigma_{xy}^{(n,s-1)}}{\partial \eta}
\end{aligned} \tag{1.14}$$

$$\begin{aligned}
G^{(n)} \frac{\partial^2 V^{(n,s)}}{\partial \zeta^2} &= R_v^{(n,s)} \\
R_v^{(n,s)} &= -F_y^{(n,s)} - G^{(n)} \frac{\partial^2 W^{(n,s-1)}}{\partial \eta \partial \zeta} - \frac{\partial \sigma_{xy}^{(n,s-1)}}{\partial \xi} - \frac{\partial \sigma_{yy}^{(n,s-1)}}{\partial \eta}
\end{aligned} \tag{1.15}$$

$$\begin{aligned}
\Delta_1^{(n)} \frac{\partial^2 W^{(n,s)}}{\partial \zeta^2} &= R_w^{(n,s)}, \quad \Delta_1^{(n)} = \frac{\beta_{11}^{(n)} - \beta_{12}^{(n)}}{\Delta^{(n)}} \\
R_w^{(n,s)} &= -F_z^{(n,s)} - \frac{\partial b_3^{(n,s)}}{\partial \zeta} - \frac{\partial \sigma_{xz}^{(n,s-1)}}{\partial \xi} - \frac{\partial \sigma_{yz}^{(n,s-1)}}{\partial \eta}
\end{aligned} \tag{1.16}$$

According to (1.14)

$$\begin{aligned}\frac{\partial U^{(n,s)}}{\partial \zeta} &= \frac{1}{G^{(n)}} \int_{\zeta_{n-1}}^{\zeta} R_u^{(n,s)} d\zeta + C_1^{(n,s)}(\xi, \eta) \\ U^{(n,s)} &= \frac{1}{G^{(n)}} \int_{\zeta_{n-1}}^{\zeta} d\zeta \int_{\zeta_{n-1}}^{\zeta} R_u^{(n,s)} d\zeta + C_1^{(n,s)} \zeta + C_2^{(n,s)}(\xi, \eta)\end{aligned}\quad (1.17)$$

by using (1.13)

$$\sigma_{xz}^{(n,s)} = \int_{\zeta_{n-1}}^{\zeta} R_u^{(n,s)} d\zeta + G^{(n)} C_1^{(n,s)} + G^{(n)} \frac{\partial W^{(n,s-1)}}{\partial \xi} \quad (1.18)$$

By satisfying the first condition (1.7), assuming $\zeta_0 = 0$, we will obtain

$$C_1^{(1,s)} = - \left(\frac{\partial W^{(1,s-1)}}{\partial \xi} \right)_{\zeta=0}, \Rightarrow C_1^{(1,0)} = 0 \quad (1.19)$$

Using (1.18), (1.19) by satisfying the first condition of contact (1.9), we will consecutively determined $C_1^{(n+1,s)}$

$$C_1^{(n+1,s)} = \frac{1}{G^{(n+1)}} \left[\sigma_{xz}^{(n,s)}(\zeta = \zeta_n) - G^{(n+1)} \left(\frac{\partial W^{(n+1,s-1)}}{\partial \xi} \right)_{\zeta=\zeta_n} \right] \quad (1.20)$$

where

$$\zeta_n = H_n/h, \quad n = 1, 2, \dots, N-1, \quad H_n = \sum_{j=1}^n h_j$$

Similarly, according to (1.15), (1.9)

$$\begin{aligned}\frac{\partial V^{(n,s)}}{\partial \zeta} &= \frac{1}{G^{(n)}} \int_{\zeta_{n-1}}^{\zeta} R_v^{(n,s)} d\zeta + C_3^{(n,s)}(\xi, \eta) \\ V^{(n,s)} &= \frac{1}{G^{(n)}} \int_{\zeta_{n-1}}^{\zeta} d\zeta \int_{\zeta_{n-1}}^{\zeta} R_v^{(n,s)} d\zeta + C_3^{(n,s)} \zeta + C_4^{(n,s)}(\xi, \eta)\end{aligned}\quad (1.21)$$

$$\begin{aligned}C_3^{(1,s)} &= - \left(\frac{\partial W^{(1,s-1)}}{\partial \eta} \right)_{\zeta=0} \Rightarrow C_3^{(1,0)} = 0 \\ C_3^{(n+1,s)} &= \frac{1}{G^{(n+1)}} \left[\sigma_{yz}^{(n,s)}(\zeta = \zeta_n) - G^{(n+1)} \left(\frac{\partial W^{(n+1,s-1)}}{\partial \eta} \right)_{\zeta=\zeta_n} \right] \\ &n = 1, 2, \dots, N-1\end{aligned}\quad (1.22)$$

According to (1.16)

$$\begin{aligned}
\frac{\partial W^{(n,s)}}{\partial \zeta} &= \frac{1}{\Delta_1^{(n)}} \int_{\zeta_{n-1}}^{\zeta} R_w^{(n,s)} d\zeta + C_5^{(n,s)}(\xi, \eta) \\
W^{(n,s)} &= \frac{1}{\Delta_1^{(n)}} \int_{\zeta_{n-1}}^{\zeta} d\zeta \int_{\zeta_{n-1}}^{\zeta} R_w^{(n,s)} d\zeta + C_5^{(n,s)} \zeta + C_6^{(n,s)}(\xi, \eta) \\
\Delta_1^{(n)} &= \frac{\beta_{11}^{(n)} - \beta_{12}^{(n)}}{(\beta_{11}^{(n)} + \beta_{12}^{(n)}) (\beta_{11}^{(n)} - 2\beta_{12}^{(n)})} \\
\sigma_{zz}^{(n,s)} &= b_3^{(n,s)} + \Delta_1^{(n)} \frac{\partial W^{(n,s)}}{\partial \zeta} = b_3^{(n,s)} + \int_{\zeta_{n-1}}^{\zeta} R_w^{(n,s)} d\zeta + C_5^{(n,s)}(\xi, \eta) \Delta_1^{(n)}
\end{aligned} \tag{1.23}$$

By satisfying the last condition (1.7), we will obtain

$$C_5^{(1,s)} = -\frac{1}{\Delta_1^{(n)}} \left(b_3^{(1,s)}(\zeta = 0) \right) \tag{1.24}$$

According to (1.9)

$$C_5^{(n+1,s)} = \frac{1}{\Delta_1^{(n+1)}} \left(\sigma_{zz}^{(n,s)} - b_3^{(n+1,s)}(\zeta = \zeta_n) \right), \quad n = 1, 2, \dots, N-1 \tag{1.25}$$

Thus, all $C_1^{(n,s)}$, $C_3^{(n,s)}$, $C_5^{(n,s)}$ are determined. From conditions (1.8), (1.9), are determined $C_2^{(n,s)}$, $C_4^{(n,s)}$, $C_6^{(n,s)}$.

According to (1.8), (1.17)

$$U^{(2,s)}(\zeta = \zeta_2) = \frac{1}{G^{(2)}} \int_{\zeta_1}^{\zeta_2} d\zeta \int_{\zeta_1}^{\zeta} R_u^{(2,s)} d\zeta + C_1^{(2,s)} \zeta_2 + C_2^{(2,s)} = u^{+(s)} \tag{1.26}$$

with

$$u^{+(0)} = \frac{u^+}{l}, \quad u^{+(s)} = 0, \quad s \neq 0$$

and

$$C_2^{(2,s)} = u^{+(s)} - C_1^{(2,s)} \zeta_2 - \frac{1}{G^{(2)}} \int_{\zeta_1}^{\zeta_2} d\zeta \int_{\zeta_1}^{\zeta} R_u^{(2,s)} d\zeta$$

By satisfying the condition

$$U^{(1,s)}(\zeta = \zeta_1) = U^{(2,s)}(\zeta = \zeta_1)$$

we will find $C_2^{(1,s)}$

$$C_2^{(1,s)} = (C_1^{(2,s)} - C_1^{(1,s)})\zeta_1 + C_2^{(2,s)} - \frac{1}{G^{(1)}} \int_0^{\zeta_1} d\zeta \int_0^{\zeta} R_u^{(1,s)} d\zeta \quad (1.27)$$

From the condition $U^{(3,s)}(\zeta = \zeta_2) = u^{+(s)}$, we will determine

$$C_2^{(3,s)} = u^{+(s)} - C_1^{(3,s)}\zeta_2 \quad (1.28)$$

From conditions $U^{(n,s)}(\zeta = \zeta_n) = U^{(n+1,s)}(\zeta = \zeta_n)$ determined the other $C_2^{(n,s)}$. We will have

$$C_2^{(n+1,s)} = U^{(n,s)}(\zeta = \zeta_n) - C_1^{(n+1,s)}\zeta_n \quad (1.29)$$

All $C_3^{(n,s)}$, $C_4^{(n,s)}$ are determined similarly. Formulas for them can be obtained from the above mentioned by cyclic permutation ($C_1, C_2, U; C_3, C_4, V$). Satisfying conditions (1.8), (1.9) relatively to W , we will obtain

$$\begin{aligned} C_6^{(2,s)} &= w^{+(s)} - C_5^{(2,s)}\zeta_2 - \frac{1}{\Delta_1^{(2)}} \int_{\zeta_1}^{\zeta_2} d\zeta \int_{\zeta_1}^{\zeta} R_w^{(2,s)} d\zeta \\ C_6^{(3,s)} &= w^{+(s)} - C_5^{(3,s)}\zeta_2, \quad w^{+(0)} = w^+/l, \quad w^{+(s)} = 0, \quad s \neq 0 \\ C_6^{(1,s)} &= C_6^{(2,s)} + (C_5^{(2,s)} - C_5^{(1,s)})\zeta_1 - \frac{1}{\Delta_1^{(1)}} \int_0^{\zeta_1} d\zeta \int_0^{\zeta} R_w^{(1,s)} d\zeta \\ C_6^{(n+1,s)} &= W^{(n,s)}(\zeta = \zeta_n) - C_5^{(n+1,s)}\zeta_n \end{aligned} \quad (1.30)$$

The above mentioned formulas make it possible to calculate the SSS of an arbitrary layer of the package and monitor its change over time based on the regularly carried out new measurements of displacements of points of the surface of contact between second and third layers.

If functions u^+ , v^+ , w^+ , included in conditions (1.8), and also θ are algebraic polynomials, the iterative process of determining unknowns breaks at a certain approximation. As a result, we obtain a mathematically exact solution in the external problem.

On the base of found solution, it is possible to calculate the accumulated potential energy of deformation (W) according to the well-known formula of elasticity theory

$$W = \frac{1}{2} \int_V (\sigma_{xx}\varepsilon_{xx} + \sigma_{yy}\varepsilon_{yy} + \sigma_{zz}\varepsilon_{zz} + \sigma_{xy}\varepsilon_{xy} + \sigma_{xz}\varepsilon_{xz} + \sigma_{yz}\varepsilon_{yz}) dV \quad (1.31)$$

and trace its change over time. When this energy reaches the critical value, global destruction—an earthquake—will occur. There is the formula that relates the potential energy of deformation and the magnitude (M) of the expected earthquake [4, 5].

$$\lg W = 11.8 + 1.5M \quad (1.32)$$

The critical deformation energy is $W_{cr} = 10^{11.8}$ J and corresponds to $M = 0$. When $W > W_{cr}$, the process becomes dynamic and fast (Foreshocks, Earthquakes, Aftershocks) and having value of W by formula (1.32), it is possible to predict the magnitude of the expected earthquake.

1.3 Investigation of Fast Dynamic Processes

For investigating associated with an earthquake fast processes, it is necessary to solve in the domain Z equations of the motion of the elasticity theory:

$$\frac{\partial \sigma_{xx}^{(n)}}{\partial x} + \frac{\partial \sigma_{xy}^{(n)}}{\partial y} + \frac{\partial \sigma_{xz}^{(n)}}{\partial z} = \rho_n \frac{\partial^2 u_x^{(n)}}{\partial t^2}, \quad (x, y, z), \quad n = 1, 2, \dots, N \quad (1.33)$$

at elasticity relations (1.5) (usually without taking into account the temperature) and full contact conditions (1.9) between adjacent layers. We consider, that measurement data is again have taken from the contact surface between second and third layers. The case when data have taken from the contact surface between arbitrarily chosen adjacent layers is considering in a similar way and does not cause any difficulties. Boundary conditions of the problem are

- at the facial surface $z = 0$ of the package from plates is free

$$\sigma_{jz}^{(1)}(x, y, 0, t) = 0, \quad j = x, y, z \quad (1.34)$$

- values of displacements of points of the contact surface between second and third layers are known

$$u_x^{(2)}(x, y, \zeta_2, t) = u_x^{(3)}(x, y, \zeta_2, t) = u^+(x, y) \exp(i\Omega t), \quad (x, y, z) \quad (1.35)$$

Ω is the vibration frequency of the contact surface of these adjacent layers.

The solution of the formulated problem will be sought in the form

$$\begin{aligned}\sigma_{\alpha\beta}^{(n)}(x, y, \zeta, t) &= \sigma_{ij}^{(n)}(x, y, \zeta) \exp(i\Omega t), \quad \alpha, \beta = x, y, z; \quad i, j = 1, 2, 3, \dots \\ u_x^{(n)}(x, y, z, t) &= \bar{u}_x^{(n)}(x, y, z) \exp(i\Omega t), \quad (x, y, z)\end{aligned}\quad (1.36)$$

In the equations of motion and elasticity relations, we again pass to dimensionless coordinates ξ, η, ζ and displacements

$$U^{(n)} = \frac{\bar{u}_x^{(n)}}{l}, \quad V^{(n)} = \frac{\bar{u}_y^{(n)}}{l}, \quad W^{(n)} = \frac{\bar{u}_z^{(n)}}{l} \quad (1.37)$$

As a result, we will obtain a new system of singularly perturbed differential equations. The solution to the external problem (I^{out}) is sought in the form

$$U^{(n)\text{out}} = \varepsilon^s U^{(n,s)}, \quad (U, V, W), \quad \sigma_{ij}^{(n)\text{out}} = \varepsilon^{-1+s} \sigma_{ij}^{(n,s)}, \quad s = \overline{0, S} \quad (1.38)$$

By substituting (1.38) into the transformed equations of motion and elasticity relations, we will obtain the following system to determine $\sigma_{ij}^{(n,s)}, U^{(n,s)}, V^{(n,s)}, W^{(n,s)}$:

$$\begin{aligned}\frac{\partial \sigma_{11}^{(n,s-1)}}{\partial \xi} + \frac{\partial \sigma_{12}^{(n,s-1)}}{\partial \eta} + \frac{\partial \sigma_{13}^{(n,s)}}{\partial \zeta} + \Omega_*^2 \rho_n U^{(n,s)} &= 0 \\ \frac{\partial \sigma_{12}^{(n,s-1)}}{\partial \xi} + \frac{\partial \sigma_{22}^{(n,s-1)}}{\partial \eta} + \frac{\partial \sigma_{23}^{(n,s)}}{\partial \zeta} + \Omega_*^2 \rho_n V^{(n,s)} &= 0 \\ \frac{\partial \sigma_{13}^{(n,s-1)}}{\partial \xi} + \frac{\partial \sigma_{23}^{(n,s-1)}}{\partial \eta} + \frac{\partial \sigma_{33}^{(n,s)}}{\partial \zeta} + \Omega_*^2 \rho_n W^{(n,s)} &= 0 \\ \frac{\partial U^{(n,s-1)}}{\partial \xi} &= \beta_{11}^{(n)} \sigma_{11}^{(n,s)} - \beta_{12}^{(n)} \sigma_{22}^{(n,s)} - \beta_{12}^{(n)} \sigma_{33}^{(n,s)} \\ \frac{\partial V^{(n,s-1)}}{\partial \eta} &= -\beta_{12}^{(n)} \sigma_{11}^{(n,s)} + \beta_{11}^{(n)} \sigma_{22}^{(n,s)} - \beta_{12}^{(n)} \sigma_{33}^{(n,s)} \\ \frac{\partial W^{(n,s)}}{\partial \zeta} &= -\beta_{12}^{(n)} \sigma_{11}^{(n,s)} - \beta_{12}^{(n)} \sigma_{22}^{(n,s)} + \beta_{11}^{(n)} \sigma_{33}^{(n,s)} \\ \frac{\partial W^{(n,s-1)}}{\partial \xi} + \frac{\partial U^{(n,s)}}{\partial \zeta} &= \frac{1}{G^{(n)}} \sigma_{13}^{(n,s)} \\ \frac{\partial W^{(n,s-1)}}{\partial \eta} + \frac{\partial V^{(n,s)}}{\partial \zeta} &= \frac{1}{G^{(n)}} \sigma_{23}^{(n,s)} \\ \frac{\partial V^{(n,s-1)}}{\partial \xi} + \frac{\partial U^{(n,s-1)}}{\partial \eta} &= \frac{1}{G^{(n)}} \sigma_{12}^{(n,s)}\end{aligned}\quad (1.39)$$

$\Omega_* = h\Omega$, $Q^{(n,m)} = 0$ when $m < 0$. From system (1.39), all stresses can be expressed in terms of displacements:

$$\begin{aligned}
\sigma_{11}^{(n,s)} &= \frac{1}{\Delta^{(n)}} \left[\beta_{12}^{(n)} \frac{\partial W^{(n,s)}}{\partial \zeta} + (\beta_{11}^{(n)} - \beta_{12}^{(n)}) \frac{\partial U^{(n,s-1)}}{\partial \xi} + \beta_{12}^{(n)} \frac{\partial V^{(n,s-1)}}{\partial \eta} \right] \\
\sigma_{22}^{(n,s)} &= \frac{1}{\Delta^{(n)}} \left[\beta_{12}^{(n)} \frac{\partial W^{(n,s)}}{\partial \zeta} + \beta_{12}^{(n)} \frac{\partial U^{(n,s-1)}}{\partial \xi} + (\beta_{11}^{(n)} - \beta_{12}^{(n)}) \frac{\partial V^{(n,s-1)}}{\partial \eta} \right] \\
\sigma_{33}^{(n,s)} &= \frac{1}{\Delta^{(n)}} \left[(\beta_{11}^{(n)} - \beta_{12}^{(n)}) \frac{\partial W^{(n,s)}}{\partial \zeta} + \beta_{12}^{(n)} \frac{\partial U^{(n,s-1)}}{\partial \xi} + \beta_{12}^{(n)} \frac{\partial V^{(n,s-1)}}{\partial \eta} \right] \\
\Delta^{(n)} &= (\beta_{11}^{(n)} + \beta_{12}^{(n)}) (\beta_{11}^{(n)} - 2\beta_{12}^{(n)}) \\
\sigma_{13}^{(n,s)} &= G^{(n)} \left(\frac{\partial U^{(n,s)}}{\partial \zeta} + \frac{\partial W^{(n,s-1)}}{\partial \xi} \right) \\
\sigma_{23}^{(n,s)} &= G^{(n)} \left(\frac{\partial V^{(n,s)}}{\partial \zeta} + \frac{\partial W^{(n,s-1)}}{\partial \eta} \right) \\
\sigma_{12}^{(n,s)} &= G^{(n)} \left(\frac{\partial V^{(n,s-1)}}{\partial \xi} + \frac{\partial U^{(n,s-1)}}{\partial \eta} \right)
\end{aligned} \tag{1.40}$$

By substituting the values of $\sigma_{13}^{(n,s)}$, $\sigma_{23}^{(n,s)}$, $\sigma_{33}^{(n,s)}$ in the first three equations of (1.39), we will obtain equations for determining the displacements:

$$\begin{aligned}
G^{(n)} \frac{\partial^2 U^{(n,s)}}{\partial \zeta^2} + \Omega_*^2 \rho_n U^{(n,s)} &= R_u^{(n,s)} \\
R_u^{(n,s)} &= -G^{(n)} \frac{\partial^2 W^{(n,s-1)}}{\partial \xi \partial \zeta} - \frac{\partial \sigma_{11}^{(n,s-1)}}{\partial \xi} - \frac{\partial \sigma_{12}^{(n,s-1)}}{\partial \eta}
\end{aligned} \tag{1.41}$$

$$\begin{aligned}
G^{(n)} \frac{\partial^2 V^{(n,s)}}{\partial \zeta^2} + \Omega_*^2 \rho_n V^{(n,s)} &= R_v^{(n,s)} \\
R_v^{(n,s)} &= -G^{(n)} \frac{\partial^2 W^{(n,s-1)}}{\partial \eta \partial \zeta} - \frac{\partial \sigma_{12}^{(n,s-1)}}{\partial \xi} - \frac{\partial \sigma_{22}^{(n,s-1)}}{\partial \eta}
\end{aligned} \tag{1.42}$$

$$\begin{aligned}
\frac{\beta_{11}^{(n)} - \beta_{12}^{(n)}}{\Delta^{(n)}} \frac{\partial^2 W^{(n,s)}}{\partial \zeta^2} + \Omega_*^2 \rho_n W^{(n,s)} &= R_w^{(n,s)} \\
R_w^{(n,s)} &= -\frac{1}{\Delta^{(n)}} \beta_{12}^{(n)} \left[\frac{\partial^2 U^{(n,s-1)}}{\partial \xi \partial \zeta} + \frac{\partial^2 V^{(n,s-1)}}{\partial \eta \partial \zeta} \right] - \frac{\partial \sigma_{13}^{(n,s-1)}}{\partial \xi} - \frac{\partial \sigma_{23}^{(n,s-1)}}{\partial \eta}
\end{aligned} \tag{1.43}$$

The solution to Eq. (1.41) is

$$U^{(n,s)} = C_{1u}^{(n,s)}(\xi, \eta) \sin \Omega_* \sqrt{\frac{\rho_n}{G^{(n)}}} \zeta + C_{2u}^{(n,s)}(\xi, \eta) \cos \Omega_* \sqrt{\frac{\rho_n}{G^{(n)}}} \zeta + \bar{U}^{(n,s)} \tag{1.44}$$

Solutions of Eqs. (1.42), (1.43) can be obtained from (1.44) by cyclic permutation (u, v, w ; $G^{(n)}, G^{(n)}, \Delta_1^{(n)}$), where

$$\Delta_1^{(n)} = \frac{\beta_{11}^{(n)} - \beta_{12}^{(n)}}{\Delta^{(n)}}.$$

According to (1.40), (1.44) we will have

$$\begin{aligned}\sigma_{13}^{(n,s)} &= \sqrt{G^{(n)}} \rho_n (C_{1u}^{(n,s)} \cos \Omega_* \sqrt{\frac{\rho_n}{G^{(n)}}} \zeta - C_{2u}^{(n,s)}(\xi, \eta) \sin \Omega_* \sqrt{\frac{\rho_n}{G^{(n)}}} \zeta) + \sigma_{13*}^{(n,s)} \\ \sigma_{13*}^{(n,s)} &= G^{(n)} \left(\frac{\partial W^{(n,s-1)}}{\partial \xi} + \frac{\partial \bar{U}^{(n,s)}}{\partial \zeta} \right)\end{aligned}\quad (1.45)$$

By satisfying condition (1.34) for $\sigma_{xz}^{(1)}$, using (1.36), (1.45), we obtain

$$C_{1u}^{(1,s)} = -\frac{1}{\sqrt{G^{(1)}} \rho_1} \sigma_{13*}^{(1,s)}(\xi, \eta, 0) \Rightarrow C_{1u}^{(1,0)} = 0 \quad (1.46)$$

Satisfaction of conditions of full contact between the first and second layers and condition (1.35) for the second layer passes to the algebraic system

$$\begin{aligned}C_{2u}^{(1,s)} b_1 \sqrt{G^{(1)}} \rho_1 + C_{1u}^{(2,s)} b_4 \sqrt{G^{(2)}} \rho_2 - C_{2u}^{(2,s)} b_3 \sqrt{G^{(2)}} \rho_2 &= d_{1u}^{(s)} \\ C_{2u}^{(1,s)} b_2 - C_{1u}^{(2,s)} b_3 - C_{2u}^{(2,s)} b_4 &= d_{2u}^{(s)} \\ C_{1u}^{(2,s)} b_5 + C_{2u}^{(2,s)} b_6 &= d_{3u}^{(s)}\end{aligned}\quad (1.47)$$

where

$$\begin{aligned}b_1 &= \sin \Omega_* \sqrt{\frac{\rho_1}{G^{(1)}}} \zeta_1, \quad b_2 = \cos \Omega_* \sqrt{\frac{\rho_1}{G^{(1)}}} \zeta_1, \quad b_3 = \sin \Omega_* \sqrt{\frac{\rho_2}{G^{(2)}}} \zeta_1 \\ b_4 &= \cos \Omega_* \sqrt{\frac{\rho_2}{G^{(2)}}} \zeta_1, \quad b_5 = \sin \Omega_* \sqrt{\frac{\rho_2}{G^{(2)}}} \zeta_2, \quad b_6 = \cos \Omega_* \sqrt{\frac{\rho_2}{G^{(2)}}} \zeta_2 \\ d_{1u}^{(s)} &= C_{1u}^{(1,s)} b_2 \sqrt{\rho_1 G^{(1)}} + \sigma_{13*}^{(2,s)}(\xi, \eta, \zeta_1)\end{aligned}\quad (1.48)$$

$$d_{2u}^{(s)} = \bar{U}^{(2,s)}(\xi, \eta, \zeta_1) - C_{1u}^{(1,s)} b_1 - \bar{U}^{(1,s)}(\xi, \eta, \zeta_1)$$

$$d_{3u}^{(s)} = U^{+(s)} - \bar{U}^{(2,s)}(\xi, \eta, \zeta_2)$$

and $U^{+(0)} = u^+ / l$, $U^{+(s)} = 0$, $s \neq 0$.

From the algebraic system (1.47), by Cramer's formula, unknowns $C_{2u}^{(1,s)}$, $C_{1u}^{(2,s)}$, $C_{2u}^{(2,s)}$ are determined:

$$C_{2u}^{(1,s)} = \frac{\delta_1^{(s)}}{\delta}, \quad C_{1u}^{(2,s)} = \frac{\delta_2^{(s)}}{\delta}, \quad C_{2u}^{(2,s)} = \frac{\delta_3^{(s)}}{\delta} \quad (1.49)$$

with

$$\delta = \begin{vmatrix} b_1 \sqrt{G^{(1)}} \rho_1 & b_4 \sqrt{G^{(2)}} \rho_2 & -b_3 \sqrt{G^{(2)}} \rho_2 \\ b_2 & -b_3 & -b_4 \\ 0 & b_5 & b_6 \end{vmatrix}, \quad d^{(s)} = \begin{vmatrix} d_{1u}^{(s)} \\ d_{2u}^{(s)} \\ d_{3u}^{(s)} \end{vmatrix}$$

δ_j is obtained from δ by replacing the j -th column with the column $d^{(s)}$. By this way, all data for the first and second layers is determined. Satisfaction of the condition (1.35) for the third layer and condition of contact relatively to stresses $\sigma_{13}^{(2,s)}$, $\sigma_{13}^{(3,s)}$ leads to the system:

$$\begin{aligned} C_{1u}^{(3,s)} b_7 + C_{2u}^{(3,s)} b_8 &= U^{+(s)} - \bar{U}^{(3,s)}(\xi, \eta, \zeta_2) = d_{4u}^{(s)} \\ C_{1u}^{(3,s)} b_8 - C_{2u}^{(3,s)} b_7 &= \frac{1}{\sqrt{G^{(3)} \rho_3}} \left(\sigma_{13}^{(2,s)}(\xi, \eta, \zeta_2) - \sigma_{13*}^{(3,s)}(\xi, \eta, \zeta_2) \right) = d_{5u}^{(s)} \\ b_7 &= \sin \Omega_* \sqrt{\frac{\rho_3}{G^{(3)}}} \zeta_2 \\ b_8 &= \cos \Omega_* \sqrt{\frac{\rho_3}{G^{(3)}}} \zeta_2 \end{aligned} \quad (1.50)$$

from where the unknowns of the third layer are determined:

$$C_{1u}^{(3,s)} = b_7 d_{4u}^{(s)} + b_8 d_{5u}^{(s)}, \quad C_{2u}^{(3,s)} = b_8 d_{4u}^{(s)} - b_7 d_{5u}^{(s)} \quad (1.51)$$

For layers with numbers $n > 3$ from conditions of full contact between adjacent layers $(n + 1)$ and (n) sequentially, knowing data of layer n , unknowns of layer $(n + 1)$ are determined:

$$\begin{aligned} C_{1u}^{(n+1,s)} &= b_{1n} d_{1un}^{(s)} + b_{2n} d_{2un}^{(s)} \\ C_{2u}^{(n+1,s)} &= b_{2n} d_{1un}^{(s)} - b_{1n} d_{2un}^{(s)} \\ b_{1n} &= \sin \Omega_* \sqrt{\frac{\rho_{n+1}}{G^{(n+1)}}} \zeta_n \\ b_{2n} &= \cos \Omega_* \sqrt{\frac{\rho_{n+1}}{G^{(n+1)}}} \zeta_n \\ d_{1un}^{(s)} &= U^{(n,s)}(\xi, \eta, \zeta_n) - \bar{U}^{(n+1,s)}(\xi, \eta, \zeta_n) \\ d_{2un}^{(s)} &= \frac{1}{\sqrt{G^{(n+1)} \rho_{n+1}}} \left[\sigma_{13}^{(n,s)}(\xi, \eta, \zeta_n) - \sigma_{13*}^{(n+1,s)}(\xi, \eta, \zeta_n) \right] \\ & \quad n = 3, 4, \dots (N - 1) \end{aligned} \quad (1.52)$$

In a similar way, remaining conditions (1.34), (1.35) are satisfied. The corresponding data can be obtained from the above mentioned by cyclic permutation

$$(U_x, U_y, U_z; u, v, w; G, G, \Delta_1; 13, 23, 33)$$

If functions U^+ , V^+ , W^+ are algebraic polynomials, mathematically exact solution of the external problem corresponds them. In all considered problems, the solution of the boundary layer is localized near the side surface. All quantities decrease exponentially with removing from the side surface. Taking into account, that tangential dimensions of the packet are much greater than its thickness, and the boundary

layer is usually neglected. If necessary, the corresponding solution can be determined by the method described in [2].

1.4 Conclusions

Earthquakes are the result of the accumulation over the years of enormous potential energy of deformation, which with reaching the critical value, causes to the global destruction—an earthquake. Seismologists established that before an earthquake, in a seismically dangerous zone, there is a significant deformation (displacement of points) of the Earth's Crust. The problem arose by data of displacements of points of this surface to determine the stress-strain state (SSS) of the corresponding block of the Earth's Crust (Rikitake problem) and based on regular measurements of displacements to track SSS change over the time. In this work, regarding that structure of Earth's Crust block is known (layering, Young's, Shear, Poisson's coefficients, density of layers, etc.), based on the data of measuring instruments (inclinometers, strainmeters, etc.), which are located at a certain depth from the surface of Earth's Crust, based on equations and relations of elasticity theory, is determined the SSS of the layered package from isotropic layers. The potential energy of deformation is determined, and the magnitude of the expected earthquake is estimated. Fast-flowing dynamic processes are studied (Foreshocks, Earthquakes, Aftershocks).

Acknowledgements The work was supported by the Science Committee of RA, in the frames of the research project No. 21T-2C075.

References

1. Aghalovyan, L.A.: On one class of three-dimensional problems of elasticity theory for plates. *Proc. A. Razmadze Math. Inst.* **155**(1), 3–10 (2011)
2. Aghalovyan, L.A.: *Asymptotic Theory of Anisotropic Plates and Shells*, World Scientific Publishing Co Pte. Ltd., Singapore, New Jersey, London, Hong Kong (2015)
3. Basar S., Coupland D., Obrist H.U.: *The Age of Earthquakes*, Penguin Random House Books (2015)
4. Gutenberg, B., Richter, C.F.: Earthquake magnitude, intensity, energy and acceleration. *Bullet. Seismol. Soc. Am.* **46**(2), 105–145 (1956)
5. Kasahara, K.: *Earthquake Mechanics*. Cambridge University Press, Cambridge (1981)
6. Pichon, H.L., Francheteau, J., Bonnin, J.: *Plate Tectonics*. Elsevier, Amsterdam (1973)
7. Rikitake, T.: *Earthquake Prediction*. Elsevier, Amsterdam (1976)

Chapter 2

Diffraction of Plane Waves in an Elastic Half-Plane Enhanced Along Its Boundary by a Semi-infinite Stringer



Karo L. Aghayan and Rafik A. Baghdasaryan

Abstract A dynamic contact problem is considered on the propagation and diffraction of plane elastic waves incident from infinity onto the boundary of an elastic half-plane reinforced by a semi-infinite stringer of small thickness. Questions related to the dynamic mutual influence of an elastic half-plane with a stringer of semi-infinite length rigidly welded to its boundary are investigated. Due to the smallness of the stringer thickness, the model of a one-dimensional elastic continuum is taken as a physical model for it [1, 2]. Based on the adopted model, with the help of the generalized Fourier transform, the problem is reduced to a Riemann-type boundary value problem in the theory of analytic functions on the real axis and, further, a closed solution of the problem is constructed using the Wiener–Hopf method. Analytical expressions are obtained that represent the distribution of wave components in all parts of the half-plane.

Keywords Surface wave · Reflection · Diffraction · Contact stresses · Wave field · Stringer

2.1 Introduction

Research in the field of the dynamic theory of elasticity related to the processes of oscillations, diffraction and propagation of various types of waves in massive bodies with stress concentrators are among the topical problems of the dynamics of the contact interaction of elastic bodies. In particular, this also applies to the problems of propagation and reflection of elastic and surface waves of the Rayleigh, Love, etc., type in an elastic plane with stress concentrators of the type stamp, crack, stringer (overlay, inclusion), strip, beam, etc.

K. L. Aghayan (✉)

Institute of Mechanics, National Academy of Sciences of Armenia, Baghramyan 24/2 ave, 0019 Yerevan, Republic of Armenia
e-mail: karo.aghayan@gmail.com

R. A. Baghdasaryan

National Polytechnic University of Armenia, 105, Teryan str, 0009 Yerevan, Republic of Armenia
e-mail: rafikbaghdasaryan@gmail.com

There are quite a lot of works on the study of plane contact and mixed boundary value problems (in static and dynamic statement) for a plane, half-plane and strip reinforced with elastic fasteners in the form of stringers. Let us briefly dwell on some of them, which are related directly to the problem considered here.

Of the static contact problems for a half-plane or plane, we note only the works [1–3], in which for the first time the model of a one-dimensional elastic continuum was adopted and substantiated as a physical model of the stringer. In turn, these works served as a kind of stimulus for the subsequent appearance of many new fundamental works in the field of contact problems.

Of the dynamic contact problems closest to the problem considered here, we note the works [4–8] and the works cited in them. In these papers, in the formulation of a plane deformation, stationary dynamic contact problems are considered for elastic space, layer and half-space. The elements in contact with massive bodies here are mainly stamps and thin layers, under various types of loading and boundary conditions.

The number of dynamic contact problems for an elastic plane or half-plane with elastic stringers is small. Of these, we point out the works [9–11]. Note that [9] is the first work in this direction and, as its author notes, it was put forward by Academician N. Kh. Harutyunyan.

In [9], two dynamic contact problems are considered on the transfer of a concentrated force harmonically varying in time to a semi-infinite elastic half-plane through an elastic infinite and semi-infinite overlay glued to its boundary. The work was done at a high mathematical level. A closed solution in the form of Fourier integrals is obtained.

The problem proposed here is related to the problems from [9]. In [9, 10], the question of the transfer of a concentrated force from a stringer to the boundary of a half-plane is considered, where the stringer plays the role of a damper, which weakens the influence of the concentrated force. In the problem considered here, as in [11], questions related to the general change in the wave field due to the mutual influence of the stringer with the boundary of the half-plane are investigated.

2.2 Statement of the Problem

An elastic half-plane with elastic characteristics (λ, μ, ρ) in the Cartesian coordinate system Oxz occupies the region $\Omega^- (-\infty < x < \infty, z < 0)$. The axis Oz is directed along the outer normal to the boundary of the half-plane. Along its boundary $z = 0$ the half-plane is reinforced with a semi-infinite stringer with a sufficiently small constant thickness h_S and with elastic parameters E_S, ν_S, ρ_S . The half-plane and the stringer are connected along the boundary $z = 0$ of the half-plane and are in full contact. With respect to the stringer, it is assumed that due to the smallness of the

thickness h_s , the bending stiffness is negligible. Then, the pressure of the stringer on the half-plane can be neglected and it can be assumed that only tangential contact stresses arise under the stringer. This allows, as in [1, 2], to take the model of a one-dimensional elastic continuum as the physical model of the stringer.

Let us study, the two-dimensional wave motion in the indicated composite half-plane, when a plane transverse SV wave falls on its boundary from infinity, described by the potential

$$\psi_\infty(x, z, t) = \psi_0(x, z)e^{-i\omega t} \quad x, z \in \Omega^- \quad (2.1)$$

$$\psi_0(x, z) = B_0 e^{i(\xi x + \eta z)}, \quad \xi = k_2 \cos \beta, \quad \eta = k_2 \sin \beta,$$

where $\psi_0(x, z)$ is a amplitude, $\beta (0 < \beta < \pi/2)$ is the angle of falling of shear wave, $k_2 = \omega/c_2$ is a wavenumber, $c_2 = \sqrt{\mu/\rho}$ is a phase velocity transverse wave, μ and ρ are shear module and density, ω is a oscillation frequency and t is a time.

Under these assumptions, it is required to determine the distribution of the wave components of the diffracted field in the half-plane and the contact stresses arising under the stringer.

2.3 Influence Function

Consider the following auxiliary plane strain problem for the above-mentioned elastic region Ω^- .

On the boundary of the elastic half-plane acts the following given load

$$\sigma_z^*(x, z, t)|_{z=0} = 0 \quad (-\infty < x < \infty) \quad (2.2)$$

$$\tau_{xz}^*(x, z, t)|_{z=0} = \tau_0(x)e^{-i\omega t}, \quad (-\infty < x < \infty) \quad (2.3)$$

and from infinity, a transverse wave falls on the boundaries of the half-plane, given by formula (2.1).

Using amplitudes $\varphi(x, z)$ and $\psi(x, z)$ of the wave potentials

$$\varphi_*(x, z, t) = \varphi(x, z)e^{-i\omega t}; \quad \psi_*(x, z, t) = \psi(x, z)e^{-i\omega t}$$

the solution to this problem can be formulated in the form of the following system of boundary value problems [12], with respect to the potentials $\varphi(x, z)$ and $\psi(x, z)$ (here and below, the harmonic factor $e^{i\omega t}$ is omitted):

$$\Delta\varphi(x, z) + k_1^2\varphi(x, z) = 0 \quad (x, z) \in \Omega^- \quad (2.4)$$

$$\Delta \Psi(x, z) + k_2^2 \Psi(x, z) = 0 \quad (x, z) \in \Omega^- \quad (2.5)$$

$$\sigma_z(x, 0) = 0; \quad \tau_{xz}(x, 0) = \tau_0(x), \quad |x| < \infty \quad (2.6)$$

$$\Psi(x, z) = \psi(x, z) - B_0 e^{i(\xi x + \eta z)} \quad (2.7)$$

Here, $\Delta = \frac{\partial^2}{\partial x^2} + \frac{\partial^2}{\partial z^2}$ is a Laplace operator, $k_1 = \frac{\omega}{c_1} = \omega \sqrt{\rho/(\lambda + 2\mu)}$ is the wavenumber, c_1 is the phase velocity of longitudinal wave, λ , μ are Lamé parameters and ρ is the density.

Applying to (2.4)–(2.7) the Fourier transform, we obtain the following system of two ordinary differential equations with respect to $\bar{\varphi}(\sigma, z)$ and $\bar{\Psi}(\sigma, z)$:

$$\frac{d^2 \bar{\varphi}(\sigma, z)}{dz^2} - \gamma_1(\sigma) \bar{\varphi}(\sigma, z) = 0 \quad (2.8)$$

$$\frac{d^2 \bar{\Psi}(\sigma, z)}{dz^2} - \gamma_2(\sigma) \bar{\Psi}(\sigma, z) = 0 \quad (2.9)$$

with boundary conditions

$$\left(\frac{d^2 \bar{\varphi}}{dz^2} - \sigma^2 \frac{\lambda}{\lambda + 2\mu} \bar{\varphi} - 2i\sigma \frac{\mu}{\lambda + 2\mu} \frac{d\bar{\psi}}{dz} \right) \Big|_{z=0} = 0 \quad (|\sigma| < \infty) \quad (2.10)$$

$$\left(\frac{d^2 \bar{\psi}}{dz^2} + \sigma^2 \bar{\psi} + 2i\sigma \frac{d\bar{\varphi}}{dz} \right) \Big|_{z=0} = -\frac{1}{\mu} \bar{\tau}_0(\sigma) \quad (|\sigma| < \infty) \quad (2.11)$$

Here

$$\gamma_1(\sigma) = \sqrt{\sigma^2 - k_1^2}; \quad \gamma_2(\sigma) = \sqrt{\sigma^2 - k_2^2} \quad (2.12)$$

$$\bar{\psi}(\sigma, z) = \bar{\Psi}(\sigma, z) + 2\pi B_0 e^{-i\eta z} \delta(\sigma + \xi) \quad (2.13)$$

and $\delta(x)$ is the Dirac delta-function.

Note that the boundary conditions (2.10), (2.11) correspond to conditions (2.6), (2.7) as a consequence of Hooke's law and the dependences of elastic displacements $U_x(x, z)$ and $U_z(x, z)$ on the potentials $\varphi(x, z)$ and $\psi(x, z)$

$$U_x(x, z) = \frac{\partial \varphi}{\partial x} - \frac{\partial \psi}{\partial z}; \quad U_z(x, z) = \frac{\partial \varphi}{\partial z} + \frac{\partial \psi}{\partial x} \quad (2.14)$$

The general solution to (2.8) and (2.9) is represented as

$$\begin{aligned}\bar{\varphi}(\sigma, z) &= A_1(\sigma)e^{\gamma_1 z} + A_2(\sigma)e^{-\gamma_1 z} \\ \bar{\Psi}(\sigma, z) &= B_1(\sigma)e^{\gamma_2 z} + B_2(\sigma)e^{-\gamma_2 z}\end{aligned}\quad (2.15)$$

where A_1, A_2, B_1, B_2 are unknown constants.

In solution (2.15), $\gamma_1(\sigma)$ and $\gamma_2(\sigma)$ given by formula (2.12) are multivalued functions. Any linear combination of expressions (2.15) corresponding to different values of multivalued functions $\gamma_1(\sigma)$ and $\gamma_2(\sigma)$ will be a solution to system of Eqs. (2.8) and (2.9).

This ambiguity in the choice of solutions can be eliminated by matching the form of expressions $\bar{\varphi}(\sigma, z)$ and $\bar{\Psi}(\sigma, z)$ with the corresponding physical requirements of the stated problem. In other words, the diffracted waves must be exponentially decreasing along z (nonuniform waves) or moving away from the boundary (uniform waves).

The points $\sigma = \pm k_1$ and $\sigma = \pm k_2$ are the branch points of the functions $\gamma_1(\alpha)$ and $\gamma_2(\alpha)$ in the complex plane $\alpha = \sigma + i\tau$.

An unambiguous analytical branch of these functions can be chosen if cuts are made in the complex plane in the form of straight lines connecting points k_1, k_2 and $-k_1, -k_2$ with a point at infinity, respectively, in the upper and lower half-planes. In the plane cut in this way, one can choose single-valued analytic branches of the functions $\gamma_1(\alpha)$ and $\gamma_2(\alpha)$ such that $\gamma_1(\alpha), \gamma_2(\alpha) \rightarrow |\alpha|$ when $\sigma \rightarrow \pm\infty$ [13]. Based on these considerations, in (2.15) one should set $A_2 = B_2 = 0$. In addition, to ensure the above two requirements, it follows that when $|\sigma| > k_1$ ($|\sigma| > k_2$) the values of the function $\gamma_1(\gamma_2)$ must be positive, i.e.

$$\gamma_1 = \sqrt{\sigma^2 - k_1^2}; \quad \gamma_2 = \sqrt{\sigma^2 - k_2^2},$$

and when $|\sigma| < k_j$ ($j = 1, 2$)

$$\gamma_1 = -i\sqrt{k_1^2 - \sigma^2}; \quad \gamma_2 = -i\sqrt{k_2^2 - \sigma^2}\quad (2.16)$$

The remaining two constants included in (2.15), taking into account (2.13), are determined from the boundary conditions (2.10) and (2.11) as follows:

$$A_1(\sigma) = 8\pi B_0 \frac{\xi\eta(\xi^2 - \eta^2)}{R(\xi)} \delta(\sigma + \xi) - i \frac{2\sigma\sqrt{\sigma^2 - k_2^2}}{\mu R(\sigma)} \bar{\tau}_0(\sigma)\quad (2.17)$$

$$B_1(\sigma) = -2\pi B_0 \frac{(\xi^2 - \eta^2)^2 - 4\xi^2\eta\sqrt{k_1^2 - \xi^2}}{R(\xi)} \delta(\sigma + \xi) - \frac{2\sigma^2 - k_2^2}{\mu R(\sigma)} \bar{\tau}_0(\sigma)\quad (2.18)$$

where $R(\sigma)$ is the Rayleigh function

$$R(\sigma) = (2\sigma^2 - k_2^2)^2 - 4\sigma^2 \sqrt{(\sigma^2 - k_1^2)(\sigma^2 - k_2^2)} \quad (2.19)$$

Substituting the values A_1, B_1 from (2.17), (2.18) into (2.15), taking into account $A_2 = B_2 = 0$, after the inverse transformation, we obtain the final expressions for the wave potentials $\varphi(x, z)$ and $\Psi(x, z)$ which solve the problem for given B_0 and $\tau_0(x)$.

Without dwelling on the details here, we note that in (2.17) and (2.18), the first components are responsible for the reflected waves, and the second for the surface waves with the wavenumber $\sigma_R (R(\sigma_R) = 0)$.

We also note that when using formulas (2.17)–(2.19), one should keep in mind (2.16) and the well-known Snell relation $k_1 \cos \beta = k_2 \cos \vartheta$, where ϑ is the angle of the reflected longitudinal wave.

Let us define the expression for the Fourier image of the horizontal displacements of the boundary points of the half-plane $\overline{U}_x(\sigma, 0)$. After applying to (2.14) Fourier transformation we will have

$$\overline{U}_x(\sigma, z) = -i\sigma \overline{\varphi}(\sigma, z) - \frac{d\overline{\psi}(\sigma, z)}{dz} \quad (2.20)$$

Now, taking into account (2.15), (2.17) and (2.18), from (2.20) we obtain

$$\overline{U}_x(\sigma, 0) = 2\pi i B_0 \eta H(\xi, \eta) \delta(\sigma + \xi) - \frac{k_2^2 \sqrt{\sigma^2 - k_2^2}}{\mu R(\sigma)} \overline{\tau}_0(\sigma), \quad (2.21)$$

$$H(\xi, \eta) = \frac{(\xi^2 - \eta^2)(3\xi^2 + \eta^2) + 4\xi^2 \eta \sqrt{k_1^2 - \xi^2}}{R(\xi)} - 1 \quad (2.22)$$

Note that when $\tau_0(x) = \delta(x)$, the $\overline{U}_x(\sigma, 0)$ represents the Green's function for the boundary value problem (2.8)–(2.11).

2.4 Solution of the Contact Problem

We will solve the problem by the method of generalized Fourier transform and will use the following notations [18]

$$f^\pm(x) = \theta(\pm x), \quad \overline{f}^\pm(\sigma) = \int_{-\infty}^{\infty} f^\pm(x) e^{i\sigma x} dx; \quad f^\pm(x) = \frac{1}{2\pi} \int_{-\infty}^{\infty} \overline{f}^\pm(\sigma) e^{-i\sigma x} d\sigma \quad (2.23)$$

where $\theta(x)$ is the Heaviside function.

Then, taking into account (2.23), (2.21) can be represented as

$$\begin{aligned} \overline{U}_x^+(\sigma, 0) + \overline{U}_x^-(\sigma, 0) &= 2\pi i B_0 \eta H(\xi, \eta) \delta(\sigma + \xi) \\ &\quad - \frac{k_2^2 \sqrt{\sigma^2 - k_2^2}}{\mu R(\sigma)} \overline{\tau}_S^+(\sigma), \quad -\infty < \sigma < \infty \end{aligned} \quad (2.24)$$

where $\overline{\tau}_S^+(\sigma)$ is the transformant of the tangential contact stress $\tau_S^+(x)$ arising under the semi-infinite stringer.

Now consider the movement of the stringer, separating it from the edge of the half-plane. Let us denote by $\tau_S(x)$ the amplitude of tangential contact stresses arising on the line of contact of the stringer with the boundary of the half-plane. Applying the d'Alembert principle to an infinitely small element of the stringer, taking into account the above model of a uniaxial stress state for it and Hooke's law, for the amplitude of horizontal displacements $U_S(x)$, we obtain a differential equation [9, 11]

$$\frac{d^2 U_S(x)}{dx^2} + q^2 U_S(x) - A_S \tau_S(x) = 0, \quad (0 < x < \infty) \quad (2.25)$$

$$q = \frac{\omega}{c_S}, \quad c_S^2 = \frac{E_S}{\rho_S(1 - \nu_S^2)}, \quad A_S = \frac{1 - \nu_S^2}{E_S h_S}$$

Here, q is a wavenumber, c_S is a phase velocity of wave in stringer (rod) and E_S , ν_S , ρ_S are shear module, Poisson's ratio and density of the stringer material.

On the other hand, for the second differential of the function $U_S^+(x) = \theta(x)U_S(x)$ we have

$$\frac{d^2 U_S^+(x)}{dx^2} = U_S(0)\delta'(x) + \theta(x)\frac{d^2 U_S(x)}{dx^2} = 0, \quad (-\infty < x < \infty). \quad (2.26)$$

Here, we took into account the well-known relations

$$\delta(x) = \theta'(x), \quad f(x)\delta(x) = f(0)\delta(x) \quad (f(0) \neq 0)$$

and the condition

$$\sigma_x^{(S)}(0) = E_S \left. \frac{dU_S}{dx} \right|_{x=+0} = 0 \quad (2.27)$$

which represents the absence of the normal stress $\sigma_x^{(S)}(x)$ in the end $x = +0$ of the stringer.

Combining (2.25) with (2.26), we get

$$\frac{d^2 U_S^+(x)}{dx^2} = U_S(0)\delta'(x) + \theta(x)[A_S \tau_S(x) - q^2 U_S(x)] \quad (2.28)$$

or after applying the generalized transformation (2.23)

$$(\sigma^2 - q^2)\overline{U}_S^+(\sigma) + A_S\overline{\tau}_S^+(\sigma) - iU_S(0)\sigma = 0 \quad (2.29)$$

where $U_S(0)$ is an unknown constant.

The contact condition between stringer and half-plane after Fourier transform has the following form:

$$\overline{U}_x^+(\sigma, 0) = \overline{U}_S^+(\sigma), \quad (-\infty < \sigma < \infty) \quad (2.30)$$

Satisfying condition (2.30) with the help of (2.24) and (2.29), we arrive at the following functional equation for the unknowns $\overline{U}_x^-(\sigma, 0)$ and $\overline{\tau}_S^+(\sigma)$:

$$\begin{aligned} & (\sigma^2 - q^2)\overline{U}_S^-(\sigma, 0) - \chi\sqrt{\sigma^2 - k_2^2}\overline{F}(\sigma)\overline{\tau}_S^+(\sigma) \\ & = 2\pi i B_0\eta H(\xi, \eta)(\sigma^2 - q^2)\delta(\sigma + \xi) - iU_S(0)\sigma \quad (-\infty < \sigma < \infty) \end{aligned} \quad (2.31)$$

where

$$\overline{F}(\sigma) = \frac{2(k_2^2 - k_1^2)R_*(\sigma)}{R(\sigma)\sqrt{\sigma^2 - k_2^2}} \quad (2.32)$$

$$R_*(\sigma) = \mu_*R(\sigma) - (\sigma^2 - q^2)\sqrt{\sigma^2 - k_2^2} \quad (2.33)$$

$$\chi = k_2^2(2\mu(k_2^2 - k_1^2))^{-1}, \quad \mu_* = \mu A_S k_2^{-2} \quad (2.34)$$

and $R(\sigma)$ is given by (2.19).

Thus, the solution of the problem has been reduced to the Riemann boundary value problem of the theory of analytic functions on the real axis (2.31) for the unknown functions $\overline{U}_x^-(\sigma, 0)$ and $\overline{\tau}_S^+(\sigma)$.

Using notation

$$\overline{K}(\sigma) = \frac{\sigma^2 - \sigma_R^2}{\sigma^2 - \sigma_{R_*}^2}\overline{F}(\sigma) \quad (2.35)$$

we represent Eq. (2.31) in the form

$$\begin{aligned} & (\sigma - q)\overline{U}_x^-(\sigma, 0) - \chi\sqrt{\sigma^2 - k_2^2}\frac{(\sigma^2 - \sigma_{R_*}^2)}{(\sigma^2 - \sigma_R^2)(\sigma + q)}\overline{K}(\sigma)\overline{\tau}_S^+(\sigma) \\ & = -2\pi i B_0\eta(\xi + q)H(\xi, \eta)\delta(\sigma + \xi) - iU_S(0)\frac{\sigma}{\sigma + q}, \quad (-\infty < \sigma < \infty) \end{aligned} \quad (2.36)$$

Here, σ_R and σ_{R_*} are roots of the equations $R(\sigma) = 0$ и $R_*(\sigma) = 0$, respectively, where $R(\sigma)$ and $R_*(\sigma)$ are given by formulas (2.19), (2.33).

Rayleigh function $R(\sigma)$ has two real roots [12, 14]: $\sigma = \pm\sigma_R$. It turns out that $R_*(\sigma)$ also has two roots: $\sigma = \pm\sigma_{R_*}$. With this [7, 9], if $\sigma_R > q$, then $\sigma_{R_*} \in (k_2, \sigma_R)$; if $\sigma_R < q$, then $\sigma_{R_*} \in (\sigma_R, q)$ and if $\sigma_R = q$, then obviously, $\sigma_{R_*} = \sigma_R$.

We construct the solution of the functional Eq. (2.36) by the factorization method [13] developed in [15, 16]. In this case, when solving (2.36) and factorization $\overline{K}(\sigma)$, it is assumed that the real axis bypasses the negative roots $\sigma = -\sigma_R, \sigma = -\sigma_{R_*}$ of the functions $R(\sigma), R_*(\sigma)$ and the point $\sigma = -q$ from above, and positive roots $\sigma = \sigma_R, \sigma = \sigma_{R_*}$ and the point $\sigma = q$ from below.

Accordingly, for the function $\gamma_j(\sigma)$ from (2.9), it is assumed that $\sqrt{\sigma^2 - k_j^2} > 0$ for $|\sigma| > k_j, \sqrt{\sigma^2 - k_j^2} = -i\sqrt{k_j^2 - \sigma^2}$, i.e. in (2.26) it is assumed that the real axis bypasses the branch points $\sigma_j = -k_j$ of the function $\gamma_j(\alpha) = \sqrt{\alpha^2 - k_j^2}$ from above, and the points $\sigma_j = k_j$ —from below.

We factorize the function $\overline{K}(\sigma)$, presenting it in the form

$$\overline{K}(\sigma) = \overline{K}_+(\sigma) \cdot \overline{K}_-(\sigma) \quad (2.37)$$

where $\overline{K}_+(\alpha)$ is regular and does not have zeros for $\text{Im}\alpha > 0$, $\overline{K}_-(\alpha)$ is regular and does not have zeros for $\text{Im}\alpha < 0$, $\alpha = \sigma + i\tau$. With this, $\overline{K}_\pm(\alpha) \rightarrow 1$ when $|\alpha| \rightarrow \infty$ in own regularity regions, and $\overline{K}_\pm(\sigma)$ are defined by formulas

$$\overline{K}_+(\sigma) = \exp(L_+(\sigma)), \quad \overline{K}_-(\sigma) = \exp(L_-(\sigma)) \quad (2.38)$$

$$\overline{L}_+(\sigma) = \frac{1}{2\pi i} \int_{-\infty}^{\infty} \frac{\ln \overline{K}(s)}{s - (\sigma + i0)} ds; \quad \overline{L}_-(\sigma) = -\frac{1}{2\pi i} \int_{-\infty}^{\infty} \frac{\ln \overline{K}(s)}{s - (\sigma - i0)} ds \quad (2.39)$$

The function $\overline{L}_+(\alpha)$ ($\overline{L}_-(\alpha)$) as an analytic continuation of $\overline{L}_+(\sigma)$ ($\overline{L}_-(\sigma)$) is bounded and regular at $\text{Im}\alpha > 0$ ($\text{Im}\alpha < 0$) and has no zeros there.

Bearing in mind the well-known representation [18]

$$\delta(\sigma) = \frac{1}{2\pi i} \left[\frac{1}{\sigma - i0} - \frac{1}{\sigma + i0} \right]; \quad \frac{1}{\sigma \pm i0} = \frac{1}{\sigma} \pm i\pi\delta(\sigma) \quad (2.40)$$

$\overline{L}_+(\sigma)$ can be calculated by formula

$$\overline{L}_+(\sigma) = \frac{1}{2} \ln \overline{K}(\sigma) + \frac{1}{2\pi i} \int_{-\infty}^{\infty} \ln \overline{K}(t) \frac{dt}{t - \sigma}$$

Using (2.37) and (2.40), we can now represent the functional equation in the form

$$\begin{aligned} & \frac{\sigma - q}{P_-(\sigma)} \overline{U}_x^-(\sigma, 0) - \frac{\overline{P}_+(\sigma)}{\sigma + q} \overline{\tau}_S^+(\sigma) \\ &= \eta(\xi + q)H(\xi, \eta) \left[\frac{1}{\sigma + \xi + i0} - \frac{1}{\sigma + \xi - i0} \right] \\ & - iU_S(0) \frac{\sigma}{(\sigma + q)P_-(\sigma)} \quad (-\infty < \sigma < \infty) \end{aligned} \quad (2.41)$$

$$\overline{P}_\pm(\sigma) = \sqrt{\chi} \sqrt{\sigma \pm k_2} \frac{\sigma \pm \sigma_{R_\pm}}{\sigma \pm \sigma_R} \overline{K}_\pm(\sigma); \quad \overline{P}_+(\xi) = i\overline{P}_-(-\xi) \quad (2.42)$$

Solving, according to the usual procedure [13], Eq. (2.42), for $\overline{\tau}_S^+(\sigma)$, we obtain the following representation

$$\overline{\tau}_S^+(\sigma) = -B_0 \frac{i\eta(\xi + q)H(\xi, \eta)}{\overline{P}_+(\xi)} \frac{\sigma + q}{\overline{P}_+(\sigma)(\sigma + \xi + i0)} + \frac{qU_S(0)}{\overline{P}_+(q)\overline{P}_+(\sigma)} \quad (2.43)$$

The unknown constant $U_S(0)$ is determined from the equilibrium condition of the semi-infinite stringer

$$\int_0^\infty \overline{\tau}_S^+(x) dx = 0 \Rightarrow \overline{\tau}_S^+(0) = 0 \quad (2.44)$$

As a result, for $\overline{\tau}_S^+(\sigma)$, finally, we get

$$\overline{\tau}_S^+(\sigma) = B_0 M(\xi, \eta) \frac{i\sigma}{(\sigma + \xi + i0)\overline{P}_+(\sigma)} \quad (2.45)$$

where

$$M(\xi, \eta) = \frac{\eta(q^2 - \xi^2)H(\xi, \eta)}{\overline{P}_+(\xi) \cdot \xi} \quad (2.46)$$

In (2.17) and (2.18), replacing $\overline{\tau}_0(\sigma)$ by $\overline{\tau}_S^+(\sigma)$ from (2.45), then substituting the result into (2.15), and applying the inverse transformation, we obtain the following representations for $\varphi(x, z)$ and $\psi(x, z)$:

$$\begin{aligned} \varphi(x, z) &= 4B_0 \frac{\xi\eta(\xi^2 - \eta^2)}{R(\xi)} e^{i(\xi x - \sqrt{k_1^2 - \xi^2}z)} \\ &+ \frac{B_0}{\pi\mu} M(\xi, \eta) \int_{-\infty}^\infty \frac{\sigma^2 \sqrt{\sigma^2 - k_2^2} e^{-i\sigma x + \sqrt{\sigma^2 - k_1^2}z}}{(\sigma + \xi + i0)R(\sigma)\overline{P}_+(\sigma)} d\sigma \end{aligned} \quad (2.47)$$

$$\begin{aligned} \psi(x, z) = & B_0 e^{i(\xi x + \eta z)} - B_0 \frac{(\xi^2 - \eta^2)^2 - 4\eta\xi^2 \sqrt{k_1^2 - \xi^2}}{R(\xi)} e^{i(\xi x - \eta z)} \\ & - \frac{iB_0}{2\pi\mu} M(\xi, \eta) \int_{-\infty}^{\infty} \frac{\sigma e^{-i\sigma x + \sqrt{\sigma^2 - k_2^2} z}}{(\sigma + \xi + i0)\bar{P}_+(\sigma)} d\sigma \end{aligned} \quad (2.48)$$

2.5 Determination of the Radiated Wave Field

Let us first turn to contact stresses. From relation (2.45), after the inverse transformation (2.23), for the amplitude of the contact stresses we obtain

$$\tau_S^+(x) = \begin{cases} \frac{B_0^*}{2\pi} \int_{-\infty}^{\infty} \frac{\sigma(\sigma + \sigma_R)}{\bar{K}_+(\sigma)\sqrt{\sigma + k_2}} \frac{e^{-i\sigma x} d\sigma}{(\sigma + \xi + i0)(\sigma + \sigma_{R_*})}, & x > 0 \\ 0, & x < 0 \end{cases}. \quad (2.49)$$

$$B_0^* = M(\xi, \eta)/\chi$$

Here, the real axis bypasses the points $-\sigma_R$, $-\sigma_{R_*}$, $-k_2$, $-k_1$, $-\xi$ from above, and the points ξ , k_1 , k_2 , σ_{R_*} , σ_R —from below.

To study the integral from (2.49), as usual, we pass into a complex plane $\alpha = \sigma + i\tau$, cut in a certain way, a detailed description of which is given in [13, 16].

Since $x > 0$, we close the integration contour in the lower half-plane. Bearing in mind the peculiarities of the analytic continuation of the integrand from (2.49) into the upper and lower half-planes of the cut plane, the amplitude of the contact stress from (2.49) can be represented as

$$\tau_S^+(x) = -\frac{iB_0^*}{\sigma_{R_*} - \xi} [\bar{M}_+(-\xi)e^{i\xi x} + \bar{M}_+(-\sigma_{R_*})e^{i\sigma_{R_*} x}] + T_S(x) \quad (2.50)$$

$$T_S(x) = \frac{B_0^* k_2}{\pi} \int_0^{k_2} \bar{M}_-(\sigma) \frac{e^{-i\sigma x} d\sigma}{(\xi - \sigma)(\sigma_{R_*} - \sigma)} + \frac{B_0^*}{\pi} \int_0^{\infty} \bar{M}_-(i\tau) \frac{e^{-\tau x} d\tau s}{(\xi - i\tau)(\sigma_{R_*} - i\tau)} \quad (2.51)$$

$$\bar{M}_+(\sigma) = \frac{\sigma(\sigma + \sigma_R)}{\bar{K}_+(\sigma)\sqrt{\sigma + k_2}}, \quad \bar{M}_-(\sigma) = \frac{\sigma(\sigma + \sigma_R)\bar{K}_-(\sigma)\sqrt{\sigma - k_2}}{\bar{K}(\sigma)\sqrt{\sigma^2 - k_2^2}} \quad (2.52)$$

It follows from (2.50) and (2.51) that the contact stress on the contact line consists of the following components: (a) component with wavenumber $\xi = k_2 \cos \beta$ due to the incident wave; (b) diffracted wave with wavenumber σ_{R_*} , due to a localized surface wave; (c) a diffracted wave with a wavenumber k_2 , due to the presence of an end point $x = +0$ of a semi-infinite stringer.

For the diffracted part of $T_S(x)$ from (2.51), we obtain an asymptotic formula

$$T_S(x) = \frac{B_0^*}{\sqrt{\pi x}} \left(e^{-i(k_2 x + \frac{\pi}{4})} + O\left(x^{-\frac{3}{2}}\right) \right) \text{ when } x \rightarrow +\infty \quad (2.53)$$

Bearing in mind that $\overline{K_+}(\sigma) \rightarrow 1$ when $|\sigma| \rightarrow \infty$; from (2.49), we obtain the following asymptotics for $\tau_S^+(x)$ at $x \rightarrow +0$:

$$\begin{aligned} \tau_S^+(x) &= \frac{B_0^*}{2\pi} \int_{-\infty}^{\infty} \frac{1}{\sqrt{\sigma + i0}} \left[1 + \frac{\xi + k_2 + \sigma_R}{\sigma} + O(|\sigma|^2) \right] e^{-i\sigma x} d\sigma \\ &= \frac{B_0^*}{\sqrt{\pi x_+}} \left(1 + O\left(x_+^{3/2}\right) \right) \end{aligned} \quad (2.54)$$

From the last expression, we see that the contact stress $\tau_S^+(x)$ at the end point of the stringer has a traditional root singularity.

Similarly, from (2.47), (2.48), we obtain the following formulas for the wave potentials:

in the region $\Omega_-^-(x < 0, z < 0)$

$$\varphi(x, z) = N_\varphi^{(1)} e^{i(\xi x - \sqrt{k_1^2 - \xi^2} z)} + N_\varphi^{(2)} e^{\sqrt{\sigma_R^2 - k_1^2} z - i\sigma_R x} + I_\varphi^{(-)}(x, z) \quad (2.55)$$

$$\psi(x, z) = B_0 e^{i(\xi x + \eta z)} - N_\psi^{(1)} e^{i(\xi x - \sqrt{k_2^2 - \xi^2} z)} + N_\psi^{(2)} e^{\sqrt{\sigma_R^2 - k_2^2} z - i\sigma_R x} + I_\psi^{(-)}(x, z) \quad (2.56)$$

where

$$\begin{aligned} N_\varphi^{(1)} &= 4B_0 \frac{\xi \eta (\xi^2 - \eta^2)}{R(\xi)}, \quad N_\varphi^{(2)} = \frac{4B_0 \eta (q^2 - \xi^2) (2\sigma_R^2 - k_2^2) \sigma_R^2}{\mu \xi P_+(\xi) \sqrt{\sigma_R + k_2} K_+(\sigma_R)} \\ N_\psi^{(1)} &= B_0 \frac{(\xi^2 - \eta^2)^2 - 4\xi^2 \eta \sqrt{k_1^2 - \xi^2}}{R(\xi)}, \quad N_\psi^{(2)} = \frac{2N_\varphi^{(2)}}{R'(\sigma_R) (\sigma_R + \sigma_{R_*}) (\sigma_R + \xi)} \end{aligned} \quad (2.57)$$

in the region $\Omega_+^-(x > 0, z < 0)$:

$$\begin{aligned} \varphi(x, z) &= N_\varphi^{(1)} e^{i(\xi x - \sqrt{k_1^2 - \xi^2} z)} + N_\varphi^{(3)} e^{i(\xi x - \sqrt{k_1^2 - \xi^2} z + \frac{\pi}{2})} \\ &\quad + N_\varphi^{(4)} e^{\sqrt{\sigma_{R_*}^2 - k_1^2} z + i(\sigma_{R_*} x + \frac{\pi}{2})} + I_\varphi^{(+)}(x, z) \end{aligned} \quad (2.58)$$

$$\psi(x, z) = B_0 e^{i(\xi x + \eta z)} - N_\psi^{(1)} e^{i(\sigma_{R_*}^2 - \sqrt{\sigma_{R_*}^2 - k_2^2} z)}$$

$$- N_{\varphi}^{(3)} e^{i(\xi x - \sqrt{k_2^2 - \xi^2} z)} + I_{\psi}^{(+)}(x, z) \quad (2.59)$$

$$N_{\varphi}^{(3)} = N_{\varphi}^{(2)} \frac{\xi^2 \sqrt{k_2^2 - \xi^2} (\sigma_R - \xi)}{\sqrt{\chi} \bar{K}_+(\xi)}, \quad N_{\varphi}^{(4)} = N_{\varphi}^{(2)} \frac{\sigma_{R_*}^2 \sqrt{\sigma_{R_*}^2 - k_2^2} (\sigma_R - \sigma_{R_*})}{\sqrt{\chi} \bar{K}_+(-\sigma_{R_*}) R(\sigma_{R_*}) (\xi - \sigma_{R_*})}$$

$$N_{\psi}^{(3)} = N_{\psi}^{(2)} \frac{(2\sigma_{R_*}^2 - k_2^2) \sigma_{R_*} (\sigma_R - \sigma_{R_*})}{\bar{K}_+(-\sigma_{R_*}) \sqrt{\sigma_{R_*}^2 - k_2^2}} \quad (2.60)$$

With the help of formulas (2.55)–(2.60) and (2.14), it is not difficult to obtain the distributions of the elastic displacement amplitudes $U_x(x, z)$ and $U_z(x, z)$ in the regions Ω^- and Ω^+ , thereby, to characterize the total wave field in the half-plane. However, this can also be done based on (2.55)–(2.60).

The functions $I_{\varphi}^{(\pm)}(x, z)$ and $I_{\psi}^{(\pm)}(x, z)$ included in formulas (2.55)–(2.59), similarly to $T_S(x)$ from (2.50), are represented as regular integrals over the edges of the corresponding cuts [14–16], which makes it possible, when considering the near field, to calculate the diffracted field directly. When considering the far field, one should study these integrals in detail and obtain asymptotic formulas corresponding to the problem posed, representing the distribution of diffracted damped body waves, which was not carried out here.

The wave field in the region Ω^- , as follows from (2.55) and (2.56), consists of incident and reflected waves, as well as diffracted damped body waves and a diffracted surface wave localized near the surface ($x < 0, z = -0$). This surface wave propagates with a velocity ω/σ_R in the direction opposite to the axis Ox and decays at $z \rightarrow -\infty$ as $O(e^{\sqrt{\sigma_R^2 - k_1^2} z})$. Obviously, the diffracted surface and body waves are due to the presence of a semi-infinite stringer.

The uniform distribution of the wave field is also obtained in the region Ω^+ , only with wave parameters that differ from the case $x < 0$. Thus, a localized surface wave propagating with a velocity ω/σ_{R_*} in the direction of the axis Ox decays at $z \rightarrow -\infty$ as $O(e^{\sqrt{\sigma_{R_*}^2 - k_1^2} z})$.

2.6 Numerical Analysis

In the problem under consideration, the mutual influence of a half-plane and a semi-infinite stringer is of particular interest, which is reflected mainly in the features of surface wave propagation. Let us carry out a numerical analysis of the dependence of the propagation velocity of a surface wave on the elastic characteristics of a half-plane and a semi-infinite stringer. Note that the roots of the wave function $R_*(\sigma)$ (2.60), in contrast to the roots of the Rayleigh function $R(\sigma)$ (2.19), depend on the frequency ω , i.e. the surface wave propagates along the line of contact with the dispersion.

The figures show plots of the dependence of the square of the ratio of the phase velocity of a surface wave c to the phase velocity c_2 of a transverse wave in the

half-plane, marked by $\zeta = c^2/c_2^2$, on the product kh_S , where k is the wavenumber of the surface wave. As variable parameters are taken: Poisson's ratio of the half-plane ν , the ratio of the velocity of elastic waves in the stringer $c_S = \sqrt{\frac{E_S}{\rho_S(1-\nu_S^2)}}$ to c_2 , marked by $\theta_S = \frac{c_S^2}{c_2^2}$ and combined parameter $A_* = \frac{E_S h_S}{\mu(1-\nu_S^2)}$, included in Eq. (2.33).

Figure 2.1 shows the curves when $\nu = 0.3$, $A_* = 2$, and the parameter θ_S takes the values $\theta_S = 0.5; 0.65; 0.8; 1.0; 5.0$.

Figure 2.2 shows the curves when $\theta_S = 0.5$, $A_* = 2$, and the Poisson's ratio takes the values $\nu = 0.16; 0.25; 0.33; 0.42$.

Figure 2.3 shows the curves when $\nu = 0.3$; $\theta_S = 0.5$, and the combined parameter A_* takes the values $A_* = 0.1; 0.5; 1.0; 2.0; 5.0$.

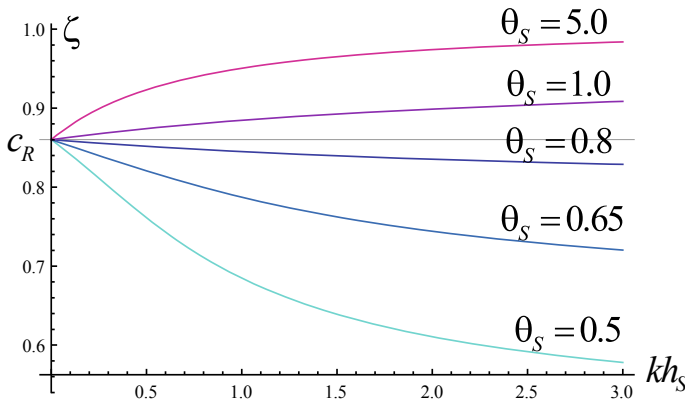


Fig. 2.1 Dependence ζ on kh_S for various values of parameter θ_S

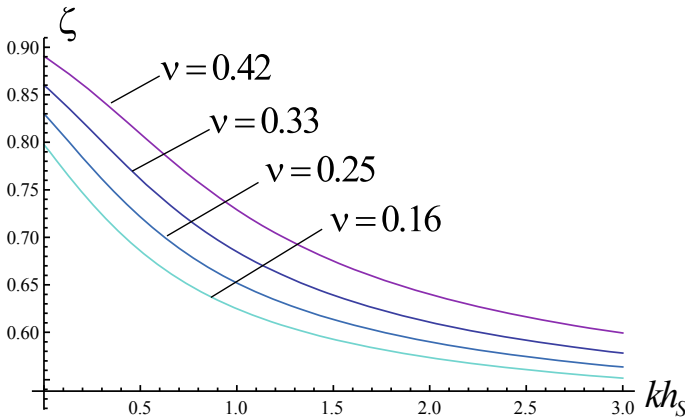


Fig. 2.2 Dependence ζ on kh_S for various values of Poisson's ratio ν

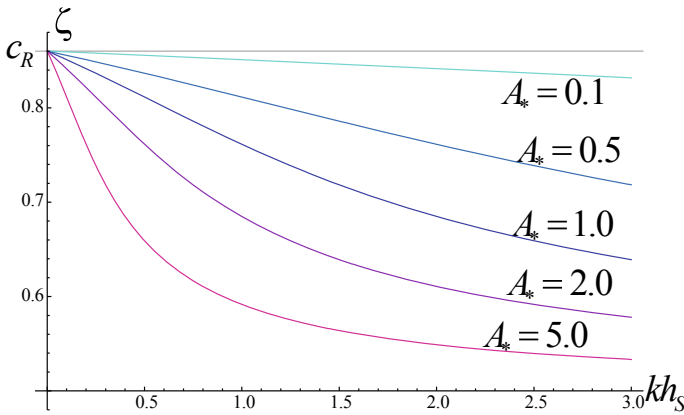


Fig. 2.3 Dependence ζ on kh_S for various values of parameter A_*

2.7 Conclusion

Questions related to the propagation and diffraction of plane elastic waves incident at a certain angle from infinity onto the boundary of an elastic half-plane reinforced with a stringer of semi-infinite length are investigated. A closed solution of the problem is obtained in the form of analytical expressions for the wave field in the half-plane and contact stresses under the stringer. The presence of a semi-infinite stringer leads to a significant change in the wave field in the composite half-plane, both qualitatively and quantitatively. It is shown that in the case of equality of the projection of the velocity of propagation of the incident wave ξ and the velocity of propagation of the wave in the stringer q , the contact shear stresses vanish.

In both quarter-planes Ω_{\pm}^- , in addition to the incident and reflected waves, diffracted surface and body waves arise, propagating at different speeds, in different directions and having different orders of decrease at infinity.

As shown by numerical calculations, depending on the relative position of the wave numbers σ_R and q , the wavenumber σ_{R_*} changes at different rates. In this case, the wave parameters strongly depend on the mechanical characteristics of the stringer.

References

1. Melan, E.: Ein Beitrag zur Theorie geschweißter Verbindungen. *Ing. Arch.* **3**, 123–129 (1932)
2. Arutiunian N.Kh.: Contact problem for a half-plane with elastic reinforcement: *PMM.* **32**(4), 632–646 (1968)
3. Muki, R., Sternberg, E.: Transfer of load from an edge-stiffener to a sheet—a reconsideration of Melan’s problem. *J. Appl. Mech.* **34**, 679–686 (1967)
4. Borodachev, N.M.: Vibrations of a stamp lying on an elastic half-space under the action of a horizontal harmonic force. In: *Proceedings of Universities. Construction and Architecture* (9) (1963) (in Russ.)
5. Belubekyan, M.V.: Surface waves in elastic media. In *Col.: Problems of Mechanics of a Deformable Solid Body*, pp. 79–96. Publ. NAS RA, Yerevan (1997) (in Russ.)
6. Belubekyan, M.V.: Reyleigh type waves in the layer-half-space system. *Proc. NAS RA Mech.* **58**(2), 9–15 (2005). (in Russ.)
7. Aghayan, K.L., Baghdasaryan, R.A.: Propagation of elastic waves in half-space with a thin elastic reinforcing layer. In: *Proceedings of VII International Conference on “The problems of dynamics of interaction of deformable media”*, Goris-Stepanakert, 19–23 September 2011, pp. 18–25 (in Russ.)
8. Amirjanyan, A.A., Belubekyan, M.V., Gevorgyan, G.Z., Darbinyan, A.Z.: Propagation of surface waves in a composite semi-plane under Navier conditions on the joint line. *Proc. NAS RA Mech.* **74**(4), 29–40 (2021). (in Russ.)
9. Grigoryan, E.Kh.: On two dynamic contact problems for a half-plane with elastic overlays. In: *Proceedings of AS SSSR, Mechanika Tverdovo Tela* (5) (1972) (in Russ)
10. Grigorian, E.Kh.: On the dynamic contact problem for a half-plane reinforced by a finite elastic strip. *J. Appl. Math. Mech.* **38**(2), 292–302 (1974)
11. Aghayan, K.L., Grigoryan, E.Kh., Jilavyan, S.H.: Diffraction of a plane shear wave on the elastic space with the semi-infinite elastic inclusion. *Proc. NAS RA Mech.* **56**(4), 3–17 (2003) (in Russ.)
12. Nowacki, W.: *Theory of Elasticity*. Mir, Moscow (1975)
13. Noble, B.: *Methods Based on the Wiener-Hopf Technique*. Pergamon Press (1958)
14. Grinchenko, V.T., Meleshko, V.V.: *Harmonic Oscillations and Waves in Elastic Bodies*. Kiev, Naukova Dumka (1981) (in Russ.)
15. Grigoryan, E.Kh., Agayan, K.L.: Radiation of a plane shear wave from an elastic waveguide to a composite elastic space. *Proc. NAS RA Mech.* **60**(3), 23–37 (2007) (in Russ.)
16. Agayan, K.L., Grigoryan, E.K., Gulyan, K.G.: Diffraction of a shear plane wave in a compound elastic space with a half-infinite crack parallel to the inhomogeneity line. *Mech. Solids* **48**, 203–209 (2013)
17. Grigoryan, E.Kh., Aghayan, K.L.: On a new method for determining asymptotic formulas in problems of wave diffraction. *Rep. NAS RA* (3), 261–271 (2010) (in Russ.)
18. Shilov, G.E.: *Mathematical Analysis. Second Special Course*. Moscow, Nauka (1965) (in Russ.)

Chapter 3

Analysis of Equivalence Conditions of Model of an Inhomogeneous Elastic Half-Space and Model of an Inhomogeneous Elastic Layer on the Elastic Foundation



Sergei M. Aizikovich, Polina A. Lapina, and Sergei S. Volkov

Abstract The paper considers contact problems on the shear of the surface of an elastic inhomogeneous by depth half-space, and on the shear of the surface of an elastic inhomogeneous by depth layer, rigidly coupled with a more rigid elastic foundation. The solution of integral equations, to which the contact problems are reduced, is constructed analytically by asymptotic methods for an inhomogeneous half-space and by a numerical–analytical method for an inhomogeneous layer on an elastic foundation. Using the explicit form of the kernel transforms of integral equations for these problems, the closeness of their solutions is studied. It is shown that for the laws of inhomogeneity, the kernel transforms of integral equations of which are close, there is a region of values of geometrical parameters, for which the distributions of contact stresses are also close.

Keywords Contact problem · Inhomogeneous material · Exponential shear modulus

3.1 Introduction

Inhomogeneous materials of various structure and composition have numerous applications: building materials [1], soils, semiconductors in microelectronics [2–4], various coatings, and implants in biomechanics [5, 6]. When calculating the stress–strain state for inhomogeneous materials, it is necessary to take into account the change in the properties of such materials by depth of the product [7–11]. Often,

S. M. Aizikovich (✉) · P. A. Lapina · S. S. Volkov
Research and Education Center «Materials», Don State Technical University, 1 Gagarin Sq,
Rostov-on-Don 344000, Russian Federation
e-mail: saizikovich@gmail.com

P. A. Lapina
e-mail: polina_azarova86@mail.ru

S. S. Volkov
e-mail: fenix_rsu@mail.ru

additional assumptions are made about the changing of the elastic properties of materials, which in some cases makes it possible to obtain analytical solutions to the corresponding differential equations. The works [12–19] consider materials which elastic properties change exponentially. In [20], the hyperbolic law of change in elastic properties is considered, in [21–23]—a power law, in [24, 25]—a linear law, and in [26–30]—an arbitrary change in elastic properties material by depth. The exponential law of inhomogeneity quite well reflects the change in the properties of some real inhomogeneous materials that may arise because of a technological or natural process [14].

The choice of an adequate mathematical model in the calculation of the stress–strain state of inhomogeneous media and the analysis of the efficacy of methods for constructing solutions is a topical issue of modern mechanics.

The present paper proposes an approach to the analysis of the equivalence of solutions for various models of inhomogeneous media, which is illustrated by the example of solving contact problems on the shear of the surface of an elastic inhomogeneous by depth half-space and the shear of the surface of an elastic inhomogeneous by depth layer rigidly linked to a more rigid base.

Using the values of the kernel transforms of the integral equations for the two proposed models of an inhomogeneous by depth half-space, the closeness of the solutions of the corresponding contact problems is investigated. A comparison of solutions to problems constructed approximately analytically using asymptotic methods is implemented in order to determine the areas of problem parameters for which the solutions are close to each other.

3.2 Statement of the Contact Problem on the Shear of the Surface of an Inhomogeneous Half-Space

Let us consider the problem of a shear of the surface of an inhomogeneous half-space by a strip punch with a flat base without friction. The equation of the theory of elasticity in stresses in the case of anti-plane deformation has the form

$$\frac{\partial \sigma_{zx}}{\partial x} + \frac{\partial \sigma_{zy}}{\partial y} = 0, \quad (3.1)$$

where stresses $\sigma_{zx}(x, y)$, $\sigma_{zy}(x, y)$ are expressed in terms of deformations $w(x, y)$ in the form

$$\sigma_{zx} = \mu(y) \frac{\partial w}{\partial x}, \quad \sigma_{zy} = \mu(y) \frac{\partial w}{\partial y}. \quad (3.2)$$

where $\mu(y)$ is the shear modulus of inhomogeneous by the coordinate y medium.

The mixed boundary conditions of the formulated contact problem of pure shear of the surface of an inhomogeneous half-space by a strip punch have the form

$$w(x, 0) = \varepsilon \quad |x| \leq a \tag{3.3}$$

$$\sigma_{yz}(x, 0) = \begin{cases} -\varphi(x) & |x| \leq a \\ 0 & a < |x| < \infty \end{cases} \tag{3.4}$$

where ε is the value, to which the punch is shifted, a is the half-width of the contact area, and $\varphi(x)$ is the contact stresses under the punch to be determined.

At infinity at $\sqrt{x^2 + y^2} \rightarrow \infty$ for $w(x, y)$ and $\frac{\partial w(x,y)}{\partial x}$, the following conditions are required:

$$\lim_{\sqrt{x^2+y^2} \rightarrow \infty} \left\{ w, \frac{\partial w}{\partial x} \right\} = 0. \tag{3.5}$$

3.3 Models of an Inhomogeneous Half-Space

In the present paper, we compared solutions for two models of an inhomogeneous medium. Figure 3.1a, b shows diagrams of two models of an inhomogeneous half-space. Model (a) was used in [17–19], and model (b) was used in [31].

The model (a) and an analytical approach to the solution were proposed in the works [17–19], where the contact problem of shear of the half-space surface with an exponential shear modulus by a strip infinite punch with a flat shape of the base was considered. The problem of determining the parameters of the exponential shear modulus from contact stresses and displacements of the free surface was also investigated there. In the works cited, the shear modulus of inhomogeneous half-space varied by depth y according to the law

$$\mu_1(y) = \mu_0 e^{2d y}, \quad 0 \leq y < \infty, \tag{3.6}$$

where μ_0 is the value of the shear modulus on the surface of the half-space, and d is the parameter characterizing the rate of change of the shear modulus by depth.

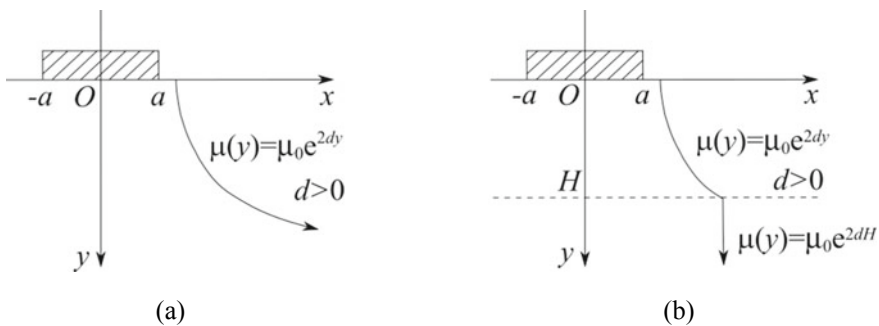


Fig. 3.1 Models of an inhomogeneous half-space

The construction of a solution for model (b) of an inhomogeneous half-space was carried out based on a numerical–analytical approach developed in [31–37]. The proposed method made it possible to construct solutions to contact problems based on the numerical calculation of the kernel transforms of integral equations and their subsequent approximations by analytical expressions. In this case, the model of an inhomogeneous half-space was used, which consisted of an inhomogeneous layer lying with adhesion on an elastic homogeneous half-space, i.e., the shear modulus of such a half-space varied according to an arbitrary law up to a certain depth H , and after that it stabilized and became constant. In the present work, it is assumed that the shear modulus of the inhomogeneous layer varies according to the exponential law

$$\mu_2(y) = \begin{cases} \mu_0 e^{2dy}, & 0 \leq y \leq H \\ \mu_0 e^{2dH}, & H < y < \infty \end{cases} \quad (3.7)$$

where H is the thickness of the surface inhomogeneous layer.

3.4 Integral Equations of Contact Problems and Solution Methods

To construct a solution of the problem (3.1)–(3.5), the integral Fourier transformation is used. The solution of the problem is reduced to the solution of an integral equation of the Fourier convolution type of the first kind with a difference kernel with respect to the unknown contact stresses $\varphi(\xi)$.

In the case of model (a), we write the integral equation in the form [17–19]

$$\int_{-a}^a \varphi(\xi) d\xi \int_{-\infty}^{\infty} K(\alpha) e^{i\alpha(\xi-x)} d\alpha = 2\pi\mu_1(0)\varepsilon, \quad |x| \leq a, \quad (3.8)$$

$$K(\alpha) = \left(d + \sqrt{d^2 + \alpha^2} \right)^{-1} \quad (3.9)$$

The kernel of the integral equation has the following asymptotic properties:

$$K(\alpha) = |\alpha|^{-1} + O(\alpha^{-2}) \text{ at } |\alpha| \rightarrow \infty, \quad (3.10)$$

$$K(\alpha) = K(0) + O(\alpha^2) \text{ at } |\alpha| \rightarrow 0, \quad (3.11)$$

After the transition in the integral equation Eq. (3.8) to dimensionless coordinates, we denote the dimensionless parameter of the problem $\lambda_1 = \frac{1}{da}$. To construct effective analytical solutions of the integral Eq. (3.8), asymptotic methods are used. For small values of the dimensionless parameter $\lambda_1 \in (0, \lambda_0)$, the solution of the

integral equation is constructed as the zero term of the Neumann series based on the Wiener–Hopf method [38] using the simplest kernel approximations of $K(\alpha)$. When constructing a solution of the integral equation in the case of large values of the parameter $\lambda_1 \in (\lambda_0, \infty)$, as in [39], expansions into power series of parameter λ_1 are used and the solution is written as a double functional series in powers of λ_1 .

In the case of model (b), we write the integral equation according to [31] for unknown contact stresses in the form

$$\int_{-a}^a \varphi(\xi) d\xi \int_{-\infty}^{\infty} \frac{1}{|\alpha|} L(\alpha) e^{i\alpha(\xi-x)} d\alpha = 2\pi\mu_2(0)\varepsilon, \quad |x| \leq a \quad (3.12)$$

Having made the transition in the integral equation Eq. (3.12) to dimensionless coordinates, we denote the dimensionless geometric parameter of the problem $\lambda_2 = \frac{H}{a}$. The kernel transform of the integral equation is constructed analytically [31–37].

The function $L(\alpha)$ from the integral Eq. (3.12) has the following asymptotic properties:

$$L(\alpha) = 1 + O(\alpha^{-2}) \text{ at } |\alpha| \rightarrow \infty, \quad (3.13)$$

$$L(\alpha) = L(0) + O(\alpha^2) \text{ at } |\alpha| \rightarrow 0, \quad (3.14)$$

The numerically constructed kernel transform of the integral equation is approximated by the following product

$$L(\alpha) = L_{\Pi}^N(\alpha) \equiv \prod_{i=1}^N \frac{\alpha^2 + A_i^2}{\alpha^2 + B_i^2}; \quad (B_i - B_k)(A_i - A_k) \neq 0 \text{ where } i \neq k \quad (3.15)$$

An approximate analytical solution of the integral equation is constructed, based on the proposed approximation. This solution is effective over the entire range of values of the dimensionless geometrical parameter λ_2 .

3.5 Numerical Analysis

Figures 3.2 and 3.3 show the kernel transforms of integral equations for two models of an inhomogeneous by depth half-space for different values of the parameters d and H . For model (a), the kernel transforms $K(\alpha)$ are constructed analytically, and the graphs show the functions $|\alpha|K(\alpha)$. For model (b), numerically constructed transforms $L(\alpha)$ are shown. The figures also schematically show the laws of inhomogeneity.

Reduced contact stresses are constructed in the area of problem parameters (d , H), at which the relative difference of the kernel transforms $|\alpha|K(\alpha)$ and $L(\alpha)$ of integral Eqs. (3.8) and (3.12), constructed analytically and numerically–analytically,

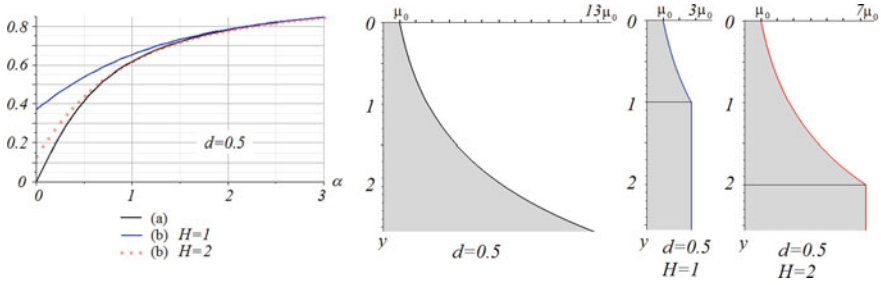


Fig. 3.2 Kernel transforms of integral equations $|\alpha|K(\alpha)$ at $d = 0.5$ for model **a** and $L(\alpha)$ at $d = 0.5$, $H = 1$ and $H = 2$ for model **b** and laws of inhomogeneity

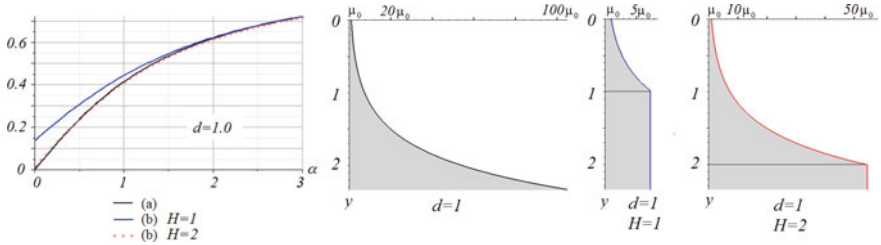


Fig. 3.3 Kernel transforms of integral equations $|\alpha|K(\alpha)$ at $d = 1$ for model **a** and $L(\alpha)$ at $d = 1$, $H = 1$ and $H = 2$ for model **b** and laws of inhomogeneity

respectively, does not exceed a few percent. Figures 3.4 and 3.5 show the reduced contact shear stresses calculated for the same parameters d and H , as in Figs. 3.2 and 3.3. In the case of model (a) in the Fig. 3.4, the solution is built in the form of a double functional series in powers of the dimensionless parameter $\lambda_1 = 2$, that corresponds to the case of large values of the parameter $\lambda_1 \in (\lambda_0, \infty)$. In the case of model (a) in the Fig. 3.5, the solution is constructed by the Wiener-Hopf method at $\lambda_1 = 1$, that corresponds to the case of small values of the dimensionless parameter $\lambda_1 \in (0, \lambda_0)$. In the case of model (b) in the Figs. 3.4 and 3.5, the solution is constructed by the bilateral asymptotic method [31, 32] at $\lambda_2 = 1$ and $\lambda_2 = 2$ and the simplest approximation of the kernel transform of the form (3.15) at $N = 1$ is used.

Numerical results show that the contact stresses constructed on the basis of two approaches in the domain of the problem parameters, in which the kernel transforms of the integral equations coincide with an accuracy of 5–7%, also give an error not exceeding 5–7%.

Fig. 3.4 Reduced contact stresses at $d = 0.5$ for model (a) and at $d = 0.5, H = 1$ and $H = 2$ for model (b)

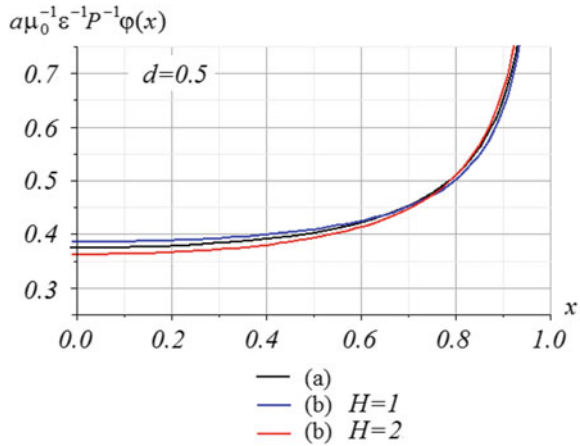
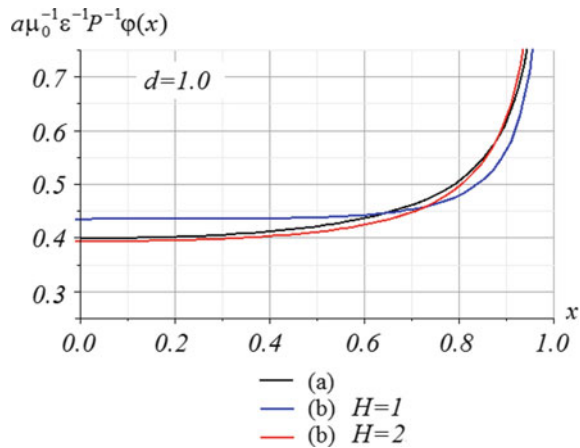


Fig. 3.5 Reduced contact stresses at $d = 1$ for model (a) and at $d = 1, H = 1$ and $H = 2$ for model (b)



3.6 Conclusion

Using the example of contact problems on the shear of the surface of an elastic half-space inhomogeneous by depth and the shear of the surface of an elastic layer inhomogeneous by depth, lying with adhesion on an elastic homogeneous half-space, a comparative analysis of solutions is carried out. The values of the characteristic parameters of the problems are determined for which the contact stresses for these two models of inhomogeneous media are close to each other.

Acknowledgements The study was supported by the Russian Science Foundation grant No. 22-19-00732.

References

1. Popov, G.Ya.: On the theory of plate bending on an elastic inhomogeneous half-space. *Isvestiya vuzov. Stroitel'stvo i arkhitektura* (11–12), 11–19 (1959)
2. Shiraki, Y., Usami, N. (eds.): *Silicon–Germanium (SiGe) Nanostructures: Production Properties and Applications in Electronics*. Woodhead Publishing, Cambridge, UK (2011)
3. Miyamoto, Y., Kaysser, W.A., Rabin, B.H., Kawasaki, A., Ford, R.G. (eds.): *Functionally Graded Materials: Design, Processing and Applications*. Springer, New York, NY, USA (1999)
4. Kuprin, A.S., Gilewicz, A., Kuznetsova, T.A., Lapitskaya, V.A., Tolmachova, G.N., Warcholinski, B., Aizikovich, S., Sadyrin, E.V.: Structure and properties of ZrON coatings synthesized by cathodic arc evaporation. *Materials* **14**(6), 1483 (2021)
5. Melnikova, G., Kuznetsova, T., Lapitskaya, V., Petrovskaya, A., Chizhik, S., Zykova, A., Safonov, V., Aizikovich, S., Sadyrin, E., Sun, W., Yakovin, S.: Nanomechanical and nanotribological properties of nanostructured coatings of tantalum and its compounds on steel substrates. *Nanomaterials* **11**(9), 2407 (2021)
6. Sadyrin, E.V.: Correlating the mechanical properties to the mineral density of brown spot lesion in dentine using nanoindentation and X-ray micro-tomography. In: *Advanced Materials Modelling for Mechanical, Medical and Biological Applications*, pp. 389–398. Springer, Cham (2022)
7. Gibson, R.E.: Some results concerning displacements and stresses in a non-homogeneous elastic half-space. *Geotechnique* **17**(1), 58–67 (1967)
8. Giannakopoulos, A.E., Suresh, S.: Indentation of solids with gradients in elastic properties: Part I. Point force. *Int. J. Solids Struct.* **34**, 2357–2428 (1997)
9. Giannakopoulos, A.E., Suresh, S.: Indentation of solids with gradients in elastic properties: Part II. Axisymmetric indentors. *Int. J. Solids Struct.* **34**(19), 2393–2428 (1997)
10. Katebi, A., Selvadurai, A.P.S.: A frictionless contact problem for a flexible circular plate and an incompressible non-homogeneous elastic half-space. *Int. J. Mech. Sci.* **90**, 239–245 (2015)
11. Aizikovich, S.M., Vasil'ev, A.S., Volkov, S.S.: The axisymmetric contact problem of the indentation of a conical punch into a half-space with a coating inhomogeneous in depth. *J. Appl. Math. Mech.* **79**(5), 500–505 (2015)
12. Guler, M.A., Erdogan, F.: Contact mechanics of graded coatings. *Int. J. Solids Struct.* **41**, 3865–3889 (2004)
13. Selvadurai, A.P.S., Singh, B.M., Vrbik, J.: A Reissner-Sagoci problem for a non-homogeneous elastic solid. *J. Elast.* **16**, 383–391 (1986)
14. Selvadurai, A.P.S., Katebi, A.: Mindlin's problem for an incompressible elastic half-space with an exponential variation in the linear elastic shear modulus. *Int. J. Eng. Sci.* **65**, 9–21 (2013)
15. Tokovyy, Y., Ma, C.-C.: An analytical solution to the three-dimensional problem on elastic equilibrium of an exponentially-inhomogeneous layer. *J. Mech.* **31**(5), 545–555 (2015)
16. Selvadurai, A.P.S., Katebi, A.: The Boussinesq–Mindlin problem for a non-homogeneous elastic halfspace. *Zeitschrift für angewandte Mathematik und Physik* **67**, 68 (2016)
17. Zelentsov, V.B., Lapina, P.A., Mitrin, B.I., Kudish, I.I.: An antiplane deformation of a functionally graded half-space. In: *Continuum Mechanics and Thermodynamics* **34**, 909–920 (2022)
18. Zelentsov, V.B., Lapina, P.A., Mitrin, B.I., Eremeyev, V.A.: Characterization of the functionally graded shear modulus of a half-space. *Mathematics* **8**(4) (2020). Article no. 640
19. Zelentsov, V.B., Lapina, P.A., Zagrebneva, A.D.: Method for determining the parameters of the exponential shear modulus of a functional-gradient half-space. In: Altenbach, H., Eremeyev, V.A., Galybin, A., Vasiliev, A. (eds.) *Advanced Materials Modelling for Mechanical, Medical and Biological Applications*. *Advanced Structured Materials*, vol. 155. Springer, Cham (2022)
20. Awojobi, A.O.: On the hyperbolic variation of elastic modulus in a non-homogeneous stratum. *Int. J. Solids Struct.* **12**, 739–748 (1976)
21. Kassir, M.K.: The Reissner-Sagoci problem for a non-homogeneous solid. *Int. J. Eng. Sci.* **8**(10), 875–885 (1970)

22. Altenbach, H., Eremeyev, V.A.: Eigen-vibrations of plates made of functionally graded material. *Comput. Mater. Continua* **9**(2), 153–177 (2009)
23. Kulchitsky-Zhyhailo, R., Bajkowski, A.: Analytical and numerical methods of solution of three-dimensional problem of elasticity for functionally graded coated half-space. *Int. J. Mech. Sci.* **54**, 105–112 (2012)
24. Gibson, R.E., Sills, G.C.: Settlement of a strip load on a non-homogeneous orthotropic incompressible elastic half-space. *Quart. J. Mech. Appl. Math.* **28**, 233–243 (1975)
25. Chen, P., Chen, S.: Contact behaviors of a rigid punch and a homogeneous half-space coated with a graded layer. *Acta Mechanica* **223**, 563–577 (2012)
26. Liu, T.-J., Wang, Y.-S., Zhang, C.-Z.: Axisymmetric frictionless contact of functionally graded materials. *Arch. Appl. Mech.* **78**, 267–282 (2008)
27. Ke, L.-L., Wang, Y.-S.: Two-dimensional sliding frictional contact of functionally graded materials. *Eur. J. Mech. A/Solids* **26**, 171–188 (2007)
28. Çömez, İ: Contact problem for a functionally graded layer indented by a moving punch. *Int. J. Mech. Sci.* **100**, 339–344 (2015)
29. Su, J., Ke, L.-L., Wang, Y.-S.: Axisymmetric frictionless contact of a functionally graded piezoelectric layered half-space under a conducting punch. *Int. J. Solids Struct.* **90**, 45–59 (2016)
30. Kudish, I.I., Pashkovski, E., Volkov, S.S., Vasiliev, A.S., Aizikovich, S.M.: Heavily loaded line EHL contacts with thin adsorbed soft layers. *Math. Mech. Solids* **25**(4), 1011–1037 (2020)
31. Aizikovich, S.M.: Shear by a stamp of an elastic inhomogeneous half-space of a special form. *Izvestiya AN SSSR. MTT.* (5), 74–80 (1978)
32. Aizikovich, S.M.: An asymptotic solution of a class of coupled equations. *J. Appl. Math. Mech.* **54**(5), 719–724 (1990)
33. Aizikovich, S., Vasiliev, A., Seleznev, N.: Inverse analysis for evaluation of the shear modulus of inhomogeneous media by torsion experiments. *Int. J. Eng. Sci.* **48**(10), 936–942 (2010)
34. Aizikovich, S.M., Vasiliev, A.S.: A bilateral asymptotic method of solving the integral equation of the contact problem of the torsion of an elastic half-space inhomogeneous in depth. *J. Appl. Math. Mech.* **77**(1), 91–97 (2013)
35. Volkov, S., Aizikovich, S., Wang, Y.-S., Fedotov, I.: Analytical solution of axisymmetric contact problem about indentation of a circular indenter into a soft functionally graded elastic layer. *Acta Mechanica Sinica* **29**(2), 196–201 (2013)
36. Krenev, L.I., Aizikovich, S.M., Tokovyy, Y.V., Wang, Y.-Ch.: Axisymmetric problem on the indentation of a hot circular punch into an arbitrarily nonhomogeneous half-space. *Int. J. Solids Struct.* **59**(1), 18–28 (2015)
37. Vasiliev, A.S., Volkov, S.S., Sadyrin, E.V., Aizikovich, S.M.: Simplified analytical solution of the contact problem on indentation of a coated half-space by a conical punch. *Mathematics* **8**(6), 983 (2020)
38. Noble, B.: *Methods Based on the Wiener-Hopf Technique for the Solution of Partial Differential Equations*. Pergamon Press, London, UK (1958)
39. Aleksandrov, V.M., Belokon', A.V.: Asymptotic solution of a class of integral equations and its application to contact problems for cylindrical elastic bodies. *J. Appl. Math. Mech.* **31**(4), 718–724 (1967)

Chapter 4

Docking of Inhomogeneous Surfaces of Piezoelectric Layers in a Composite Waveguide as a Harvesters of Wave Energy



Ara S. Avetisyan and Andranik A. Kamalyan

Abstract A piezoelectric waveguide, consisting of two layers rigidly connected to each other along non-smooth surfaces, is modeled as a three-layer sandwich with an internal periodically inhomogeneous thin layer. Taking into account the periodicity of the inhomogeneity of the simulated waveguide, in order to study the propagation of normal waves in it, according to the Lyapunov–Floquet theory, the boundary value problem of electro elasticity is solved by the width of the formed periodic cell. The systems of quasi-static equations of electroacoustics are solved in the rectangular-shaped virtual cuts formed in two main homogeneous piezoelectric layers. In the newly formed rectangles of the inner inhomogeneous thin layer, hypothetical solutions are constructed, taking into account the hypothetical inhomogeneity of the material both over the thickness of this layer and its periodicity along the waveguide. In the case of particular longitudinal inhomogeneities of the inner layer, the propagation of a high-frequency electroacoustic signal of antiplane deformation, when the length of the short-wavelength signal is comparable to the linear dimensions of the surface roughness, is studied. The regions of permissible lengths of a propagating wave in a periodic structure are determined. A dispersion equation is obtained for the propagation of a normal electroacoustic signal in a composite waveguide. A strong localization of wave energy near an inhomogeneous junction of piezoelectric layers is revealed. It is shown that the seam along the surface roughness of the layers can become a harvester for a wave energy in a composite waveguide.

Keywords Piezoelectric waveguide · Non-smooth surfaces · Periodically inhomogeneous · Hypothetical solutions · Antiplane deformation · Electroacoustic signal · Permissible length · Wave energy harvester

A. S. Avetisyan (✉) · A. A. Kamalyan
Institute of Mechanics of National Academy of Sciences of Armenia,
24b Baghramyan Ave., 0019 Yerevan, Republic of Armenia
e-mail: ara.serg.avetisyan@gmail.com

A. A. Kamalyan
e-mail: Kamalyan.Andranik@yahoo.com

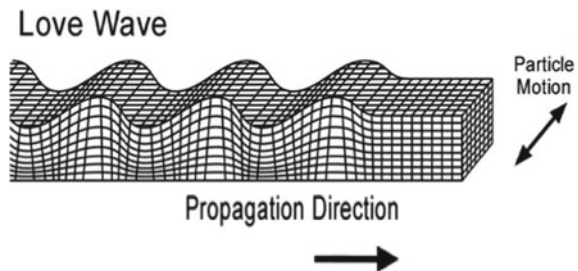
4.1 Introduction

An important problem in modern technical problems is the harvesting of energy (or part of the energy) of a dynamic process. In many ways, the possibility of energy harvesting is determined by the composition of its carriers and the nature of the assembly element. An interesting example of wave energy propagation is a relatively simple dynamic process: the propagation of an electroactive elastic shear wave, type SH , in a layered piezoelectric waveguide. A two-component wave transfers the energy of an elastic wave and the energy of an electric field oscillation that accompanies it. In the case of propagation of a high-frequency (short-wavelength) wave signal in a composite waveguide, wave energy can be localized near the interfaces of the layers.

In 1911, Love showed that, in contrast to elastic waves of plane deformation, the localization of the wave energy of elastic pure shear waves (SH waves) is possible in the near-surface zone of an elastic half-space at the junction with a layer of softer material [1] (Fig. 4.1). This showed that the localization of the wave energy of elastic shear waves of the SH type can be a consequence of discontinuities in the physical and mechanical characteristics (properties) of the material at the interface between the media, or a consequence of near-surface inhomogeneities of the material. In 1968 Bleustein [2], and in 1969, Gulyaev [3] confirmed the assumption about the existence of localization of the wave energy of an electroactive elastic wave (SH type) near a mechanically free smooth surface of a piezoelectric medium of a certain symmetry, under different boundary conditions on the accompanying electric field [4]. However, as shown in [5], the formulation of the electroelastic problem of antiplane deformation in an anisotropic piezoelectric material is possible only in certain sagittal planes of piezoelectric media. This means that the existence of Gulyaev-Bleustein waves is not possible in all piezoelectric homogeneous bodies. Electroelastic waves of SH polarization exist in the corresponding layered Love schemes, with a piezoelectric substrate [6–10]. Depending on the ratio of the physical and mechanical characteristics of the materials of the piezoelectric substrate and the thin layer, in some of these schemes, along with the multimode Love wave, there is a single-mode Gulyaev–Bleustein wave.

Thermomechanical technological processing of the surface of a solid deformable element practically does not ensure the ideal smoothness of this surface. To ensure the

Fig. 4.1 Structural diagram of the Love wave



required smoothness on the outer surfaces in the composite waveguide, the residual geometric inhomogeneities of the layers (roughness) are poured with a softer material and smoothed out. Smoothness on the internal surfaces of the adhesion of layers in a composite waveguide is provided by thermal pressing of the layers one into another, or by ultrasonic welding of non-smooth surfaces.

In both cases, thermal diffusion occurs and inhomogeneous thin layers appear on the surfaces of the main layers. Depending on the ratio of the physical and mechanical characteristics of the materials, the emerging layers can become energy collectors of the high-frequency wave propagating along the composite waveguide.

Without violating the generality of reasoning, we will consider the case of only the roughness of the inner surfaces at the junction of the piezoelectric layers. The roughness of the outer surfaces is neglected.

4.2 Modeling of a Two-Layer Piezoelectric Waveguide, Taking into Account the Roughness of the Surfaces of the Constituent Layers

Let two homogeneous 6mm class piezoelectric layers of hexagonal symmetry, with thicknesses, respectively, H_1 and H_2 , and with surface periodic irregularities $h_{1\pm}(x) = h_{1\pm}(x + d_1)$ and $h_{2\pm}(x) = h_{2\pm}(x + d_2)$, respectively, are pressed, providing perfect adhesion between them. Then, if $R_{1\pm} = \max |h_{1\pm}(x)|$ and $R_{2\pm} = \max |h_{2\pm}(x)|$ are considered, as the maximum deviations of the roughness of these surface irregularities, then an inhomogeneous thin layer with a thickness of $|h_{1-}(x)| + |h_{2+}(x)| \leq R_{1-} + R_{2+} = 2R_0$ is appear between the main layers (Fig. 4.2).

Considering thermal diffusion, it can be assumed that the material of the newly formed surface layer will be inhomogeneous. Then, the physical and mechani-

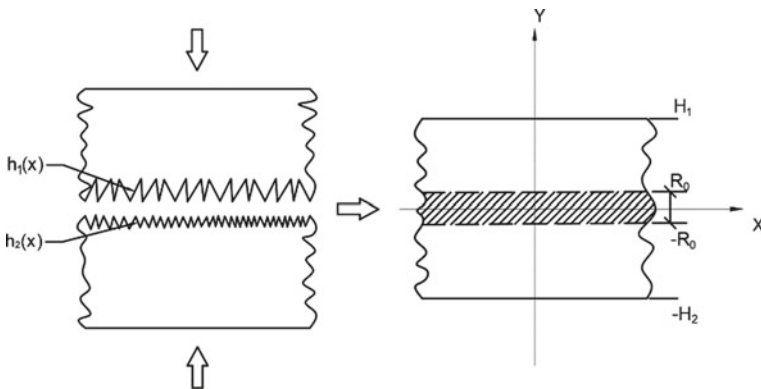


Fig. 4.2 Layered waveguide of two pressed piezoelectric layers with non-smooth surfaces.eps

cal characteristics of the formed inhomogeneous piezoelectric layer will change along the thickness of the formed layer $\gamma_0(x, y) = \gamma_{p1}(x)[\gamma_{p1}(x)/\gamma_{p2}(x)]^{(y-R_0)/2R_0}$, taking on the virtually selected surfaces of the layer $y = R_0$ and $y = -R_0$ the values of the materials of the neighboring main homogeneous piezoelectric layers $\gamma_{p1} \in \{c_{44}^{(p1)}, \rho_{p1}, e_{15}^{(p1)}, \varepsilon_{11}^{(p1)}\}$ and $\gamma_{p2} \in \{c_{44}^{(p2)}, \rho_{p2}, e_{15}^{(p2)}, \varepsilon_{11}^{(p2)}\}$ [11, 12]

$$\begin{aligned} c_{44}^{(0)}(x, y) &= c_{44}^{(p1)}(x, R_0)[c_{44}^{(p1)}(x, R_0)/c_{44}^{(p2)}(x, -R_0)]^{\frac{y-R_0}{2R_0}}, \\ \rho_0(x, y) &= \rho_{p1}(x, R_0)[\rho_{p1}(x, R_0)/\rho_{p2}(x, -R_0)]^{\frac{y-R_0}{2R_0}}, \end{aligned} \quad (4.1)$$

$$\begin{aligned} e_{15}^{(0)}(x, y) &= e_{15}^{(p1)}(x, R_0)[e_{15}^{(p1)}(x, R_0)/e_{15}^{(p2)}(x, -R_0)]^{\frac{y-R_0}{2R_0}}, \\ \varepsilon_{11}^{(0)}(x, y) &= \varepsilon_{11}^{(p1)}(x, R_0)[\varepsilon_{11}^{(p1)}(x, R_0)/\varepsilon_{11}^{(p2)}(x, -R_0)]^{\frac{y-R_0}{2R_0}} \end{aligned} \quad (4.2)$$

The interlayer formed between the main layers will also be periodically inhomogeneous along the waveguide. The physical and mechanical characteristics of the material of the formed interlayer will change along the waveguide. In particular, in (4.1) and (4.2) for the material characteristics can be represented

$$\begin{aligned} c_{44}^{(p1)}(x) &= c_{44}^{(1)}f_1(x), \quad \rho_{p1}(x) = \rho_1f_1(x), \\ e_{15}^{(p1)}(x) &= e_{15}^{(1)}f_1(x), \quad \varepsilon_{11}^{(p1)}(x) = \varepsilon_{11}^{(1)}f_1(x) \end{aligned} \quad (4.3)$$

in $(m-1)d - d_1 < x < (m-1)d$

$$\begin{aligned} c_{44}^{(p2)}(x) &= c_{44}^{(2)}f_2(x), \quad \rho_{p2}(x) = \rho_2 \cdot f_2(x), \\ e_{15}^{(p2)}(x) &= e_{15}^{(2)}f_2(x), \quad \varepsilon_{11}^{(p2)}(x) = \varepsilon_{11}^{(2)} \cdot f_2(x) \end{aligned} \quad (4.4)$$

in $(m-1)d < x < md - d_1$,

where $f_1(x) = \exp[a_1(x - (m-1)d)]$ and $f_2(x) = \exp[a_2(x - (m-1)d)]$ are the functions of the longitudinal inhomogeneity in each given section $m \in \mathbb{N}^+$ of the cell of the formed interlayer [13].

Inhomogeneous both in thickness and length, a piezoelectric layer with transverse cells $(m-1)d - d_1 < x < (m-1)d \cup (m-1)d < x < md - d_1$, is modeled as a multi-cell three-layer waveguide, with a thin, periodically inhomogeneous piezoelectric layer $\{|x| < \infty; |y| < R_0; |z| < \infty\}$ between two homogeneous piezoelectric layers

$$\{|x| < \infty; -H_2 - R_0 \leq |y| \leq -R_0; |z| < \infty\}$$

and

$$\{|x| < \infty; R_0 \leq |y| \leq H_1 - R_0; |z| < \infty\}.$$

4.3 Formulation of a Mathematical Boundary Value Problem in a Three-Layer Sandwich with a Thin Inhomogeneous Filling

In the problem of electroactive antiplane deformation, in the main layers

$$\{|x| < \infty; R_0 \leq |y| \leq H_1 - R_0; |z| < \infty\}$$

and

$$\{|x| < \infty; -H_2 - R_0 \leq |y| \leq -R_0; |z| < \infty\}$$

of the layered waveguide “*piezoelectric-1*” and “*piezoelectric-2*” from piezoelectric materials of class 6mm of hexagonal symmetry, not zero mechanical stresses $\sigma_{zx}^{(n,m)}(x, y, t)$ and $\sigma_{yz}^{(n,m)}(x, y, t)$, but also the components of the electric displacement vector $D_x^{(n,m)}(x, y, t)$ and $D_y^{(n,m)}(x, y, t)$ are written in the known form

$$\begin{aligned} \sigma_{zx}^{(n,m)}(x, y, t) &= c_{44}^{(n)} w_{nm,x}(x, y, t) + e_{15}^{(n)} \varphi_{nm,x}(x, y, t), \\ \sigma_{yz}^{(n,m)}(x, y, t) &= c_{44}^{(n)} w_{nm,y}(x, y, t) + e_{15}^{(n)} \varphi_{nm,y}(x, y, t), \end{aligned} \quad (4.5)$$

$$\begin{aligned} D_x^{(n,m)}(x, y, t) &= e_{15}^{(n)} w_{nm,x}(x, y, t) - \varepsilon_{11}^{(n)} \varphi_{nm,x}(x, y, t), \\ D_y^{(n,m)}(x, y, t) &= e_{15}^{(n)} w_{nm,y}(x, y, t) - \varepsilon_{11}^{(n)} \varphi_{nm,y}(x, y, t). \end{aligned} \quad (4.6)$$

In formed rectangles of these homogeneous piezoelectric layers, numbered $n = \{1; 2\}$, respectively, the well-known quasi-static equations of electroactive antiplane deformation will be solved

$$\begin{aligned} w_{nm,xx}(x, y) + w_{nm,yy}(x, y) &= -\omega^2 \left(\rho_n \tilde{c}_{44}^{(n)} \right) w_{nm}(x, y), \\ \varphi_{nm,xx}(x, y) + \varphi_{nm,yy}(x, y) &= \left(e_{15}^{(n)} / \varepsilon_{11}^{(n)} \right) [w_{nm,xx}(x, y) + w_{nm,yy}(x, y)] \end{aligned} \quad (4.7)$$

In the systems of Eq. (4.7), $\tilde{c}_{44}^{(n)} = c_{44}^{(n)} (1 + \chi_n^2)$ is the reduced shear stiffness, and $\chi_n^2 = [e_{15}^{(n)}]^2 / (c_{44}^{(n)} \varepsilon_{11}^{(n)})$ is the coefficient of electromechanical coupling of a homogeneous piezoelectric medium under the number “ n ”.

In a virtually isolated inhomogeneous piezoelectric layer $\{|x| < \infty; |y| < R_0; |z| < \infty\}$, the adhesion of two piezoelectrics, non-zero components of the mechanical stress tensor and the electric displacement vector in the problem of electroactive antiplane deformation, are also written in the form (4.5) and (4.6), but with variable coefficients (4.1) and (4.2)

$$\begin{aligned} \sigma_{zx}^{(0m)}(x, y, t) &= c_{44}^{(0)}(x, y) w_{0m,x}(x, y, t) - e_{15}^{(0)}(x, y) \varphi_{0m,x}(x, y, t), \\ \sigma_{yz}^{(0m)}(x, y, t) &= c_{44}^{(0)}(x, y) w_{0m,y}(x, y, t) - e_{15}^{(0)}(x, y) \varphi_{0m,y}(x, y, t), \end{aligned} \quad (4.8)$$

$$\begin{aligned} D_x^{(0m)}(x, y, t) &= e_{15}^{(0)}(x, y)w_{0m,x}(x, y, t) + \varepsilon_{11}^{(0)}(x, y)\varphi_{0m,x}(x, y, t), \\ D_y^{(0m)}(x, y, t) &= e_{15}^{(0)}(x, y)w_{0m,y}(x, y, t) + \varepsilon_{11}^{(0)}(x, y)\varphi_{0m,y}(x, y, t). \end{aligned} \quad (4.9)$$

Taking into account the periodic inhomogeneity of the formed interlayer, the desired values $w_0(x, y, t)$ and $\varphi_0(x, y, t)$ in this interlayer will be further represented in the form of Bloch-Floquet waves $f_0(x + s, y, t) = \mu(\omega)f_0(x, y, t)$, where $\mu(\omega) = \exp[isk(\omega)]$ the coefficient of periodicity of the Floquet waves is. Then, the system of equations of electroactive antiplane deformation in the interlayer can be conveniently written as

$$\begin{aligned} -\sigma_{yz,y}^{(0m)}(x, y) &= c_{44}^{(0)}(x, y)w_{0m,xx}(x, y) + e_{15}^{(0)}(x, y)\varphi_{0m,xx}(x, y) \\ &\quad + c_{44,x}^{(0)}(x, y)w_{0m,x}(x, y) + e_{15,x}^{(0)}(x, y)\varphi_{0m,x}(x, y) + \omega^2\rho_0(x, y)w_0(x, y), \\ -D_{y,y}^{(0m)}(x, y) &= e_{15}^{(0)}(x, y)w_{0m,xx}(x, y) - \varepsilon_{11}^{(0)}(x, y)\varphi_{0m,xx}(x, y) \\ &\quad + e_{15,x}^{(0)}(x, y)w_{0m,x}(x, y) - \varepsilon_{11,x}^{(0)}(x, y)\varphi_{0m,x}(x, y) \end{aligned} \quad (4.10)$$

The conditions of conjugation of electromechanical fields on virtually drawn surfaces $y = -R_0$ and $y = R_0$, respectively, will be written in the form

$$\begin{aligned} c_{44}^{(2)}w_{2,y}(x, -R_0) + e_{15}^{(2)}\varphi_{2,y}(x, -R_0) \\ = c_{44}^{(0)}(x, -R_0)w_{0,y}(x, -R_0) + e_{15}^{(0)}(x, -R_0)\varphi_{0,y}(x, -R_0) \\ e_{15}^{(2)}w_{2,y}(x, -R_0) - \varepsilon_{11}^{(2)}\varphi_{2,y}(x, -R_0) \\ = e_{15}^{(0)}(x, -R_0)w_{0,y}(x, -R_0) - \varepsilon_{11}^{(0)}(x, -R_0)\varphi_{0,y}(x, -R_0) \end{aligned} \quad (4.11)$$

$$w_2(x, -R_0) = w_0(x, -R_0); \quad \varphi_2(x, -R_0) = \varphi_0(x, -R_0) \quad (4.12)$$

$$\begin{aligned} c_{44}^{(1)}w_{1,y}(x, R_0) + e_{15}^{(1)}\varphi_{1,y}(x, R_0) \\ = c_{44}^{(0)}(x, R_0)w_{0,y}(x, R_0) + e_{15}^{(0)}(x, R_0)\varphi_{0,y}(x, R_0) \\ e_{15}^{(1)}w_{1,y}(x, R_0) - \varepsilon_{11}^{(1)}\varphi_{1,y}(x, R_0) \\ = e_{15}^{(0)}(x, R_0)w_{0,y}(x, R_0) - \varepsilon_{11}^{(0)}(x, R_0)\varphi_{0,y}(x, R_0) \end{aligned} \quad (4.13)$$

$$w_1(x, R_0) = w_0(x, R_0); \quad \varphi_1(x, R_0) = \varphi_0(x, R_0). \quad (4.14)$$

On the external surfaces $y = H_1$ and $y = -H_2$ of a piezoelectric layered waveguide, we consider the case of mechanically free and electrically open smooth surfaces in which the localization of wave energy is not possible [11, 12]. These conditions correspond to the case of strong dielectric piezoelectrics, for which $\varepsilon_{11}^{(p1)} \gg \varepsilon_0$. In this case, the surface conditions take on a rather simple form

$$w_{1,y}(x, y)\Big|_{y=H_1} = 0; \quad \varphi_{1,y}(x, y)\Big|_{y=H_1} = 0. \quad (4.15)$$

$$w_{2,y}(x, y)\Big|_{y=-H_2} = 0; \quad \varphi_{2,y}(x, y)\Big|_{y=-H_2} = 0. \quad (4.16)$$

4.4 Solution of the Mathematical Boundary Problem

According to the Lyapunov–Floquet theory, the propagation of normal waves requires consideration of the electro elasticity equations along the width of the specified cell. Taking into account the homogeneous surface conditions (4.15) and (4.16) on the mechanically free and electrically open surfaces of the waveguide, in each interlayer $m \in \{1; 2\}$ of a periodic cell

$$\{(m-1)d - d_1 < x < (m-1)d\} \cup \{(m-1)d < x < md - d_1\},$$

the short-wavelength solutions of the systems of quasi-static equations (4.7) in the form of normal waves can be written in the well-known form

$$\begin{aligned} w_{1m}(x, y, t) &= W_{1m}(R_0) \exp[-\alpha_{1m}k_m(\omega)(y - R_0)] \exp[i(k_m(\omega)x - \omega t)], \\ \varphi_{1m}(x, y, t) &= \frac{\Phi_{1m}(R_0)}{1 - \alpha_{1m}(e_{15}^{(1)}/\varepsilon_{11}^{(1)})} \cdot \\ &\cdot \frac{1 - \alpha_{1m}(e_{15}^{(1)}/\varepsilon_{11}^{(1)}) \exp[(\alpha_{1m} - 1)k_m(\omega)(y - R_0)]}{\exp[-\alpha_{1m}k_m(\omega)(y - R_0)]} \exp[i(k_m(\omega)x - \omega t)], \end{aligned} \quad (4.17)$$

$$\begin{aligned} w_{2m}(x, y, t) &= W_{2m}(-R_0) \exp[-\alpha_{2m}k_m(\omega)(y + R_0)] \exp[i(k_m(\omega)x - \omega t)], \\ \varphi_{2m}(x, y, t) &= \frac{\Phi_{2m}(-R_0)}{1 - \alpha_{2m}(e_{15}^{(2)}/\varepsilon_{11}^{(2)})} \cdot \\ &\cdot \frac{1 - \alpha_{2m}(e_{15}^{(2)}/\varepsilon_{11}^{(2)}) \exp[(1 - \alpha_{2m})k_m(\omega)(y + R_0)]}{\exp[\alpha_{2m}k_m(\omega)(y + R_0)]} \exp[i(k_m(\omega)x - \omega t)]. \end{aligned} \quad (4.18)$$

The wave formation parameters $\alpha_{1m}(\omega, k_m(\omega))$ and $\alpha_{2m}(\omega, k_m(\omega))$ in the main piezoelectric layers of the waveguide are defined as

$$\alpha_{nm}(\omega, k_m(\omega)) = \sqrt{1 - [C_{nt}\omega/k_m(\omega)]^2}.$$

$W_{1m}(R_0)$, $W_{2m}(-R_0)$, $\Phi_{1m}(R_0)$ and $\Phi_{2m}(-R_0)$ amplitudes of electroacoustic shear waves on virtually vibrated surfaces of a thin inhomogeneous layer of the waveguide. Based on the surface conditions (4.12) and (4.14), and taking into account the thinness of the formed internal inhomogeneous layer compared to the thicknesses of the main layers of the waveguide $2R_0 \ll \min\{H_1; H_2\}$, for elastic shear $w_{0m}(x, y, t)$ and the electric potential $\varphi_{0m}(x, y, t)$ of high-frequency electroacoustic waves in the inhomogeneous layer, we can hypothetically represent in the form [11, 12].

$$w_{0m}(x, y, t) = \left\{ \frac{\sin[\alpha_{0m}k_m(\omega)(y - R_0)]}{\sin[2\alpha_{0m}R_0k_m(\omega)]} [w_{1m}(-R_0) - w_{2m}(-R_0)] + w_{1m}(-R_0) \right\} \cdot \exp [i(k_m(\omega)x - \omega t)], \quad (4.19)$$

$$\varphi_{0m}(x, y, t) = \left\{ \frac{\sin[k_m(\omega)(y - R_0)]}{\sin[2\alpha_{0m}R_0k_m(\omega)]} [\Phi_{1m}(-R_0) - \Phi_{2m}(-R_0)] + \Phi_{1m}(-R_0) \right\} \cdot \exp [i(k_m(\omega)x - \omega t)]. \quad (4.20)$$

By choosing the representations of solutions (4.19) and (4.20), the surface conditions (4.12) and (4.14) are satisfied automatically, and the wave formation functions

$$\sin[\alpha_{0m}k_m(\omega)(y - R_0)]/\sin[2\alpha_{0m}R_0k_m(\omega)]$$

and

$$\sin[k_m(\omega)(y - R_0)]/\sin[2R_0k_m(\omega)]$$

describe the amplitude changes in the sought-for components of the wave field over the thickness of the virtual inhomogeneous interlayer. The wave formation coefficient of an electroactive elastic shear wave in them is defined as

$$\alpha_{0m}(\omega, k_m(\omega)) = \sqrt{\eta_{0m}^2(\omega, k_m(\omega)) - 1},$$

in which the phase velocity averaged over the thickness in an inhomogeneous layer will be represented as $\eta_{0m}(\omega, k_m(\omega)) = \omega/(\bar{C}_{0r}k_m(\omega))$. The averaged over the thickness velocity of a bulk shear wave $\bar{C}_{0r}(C_{p1}, C_{p2}) = \text{const}$ in an inhomogeneous thin piezoelectric layer is defined as

$$\begin{aligned} \bar{C}_{0r}^2(C_{p1}, C_{p2}) &= \frac{1}{2R_0} \int_{-R_0}^{R_0} \frac{c_{44}^{(0)}(\xi)}{\rho_0(\xi)} \left[1 + \frac{[e_{15}^{(0)}(\xi)]^2}{c_{44}^{(0)}(\xi)\varepsilon_{11}^{(0)}(\xi)} \right] d\xi \\ &= \left| \frac{C_{p1}^2 - C_{p2}^2}{\ln C_{p1}^2 - \ln C_{p2}^2} \right| + \left| \frac{\tilde{C}_{p1}^2 - \tilde{C}_{p2}^2}{\ln \tilde{C}_{p1}^2 - \ln \tilde{C}_{p2}^2} \right|. \end{aligned} \quad (4.21)$$

In the case of propagation of a long-wave electroacoustic wave signal, when $2R_0k(\omega) \ll 1$, the internal inhomogeneous layer does not affect the propagation of a normal wave. In the case of propagation of a short-wave (high-frequency) signal of an electroacoustic wave, when $2R_0k_m(\omega) \gg 1$, by substituting solutions (4.17)–(4.20) into surface conditions (4.11) and (4.13), a defining system of algebraic equations is obtained.

$$\begin{aligned}
& c_{44}^{(2)} \alpha_{0m} \text{ctg}[2\alpha_{0m} R_0 k_m(\omega)] W_{1m}(-R_0) \\
& + c_{44}^{(2)} [\alpha_{2m} - \alpha_{0m} \text{ctg}[2\alpha_{0m} R_0 k_m(\omega)]] W_{2m}(-R_0) \\
& + e_{15}^{(2)} \text{ctg}[2R_0 k_m(\omega)] \Phi_{1m}(-R_0) - e_{15}^{(2)} [(1 - \alpha_{2m}) \\
& - \text{ctg}[2R_0 k_m(\omega)]] \Phi_{2m}(-R_0) = 0, \\
& e_{15}^{(2)} \alpha_{0m} \text{ctg}[2\alpha_{0m} R_0 k_m(\omega)] W_{1m}(-R_0) \\
& + e_{15}^{(2)} [\alpha_{2m} - \alpha_{0m} \text{ctg}[2\alpha_{0m} R_0 k_m(\omega)]] W_{2m}(-R_0) \\
& - \varepsilon_{11}^{(2)} \text{ctg}[2R_0 k_m(\omega)] \Phi_{1m}(-R_0) + \varepsilon_{11}^{(2)} [(1 - \alpha_{2m}) \\
& + \text{ctg}[2R_0 k_m(\omega)]] \Phi_{2m}(-R_0) = 0, \\
& c_{44}^{(1)} [\alpha_{1m} + \alpha_{0m} \sec[2\alpha_{0m} R_0 k_m(\omega)]] W_{1m}(-R_0) \\
& - c_{44}^{(1)} \alpha_{0m} \cdot \sec[2\alpha_{0m} R_0 k_m(\omega)] W_{2m}(-R_0) \\
& + e_{15}^{(1)} [\sec[2R_0 k_m(\omega)] - 1] \Phi_{1m}(R_0) - e_{15}^{(1)} \sec[2R_0 k_m(\omega)] \Phi_{2m}(-R_0) = 0, \\
& e_{15}^{(1)} [\alpha_{1m} + \alpha_{0m} \sec[2\alpha_{0m} R_0 k_m(\omega)]] W_{1m}(-R_0) \\
& - e_{15}^{(1)} \alpha_{0m} \sec[2\alpha_{0m} R_0 k_m(\omega)] W_{2m}(-R_0) \\
& - \varepsilon_{11}^{(1)} [\sec[2R_0 k(\omega)] - 1] \Phi_{1m}(R_0) + \varepsilon_{11}^{(1)} \sec[2R_0 k_m(\omega)] \Phi_{2m}(-R_0) = 0.
\end{aligned} \tag{4.22}$$

To determine the wave numbers in the periodic interlayers of a three-layer waveguide, the dispersion equations are derived from this [14]

$$\text{tg}[2R_0 \alpha_{01}(\omega) k_1(\omega)] = c_{44}^{(0)} \alpha_{01}(\omega) \frac{c_{44}^{(p1)} \alpha_{11}(\omega) + c_{44}^{(p2)} \alpha_{21}(\omega)}{\left[c_{44}^{(p1)} \alpha_{11}(\omega) c_{44}^{(p2)} \alpha_{21}(\omega) - \left(c_{44}^{(0)} \alpha_{01}(\omega) \right)^2 \right]} \tag{4.23}$$

$$\text{tg}[2R_0 \alpha_{02}(\omega) k_2(\omega)] = c_{44}^{(0)} \alpha_{02}(\omega) \frac{c_{44}^{(p1)} \alpha_{12}(\omega) + c_{44}^{(p2)} \alpha_{22}(\omega)}{\left[c_{44}^{(p1)} \alpha_{12}(\omega) c_{44}^{(p2)} \alpha_{22}(\omega) - \left(c_{44}^{(0)} \alpha_{02}(\omega) \right)^2 \right]} \tag{4.24}$$

The system of dispersion relations (4.23) and (4.24) itself represents the dispersion equation of wave formation through the thickness of composite waveguide. Their joint solution provides synchronized values of wave numbers $k_1(\omega)$ and $k_2(\omega)$ in components of waveguide. The dispersion curves of localized shear micrometer waves $\lambda \sim 10^{-6}$ m at the junction of pairs of piezoelectrics PZT-4 with Cadmium Sulfide and PZT-5 with Zinc Oxide, for micrometer height $R_0 = 10^{-6}$ m and micrometer widths of protrusions and cavities of surface protrusions $d_1 = 10^{-6}$ m and $d_2 = 5 \times 10^{-7}$ m (Fig. 4.3).

High frequency shear Love and Gulyaev–Bleustein types waves for which $\min\{c_{1t}; c_{2t}\} \leq \omega/k(\omega) < \max\{c_{1t}; c_{2t}\}$ already will propagate in the composite

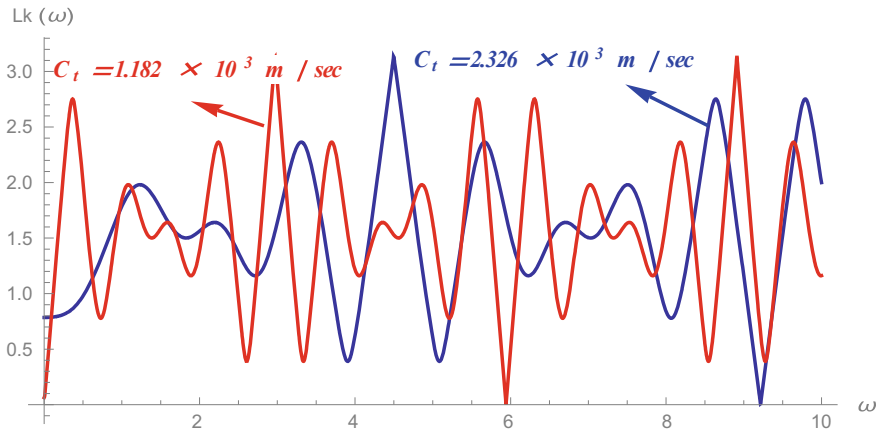


Fig. 4.3 The dispersion curves of localized shear micrometer waves $\lambda \sim 10^{-6}$ m at the junction of pairs of piezoelectrics **PZT-4 with Cadmium Sulfide** and **PZT-5 with Zinc Oxide**, for micrometer height $R_0 = 10^{-6}$ m and micrometer widths of protrusions and cavities of surface protrusions $d_1 = 10^{-6}$ m and $d_2 = 5 \times 10^{-7}$ m

waveguide of the same materials outside of frequency bands

$$0 < \omega \leq (\pi/R_0) \cdot [c_{1t}c_{2t}/(c_{1t}^2 - c_{2t}^2)]$$

(see Fig. 4.4). In this case, the forbidden (or allowed) frequency zones of localized Love and Gulyaev–Bleustein type waves are also determined from the dispersion equation

$$\begin{aligned} & \cos[Lk_F(\omega)] \\ &= \cos[ak_1(\omega)] \cos[bk_2(\omega)] - \frac{G_2^2 k_2^2(\omega) + G_1^2 k_1^2(\omega)}{2G_1 k_1(\omega) G_2 k_2(\omega)} \sin[ak_1(\omega)] \sin[bk_2(\omega)] \end{aligned} \quad (4.25)$$

already taking into account the frequency in the definition area

$$\omega \geq (\pi/R_0) \cdot [c_{1t}c_{2t}/(c_{1t}^2 - c_{2t}^2)]$$

(see Fig. 4.3).

Synchronization of shear wave propagation in general assumes the same allowed wave number, determined from (4.25)

$$\begin{aligned} k(\omega) = \frac{1}{L} \arccos \left\{ \frac{1}{4G_1 k_1(\omega) \cdot G_2 k_2(\omega)} \cdot \right. \\ \left. \cdot \left[[G_2 k_2(\omega) + G_1 k_1(\omega)]^2 \cos[d_1 k_1(\omega) + d_2 k_2(\omega)] - \right] \right\} \quad (4.26) \\ \left. \left[-[G_2 k_2(\omega) - G_1 k_1(\omega)]^2 \cos[d_1 k_1(\omega) - d_2 k_2(\omega)] \right] \right\} \end{aligned}$$

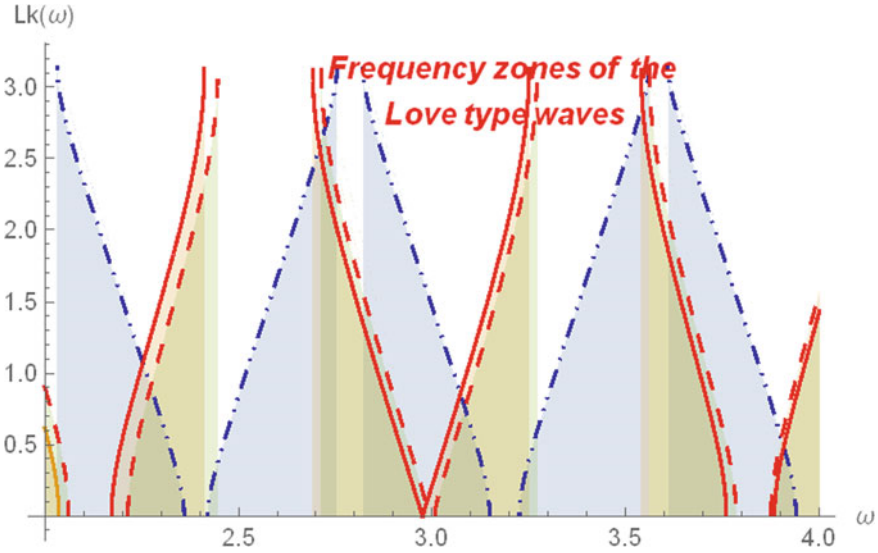


Fig. 4.4 Forbidden and/or allowed frequency zones for shear localized slow waves (Love type waves) in composite waveguide piezoelectrics **PZT-4 with Cadmium Sulfide** and **PZT-5 with Zinc Oxide**

Considering the received relations as an area of definition for the allowed lengths of the wave signal in the periodic structure, from (4.26) we get

$$\lambda(\omega) = 2\pi(d_1 + d_2)\arccos^{-1} \left\{ \frac{[G_2k_2(\omega) + G_1k_1(\omega)]^2}{4G_1k_1(\omega) \cdot G_2k_2(\omega)} \cdot \left[\begin{array}{l} \cos[d_1k_1(\omega) + d_2k_2(\omega)] - \\ - \frac{[G_2k_2(\omega) - G_1k_1(\omega)]^2}{[G_2k_2(\omega) + G_1k_1(\omega)]^2} \cos[d_1k_1(\omega) - d_2k_2(\omega)] - \end{array} \right] \right\} \quad (4.27)$$

It follows from more visual graphs of high-frequency propagation (Fig.4.5), that forbidden frequency zones do not form in this task, in which wave numbers $k(\omega)$ do not exist. In this case, the dispersion lines have clearly outlined envelopes at top and bottom. It is also obvious, that the different stiffness of the materials of half-spaces lead to frequency shear of the dispersion curves between each other.

It is interesting, that in all these cases the nature of changes of phase speeds are the same in the virtually selected layers (Fig.4.5), while the phase speed in the cavity layer $d_1 \leq x \leq d_1 + d_2$ is less than the phase speed in the protrusion layer $0 \leq x \leq d_1$. Based on the fineness of the isolated inner inhomogeneous layer $\{|x| < \infty; |y| \leq R_0; |z| < \infty\}$, taking into account the boundary conditions (4.11), (4.13) and the electro elasticity equations (4.10), it can be replaced by the action of equivalent electromechanical loads on the surfaces $y = \mp R_0$ of the main layers. The difference in mechanical surface shear stresses on the surfaces $y = \mp R_0$ of the seen layer can be represented as

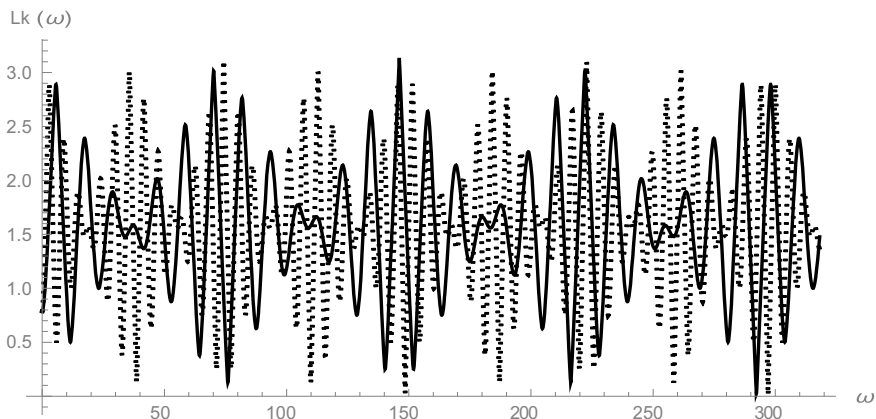


Fig. 4.5 Dispersion curves of localized shear nanometer waves $\lambda(\omega) \sim 10^{-9}$ m at the junction of pairs of piezoelectrics PZT-4 with Zinc Oxide and PZT-5 with Cadmium Sulfide, for micrometer height $R_0 = 10^{-6}$ m and micrometer widths of protrusions and cavities of surface protrusions $d_1 = 10^{-8}$ m and $d_2 = 5 \times 10^{-7}$ m

$$\begin{aligned}
 & - \Delta \sigma_{yz}^{(0m)} (\mp R_0) \\
 & \frac{c_{44}^{(p1)} w_{1,y}(x, R_0) + {}_{15}^{(p1)} \varphi_{1,y}(x, R_0) - c_{44}^{(p2)} w_{2,y}(x, -R_0) - {}_{15}^{(p2)} \varphi_{2,y}(x, -R_0)}{2R_0 [W_2(-R_0) - W_1(R_0)] k_*^2} \\
 & = [\omega^2 / k_*^2] \rho_{p1} \frac{[\alpha_0 k_* R_0 \text{ctg}(2\alpha_0 k_* R_0) - 2[\rho_{p1} / \rho_{p2}] \alpha_0 k_* R_0 \text{csc}(2\alpha_0 k_* R_0) + \ln[\rho_{p1} / \rho_{p2}]]}{[\rho_{p1} / \rho_{p2}] (4\alpha_0^2 k_*^2 R_0^2 + 2 \ln[\rho_{p1} / \rho_{p2}])} \\
 & - c_{44}^{(p1)} \frac{[\alpha_0 k_* R_0 \text{ctg}(2\alpha_0 k_* R_0) - 2[c_{44}^{(p1)} / c_{44}^{(p2)}] \alpha_0 k_* R_0 \text{csc}(2\alpha_0 k_* R_0) + \ln[c_{44}^{(p1)} / c_{44}^{(p2)}]]}{[c_{44}^{(p1)} / c_{44}^{(p2)}] (4\alpha_0^2 k_*^2 R_0^2 + 2 \ln[c_{44}^{(p1)} / c_{44}^{(p2)}])} \\
 & - \frac{\Phi_2(-R_0) - \Phi_1(R_0)}{W_2(-R_0) - W_1(R_0)} e_{15}^{(p1)} \cdot \\
 & \quad \cdot \frac{[2k_* R_0 \text{ctg}(2k_* R_0) - 2[e_{15}^{(p1)} / e_{15}^{(p2)}] k_* R_0 \text{csc}(2k_* R_0) + \ln[e_{15}^{(p1)} / e_{15}^{(p2)}]]}{[e_{15}^{(p1)} / e_{15}^{(p2)}] (4k_*^2 R_0^2 + 2 \ln[e_{15}^{(p1)} / e_{15}^{(p2)}])} \\
 & + \frac{W_1(R_0)}{2R_0 [W_2(-R_0) - W_1(R_0)]} \left[\frac{c_{44}^{(p1)} - c_{44}^{(p2)}}{\ln[c_{44}^{(p1)} / c_{44}^{(p2)}]} - \omega^2 \frac{\rho_{p1} - \rho_{p2}}{\ln[\rho_{p1} / \rho_{p2}]} \right] \\
 & + \frac{\Phi_1(R_0)}{2R_0 [W_2(-R_0) - W_1(R_0)]} \frac{e_{15}^{(p1)} - e_{15}^{(p2)}}{\ln[e_{15}^{(p1)} / e_{15}^{(p2)}]}, \tag{4.28}
 \end{aligned}$$

The difference of the normal electrical displacement to surfaces $y = \mp R_0$ of the seen layer can be represented as

$$\begin{aligned}
& - \Delta D_y^{(0m)}(\mp R_0) \\
& = \frac{e_{15}^{(p1)} W_{1,y}(x, R_0) - \varepsilon_{11}^{(p1)} \varphi_{1,y}(x, R_0) - e_{44}^{(p2)} W_{2,y}(x, -R_0) + \varepsilon_{11}^{(p2)} \varphi_{2,y}(x, -R_0)}{2R_0 [W_2(-R_0) - W_1(R_0)] k_*^2} \\
& = -e_{15}^{(p1)} \frac{\left[\alpha_0 k_* R_0 \operatorname{ctg}(2\alpha_0 k_* R_0) - 2[e_{15}^{(p1)}/e_{15}^{(p2)}] \alpha_0 k_* R_0 \operatorname{csc}(2\alpha_0 k_* R_0) + \ln[e_{15}^{(p1)}/e_{15}^{(p2)}] \right]}{[c_{44}^{(p1)}/c_{44}^{(p2)}] \left(4\alpha_0^2 k_*^2 R_0^2 + 2 \ln [c_{44}^{(p1)}/c_{44}^{(p2)}] \right)} \\
& + \frac{\Phi_2(-R_0) - \Phi_1(R_0)}{W_2(-R_0) - W_1(R_0)} \varepsilon_{11}^{(p1)} \cdot \\
& \quad \cdot \frac{\left[2k_* R_0 \operatorname{ctg}(2k_* R_0) - 2[\varepsilon_{11}^{(p1)}/\varepsilon_{11}^{(p2)}] k_* R_0 \operatorname{csc}(2k_* R_0) + \ln[\varepsilon_{11}^{(p1)}/\varepsilon_{11}^{(p2)}] \right]}{[\varepsilon_{11}^{(p1)}/\varepsilon_{11}^{(p2)}] \left(4k_*^2 R_0^2 + 2 \ln [\varepsilon_{11}^{(p1)}/\varepsilon_{11}^{(p2)}] \right)} + \\
& + \frac{W_1(R_0)}{2R_0 [W_2(-R_0) - W_1(R_0)]} \frac{e_{15}^{(p1)} - e_{15}^{(p2)}}{\ln [e_{15}^{(p1)}/e_{15}^{(p2)}]} + \frac{\Phi_1(R_0)}{2R_0 [W_2(-R_0) - W_1(R_0)]} \frac{\varepsilon_{11}^{(p1)} - \varepsilon_{11}^{(p2)}}{\ln [\varepsilon_{11}^{(p1)}/\varepsilon_{11}^{(p2)}]}
\end{aligned} \tag{4.29}$$

In both intervals of longitudinal inhomogeneity $0 \leq x \leq d_1$ and $d_1 \leq x \leq d_1 + d_2$, the wave number of the propagating wave is determined from (4.26).

4.5 Conclusion

As a wave energy harvester, a model of a two-layer piezoelectric waveguide is proposed, taking into account the roughness of the joining surfaces of the layers. The docking of two different piezoelectric salts leads to the formation of an internal, thin, inhomogeneous layer both in thickness and along the interlayer. The longitudinal periodic inhomogeneity of the formed interlayer transforms the electroacoustic signal into waves of the Floquet type. The inhomogeneity of the formed interlayer in thickness leads to the appearance of differential mechanical stresses and electrical displacement on the surfaces of the seen interlayer. Localization of high-frequency electroacoustic shear waves occurs in the formed inhomogeneous interlayer and near it. It is shown that if in a layered waveguide with an internal millimeter inhomogeneous layer, millimeter electroacoustic waves have a periodic structure (Floquet type waves) and there are forbidden frequency zones, then in the case of a nanometer wave signal, there are no forbidden frequency zones. In this case, the wave energy is strongly localized near the inhomogeneous interlayer for all frequencies of the wave ultrasonic signal.

References

1. Love, A.E.H.: Some Problems of Geodynamics, first published in (1911) by the Cambridge University Press and published again in (1967) by Dover, New York, USA (Chapter 11: Theory of the propagation of seismic waves)
2. Bleustein, J.L.: A new surface wave in piezoelectric materials. *Appl. Phys. Lett.* **13**(12), 412–413 (1968). <https://doi.org/10.1063/1.1652495>
3. Gulyaev, Yu.V.: Surface electroacoustic waves in solids. *Sov. Phys. JETP Lett* **9**, 37–38 (1969). [in Russ.]
4. Kaganov, M.I., Sklovskaya, I.L.: Surface wave in piezoelectric. *Sov. Phys.-Solid State*, **8**, 2789 (1967). [in Russ.]
5. Avetisyan A.S.: Two dimensional problems of electro acoustics in homogeneous piezoelectric crystals. *Mech. Proc. NAS Armenia* **72**(3), 56–79
6. Zolotova, O.P., Burkov, S.I., Sorokin, B.P., Telichko, A.V.: Waves, elastic, in piezoelectric layers structures. *J. Siberian Federal Univ. Math. Phys.* **5**(2), 164–186 (2012)
7. Liu J., Wang, Y., Wang, B.: Propagation of shear horizontal surface waves in a layered piezoelectric half-space with an imperfect interface. In: *IEEE Trans. Ultrasonic, Ferroel. and Freq. Control* **57**(8), 1875–1879
8. Liu, J., He, S.: Properties of love waves in layered piezoelectric structures. *Int. J. Solids Struct.* **47**, 169–174 (2010)
9. Maugin, G.A.: Elastic surface waves with transverse horizontal polarization. *Adv. Appl. Mech.* **23**, 373–434 (1983)
10. Li, Z.-N., Wang, Y.-Z., Wang, Y.-S.: Nonreciprocal phenomenon in nonlinear elastic wave metamaterials with continuous properties. *Int. J. Solids Struct.* **150**(1), 125–134 (2018)
11. Avetisyan, A.S.: The mixed boundary conditions problem of layered composites with meta-surfaces in electro elasticity. In: Sumbatyan M.A. (ed.) *Book: Advanced Structured Materials 109, Wave Dynamics, Mechanics and Physics of Microstructured Metamaterials*. Springer Nature, pp. 73–96 (2019)
12. Avetisyan, A.S., Hunanyan, A.A.: The efficiency of application of virtual cross-sections method and hypotheses MELS in problems of wave signal propagation in elastic waveguides with rough surfaces. *J. Adv. Phys.* **11**(7), 3564–3574 (2016)
13. Ghazaryan, K.B., Kazaryan, R.A., Papyan, A.A.: Floquet waves in an inhomogeneous periodic rod. In: *Problems of Solid Mechanics*, pp. 110–117 (2017)
14. Avetisyan, A.S., Belubekyan, M.V., Ghazaryan, K.B.: The propagation of high-frequency shear elastic waves on interface of isotropic elastic half-spaces with canonical surface protrusions. *Am. J. Earth Sci. Eng.* **1**(2), 114–128 (2018)

Chapter 5

About One Approach in Prevention of the Emerging Dangerous Phenomena Caused by the Existence of Defect in Continuous Media



Vladimir A. Babeshko, Ilya S. Telyatnikov, Alla V. Pavlova,
and Maksim N. Kolesnikov

Abstract We consider the case of the formation for a defect of the vertical crack type, including a new type, arising in the coating of the deformable material. New models of pre-landslide phenomena, when the landslide-prone environment is enclosed in a thin-walled coating, a sarcophagus, which acquires a vertical crack, lead us to similar problems. Also, such problems arise in the following cases: underground structures such as mines with a set of parallel tunnels, in bearing pairs in mechanical engineering, in problems of seismology. One of the approaches consists in a possible, controlled impact on such structures, preventing large-scale destructive processes, with significant material damage and human casualties. It consists in vibration action at certain frequencies, up to high, close to shock ones, as well as the selection of areas for the application of such action, in relation to the defect. This approach aims to defuse the emerging dangerous phenomena, preventing the development of the process to a critical point which can cause tremendous damage. This study aims to further the development of the theory for cracks of a new type. The research is based on factorization approaches, the block element method and functional analysis methods. Depending on the goals set, the possibilities of different study approaches for the problems under consideration are discussed.

Keywords Block element method · Kirchhoff plate · Vertical crack · Eigenfunction method · Factorization

V. A. Babeshko (✉)

Southern Scientific Center, Russian Academy of Sciences, 41 Chehova st., 344006
Rostov-on-Don, Russian Federation
e-mail: babeshko41@mail.ru

I. S. Telyatnikov · A. V. Pavlova · M. N. Kolesnikov

Kuban State University, 149 Stavropolskaya st., 350040 Krasnodar, Russian Federation
e-mail: ilux_t@list.ru

A. V. Pavlova

e-mail: pavlova@math.kubsu.ru

M. N. Kolesnikov

e-mail: kolesnikov@kubsu.ru

5.1 Introduction

The problem of studying the behavior of deformable bodies in the presence of defects such as cracks has been studied by many authors [1–36]. Most of the work considers the defects in the form of Griffith cracks. Cases of cracks in multilayer deformable media with crack planes parallel to the boundary of the multilayer media are described. Analytical, numerical-analytical and fully numerical approaches can be noted, which turn out to be effective for certain boundary problems. For example, in problems associated with cracks, boundaries of which go to infinity, and analytical methods prove themselves more effective than the others. And vice versa, in problems with flat limited cracks, numerical methods turn out to be more effective. Problem statements for media with Griffith cracks are quite diverse depending on the method of applying external influences to crack faces. The conditions of the cracks destruction and approaches to studying the directions of crack development after their destruction at the tip also vary widely. Along with cracks in a homogeneous medium, we also considered cracks at the layer boundaries in a multilayer medium.

Each of the studied problems has its own specifics, aimed primarily at identifying the conditions for the defects influence on the strength properties of the structure and finding ways to reduce the vulnerability of the latter during crack propagation, or to avoid its destruction.

Along with Griffith cracks, we have found cracks of a new type [37], which complement Griffith cracks. Griffith cracks have a smooth boundary. At the crack tip, the boundary represents the rounding of an elliptic curve. The destruction of a crack consists in breaking this boundary. A crack of a new type has a piece-wise-smooth boundary. They are formed in the coated medium, occupying a position perpendicular to its boundary. At the tip, the crack boundary is described by the cavity boundary in the form of a half-strip. The mechanism of its destruction consists in the formation of singular contact stresses with the complete convergence of the crack edges.

Cracks of a new type appear in models of pre-landslide phenomena, when a landslide structure is enclosed in a thin-walled coating—a sarcophagus [38]. The destruction of the latter occurs due to the formation of through defects in it, perpendicular to the boundary and representing cracks of a new type. Similar problems for the cases of non-converged crack edges of this type also arise in the problem of stability for the underground structures, such as mines with a set of parallel adits. Here, the problem arises in the assessment of the underground structure mechanical state and its changes associated with stresses redistribution due to the constant extraction of ore from adits. In addition, the issues caused by the influence of the slow movement of lithospheric plates, which, after a long time, cause noticeable displacements in the underground structure, have not been studied [39].

Cracks of a new type can occur in the bearing pairs, important products used in mechanical engineering. Relevant for these products is the problem of structural stability and degree of performance in the event of microcracks formation, including cracks of a new type [40].

In seismology [41], it was found that when the ends of lithospheric plates moving along the Konrad boundary approach each other, cracks of a new type, representing tectonic faults, are also formed. This fact made it possible to reveal a new type of earthquakes, called “starting,” which occur at the moment of complete convergence of the lithospheric plate edges before the start of interaction. A comparison between the theoretical calculated displacements of the Earth’s surface at the epicenters of starting earthquakes shows a qualitative concurrence with the displacements of real earthquakes in these areas [41].

The issue of controlling a new type of cracks is poorly studied. One of the approaches developed in this article is to use the geometric properties of the new type cracks, namely, their location perpendicular to the boundary. An available means of influencing the latter is the possibility of the surface waves excitation caused by sources of various types. These include both vibroseismic and explosive. Both those sources are ultimately associated with certain frequencies of signal excitation by surface sources.

In this work, we study the excitation of waves caused by a surface harmonic source in a coating with a defect in the form of a new type crack.

5.2 Formulation of the Problem

A block structure is considered, consisting of two-dimensional horizontally arranged plates of different types in the form of half-planes, contacting each other along a rectilinear boundary. The block structure is located on the surface of a three-dimensional linearly deformable substrate. The considered block structures are under vertical harmonic external action. The case of static actions was considered in [41], and it led to the discovery of a new type of earthquakes, called the starting ones. The present study is based on the method developed in the aforementioned work. We consider that the coatings are half-planes with parallel boundaries, located on a linearly deformable foundation at a distance 2θ from each other. Plates are modeled with Kirchhoff plates. We consider that the space between plates of different types is free from external influences, and forces directed vertically act on the ends of the plates. In the local coordinate system $x_1x_2x_3$ with the origin in the plane x_1Ox_2 , coinciding with the middle plane of the plate. The axis Ox_3 is directed upward along the normal to the plate, the axis Ox_1 is directed tangentially to the fault boundary, and the axis Ox_2 —along the normal to its boundary. The area $|x_1| \leq \infty, x_2 \leq -\theta$, occupied by the left plate, is denoted by the index λ , and the area $|x_1| \leq \infty, x_2 \geq \theta$, occupied by the right plate—by the index r . The area between the plates $|x_1| \leq \infty, -\theta < x_2 < \theta$, is denoted by the index θ .

The Kirchhoff equation for the fragments b of the coating, $b = \lambda, r$, occupying areas Ω_b with boundaries $\partial\Omega_b$, relative to the displacements of the middle surface of the plates $\mathbf{u}_b = \{u_{1b}, u_{2b}, u_{3b}\} \exp(-i\omega t)$ under vertical harmonic (with frequency ω) effects $\mathbf{t}_b = \{0, 0, t_{3b}\} \exp(-i\omega t)$ from above and $\mathbf{g}_b = \{0, 0, g_{3b}\} \exp(-i\omega t)$ —from below, after the exclusion of the time parameter, has the form

$$\mathbf{R}_b (\partial x_1, \partial x_2) \mathbf{u}_b - \mathbf{E}_b (\mathbf{t}_b - \mathbf{g}_b) \equiv (\nabla^4 - \varepsilon_{4b}) u_{3b} + \varepsilon_{5b} (t_{3b} - g_{3b}) = 0, \quad (5.1)$$

where

$$\mathbf{E}_b = \text{diag} \{-\varepsilon_{b5}, -\varepsilon_{b5}, \varepsilon_{b5}\},$$

$$\varepsilon_{4b} = \omega^2 \rho_b \frac{12(1 - \nu_b^2) H^4}{E h_b^2}, \quad \varepsilon_{5b} = \frac{12(1 - \nu_b^2) H^4}{E_b h_b^3},$$

$$\nabla^4 = \frac{\partial^4}{\partial x_1^4} + 2 \frac{\partial^4}{\partial x_1^2 \partial x_2^2} + \frac{\partial^4}{\partial x_2^4}.$$

Here, for plates, we use the designations ρ_b —density, E_b —Young's modulus, ν_b —Poisson's ratio, h_b —plate thickness.

At the same time, at the boundaries of the plates, we can set the bending moments

$$M_b = -D_{b1} \left(\frac{\partial^2 u_{3b}}{\partial x_2^2} + \nu_b \frac{\partial^2 u_{3b}}{\partial x_1^2} \right), \quad D_{b1} = \frac{D_b}{H^2}, \quad D_{b2} = \frac{D_b}{H^3},$$

where $D_b = \frac{E_b h_b^3}{12(1 - \nu_b^2)}$ are the rigidities of the plates, H is the dimensional parameter of the substrate, for example, the layer thickness; cutting forces

$$Q_b = -D_{b2} \left(\frac{\partial^3 u_{3b}}{\partial x_2^3} + (2 - \nu_b) \frac{\partial^3 u_{3b}}{\partial x_1^2 \partial x_2} \right) = f_{4b} (\partial \Omega_b);$$

displacements— $u_{3b} = f_{1b} (\partial \Omega_b)$, rotation angles of the median plane around the axis x_1 , in the coordinate system $x_1 O x_2$ —

$$\frac{1}{H} \frac{\partial u_{3b}}{\partial x_2} = f_{2b} (\partial \Omega_b).$$

By applying the two-dimensional Fourier transform in horizontal coordinates to system (5.1), we obtain

$$R_b (-i\alpha_1, -i\alpha_2) U_{3b} = \left[(\alpha_1^2 + \alpha_2^2)^2 - \varepsilon_{43b} \right] U_{3b}, \quad b = \lambda, r,$$

$$U_{3b} (\alpha_1, \alpha_2) = \mathbf{F}_2 u_{3b} (x_1, x_2), \quad G_{3b} (\alpha_1, \alpha_2) = \mathbf{F}_2 g_{3b} (x_1, x_2),$$

$$T_{3b} (\alpha_1, \alpha_2) = \mathbf{F}_2 t_{3b} (x_1, x_2).$$

From here on, $\mathbf{F}_2 \equiv \mathbf{F}_2 (\alpha_1, \alpha_2)$ and $\mathbf{F}_1 \equiv \mathbf{F}_1 (\alpha_1)$ are the two-dimensional and one-dimensional Fourier transform operators, respectively.

The relationship between boundary stresses and displacements on the surface of an elastic medium under the plates has the form

$$u_3(x_1, x_2) = \varepsilon_6^{-1} \sum_{n=1}^2 \iint_{\Omega_n} k(x_1 - \xi_1, x_2 - \xi_2) g_{3n}(\xi_1, \xi_2) d\xi_1 d\xi_2, \\ (x_1, x_2) \in \Omega_m, \quad m = \overline{1, 3}, \quad (5.2)$$

where

$$\varepsilon_6^{-1} = \frac{(1 - \nu) H}{\mu}.$$

Here, index 1 corresponds to λ , 2— r , 3— θ , so $g_{31} = g_{3\lambda}$, $g_{32} = g_{3r}$,

$$\Omega_1 \equiv \Omega_\lambda = \{(x_1, x_2) : |x_1| \leq \infty; x_2 \leq -\theta\}, \\ \Omega_2 \equiv \Omega_r = \{(x_1, x_2) : |x_1| \leq \infty; x_2 \geq \theta\}, \\ \Omega_3 \equiv \Omega_\theta = \{(x_1, x_2) : |x_1| \leq \infty, -\theta < x_2 < \theta\}.$$

Relations (5.2) can be represented as

$$u_3(x_1, x_2, 0) = \frac{1}{4\pi^2 \varepsilon_6} \sum_{n=1}^2 \int_{\sigma_1} \int_{\sigma_2} K(\alpha_1, \alpha_2, 0) G_{3n}(\alpha_1, \alpha_2) \exp(-i\langle \alpha, \mathbf{x} \rangle) d\alpha_1 d\alpha_2,$$

$$\varepsilon_6 = \frac{\mu}{H(1 - \nu)}, \quad \langle \alpha, \mathbf{x} \rangle = \alpha_1 x_1 + \alpha_2 x_2,$$

$$K(\alpha_1, \alpha_2, 0) = O(A^{-1}), \quad A = \sqrt{\alpha_1^2 + \alpha_2^2} \rightarrow \infty.$$

Here, $K(\alpha_1, \alpha_2, x_3)$ is an analytic function of two complex variables α_k , $k = 1, 2$, in particular, meromorphic; numerous examples are given in [42, 43].

Using of the block element method leads to the introduction of external forms ω_b . By applying the approach of [41] in the variant of the harmonic oscillations presence, the functional equations of the boundary value problem can be represented in the form

$$R_b(-i\alpha_1, -i\alpha_2) U_{3b} \equiv \left[(\alpha_1^2 + \alpha_2^2)^2 - \varepsilon_{4b} \right] U_{3b} \\ = - \left[\int_{\partial\Omega_b} \omega_b - \varepsilon_{5b} S_{3b}(\alpha_1, \alpha_2) \right], \quad (5.3)$$

$$S_{3b}(\alpha_1, \alpha_2) = \mathbf{F}_2(\alpha_1, \alpha_2) (t_{3b} - g_{3b}), \quad b = \lambda, r.$$

The solution representation for each plate has the form

$$u_{3b} = -\mathbf{F}_2^{-1}(\alpha_1, \alpha_2) \frac{1}{(\alpha_1^2 + \alpha_2^2)^2 - \varepsilon_{4b}} \left[\int_{\partial\Omega_b} \omega_b - \varepsilon_{5b} S_{3b}(\alpha_1, \alpha_2) \right].$$

The external forms participating in representation (5.3) have the form

$$\begin{aligned} \omega_b = e^{i(\alpha, x)} \left\{ -i \left[\alpha_2 \mathbf{M} \mathbf{D}^{-1} - \mathbf{Q} \mathbf{D}^{-1} - (\alpha_2^2 + \nu_b \alpha_1^2) \frac{\partial u_{3b}}{\partial x_2} \right. \right. \\ \left. \left. + i \alpha_2 [\alpha_2^2 + (2 - \nu_b) \alpha_1^2] u_{3b} \right] \right\} dx_1. \end{aligned}$$

Taking into account the adopted notation, we can represent the pseudo-differential equations for the left plate

$$\begin{aligned} \mathbf{F}_1^{-1}(\xi_1^\lambda) \left\{ - \int_{\partial\Omega_\lambda} \left[i \alpha_{21-} \mathbf{D}_{\lambda 1}^{-1} \mathbf{M}_\lambda - \mathbf{D}_{\lambda 2}^{-1} \mathbf{Q}_\lambda - (\alpha_{21-}^2 + \nu_\lambda \alpha_1^2) \frac{\partial u_{3\lambda}}{\partial x_2} \right. \right. \\ \left. \left. + i \alpha_{21-} (\alpha_{21-}^2 + (2 - \nu_\lambda) \alpha_1^2) u_{3\lambda} \right] \exp(i\alpha_1 x_1) dx_1 - \varepsilon_{5\lambda} S_{3\lambda}(\alpha_1, \alpha_{21-}) \right\} = 0, \end{aligned}$$

$$\xi_1^\lambda \in \partial\Omega_\lambda;$$

$$\begin{aligned} \mathbf{F}_1^{-1}(\xi_1^\lambda) \left\{ - \int_{\partial\Omega_\lambda} \left[i \alpha_{22-} \mathbf{D}_{\lambda 1}^{-1} \mathbf{M}_\lambda - \mathbf{D}_{\lambda 2}^{-1} \mathbf{Q}_\lambda - (\alpha_{22-}^2 + \nu_\lambda \alpha_1^2) \frac{\partial u_{3\lambda}}{\partial x_2} \right. \right. \\ \left. \left. + i \alpha_{22-} (\alpha_{22-}^2 + (2 - \nu_\lambda) \alpha_1^2) u_{3\lambda} \right] \exp(i\alpha_1 x_1) dx_1 - \varepsilon_{5\lambda} S_{3\lambda}(\alpha_1, \alpha_{22-}) \right\} = 0, \end{aligned}$$

$$\xi_1^\lambda \in \partial\Omega_\lambda.$$

Similarly for the right plate

$$\begin{aligned} \mathbf{F}_1^{-1}(\xi_1^r) \left\{ - \int_{\partial\Omega_\lambda} \left[i \alpha_{21+} \mathbf{D}_{r 1}^{-1} \mathbf{M}_r - \mathbf{D}_{r 2}^{-1} \mathbf{Q}_\lambda - (\alpha_{21+}^2 + \nu_r \alpha_1^2) \frac{\partial u_{3r}}{\partial x_2} \right. \right. \\ \left. \left. + i \alpha_{21+} (\alpha_{21+}^2 + (2 - \nu_r) \alpha_1^2) u_{3r} \right] \exp(i\alpha_1 x_1) dx_1 - \varepsilon_{5r} S_{3r}(\alpha_1, \alpha_{21+}) \right\} = 0, \end{aligned}$$

$$\xi_1^r \in \partial\Omega_r;$$

$$\mathbf{F}_1^{-1}(\xi_1^r) \left\{ - \int_{\partial\Omega_\lambda} \left[i\alpha_{22+} D_{r1}^{-1} M_r - D_{r2}^{-1} Q_\lambda - (\alpha_{22+}^2 + \nu_r \alpha_1^2) \frac{\partial \mathbf{u}_{3r}}{\partial x_2} + \right. \right. \\ \left. \left. + i\alpha_{22+} (\alpha_{22+}^2 + (2 - \nu_r) \alpha_1^2) \mathbf{u}_{3r} \right] \exp(i\alpha_1 x_1) dx_1 - \varepsilon_{5r} \mathbf{S}_{3r}(\alpha_1, \alpha_{22+}) \right\} = 0, \\ \xi_1^r \in \partial\Omega_r.$$

$$\alpha_{21-} = -i\sqrt{\alpha_1^2 - \sqrt{\varepsilon_{4\lambda}}}, \quad \alpha_{22-} = -i\sqrt{\alpha_1^2 + \sqrt{\varepsilon_{4\lambda}}},$$

$$\alpha_{21+} = i\sqrt{\alpha_1^2 - \sqrt{\varepsilon_{4r}}}, \quad \alpha_{22+} = i\sqrt{\alpha_1^2 + \sqrt{\varepsilon_{4r}}}.$$

The problem posed for $\theta = 0$ is dynamically reduced by the block element method to the Wiener–Hopf functional Eq. [41], presented in the following form

$$\left[\varepsilon_{5r} (\alpha_1^2 + \alpha_2^2 - \varepsilon_{4r})^{-2} + \varepsilon_6^{-1} K_1(\alpha_1, \alpha_2) \right] G^+(\alpha_1, \alpha_2) \\ = - \left[\varepsilon_{5\lambda} (\alpha_1^2 + \alpha_2^2 - \varepsilon_{4r})^{-2} + \varepsilon_6^{-1} K_1(\alpha_1, \alpha_2) \right] G^-(\alpha_1, \alpha_2) \\ + (\alpha_1^2 + \alpha_2^2 - \varepsilon_{4r})^{-2} [A_r k_{1r} + B_r k_{2r} + \varepsilon_{5r} T^-(\alpha_1, \alpha_2)] \\ + (\alpha_1^2 + \alpha_2^2 - \varepsilon_{4r})^{-2} [A_\lambda k_{1\lambda} + B_\lambda k_{2\lambda} + \varepsilon_{5\lambda} T^+(\alpha_1, \alpha_2)], \quad \theta = 0.$$

This functional equation describes a crack of the new type [37], which, in seismological problems, is a tectonic fault. A detailed study of them made it possible to reveal the occurrence of starting earthquakes under multidirectional effects on the crack edges [41].

The block element method makes it possible to analytically reveal important qualitative properties of solutions to boundary value problems. Another approach, based on the method of eigenfunctions, makes it possible to detail the wave processes arising in a block structure with the subsequent possibility of their application to affect the edges of a defect. Below is a short summary of it.

5.3 Eigenfunction Method in the Plane Problem of Vertical Vibrations for a Plate with a New Type Crack

We consider the boundary value problem described above in a flat formulation for a block structure with $\theta = 0$. Vertical harmonic influences affect the previously described block structure. An elastic layer is considered as a deformable substrate. Omitting the details, we represent the equations of plate vibration (5.1) after separating the time factor in the form

$$R_{\pm}(\partial x_2) u_{\pm}(x_2) - \varepsilon_{\pm,5} g_{\pm}(x_2) = b_{\pm}(x_2), \quad \pm x_2 > 0, \quad (5.4)$$

$$R_{\pm}(\partial x_2) = \varepsilon_{\pm,3} \frac{\partial^4}{\partial x_2^4} - \varepsilon_{\pm,4}, \quad b_{\pm}(x_2) = -\varepsilon_{\pm,5} t_{\pm}(x_2).$$

Concentrated load $t_{+}(x_2) = A\delta(x_2 - x_2^0)$, $x_2^0 > 0$ is the point of its application, intensity $A > 0$; $t_{-}(x_2) = 0$. The nonzero component of the displacement vector is $u_{\pm,3}(x_2)$. Here, the index “+” corresponds to the right plate, generally denoted by the index r , index “-” corresponds to the left one, denoted in the previous section by the index λ .

Displacements at the upper boundary of the elastic layer (5.2) are now written in the form

$$u(x_2) = \varepsilon_6^{-1} \int_{-\infty}^{\infty} k(\xi_2 - x_2) g(x_2) d\xi_2,$$

where $u(x_2)$ and $g(x_2)$ are the displacement and stress amplitudes, respectively,

$$k(x_2) = \frac{1}{2\pi} \int_{\sigma} K(\alpha_2) \exp(-i\alpha_2 x_2) d\alpha_2.$$

Green’s function $K(\alpha_2) = K_{3,3}(\alpha_2, 0)$.

The functional relation for the integral characteristics of displacements and contact pressures between the foundation and the coating has the form

$$U(\alpha_2) = K(\alpha_2) G(\alpha_2), \quad \alpha_2 \in \sigma, \quad (5.5)$$

where

$$U(\alpha_2) = \mathbf{F}_1 u(x_2), \quad G(\alpha_2) = \mathbf{F}_1(\alpha_2) g(x_2).$$

The ideal connection of slabs and foundation involves: $u_{\pm}(x_2) = u(x_2)$, $g_{\pm}(x_2) = g(x_2)$, $\pm x_2 > 0$. Taking into account (5.5) in the Fourier transforms, this can be written

$$U(\alpha_2) = U_{+}(\alpha_2) + U_{-}(\alpha_2), \quad G(\alpha_1) = G_{+}(\alpha_2) + G_{-}(\alpha_2), \quad \alpha_2 \in \sigma. \quad (5.6)$$

The papers [44, 45] describe a solution method related to the transformation of the differential operator for the problem. The eigenfunction method gives the following representation of general solutions (5.4) that satisfy the boundedness condition in given planes and correspond to the limiting absorption principle [41].

$$u_{\pm}(x_2) = A_{\pm 1} \exp(\mp q_{\pm} x_2) + A_{\pm 2} \exp(\pm i q_{\pm} x_2) + \mathbf{F}_1^{-1}(x_2) \left[R_{\pm}^{-1}(\alpha_2) (\varepsilon_{\pm,5} G_{\pm}(\alpha_2) + B_{\pm}(\alpha_2)) \right], \quad \pm x_2 > 0,$$

where $A_{\pm j}$, $j = \overline{1, 2}$ are arbitrary constants; $q_{\pm} \in \mathbb{R}$, $q_{\pm} > 0$ are the roots of the equations

$$R_{\pm}(\alpha_2) = 0; \quad R_{\pm}(\alpha_2) = \varepsilon_{\pm,3}(\alpha_2 - q_{\pm})(\alpha_2 - iq_{\pm})(\alpha_2 + q_{\pm})(\alpha_2 + iq_{\pm});$$

$$B_+(\alpha_2) = \exp(i\alpha_2 x_2^0); \quad B_-(\alpha_2) = 0.$$

In the Fourier transforms, these relations take the form

$$U_{\pm}(\alpha_2) = \frac{\pm i A_{\pm 1}}{\alpha_2 \pm iq_{\pm}} + \frac{\pm i A_{\pm 2}}{\alpha_2 \pm q_{\pm}} + \left\{ R_{\pm}^{-1}(\alpha_2) [\varepsilon_{\pm,5} G_{\pm}(\alpha_2) + B_{\pm}(\alpha_2)] \right\}_{\sigma}^{\pm}, \quad \alpha_2 \in \sigma.$$

When choosing σ sufficiently close to the real axis, $G_+(\alpha_2)$ will be regular in the area $\alpha_2 \in \Theta_+^{\sigma}$, and $G_-(\alpha_2)$ —in the area $\alpha_2 \in \Theta_-^{\sigma}$. The last terms on the right-hand side can be represented

$$\left\{ R_{\pm}^{-1}(\alpha_2) [\varepsilon_{\pm,5} G_{\pm}(\alpha_2) + B_{\pm}(\alpha_2)] \right\}_{\sigma}^{\pm}$$

$$= R_{\pm}^{-1}(\alpha_2) [\varepsilon_{\pm,5} G_{\pm}(\alpha_2) + B_{\pm}(\alpha_2)] - \left\{ R_{\pm}^{-1}(\alpha_2) [\varepsilon_{\pm,5} G_{\pm}(\alpha_2) + B_{\pm}(\alpha_2)] \right\}_{\sigma}^{\mp}.$$

wherein

$$\left\{ R_{\pm}^{-1}(\alpha_2) [\varepsilon_{\pm,5} G_{\pm}(\alpha_2) + B_{\pm}(\alpha_2)] \right\}_{\sigma}^{\mp}$$

$$= \pm \frac{1}{4q_{\pm}^3 \varepsilon_{\pm,3}} \left[\frac{\varepsilon_{\pm,5} G_{\pm}(\pm q_{\pm})}{\alpha_2 \mp q_{\pm}} + \frac{i \varepsilon_{\pm,5} G_{\pm}(\pm iq_{\pm})}{\alpha_2 \mp iq_{\pm}} + \frac{B_{\pm}(\pm q_{\pm})}{\alpha_2 \mp q_{\pm}} + \frac{i B_{\pm}(\pm iq_{\pm})}{\alpha_2 \mp iq_{\pm}} \right],$$

where $B_+(q_+) = \exp(iq_+ x_2^0)$, $B_+(iq_+) = \exp(-q_+ x_2^0)$, $B_-(-q_-) = 0$, $B_-(-iq_-) = 0$, values $G_{\pm}(\pm q_{\pm})$ are subject to determination. Then we can write

$$U_{\pm}(\alpha_2) = \frac{\pm i A_{\pm 1}}{\alpha_2 \pm iq_{\pm}} + \frac{\pm i A_{\pm 2}}{\alpha_2 \pm q_{\pm}} + R_{\pm}^{-1}(\alpha_2) [\varepsilon_{5,\pm} G_{\pm}(\alpha_2) + B_{\pm}(\alpha_2)]$$

$$\mp \frac{1}{4q_{\pm}^3 \varepsilon_{\pm,3}} \left[\frac{\varepsilon_{5,\pm} G_{\pm}(\pm q_{\pm})}{\alpha_2 \mp q_{\pm}} + \frac{i \varepsilon_{5,\pm} G_{\pm}(\pm iq_{\pm})}{\alpha_2 \mp iq_{\pm}} + \frac{B_{\pm}(\pm q_{\pm})}{\alpha_2 \mp q_{\pm}} + \frac{i B_{\pm}(\pm iq_{\pm})}{\alpha_2 \mp iq_{\pm}} \right], \quad (5.7)$$

$$\alpha_2 \in \sigma.$$

From (5.7), it is possible to express the integral characteristics of the contact stresses between the plates and the foundation

$$G_{\pm}(\alpha_2) = \varepsilon_{5,\pm}^{-1} R_{\pm}(\alpha_2) U_{\pm}(\alpha_2) - \varepsilon_{5,\pm}^{-1} B_{\pm}(\alpha_2)$$

$$- A_{\pm 1} \frac{\pm i R_{\pm}(\alpha_2)}{\varepsilon_{5,\pm}(\alpha_2 \pm iq_{\pm})} - A_{\pm 2} \frac{\pm R_{\pm}(\alpha_2)}{i \varepsilon_{5,\pm}(\alpha_2 \pm q_{\pm})}$$

$$\pm \frac{R_{\pm}(\alpha_2)}{\varepsilon_{5,\pm} 4q_{\pm}^3 \varepsilon_{\pm,3}} \left[\frac{\varepsilon_{5,\pm} G_{\pm}(\pm q_{\pm})}{\alpha_2 \mp q_{\pm}} + \frac{i \varepsilon_{5,\pm} G_{\pm}(\pm iq_{\pm})}{\alpha_2 \mp iq_{\pm}} + \frac{B_{\pm}(\pm q_{\pm})}{\alpha_2 \mp q_{\pm}} + \frac{i B_{\pm}(\pm iq_{\pm})}{\alpha_2 \mp iq_{\pm}} \right].$$

From (5.5)–(5.7) by a series of transformations, we obtain a system of functional equations with respect to $U_{\pm}(\alpha_2)$, which is solved using the Wiener–Hopf method [46]. As a result of the expression for the Fourier transforms $U_{\pm}(\alpha_2)$ of the desired surface displacements

$$\begin{aligned}
 U_{\pm} = (N_{\pm}^{\sigma})^{\pm 1} & \left[\{D_+ Q_{0,+}\}_{\sigma}^{\pm} + \{D_- Q_{0,-}\}_{\sigma}^{\pm} \right. \\
 & + \sum_{j=1}^2 \left(A_{+j} \{D_+ Q_{j,+}\}_{\sigma}^{\pm} + A_{-j} \{D_- Q_{j,-}\}_{\sigma}^{\pm} \right) \\
 & + G_+(q_+) \{D_+ Q_{1,+}^q\}_{\sigma}^{\pm} + G_+(iq_+) \{D_+ Q_{2,+}^q\}_{\sigma}^{\pm} \\
 & \left. + G_-(-q_-) \{D_- Q_{1,-}^q\}_{\sigma}^{\pm} + G_-(-iq_-) \{D_- Q_{2,-}^q\}_{\sigma}^{\pm} \right]. \quad (5.8)
 \end{aligned}$$

In (5.8), $N_{\pm}^{\sigma}(\alpha_2)$ is the result of factorization with respect to the contour σ in the form of a product $N(\alpha_2) = N_+^{\sigma}(\alpha_2) N_-^{\sigma}(\alpha_2)$ of the function

$$N(\alpha_2) = N_1^{-1}(\alpha_2) N_2(\alpha_2), \quad N_1(\alpha_2) = \bar{N}_1(\alpha_2) R_+(\alpha_2);$$

$$N_2(\alpha_2) = \bar{N}_2(\alpha_2) R_-(\alpha_2); \quad \bar{N}_1(\alpha_2) = \varepsilon_{5,+}^{-1} K(\alpha_2) - R_+^{-1}(\alpha_2);$$

$$\bar{N}_2(\alpha_2) = \varepsilon_{5,-}^{-1} K(\alpha_2) - R_-^{-1}(\alpha_2); \quad D_{\pm} = \varepsilon_{5,\pm} (N_{\pm}^{\sigma})^{-1} N_1^{-1} K;$$

$$Q_{1,\pm} = \frac{\pm i R_{\pm}}{\alpha_2 \pm iq_{\pm}}; \quad Q_{2,\pm} = \frac{\pm i R_{\pm}}{\alpha_2 \pm q_{\pm}};$$

$$Q_{0,\pm} = B_{\pm} \pm \frac{R_{\pm}}{4q_{\pm}^3 \varepsilon_{\pm,3}} \left[\frac{B_{\pm}(\pm q_{\pm})}{\alpha_2 \mp q_{\pm}} + \frac{i B_{\pm}(\pm iq_{\pm})}{\alpha_2 \mp iq_{\pm}} \right];$$

$$Q_{1,\pm}^q = \pm \frac{R_{\pm}}{4q_{\pm}^3 \varepsilon_{\pm,3}} \frac{\varepsilon_{5,\pm}}{\alpha_2 \mp q_{\pm}}; \quad Q_{2,\pm}^q = \pm \frac{R_{\pm}}{4q_{\pm}^3 \varepsilon_{\pm,3}} \frac{i \varepsilon_{5,\pm}}{\alpha_2 \mp iq_{\pm}}.$$

The factorization of the function $N(\alpha_2)$ is carried out approximately; for this purpose, an approximating function $N^A(\alpha_2)$ and $N(\alpha_2) \approx N_+^{A,\sigma}(\alpha_2) N_-^{A,\sigma}(\alpha_2)$ is constructed. In [45], where a method for solving problems concerning an elastic layer with a composite coating consisting of extended plates, based on the transformation of the differential operator for a boundary value problem, is presented, the approximation of functions subject to factorization is described in detail.

Like $K(\alpha_2)$ and $\bar{N}_1(\alpha_2)$, $\bar{N}_2(\alpha_2)$ are even functions with a finite number of simple real poles and zeros. Their poles are the real poles of the function $K(\alpha_2) \pm p_j$, $j = 1, M_p$, as well as $\pm q_+$ —for the function $\bar{N}_1(\alpha_2)$ and $\pm q_-$ —for the function $\bar{N}_2(\alpha_2)$. The number of poles $K(\alpha_2)$ and their value determine the number and speed of propagation for surface waves in an elastic foundation. Let us introduce

the notation $z_{\bar{N}_k, j} \in \mathbf{R}$, $j = \overline{1, N_z^{\bar{M}_k}}$ for positive zeros $\bar{N}_k(\alpha_2)$, $k = \overline{1, 2}$. Further we consider functions of the form

$$\bar{N}_{k,R}(\alpha_2) = \Pi_{\bar{N}_k}^{-1}(\alpha_2) \bar{N}_k(\alpha_2), \quad k = \overline{1, 2},$$

$$\Pi_{\bar{N}_{1/2}}(\alpha_2) = \frac{(\alpha_2^2 + l^2)^{M_p+1} \prod_{j=1}^{M_z^{\bar{N}_{1/2}}} (\alpha_2^2 - z_{\bar{N}_{1/2}, j}^2)}{(\alpha_2^2 + l^2)^{M_z^{\bar{N}_{1/2}}} (\alpha_2^2 - q_{+/-}^2) \prod_{j=1}^{M_p} (\alpha_2^2 - p_j^2)}, \quad l > 0, \quad l \in \mathbf{R}.$$

Here, $z_{k,j} > 0$, $j = \overline{1, M_z^k}$ are real zeros of \bar{N}_k . The obtained $\bar{N}_{k,R}(\alpha_2)$, $k = \overline{1, 2}$ do not have zeros and poles on the real axis and behave at infinity in the same way as $\bar{N}_k(\alpha_2)$, $k = \overline{1, 2}$, $\bar{N}_{k,R}(\alpha_2) \sim O(\alpha_2^{-1})$.

Approximating the functions

$$\frac{\sqrt{\alpha_2^2 + l_0^2}}{\kappa_{\bar{M}_k}} \bar{N}_{k,R}(\alpha_2), \quad l_0 > l, \quad l_0 \in \mathbf{R}, \quad k = \overline{1, 2}$$

with Bernstein polynomials of degree N_A [43]

$$\bar{M}_{k,R}(\alpha_2) \approx \bar{M}_{k,R}^A(\alpha_2) = \frac{\kappa_{\bar{M}_k} \prod_{j=1}^{N_A} (\alpha_2 - z_{\bar{M}_k, j}^A) (\alpha_2 + z_{\bar{M}_k, j}^A)}{\sqrt{\alpha_2^2 + l_0^2} (\alpha_2^2 + l^2)^{N_A}},$$

$$k = \overline{1, 2}, \quad \alpha_2 \in \sigma,$$

where $\kappa_{\bar{N}_k} = \lim_{\alpha_2 \rightarrow \infty} \alpha_2 \bar{N}_k(\alpha_2)$, we can find

$$\bar{N}_k(\alpha_2) \approx \bar{N}_k^A(\alpha_2) = \Pi_{\bar{N}_k}(\alpha_2) \bar{N}_{k,R}^A(\alpha_2),$$

$$N_{1/2}(\alpha_2) \approx N_{1/2}^A(\alpha_2) = \bar{N}_{1/2}^A(\alpha_2) R_{+/-}(\alpha_2),$$

$$k = \overline{1, 2}, \quad \alpha_2 \in \sigma.$$

Then, the function $N^A(\alpha_2)$ is approximately constructed and factorized. After factorization, it takes the form

$$N^A(\alpha_2) = N_+^{A,\sigma}(\alpha_2) N_-^{A,\sigma}(\alpha_2),$$

$$N_{\pm}^{\sigma}(\alpha_2) \approx N_{\pm}^{A,\sigma}(\alpha_2) = \frac{\sqrt{\frac{\kappa_{\bar{N}_2} \varepsilon_{-,3}}{\kappa_{\bar{N}_1} \varepsilon_{+,3}}} (\alpha_2 \pm il)^{M_z^{\bar{N}_1}} (\alpha_2 \pm iq_-) \prod_{j=1}^{M_z^{\bar{N}_2}} (\alpha_2 \pm z_{\bar{N}_2,j}) \prod_{j=1}^{M_A} (\alpha_2 \pm z_{\bar{N}_2,j}^A)}{(\alpha_2 \pm il)^{M_z^{\bar{N}_2}} (\alpha_2 \pm iq_+) \prod_{j=1}^{M_z^{\bar{N}_1}} (\alpha_2 \pm z_{\bar{N}_1,j}) \prod_{j=1}^{M_A} (\alpha_2 \pm z_{\bar{N}_1,j}^A)}.$$

Approximation for functions $K(\alpha_2)$ and $N_1(\alpha_2)$ with given accuracy in the form of easily factorizable functions $K^A(\alpha_2)$ and $N_1^A(\alpha_2)$ allows us to analytically find the originals from the Fourier transforms of relations (5.8). Approximate values of the Fourier transforms for the desired displacements $U_{\pm}^A(\alpha_2) \approx U_{\pm}(\alpha_2)$, $\alpha_2 \in \sigma$,

$$U_{\pm}^A = \left(N_{\pm}^{A,\sigma}\right)^{\pm 1} \left[\{D_+^A Q_{0,+}\}_{\sigma}^{\pm} + \{D_-^A Q_{0,-}\}_{\sigma}^{\pm} + \sum_{j=1}^2 \left(A_{+j} \{D_+^A Q_{j,+}\}_{\sigma}^{\pm} + A_{-j} \{D_-^A Q_{j,-}\}_{\sigma}^{\pm} \right) + G_+(q_+) \{D_+^A Q_{1,+}^q\}_{\sigma}^{\pm} + G_+(iq_+) \{D_+^A Q_{2,+}^q\}_{\sigma}^{\pm} + G_-(-q_-) \{D_-^A Q_{1,-}^q\}_{\sigma}^{\pm} + G_-(-iq_-) \{D_-^A Q_{2,-}^q\}_{\sigma}^{\pm} \right],$$

where

$$D_{\pm}^A = \left(N_+^{A,\sigma}\right)^{-1} \left(N_1^A\right)^{-1} K^A \varepsilon_{5,\pm}.$$

5.4 Numerical Implementation Results

As a result of the numerical implementation of the developed algorithms for various boundary conditions at the junction of plates, we carried out calculations with varying properties of the coating and the elastic substrate.

All the results further are presented in a dimensionless form, where the linear dimensions are related to the characteristic size, and the density is related to the density value of the right coating plate. Dimensionless frequency is given by the formula $\bar{\omega} = \omega h_+ \sqrt{\frac{\rho_+}{\mu_+}}$, where ω is the dimensional frequency. In the numerical examples for plates, dimensionless parameters are fixed: $\rho_+ = \rho_- = 1$, $\mu_+ = 1$, $\nu_+ = \nu_- = 0.125$. For the elastic material of foundation $\rho = 1$. The vertical load is applied at the $x_0 = 5$.

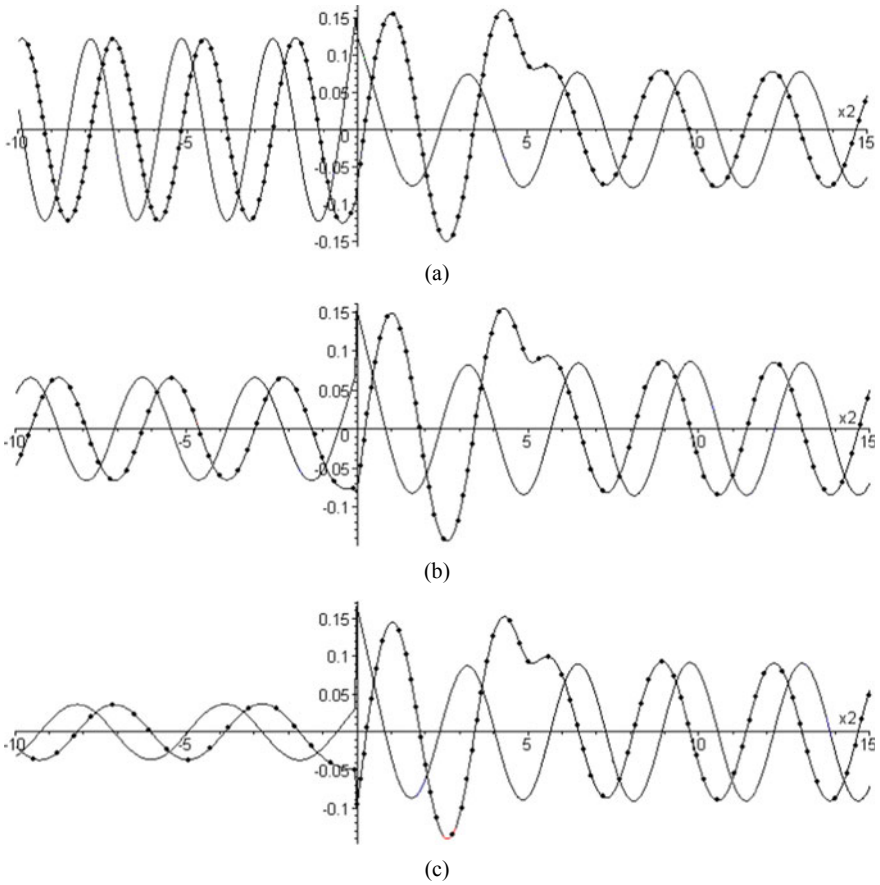


Fig. 5.1 Displacement of the surface of the system on condition of free displacement of the plates at the junction ($\nu = 0.25, \mu = 1.58$)

If the edges of the plates on the fault move freely, the bending moments $-D_{\pm} \frac{\partial^2 u_{\pm}}{\partial x_2^2}$ and transverse shear forces $-D_{\pm} \frac{\partial^3 u_{\pm}}{\partial x_2^3}, D_{\pm} = \frac{E_{\pm} h_{\pm}^2}{12(1-\nu_{\pm}^2)}$, in this area are equal to zero:

$$\left. \frac{\partial^2 u_{\pm}}{\partial x_2^2} \right|_{x_2=0} = 0, \quad \left. \frac{\partial^3 u_{\pm}}{\partial x_2^3} \right|_{x_2=0} = 0.$$

Figures 5.1 and 5.2 show graphs of real (line with markers) and imaginary (solid line) parts of surface displacement amplitudes under the condition of free displacement of the fault edges at a frequency $\bar{\omega} = 2$. Figure 5.1 corresponds to the values for the substrate $h = 2, \nu = 0.25, \mu = 1.58$. A variant of a softer foundation is illustrated in Fig. 5.2, here $\nu = 0.125, \mu = 0.67$ at the same dimensionless layer thickness.

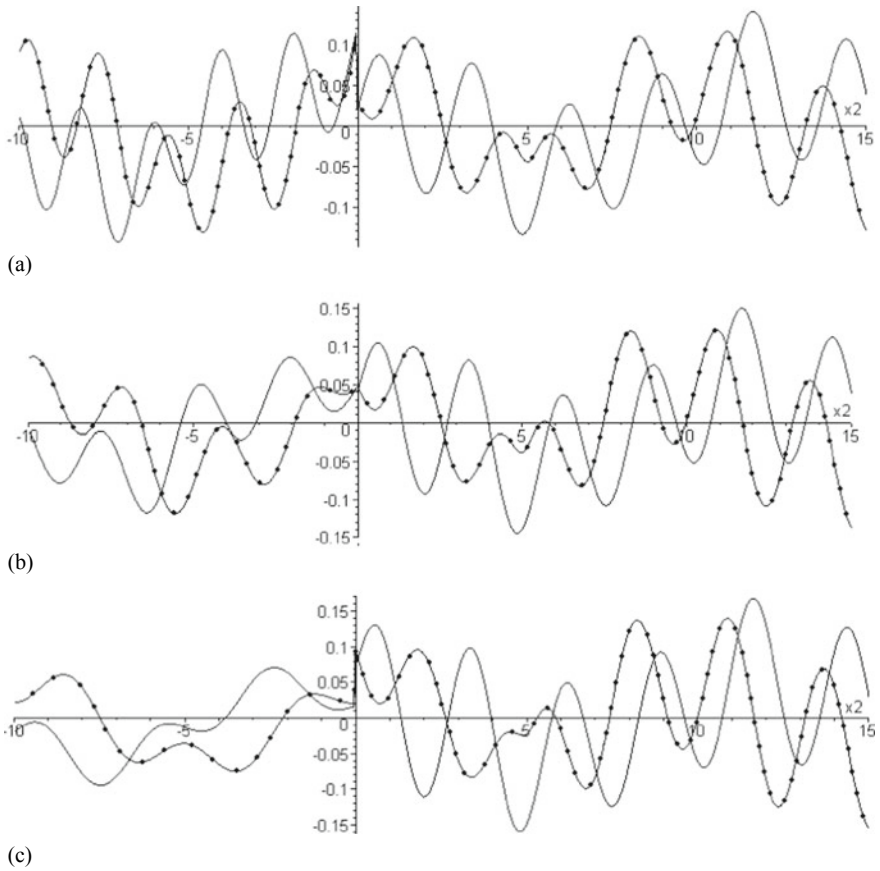
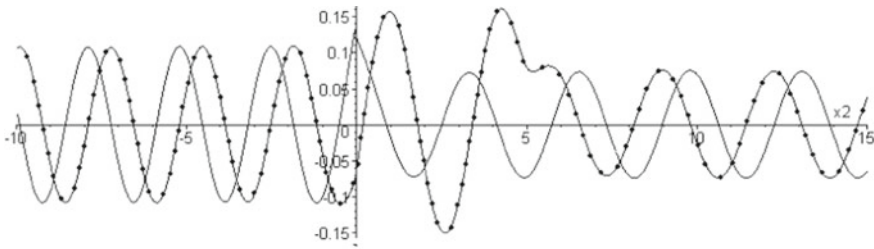


Fig. 5.2 Displacement of the surface of the system on condition of free displacement of the plates at the junction ($\nu = 0.125, \mu = 0.67$)

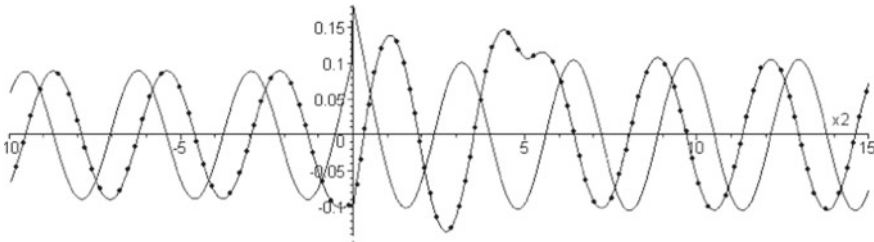
We also considered the condition for “viscous contact” of the plates in the conjugation area, while the cutting force on the plate boundary is proportional to the difference in the velocities for the edges of the plates, and the condition of zero bending moments is also satisfied

$$-D_{\pm} \frac{\partial^2 u_{\pm}}{\partial x_2^2} \Big|_{x_2=0} = 0; \quad -D_{\pm} \frac{\partial^3 u_{\pm}}{\partial x_2^3} \Big|_{x_2=0} = -ki\omega [u_{\mp}(x_2) - u_{\pm}(x_2)].$$

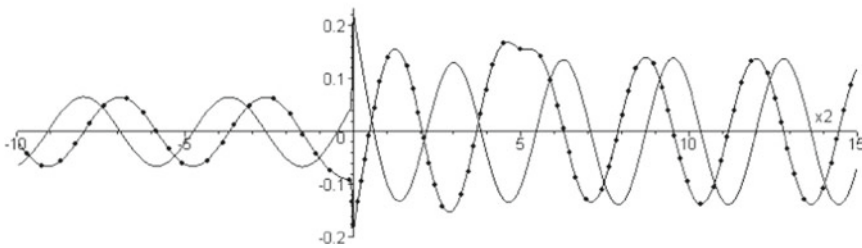
Figures 5.3 and 5.4 correspond to these boundary conditions, and Fig. 5.3 shows the results for a more rigid foundation ($\nu = 0.25, \mu = 1.58$), Fig. 5.4—for a softer



(a)



(b)



(c)

Fig. 5.3 Displacement of the surface of the system for “viscous” contact of the plates at the junction ($\nu = 0.25$, $\mu = 1.58$)

one ($\nu = 0.125$, $\mu = 0.67$), in both cases $k = 0.5$. In all Figs. 5.1, 5.2, 5.3 and 5.4, graph (a) corresponds to the case of a more rigid right plate ($\mu_- = 0.2$), graph (b)—to plates with the same properties, graph (c)—to the case of a more rigid left plate ($\mu_- = 5$).

The presented results of model calculations demonstrate the dependence of the system surface oscillations on the properties of the coating plates and foundation. For a more rigid foundation, the amplitude of displacements after passing through the fault is the smaller, the more rigid the left plate is. The wave fields for plates of different rigidity differ significantly, and the difference between the amplitudes of the wave fields on the right and left is the greater, the more contrast the properties of the plates. A softer foundation changes the pattern of displacements, violating the periodic nature of the graph and the dependence of the amplitudes on the hardness of the coating. It should also be noted that with a decrease in the vibration frequency,

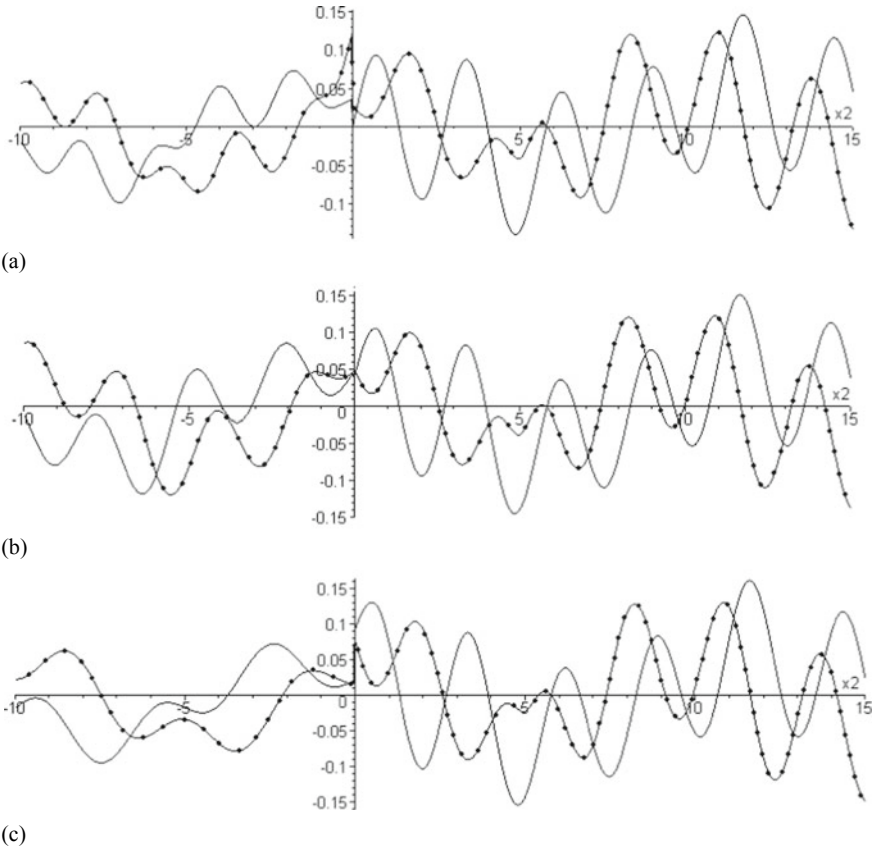


Fig. 5.4 Displacement of the surface of the system for “viscous” contact of the plates at the junction ($\nu = 0.125$, $\mu = 0.67$)

the displacement amplitudes of the left plate decrease in comparison with the right one, and the effect of the plate properties becomes less pronounced (Fig. 5.5). In Fig. 5.5, option (a) corresponds to the case of a more rigid right plate ($\mu_- = 0.2$), graph (b) corresponds to the case of a more rigid left plate ($\mu_- = 5$) for the frequency $\omega = 0.95$. The numerical results of the implementation for the method of solving the scalar problem based on the transformation of its differential operator [44, 45] match aforementioned results.

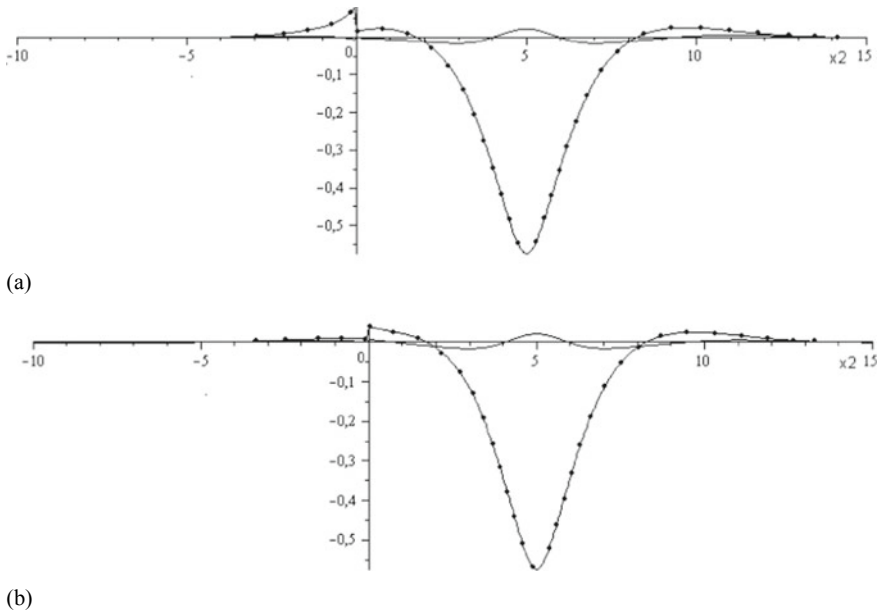


Fig. 5.5 Displacement of the surface of the system on condition of free displacement of the plates at the junction ($\omega = 0.95$)

5.5 Conclusion

We have outlined two approaches that make it possible to study both the qualitative features of the dynamic behavior of a block structure with a vertical defect in the form of the new type crack, and quantitative ones, which allows us to assess the degree of a harmonic source influence on the defect.

We have developed and implemented an analytic-numerical factorization method for solving boundary value problems of steady vibrations for an elastic medium with a coating in the form of extended plates, which allows us to investigate the nature of the harmonic signal propagation in the described structure for plates of different types as well as for plates of the same type under various contact conditions and substrate properties. The approach used in the work can be applied to problems of engineering practice and other important areas where objects with coatings are used. Here, the method can serve the purpose of evaluating a resource with an emerging defect. In other tasks, seismology and geophysics, it can serve the purposes of predicting imminent dangerous natural phenomena.

Acknowledgements The study was conducted with financial support from the RSF and KSF (project No. 22-21-20032, <https://rscf.ru/en/project/22-21-20032/>).

References

1. Cocou, M., Scarella, G.: Analysis of a dynamic unilateral contact problem for a cracked viscoelastic body. *Z. Angew. Math. Phys.* **57**, 523–546 (2006). <https://doi.org/10.1007/s00033-005-0013-x>
2. Kopp, J.B., Schmittbuhl, J., Noel, O., Lin, J., Fond, C.: Fluctuations of the dynamic fracture energy values related to the amount of created fracture surface. *Eng. Fracture Mech.* **126**, 178–189 (2014). <https://doi.org/10.1016/j.engfracmech.2014.05.014>
3. Zemlyanova, A.Y., Walton, J.R.: Modeling of a curvilinear planar crack with a curvature-dependent surface tension. *SIAM J. Appl. Math.* **72**, 1474–1492 (2012). <https://doi.org/10.48550/arXiv.1112.5235>
4. Kumar, S., Curtin, W.A.: Crack interaction with microstructure. *Mater. Today* **10**, 34–44 (2007). [https://doi.org/10.1016/S1369-7021\(07\)70207-9](https://doi.org/10.1016/S1369-7021(07)70207-9)
5. Becker, T.L., Cannon, R.M., Ritchie, R.O.: Statistical fracture modeling: crack path and fracture criteria with application to homogeneous and functionally graded materials. *Eng. Fract. Mech.* **69**, 1521–1555 (2002). [https://doi.org/10.1016/S0013-7944\(02\)00047-4](https://doi.org/10.1016/S0013-7944(02)00047-4)
6. Bassani, J., Qu, J.: Finite crack on bimaterial and bicrystal interfaces. *J. Mech. Phys. Solids* **37**(4), 435–453 (1989). [https://doi.org/10.1016/0022-5096\(89\)90023-9](https://doi.org/10.1016/0022-5096(89)90023-9)
7. Suo, Z.: Singularities, interfaces and cracks in dissimilar anisotropic media. *Proceeding of the Royal Society of London. Series A, Math. Phys.* **427**(1873), 331–358 (1990). <https://doi.org/10.1098/rspa.1990.0016>
8. Ni, L., Nemat-Nasser, S.: Interface cracks in anisotropic dissimilar materials: an analytic solution. *J. Mech. Phys. Solids* **29**(1), 113–144 (1991). [https://doi.org/10.1016/0022-5096\(91\)90033-K](https://doi.org/10.1016/0022-5096(91)90033-K)
9. Kim, C.I., Schiavone, P., Ru, C.-Q.: Effect of surface elasticity on an interface crack in plane deformations. *Proc. Royal Soc. London A: Math. Phys. Eng. Sci.* **467**, 3530–3549 (2011). <https://doi.org/10.1098/rspa.2011.0311>
10. Perelmuter, M.N.: An interface crack with non-linear bonds in a bridged zone. *J. Appl. Math. Mech.* **75**(1), 106–118 (2011). <https://doi.org/10.1016/j.jappmathmech.2011.04.016>
11. Goldstein, R.V., Perelmuter, M.N.: Kinetics of crack formation and growth on the material interface. *Mech. Solids* **47**(4), 400–414 (2012). <https://doi.org/10.3103/S002565441204005X>
12. Perelmuter, M.: Boundary element analysis of structures with bridged interfacial cracks. *Comput. Mech.* **51**(4), 523–534 (2013). <https://doi.org/10.1007/s00466-012-0817-4>
13. Perelmuter, M.N.: A criterion for the growth of cracks with bonds in the end zone. *J. Appl. Math. Mech.* **71**(1), 137–153 (2007). <https://doi.org/10.1016/j.jappmathmech.2007.03.002>
14. Morini, L., Piccolroaz, A.: Boundary integral formulation for interfacial cracks in thermofusible bimaterials. *Proc. R. Soc. A* **471**, 20150284 (2015). <https://doi.org/10.1098/rspa.2015.0284>
15. Morini, L., Radi, E., Movchan, A.B., Movchan, N.V.: Stroh formalism in analysis of skew-symmetric and symmetric weight functions for interfacial cracks. *Math. Mech. Solids* **18**, 135–153 (2013). <https://doi.org/10.1177/1081286512462299>
16. Piccolroaz, A., Mishuris, G., Movchan, A.B.: Symmetric and skew symmetric weight functions in 2D perturbation models for semi-infinite interfacial cracks. *J. Mech. Phys. Solids* **57**, 1657–1682 (2009). <https://doi.org/10.1016/j.jmps.2009.05.003>
17. Morini, L., Piccolroaz, A., Mishuris, G., Radi, E.: Integral identities for a semi-infinite interfacial crack in anisotropic elastic bimaterials. *Int. J. Solids. Struct.* **50**, 1437–1448 (2013). <https://doi.org/10.48550/arXiv.1205.1321>
18. Agrawal, A., Karlsson, A.M.: Obtaining mode mixity for a bimaterial interface crack using the virtual crack closure technique. *Int. J. Fract.* **141**, 75–98 (2006). <https://doi.org/10.1007/s10704-006-0069-4>
19. Beuth, J.L.: Separation of crack extension modes in orthotropic delamination models. *Int. J. Fract.* **77**, 305–321 (1996). <https://doi.org/10.1007/BF00036249>

20. Bjerken, C., Persson, C.: A numerical method for calculating stress intensity factors for interface cracks in bimaterials. *Eng. Fract. Mech.* **68**, 235–246 (2001). [https://doi.org/10.1016/S0013-7944\(00\)00098-9](https://doi.org/10.1016/S0013-7944(00)00098-9)
21. Hemanth, D., Shivakumar Aradhya, K.S., Rama Murthy, T.S., Govinda Raju, N.: Strain energy release rates for an interface crack in orthotropic media—A finite element investigation. *Eng. Fract. Mech.* **72**, 759–772 (2005). <https://doi.org/10.1016/j.engfracmech.2004.06.002>
22. Krueger, R.: Virtual crack closure technique: history, approach, and applications. *Appl. Mech. Rev.* **57**, 109–143 (2004). <https://doi.org/10.1115/1.1595677>
23. Mantič, V., París, F.: Relation between SIF and ERR based measures of fracture mode mixity in interface cracks. *Int. J. Fract.* **130**, 557–569 (2004). <https://doi.org/10.1023/B:FRAC.0000049496.77533.d5>
24. Oneida, E.K., van der Meulen, M.C.H., Ingrassia, A.R.: Methods for calculating G, GI and GII to simulate crack growth in 2D, multiple-material structures. *Eng. Fract. Mech.* **140**, 106–126 (2015)
25. Sun, C.T., Qian, W.: The use of finite extension strain energy release rates in fracture of interfacial cracks. *Int. J. Solids Struct.* **34**, 2595–2609 (1997). [https://doi.org/10.1016/S0020-7683\(96\)00157-6](https://doi.org/10.1016/S0020-7683(96)00157-6)
26. Sun, S., Chen, X., Badwe, N., Sieradzki, K.: Potential-dependent dynamic fracture of nanoporous gold. *Nature materials* **14**(9), 894–898 (2015). <https://doi.org/10.1038/nmat4335>
27. Chen, C.-H., Cambonie, T., Lazarus, V., Nicoli, M., Pons, A.J., Karma, A.: Crack front segmentation and facet coarsening in mixed-mode fracture. *Phys. Rev. Lett.* **115**, 265503 (2015). <https://doi.org/10.1103/PhysRevLett.115.265503>
28. Ronsin, O., Caroli, C., Baumberger, T.: Crack front échelon instability in mixed mode fracture of a strongly nonlinear elastic solid. *Europhys. Lett.* **105**(3), 34001 (2014). <https://doi.org/10.1209/0295-5075/105/34001>
29. Sator, C., Becker, W.: Closed-form solutions for stress singularities at plane bi- and trimaterial junctions. *Arch. Appl. Mech.* **82**, 643–658 (2012). <https://doi.org/10.1007/s00419-011-0580-6>
30. Rice, J.R., Sih, G.C.: Plane problems of cracks in dissimilar media. *Trans. ASME. J. Appl. Mech.* **32**, 218–224 (1965). <https://doi.org/10.1115/1.3625816>
31. Rice, J.R.: Elastic fracture mechanics concepts for interface cracks. *Trans. ASME. J. Appl. Mech.* **55**, 98–103 (1988). <https://doi.org/10.1115/1.3173668>
32. Sinclair, G.B.: Stress singularities in classical elasticity—I: removal, interpretation, and analysis. *Appl. Mech. Rev.* **57**, 251–298 (2004). <https://doi.org/10.1115/1.1762503>
33. Sinclair, G.B.: Stress singularities in classical elasticity—II: asymptotic identification. *Appl. Mech. Rev.* **57**, 385–439 (2004). <https://doi.org/10.1115/1.1767846>
34. Morozov, N.F.: *Mathematical Questions of the Theory of Cracks*. Nauka, Moscow (1984). [in Russian]
35. Cherepanov, G.P.: *Brittle Fracture Mechanics*. Nauka, Moscow (1974). [in Russian]
36. Barsukov, S.A., Glushkov, E.V., Glushkova, N.V.: Stress singularity at front corner points of an interfacial crack between two media. *Izvestia RAN. Mekh. Tverdogo Tela* **2**, 77–85 (2002). [in Russian]
37. Babeshko, V.A., Evdokimova, O.V., Babeshko, O.M.: A new type of cracks adding to Griffith-Irwin cracks. *Doklady Phys.* **64**(2), 102–105 (2019). <https://doi.org/10.1134/S10283358191030042>
38. Babeshko, V.A., Evdokimova, O.V., Babeshko, O.M.: On a new model for predicting landslide events. In: Irschik, H., Krommer, M., Matveenko, V.P., Belyaev, A.K. (eds.) *Dynamics and control of advanced structures and machines*. *Adv. Struct. Mater.* **156** (2022). Springer, Cham. https://doi.org/10.1007/978-3-030-79325-8_2
39. Babeshko, V.A., Evdokimova, O.V., Babeshko, O.M., Pavlova, A.B., Telatnikov, I.S., Fedorenko, A.G.: The theory of block structures in problems on the strength of galleries and constructions with multiple connections. *Doklady Phys.* **64**(1), 4–8 (2019). <https://doi.org/10.1134/S1028335819010014>

40. Babeshko, V.A., Evdokimova, O.V., Babeshko, O.M., Evdokimov, V.S., Uafa, S.B.: On bearing resources and on the mechanics of subduction processes. *Mech. Solids* **55**(3), 309–315 (2020). <https://doi.org/10.3103/S0025654420030036>
41. Babeshko, V.A., Evdokimova, O.V., Babeshko, O.M.: On the possibility of predicting some types of earthquake by a mechanical approach. *Acta Mech.* **229**(5), 2163–2175 (2018). <https://doi.org/10.1007/s00707-017-2092-0>
42. Vorovich, I.I., Babeshko, V.A.: *Dynamic Mixed Problems of Elasticity Theory for Non-classical Domains*. Nauka, Moscow (1979). [in Russian]
43. Vorovich, I.I., Babeshko, V.A., Pryakhina, O.D.: *The Dynamics of Massive Bodies and Resonance Phenomena in Deformable Media*. Nauchny Mir, Moscow (1999). [in Russian]
44. Kolesnikov, M.N., Telyatnikov, I.S.: To the research methods of faults under the vibration impacts. *Sci. J. KubSAU* (7), 647–659 (2016). Available at: <http://ej.kubagro.ru/2016/07/pdf/33.pdf>. [in Russian]
45. Kolesnikov, M.N., Telyatnikov, I.S.: About method of studying the dynamics of contacting lithospheric structures. *Ecolog. Bullet. Sci. Centers of the BSEC* (4 pt. 1), 50–61 (2017). [in Russian]
46. Noble, B.: *Methods Based on the Wiener-Hopf Technique for the Solution of Partial Differential Equations*. Pergamon Press, New York (1958)

Chapter 6

Stress–Strain State of a Magnetoelastic Ferromagnetic Plane with a Crack Under the Action of a Magnetic Field



Gevorg Y. Baghdasaryan

Abstract This work is devoted to investigation of the stress–strain state of an elastic ferromagnetic plane with a crack under the action of an external magnetic field. The main characteristics of the stress–strain state and the magnetic field induced in the medium are determined. Their features near the crack are investigated depending on the medium properties and on the intensity of the external magnetic field. The conditions for the occurrence of concentrations of magnetoelastic stresses and components of the induced magnetic field at the ends of the crack are obtained. It is shown that the occurrence of concentration in ferromagnetic bodies with cracks substantially depends on the sign of the magnetostriction constant. It is established that in a magnetically soft ferromagnet with a crack, concentrations of magnetoelastic quantities arise only in those cases when the relative magnetic permeability of the material is sufficiently large. Formulas that determine the intensity factors for both magnetoelastic stresses and for the components of the induced magnetic fields are derived.

Keywords Magnetostriction · Crack · Crack intensity factor · Concentration

6.1 Introduction

The problem of the stress–strain state of an elastic magnetostrictive plane with a straight crack is considered. The only source that causes elastic deformations and an induced magnetic field in a medium is an external magnetic field. The study was carried out based on linear equations and boundary conditions for the magnetoelasticity of a ferromagnetic body [1], obtained using the main provisions of the nonlinear theory of magnetoelastic interactions in these mediums [2–5]. The main characteristics of the stress–strain state and induced magnetic field in the medium are determined. Their features near the crack are studied depending on the orientation of the external magnetic field, the magnitude of the magnetostrictive constants of

G. Y. Baghdasaryan (✉)

Institute of Mechanics, National Academy of Sciences of Armenia, 24B Baghramyan Ave,
Yerevan 0019, Republic of Armenia
e-mail: gevorg.baghdasaryan@rau.am

the medium and the intensity of the given magnetic field. It has been established that if the external magnetic field is directed obliquely to the plane of the crack, then in addition to the plane problem of determining the stress–strain state of a magnetoelastic system with a crack [6–8], there also arises the problem of a longitudinal shear crack (antiplane problem). Note that if the magnetic field is perpendicular to the plane of the crack, then the antiplane problem does not arise [6–8]. The conditions for the appearance of concentrations of magnetoelastic stresses and components of the induced magnetic field at the ends of a crack are obtained. It is shown that: (a) the occurrence of concentration in magnetostrictive bodies with a crack depends significantly on the sign of the magnetostriction constants; (b) if the material of the medium does not have magnetostrictive properties, then concentrations of magnetoelastic quantities appear in a magnetically soft ferromagnet with a crack only in cases where the relative magnetic permeability of the material is sufficiently large; (c) shear stresses of magnetoelastic origin take maximum values of about forty-five degrees of the magnetic field inclination angle. Formulas are also obtained that determine the intensity factors both for magnetoelastic stresses and for the components of induced magnetic fields. Similar problems on the concentrations of elastic stresses and the induced magnetic field near a crack, when the material of the body does not have magnetostrictive properties, are considered in [6–8]. The results revealed in this article have numerous applications in various fields, such as fracture mechanics, geophysics, optics, acoustics and can become a means of detecting defects in magnetoactive bodies using magnetic fields.

6.2 Statement of the Problem

It is known that when a ferromagnetic body is placed in a magnetic field, the material is magnetized, which leads both to a change in the magnetic field intensity throughout the space and to the appearance of body and surface forces. Under the action of these forces, deformations arise in the medium, which excite an additional (induced) magnetic field. Based on this, the characteristics of the magnetic field are presented in the form

$$\vec{H} = \vec{H}_0 + \vec{h}, \quad \vec{B} = \vec{B}_0 + \vec{b}, \quad \vec{M} = \vec{M}_0 + \vec{m},$$

where \vec{H}_0 , \vec{B}_0 and \vec{M}_0 , respectively, are the vectors of intensity, magnetic induction and magnetization of the magnetic field of an undeformed body and \vec{h} , \vec{b} and \vec{m} are additions to the indicated quantities due to the deformation of the medium. In vacuum, the vectors \vec{B} and \vec{H} are related by the relation $\vec{B}^{(e)} = \mu_0 \vec{H}_0^{(e)}$, where μ_0 is the absolute magnetic constant ($\mu_0 = 4\pi \cdot 10^{-7} \text{N/m}$) and the index e hereinafter means belonging to the external (surrounding the body) medium, the electromagnetic properties of which are equivalent to those of vacuum.

The characteristics of the magnetic field of an undeformed body are determined from the solution of the following problem of magnetostatics:

$$\begin{aligned} \operatorname{rot} \vec{H}_0 &= 0, \quad \operatorname{div} \vec{B}_0 = 0, \quad \vec{B}_0 = \mu_0 \mu_r \vec{H}_0; \\ \vec{n} \cdot (\vec{H}_0 - \vec{H}_0^{(e)}) &= 0, \quad \vec{n} \times (\vec{H}_0 - \vec{H}_0^{(e)}) = 0 \quad \text{for } (x_1, x_2, x_3) \in S_0; \\ \vec{H}_0^{(e)} &\rightarrow \vec{H}^{(0)} \quad \text{for } |\vec{r}| \rightarrow \infty; \end{aligned} \quad (6.2.1)$$

where \vec{n} is the unit vector of the outer normal to the undeformed surface of the S_0 body, \vec{r} is the radius vector, x_i are the Cartesian coordinates of the considered point, μ_r is the relative magnetic permeability of the medium and $\vec{H}^{(0)}$ is the intensity of the given magnetic field at infinity in the absence of a ferromagnetic body.

The stress–strain state of the medium and the magnetic field induced in it are determined from the equations and boundary conditions of magnetoelasticity of magnetostrictive ferromagnetic bodies. Based on the main provisions of the theory of small perturbations, it is assumed that both the deformations and the magnetic quantities due to them are small ($\varepsilon_{ij} \ll 1$, $|\vec{h}/\vec{H}_0| \ll 1$, $|\vec{b}/\vec{B}_0| \ll 1$, $|\vec{m}/\vec{M}_0| \ll 1$, where ε_{ij} are the components of the linear strain tensor). On this basis, the equations and boundary conditions are linearized. As a result, at $|M_{0j}u_{i,j}| \ll |m_i|$, the following linear equations and boundary conditions of magnetoelasticity are obtained, given in [1, 3]:

- System of differential equations of the deformable state

$$\begin{aligned} t_{ik,k} + \mu_0(M_{0k}H_{0i,k} + M_{0k}h_{i,k} + m_k H_{0i,k}) &= 0, \\ \varepsilon_{ijk}h_{k,j} = 0, \quad b_{j,j} = 0, \quad (\vec{b} = \mu_0\mu_r\vec{h}), \end{aligned} \quad (6.2.2)$$

where t_{ij} is the tensor of magnetoelastic stresses and μ_r is the relative magnetic permeability of the medium;

- Equations of state

$$t_{ij} = t_{ij}^{(0)} + C_{ijkl}u_{k,l} + 2\mu_0 B_{ijkl}M_{0l}m_k + \mu_0(H_{0j}m_i + H_{0i}m_j), \quad m_i = \chi h_i, \quad (6.2.3)$$

where

$$t_{ij}^{(0)} = \mu_0 \chi^{-1} M_{0i} M_{0j} + \frac{1}{2} \mu_0 B_{ijkl} M_{0k} M_{0l};$$

- Boundary conditions at the interfaces of two media

$$\varepsilon_{ijk} \left\{ n_j \left[h_k - h_k^{(e)} \right] - n_m \left[H_{0k} - H_{0k}^{(e)} \right] u_{m,j} \right\} = 0,$$

$$\begin{aligned} n_j [b_i - b_i^{(e)}] &= n_m [B_{0i} - B_{0i}^{(e)}] u_{m,i}, \\ n_i [t_{ij} - t_{ij}^{(e)}] &= [T_{ki}^{(e)} - T_{ki}] n_k. \end{aligned} \quad (6.2.4)$$

In (6.2.2)–(6.2.4), C_{ijkl} and B_{ijkl} are the tensors of elastic constants and magnetostrictive coefficients, respectively, u_k are the components of the displacement vector of points in the medium, ε_{ijk} is the Levy-Civita symbol, the $\chi = \mu_r - 1$ magnetic susceptibility of the material of the medium and $T_{ki}^{(e)}$ and T_{ki} the Maxwell stress tensors in vacuum and in a magnetostrictive medium, respectively. Over repeated indices, summation is assumed, and the notation $f_{,k}$ means $\partial f / \partial x_k$.

We note that in deriving the last three conditions from (6.2.4), we used the Maxwell stress tensor T_{ij}

$$\begin{aligned} T_{ki}^{(e)} &= \mu_0 \left(H_i^{(e)} H_k^{(e)} + H_i^{(e)} h_k^{(e)} + H_k^{(e)} h_i^{(e)} \right) \\ &\quad - \mu_0 \delta_{ik} \left(\frac{1}{2} H_j^{(e)} H_j^{(e)} + H_j^{(e)} h_j^{(e)} \right), \\ T_{ki} &= \mu_0 \mu_r (H_{0i} H_{0k} + H_{0i} h_k + H_{0k} h_i) \\ &\quad - \mu_0 \delta_{ik} \left(\frac{1}{2} H_{0j} H_{0j} + H_{0j} h_j \right). \end{aligned} \quad (6.2.5)$$

In what follows, only isotropic media are considered. For such media, the tensor C_{ijkl} has the following well-known representation:

$$C_{ijkl} = \lambda \delta_{ij} \delta_{kl} + \mu (\delta_{ik} \delta_{jl} + \delta_{il} \delta_{jk}), \quad (6.2.6)$$

and the tensor B_{ijkl} according to [3, 9–12] is represented as [13]

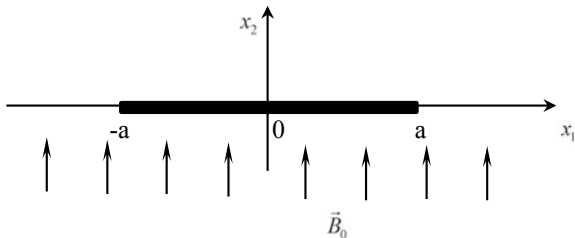
$$B_{ijkl} = e_2 \delta_{ij} \delta_{kl} + \frac{1}{2} (e_1 - e_2) (\delta_{ik} \delta_{jl} + \delta_{il} \delta_{jk}), \quad (6.2.7)$$

Here λ and μ are the Lamé parameters, e_1 and e_2 are the magnetostriction coefficients of the material of the medium.

6.3 Solution of the Problem in the Case of a Constant Transverse Magnetic Field

Based on the above equations and boundary conditions, the formulation of the plane problem of the concentration of elastic stresses and the induced magnetic field near a crack caused by an external transverse magnetic field is formulated below. The rectangular Cartesian coordinate system is (x_1, x_2, x_3) chosen so that the cross-section of the crack (the edges of which are free from external mechanical loads) is in

Fig. 6.1 A crack of finite dimensions in a magnetostrictive body



the plane $(x_1, 0, x_2)$ and occupies an area $[-a, a]$ on the coordinate axis $0x_1$. The medium is placed in a constant magnetic field $\vec{B}^{(0)}(0, B_0, 0)$ (which is the only source of external influences) and is under conditions of plane deformation in the plane $(x_1, 0, x_2)$ (Fig. 6.1).

Note that for the case under consideration problem (6.2.1) has the following solution:

$$\begin{aligned}\vec{B}_0^{(e)} &= B_0 \vec{i}_2, \quad \vec{B}_0 = \vec{B}_0^{(e)}, \\ \vec{H}_0^{(e)} &= \vec{B}_0^{(e)} \mu_0^{-1}, \quad \vec{H}_0 = \vec{B}_0 (\mu_0 \mu_r)^{-1},\end{aligned}\quad (6.3.1)$$

where \vec{i}_k are the unit vectors of the coordinate axes. In (6.3.1) and in what follows, the index e means belonging to the crack region.

By virtue of (6.2.3) and (6.3.1), from (6.2.2) for the problem under consideration, the following equations of magnetoelasticity of the deformed state are obtained:

$$\begin{aligned}\Delta u_1 + \frac{1}{1-2\nu} \frac{\partial}{\partial x_1} \left(\frac{\partial u_1}{\partial x_1} + \frac{\partial u_2}{\partial x_2} \right) + \frac{2\chi B_0}{\mu_r \mu} s \frac{\partial h_1}{\partial x_2} &= 0, \\ \Delta u_2 + \frac{1}{1-2\nu} \frac{\partial}{\partial x_2} \left(\frac{\partial u_1}{\partial x_1} + \frac{\partial u_2}{\partial x_2} \right) + \frac{2\chi B_0}{\mu_r \mu} s \frac{\partial h_2}{\partial x_2} &= 0;\end{aligned}\quad (6.3.2)$$

$$\begin{aligned}\Delta \Phi &= 0, \quad \Delta \Phi^{(e)} = 0, \\ h_k &= \frac{\partial \Phi}{\partial x_k}, \quad h_k^{(e)} = \frac{\partial \Phi^{(e)}}{\partial x_k},\end{aligned}\quad (6.3.3)$$

where Δ is the two-dimensional Laplace operator, ν is the Poisson ratio and s is the coefficient characterizing the properties of the magnetostriction of the material of the medium

$$s = 1 + \chi \frac{e_1 + e_2}{2},$$

Φ and $\Phi^{(e)}$ are the potentials of induced magnetic fields.

Similarly, from (6.2.3) and (6.2.4), considering the symmetry of the problem, the following boundary conditions on the plane are obtained $x_2 = 0$:

$$\begin{cases} h_1(x_1, 0) = h_1^{(e)}(x_1, 0) + \frac{\chi B_0}{\mu_0 \mu_r} u_{2,1}(x_1, 0), \\ \mu_r h_2(x_1, 0) = h_2^{(e)}(x_1, 0), \\ \Phi^{(e)}(x_1, 0) = 0, \\ t_{22}(x_1, 0) = \frac{\chi^2}{\mu_r} \left[\frac{B_0^2}{2\mu_0 \mu_r} + B_0 h_2(x_1, 0) \right] \end{cases} \quad \text{for } |x_1| < a \quad (6.3.4)$$

$$\Phi(x_1, 0) = 0, \quad u_2(x_1, 0) = 0 \quad \text{for } |x_1| > a \quad (6.3.5)$$

$$t_{12}(x_1, 0) = 0 \quad \text{for } |x_1| < \infty \quad (6.3.6)$$

In addition to conditions (6.3.4)–(6.3.6), the conditions at infinity must also be satisfied, according to which $\lim_{h_i} = 0 (i = 1, 2)$. Thus, if the magnetic field is perpendicular to the plane of the crack, then the problem of determining the stress–strain state of the medium is flat and is represented by Eqs. (6.3.2)–(6.3.4) and conditions (6.3.4)–(6.3.6).

6.4 Solution of the Problem

Solutions of Eqs. (6.3.4) and (6.3.5) satisfying the conditions at infinity, where $x_2 > 0$ can be represented as

$$\begin{aligned} u_1 &= \frac{2}{\pi} \int_0^\infty \left\{ \left[c_1(\alpha) - \frac{3 - 4\nu - x_2 \alpha}{\alpha} c_2(\alpha) \right] e^{-\alpha x_2} \right. \\ &\quad \left. + s \cdot \frac{2(1 - 2\nu)\chi}{\mu_r \mu} B_0 c_3(\alpha) e^{-\alpha x_2} \right\} \sin \alpha x_1 d\alpha, \\ u_2 &= \frac{2}{\pi} \int_0^\infty [c_1(\alpha) + x_2 c_2(\alpha)] e^{-\alpha x_2} \cos \alpha x_1 d\alpha, \end{aligned} \quad (6.4.1)$$

$$\begin{aligned} \Phi &= \frac{2}{\pi} \int_0^\infty c_3(\alpha) e^{-\alpha x_2} \cos \alpha x_1 d\alpha, \\ \Phi^{(e)} &= \frac{2}{\pi} \int_0^\infty c_3^{(e)}(\alpha) \operatorname{sh} \alpha x_2 \cos \alpha x_1 d\alpha, \end{aligned} \quad (6.4.2)$$

where $c_i(\alpha) (i = 1, 2, 3)$ and $c_3^{(e)}(\alpha)$ are unknown functions, which are determined by satisfying the boundary conditions (6.3.4)–(6.3.6).

Substituting (6.4.1) and (6.4.2) into (6.2.3) and (6.2.5), we determine the magnetoelastic stresses t_{ij} and Maxwell stresses T_{ij} . In particular, for normal stresses t_{22} and T_{22} , we obtain the following expressions:

$$t_{22} = \frac{4\mu}{\pi} \int_0^{\infty} \left\{ -\alpha c_1 + (1 - 2\nu - \alpha x_2) c_2 - \frac{\chi B_0}{\mu_r \mu} [1 - 2\nu - \nu \chi (e_1 + e_2)] \alpha c_3 \right\} e^{-\alpha x_2} \cos \alpha x_1 d\alpha + \frac{\chi B_0^2}{2\mu_0 \mu_r^2} (2 + \chi e_1),$$

$$T_{22} = \frac{2\chi + 1}{\mu_r} B_0 \left[\frac{B_0}{2\mu_0 \mu_r} - \frac{2}{\pi} \int_0^{\infty} \alpha c_3(\alpha) e^{-\alpha x_2} \cos \alpha x_1 d\alpha \right]. \quad (6.4.3)$$

Let us pass to the definition of unknown functions $c_i(\alpha)$ ($i = 1, 2, 3$) and $c_3^{(e)}(\alpha)$ by satisfying the boundary conditions (6.3.4)–(6.3.6). The boundary condition (2.13) leads to the following relation between the unknown functions:

$$\alpha c_1(\alpha) = 2(1 - \nu) c_2(\alpha) - \frac{B_0 \chi}{2\mu \mu_r} \{3 - 4\nu + 2\chi[(1 - \nu)e_1 - \nu e_2]\} \alpha c_3(\alpha). \quad (6.4.4)$$

Using (6.4.4), it is easy to show that the representations (6.4.1) satisfy the boundary conditions (6.3.4) and (6.3.5) (except for the second condition from (2.11)), if the unknown functions $c_1(\alpha)$ and $c_3(\alpha)$ are solutions of the following system of dual integral equations:

$$\int_0^{\infty} c_1(\alpha) \cos \alpha x_1 d\alpha = 0, \quad |x_1| > a$$

$$\int_0^{\infty} \alpha c_1(\alpha) \cos \alpha x_1 d\alpha = \frac{\pi(1 - \nu)(2 - \chi + \chi e_1)}{4\mu_0 \mu \mu_r^2} \chi B_0^2, \quad |x_1| < a \quad (6.4.5)$$

$$+ \frac{\chi B_0 f_1(e_1, e_2)}{2\mu \mu_r} \int_0^{\infty} \alpha c_3(\alpha) \cos \alpha x_1 d\alpha;$$

$$\int_0^{\infty} c_3(\alpha) \cos \alpha x_1 d\alpha = 0, \quad |x_1| > a$$

$$\int_0^{\infty} \alpha \left[c_3(\alpha) - \frac{\chi B_0}{\mu_0 \mu_r} c_1(\alpha) \right] \sin \alpha x_1 d\alpha = 0, \quad |x_1| < a \quad (6.4.6)$$

where

$$f_1(e_1, e_2) = 2\nu - 1 + 2(1 - \nu)\chi + 2\chi[e_1 - \nu(e_1 - e_2)].$$

The solution of the system of dual integral Eqs. (6.4.5)–(6.4.6), following [6, 14], can be represented as

$$\begin{aligned} c_1(\alpha) &= \int_0^a \varphi(\zeta) J_0(\alpha\zeta) d\zeta, \\ c_3(\alpha) &= \int_0^a \psi(\zeta) J_0(\alpha\zeta) d\zeta, \end{aligned} \quad (6.4.7)$$

where $J_0(\alpha\zeta)$ is the Bessel function of the real argument and $\varphi(\xi)$ and $\psi(\xi)$ are the new unknown functions.

By (6.4.7), the first equation in (6.4.5) and (6.4.6) is identically satisfied for any integrable functions $\varphi(\xi)$ and $\psi(\xi)$, and the second equations from (6.4.5) and (6.4.6) give the following system of integral equations for $\varphi(\xi)$ and $\psi(\xi)$:

$$\begin{aligned} \frac{d}{dx_1} \int_{x_1}^a \left[\psi(\xi) - \frac{\chi B_0}{\mu_0 \mu_r} \varphi(\xi) \right] \frac{d\xi}{\sqrt{\xi^2 - x_1^2}} &= 0, & |x_1| < a \\ \frac{d}{dx_1} \int_0^{x_1} \left[\frac{\chi B_0 f_1}{2\mu\mu_r} \psi(\xi) - \varphi(\xi) \right] \frac{d\xi}{\sqrt{x_1^2 - \xi^2}} &= \frac{\chi B_0^2}{4\mu_0 \mu \mu_r^2} f_2, & |x_1| < a \end{aligned} \quad (6.4.8)$$

where

$$f_2 = \pi(1 - \nu)(\chi - 2 - \chi e_1).$$

It follows from (6.4.8) that the unknowns φ and ψ are solutions of the following system of linear algebraic equations:

$$\begin{aligned} \psi(\xi) - \frac{\chi B_0}{\mu_0 \mu_r} \varphi(\xi) &= 0, \\ \frac{\chi B_0 f_1 (e_1, e_2)_1}{2\mu\mu_r} \psi(\xi) - \varphi(\xi) &= \frac{\chi B_0^2}{4\mu_0 \mu \mu_r^2} f_2 \cdot \xi, \end{aligned} \quad (6.4.9)$$

Substituting $\varphi(\xi)$ and $\psi(\xi)$, which are solutions of system (6.4.9) into representations (3.7), for the unknowns $c_1(\alpha)$ and $c_3(\alpha)$, we obtain the following expressions:

$$\begin{aligned} c_1(\alpha) &= a A_1 \alpha^{-1} J_1(a\alpha), \\ c_3(\alpha) &= a A_3 \alpha^{-1} J_1(a\alpha), \end{aligned} \quad (6.4.10)$$

where

$$\begin{aligned}
A_1 &= -\frac{\chi B_0^2}{2\mu_0\mu} \frac{f_2(e_1)}{\Delta}, \\
A_3 &= -\frac{B_0}{2\mu_0\mu_r} \frac{\chi^2 B_0^2}{\mu_0\mu} \frac{f_2(e_1)}{\Delta}, \\
\Delta &= 2\mu_r^2 - \frac{\chi^2 B_0^2}{\mu_0\mu} f_1(e_1, e_2),
\end{aligned} \tag{6.4.11}$$

$J_1(a\alpha)$ is the Bessel function of a real argument, and formulas (6.4.10) are obtained under the assumption that the determinant Δ of system (6.4.9) is nonzero.

On the basis of (6.4.4) and (6.4.10) from (6.4.1) and (6.4.2), we find the displacements u_i ($i = 1, 2$) and the potential of the induced magnetic field Φ . Substituting the found expressions for u_i and Φ into (6.2.3) and (6.2.5), we determine the magnetoelastic stresses t_{ij} and the induced magnetic field \vec{h} in the medium. In particular, using (6.4.1), (6.4.3) and (6.4.10), for h_i , t_{22} , T_{22} and u_2 for $x_2 = 0$, we obtain the following expressions:

$$\begin{aligned}
h_1(x_1, 0) &= \begin{cases} 0, & \text{for } |x_1| > a \\ -\frac{2A_3}{\pi} \frac{x_1}{\sqrt{a^2 - x_1^2}}, & \text{for } |x_1| < a \end{cases} \\
h_2(x_1, 0) &= \frac{2A_3}{\pi} \begin{cases} \frac{a^2}{\sqrt{x_1^2 - a^2} [x_1 + \sqrt{x_1^2 - a^2}]}, & \text{for } |x_1| > a \\ -1, & \text{for } |x_1| < a \end{cases}
\end{aligned} \tag{6.4.12}$$

$$\begin{aligned}
t_{22} &= \frac{\chi B_0^2}{2\mu_0\mu_r^2} (2 + \chi e_1) \\
&+ \frac{2\mu A_1}{\pi(1 - \nu)} \left\{ 1 - \frac{\chi^2 B_0^2}{2\mu_0\mu\mu_r^2} [f_1 - 2(1 - \nu)\chi] \right\} \frac{a^2}{\sqrt{x_1^2 - a^2} [x_1 + \sqrt{x_1^2 - a^2}]}
\end{aligned}$$

for $|x_1| > a$

$$\begin{aligned}
T_{22} &= \frac{(2\chi + 1)B_0^2}{2\mu_0\mu_r^2} \\
&+ \frac{2(2\chi + 1)B_0}{\pi\mu_r} \frac{a^2 A_3}{\sqrt{x_1^2 - a^2} [x_1 + \sqrt{x_1^2 - a^2}]} \quad \text{for } |x_1| > a
\end{aligned} \tag{6.4.13}$$

$$u_2(x_1, 0) = \frac{2A_1}{\pi} \sqrt{a^2 - x_1^2}, \quad \text{for } |x_1| < a \tag{6.4.14}$$

Formulas (6.4.12) and (6.4.13) show that the presence of cracks in magnetostrictive ferromagnetic deformable bodies (which are only under the action of an external stationary magnetic field) leads to the appearance of a concentration of both magnetoelastic stresses and stresses of the magnetic field induced in the body. These results were also found in the case of magnetically soft ferromagnetic bodies in [6, 9].

6.5 Coefficients of Intensity of Magnetoelastic Stresses and Induced Magnetic Field

Using (6.4.12) and (6.4.13), it is easy to find the following expressions for the intensity factors of magnetoelastic stresses and the stress components of the magnetic field induced in the body:

- For total magnetoelastic stresses $t_{22}^C = t_{22} + T_{22}$

$$K_1 = \lim_{x_1 \rightarrow a+0} \sqrt{2(x_1 - a)} t_{22}^C|_{x_2=0} = [\chi(e_1 - 1) + 2] \frac{b_c^2 R_1 \mu}{2\Delta} \sqrt{a}, \quad (6.5.1)$$

where

$$R_1 = 2\chi + \left(\frac{\chi b_c}{\mu_r} \right)^2 \{2(1 - \nu + (5 + 6\nu)\chi - 2\chi^2[e_1 - \nu(e_1 - e_2)])\},$$

$$\Delta = 2\mu_r^2 - (\chi b_c)^2 f_1(e_1, e_2), \quad b_c^2 = \frac{B_0^2}{\mu_0 \mu};$$

- For the components of the induced magnetic field

$$K_2 = \lim_{x_1 \rightarrow a+} \sqrt{2(x_1 - a)} h_2|_{x_2=0}$$

$$= [\chi(e_1 - 1) + 2] \frac{B_0}{\mu_0 \mu_r} \frac{(\chi b_c)^2}{\Delta} (1 - \nu) \sqrt{a}. \quad (6.5.2)$$

Bearing in mind that equal in magnitude and oppositely directed normal forces act on the crack faces, it is assumed that concentrations of magnetoelastic stresses and components of the induced magnetic field appear at the ends of the crack, if $u_2(x_1, 0) > 0$ at $|x_1| < a$. Because of this, it follows from (6.4.11) and (6.4.14) that the normal displacement of the crack edge $x_2 = 0^+$ will be positive if

$$f_2(e_1) \cdot (\Delta)^{-1} < 0. \quad (6.5.3)$$

Consequently, inequality (6.5.3) is the condition for the occurrence of concentrations of the quantities indicated above at the ends of the crack.

In the case of magnetically soft ferromagnetic materials that do not have magnetostrictive properties ($e_1 = e_2 = 0$), condition (6.5.3) has the form

$$\frac{\pi(1 - \nu)(\chi - 2)}{2\mu_r^2 - (\chi b_c)^2 [2\nu - 1 + 2(1 - \nu)\chi]} < 0. \quad (6.5.4)$$

Considering that $B_0 \leq B_s$ (where B_s is the saturation induction and $B_s \leq 2T$), it is easy to check that inequality (6.5.4) in the case of soft magnetic materials will be

satisfied if $\mu_r > 10^4$. Those only for such magnetically soft materials, which have the indicated relatively high relative magnetic permeability, will concentrations of magnetoelastic stresses and components of the magnetic field intensity appear at the ends of the crack.

Let us return to condition (6.5.3), when the materials of the media have a magnetostrictive property. Bearing in mind that, according to [11, 13, 15], $e_2 \approx -0.5e_1$ and for the main magnetostrictive materials, we note $|e_1| > 20$ from the expressions for $f_1(e_1, e_2)$ and $f_2(e_1)$ that the sign of the quantity $f_1(e_1, e_2)$ coincides with the sign of the constant e_1 , while the converse assertion is true for $f_2(e_1)$. In a similar way, it is shown that the determinant Δ at $B_0 < B_s$ is positive, regardless of the signs of the magnetostrictive parameters e_i , in contrast to the case of magnetically soft ferromagnets. Considering the above, we conclude that in the cases of basic magnetostrictive materials:

- (a) If $e_1 < 0$, then condition (6.5.3) is violated and consequently, for such materials at the ends of the crack, there is no stress concentration (both magnetoelastic and induced magnetic field).
- (b) If $e_1 > 0$, then (6.5.3) holds and consequently, there is a stress concentration at the end of a crack in a magnetostrictive material with the indicated property.

6.6 Occurrence of Concentrations of Magnetoelastic Stresses Due to Longitudinal Shear Due to the Orientation of the External Magnetic Field

Let in an infinite elastic ferromagnetic space be a rectilinear tunneling crack with a width $2a$, the edges of which are free from external mechanical loads. The rectangular system of Cartesian coordinates is chosen so that the cross-section of the crack is in the plane $x_1 0x_2$ and occupies an area $(-a, a)$ on the coordinate plane $0x_1$. The space, the material of which is isotropic, homogeneous and magnetically soft, is placed in a constant magnetic field $\vec{B}_0(0, B_{02}, B_{03})$ with a magnetic induction vector $\vec{B}_0(0, B_0 \cos \varphi, B_0 \sin \varphi)$, where φ the angle between the magnetic field and the axis $0x_2$, $B_0^2 = B_{02}^2 + B_{01}^2$. The specified magnetic field is the only source of external influences.

For the considered case, problem (6.2.1) has the following solution:

$$\begin{aligned} \vec{B}_0^{(e)} &= B_{02}i_2 + B_{03}i_3, & \vec{B}_0 &= B_{02}i_2 + \mu_r B_{03}i_3, \\ \vec{H}_0^{(e)} &= \mu_0^{-1} \vec{B}_0^{(e)}, & \vec{H}_0 &= (\mu_0 \mu_r)^{-1} \vec{B}_0, \end{aligned} \quad (6.6.1)$$

where the index “ e ” means belonging to the crack area and i_k are the unit vectors of the coordinate axes. Assuming that no required quantities depend on the coordinate x_3 . From (6.2.2), by (6.2.3) and (6.4.1) for B_{ijkl} , we obtain the following equations for the magnetoelasticity of the deformed state:

- Relatively $u_1(x_1, x_2, t)$ and $u_2(x_1, x_2, t)$

$$\begin{aligned} \Delta u_i + \frac{1}{1-2\nu} \theta_{,i} + F_i &= 0, \quad (i = 1, 2) \\ \Delta \Phi &= 0, \quad \Delta \Phi^{(e)} = 0 \end{aligned} \quad (6.6.2)$$

- Relatively $u_3(x_1, x_2, t)$

$$\Delta u_3 = 0 \quad (6.6.3)$$

whereas before, $\Phi^{(e)}$ and Φ are the potentials of the induced magnetic field in the crack region and in the medium, respectively, Δ is the two-dimensional Laplace operator,

$$\begin{aligned} \theta &= u_{1,1} + u_{2,2}, \quad F_1 = \frac{2\chi B_{02}}{\mu\mu_r} h_{i,2}, \\ h_k &= \Phi_{,k}, \quad h_k^{(e)} = \Phi_{,k}^{(e)}, \quad f_{,k} \equiv \frac{\partial f}{\partial x_k}. \end{aligned} \quad (6.6.4)$$

Similarly, from (6.6.2) to (6.6.4), the following boundary conditions are obtained on the coordinate axis $0x_1$ in the plane $x_2 = 0$:

$$\begin{aligned} \Delta u_2 &= 0, \quad \Phi = 0 && \text{for } |x_1| > a \\ t_{12} + \frac{2\chi B_{02}^2}{\mu_0\mu_r} u_{2,1} &= 0 && \text{for } |x_1| < \infty \\ t_{22} &= \frac{\chi^2}{\mu_r} \left(\frac{B_{02}^2}{2\mu_0\mu_r} + B_{02}\Phi_{,2} \right) && \text{for } |x_1| < a \\ \Phi_{,1} - \Phi_{,1}^{(e)} &= \frac{B_{02}^2}{\mu_0\mu_r} u_{2,1} && \text{for } |x_1| < a \\ \Phi^{(e)} &= 0, \quad \Phi_{,2}^{(e)} = \mu_r \Phi_{,2} && \text{for } |x_1| < a \end{aligned} \quad (6.6.5)$$

and the following conditions regarding $u_3(x_1, x_2, t)$

$$\begin{cases} u_{3,1} = 0 & \text{for } |x_1| > a \\ u_{3,2} = -\frac{\chi B_{03}^{(e)}}{\mu} \left(\frac{B_{02}}{\mu_0\mu_r} + h_2 \right) & \text{for } |x_1| < a \end{cases} \quad (6.6.6)$$

In addition to conditions (6.6.5) and (6.6.6), the conditions at infinity must also be satisfied, according to which all the required quantities due to the deformation of the medium must tend to zero at $|\vec{r}| \rightarrow \infty$.

From (6.6.2)–(6.6.6), due to (6.2.5), it is seen that:

- Problem (6.6.2), (6.6.5) (a plane problem for determining u_1 and u_2) is separated from problem (6.6.3)–(6.6.6) (an antiplane problem for determining u_3);
- To solve the antiplane problem, it is necessary to have a boundary value for the component h_2 of the magnetic field induced in the medium, which arises as a result of plane deformation;
- the existence of an antiplane problem is possible only under the condition $B_{02} \cdot B_{03} \neq 0$ with respect to the components of the unperturbed magnetic field.

The plane problem (6.2.2), (6.2.5) was solved in the previous subsection, and for the quantity of interest to us h_2 on the crack faces at $B_{ijkl} = 0$ (soft magnetic material), the following value was obtained:

$$h_2(x_1, 0) \equiv h_2^{(0)} = \frac{(1 - \nu)(\chi - 2)\chi^2 b_0^2}{2\mu_r^2 + b_0^2 \chi [1 - 2\nu - 2(1 - \nu)\chi]} \frac{B_{02}}{\mu_0 \mu_r} \quad (6.6.7)$$

where $b_0^2 = \frac{B_{02}}{\mu_0 \mu_r}$, which coincides with the indicated value obtained in [6].

The solution of Eq. (6.2.3), taking into account the condition at infinity, can be represented as ($x_2 > 0$)

$$u_3(x_1, x_2) = \int_{-\infty}^{\infty} A(\alpha) \exp(-|\alpha|x_2) \exp(-i\alpha x_1) d\alpha \quad (6.6.8)$$

The unknown function $A(\alpha)$ entering (6.6.8) is determined by satisfying the boundary conditions (6.2.6). For this purpose, we introduce a new unknown function $\varphi(x_1)$ as follows:

$$\varphi(x_1) = u_{3,1}(x_1, 0) \quad \text{for } |x_1| < a \quad (6.6.9)$$

Satisfying the boundary conditions (6.2.6) at $B_{ijkl} = 0$ (soft magnetic material), it can be shown [16] that $\varphi(x_1)$ is the solution of the following singular integral equation:

$$\frac{1}{\pi} \int_{-a}^a \frac{\varphi(s) ds}{x - s} = \lambda \quad (6.6.10)$$

satisfying the condition

$$\frac{1}{\pi} \int_{-a}^a \varphi(s) ds = 0 \quad (6.6.11)$$

where

$$\lambda = -\frac{\chi}{\mu \mu_r} B_{02} \frac{B_{03}^{(e)}}{\mu_0} - B_{03}^{(e)} \frac{\chi}{\mu_r} h_2^{(0)}$$

Integral Eq. (6.6.10) in the class of unbounded functions has the following solution that satisfies condition (6.4.11) [16]

$$\varphi(x_1) = -\lambda \frac{x_1}{\sqrt{a^2 - x_1^2}} \tag{6.6.12}$$

Based on (6.6.12) from (6.6.9), we determine the displacement u_3 . Substituting the found expression for u_3 in (6.6.2), we determine the magnetoelastic stresses S_{23} in the medium. In particular, for S_{23} at $x_2 = 0$, we obtain the expressions

$$\frac{S_{23}(x, 0)}{\mu} = \begin{cases} S_0 & \text{for } |x| < 1 \\ S_0 - \left[\lambda - \frac{2\mu_r - 1}{\mu} B_{03}^{(e)} h_2^{(0)} \right] \frac{x}{\sqrt{x^2 - 1}} & \text{for } |x| > 1 \end{cases} \tag{6.6.13}$$

where

$$S_0 = \frac{2\mu_r - 1}{\mu\mu_r} \frac{B_{02} B_{03}^{(e)}}{\mu_0} + \lambda + \frac{2\mu_r - 1}{\mu} B_{03}^{(e)} h_2^{(0)}, \quad x = \frac{x_1}{a}.$$

Based on formulas (6.6.13), numerical calculations were made, the results of which are given in Tables 6.1 and 6.2. Table 6.1 gives the values $10^3 S_{23}/\mu$ at various points $x_1 > a$ at $B_{02} = B_{03} = 1$.

Table 6.1 is for the following ferromagnetic materials:

- Alfer alloy ($\nu = 0.3$; $\mu = 6.3 \cdot 10^{10} \text{N/m}^2$; $\mu_r = 30$),
- F-107 ferrite ($\nu = 0.3$; $\mu = 6.8 \cdot 10^{10} \text{N/m}^2$; $\mu_r = 110$) and
- Technical iron ($\nu = 0.28$; $\mu = 1.1 \cdot 10^{11} \text{N/m}^2$; $\mu_r = 2.5 \cdot 10^3$).

Table 6.1 Values $10^3 S_{23}/\mu$ at various points $x_1 > a$ at $B_{02} = B_{03} = 1$

$10^3 S_{23}/\mu$	Alfer alloy	F-107 ferrite	Technical iron
1.2	0.2208	0.2061	0.1260
1.3	0.2019	0.1889	0.1154
1.4	0.1913	0.1792	0.1095
1.6	0.1798	0.1688	0.1030
1.7	0.1763	0.1657	0.1011
1.8	0.1737	0.1633	0.9968

Table 6.2 Dependence $10^5 S_{23}/\mu$ on the intensity of the external magnetic field in the case of technical iron at $B_{02} = B_{03} = B_0$

$10^5 S_{23}/\mu$	$B_0 = 0.2T$	$B_0 = 0.4T$	$B_0 = 0.8T$
1.2	0.5103	2.038	8.103
1.3	0.4660	1.862	7.414
1.4	0.4413	1.763	7.029
1.6	0.4145	1.657	6.611
1.7	0.4064	1.625	6.485
1.8	0.4003	1.601	6.389

The dependence $10^5 S_{23}/\mu$ on the intensity of the external magnetic field in the case of technical iron at $B_{02} = B_{03} = B_0$ is given in Table 6.2.

Formulas (6.6.13) and the above calculations show that: (a) the problem of a longitudinal shear crack arises due to the fact that $B_{02} \cdot B_{03} \neq 0$ and (b) there is such a value of the B_{0*} for B_{02}

$$\frac{B_{02}^2}{\mu_0 \mu} = \frac{2\mu_r^2}{\chi} \frac{1}{\mu_r(\chi - 2)(1 - \nu) + 2(1 - \nu)\chi - 1}$$

that at $B_{02} = B_{0*}$, the shear stress intensity factor vanishes, (c) with an increase in the intensity of the external magnetic field, the stress S_{23} increases monotonically and (d) the magnitude of the stresses S_{23} on the crack faces $B_0^2(\mu_0\mu)^{-1} \ll 1$ can be replaced with accuracy by the expression

$$S_{23} = S_0\mu \approx \frac{B_{02}B_{03}^{(e)}}{\mu_0} = \frac{B_0^2}{2\mu_0} \sin 2\varphi$$

from which it can be seen that the influence of the magnetic field is strongest near $\varphi = \pi/4$.

References

1. Pao, Y.-H., Yen, C.-S.: A linear theory for soft ferromagnetic elastic solids. *Int. J. Eng. Sci.* **11**(4), 415–436 (1973)
2. Maugin, G.A.: *Continuum Mechanics of Electromagnetic Solids*, North-Holland Series in Applied Mathematics and Mechanics, vol. 33 (2013)
3. Baghdasaryan, G.Y.: *Vibrations and Stability of Magnetoelastic Systems*. YSU Publishing House, Yerevan (1999). (in Russ.)
4. Baghdasaryan, G., Danoyan, Z.: *Magnetoelastic Waves*. Springer (2018)
5. Brown, W.F.: Structure and energy of one-dimensional domain walls in ferromagnetic thin films. *J. Appl. Phys.* **36**(4), 1380 (1965). <https://doi.org/10.1063/1.1714314>
6. Shindo, Y.: Magnetoelastic interaction of a soft ferromagnetic elastic solid with a penny-shaped crack in a constant axial magnetic field. *ASME J. Appl. Mech.* **44**, 47–50 (1977). <https://doi.org/10.1115/1.3424290>
7. Asanyan, D.D., Aslanyan, A.A., Bagdasaryan, G.E.: On concentrations of elastic stresses and induced magnetic field near a crack resulting from an external magnetic field. *Mech. Proc. Natl. Acad. Sci. Armenia* **41**, 15–25 (1988)
8. Baghdasaryan, G.Y., Hasanyan, D.J.: Magnetoelastic interaction between a soft ferromagnetic elastic half plane with a crack and a constant magnetic field. *Int. J. Solids Struct.* **37**, 5371–5383 (2000). [https://doi.org/10.1016/S0020-7683\(99\)00219-X](https://doi.org/10.1016/S0020-7683(99)00219-X)
9. Sirotnin, Yu.I., Shaskolskaya, M.P.: *Foundations of Crystal Physics*. 2nd ed., revised. M.: Nauka (1979) (in Russ.)
10. Syrkin, L.N.: *Piezomagnetic Ceramics*, 2nd ed., revised and supplemented. Energy (1980) (in Russ)
11. Vlasov, K.B.: Several issues of elastic ferromagnetic (magnetostrictive) environments theory. *Phys. Proc. Acad. Sci. USSR* **21**(8), 1140–1148 (1957) (in Russ.)
12. Bagdasaryan, G.Y., Danoyan, E.A.: Mathematical modeling of vibrations of two-layered magnetostrictive plates. *MTT* **3**, 87–94 (1992). (in Russ.)

13. Bagdasaryan, G.E., Danoyan, Z.N., Danoyan, E.O.: Reports of the National Academy of Sciences of Armenia, vol. 110(4) (2010) (in Russ.)
14. Sneddon, I.N.: Mixed Boundary Value Problems in Potential Theory. Wiley, New York (1966)
15. Berlincourt, D., Keran, D., Joffe, G.: In: Mezon, W. (ed.) Physical Acoustics, vol. 1. Methods and Devices for Ultrasonic Research, pp. 204–326. M. Mir (1966) (in Russ.)
16. Gakhov, V.D.: Boundary Problems. Nauka, Moscow (1977).(in Russ)

Chapter 7

The Effect of Longitudinal Oscillations Resonance on Stability and Domains of Attraction in the Generalized Kapitza Problem



Alexander K. Belyaev, Oksana R. Polyakova, and Tatyana P. Tovstik

Abstract We study the effect of stabilization of a pendulum with internal degree of freedom in the upper inverted equilibrium position subject to vertical vibration of the support. A small amplitude parameter of support vibration is introduced. The method of two-scale expansions is used to obtain the averaged motion equation of the pendulum. Stability conditions for the upper equilibrium position are found depending on the parameters of the elastic element of the pendulum. Critical values of the pendulum deflection angle are obtained, which control the boundary of the stable oscillation zone.

Keywords Kapitza's pendulum · Stability · Attraction basin · Two-scale asymptotic expansion · Solid body with internal degree of freedom · Resonance

7.1 Introduction

Stabilization effect of the upper vertical position of a pendulum with vibrating support is studied. Stephenson [1] first described this effect. Later, Kapitza [2] gave theoretical and experimental evidences for this effect. Chelomei [3] considered a similar problem, with a weight sliding along a rod. For recent studies on this problem and various generalizations thereof, see [4–7]. It is also worth mentioning the paper [8] describing experiments with a working model of a three-link pendulum [8]. The Kapitza effect occurs with sufficiently strong vibrations of the support. Another condition for stabilization of the pendulum in the classical Kapitza problem is the

A. K. Belyaev · T. P. Tovstik (✉)

Institute for Problems in Mechanical Engineering of the Russian Academy of Sciences, St. Petersburg, Russia

e-mail: tovstik_t@mail.ru

A. K. Belyaev

e-mail: vice.ipme@gmail.com

O. R. Polyakova

Saint-Petersburg State University of Architecture and Civil Engineering, St. Petersburg, Russia

e-mail: ksempolyaor@yandex.ru

small oscillation amplitude requirement of the support with respect to the length of the pendulum itself.

The present paper is concerned with the study of the behavior of a compressible Kapitza pendulum as a function of the natural frequency of longitudinal vibrations of the elastic element of the pendulum. Stability analysis of the upper equilibrium position is carried out, and the domain of attraction of the stable solution is found. An averaged equation describing the pendulum motion is established, and its solution is studied. The error of the averaged solution of the nonlinear problem is estimated. A stability condition for the upper vertical position of a pendulum is obtained with due account of its compressibility.

7.2 Model of a Compressed Pendulum. Complete Nonlinear System of Equations

Let us consider the generalized Kapitza pendulum implemented as follows (Fig. 7.1). A body of point mass m is attached via a weightless spring of rigidity c to the pendulum hinged support vibrating in the vertical direction. Both the rod and the point mass of the pendulum are located in a tube that prevents the spring from bending. The tube mass is $m_1 = \kappa m$, where the coefficient κ assumes arbitrary values in the interval $\kappa \in (0, \infty)$. The mass is distributed uniformly over the length l of the tube, and the tube thickness is neglected. The pendulum is subjected to a gravitational force. Let l_0 be the spring length in the unstressed state, and let l be its length in the upper equilibrium position, $l = l_0 - mg/c$. The string length l will be considered as a reference value, and the actual length of the string will be denoted by $l + s(t)$, where $s(t) \ll l$. The deformation δ of the string is $\delta = l + s(t) - l_0 = s(t) - mg/c$.

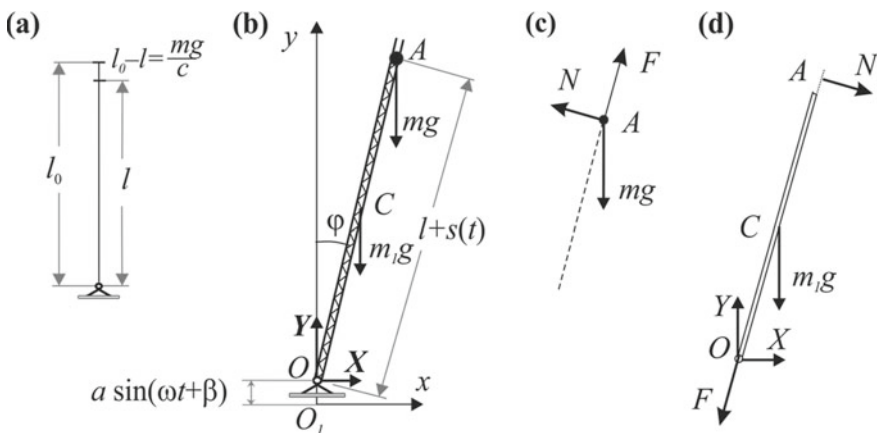


Fig. 7.1 Model of a compressible Kapitza pendulum. **a** Equilibrium position of a compressed spring. **b** Kapitza pendulum. **c** Forces acting on the weight. **d** Forces acting on the tube

Note that the real length of the tube exceeds l , but we will neglect the mass of the small part of the tube above the level l .

Assume that the pendulum support vibrates in the vertical direction according to the law $y_O(t) = a \sin(\omega t + \beta)$ with constant values of the amplitude, frequency, and the initial phase a , ω , β , respectively.

Let us write down the motion equations separately for the weight and the tube, as subject to the external forces shown in Fig. 7.1. Here, X , Y are the forces acting on the tube from the hinge side, N is the interaction force between the weight and the tube (this force is orthogonal to the pendulum axis), and $F = -c\delta$ is the force acting along the deformed weightless spring. As the unknown variables, we take $s(t)$, which is the small (relative to l) deflection of the weight along the pendulum axis, and $\varphi(t)$, which is the angle of rotation of the pendulum from the upper vertical position, in the counter-clockwise sense—and this quantity is not small in general. So, we have

$$\begin{cases} m \frac{d^2}{dt^2} ((l + s(t)) \sin \varphi(t)) = F(t) \sin \varphi(t) - N(t) \cos \varphi(t), & F(t) = -cs(t) + mg, \\ m \frac{d^2}{dt^2} (a \sin(\omega t + \beta) + (l + s(t)) \cos \varphi(t)) = F(t) \cos \varphi(t) + N(t) \sin \varphi(t) - mg, \\ m_1 \frac{d^2}{dt^2} \left(\frac{l}{2} \sin \varphi(t) \right) = X(t) - F(t) \sin \varphi(t) + N(t) \cos \varphi(t), \\ m_1 \frac{d^2}{dt^2} \left(a \sin(\omega t + \beta) + \frac{l}{2} \cos \varphi(t) \right) = Y(t) - F(t) \cos \varphi(t) - N(t) \sin \varphi(t) - m_1 g, \\ \frac{m_1 l^2}{12} \frac{d^2 \varphi(t)}{dt^2} = \left(\frac{l}{2} + s(t) \right) N(t) + \frac{l}{2} Y(t) \sin \varphi(t) - \frac{l}{2} X(t) \cos \varphi(t). \end{cases}$$

Transforming the first two equations, we get

$$\begin{cases} \ddot{s} + \frac{c}{m} s - (l + s) \dot{\varphi}^2 - a \omega^2 \sin(\omega t + \beta) \cos \varphi - g(1 - \cos \varphi) = 0, \\ (l + s) \ddot{\varphi} + 2\dot{s} \dot{\varphi} + a \omega^2 \sin(\omega t + \beta) \sin \varphi + \frac{N}{m} - g \sin \varphi = 0, \end{cases} \quad (7.1)$$

and excluding X , Y from the three equations in curly brackets, we obtain

$$\frac{2}{3} \ddot{\varphi} l + a \omega^2 \sin(\omega t + \beta) \sin \varphi = g \sin \varphi + \left(2 + \frac{2s}{l} \right) \frac{N}{m_1}. \quad (7.2)$$

Let us change to the dimensionless variables in length and time

$$\tilde{s} = \frac{s}{l}, \quad \varepsilon = \frac{a}{l}, \quad \tilde{t} = \omega t, \quad (7.3)$$

(the tilde will be dropped in what follows). The quantity ε will be considered as the small parameter of the problem. We set

$$v^2 = \frac{c}{m\omega^2}, \quad \varepsilon^2 q = \frac{g}{l\omega^2}, \quad (7.4)$$

where v is the ratio of the natural vibration frequency of the spring loaded weight to the given oscillation frequency of the pendulum support, and $\varepsilon^2 q$ is the squared ratio of the frequency of free vibrations of the mathematical pendulum of length l in a gravity field to the given oscillation frequency of the support. On the boundary of the stability region in the classical Kapitsa problem [5], the quantity $\varepsilon^2 q = g/l\omega^2$ is of second order of smallness with respect to the small quantity $\varepsilon = a/l$. In this problem, the destabilizing term, which is consequent on the gravity force, has the above order of smallness, as in the classical setting. Note that by making $\kappa \rightarrow \infty$ we transform the problem into the classical problem on oscillation of an inextensible rod on a vibrating support.

In the dimensionless form, in view of (7.2) system (7.1) assumes the form

$$\begin{cases} \ddot{s} + v^2 s - (1+s)\dot{\varphi}^2 - \varepsilon \sin(t+\beta) \cos \varphi + \varepsilon^2 q (1 - \cos \varphi) = 0, \\ \left(1 + s + \frac{\kappa}{3(1+s)}\right) \ddot{\varphi} + 2\dot{s}\dot{\varphi} + \varepsilon \left(1 + \frac{\kappa}{2(1+s)}\right) \sin(t+\beta) \sin \varphi - \varepsilon^2 q \left(1 + \frac{\kappa}{2(1+s)}\right) \sin \varphi = 0. \end{cases} \quad (7.5)$$

Let us specify the initial conditions. Assume that initially, at $t = 0$, the pendulum was deflected by an angle φ_0 without the initial angular velocity and the spring was in equilibrium:

$$\varphi(0) = \varphi_0, \quad \dot{\varphi}(0) = 0, \quad s(0) = s_0 = \frac{\varepsilon^2 q}{v^2} (1 - \cos \varphi_0), \quad \dot{s}(0) = 0, \quad (7.6)$$

Moreover, the initial phase of oscillations of the support is equal to some β .

Assuming that oscillation decay insignificantly, one can pose the problem on the convergence of the solution $\varphi(t)$ to zero and find sufficient conditions for this convergence.

7.3 Averaged Motion Equation of the Pendulum

We will assume that s is a small quantity of order ε . Introducing the slow time $\theta = \varepsilon t$, we will solve system (7.5) by the method of two-scale expansions [9]. The solution will be obtained as series with respect to the small parameter:

$$\begin{aligned} \varphi(t, \theta, \varepsilon) &= \sum_{m=0}^{\infty} (U_m(\theta) + V_m(t, \theta)) \varepsilon^m, \quad s(t, \theta, \varepsilon) = \sum_{m=1}^{\infty} (r_m(\theta) + s_m(t, \theta)) \varepsilon^m, \\ \theta = \varepsilon t, \quad \int_0^{2k\pi} V_m(t, \theta) dt &= 0, \quad \int_0^{2k\pi} s_m(t, \theta) dt = 0, \quad m = 1, 2, \dots, \end{aligned} \quad (7.7)$$

where the integer quantity k is fixed so that, with a sufficient degree of accuracy, an integer number of oscillations with frequency ν would occur over the time period $2k\pi$. We will assume that the frequency ν is not equal to the frequency of support oscillations, i.e., $\nu \neq 1$.

Taking into account the equalities

$$\begin{aligned} \frac{d\varphi}{dt} &= \frac{\partial\varphi}{\partial t} + \varepsilon \frac{\partial\varphi}{\partial\theta}, & \frac{d^2\varphi}{dt^2} &= \frac{\partial^2\varphi}{\partial t^2} + 2\varepsilon \frac{\partial^2\varphi}{\partial t \partial\theta} + \varepsilon^2 \frac{\partial^2\varphi}{\partial\theta^2}, \\ \frac{ds}{dt} &= \frac{\partial s}{\partial t} + \varepsilon \frac{\partial s}{\partial\theta}, & \frac{d^2s}{dt^2} &= \frac{\partial^2 s}{\partial t^2} + 2\varepsilon \frac{\partial^2 s}{\partial t \partial\theta} + \varepsilon^2 \frac{\partial^2 s}{\partial\theta^2}, \end{aligned} \quad (7.8)$$

Substituting series (7.7) into the system of Eq. (7.5), we equate the terms involving ε^0 , ε^1 , ε^2 . Our aim is to find the averaged value of the angle in the zero approximation $U_0(\theta)$. For the terms multiplying ε^0 , ε^1 , we get

$$V_0(t, \theta) = 0, \quad V_1(t, \theta) = \sin(t + \beta) \sin U_0(\theta), \quad (7.9)$$

and hence, in view of (7.7), (7.8)

$$\dot{\varphi}(t, \theta, \varepsilon), \ddot{\varphi}(t, \theta, \varepsilon) = O(\varepsilon), \quad (7.10)$$

$$r_1(\theta) = 0, \quad \frac{\partial^2 s_1(t, \theta)}{\partial t^2} + \nu^2 s_1(t, \theta) = \sin(t + \beta) \cos U_0(\theta). \quad (7.11)$$

The initial conditions for Eq. (7.11) are obtained from (7.6) in view of (7.7):

$$s_1(t, \theta) = 0, \quad \dot{s}_1(t, \theta) = 0, \quad t = 0. \quad (7.12)$$

Solving Eq. (7.11) with initial conditions (7.12), we obtain

$$s_1(t, \theta) = \frac{\cos U_0(\theta)}{\nu^2 - 1} \left(\frac{-\cos \beta}{\nu} \sin \nu t - \sin \beta \cos \nu t + \sin(t + \beta) \right), \quad (7.13)$$

$$\begin{aligned} s(t, \theta, \varepsilon) &= \varepsilon s_1 + O(\varepsilon^2) \\ &= \varepsilon \frac{\cos U_0(\theta)}{\nu^2 - 1} \left(\frac{-\cos \beta}{\nu} \sin \nu t - \sin \beta \cos \nu t + \sin(t + \beta) \right) + O(\varepsilon^2) \end{aligned} \quad (7.14)$$

We simplify the second equation in (7.5) in the second approximation by getting rid of the trigonometric functions in the denominator and using the expansion $\frac{1}{(1+\varepsilon s_1)} = 1 - \varepsilon s_1 + O(\varepsilon^2)$. Substituting (7.9) and (7.14) into the second equation in (7.5), and averaging with the help of (7.7), (7.8), we get the following equation with respect to the unknown function of the averaged deflection angle of the pendulum:

$$\begin{aligned}
 a_1 U_0''(\theta) + b_1 \sin U_0(\theta) \cos U_0(\theta) - c_1 q \sin U_0(\theta) &= 0, \\
 a_1 = 1 + \frac{\kappa}{3}, \quad b_1 = \frac{1}{2} \frac{\nu^2}{\nu^2 - 1} + \frac{3\kappa^2 + 8\kappa}{8\kappa + 24}, \quad c_1 = 1 + \frac{\kappa}{2}.
 \end{aligned} \tag{7.15}$$

We augment this equation with the initial conditions obtained from the given initial conditions for the function φ :

$$\begin{aligned}
 \varphi = U_0 + O(\varepsilon), \quad \frac{d\varphi}{dt} = \varepsilon \left(U_0' + \frac{\partial V_1}{\partial t} \right), \\
 \varphi(0) = \varphi_0, \quad \dot{\varphi}(0) = 0, \quad \Rightarrow \quad U_0(0) = \varphi_0, \quad U_0'(0) = -\cos \beta \sin \varphi_0.
 \end{aligned} \tag{7.16}$$

7.4 Stability Conditions for the Upper Equilibrium Position

Problems (7.15)–(7.16) give the zero approximation U_0 to the complete nonlinear system of Eqs. (7.5), (7.6) and can be studied analytically. For small deflection angles U_0 , the linearized Eq. (7.15) has the form

$$a_1 U_0''(\theta) + (b_1 - c_1 q) U_0(\theta) = 0, \tag{7.17}$$

which gives conditions for stability of oscillations near $U_0 = 0$:

$$b_1 - c_1 q = \frac{1}{2} \frac{\nu^2}{\nu^2 - 1} + \frac{3\kappa^2 + 8\kappa}{8\kappa + 24} - \left(1 + \frac{\kappa}{2} \right) q > 0. \tag{7.18}$$

Making $\kappa \rightarrow \infty$ and neglecting the compressibility of the pendulum, condition (7.18) assumes the form known for the classical Kapitza pendulum (see [7]):

$$q = \frac{lg}{a^2 \omega^2} < \frac{3}{4}. \tag{7.19}$$

Let us return back to Eq. (7.15). A necessary condition for stability of oscillation of $U_0(\theta)$ near $U_0 = 0$ is the positivity of the coefficient b_1 .

The dashed region in Fig. 7.2 corresponds to the region of possible values of the parameters $\nu = \sqrt{\frac{c}{m} \frac{1}{\omega}}$, $\kappa = \frac{m_1}{m}$ that give $b_1 > 0$. For these values of the parameters, the solution on the phase plane will have a stable rest point $(U_0, U_0') = (0, 0)$.

7.5 Oscillation Stability Zone

The separatrix equation for the solution of problem (7.15)–(7.16) on the phase plane has the form

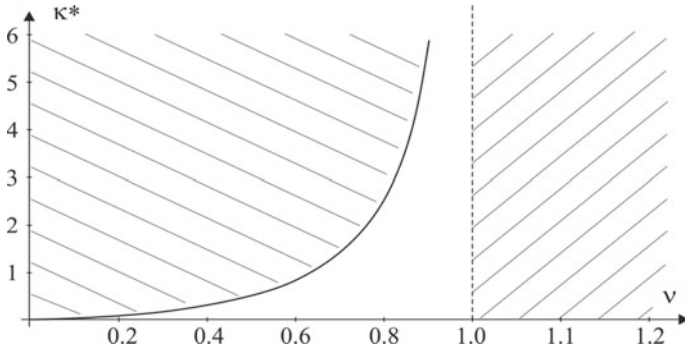


Fig. 7.2 Possible values of the parameters ν, κ

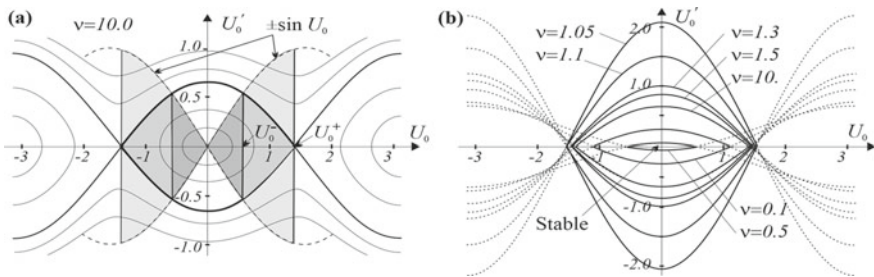


Fig. 7.3 Phase plane (U_0, U'_0) for $\kappa = 1, q = 0.1$ **a** U_0^- and U_0^+ on the phase plane. **b** Separatrices for $\nu = 0.1, \dots, 10.0$

$$(U'_0)^2 = \frac{1}{a_1 b_1} (b_1 \cos U_0 - c_1 q)^2. \tag{7.20}$$

The separatrix in the phase plane is shown in Fig. 7.3. The initial conditions $U_0(0)$, as from the range $0 < U_0(0) < U_0^-$, give a stable solution for all values β of the initial phase of oscillations of the support. The initial values from the range $U_0^- < U_0(0) < U_0^+$ give a stable solution for some values β of the initial phase. From Eq. (7.20), we get

$$U_0^+ = \arccos\left(\frac{c_1 q}{b_1}\right). \tag{7.21}$$

7.6 Conclusion

A numerical solution of problem (7.5)–(7.6), of the second approximation of problem (7.5)–(7.6) for small ε , and of the averaged problem (7.15)–(7.16) was given. Critical

values for the initial conditions φ_{0*} and U_{0*} for various parameters of the problem and the initial phase of oscillation of the support β were compared. The averaged method gives a certain error caused mainly by discarding the terms above the second order of smallness.

In view of the above results, the conclusion can be made that the effect of compressibility of the rod (per the above model) can either reduce or extend the pendulum stability region. For small eigenfrequencies of a compressible rod, the Kapitza effect can hardly be achieved near resonance in the subresonance region, and, vice versa, this effect takes place for much broader values of parameters in the superresonance region.

Acknowledgements This research was carried out with the financial support of the Russian Foundation for Basic Research (grant no. 20-51-S52001 MHT-a).

References

1. Stephenson, A.: On an induced stability. *Phil. Mag.* **15**, 233–236 (1908)
2. Kapitza, P.L.: The pendulum in vibrating support. *Uspekhi fizicheskikh nauk* **44**(1), 7–20 (1951). (in Russ.)
3. Chelomei, V.N.: Mechanical paradoxes caused by vibrations. *Dokl. Akad. Nauk SSSR* **270**(1), 62 (1983)
4. Blekhman, I.I.: *Vibrational Mechanics*. World Scientific, Singapore (2000)
5. Belyaev, A.K., Morozov, N.F., Tovstik, P.E., Tovstik, T.M., Tovstik, T.P.: Classical Kapitza's problem of stability of an inverted pendulum and some generalizations. *Acta Mechanica* **232**, 1743–1759 (2021)
6. Morozov, N.F., Belyaev, A.K., Tovstik, P.E., Tovstik, T.P.: Stability of a vertical rod on a vibrating support. *Dokl. Phys.* **63**(9), 380–384 (2018)
7. Belyaev, A.K., Morozov, N.F., Tovstik, P.E., Tovstik, T.P.: Stability of a flexible vertical rod on a vibrating support. *Vestnik St.Petersburg Univ. Math. Mech. Astron.* **51**(3), 296–304 (2018)
8. Gordin, Ya.D., Gribkov, V.A.: On root causes of mismatch between theoretical and experimental stability domains of inverted regulated pendula. In: XII All-Russian Conference of Fundamental Problems of Theoretical and Applied Mechanics. Vol. 1: General and Applied Mechanics, pp. 65–68. RITs BashGU, Ufa (2019) (in Russ.)
9. Bogoliubov, N.N., Mitropolski, Y.A.: *Asymptotic Methods in the Theory of Non-linear Oscillations*. Gordon and Breach, New York (1961)

Chapter 8

Band Gaps of Metastructure with Periodically Attached Piezoelectric Patches and Internal Hinges



Karen Ghazaryan, Samvel Jilavyan, Davit Piliposyan, and David Aznaurov

Abstract In this paper, we investigate the problem of band gaps for flexural waves in a beam with periodically attached piezoelectric patches and internal hinges for the purpose of vibration energy harvesting. Based on Euler–Bernoulli beam theory, general solutions of the finite length periodic beam for two topological systems (beam with patches, beam with patches and internal hinges) are obtained using the transfer matrix method. By applying the Floquet theory, the explicit expressions are derived defining the band gap structure. The corresponding band gap dispersion curves are plotted. The innovation of this paper is the results concerning widening of the resonant bandwidth of a piezoelectric harvester based on phononic band gaps generated by internal hinges, not by patches.

Keywords Piezoelectric · Energy harvesting · Band gaps · Resonance frequency

8.1 Introduction

New developments in wireless and microelectro-mechanical systems have increased the demand for portable electronics and wireless sensors, making power supply of these portable devices a crucial issue. Nowadays, the most appropriate solution to extend the life of various devices is to harvest the ambient energy and generate

K. Ghazaryan (✉) · D. Piliposyan · D. Aznaurov
Institute of Mechanics, National Academy of Sciences, 24 Bagramyan ave., 0019, Yerevan,
Republic of Armenia
e-mail: kghazaryan@mechins.sci.am

D. Piliposyan
e-mail: piliposyan@mechins.sci.am

D. Aznaurov
e-mail: azn.david.08@gmail.com

S. Jilavyan
Faculty of Mathematics and Mechanics, Yerevan State University, Alex Manoogian 1, 0025,
Yerevan, Republic of Armenia
e-mail: samjilavyan@ysu.am

electrical energy, which is called energy harvesting [1–3]. Piezoelectric vibration energy harvesting can harvest electrical energy from mechanical vibrations based on the direct piezoelectric effect. Elastic beams and plates are widely used in the most piezoelectric vibration energy harvesting devices [4–13].

Recently, artificial materials and structures called mechanical metamaterials have become the centerpiece of many research studies and engineering applications. Due to structural periodicity, these materials exhibit exotic physical properties including negative refraction, frequency stop-bands, cloaking and energy harvesting, all unachievable in naturally occurring materials. Waves in metamaterials can only propagate within specific frequency bands and are completely blocked within forbidden band gaps [14–17].

The use of metamaterial structures for generating electric power via energy harvesting has been widely investigated recently [18–24]. In phonon metamaterial structures, external stimulations will cause mechanical vibrations that will propagate through the beam. Due to the presence of local resonators, there will be oscillations in certain frequency bands which cannot propagate through periodic cells, creating band gaps. Energy of these vibrations will localize in the form of an oscillatory motion of the internal structural elements, and the piezoelectric effect can be exploited to convert the localized vibration energy into electrical energy [18, 20].

The review of the most recent developments in piezoelectric energy harvesting methods for converting localized mechanical wave energy into electrical energy using artificially designed mechanical structures are given in Lee et al. [25].

8.2 Band Gaps of a Beam with Periodically Attached Piezoelectric Patches

We consider a finite elastic beam of length nd with periodically attached piezoelectric patches at $z = (n - 1/2)d$, $n = 1, 2, \dots, N$, distanced d from each other and each patch having a mass μ (Fig. 8.1) The equation of motion of Euler–Bernoulli beam can be cast as

$$EI \frac{\partial^4 U_0}{\partial z^4} + \rho A \frac{\partial^2 U_0}{\partial t^2} = 0, \quad (8.1)$$

where $U_0(z, t)$ is the dynamic deflection of the beam's neutral axis at the point z , E is the elastic modulus, I is the area moment of inertia with respect to the axis

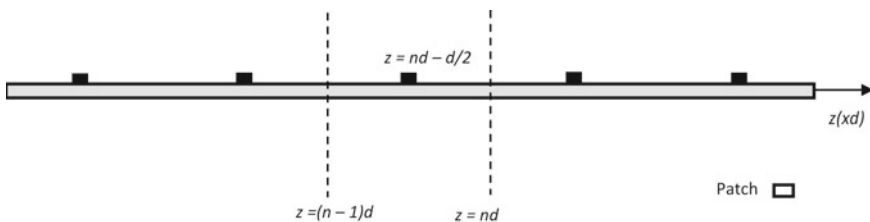


Fig. 8.1 Schematic of the beam with patches, basic unit cell

perpendicular to the beam axis, ρ is the bulk density and A is the cross-sectional area of the beam.

We assume that $U_0(z, t) = U(z)e^{i\omega t}$, where $U(z)$ is the amplitude of the free vibration response of the beam at z and ω is the beam's vibration frequency. The amplitude $U(z)$ satisfies to the following equation

$$\frac{d^4 U}{dz^4} - \frac{A\rho\omega^2}{EI}U = 0. \quad (8.2)$$

Introducing a dimensionless coordinate $x = z/d$, we consider the beam's motion in a basic unit cell $x \in (n-1, n)$. The solutions for the amplitude in each unit cell can be written as

$$U_{\pm} = C_{\pm 1} \sin(px) + C_{\pm 2} \sinh(px) + C_{\pm 3} \cos(px) + C_{\pm 4} \cosh(px), \quad (8.3)$$

where $p = \sqrt{\Omega}$, $\Omega = \omega d^2 \sqrt{(EI)^{-1} \rho A}$, Ω is the dimensionless bending frequency, subscripts (\pm) denote regions: $(-)$ $\rightarrow x \in ((n-1), n-1/2)$, $(+)$ $\rightarrow x \in (n-1/2, n)$.

Contact conditions at points where the patches of mass μ are attached can be cast as

$$EI \frac{\partial^3 U_{0+}}{\partial z^3} - EI \frac{\partial^3 U_{0-}}{\partial z^3} = -\mu \frac{\partial^2 U_{0\pm}}{\partial t^2}, \quad (8.4)$$

$$\frac{\partial^2 U_{0+}}{\partial z^2} = \frac{\partial^2 U_{0-}}{\partial z^2}, \quad (8.5)$$

$$\frac{\partial U_{0+}}{\partial z} = \frac{\partial U_{0-}}{\partial z}, \quad U_{0+} = U_{0-}. \quad (8.6)$$

For the amplitudes U_{\pm} , we have the following conditions at $x = n-1/2$

$$\frac{d^3 U_+}{dx^3} - \frac{d^3 U_-}{dx^3} = fp^4 U_{\pm}, \quad (8.7)$$

$$\frac{d^2 U_+}{dx^2} = \frac{d^2 U_-}{dx^2}, \quad (8.8)$$

$$\frac{dU_+}{dx} = \frac{dU_-}{dx}, \quad U_+ = U_-. \quad (8.9)$$

Here the dimensionless parameter $f = \mu/(\rho Ad)$ determines the ratio of the patch mass to the mass of a beam of length d . Since the interface contact conditions are imposed on the beam deflection $U(x)$, the slope $\frac{dU(x)}{dx}$, the bending moment $EI \frac{d^2 U(x)}{dx^2}$ and the shear force $EI \frac{d^3 U(x)}{dx^3}$, it is convenient to introduce the following vectors

$$\mathbf{W}_{\pm}(x) = \left(U_{\pm}(x), \frac{dU_{\pm}(x)}{dx}, EI \frac{d^2U_{\pm}(x)}{dx^2}, EI \frac{d^3U_{\pm}(x)}{dx^3} \right)^T, \quad (8.10)$$

$$\mathbf{C}_{\pm}(x) = (C_{1\pm}, C_{2\pm}, C_{3\pm}, C_{4\pm})^T. \quad (8.11)$$

Using Eq. (8.3) we can write the solutions in the following matrix form

$$\mathbf{W}_{\pm}(x) = \hat{P}(x)\mathbf{C}_{\pm}(x), \quad (8.12)$$

where

$$\hat{P}(x) = \begin{pmatrix} \sin(px) & \sinh(px) & \cos(px) & \cosh(px) \\ p \cos(px) & p \cosh(px) & -p \sin(px) & p \sinh(px) \\ -EI p^2 \sin(px) & EI p^2 \sinh(px) & -EI p^2 \cos(px) & EI p^2 \cosh(px) \\ -EI p^3 \cos(px) & EI p^3 \cosh(px) & -EI p^3 \sin(px) & EI p^3 \sinh(px) \end{pmatrix}. \quad (8.13)$$

A propagator matrix method can be used to link field values of the vectors $\mathbf{W}_+(n)$ and $\mathbf{W}_-(n)$ in unit a cell. Considering values of field vectors $\mathbf{W}_+(x)$ at points $x = n$ and $x = n - 1/2$ the following relations can be written

$$\mathbf{W}_+(n) = \hat{P}(n)\mathbf{C}_+, \quad \mathbf{W}_+(n - 1/2) = \hat{P}(n - 1/2)\mathbf{C}_+. \quad (8.14)$$

Eliminating vectors \mathbf{C}_+ from (8.14), the following relation linking vector field values within (+) sub-unit can be found:

$$\mathbf{W}_+(n) = \hat{M}\mathbf{W}_+(n - 1/2), \quad \hat{M} = \hat{P}(n)\hat{P}^-(n - 1/2). \quad (8.15)$$

Similarly, we can find the relation linking the vector field values within a (-) sub-unit:

$$\mathbf{W}_-(n - 1/2) = \hat{M}\mathbf{W}_-(n - 1). \quad (8.16)$$

Herein \hat{M} is the following unimodular transfer matrix in an each sub-layer

$$\hat{M} = \begin{pmatrix} g_1 & \frac{g_2}{p} & \frac{g_4}{EI p^2} & \frac{g_3}{EI p^3} \\ g_3 p & g_1 & \frac{g_2}{EI p} & \frac{g_4}{EI p^2} \\ EI g_4 p^2 & EI g_3 p & g_1 & \frac{g_2}{p} \\ EI g_2 p^3 & EI g_4 p^2 & g_3 p & g_1 \end{pmatrix}, \quad (8.17)$$

where

$$g_{1,4} = \frac{1}{2} \left(\pm \cos \frac{p}{2} + \cosh \frac{p}{2} \right), \quad g_{2,3} = \frac{1}{2} \left(\pm \sin \frac{p}{2} + \sinh \frac{p}{2} \right). \quad (8.18)$$

We can also write contact conditions for the amplitude at $x = n - 1/2$ in a matrix form as:

$$\mathbf{W}_+(n - 1/2) = \hat{S}\mathbf{W}_-(n - 1/2), \quad (8.19)$$

where

$$\hat{S} = \begin{pmatrix} 1 & 0 & 0 & 0 \\ 0 & 1 & 0 & 0 \\ 0 & 0 & 1 & 0 \\ fp^4 & 0 & 0 & 1 \end{pmatrix}. \quad (8.20)$$

Using (8.20), we come finally to the following relation

$$\mathbf{W}_+(n) = \hat{M}\hat{S}\mathbf{W}_-(n - 1), \quad \mathbf{W}_+(n) = \hat{Q}\mathbf{W}_-(n - 1), \quad \hat{Q} = \hat{M}\hat{S}\hat{M}. \quad (8.21)$$

Herein \hat{Q} is a unimodal propagator matrix for the Euler–Bernulli beam, which links the field vectors at the ends of the n -th cell. Note that the elements of matrix \hat{Q} do not depend on cell number n .

Repeating this procedure n times, the propagator unimodal matrix \hat{Q}^n can be found, which connects the vectors at $x = 0$ and $x = n$ points of the finite beam of length nd :

$$\mathbf{W}_+(n) = \hat{Q}^n \mathbf{W}_-(0), \quad n = 1, 2, \dots, N. \quad (8.22)$$

By applying the Bloch–Floquet periodicity condition $\mathbf{W}_+(n) = \lambda \mathbf{W}_-(n - 1)$ at both ends of unit cell we come to following matrix eigenvalue problem [16, 17]

$$(\hat{Q} - \lambda \hat{I})\mathbf{W}_-(n - 1) = 0. \quad (8.23)$$

To determine the eigenvalues of the periodic structure, the roots of the following equation should be found:

$$\text{Det}(\hat{Q} - \lambda \hat{I}) = 0 \Rightarrow 2 + g\lambda + r\lambda^2 + g\lambda^3 + 2\lambda^4 = 0, \quad (8.24)$$

where \hat{I} is a 4×4 identity matrix,

$$g = fp(\sin(p) - \sinh(p)) - 4(\cos(p) + \cosh(p)), \quad (8.25)$$

$$r = 2pf(\cos(p)\sinh(p) - \sin(p)\cosh(p)) + 8\cos(p)\cosh(p) + 4. \quad (8.26)$$

Taking into account that $\lambda = \exp(ikd)$ the dispersion equations (8.24) can be witten as

$$r + 2g \cos(kd) + 4 \cos(2kd) = 0 \quad (8.27)$$

with solutions

$$\cos(kd) = -\frac{1}{8}(g \pm s), \quad s = \sqrt{32 + g^2 - 8r}. \quad (8.28)$$

A similar type of equation has been obtained and discussed in [26] for a vibrating piecewise bi-material periodic beam. When there are no patches ($\mu = 0$) then the solutions are $\cos(kd) \rightarrow \cos(p)$, and $\cos(kd) \rightarrow \cosh(p)$.

Equations (8.27) and (8.28) determine the two Floquet spectrum of beam frequencies. Since the Euler–Bernoulli beam vibration equation is not hyperbolic, one of the spectrum is the Floquet pseudo spectrum [26] which corresponds to the case when $\cos(kd) \rightarrow \cosh(p)$.

The elements of matrix \hat{Q}^n expressed via elements of matrix \hat{Q} can be written by means of Sylvester’s matrix polynomial theorem [27]:

$$\hat{Q}^n = \sum_{m=1}^4 \left(\lambda_m^n \prod_{m \neq j} \frac{\lambda_j \hat{I} - \hat{Q}}{\lambda_m - \lambda_j} \right), \tag{8.29}$$

where

$$\lambda_{1,2} = -\frac{1}{8} \left(g + s \pm \sqrt{((g + s)^2 - 64)} \right), \quad \lambda_{3,4} = -\frac{1}{8} \left(g - s \pm \sqrt{((g - s)^2 - 64)} \right) \tag{8.30}$$

are the solutions of dispersion equation (8.24).

8.3 Band Gaps of a Beam with Periodically Attached Piezoelectric Patches and Internal Hinges

We now consider a finite elastic beam of length nd with periodically attached piezoelectric patches of masses μ and internal hinges. The distances between patches and hinges are d . Introducing the dimensionless coordinate $x = z/d$, we consider the beam motion in a unit cell $x \in (n - 1, n)$. Patches are attached at points $x = n - 1/2$, internal hinges are located at points $x = n$ and $x = n - 1$ (Fig. 8.2).

At points where the hinges are attached the following conditions are valid

$$\frac{d^2U_+}{dx^2} = 0, \quad \frac{d^2U_-}{dx^2} = 0, \quad \frac{dU_+^3}{dx^3} = \frac{dU_-^3}{dx^3}, \quad U_+ = U_- \tag{8.31}$$

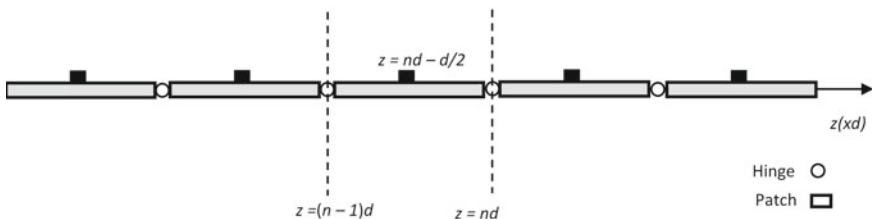


Fig. 8.2 Schematic of the beam with patches and internal hinges, basic unit cell

The piezoelectric patches are periodically attached at points $x = n - 1/2$. Solutions satisfying the first and second conditions of (8.31) can be written as

$$U_+(x) = C_1 \sin(p(x - n)) + C_2 \sinh(p(x - n)) + C_0 (\cos(p(x - n)) + \cosh(p(x - n))), \quad (8.32)$$

$$U_-(x) = A_1 \sin(p(x - n + 1)) + A_2 \sinh(p(x - n + 1)) + A_0 (\cos(p(x - n + 1)) + \cosh(p(x - n + 1))), \quad (8.33)$$

Using the contact conditions (8.7)-(9) at points $x = n - 1/2$, we find the following relations for the constants C_1 , C_2 , A_1 and A_2 expressed via two constants C_0 and A_0 :

$$\begin{aligned} \vartheta C_1 = & C_0 \csc\left(\frac{p}{2}\right) \left(fp \left(\cos(p) \csc\left(\frac{p}{2}\right) \sinh\left(\frac{p}{2}\right) - 1 \right) \right. \\ & + \csc\left(\frac{p}{2}\right) \cosh\left(\frac{p}{2}\right) (4 \cos(p) - fp \sin(p)) \Big) \\ & - A_0 \csc^2\left(\frac{p}{2}\right) \left(fp \left(\sin\left(\frac{p}{2}\right) + \sinh\left(\frac{p}{2}\right) \right) + 4 \cosh\left(\frac{p}{2}\right) \right) \end{aligned} \quad (8.34)$$

$$\begin{aligned} \theta C_2 = & -A_0 \operatorname{csch}\left(\frac{p}{2}\right) \left(fp \csc\left(\frac{p}{2}\right) + \operatorname{csch}\left(\frac{p}{2}\right) (fp - 4 \cot\left(\frac{p}{2}\right)) \right) - C_0 \operatorname{csch}\left(\frac{p}{2}\right) \times \\ & \left(fp \csc\left(\frac{p}{2}\right) + 2fp \cot\left(\frac{p}{2}\right) \cosh\left(\frac{p}{2}\right) + \cosh(p) \operatorname{csch}\left(\frac{p}{2}\right) (4 \cot\left(\frac{p}{2}\right) - fp) \right) \end{aligned} \quad (8.35)$$

$$\begin{aligned} \theta A_1 = & C_0 \csc^2\left(\frac{p}{2}\right) \left(fp \left(\sin\left(\frac{p}{2}\right) + \sinh\left(\frac{p}{2}\right) \right) + 4 \cosh\left(\frac{p}{2}\right) \right) - \\ & - A_0 \csc\left(\frac{p}{2}\right) \left(fp \left(\cos(p) \csc\left(\frac{p}{2}\right) \sinh\left(\frac{p}{2}\right) - 1 \right) + \csc\left(\frac{p}{2}\right) \cosh\left(\frac{p}{2}\right) \times \right. \\ & \left. (4 \cos(p) - fp \sin(p)) \right). \end{aligned} \quad (8.36)$$

$$\theta A_2 = A_0 \operatorname{csch}\left(\frac{p}{2}\right) \times$$

$$\begin{aligned} & \left(fp \csc\left(\frac{p}{2}\right) + 2fp \cot\left(\frac{p}{2}\right) \cosh\left(\frac{p}{2}\right) + \cosh(p) \operatorname{csch}\left(\frac{p}{2}\right) (4 \cot\left(\frac{p}{2}\right) - fp) \right) + \\ & C_0 \operatorname{csch}\left(\frac{p}{2}\right) \left(fp \csc\left(\frac{p}{2}\right) + C_0 \operatorname{csch}\left(\frac{p}{2}\right) (fp - 4 \cot\left(\frac{p}{2}\right)) \right). \end{aligned} \quad (8.37)$$

Here

$$\theta = 2fp \cot\left(\frac{p}{2}\right) + \coth\left(\frac{p}{2}\right) \left(8 \cot\left(\frac{p}{2}\right) - 2fp \right), \quad (8.38)$$

$$\vartheta = 2 \cosh\left(\frac{p}{2}\right) \left(fp - 4 \cot\left(\frac{p}{2}\right) \right) - 2fp \cot\left(\frac{p}{2}\right) \sinh\left(\frac{p}{2}\right). \quad (8.39)$$

Introducing column vectors

$$\mathbf{U}_{\pm}(x) = \begin{pmatrix} U_{\pm}(x) \\ \frac{d^3 U_{\pm}}{dx^3} \end{pmatrix}, \quad (8.40)$$

we can express the values of $\mathbf{U}_{+}(n)$ and $\mathbf{U}_{-}(n-1)$ via two constants C_0 and A_0 . After eliminating these constants, we find the following relation

$$\mathbf{U}_{+}(n) = \hat{F}\mathbf{U}_{-}(n-1). \quad (8.41)$$

Herein \hat{F} is a unimodal propagator matrix for the Euler–Bernulli beam’s wave field, which links the field vectors at the ends of the n -th cell with attached piezoelectric patches, where the internal hinges are placed.

The elements of this matrix do not depend on the unit cell number and can be cast as

$$\begin{aligned} F_{11} &= fp \left(\cos(p) - \cosh(p) + 4 \sin\left(\frac{p}{2}\right) \sinh\left(\frac{p}{2}\right) + 2 \sin(p) \sinh(p) \right) \\ &\quad + 4 \sin(p) \cosh(p) - 4 \cos(p) \sinh(p), \\ F_{22} &= F_{11}, \end{aligned}$$

$$\begin{aligned} F_{12} &= 2p^{-3} (fp(-\sin(p) - \sinh(p) + \cos(p) \sinh(p) + \sin(p) \cosh(p)) + 4 \sin(p) \sinh(p)), \\ F_{21} &= fp^4 \left(\sin(p) - 4 \cos\left(\frac{p}{2}\right) \sinh\left(\frac{p}{2}\right) - (\cos(p) + 1) \sinh(p) + 4 \sin\left(\frac{p}{2}\right) \cosh\left(\frac{p}{2}\right) \right. \\ &\quad \left. + \sin(p) \cosh(p) - 4p^3(\cos(p) \cosh(p) - 1), \right. \\ \Delta &= 4 \sin(p) - 4 \sinh(p) - 2fp \left(\sin\left(\frac{p}{2}\right) + \sinh\left(\frac{p}{2}\right) \right)^2. \end{aligned}$$

According to Sylvester’s matrix polynomial theorem for 2×2 matrices, the elements of the n -th power of a unimodal matrix \hat{F} can be written as [27]

$$\hat{F}^n = \begin{pmatrix} M_{11} & M_{12} \\ M_{21} & M_{22} \end{pmatrix}, \quad (8.42)$$

and can be simplified using the following matrix identity

$$\begin{aligned} M_{11} &= F_{11}S_{n-1}(\eta) - S_{n-2}(\eta), & M_{12} &= F_{12}S_{n-1}(\eta), \\ M_{21} &= F_{21}S_{n-1}(\eta), & M_{22} &= F_{22}S_{n-1}(\eta) - S_{n-2}(\eta), \end{aligned}$$

where $S_n(\eta)$ are the Chebyshev polynomials of second kind, namely

$$S_n(\eta) = \frac{\sin((n+1)\phi)}{\sin(\phi)}, \quad \cos(\phi) = \eta, \quad \eta = \frac{F_{11}}{\Delta}. \quad (8.43)$$

Matrix \hat{F}^n connects the vectors at points $x = 0$ and $x = n$ of the finite beam of length nd :

$$U_+(n) = \hat{F}^n U_0(n), \quad n = 1, 2, \dots, N. \quad (8.44)$$

By applying the Bloch–Floquet periodicity condition at both ends of a unit cell

$$\mathbf{U}_+(n) = \lambda \mathbf{U}_-(n-1),$$

the problem reduces to the following eigenvalue problem

$$(\hat{F} - \lambda \hat{I}) U_{n-1} = 0 \Rightarrow 1 - 2\lambda(F_{11}/\Delta) + \lambda^2 = 0,$$

where \hat{I} is a 2×2 identity matrix. Taking into account that $\lambda = \exp(ikd)$, the equation defining the gaps of the beam with external hinges and patches can be found as

$$\cos(kd) = \frac{F_{11}}{\Delta}. \quad (8.45)$$

8.4 Analysis and Conclusions

Note that relations (8.23) and (8.41) that have been obtained for a metastructure of a finite length can be used for as solutions of problems of free and forced vibration of metastructures. The dispersion curves defining band gaps are presented in Figs. 8.3, 8.4 and 8.5. The dashed curves correspond to a beam with patches and solid curves correspond to a beam with internal hinges and patches. The dispersion curves are given in the first Brillouin zone $0 < kd < \pi$, for different values of dimensionless parameter $f = \mu/(\rho AD)$, Ω is the dimensionless bending frequency of the metastructure.

The dispersion curves are plotted in accordance with the analytical expression (8.28) for the beam with patches (BP) and (8.45) for the beam with patches and hinges (BPH). Vibrational energy is localized and converted into kinetic energy by piezoelectric patches within the frequency band gaps. The maximum bending deformations occur within the first band gap; therefore, most of the energy harvesting will occur within the first band gap of the metamaterial structure [18, 19].

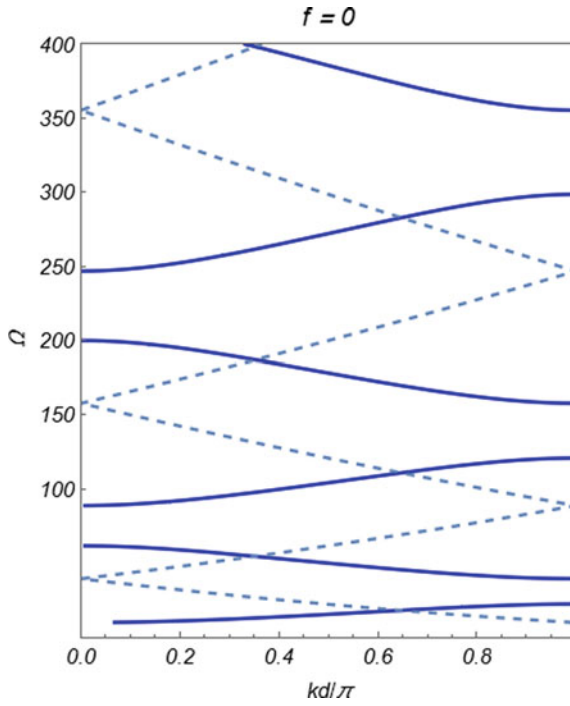


Fig. 8.3 Band structures of a beam with hinges when patches are absent

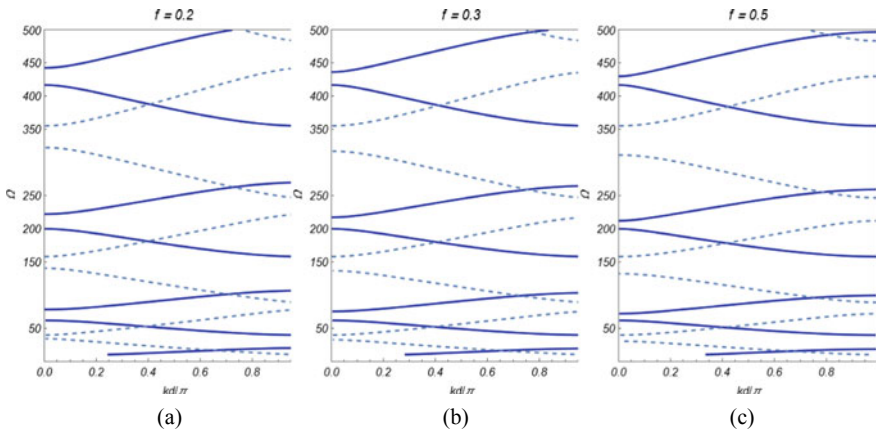


Fig. 8.4 Band structures of a beam with hinges and patches for different values of f

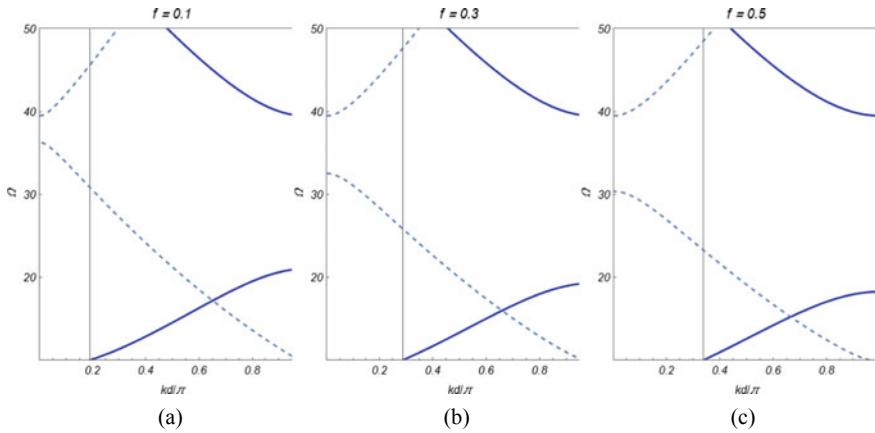


Fig. 8.5 First low-frequency band gap of a beam with hinges and patches for different values of f

The analysis of the band gaps structures can be summarized as follows:

1. Increasing of parameter f increase the gap bandwidth and shift the center frequency of the vibration band gaps to low-frequency regions
2. Increasing of parameter f slightly changes the gap bandwidth of (BPH) and significantly changes the gap bandwidth of (BP).
3. The band bandwidth of the BPH is wider than the band bandwidth of the BP.
4. All gaps of the BP are located within the gaps of the BPH.
5. Widening of the resonant bandwidths of a piezoelectric harvester with phononic band gaps generated by internal hinges is more significant than widening of the resonant bandwidths due to increase of the patch parameter f .

We can conclude finally that the novelty of this paper is the results concerning the widening of the resonant bandwidths of a piezoelectric harvester based on phononic band gaps generated by the internal hinges, not by the patches. The impact of the patches on the gap formation is insignificant in this metastructure with internal hinges.

Acknowledgements The work was supported by the Science Committee of RA, in the framework of the research project 21T-2C299.

References

1. Stephen, N.G.: On energy harvesting from ambient vibration. *J. Sound Vibration* **293**(1–2), 409–425 (2006)
2. Hame, R.L.: Theoretical investigations of energy harvesting efficiency from structural vibrations using piezoelectric and electromagnetic oscillators. *J. Acoustical Soc. Am.* **132**(1), 162–172 (2012)

3. Lu, Y., Wang, Z., Zhu, X., Hu, C., Yang, J., Wu, Y.: Vibration energy harvesting from the subwavelength interface state of a topological metamaterial beam. *Micromachines* **13**(6), 862 (2022)
4. Liao, Y., Sodano, H.A.: Optimal placement of piezoelectric material on a cantilever beam for maximum piezoelectric damping and power harvesting efficiency. *Smart Mater. Struct.* **21**(10), 105014 (2012)
5. Wang, Q., Wu, N.: Optimal design of a piezoelectric coupled beam for power harvesting. *Smart Mater. Struct.* **21**(8), 085013 (2012)
6. Erturk, A., Inman, D.J.: An experimentally validated bimorph cantilever model for piezoelectric energy harvesting from base excitations. *Smart Mater. Struct.* **18**(2), 025009 (2009)
7. Doaré, O., Michelin, S.: Piezoelectric coupling in energy-harvesting fluttering flexible plates: linear stability analysis and conversion efficiency. *J. Fluids Struct.* **27**(8), 1357–1375 (2011)
8. Friswell, M.I., Bilgen, O., Ali, S.F., Litak, G., Adhikari, S.: The effect of noise on the response of a vertical cantilever beam energy harvester. *ZAMM* **95**(5), 433–443 (2015)
9. Eichhorn, C., Goldschmidtboeing, F., Woias, P.: A frequency tunable piezoelectric energy converter based on a cantilever beam. *Proc. PowerMEMS* **9**(12), 309–312 (2008)
10. Li, H., WeiYang, Q.: Dynamics and coherence resonance of a laminated piezoelectric beam for energy harvesting. *Nonlinear Dyn.* **81**(4), 1751–1757 (2015)
11. Piliposian, G., Hasanyan, A., Piliposyan, D.: The effect of the location of piezoelectric patches on the sensing, actuating and energy harvesting properties of a composite plate. *J. Phys. D: Appl. Phys.* **52**(44), 445501 (2019)
12. Piliposian, G., Hasanyan, A., Piliposyan, G., Jilavyan, H.: On the sensing, Actuating and energy harvesting properties of a composite plate with piezoelectric patches. *Int. J. Precision Eng. Manuf.-Green Technol.* **7**, 657–668 (2020)
13. Doaré, O., Michelin, S.: Piezoelectric coupling in energy-harvesting fluttering flexible plates: linear stability analysis and conversion efficiency. *J. Fluids Struct.* **27**(8), 1357–1375 (2011)
14. Ghazaryan, K., Piliposyan, D.: Interfacial effects for shear waves in one dimensional periodic piezoelectric structure. *J. Sound Vibration* **330**(26), 6456–6466 (2011)
15. Piliposyan, D.: Piezoelectricity induced defect modes for shear waves in a periodically stratified superlattice. *J. Sound Vibration* **412**, 242–255 (2018)
16. Adams, S., Craster, R.V., Guenneau, S.: Bloch waves in periodic multi-layered acoustic layers. In: *Proceedings of the Royal Society of London A: Mathematical, Physical and Engineering Sciences*, vol. 464, no. 2098 (2008)
17. Hussein, M.I., Leamy, M.J., Ruzzene, M.: Dynamics of phononic materials and structures: historical origins, recent progress, and future outlook. *Appl. Mech. Rev.* **66**, 040802/1-38 (2014)
18. Anigbogu, W., Nguyen, H., Bardaweel, H.K.: Layered metamaterial beam structures with local resonators for vibration attenuation: model and experiment. *Front. Mech. Eng.* **7** (2021). <https://doi.org/10.3389/fmech.2021.768508>
19. Anigbogu, W., Bardaweel, H.: A metamaterial inspired structure for simultaneous vibration attenuation and energy harvesting. In: *Shock and Vibration*, vol. 2020, Article ID 4063025, pp. 1–12 (2020)
20. Motaei, F., Bahrami, A.: Energy harvesting from sonic noises by phononic crystal fibers. *Sci. Rep.* **12**(1), 1–8 (2022)
21. Ma, T.X., Fan, Q.S., Zhang, C., Wang, Y.S.: Flexural wave energy harvesting by the topological interface state of a phononic crystal beam. *Extreme Mech. Lett.* **50**, 101578 (2022)
22. Zhenkun, L., Al, Ba.'ba' a H., Tol, S.: Piezoelectric metastructures for simultaneous broadband energy harvesting and vibration suppression of traveling waves. *Smart Mater. Struct.* **30**, 075037 (2021)
23. Carrara, M., Cacan, M.R., Toussaint, J., Leamy, M.J., Ruzzene, M., Erturk, A.: Metamaterial-inspired structures and concepts for elasto-acoustic wave energy harvesting. *Smart Mater. Struct.* **22**(6), 065004 (2013)
24. Hu, G., Tang, L., Banerjee, A., Das, R.: Metastructure with piezoelectric element for simultaneous vibration suppression and energy harvesting. *J. Vibration Acoustics* **139**(1), 011012 (2017)

25. Lee, G., Lee, D., Park, J., Jang, Y., Kim, M., Rho, J.: Piezoelectric energy harvesting using mechanical metamaterials and phononic crystals. *Commun. Phys.* **5**(1), 1–16 (2022)
26. Papanicolaou, V.: The periodic Euler-Bernoulli equation. *Trans. Am. Math. Soc.* **355**(9), 3727–3759 (2003)
27. Tovar, A.A., Casperson, W.: Generalized Sylvester theorems for periodic applications in matrix optics. *J. Opt. Soc. Am. A* **12**, 578–590 (1995)

Chapter 9

Periodic Contact Problem for a Two-level System of Punches and a Viscoelastic Half-space



Irina G. Goryacheva and Anastasiya A. Yakovenko

Abstract The paper presents a solution of the contact problem for a periodic two-level system of axisymmetric punches and a viscoelastic half-space. The case of a constant nominal pressure applied to the punch system is considered. The variation of the real contact area in time and the conditions that provide the contact of the punches of both levels with the half-space are investigated. The influence of the geometric parameters of the punch system and the mechanical properties of the viscoelastic half-space on the contact characteristics are analyzed. Numerical results are presented for the system of punches located in the nodes of a square lattice and penetrated into a viscoelastic half-space modeled by a standard linear solid. It is shown that the real contact area may increase greatly if the second level punches come into contact with the half-space at some instant of time.

Keywords Periodic contact · Linear viscoelasticity · Multi-level system of punches · Time dependent contact characteristics

9.1 Introduction

Discrete contact problems are of great theoretical and practical importance. These problems mainly arise in study of the contact of bodies taking into account their surface microrelief, which is formed by a surface roughness. Solutions of these problems differ considerably from the classical solutions of the contact problems for absolutely smooth bodies. The most significant difference is that the real contact area consists of the system of contact spots may be several times smaller than the nominal one. This fact is essential in analysis of many important operational properties of tribounits.

I. G. Goryacheva · A. A. Yakovenko (✉)
Ishlinsky Institute for Problems in Mechanics RAS, Prospekt Vernadskogo, 101-1, Moscow
119526, Russian Federation
e-mail: anastasiya.yakovenko@phystech.edu

I. G. Goryacheva
e-mail: goryache@ipmnet.ru

The characteristics of the contact interaction are determined not only by the geometry of the contact surfaces of the bodies, but also by their mechanical properties. Many materials are characterized by viscoelastic properties, that is, their stress-strain state is time-dependent. For example, soft polymers belong to this type of materials. Polymers are widely used in many industries such as automotive, aerospace, construction, textile, medicine and others [1]. They are applied to produce food wraps, containers, adhesives, electric- and thermal insulation, lenses, windows, clothing, etc. Hence, the problems of discrete contact of viscoelastic bodies are of great relevance. An extensive study of the stress state of viscoelastic bodies is presented in the book of Arutunyan [2].

The roughness of surfaces has often a statistical nature; however, it can also be regular, for example, in the case when it is produced by artificial methods. Currently, numerical methods are widely used to solve the problems of contact of rough surfaces. Such approach makes it possible to consider any contact geometry of bodies and their mechanical properties. For example, numerical calculations were used in [3] to analyze the viscoelastic contact of tires with the road. In this study, the authors proposed to consider the contact at the macrolevel with limited number of asperities. The conjugate gradient method was used in [4] to solve the problem of the contact of a rigid smooth spherical indenter with a viscoelastic rough half-space. The problem of the rough viscoelastic contact is also numerically solved in [5] using both spatial and time discretization.

Despite a huge variety of problems that can be solved by numerical methods, analytical approaches to solving the discrete contact problems also do not lose their relevance. There are a number of analytical methods of solving the contact problems for viscoelastic bodies with regular and irregular microrelief. In the case of irregular roughness, the contact model is in general based on the Greenwood–Williamson approach [6], which respects the height distribution of asperities. The first attempt to extend the application of this model to the viscoelastic case has been performed in [7]. To take into account the viscoelasticity of bodies, the authors simply replaced the Young's modulus with the time-dependent relaxation function. However, this procedure is incorrect, as was shown in [8], where the accurate solution was derived. The solution obtained in [8] allows us to take into account the fact that asperities of different heights come into contact at various times. In addition to the Greenwood–Williamson statistical model, fractal geometry is also used to describe the contact of rough surfaces in the viscoelastic case (see, for example, [9]). Another approach to solving the contact problems for rough bodies based on the probabilistic method and the diffusion equation can be found in the Persson's works. In [10], this approach was used to solve the contact problem in the viscoelastic case for fixed nominal pressure. Later, the Persson's theory was extended to the viscoelastic contact under an arbitrarily time-varying applied load [11]. Despite the fact that the Persson's theory for the rough contact gives quite simple results, its justification is not strict enough that is noted, for example, in [12].

Analytical methods have also been developed to study the contact of bodies with periodic roughness. In [13], the localization method was suggested to solve the contact problems for a periodic system of axisymmetric punches and an elastic

half-space. This method allows us to consider both single-level periodic systems of punches and systems of punches with different heights. Application of the localization method to solve the periodic problem with a viscoelastic half-space is carried out in [14], where the analytical solution for a single-level system of spherical punches which is in contact with the viscoelastic base was reduced. However, the surface roughness is often uneven in height, which is essential for studying the contact of bodies with rheological properties. In this study, using the localization principle, the contact of a two-level periodic system of axisymmetric punches with a viscoelastic half-space is analyzed.

The article is structured as follows. In Sect. 9.2, the formulation of the contact problem for the two-level periodic system of punches indenting into the viscoelastic half-space is presented. In Sect. 9.3, the one-level contact of the system of punches with the half-space is studied and the conditions of the second level punches coming into contact are analyzed. In Sect. 9.4, the two-level contact is investigated and the dependence of the real contact area on time is analyzed. Section 9.5 provides some main conclusions.

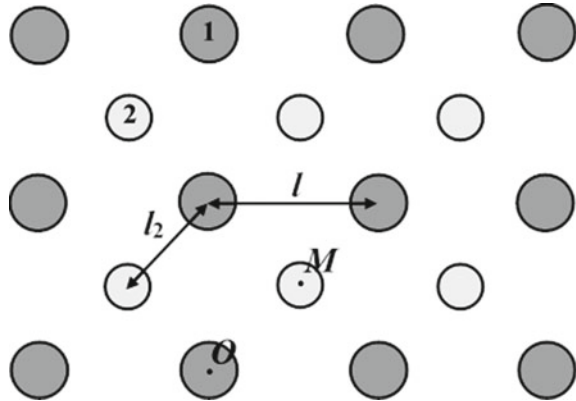
9.2 Statement of the Contact Problem

The indentation of a two-level periodic system of axisymmetric punches into a viscoelastic half-space is considered. The difference in the heights of the punches of the two levels is given and equal to Δh . The shape of the contact surface of the punches is described by the function $f(r) = Cr^s / R^{s-1}$, where $s = 1, 2, \dots$, R is the characteristic punch size, C is the dimensionless constant. The axes of symmetry of the punches are perpendicular to the boundary of the half-space. We connect the coordinate system with some fixed punch of the i th level ($i = 1, 2, \dots$) in such a way as to the axis Oz coincides with the axis of rotation of the fixed punch, and the plane $Or\theta$ coincides with the undeformed surface of the half-space. We also assume that the each contact spot of the i th level is bounded by a circle of radius $a_i(t)$ (Fig. 9.1) that is valid for not very tight contact.

The boundary conditions of the problem are of a mixed type, since normal displacements of the half-space boundary are known at all contact spots, and outside the contact area, we have the condition of zero normal stresses. It is also assumed that the shear stresses are zero on the entire boundary of the half-space. In addition, as initial conditions, we suppose that before the interaction process begins, the viscoelastic half-space is not stressed and is at rest.

For certainty, we consider a system of punches located at each level in nodes of a square lattice, that is, at vertices of squares of one size $l \times l$ (Fig. 9.1). The punch system is loaded with a nominal pressure $\bar{p}(t) = \bar{p}_0 H(t)$ acting within one period. Here \bar{p}_0 is a given constant and $H(t)$ is the Heaviside function. We assume that the material of the half-space is homogeneous, isotropic, linearly viscoelastic, and has the constant Poisson's ratio ν . In this case, one relaxation function is sufficient

Fig. 9.1 Scheme of the location of punches in a two-level periodic system



to describe mechanical behavior of the material [15]. For example, we can use the relaxation function $E(t)$ corresponding to uniaxial tension/compression or the creep function $J(t)$ related to it.

9.3 Contact Problem Solution for the First Level Punches

If the value of the nominal pressure $\bar{p}(t)$ is not sufficient to immediately provide the two-level contact, only the first level punches come into contact with the half-space at the beginning of the contact interaction. In this part, the contact problem analysis for the one-level system of punches is presented and the condition when the second level of punches comes into contact is derived.

9.3.1 Derivation of the Main Equations for Calculation of the First Level Contact Characteristics

The solution of the problem of the indentation of a one-level punch system into a viscoelastic half-space is obtained in [16]. This solution is constructed using the extended correspondence principle [17] and the localization method [13]. In [14, 16], the one-level periodic contact problem is solved in the simplest case, when the real pressure distribution is taken into account only under the fixed punch, and the action of all the others is replaced by the nominal pressure. In this research, in order to improve the calculation accuracy, one more series of punches is added to consideration, and their action is replaced by the load of intensity $4P_1(t)$ distributed over a circle of radius l . In this case, the solution of the single-level problem takes the following form

$$\begin{aligned}
 p_1(r, t) = \int_{0^-}^t E(t - \tau) \frac{\partial}{\partial \tau} & \left(\frac{Cp_{(k,m)}(r, \tau)}{\pi (1 - \nu^2) R^{s-1}} + \frac{2}{\pi^2} \left(\int_{0^-}^{\tau} J(\tau - \tau') \frac{dP_1(\tau')}{d\tau'} d\tau' \right) \right) \\
 & \cdot \left(\frac{2}{l^2 - r^2} \sqrt{\frac{a_1^2(\tau) - r^2}{l^2 - a_1^2(\tau)}} + \frac{5}{A_1^2} \arctan \sqrt{\frac{a_1^2(\tau) - r^2}{A_1^2 - a_1^2(\tau)}} \right) d\tau, \tag{9.1}
 \end{aligned}$$

$$\begin{aligned}
 & \frac{a_1^{s+1}(t)}{10 \left(\arccos \left(\frac{a_1(t)}{A_1} \right) + \frac{a_1(t)}{A_1^2} \sqrt{A_1^2 - a_1^2(t)} \right) - 8 \left(\arccos \left(\frac{a_1(t)}{l} \right) + \frac{a_1(t)}{\sqrt{l^2 - a_1^2(t)}} \right)} \\
 & = \frac{(1 - \nu^2) (s + 1) \Gamma(s) R^{s-1}}{\pi 2^{s-1} s^2 C \Gamma^2 \left(\frac{s}{2} \right)} \int_{0^-}^t J(t - \tau) \frac{dP_1(\tau)}{d\tau} d\tau, \tag{9.2}
 \end{aligned}$$

where $\Gamma(x)$ is the gamma function, $p_1(r, t)$ is the contact pressure under the first level punch, $P_1(t)$ is the load applied to a single first level punch, and A_1 is the radius of the circle outside of which the nominal pressure is distributed, which replaces the action of all punches except the fixed one and four nearby punches. The functions $p_{(k)}(r, t)$ and $p_{(m)}(r, t)$ in Eq. (9.1) are determined by the parity of the exponent s of the function $f(r)$ and have the following form

$$\begin{aligned}
 p_{(k)}(r, t) & = \left(\frac{(2k + 1)!!}{(2k)!!} \right)^2 r^{2k} \\
 & \cdot \left(\cosh^{-1} \left(\frac{a_1(t)}{r} \right) + \sqrt{1 - \left(\frac{r}{a_1(t)} \right)^2} \sum_{i=1}^k \frac{(2i - 2)!!}{(2i - 1)!!} \left(\frac{a_1(t)}{r} \right)^{2i} \right), \\
 p_{(m)}(r, t) & = \left(\frac{(2m)!!}{(2m - 1)!!} \right)^2 a_1^{2m-1}(t) \sqrt{1 - \left(\frac{r}{a_1(t)} \right)^2} \sum_{i=1}^m \frac{(2i - 3)!!}{(2i - 2)!!} \left(\frac{r}{a_1(t)} \right)^{2(m-i)},
 \end{aligned}$$

where k are m are integers. The function with index k corresponds to the odd exponent s , that is, $s = 2k + 1$, and the function with index m corresponds to an even exponent s , that is, $s = 2m$. According to the localization principle, the radius A_1 of the circle is determined by the average number \bar{N}_1 of contact spots per unit area and the number M_1 of punches located inside this circle, namely

$$\pi A_1^2 = \frac{M_1}{\bar{N}_1}. \tag{9.3}$$

During the single-level contact $\bar{p}(t) = \bar{N}_1 P_1(t)$, so Eqs. (9.1) and (9.2) can be written in terms of the nominal pressure. Provided the constant value of the applied nominal pressure, we obtain

$$p_1(r, t) = \int_{0^-}^t E(t - \tau) \frac{\partial}{\partial \tau} \left(\frac{C p_{k,m}(r, \tau)}{\pi (1 - \nu^2) R^{s-1}} + \frac{2}{5\pi} \bar{p}_0 J(\tau) \right. \\ \left. \cdot \left(\frac{2A_1^2}{l^2 - r^2} \sqrt{\frac{a_1^2(\tau) - r^2}{l^2 - a_1^2(\tau)}} + 5 \arctan \sqrt{\frac{a_1^2(\tau) - r^2}{A_1^2 - a_1^2(\tau)}} \right) \right) d\tau, \quad (9.4)$$

$$\frac{a_1^{s+1}(t)}{10 \left(\arccos \left(\frac{a_1(t)}{A_1} \right) + \frac{a_1(t)}{A_1} \sqrt{A_1^2 - a_1^2(t)} \right) - 8 \left(\arccos \left(\frac{a_1(t)}{l} \right) + \frac{a_1(t)}{\sqrt{l^2 - a_1^2(t)}} \right)} = \frac{(1 - \nu^2) (s + 1) \Gamma(s) R^{s-1} A_1^2 \bar{p}_0 J(t)}{2^{s-1} 5 s^2 C \Gamma^2 \left(\frac{s}{2} \right)}. \quad (9.5)$$

Equations (9.4) and (9.5) are used to calculate the pressure distribution at the initial stage of indentation process when only the first level punches come into contact.

9.3.2 Determination of the Instant of Time When the Second Level of Punches Comes into Contact with the Half-space

Let us find the time instant t_* when the second level punches come into the contact with the viscoelastic half-space. For this purpose, first it needs to investigate the variation in time of the vertical displacement of the point M of the half-space boundary (Fig. 9.1). The point M is located at the center of the square and the vertices of which are centers of the contact spots of the first level punches. For simplicity, the action of these four punches is replaced by the load of intensity $4P_1(t)$ distributed along the circumference of radius $l_2 = l/\sqrt{2}$, and the action of other first level punches is replaced by the nominal pressure distributed outside the circle of radius A . Based on (9.3), the radius A is determined from the condition $\pi A^2 = 4/\bar{N}_1$.

The vertical displacement $u_z(r, t)$ of the viscoelastic half-space (characterized by the constant Poisson ratio) due to the action of the axisymmetric normal pressure $p(r, t)$ applied over a circular area of radius $a(t)$ is determined by the following expression [18]

$$u_z(r, t) = \frac{4(1-\nu^2)}{\pi} \int_{0^-}^t J(t-\tau) \frac{\partial}{\partial \tau} \left(\int_0^{a(\tau)} p(\rho, \tau) \mathbf{K} \left(\frac{2\sqrt{\rho r}}{\rho+r} \right) \frac{\rho d\rho}{\rho+r} \right) d\tau, \quad (9.6)$$

where $\mathbf{K}(x)$ is the complete elliptic integral of the first kind. It is convenient to put the origin at the point M (Fig. 9.1). Based on the proposed replacement of the action of punches with the circumferentially distributed load $2P_1(t)\delta(r-l_2)/(\pi r)$ ($\delta(x)$ is the Dirac delta function) and the nominal pressure $\bar{p}(t)$, we obtain from Eq. (9.6) the following expression for the half-space boundary displacement for $r < l_2$

$$u_z(r, t) = \frac{8(1-\nu^2)}{\pi^2 l_2} \mathbf{K} \left(\frac{r}{l_2} \right) \int_{0^-}^t J(t-\tau) \frac{dP_1(\tau)}{d\tau} d\tau + D_\infty - \frac{4(1-\nu^2)}{\pi} \mathbf{AE} \left(\frac{r}{A} \right) \int_{0^-}^t J(t-\tau) \frac{d\bar{p}(\tau)}{d\tau} d\tau, \quad (9.7)$$

where $\mathbf{E}(x)$ is the complete elliptic integral of the second kind and D_∞ is the displacement of the half-space boundary loaded everywhere with the nominal pressure. Hence, the displacement of the point M , i.e., $r = 0$, provided the constant nominal pressure \bar{p}_0 applied to the system, as follows from (9.7) and the equilibrium condition $\pi A_1^2 \bar{p}(t) = 5P_1(t)$, is

$$u_z(0, t) = 2(1-\nu^2) \left(\frac{2A_1^2}{5l_2} - A \right) \bar{p}_0 J(t) + D_\infty. \quad (9.8)$$

The vertical displacement of any fixed first level punch is determined by the magnitude of the indentation depth $D(t)$ of the periodic system of the first level punches under the given load $\bar{p}(t)$. By analogy with [14], we find the function of the additional displacement $d(t)$, which is

$$d(t) = D(t) - D_\infty = \frac{s\Gamma^2\left(\frac{s}{2}\right) C a_1^s(t)}{2^{2-s}\Gamma(s)R^{s-1}} - 2(1-\nu^2) \left(\sqrt{A_1^2 - a_1^2(t)} - \frac{2A_1^2}{5\sqrt{l_2^2 - a_1^2(t)}} \right) \bar{p}_0 J(t). \quad (9.9)$$

For further investigation, we introduce a function $h(t)$ equal to the difference between the displacements of the points O and M (Fig. 9.1). Based on Eqs. (9.8) and (9.9), this function is calculated by the following expression

$$\begin{aligned}
 h(t) = D(t) - u_z(0, t) = & \frac{s\Gamma^2\left(\frac{s}{2}\right)Ca_1^s(t)}{2^{2-s}\Gamma(s)R^{s-1}} \\
 & - 2(1 - \nu^2) \left(\sqrt{A_1^2 - a_1^2(t)} - \frac{2A_1^2}{5\sqrt{l^2 - a_1^2(t)}} + \frac{2A_1^2}{5l^2} - A \right) \bar{p}_0 J(t).
 \end{aligned}
 \tag{9.10}$$

Together with Eq. (9.5), which determines the dependence of the radius of a single contact spot on time, Eq. (9.10) allows us to calculate the value of the function $h(t)$ at each time. The time instant t_* when the value of the function $h(t)$ becomes equal Δh , i.e., $\Delta h = h(t_*)$, determines the moment when the second level punches come into contact with the half-space. It also follows that if $h(0) \geq \Delta h$, then the two-level contact occurs immediately from the beginning of the interaction process.

9.3.3 Analysis of the Indentation of the First Level Punches into the Half-space

Let us first analyze the dependence $h(a_1)$. Based on Eqs. (9.5) and (9.10), we get

$$\begin{aligned}
 h(a_1) = & \frac{s\Gamma^2\left(\frac{s}{2}\right)Ca_1^s}{2^{2-s}\Gamma(s)R^{s-1}} \left(1 \right. \\
 & \left. - \frac{20sa_1 \left(\sqrt{A_1^2 - a_1^2} - \frac{2A_1^2}{5\sqrt{l^2 - a_1^2}} + \frac{2A_1^2}{5l^2} - A \right)}{(s+1)A_1^2 \left(10 \left(\arccos\left(\frac{a_1}{A_1}\right) + \frac{a_1}{A_1} \sqrt{A_1^2 - a_1^2} \right) - 8 \left(\arccos\left(\frac{a_1}{l}\right) + \frac{a_1}{\sqrt{l^2 - a_1^2}} \right) \right)} \right).
 \end{aligned}$$

Figure 9.2 illustrates the function $h(a_1)$ and its derivative for three values of the exponent s of the shape function $f(r)$ for the quadratic lattice (in this case, the average number of the contact spots per unit area is defined by the expression $\bar{N}_1 = 1/l^2$). As follows from the results of calculations, the function $h(a_1)$ is monotonically increasing (Fig. 9.2b shows that the derivative of the function $h(a_1)$ is positive everywhere). As shown in [14], at a constant nominal pressure, the dependence of the radius of the contact spot of the single first level punch with the viscoelastic half-space is described by a monotonically increasing function. Consequently, the difference in the displacements of the points O (the center of the contact area of the first level punch with the half-space) and M (the square center where the contact of the second level punch with the half-space should begin) also increases with time.

Let us analyze the dependence of the difference in the displacements of the points O and M (Fig. 9.1) on time for certain types of the creep function $J(t)$. We consider the viscoelastic model of the standard linear solid and the creep function of which has the following form [19]

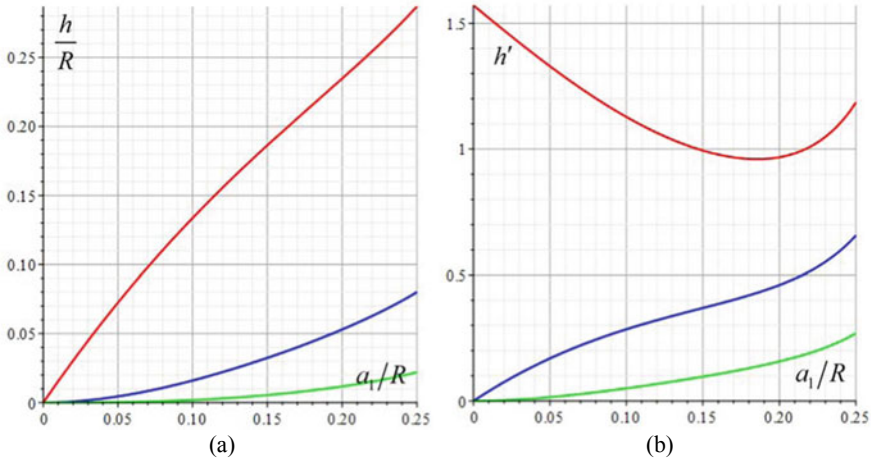


Fig. 9.2 Dependence of the function h (a) and its derivative (b) on the radius of the single contact spot a_1 for different punch shapes ($s = 1$ for the red lines, $s = 2$ for the blue lines, $s = 3$ for the green lines), and $C = 1, l = 0.5R$

$$J(t) = \frac{T_\varepsilon}{E_0 T_\sigma} \left(1 - \left(1 - \frac{T_\sigma}{T_\varepsilon} \right) \exp \left(-\frac{t}{T_\varepsilon} \right) \right), \tag{9.11}$$

where E_0 is the instantaneous elastic modulus, T_σ is the relaxation time and T_ε is the creep (retardation) time. Substituting Eq. (9.11) into Eq. (9.10), we obtain an expression that with Eq. (9.5) allows us to determine the moment t_* when the second level punches come into contact with the half-space. This moment is determined from the condition $h(t_*) = \Delta h$.

Figure 9.3 illustrates the dependence $h(t)$ for spherical punches with $f(r) = r^2/(2R)$ for different values of the ratio of creep and relaxation times, as well as for different densities of location of punches in the system (the different pitch l of the quadratic lattice). As follows from the calculation results, the value h for a fixed instant of time grows with an increase in the parameter $T = T_\varepsilon/T_\sigma$ (for a fixed instantaneous elastic modulus E_0), that is, in the viscosity of the half-space material, and with an increase in the pitch l of the quadratic lattice. Therefore, these parameters, as well as the values of the height difference Δh and the applied nominal pressure \bar{p}_0 , influence the fact whether the second level punches will come into contact with the viscoelastic half-space. So, if $\Delta h = 0.04R$, then with the values of the parameters under consideration, the two-level contact does not occur at $T = 2$ or at $l = 0.5R$. Note that in the graphs of Fig. 9.3, the dotted lines correspond to the elastic case with the long-term (equilibrium) elastic modulus $E_\infty = E_0 T_\sigma/T_\varepsilon$.

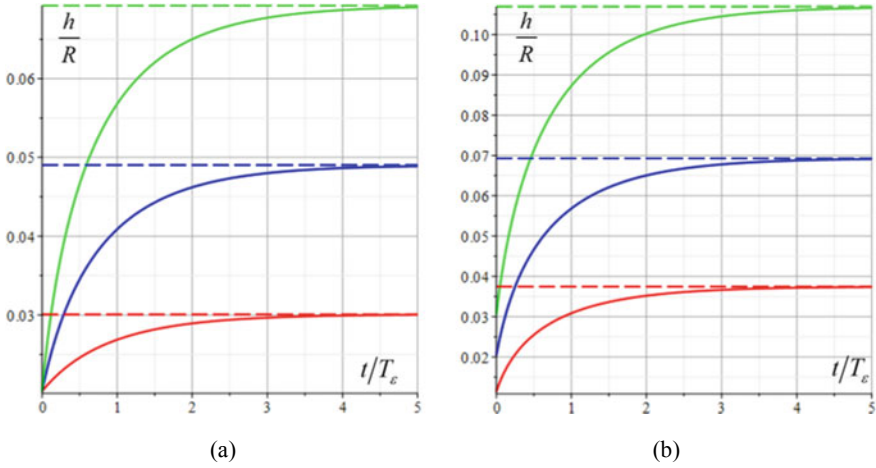


Fig. 9.3 Dependencies of the difference of the displacements of the points O and M on time (a) for different values of T ($T = 2$ for the red line, $T = 5$ for the blue line, $T = 10$ for the green line) at $l = 0.75R$; and (b) for different values of the pitch l ($l = 0.5R$ for the red line, $l = 0.75R$ for the blue line, $l = R$ for the green line) at $T = 10$; $\bar{p}_0 = 0.01E_0 / (1 - \nu^2)$

9.4 Two-level Contact of the System of Punches and the Half-space

If the conditions for the second level punches coming into contact are fulfilled, the two-level contact occurs. For the asymptotic analysis of the contact characteristics in the two-level contact, we use the correspondence elastic solution with instantaneous and long-term elastic modules of the viscoelastic material under consideration.

9.4.1 Asymptotic Analysis of the Contact Characteristics

A general approach to solving the problems of indentation of a multi-level periodic system of punches into an elastic half-space is presented in [20]. Fixing the punch of one of the two levels and replacing the action of the nearby four punches of another level, as well as four punches of the same level with loads distributed over the circles of radii l_2 and l , respectively, and all other punches of both levels with the nominal pressure, we obtain the following system of equations ($i = 1, 2$)

$$\bar{p} = \frac{1}{j_2} (P_1 + P_2), \tag{9.12}$$

$$\pi A_i^2 \bar{p} = 5P_i + 4P_j, \tag{9.13}$$

$$\begin{aligned}
 P_i = & \frac{2^{s-1} s^2 \Gamma^2\left(\frac{s}{2}\right) E C a_i^{s+1}}{(s+1) \Gamma(s) (1-\nu^2) R^{s-1}} + \frac{8 P_j}{\pi} \left(\frac{a_i}{\sqrt{l_2^2 - a_i^2}} - \arcsin\left(\frac{a_i}{l_2}\right) \right) \\
 & + \frac{8 P_i}{\pi} \left(\frac{a_i}{\sqrt{l^2 - a_i^2}} - \arcsin\left(\frac{a_i}{l}\right) \right) + 2 \bar{p} \left(A_i^2 \arcsin\left(\frac{a_i}{A_i}\right) - a_i \sqrt{A_i^2 - a_i^2} \right),
 \end{aligned}
 \tag{9.14}$$

$$\begin{aligned}
 \Delta h = & \frac{1-\nu^2}{\pi E} \left(\frac{\pi s \Gamma^2\left(\frac{s}{2}\right) C E (a_1^s - a_2^s)}{2^{2-s} \Gamma(s) R^{s-1} (1-\nu^2)} - \left(\frac{4 P_1}{\sqrt{l_2^2 - a_2^2}} - \frac{4 P_2}{\sqrt{l_2^2 - a_1^2}} \right) \right. \\
 & \left. - \left(\frac{4 P_2}{\sqrt{l^2 - a_2^2}} - \frac{4 P_1}{\sqrt{l^2 - a_1^2}} \right) - 2 \pi \bar{p} \left(\sqrt{A_1^2 - a_1^2} - \sqrt{A_2^2 - a_2^2} \right) \right).
 \end{aligned}
 \tag{9.15}$$

Note that in Eqs. (9.13) and (9.14) $i \neq j$.

Table 9.1 gives the values P_i, a_i, A_i for spherical punches of each level ($i = 1, 2$) calculated by Eqs. (9.12)–(9.15) for the instantaneous and long-term elastic modulus presented in the table at $\bar{p}_0 = 0.06 E_0 / (1 - \nu^2), l = 0.75 R, \Delta h = 0.05 R$. It follows from the results that the load applied to the single punch of the first level decreases, and the load applied to the single punch of the second level increases with time. The contact spot’s radii a_i for punches of both levels increase over time. Note that the growth of the contact radius is limited by the condition $a_1 + a_2 \leq l_2$, that is, the sum of the radii of the contact spots does not exceed a half of the length of the diagonal of the lattice square.

The radii A_i ($i = 1, 2$) of the areas ($r > A_i$) in which, according to the used model, the nominal pressure acts are practically constant as follows from the calculation results presented in Table 9.1. Therefore, for the correct application of the localization principle for investigating the two-level contact in the viscoelastic case, we assume that the radii A_1 and A_2 do not change in time: $A_1(t) = A_1(t_*)$ and $A_2(t) = A_2(t_*)$, where $t_* \geq 0$.

Table 9.1 Instantaneous and long-term values of the contact characteristics of the two-level contact

E	$\frac{P_1(1-\nu^2)}{R^2 E_0}$	$\frac{P_2(1-\nu^2)}{R^2 E_0}$	$\frac{a_1}{R}$	$\frac{a_2}{R}$	$\frac{A_1}{R}$	$\frac{A_2}{R}$
E_0	0.0335	0.0003	0.2815	0.0567	0.9454	0.8472
$E_\infty = 0.8 E_0$	0.0327	0.0011	0.2976	0.0926	0.9432	0.8497
$E_\infty = 0.5 E_0$	0.0308	0.0029	0.3302	0.1455	0.9379	0.8555
$E_\infty = 0.4 E_0$	0.03	0.0038	0.3447	0.1662	0.9355	0.8581

9.4.2 Solution of the Viscoelastic Two-level Periodic Problem

As it was shown in Sect. 9.4.1, if the condition $a_1 + a_2 \leq l_2$ is precisely satisfied, the radii a_1 and a_2 increase over time. This fact makes it possible to derive the viscoelastic solution based on the solution of the similar elastic problem using the extended correspondence principle [15]. According to this principle, by replacing p_i/E with

$$\int_{0^-}^t J(t - \tau) (\partial p_i / \partial \tau) d\tau$$

and, consequently, \bar{p}/E and P_i/E with

$$\int_{0^-}^t J(t - \tau) (d\bar{p}/d\tau) d\tau$$

and

$$\int_{0^-}^t J(t - \tau) (dP_i/d\tau) d\tau,$$

respectively, and taking into account Eqs. (9.14)–(9.15) and the assumption that the radii A_1 and A_2 do not depend on time, we obtain the following system of equations for calculation of the contact characteristics in the two-level periodic contact problem for the viscoelastic half-space

$$\begin{aligned} Q_i(t) = & \frac{2^{s-1} s^2 \Gamma^2\left(\frac{s}{2}\right) C a_i^{s+1}(t)}{(s+1)\Gamma(s)(1-\nu^2)R^{s-1}} + \frac{8Q_j(t)}{\pi} \left(\frac{a_i(t)}{\sqrt{l_2^2 - a_i^2(t)}} - \arcsin\left(\frac{a_i(t)}{l_2}\right) \right) \\ & + \frac{8Q_i(t)}{\pi} \left(\frac{a_i(t)}{\sqrt{l^2 - a_i^2(t)}} - \arcsin\left(\frac{a_i(t)}{l}\right) \right) + 2\bar{p}_0 J(t) \left(A_i^2 \arcsin\left(\frac{a_i(t)}{A_i}\right) - \right. \\ & \left. - a_i(t) \sqrt{A_i^2 - a_i^2(t)} \right), \end{aligned} \quad (9.16)$$

$$\begin{aligned} \Delta h = & \frac{s\Gamma^2\left(\frac{s}{2}\right) C (a_1^s(t) - a_2^s(t))}{2^{2-s}\Gamma(s)R^{s-1}} - \frac{4(1-\nu^2)}{\pi} \left(\frac{Q_1(t)}{\sqrt{l_2^2 - a_2^2(t)}} - \frac{Q_2(t)}{\sqrt{l_2^2 - a_1^2(t)}} \right) \\ & - \frac{4(1-\nu^2)}{\pi} \left(\frac{Q_2(t)}{\sqrt{l^2 - a_2^2(t)}} - \frac{Q_1(t)}{\sqrt{l^2 - a_1^2(t)}} \right) - 2(1-\nu^2) \bar{p}_0 J(t) \left(\sqrt{A_1^2 - a_1^2(t)} \right. \\ & \left. - \sqrt{A_2^2 - a_2^2(t)} \right), \end{aligned} \quad (9.17)$$

where $Q_i(t) = \int_{0^-}^t J(t - \tau) (dP_i/d\tau) d\tau$ ($i = 1, 2$). It is also necessary to add the equilibrium condition (9.12) to (9.16)–(9.17). The values of the radii A_1 and A_2 are taken as follows

$$\pi A_i^2(t_*) \bar{p}_0 = 5P_i(t_*) + 4P_j(t_*). \tag{9.18}$$

In particular, if $t_* \neq 0$, that is, when the value of the nominal pressure is not sufficient for the two-level contact to occur immediately, the values $A_1(t) = A_1(t_*)$ and $A_2(t) = A_2(t_*)$ are calculated from the following expressions

$$\pi A_1^2(t_*) \bar{p}_0 = 5P_1(t_*) + 4P_2(t_*) = 5l^2 \bar{p}_0 \implies A_1 = \sqrt{\frac{5}{\pi}} l,$$

$$\pi A_2^2(t_*) \bar{p}_0 = 5P_2(t_*) + 4P_1(t_*) = 4l^2 \bar{p}_0 \implies A_2 = \frac{2l}{\sqrt{\pi}}.$$

Equation (9.12) for this case takes the following form

$$\int_{0^-}^t J(t - \tau) \frac{d\bar{p}(\tau)}{d\tau} d\tau = \frac{1}{l^2} (Q_1(t) + Q_2(t)). \tag{9.19}$$

The resulting system of Eqs. (9.16)–(9.19) enables to determine the dependencies on time of the radii of the contact spots of the punches of both levels, as well as the functions $Q_1(t)$ and $Q_2(t)$, which are then used to calculate the dependencies on time of the load distribution between the punches of both levels, that is, the functions $P_1(t)$ and $P_2(t)$.

Figure 9.4 illustrates the dependencies $a_1(t)$ and $a_2(t)$ for two values of the nominal pressure \bar{p}_0 , one of which immediately provides the two-level contact, and the other provides it after some time. The results are calculated for the system of spherical punches ($f(r) = r^2/(2R)$). As follows from the results, the radii of the contact spots increase in time, tending to the constant values that correspond to the elastic solutions with the long-term elastic modulus. Note that the radii of the contact spots of the second level punches (red lines) increase significantly compared with the punches of the first level. For example, for the parameters used in calculations, in the case when the two-level contact occurs from the beginning of the indentation process (Fig. 9.4a), the radius a_1 increases about 1.2 times, while the radius a_2 increases 2.7 times to the time instant $t = 5T_\varepsilon$. Figure 9.4b illustrates the case when the second level punches come into contact with the half-space only some time after the beginning of the indentation process.

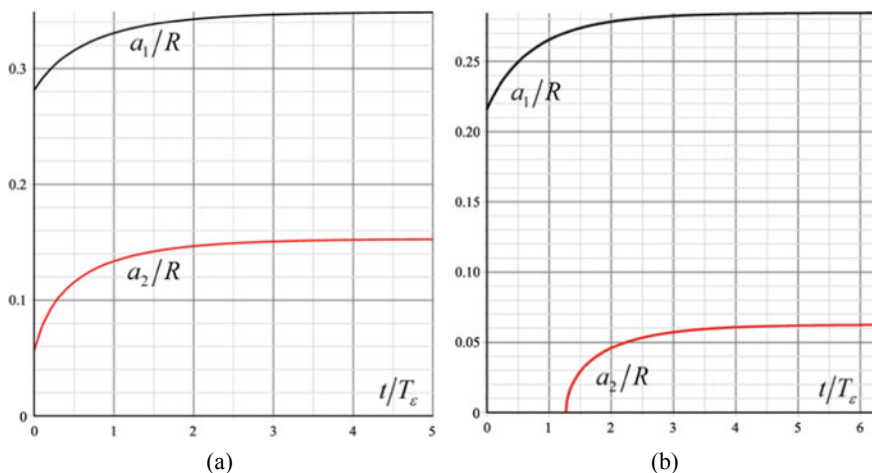


Fig. 9.4 Dependencies of the radii a_i ($i = 1, 2$) of the contact spots of each level on time at $l = 0.75R$, $T = 2.5$, $\Delta h = 0.05R$ and $\bar{p}_0 = 0.06E_0/(1 - \nu^2)$ (a); $\bar{p}_0 = 0.025E_0/(1 - \nu^2)$ (b)

9.4.3 Analysis of the Dependence of the Real Contact Area on Time

Let us introduce the following function that characterizes the evolution in time of the relative contact area for the two-level system of punches located in the nodes of quadratic lattice (Fig. 9.1)

$$\lambda(t) = \pi a_1^2(t) \bar{N}_1 + \pi a_2^2(t) \bar{N}_2 = \frac{\pi}{l^2} (a_1^2(t) + a_2^2(t)). \quad (9.20)$$

Figure 9.5 illustrates the dependencies of the relative contact area on time at different values of the pitch l of the quadratic lattice and different values of the height difference of the spherical punches of the two levels. The results are obtained for the viscoelastic model of the standard linear solid with $T = 2.5$. The results indicate that a decrease in the punch height difference and the distance between them leads to an increase in the relative contact area. Depending on the distance between the punches and their height difference, the contact area forms from interaction with the half-space of the only first level punches or both levels. So, if $\bar{p}_0 = 0.025E_0/(1 - \nu^2)$, the transition from the single-level contact to the two-level contact occurs only for the square lattice with $l = 0.75R$ as follows from the results presented in Fig. 9.5a (red line). In the other two cases, the two-level contact is observed from the beginning of the interaction process. For the higher nominal pressure $\bar{p}_0 = 0.06E_0/(1 - \nu^2)$, in the case of the system with $\Delta h = 0.05R$, the punches of the second level are in contact with the half-space from the beginning of the interaction process, for the system with $\Delta h = 0.075R$ the second level of punches comes into contact at $t = 1.03T_\varepsilon$

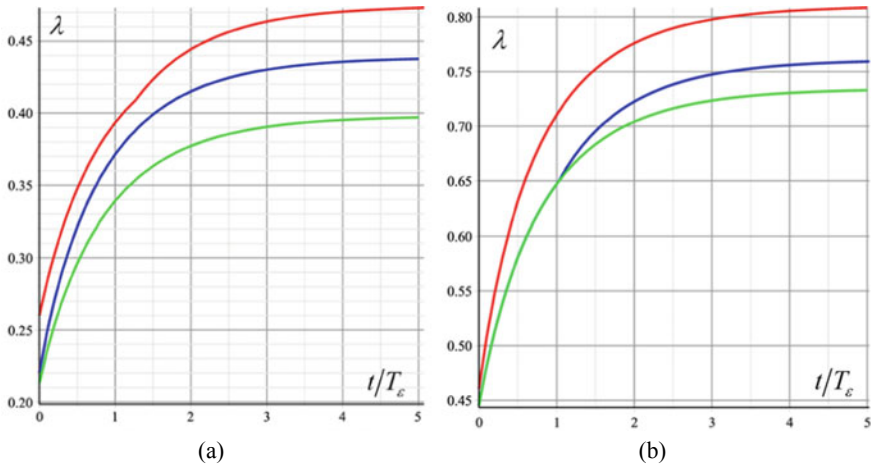


Fig. 9.5 Dependencies of the relative contact area on time **a** at $\Delta h = 0.05R$ and $\bar{p}_0 = 0.025E_0 / (1 - \nu^2)$ ($l = 0.75R$ for the red line, $l = R$ for the blue line, $l = 1.25R$ for the green line); **b** at $l = 0.75R$ and $\bar{p}_0 = 0.06E_0 / (1 - \nu^2)$ ($\Delta h = 0.05R$ for the red line, $\Delta h = 0.075R$ for the blue line, $\Delta h = 0.1R$ for the green line)

(blue line), and in the case of the system with $\Delta h = 0.1R$, the two-level contact is not possible (see Fig. 9.5b).

9.5 Conclusions

This study investigates the contact of the two-level periodic system of axisymmetric punches with the viscoelastic half-space under the action of the constant nominal pressure. Application of the localization method and the extended correspondence principle make it possible to analyze the dependence on time of the real contact area of the punch system with the half-space, and to study the conditions provided the contact of the punches of both levels with the half-space.

It is shown that the contact of the second level punches with the viscoelastic half-space is guaranteed not only by the specific geometric parameters of the system (the pitch of the periodic lattice and the height difference of the punches of the two levels), but also by the defined values of the viscoelastic properties of the half-space material. In this connection, there are three possible cases: the two-level contact occurs immediately, the two-level contact occurs after some time, or the two-level contact will never occur. The latter is valid only if the material of the viscoelastic half-space has a non-zero long-term elastic modulus, that is, the material is characterized by the limited creep.

Analysis of the real contact area evolution showed that the radii of contact spots of the punches of both levels increase in time at least for not tight contact. If the second

level punches come into contact (note that this condition is realized for the certain geometric characteristics of the periodic punch system and the certain viscoelastic properties of the half-space), the relative real contact area may grow considerably over time. This fact must be taken into account for analysis of the contact characteristics of various tribounits.

Acknowledgements This study was funded by RFBR according to the research project No. 20-01-00400 (Sects. 9.1–9.3 and 9.4.2) and by RSF according to the research project No. 18-19-00574 (Sects. 9.4.1 and 9.4.3).

References

1. Brinson, H.F., Brinson, L.C.: Characteristics, applications and properties of polymers. In: Brinson, H.F., Brinson, L.C. Polymer engineering science and viscoelasticity. An Introduction, pp. 57–100. Springer, Boston, MA (2015)
2. Arutunyan, N.K.: Some Problems in the Theory of Creep. Pergamon Press, Oxford (1966)
3. Dubois, G., Cesbron, J., Yin, H.P., Anfosso-Lédée, F.: Macro-scale approach for rough frictionless multi-indentation on a viscoelastic half-space. *Wear* **272**(1), 69–78 (2011). <https://doi.org/10.1016/j.wear.2011.07.011>
4. Chen, W.W., Wang, Q.J., Huan, Z., Luo, X.: Semi-analytical viscoelastic contact modeling of polymer-based materials. *J. Tribol.* **133**(4), 041404 (2011). <https://doi.org/10.1115/1.4004928>
5. Spinu, S., Cerlinca, D.: Modelling of rough contact between linear viscoelastic materials. *Model. Simul. Eng.* (2017). <https://doi.org/10.1155/2017/2521903>
6. Greenwood, J.A., Williamson, J.B.P.: Contact of nominally flat surfaces. *Proc. R. Soc. Lond. A* **295**300-319 (1966). <https://doi.org/10.1098/rspa.1966.0242>
7. Creton, C., Leibler, L.: How does tack depend on time of contact and contact pressure? *J. Polym. Sci. B* **34**, 545–554 (1996). [https://doi.org/10.1002/\(SICI\)1099-0488\(199602\)34:3<545::AID-POLB13>3.0.CO;2-I](https://doi.org/10.1002/(SICI)1099-0488(199602)34:3<545::AID-POLB13>3.0.CO;2-I)
8. Hui, C.Y., Lin, Y.Y., Baney, J.M.: The mechanics of tack: viscoelastic contact on a rough surface. *J. Polym. Sci. B* **38**, 1485–1495 (2000). [https://doi.org/10.1002/\(SICI\)1099-0488\(20000601\)38:11<1485::AID-POLB80>3.0.CO;2-1](https://doi.org/10.1002/(SICI)1099-0488(20000601)38:11<1485::AID-POLB80>3.0.CO;2-1)
9. Abuzeid, O.M., Eberhard, P.: Linear viscoelastic creep model for the contact of nominal flat surfaces based on fractal geometry: standard linear solid (SLS) material. *J. Tribol.* **129**(3), 461–466 (2007). <https://doi.org/10.1115/1.2736427>
10. Persson, B.N.J., Albohr, O., Creton, C., Peveri, V.: Contact area between a viscoelastic solid and a hard, randomly rough, substrate. *J. Chem. Phys.* **120**(18), 8779 (2004). <https://doi.org/10.1063/1.1697376>
11. Papangelo, A., Ciavarella, M.: Viscoelastic normal indentation of nominally flat randomly rough contacts. *Int. J. Mech. Sci.* **211**, 106783 (2021). <https://doi.org/10.1016/j.ijmecsci.2021.106783>
12. Manners, W., Greenwood, J.A.: Some observations on Persson's diffusion theory of elastic contact. *Wear* **261**(5–6), 600–610 (2006). <https://doi.org/10.1016/j.wear.2006.01.007>
13. Goryacheva, I.G.: The periodic contact problem for an elastic half-space. *J. Appl. Math. Mech.* **62**(6), 959–966 (1998). [https://doi.org/10.1016/S0021-8928\(98\)00122-1](https://doi.org/10.1016/S0021-8928(98)00122-1)
14. Yakovenko, A., Goryacheva, I.: The periodic contact problem for spherical indenters and viscoelastic half-space. *Tribol. Int.* **161**, 107078 (2021). <https://doi.org/10.1016/j.triboint.2021.107078>
15. Christensen, R.: *Theory of Viscoelasticity: An Introduction*. Academic Press, London (1971)
16. Goryacheva, I.G., Yakovenko, A.A.: Indentation of a rigid cylinder with a rough flat base into a thin viscoelastic layer. *J. Appl. Mech. Tech. Phys.* **62**(5), 723–735 (2021). <https://doi.org/10.1134/S0021894421050035>

17. Graham, G.A.C.: The correspondence principle of linear viscoelasticity theory for mixed boundary value problems involving time-dependent boundary regions. *Q. Appl. Math.* **XXVI**(2), 167–174 (1968). <http://orcid.org/10.1090/qam/99860>
18. Ting, T.C.T.: The contact stresses between a rigid indenter and a viscoelastic half-space. *J. Appl. Mech.* **33**(4), 845–854 (1966). <https://doi.org/10.1115/1.3625192>
19. Mainardi, F., Spada, G.: Creep, relaxation and viscosity properties for basic fractional models in rheology. *Eur. Phys. J. Spec. Top.* **193**(1), 133–160 (2011). <https://doi.org/10.1140/epjst/e2011-01387-1>
20. Goryacheva, I.G.: *Contact Mechanics in Tribology*. Springer, Dordrecht (1998)

Chapter 10

On an Axisymmetric Contact Problem for a Piecewise-Homogeneous Space with Disk-Shaped Crack



Vahram N. Hakobyan, Aram H. Grigoryan, and Harutyun A. Amirjanyan

Abstract The article discusses an axisymmetric stress state of a piecewise-homogeneous space of two dissimilar half-spaces, which on the plane of the junction of dissimilar half-spaces contains a circular disk-shaped interfacial crack, on one of the sides of which an absolutely rigid stamp (circular shim) is pressed with adhesion, the radius of which is less than the radius of the crack. The governing equation of the problem is derived in the form of a single singular integral equation of the second kind with respect to the complex combination of reduced unknown contact stresses, the solution of which is constructed by the numerical-analytical method of mechanical quadratures. A numerical calculation was carried out and the regularities of the change in the Cherepanov-Rice integral on the boundary circle of the crack and the rigid displacement of the shim depending on the physical–mechanical and geometric characteristics of the problem were studied.

Keywords Elasticity · Compound space · Interfacial coin-shaped crack · Stamp · Axisymmetric contact problem

10.1 Introduction

The development of contact and mixed boundary value problems of the theory of elasticity and fracture mechanics is aimed at developing new methods for more accurate calculations of various constructions and their parts containing various types of stress concentrators in order to increase their durability. Many fundamental results in this direction are given in well-known monographs [1–5]. In this area, we note axisymmetric contact and mixed problems, the solution of which often leads to

V. N. Hakobyan (✉) · A. H. Grigoryan · H. A. Amirjanyan
Institute of Mechanics NAS RA, Baghranyan Ave. 24/2, 0019 Yerevan, Republic of Armenia
e-mail: vhakobyan@sci.am

A. H. Grigoryan
e-mail: grigoryanaram4@gmail.com

H. A. Amirjanyan
e-mail: amirjanyan@gmail.com

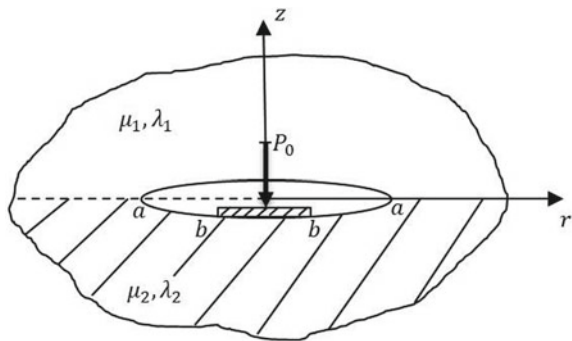
mathematical and computational difficulties. Here it should be noted that the use of rotation operators in solving axisymmetric contact and mixed problems leads them to plane problems. However, after solving these problems, when determining the real stresses or displacements, often mathematical or computational difficulties arise. Let us point out [6–11], where solutions are constructed for several axisymmetric contact and mixed problems for homogeneous and piecewise-homogeneous spaces with disk-like defects. In [8–11], exact solutions of some problems were constructed for a homogeneous and piecewise-homogeneous space with a disk-shaped crack, on one of the sides of which a rigid disk-shaped inclusion is pressed, the radius of which is equal to the radius of the crack, under different contact conditions. Similar problems when the inclusion radius is less than the crack radius, as we know, for both homogeneous and piecewise-homogeneous space with a disk-shaped crack have not been considered. Here we consider the axisymmetric stress state of a piecewise-homogeneous space with a disk-shaped crack, one of the edges of which is pressed in by a rigid shim whose radius is less than the crack radius.

10.2 Statement of the Problem and Derivation of Governing Equations

Let us consider the axisymmetric stress state of a piecewise-homogeneous space obtained by connecting two heterogeneous half-spaces with Lamé coefficients μ_1, λ_1 and μ_2, λ_2 , respectively, occupying half-spaces $z \geq 0$ and $z \leq 0$, respectively, in a cylindrical coordinate system $Or\varphi z$. It is assumed that a piecewise-homogeneous space on the plane of the junction of dissimilar half-spaces $z = 0$ contains a circular disk-shaped interfacial crack with a radius a . On the lower side of the space, using a concentrated load of magnitude P_0 with adhesion, a rigid stamp (circular washer) is pressed with a flat base of a radius b that is less than the radius of the crack ($b < a$). Figure 10.1 shows the axial section of the piecewise-homogeneous space.

The problem can be mathematically represented as the following boundary value problem:

Fig. 10.1 Axial section of the piecewise-homogeneous space



$$\begin{cases} u_1(r, 0) = u_2(r, 0); \\ w_1(r, 0) = w_2(r, 0); \\ \sigma_z^{(1)}(r, 0) = \sigma_z^{(2)}(r, 0); \\ \tau_{rz}^{(1)}(r, 0) = \tau_{rz}^{(2)}(r, 0); \end{cases} \quad (a < r < \infty) \quad (10.1a)$$

$$\begin{cases} \sigma_z^{(1)}(r, 0) = 0; \quad \tau_{rz}^{(1)}(r, 0) = 0; \quad (0 < r < a) \\ \sigma_z^{(2)}(r, 0) = 0; \quad \tau_{rz}^{(2)}(r, 0) = 0; \quad (b < r < a) \\ w_2(r, 0) = -\delta; \quad u_2(r, 0) = 0. \quad (0 < r < b) \end{cases} \quad (10.1b)$$

Here, $w_j(r, z)$ and $u_j(r, z)$ ($j = 1, 2$) are the normal and radial displacement components, respectively, for the upper and lower half-spaces in a cylindrical coordinate system, $\sigma_z^{(j)}(r, z)$ and $\tau_{rz}^{(j)}(r, z)$ are the normal and tangential stress components, and δ is the rigid displacement of the stamp. It is required to study the behavior of rigid displacement of the stamp and the Cherepanov-Rice J -integral depending on the physical-mechanical and geometrical parameters of the problem.

To solve the problem, we will use discontinuous solutions of the equations of the axisymmetric theory of elasticity for a piecewise-homogeneous space [10]:

$$\begin{aligned} u_2(r, 0) &= -\frac{b_0}{\Delta} L_{1,1}^1[u] - \frac{b_1}{\Delta} L_{1,0}^1[w] + \frac{d_0}{\Delta} L_{1,0}^0[\sigma] - \frac{d_1}{\Delta} L_{1,1}^0[\tau]; \\ w_2(r, 0) &= -\frac{b_1}{\Delta} L_{0,1}^1[u] - \frac{b_0}{\Delta} L_{1,0}^1[w] - \frac{d_1}{\Delta} L_{0,0}^0[\sigma] + \frac{d_0}{\Delta} L_{0,1}^0[\tau]; \\ \sigma_z^{(1)}(r, 0) &= \frac{b_2}{\Delta} L_{0,1}^2[u] + \frac{b_3}{\Delta} L_{0,0}^2[w] + \frac{b_0}{\Delta} L_{0,0}^1[\sigma] + \frac{b_1}{\Delta} L_{0,1}^1[\tau]; \\ \tau_{rz}^{(1)}(r, 0) &= \frac{b_3}{\Delta} L_{1,1}^2[u] + \frac{b_2}{\Delta} L_{1,0}^2[w] + \frac{b_1}{\Delta} L_{1,0}^1[\sigma] + \frac{b_0}{\Delta} L_{1,1}^1[\tau]; \\ u_1(r, 0) &= u_2(r, 0) + u(r); \quad w_1(r, 0) = w_2(r, 0) + w(r); \\ \sigma_z^{(2)}(r, 0) &= \sigma_z^{(1)}(r, 0) - \sigma(r); \quad \tau_{rz}^{(2)}(r, 0) = \tau_{rz}^{(1)}(r, 0) - \tau(r). \end{aligned} \quad (10.2)$$

The notation introduced in [10] is retained here:

$$\begin{aligned} L_{m,n}^k[\varphi] &= \int_0^a W_{m,n}^k(r, \xi) \varphi(\xi) d\xi; \quad W_{m,n}^k(r, \xi) = \int_0^\infty t^k J_m(\text{tr}) J_n(t\xi) dt \\ d_0 &= \frac{\theta_1^{(1)} - \theta_1^{(2)}}{2}; \quad d_1 = \frac{\theta_2^{(2)} + \theta_2^{(1)}}{2}; \quad b_0 = \theta_2^{(1)} (\theta_2^{(1)} + \theta_2^{(2)}) - \theta_1^{(1)} (\theta_1^{(1)} - \theta_1^{(2)}); \\ b_1 &= \theta_1^{(1)} (\theta_2^{(1)} + \theta_2^{(2)}) - \theta_2^{(1)} (\theta_1^{(1)} - \theta_1^{(2)}); \\ \Delta &= \left[(\theta_2^{(2)} + \theta_2^{(1)})^2 - (\theta_1^{(2)} - \theta_1^{(1)})^2 \right]; \end{aligned}$$

$$\theta_1^{(j)} = \frac{\mu_j^2}{\lambda_j + 3\mu_j}; \quad \theta_2^{(j)} = \frac{\mu_j(\lambda_j + 2\mu_j)}{\lambda_j + 3\mu_j} \quad (j = 1, 2)$$

$$b_2 = 2\left(\theta_1^{(1)}b_0 + \theta_2^{(1)}b_1 - \theta_1^{(1)}\Delta\right); \quad b_3 = 2\left(\theta_1^{(1)}b_1 + \theta_2^{(1)}b_0 - \theta_2^{(1)}\Delta\right)$$

It is not difficult to verify that in this case

$$\begin{aligned} \sigma_z^{(1)}(r, 0) - \sigma_z^{(2)}(r, 0) &= -\sigma_z^{(2)}(r, 0) = \sigma(r); \\ \tau_{rz}^{(1)}(r, 0) - \tau_{rz}^{(2)}(r, 0) &= -\tau_{rz}^{(2)}(r, 0) = \tau(r); \end{aligned} \quad (10.3)$$

where $\sigma(r)$ and $-\tau(r)$ are, respectively, unknown contact pressure and tangential contact stresses acting under the stamp.

Using the last two relations (10.2), we satisfy the first two conditions (10.1b). Further, following the works [8, 10], we apply to the first and second of the obtained equations, respectively, the known rotation operators I , I_1 , and introduce the functions

$$\begin{aligned} \{w_*(t); \sigma_*(t)\} &= \frac{2}{\pi} \int_t^a \frac{\xi \{w(\xi); \sigma(\xi)\}}{\sqrt{\xi^2 - t^2}} d\xi; \\ \{u_*(t); \tau_*(t)\} &= \frac{2t}{\pi} \int_t^a \frac{\{u(\xi); \tau(\xi)\}}{\sqrt{\xi^2 - t^2}} d\xi; \end{aligned} \quad (10.4)$$

and their complex combinations

$$\begin{aligned} \chi_*(x) &= \sigma_*(x) - i\tau_*(x); \quad V'_*(x) = u'_*(x) + iw'_*(x); \\ (w_*(-t) &= w_*(t); \quad u_*(-t) = -u_*(t); \quad \sigma_*(-t) = \sigma_*(t); \quad \tau_*(-t) = -\tau_*(t)). \end{aligned} \quad (10.5)$$

As a result, at the following relation is obtained:

$$\begin{aligned} b_3 V'_*(x) + b_1 \chi_*(x) + \frac{ib_0}{\pi} \int_{-a}^a \frac{\chi_*(t)}{t-x} dt + \frac{ib_2}{\pi} \int_{-a}^a \frac{V'_*(t)}{t-x} dt &= \frac{2\Delta c_*}{\pi} \quad (-a < x < a), \\ \left(c_* = \frac{\pi b_1}{2\Delta} \sigma_*(0) + \frac{\pi b_3}{2\Delta} u'_*(0) + \frac{b_0}{2\Delta} \int_{-a}^a \frac{\tau_*(t)}{t} dt + \frac{b_2}{2\Delta} \int_{-a}^a \frac{w'_*(t)}{t} dt \right). \end{aligned} \quad (10.6)$$

Note that in this case, the conditions for the equilibrium of the stamp and the continuity of displacements at the end points of the crack must be met. These conditions are written using the functions $\chi_*(x)$ and $V'_*(x)$ as follows [10]

$$\int_{-a}^a \chi_*(x) dx = \frac{P_0}{\pi}; \quad \int_{-a}^a V'_*(x) dx = 0. \tag{10.7}$$

We consider relation (10.6) as a singular integral equation with respect to the function $V'_*(x)$ and write it in the form:

$$V'_*(x) - \frac{q}{i\pi} \int_{-a}^a \frac{V'_*(t) dt}{t-x} = F(x) \quad (-a < x < a) \tag{10.8}$$

Here

$$F(x) = -\frac{b_1}{b_3} \chi_*(x) - \frac{ib_0}{\pi b_3} \int_{-a}^a \frac{\chi_*(t)}{t-x} dt + \frac{2\Delta c_*}{\pi b_3}; \quad q = \frac{b_2}{b_3}.$$

We solve the singular integral Eq. (10.8) under the second condition (10.7) and express the function $V'_*(x)$ in terms of the function $\chi_*(x)$. It is not difficult to verify that the ends of the integration interval $\pm a$ are automatic boundedness points and, therefore, solution (10.8) has the following form [12]:

$$V'_*(x) = \frac{1}{1-q^2} \left[F(x) + \frac{q\omega(x)}{\pi i} \int_{-a}^a \frac{F(s) ds}{\omega(s)(s-x)} \right] \quad (-a < x < a) \tag{10.9}$$

$$\omega(x) = \left(\frac{a+x}{a-x} \right)^{i\beta}; \quad \beta = \frac{1}{2\pi} \ln G; \quad G = \frac{1+q}{1-q} = \frac{\mu_1 + \mathfrak{a}_1\mu_2}{\mu_2 + \mathfrak{a}_2\mu_1} > 0;$$

$$\mathfrak{a}_j = \frac{\lambda_j + 3\mu_j}{\lambda_j + \mu_j}.$$

Substituting in (10.9) the value of the function $F(x)$, using the Poincaré-Bertrand formula [13],

$$\int_L \frac{dt}{(t-t_0)} \int_L \frac{\varphi(t, t_1) dt_1}{t_1-t} = -\pi^2 \varphi(t_0, t_0) + \int_L dt_1 \int_L \frac{\varphi(t, t_1) dt_1}{(t_1-t)(t-t_0)},$$

integral value [14]

$$\int_{-a}^a \frac{ds}{\omega(s)(s-x)} = \frac{\pi i}{\text{sh}(\pi\beta)} \left[1 - \frac{\text{ch}(\pi\beta)}{\omega(x)} \right]$$

and taking into account that in the considered case $\chi_*(x) = 0$ outside the interval $(-b, b)$, we obtain the following formula for the function $V'_*(x)$:

$$\begin{aligned}
 V'_*(x) &= \left(\frac{B}{1-q^2} - \frac{b_0}{b_2} \right) \chi_*(x) \\
 &+ \frac{qB\omega(x)}{\pi i(1-q^2)} \int_{-b}^b \frac{\chi_*(s)ds}{\omega(s)(s-x)} + f(x) \quad (-a < x < a) \quad (10.10) \\
 \left(f(x) &= \frac{Aq\omega(x)}{(1-q^2)\text{sh}(\pi\beta)}; \quad A = \frac{2\Delta c_*}{\pi b_3}; \quad B = \frac{b_0 b_3 - b_1 b_2}{b_2 b_3}; \right)
 \end{aligned}$$

Further, using (10.10), satisfying the second of conditions (10.7), taking into account the first condition (10.7), we obtain another relation

$$\begin{aligned}
 \int_{-b}^b \frac{\chi_*(s)}{\omega(s)} ds &= A_* C_* - B_* P_0, \quad (10.11) \\
 \left(A_* &= \frac{2\alpha_1 \alpha_2 \beta}{\vartheta_2^{(2)} \mu_1^2 \text{sh}(\pi\beta)}; \quad B_* = \frac{2b_0 \mu_2^2}{\pi \alpha_2 \vartheta_2^{(2)} b_2} \text{sh}(\pi\beta) \right).
 \end{aligned}$$

which must be satisfied by the function $\chi_*(x)$ —except for the first condition (10.7).

Now let us turn to the last two conditions (10.1b). Using the first two relations (10.3), we satisfy these conditions. Then, applying the operator I_1 to the first of the equations obtained, the operator I to the second, differentiating the resulting equations with respect to x and passing to the functions $V'_*(x)$ and $\chi_*(x)$, we obtain the following integral equation:

$$V'_*(x) + \frac{d_1}{b_1} \chi_*(x) + \frac{ib_0}{\pi b_1} \int_{-a}^a \frac{V'_*(s)ds}{(s-x)} - \frac{id_0}{\pi b_1} \int_{-b}^b \frac{\chi_*(s)ds}{(s-x)} = \frac{\Delta\delta}{\pi b_1} \quad (-b < x < b)$$

Further, with the help of relations (10.6) and (10.10), the function $V'_*(x)$ is excluded. As a result, after some calculations, to determine the complex combination of contact stresses under the stamp, the following singular integral equation of the second kind is obtained:

$$\chi_*(x) - \frac{q_*}{\pi i} \int_{-b}^b \frac{\chi_*(s) ds}{(s-x)} + \int_{-b}^b K(x,s)\chi_*(s) ds = Q(x) \quad (-b < x < b), \quad (10.12)$$

which must be considered under the first condition (10.7) and condition (10.11). Here

$$\begin{aligned} K(x,s) &= -\frac{2\vartheta_2^{(2)}\mu_1^2}{\pi i \mathfrak{a}_1 b_2} \left[\frac{\omega(x)}{\omega(s)} - 1 \right] \frac{1}{s-x}; \\ Q(x) &= -\frac{2C_*}{\pi} g(x) + \frac{2\mu_2^2}{\pi \mathfrak{a}_2 \vartheta_2^{(2)}} \delta; \\ g(x) &= \frac{\omega(x)}{\text{sh}(\pi\beta)} + \frac{2b_0\mu_2^2}{\mathfrak{a}_2 b_2 \vartheta_2^{(2)}}; \quad q_* = \frac{\vartheta_1^{(2)}}{\vartheta_2^{(2)}}. \end{aligned}$$

10.3 Solution of the Governing Singular Integral Equation

The solution of Eq. (10.12) will be constructed by the method of mechanical quadratures [16]. Using a change of variables $s = b\xi$, $x = b\eta$, we formulate Eq. (10.12) and conditions (10.7) and (10.11) on the interval $(-1, 1)$ and introduce the dimensionless unknown function $\varphi(\eta)$, the constants δ_* and \bar{C} by the formulas

$$\varphi(\xi) = \frac{b\chi_*(b\xi)}{P_0}; \quad \delta_* = \frac{\mu_2 b \delta}{P_0}; \quad \bar{C} = \frac{2bC_*}{\pi P_0}$$

the following singular integral equation is obtained:

$$\begin{aligned} \varphi(\xi) - \frac{q_*}{\pi i} \int_{-1}^1 \frac{\varphi(\xi) d\xi}{(\xi - \eta)} + \int_{-1}^1 K_*(\eta, \xi)\varphi(\xi) d\xi &= -\bar{C} g_*(\eta) + \frac{2\mu_2}{\pi \mathfrak{a}_2 \vartheta_2^{(2)}} \delta_* \\ (-1 < x < 1) \end{aligned} \quad (10.13)$$

under conditions

$$\int_{-1}^1 \varphi(\xi) d\xi = \frac{1}{\pi}; \quad \int_{-1}^1 \frac{\varphi(\xi) d\xi}{\omega_*(\xi)} = \bar{A}_* \bar{C} - B_* \quad (10.14)$$

here

$$K_*(\eta, \xi) = -\frac{2\vartheta_2^{(2)}\mu_1^2}{\pi i \alpha_1 b_2} \left(\frac{\omega_*(\eta) - \omega_*(\xi)}{\omega_*(\xi)(\xi - \eta)} \right); \quad \omega_*(\eta) = \left(\frac{\lambda - \xi}{\lambda + \xi} \right)^{-i\beta};$$

$$g_*(\eta) = \frac{\omega_*(\eta)}{sh(\pi\beta)} + \frac{2b_0\mu_2^2}{\alpha_2 b_2 \vartheta_2^{(2)}};$$

$$\overline{A}_* = \frac{\pi \lambda \alpha_1 b_2 \beta}{\mu_1^2 \vartheta_2^{(2)} sh(\pi\beta)}; \quad B_* = \frac{2b_0 \mu_2^2 sh(\pi\beta)}{\pi \alpha_2 b_2 \vartheta_2^{(2)}}; \quad \lambda = \frac{a}{b} > 1.$$

The solution of Eq. (10.13) under conditions (10.14) can be represented as the sum of two solutions:

$$\varphi(\eta) = \overline{C} \varphi_1(\eta) + \delta_* \varphi_2(\eta),$$

where $\varphi_1(\eta)$ is the solution of (10.13) in the case when the right side is $-g_*(\eta)$, and $\varphi_2(\eta)$ is the solution of (10.13) in the case when the right side is $2\mu_2/\pi \alpha_2 \vartheta_2^{(2)}$. Then from the conditions (10.14) for determining the constants \overline{C} and δ_* the following system of algebraic equations is obtained:

$$\begin{cases} \overline{C} \int_{-1}^1 \varphi_1(\eta) d\eta + \delta_* \int_{-1}^1 \varphi_2(\eta) d\eta = 1/\pi \\ \overline{C} \left[\int_{-1}^1 \frac{\varphi_1(\eta) d\eta}{\omega_*(\eta)} - A_* \right] + \delta_* \int_{-1}^1 \frac{\varphi_2(\eta) d\eta}{\omega_*(\eta)} = -B_* \end{cases} \quad (10.15)$$

As above, it is easy to check that the end points of the integration interval are points of automatic boundedness and the solution of Eq. (10.14) can be represented as:

$$\varphi_j(\eta) = \varphi_j^*(\eta)(1 + \eta)^{i\gamma}(1 - \eta)^{-i\gamma} \quad (j = 1, 2) \quad (10.16)$$

here

$$\gamma = \frac{\ln G}{2\pi} = \frac{1}{2\pi} \ln \alpha_2, \quad G = \frac{1 + q_*}{1 - q_*},$$

and $\varphi_j^*(\eta)$ ($j = 1, 2$)—smooth continuous bounded functions on the interval $[-1, 1]$. Then, substituting the value of the functions $\varphi_j(t)$ ($j = 1, 2$) from (10.16) into (10.14) and (10.15), using the quadrature formulas [16], according to the usual procedure, the systems of algebraic equations with respect to the values of the unknown functions $\varphi_j^*(\eta_i)$ ($j = 1, 2$; $i = 1 - N$) at the collocation points and constants δ_* and \overline{C} .

After solving these systems, using the Lagrange formula, you can restore the functions $\varphi_j^*(\eta)$ and determine all the necessary mechanical characteristics. In particular,

for dimensionless crack opening, we can use the formula

$$w(r) = -\frac{1}{r} \frac{d}{dr} \int_r^a \frac{sw_*(s)}{\sqrt{s^2 - r^2}} ds = -\int_r^a \frac{w'_*(s)}{\sqrt{s^2 - r^2}} ds = -\text{Im} \int_r^a \frac{V'_*(s)}{\sqrt{s^2 - r^2}} ds,$$

from which we get

$$V(x) = \frac{w(ax)}{a} = -\text{Im} \int_x^1 \frac{\psi(t)}{\sqrt{t^2 - x^2}} dt \quad \left(\psi(t) = \frac{V'_*(at)}{a} \right),$$

where the function $V'_*(t)$ is given by formula (10.10) and the function $\psi(t)$ using the unknown function $\varphi(t)$ can be written as follows:

$$\psi(t) = \begin{cases} \frac{\alpha_2 \vartheta_1^{(2)} P_0}{2ab\mu_2^2} \varphi(\lambda t) + f_*(at)\omega(at) & (0 < t < \frac{b}{a}) \\ f_*(at)\omega(at) & (\frac{b}{a} < t < 1) \end{cases} \quad (10.17)$$

$$f_*(at) = \frac{\alpha_2 \vartheta_2^{(2)}}{2\lambda i \mu_2} \left[\int_{-1}^1 \frac{\varphi(\xi) d\xi}{\omega_*(\xi)(\xi - \lambda t)} - \frac{\pi i \alpha_1 b_2 \bar{C}}{2\vartheta_2^{(2)} \mu_1^2 s h(\pi\beta)} \right] P_0^* \left(P_0^* = \frac{P_0}{\pi b^2 \mu_2} \right).$$

Let us also write a formula for determining the Cherepanov-Rice J -integral. To do this, we will use the expressions for the real stresses outside the crack on the plane of the junction of heterogeneous half-spaces through the images of the functions of stress jumps and displacements on the crack [10]:

$$\begin{aligned} \sigma_z^{(1)}(r, 0) &= \frac{b_1}{r\Delta} \frac{d}{dr} \int_0^b \frac{t\tau_*(t)dt}{\sqrt{r^2 - t^2}} - \frac{b_3}{\Delta r} \frac{d}{dr} \int_0^a \frac{tw'_*(t)dt}{\sqrt{r^2 - t^2}}; \quad (r > a) \\ \tau_{rz}^{(1)}(r, 0) &= -\frac{b_1}{\Delta} \frac{d}{dr} \int_0^b \frac{\sigma_*(t)dt}{\sqrt{r^2 - t^2}} - \frac{b_3}{\Delta} \frac{d}{dr} \int_0^a \frac{u'_*(t)dt}{\sqrt{r^2 - t^2}}. \end{aligned} \quad (10.18)$$

Obviously, the first terms in both relations (10.18) are bounded functions on the circle $r = a$. Further, considering that

$$\frac{d}{dr} \int_0^a \frac{tw'_*(t)dt}{\sqrt{r^2 - t^2}} = r \frac{d}{dr} \int_0^a \frac{w'_*(t)dt}{\sqrt{r^2 - t^2}} + \int_0^a \frac{w'_*(t)dt}{\sqrt{r^2 - t^2}} - \frac{d}{dr} \int_0^a \frac{w'_*(t)dt}{\sqrt{r+t}},$$

relations (10.18) can be represented as:

$$\sigma_z^{(1)}(r, 0) - i\tau_{rz}^{(1)}(r, 0) = \frac{ib_3}{\Delta} \frac{d}{dr} \int_0^a \frac{V'_*(t)dt}{\sqrt{r^2 - t^2}} + \Phi(r) \quad (r > a) \quad (10.19)$$

here

$$\begin{aligned} \Phi(r) = & \frac{b_1}{r\Delta} \frac{d}{dr} \int_0^b \frac{t\tau_*(t)dt}{\sqrt{r^2 - t^2}} + \frac{ib_1}{\Delta} \frac{d}{dr} \int_0^b \frac{\sigma_*(t)dt}{\sqrt{r^2 - t^2}} \\ & - \frac{b_3}{\Delta r} \left[\int_0^a \frac{w'_*(t)dt}{\sqrt{r^2 - t^2}} - \frac{d}{dr} \int_0^a \frac{w'_*(t)dt}{\sqrt{r + t}} \right] \end{aligned}$$

bounded function on the circle $r = a$.

Using the value of function $\psi(t)$ formula (10.19) will take the following form:

$$\sigma_z^{(1)}(ax, 0) - i\tau_{rz}^{(1)}(ax, 0) = \frac{ib_3}{\Delta} \frac{d}{dx} \int_0^a \frac{\psi(t)dt}{\sqrt{x^2 - t^2}} + \Phi(ax) \quad (x > 1) \quad (10.20)$$

Substituting the value $\psi(t)$ from (10.17) into (10.20), after some transformations, using the values of the integral [14]

$$\begin{aligned} & \int_a^b (y - a)^{\alpha-1} (b - y)^{\beta-1} (cy + d)^\gamma dy \\ & = \frac{(b - a)^{\alpha+\beta-1}}{(ac + d)^{-\gamma}} B(\alpha, \beta) {}_2F_1\left(\alpha, -\gamma, \alpha + \beta, \frac{c(a - b)}{ac + d}\right); \\ & (Re\alpha, Re\beta > 0, \arg(d + cb)/(d + ca) < \pi) \end{aligned}$$

For case $a = 0$, $b = 1$, $c = -1$, $d = x$, $\alpha \rightarrow 1 + i\beta$, $\beta \rightarrow 1 - i\beta$, $\gamma = -1/2$ and relation for hypergeometric functions ${}_2F_1(\alpha, \beta, \gamma, z)$ [15]

$$\begin{aligned} {}_2F_1(\alpha, \beta, \gamma, z) = & (1 - z)^{\gamma-\alpha-\beta} \frac{\Gamma(\gamma)\Gamma(\alpha + \beta - \gamma)}{\Gamma(\alpha)\Gamma(\beta)} \\ & {}_2F_1(\gamma - \alpha; \gamma - \beta; \gamma - \alpha - \beta + 1; 1 - z) + \\ & + \frac{\Gamma(\gamma)\Gamma(\gamma - \alpha - \beta)}{\Gamma(\gamma - \alpha)\Gamma(\gamma - \beta)^2} F_1(\alpha; \beta; \alpha + \beta - \gamma + 1; 1 - z), \end{aligned}$$

the complex combination of real stresses can be represented in the following form:

$$\sigma_z^{(1)}(ax, 0) - i\tau_{rz}^{(1)}(ax, 0) = - \frac{i\sqrt{\pi}b_3\Gamma(1 - i\beta)f_*(a)(x + 1)^{i\beta}}{\sqrt{2}\Delta\text{ch}(\pi\beta)\Gamma(1/2 - i\beta)(x - 1)^{1/2+i\beta}} + \Phi_*(x)$$

($x > 1$)

where $\Phi_*(x)$ is a bounded function on the circle $x = 1$, the value of which is not given here because of its cumbersomeness. Then for the complex stress intensity factor on the circle $r = a$ we obtain the expression:

$$\begin{aligned} K_I(a) - iK_{II}(a) &= \lim_{r \rightarrow a+0} \sqrt{2\pi}(x - 1)^{1/2+i\beta} [\sigma_z^{(1)}(ax, 0) - i\tau_{rz}^{(1)}(ax, 0)] \\ &= - \frac{\pi 2^{i\beta} b_3 \Gamma(1 - i\beta) f_*(a)}{\Delta\text{ch}(\pi\beta)\Gamma(1/2 - i\beta)}. \end{aligned} \tag{10.21}$$

Using the value of the complex stress intensity factor from (10.21) and expressing $f_*(a)$ through the unknown function $\varphi(\xi)$, for the Cherepanov-Rice J -integral we obtain the following formula [17]

$$\begin{aligned} J(a) = \bar{\mu}|K_I(a) - iK_{II}(a)| &= \frac{\pi[\mu(1 - \nu_1) + 1 - \nu_2] \mathfrak{a}_2 \vartheta_2^{(2)} b_3}{2\lambda \Delta \mu_1 \mu_2 \text{ch}(\pi\beta)} \times \left| \frac{\Gamma(1 - i\beta)}{\Gamma(1/2 - i\beta)} \right| \\ &\times \left| \int_{-1}^1 \frac{\varphi(\xi) d\xi}{\omega_*(\xi)(\xi - \lambda)} - \frac{\pi i \mathfrak{a}_1 b_3}{2\vartheta_2^{(2)} \mu_1^2 \text{ch}(\pi\beta)} \bar{C} \right| P_0^* \end{aligned} \tag{10.22}$$

$$\left(\mu = \frac{\mu_1}{\mu_2}; \quad \tilde{\mu} = \frac{1}{2} \left(\frac{1 - \nu_1^2}{E_1} + \frac{1 - \nu_2^2}{E_2} \right) = \frac{[\mu(1 - \nu_2) + 1 - \nu_1]}{4\mu_1} \right).$$

Thus, after solving the defining equation, the Cherepanov-Rice J -integral can be determined by formula (10.22).

10.4 Numerical Analysis

A numerical calculation has been carried out and regularities of changes in the contact stresses acting under the stamp, crack opening, dimensionless rigid displacement of the stamp and Cherepanov-Rice $J(a)$ -integrals on a circle $r = a$ depending on the ratio $\mu = \mu_1/\mu_2$ and parameter $\lambda = a/b > 1$ in the case of fixed values of Poisson's ratios $\nu_1 = 0.25$; $\nu_2 = 0.3$ have been carried out and studied. At the same time, it is assumed that $P_0^* = 0.1$. The results of numerical calculations are presented in the form of graphs. In Figs. 10.1 and 10.2, respectively, graphs of crack opening depending on the parameters μ and $\lambda = a/b > 1$.

Fig. 10.2 Rigid displacement δ_* of the stamp depending on λ

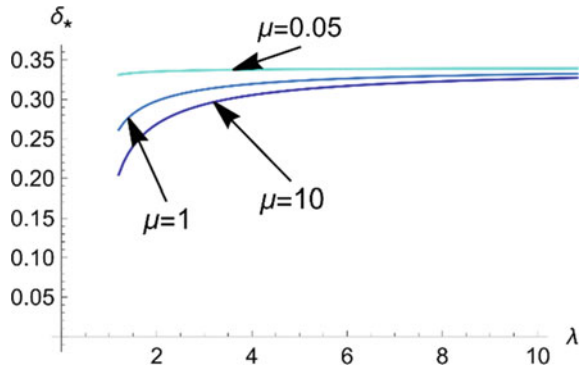
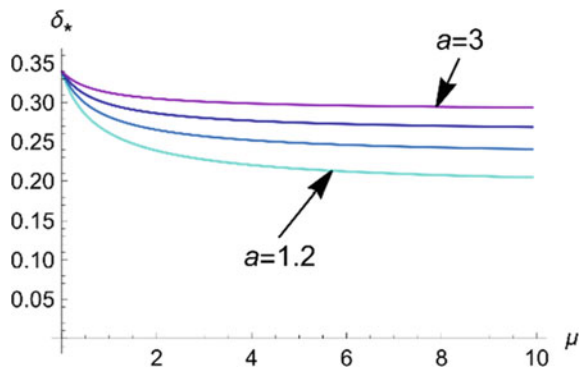


Fig. 10.3 Rigid displacement δ_* of the stamp depending on μ



Figures 10.2 and 10.3 shows, respectively, the graphs of the dimensionless rigid displacement δ_* of the stamp depending on the parameters μ and λ .

Figures show that with an increase in the parameter λ , which can be interpreted as an increase in the crack radius at a constant stamp radius, the rigid displacement of the stamp increases tending to a certain limit, which is a rigid displacement of the stamp pressed into the elastic half-space made of the second material (Fig. 10.2). An increase of the parameter μ , which can be interpreted as an increase μ_1 at a constant μ_2 , the reduced rigid displacement decreases tending to a certain limit, which corresponds to the case when the upper half-space is rigid (Fig. 10.3).

Figures 10.4 and 10.5 show, respectively, the graphs of the Cherepanov-Rice J -integrals on a circle $r = a$ depending on the same parameters.

It is clear from the graphs that J -integral Cherepanov-Rice decreases with decreasing stamp radius (Fig. 10.4). Figure 10.5 displays that as the parameter μ increases; J -integral Cherepanov-Rice tends to a certain limit as well.

Fig. 10.4 Cherepanov-rice J -integrals depending on λ

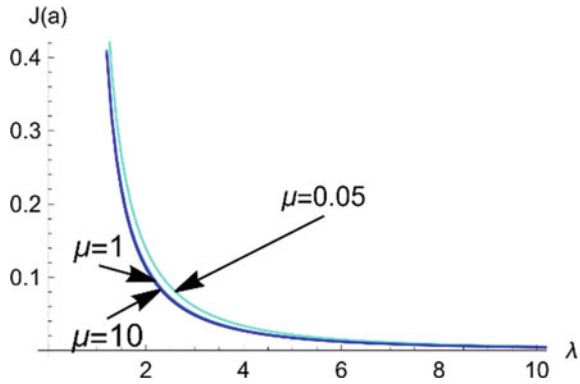
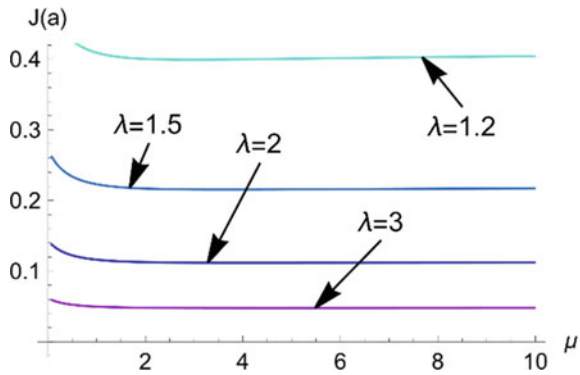


Fig. 10.5 Cherepanov-rice J -integrals depending on μ



10.5 Conclusion

Thus, by combining the methods of singular integral equations and the numerical-analytical method of mechanical quadratures, the solution of the axisymmetric contact problem for a piecewise-homogeneous space with a disk-shaped interfacial crack is constructed. One of the sides of the space is a rigid shim, which is pressed with adhesion, the radius of which is less than the radius of the crack. Using numerical calculations, the patterns for change of the reduced rigid displacement of the stamp and the Cherepanov-Rice J -integral depending on the ratio of the elastic characteristics of heterogeneous half-spaces and the radii of the crack and the circular shim are clarified. It is shown that as the circular shim radius approaches the crack radius, the Cherepanov-Rice J -integral increases, i.e., increases the likelihood of crack propagation. It has also been found that the more rigid the half-space onto which the stamp is pressed, the greater the probability of crack propagation.

References

1. Berezhnitsky, L., Panasiuk, V., Staschuk, N.: Interaction of Rigid Linear Inclusions and Cracks in Deformable Body (in Russ.). Kiev, Naukova Dumka (1983)
2. Galin, L.A.: Contact Problems in the Theory of Elasticity and Viscoelasticity (in Russ.). Nauka (1980)
3. Popov, G.Y.: Concentration of Elastic Stresses Near the Punches, Slits, Thin Inclusions and Stiffened Constructions (in Russ.). Moscow, Nauka (1982)
4. Panasiuk, V., Savruk, M., Dacyshin, A.: Distribution of Stresses near the Cracks in Plates and Shells. Naukova Dumka, Kiev (1976)
5. Muskhelishvili, N.I.: Some Basic Problems of the Mathematical Theory of Elasticity. Springer, Dordrecht (1977)
6. Wang, Z.Y., Zhang, H.T., Chou, Y.T.: Characteristics of the elastic field of a rigid line in homogeneity. Trans. ASME. J. Appl. Mech. **52**(4), 818–822 (1985)
7. Willis, J.R.: The penny-shaped crack on an interface. Quart. J. Mech. Appl. Math. **25**(3), 367–385 (1972)
8. Popov, G., Ya.: About Concentration of the Elastic Stresses Near Thin Detached Inclusion. “Contemporary Problems of Mechanics and Aviation”, Dedicated to I. Obrascov, pp. 156–162 (1980)
9. Hakobyan, V.N.: The stresses near the absolutely rigid coin-type inclusion in piecewise homogeneous space. In: Proceeding of International Conference dedicated to the 100th Anniversary of Academician Nagush Kh. Arutyunyan “Topical Problems of Continuum Mechanics”, pp. 45–51 (2007)
10. Hakobyan, V.N., Mirzoyan, S.T., Dashtoyan, L.L.: Axisymmetric mixed boundary value problem for composite space with coin-shaped crack. herald of the Bauman Moscow State Technical University. Series Nat. Sci. **3**, 31–46 (2015). <https://doi.org/10.18698/1812-3368-2015-3-31-46>
11. Hakobyan, V.N., Amirjanyan, H.A.: Axisymmetric mixed boundary problem for a composite space with a circular disc-shaped crack. Mech. Proc. National Acad. Sci. Armenia. **74**(3), 3–18 (2021)
12. Gakhov, F.D.: Boundary Problems (in Russ.). Moscow, Nauka (1977)
13. Muskhelishvili, N.I.: Singular Integral Equations. Wolters-Noordhoff, Groningen (1958)
14. Prudnikov, A.P., Brychkov, Yu.A., Marichev, O.I.: Integrals and Series (Elementary Functions), in Russ. Nauka, Moscow (1981)
15. Gradshteyn, I.S., Ryzhik, I.M., Geronimus, Y.V., Tseytlin, M.Y., Jeffrey, A.: Tables of Integrals, Series and Products (ed. by D. Zwillinger, V.H. Moll). Academic Press, Amsterdam et al. (2015)
16. Sahakyan, A.V., Amirjanyan, H.A.: Method of mechanical Quadrature’s for solving singular integral equations of various types. IOP Conf. Ser.: J. Phys.: Conf. Ser. **991**, 012070. <https://doi.org/10.1088/1742-6596/991/1/01207> (2018)
17. Murakami, Y. (ed.): Stress Intensity Factors Handbook. Pergamon Press, Oxford (1987)

Chapter 11

High-Temperature Creep of Cast Irons



Abhijit Joshi, Konstantinos P. Baxevanakis, and Vadim V. Silberschmidt

Abstract Cast irons are a family of ferrous alloys with carbon content ranging from 2.5 to 5%. They have a wide range of applications in automotive, industrial, agriculture, and construction industries. Primary classification of cast irons is based on the graphite morphology, which can be in the form of flakes, vermicular, or spheroidal. Mechanical properties of cast irons depend on matrix microstructure and graphite morphology; different alloying elements can be added to improve their high-temperature mechanical performance. Creep is an important deformation mechanism for high-temperature applications of cast irons. A literature review covering models and studies of creep in cast irons are presented in this chapter. The review highlights limited research on the creep behaviour of cast irons especially for compacted graphite iron (CGI). Original results from tensile and compression creep tests on CGI are also presented, which emphasize a significant difference in creep behaviour under tensile and compressive loading.

Keywords Cast iron · Microstructure · High-temperature · Creep · Creep models · Creep testing

11.1 Introduction to Cast Iron

Iron and steels have an extremely broad range of applications ranging from industrial, farming, building and infrastructure, domestic appliances to electronic equipment.

A. Joshi · K. P. Baxevanakis · V. V. Silberschmidt (✉)
Wolfson School of Mechanical, Electrical and Manufacturing Engineering, Loughborough
University, Loughborough, Leicestershire LE11 3TU, UK
e-mail: V.Silberschmidt@lboro.ac.uk

A. Joshi
e-mail: A.Joshi2@lboro.ac.uk

K. P. Baxevanakis
e-mail: K.Baxevanakis@lboro.ac.uk

High-temperature applications of steels and cast irons include automotive applications (cylinder heads, brakes, and exhaust manifolds), power plants (shafts and casings), pressure vessels, etc. [1].

Steel and cast iron are alloys formed by combination of iron and carbon. Carbon content in steel is up to 2.06% and in cast iron it ranges from 2.5 to 5%. Steel and cast iron offer a wide range of material properties with yield strength ranging from 200 to 2000 MPa, high levels of temperature resistance, thermal conductivity and toughness as well as good damping properties, high wear and corrosion resistance, good manufacturability, and good weldability. These alloys are also almost 100% recyclable [2].

Unlike steels and other alloys, cast irons are usually not classified according to their chemical composition. The microstructure of final product depends strongly upon foundry practice, the shape and size of the castings, and heat treatments used. So, several entirely different types of cast iron can be produced starting with the same nominal composition [2]. Based on graphite morphology, the cast irons can be classified as grey cast iron or flake graphite iron (FGI), compacted graphite iron (CGI), and spheroidal graphite iron (SGI). The different graphite morphologies are shown in Fig. 11.1, and main cast irons briefly introduced below.

Grey cast iron, or flake graphite iron (FGI), contains graphite in the shape of flakes. Under tensile load, tips of the flakes act as crack-initiation sites while the flakes themselves provide a path for crack propagation. This failure mechanism leads to the brittle behaviour of grey cast iron. FGI offers good wear resistance, castability, thermal conductivity, and damping properties. Typical applications of FGI include machine bases, brake discs and drums, engine blocks, gears, and flywheels [2].

Ductile cast iron, or spheroidal graphite iron (SGI), has graphite in nodular or spheroidal form. Compared to FGI, round graphite particles in SGI neither act as obvious crack-initiation sites nor provide crack-propagation paths; hence, SGI has much higher tensile strength. Ductile cast iron also has high levels of modulus of

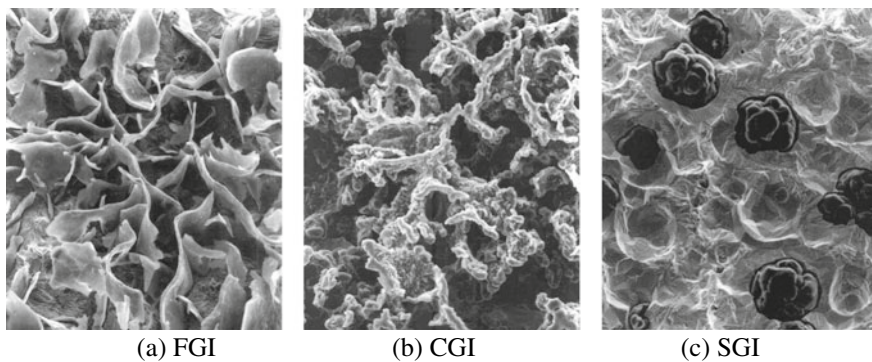


Fig. 11.1 Different graphite morphologies observed in deep etched cast irons [3]

elasticity, yield strength, wear resistance, and ductility. It has good machinability and better fatigue strength; however, the damping capacity and thermal conductivity are lower than in grey iron. Ductile iron is used in applications such as valve and pump bodies, crankshafts, in heavy-duty gears or automobile door hinges, and nowadays also as engine blocks [2].

Compacted graphite iron (CGI), or vermicular iron, contains graphite particles in ‘worm-shaped’, or vermicular form. Such particles are shorter, thicker and have rounded edges. They are interconnected, forming complex coral-like morphology that results in strong adhesion between the graphite and the iron matrix. Such microstructure inhibits initiation and propagation of cracks, and is the main reason of superior mechanical properties of CGI compared to FGI [4, 5]. CGI has applications in automobile exhaust manifolds, cylinder heads, cylinder blocks, pistons, cylinder liners, brake drums, castings in hydraulic components, and machine tools.

Other variations of cast irons include white cast iron, malleable iron, and high alloy iron.

White cast iron has of cementite and pearlite in its matrix, formed by fast cooling. The designation for this form of cast iron is based on white-appearing crystalline fracture surfaces. It has excellent wear resistance and high compressive strength, but brittleness is its main disadvantage. Typical applications of white cast iron are mill liners, shot-blasting nozzles, railway brake shoes, rolling mill rolls, brick-making equipment, crushers, and pulverizes [2].

Malleable iron contains carbon in the form of irregularly shaped graphite nodules called *temper carbon*. Typical applications include heavy-duty bearing surfaces in automobiles, trucks, railroad rolling stock as well as farm, and construction machinery [2].

High-alloy irons have of content of alloying elements greater than 4% and are used in some specific applications. The nickel-alloyed **austenitic graphitic irons** are typically used in seawater pumps and valves, oil and gas production, chemical processing plants, gas turbine casings, exhaust manifolds, and turbochargers. **High-silicon irons** are used for components requiring oxidation resistance. **Si-Mo ductile irons** are commonly employed for turbo manifolds, with high-temperature-fatigue capability being a major criterion [6].

11.2 Microstructure of Cast Iron

The microstructure of cast iron includes graphite particles embedded in the matrix. The matrix could be primarily ferritic or pearlitic, or a combination of both phases. The ferritic matrix is a softer material with lower strength compared to the pearlitic one, which is harder and stronger [7]. The features of cast irons such as ferrite/pearlite content, graphite morphology, and nodularity play a key role in determining the physical and mechanical properties. The final microstructure depends on the chemical composition, cooling rates, and subsequent heat treatments (if any). FGI, CGI,

and SGI are commercially available in different grades based on minimum ultimate strength of the material.

SEM micrographs of CGI specimens manufactured according to EN-GJV-450 standard (Fig. 11.2a) demonstrate that most of the graphite is of vermicular form but its other forms (mostly spheroidal) are also present. Etching of specimen reveals the presence of ferrite, pearlite, and graphite (Fig. 11.2b). In case of CGI, the main requirement is for a minimum of 80% graphite particles to be primarily in vermicular (compacted) form with remaining 20% graphite particles in nodular form. Presence of flake graphite is not permitted in CGI except in the rim zone of castings [8]. There is no standard requirement on the chemical composition or the method of manufacture, and these are determined by the manufacturer [9, 10].

11.3 Chemical Composition of Cast Iron

Typical chemical compositions of the main types of cast irons are given in Table 11.1 [11–13].

Silicon is one of the main ingredients of cast irons. The percentages of silicon and carbon can be altered with respect to each other to produce different microstructures in cast irons. A higher silicon fraction of about 4% is sometimes used to improve the oxidation resistance of cast irons. However, silicon has strong graphitizing influence, which leads to a process called *graphitization*, with pearlite converted into ferrite and graphite. Pearlite is stable up to about 425 °C but gradual graphitization occurs around 530 °C and accelerates significantly around 650 °C [14].

The manganese content is determined by the type of matrix required in the cast iron. Mn is a strong pearlite promoter, so it can be as low as 0.1% for a ferritic matrix or can be increased to 1.2% to obtain a pearlitic one [15]. Without manganese in the iron, undesired iron sulphide (FeS) can form at grain boundaries, potentially leading to filling defects in the castings [15, 16]. Phosphorus and sulphur are the minor elements always present in the cast iron composition. S is generally harmful in grey iron and should be kept to below 0.12% for grey iron and below 0.02% for high-quality CGI. P increases the fluidity of all cast irons, but this can lead to difficulties in casting process. For most engineering castings, it should be kept below 0.12%, but up to 1.0% may be allowed to improve the manufacturing of thin-section castings where high strength is not required [15].

Mg plays a significant role in defining the graphite morphology of cast irons that can change from flake to compacted and spheroidal as magnesium content varies (Fig. 11.3). For instance, compacted graphite is formed for Mg in a range of 0.005–0.015%. The loss of even 0.001% of magnesium at the lower end can lead to formation of flake-type graphite.

Different alloying elements can be added to improve high-temperature mechanical properties of cast irons. Addition of molybdenum in cast irons provides a significant improvement in high-temperature tensile, fatigue, and creep strengths [17–19].

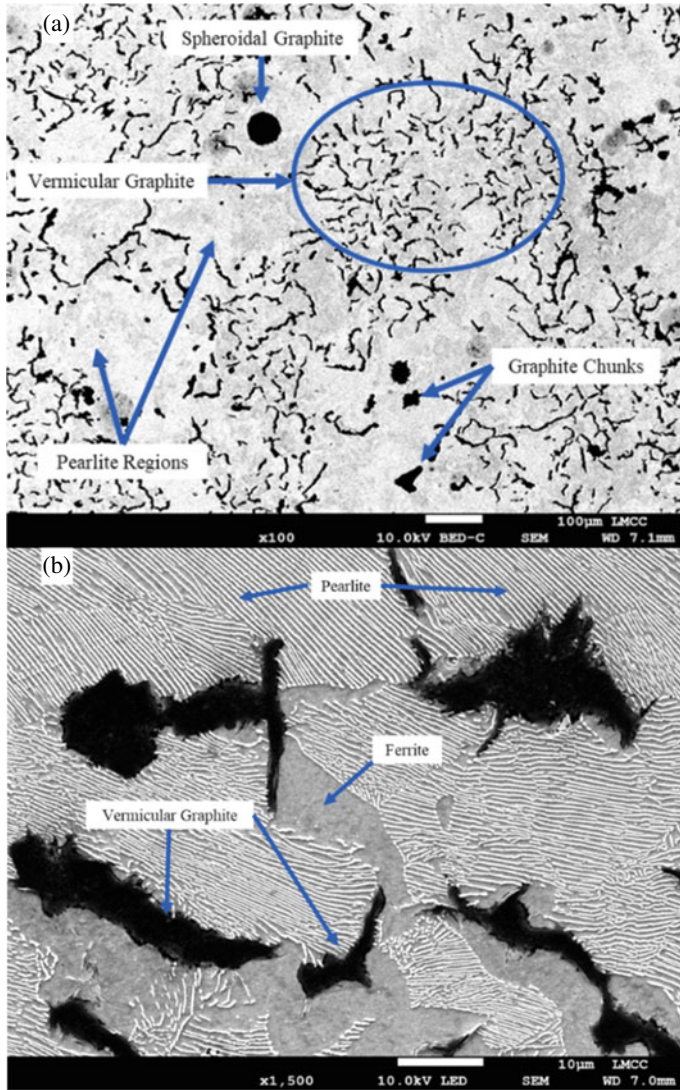
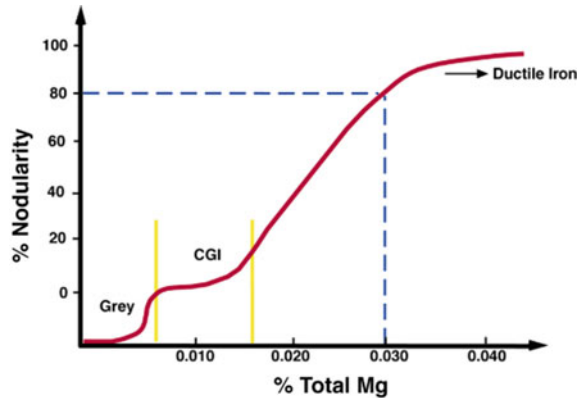


Fig. 11.2 SEM micrographs of CGI microstructure: **a** unetched specimen; **b** etched specimen

Table 11.1 Chemical composition of different cast irons (Fe—balance)

Cast iron	Carbon equivalent (%)	C (%)	Si (%)	Mn (%)	S (%)	P (%)
FGI	3.7–4.5	3.0–3.7	1.8–2.8	0.7–0.8	< 0.15	0.1–0.5
CGI	4.2–4.6	3.5–3.8	2.0–2.6	0.20–0.5	< 0.025	< 0.05
SGI	4.4–4.5	3.4–3.8	2.0–2.8	0.2–1	< 0.02	< 0.05

Fig. 11.3 Schematic of stable range of Mg for different cast irons [16]



This improvement is due to the formation and retention of carbides with chemical compositions such as $\text{Fe}_4\text{Mo}_2\text{C}$ or $\text{Fe}_3\text{Mo}_3\text{C}$.

Other alloying elements such as Cr, Co, and Al are often used in cast irons for high-temperature applications. The first two enhance structural stability of cast irons, i.e. retention of properties at high temperatures. The last stabilizes the ferrite phase and improves the oxidation resistance by formation of strong oxide (Al_2O_3) layers.

11.4 Mechanical Properties of Cast Iron

Some key mechanical properties of FGI, CGI, and SGI at room temperature are presented in Table 11.2. Apparently, SGI has high ductility and the highest tensile strength but low thermal conductivity. FGI, on the other hand, demonstrates the lowest strength and high thermal conductivity, while its close to zero elongation highlights its brittle nature. The properties of CGI are typically between those of FGI and SGI. Temperature has a strong effect on yield strength, tensile strength, and elastic modulus of FGI, CGI, and SGI (Table 11.3). It can be noted that unalloyed SGI has better tensile strength compared to FGI at room temperature, but it degrades more rapidly with temperature.

Table 11.2 Typical material properties of FGI, CGI, and SGI at room temperature [7, 8]

Property	FGI	CGI	SGI
Tensile strength (MPa)	160–320	300–600	400–700
Elongation (%)	~ 0	3–6	6–25
Elastic modulus (GPa)	96–110	140–160	170–190
Thermal conductivity at 100 °C (W/mK)	45–65	35–45	29–40

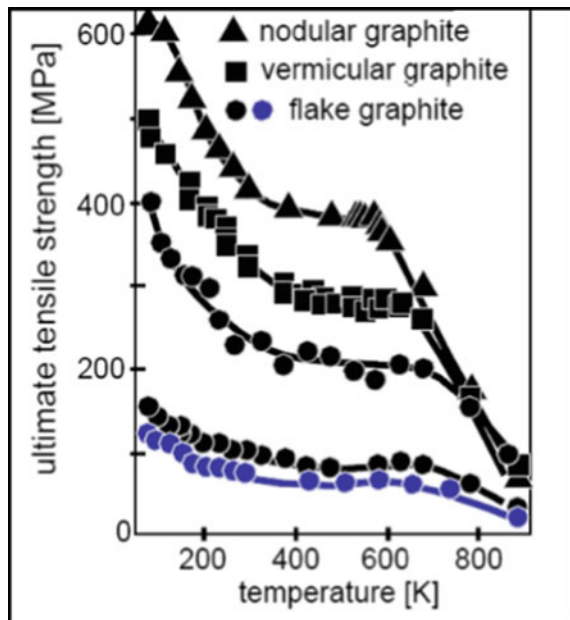
Table 11.3 Effect of temperature on tensile properties of unalloyed FGI, CGI, and SGI with fully pearlitic matrix [20]

Cast iron	Room temperature			540 °C		
	Yield strength (MPa)	Tensile strength (MPa)	Elastic modulus (GPa)	Yield strength (MPa)	Tensile strength (MPa)	Elastic modulus (GPa)
FGI	212	268	109	159	185	65
CGI	324	405	130	183	220	72
SGI	424	476	158	232	336	122

The variation of tensile strength of FGI, CGI, and SGI with temperature is demonstrated in Fig. 11.4. The figure highlights a steep increase in rate of strength reduction between 600–800 K (327–527 °C). Similar variation is reported in the literature [21, 22], with a slow reduction in tensile strength up to 400 °C followed by a significant drop around 500 °C. Comparable observation was made by Zou et al. [22] regarding fatigue strength which that increased up to 400 °C and then decreased significantly at 500 °C. The increase in fatigue strength around 300–400 °C was attributed to strain hardening, dynamic strain ageing, and precipitation strengthening effects. The significant reduction in tensile and fatigue strengths around 500 °C was attributed to high levels of oxidation, diffusion of vacancies, and grain-boundary softening.

A unique feature of cast iron is the difference in material strength under tension and compression, with compressive strength being higher compared to tensile strength.

Fig. 11.4 Influence of temperature on tensile strength of FGI, CGI, and SGI [20]



Under compression, the graphite particles are held tightly closed, and the bulk material acts very much like steel, resulting in superior strength. Under tension, the graphite particles bear almost no load and act as crack-initiation sites. In case of FGI, the ratio of compressive strength to tensile strength is typically around 2 [23], but it could be as high as 5 [24]. The tension–compression asymmetry is less pronounced in SGI compared to FGI [25], probably because the nodular graphite form does not provide a direct path for crack initiation under tensile loading.

Comparison of stress–strain curves under tension and compression loading for CGI vividly demonstrates the asymmetrical tension–compression behaviour of CGI at room and elevated temperatures (Fig. 11.5). The magnitude of 0.2% proof strength at room temperature in compression (451 MPa) is 1.31 times that in tension (344 MPa). This ratio remains similar at 500 °C. The compressive strength to tensile strength ratio of 1.31 compares well with ratios of about 1.4–1.6 are reported in literature for CGI [26, 27]. The figures also show that the elastic modulus in tension and compression are identical at room temperature (135 GPa) and at 500 °C (125 GPa).

11.5 High-Temperature Applications of Cast Irons

The properties of cast irons start degrading at around 425 °C, with creep becoming a concern above this temperature. Applications of cast iron in the automobile industry include these levels of temperature, with cylinder blocks and cylinder heads reaching temperatures around 400 to 450 °C while exhaust manifolds and turbocharger housings reaching temperatures around 800 °C [14].

The cylinder heads are traditionally manufactured from FGI, but with peak cycle pressures of about 25 MPa and temperature close to 400 °C, those designs are approaching its mechanical limit. CGI is seen as a candidate to replace grey iron and allow higher pressures and temperatures of around 450 °C [14, 28]. Cylinder blocks and cylinder heads have multiple intake and exhaust ports, coolant passages, and water jackets. As a result, during operation of these components, significant thermal gradients occur due to the movement of exhaust gases, coolants, and different rates of heat dissipation at various locations. The high operating temperature, high-frequency combustion, and multiple engine start-stop cycles lead to a combination of low-cycle and high-cycle thermo-mechanical fatigue problems in the cylinder heads. The start-up and shutdown cycles can lead to tensile and compressive stresses in the valve bridges as the temperature increases and held for long periods of time, resulting in creep, stress relaxation and, eventually, initiation, and propagation of cracks [28, 29].

Examples of cast irons mainly used in exhaust manifolds and turbochargers of heavy-duty diesel and petrol engines are alloyed cast irons such as SiMo51, SiMo1000, and Ni-Resist D-5S. SiMo51 is ferritic spheroidal cast iron with typically about 4% of Si and about 1% of Mo. SiMo1000 is also ferritic nodular cast iron, with typically around 2.5% Si, 1% Mo, and about 3% Al. D-5S is austenitic cast iron with

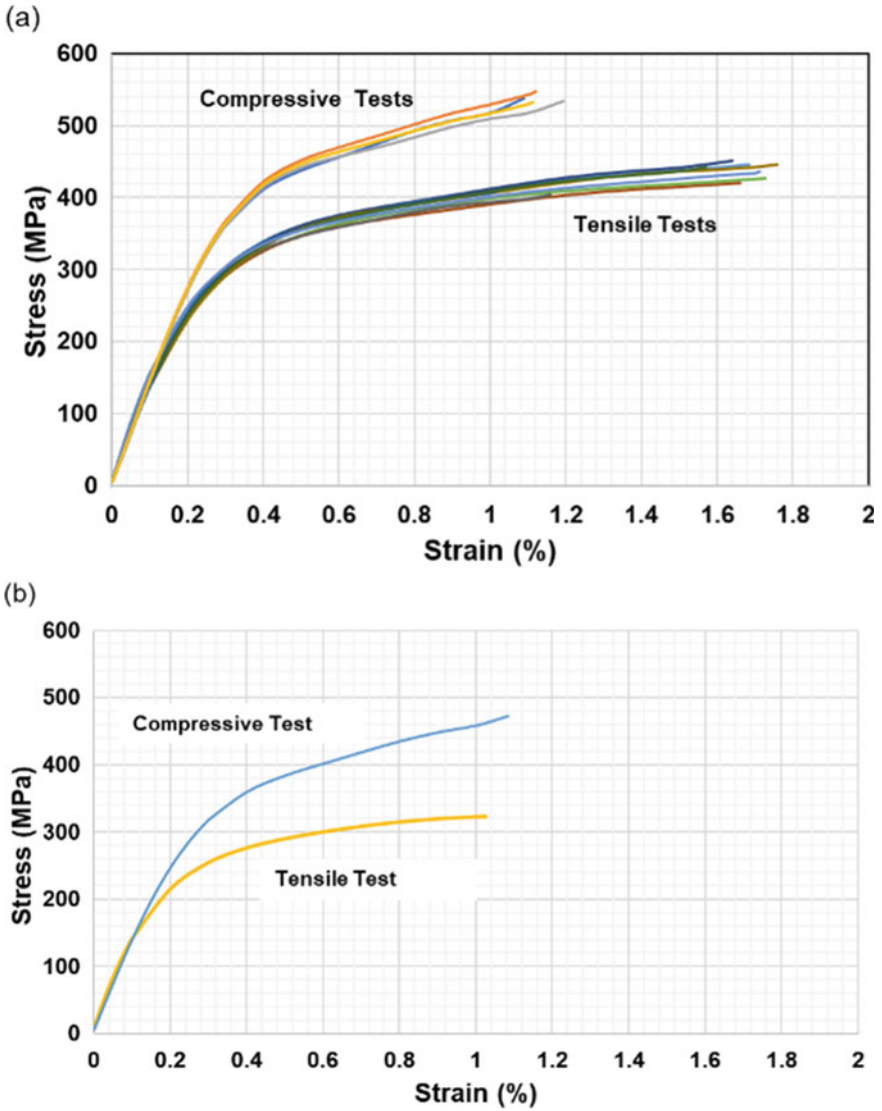


Fig. 11.5 Comparison of stress–strain curves under tension and compression loading: **a** room temperature; **b** 500 °C

about 33–35% of Ni. These materials are used in the temperature range from 700 to 900 °C [28, 30–33].

11.6 Introduction to Creep

Creep is a time-dependent, permanent deformation of material under constant stress even if the applied stress is below its yield point. The level of creep strain generated depends on the material, stress, temperature, and time spent at a particular temperature and stress level.

The idealized shape of a creep curve for a constant uniaxial load at a constant temperature is shown in Fig. 11.6. When the load is first applied, a small instantaneous strain is generated in material. The creep strain is obtained by subtracting the instantaneous strain from the total strain.

The time-dependent response is a slow increase of strain with a variable rate, which, according to Andrade [34], can be divided into three stages: primary creep, secondary creep, and the tertiary creep. During primary creep, the creep rate decreases rapidly with time. This reduction is due to the strain hardening as the dislocations encounter obstacles and are immobilized resulting in higher dislocation density [35, 36]. At the end of the primary-creep stage, the creep rate becomes almost constant, and this region is called *secondary creep*. At this stage, the strain-hardening mechanism is balanced by the recovery due to thermal softening caused by annihilation of dislocations [36, 37]. The average creep rate during secondary creep, determined by the constant slope of the creep curve, is known as *minimum creep rate*. At the end of the secondary-creep stage, the creep rate increases rapidly, ultimately leading to failure. This region of increasing creep rate is called *tertiary creep*. Temperature and stress are the two dominant external variables that affect the shape of creep curve.

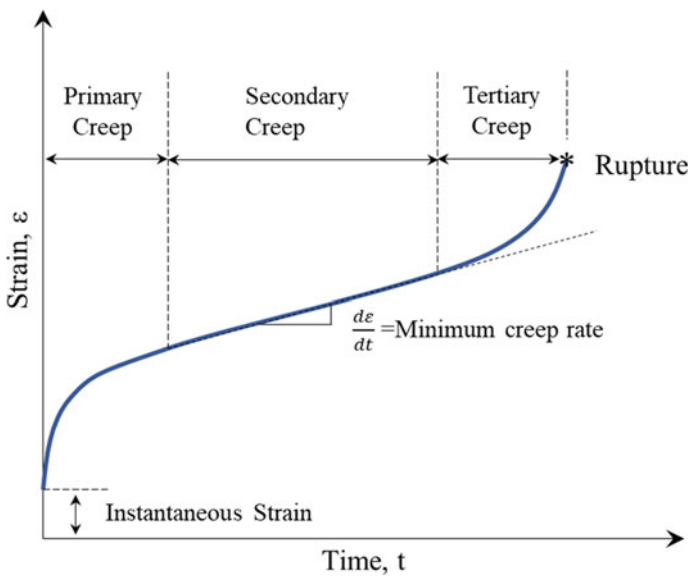


Fig. 11.6 Constant-temperature curve showing three distinct stages of creep

11.7 Creep Models

Models used to describe the creep behaviour can be broadly classified as empirical models, mechanism-based models, as well as continuum-mechanics, and micromechanical models [37, 38].

11.7.1 Empirical Models

Empirical creep models provide relationships between the creep rate, stress, temperature, and time. They can be also used to predict life of structures for given levels of stress and temperature. These relations are mainly based on experimental data from uniaxial creep tests. The empirical models are useful in early design stages to arrive at component sizing, choosing the correct materials for the application. These models do not consider stress redistribution, creep-plasticity interaction, cyclic strain accumulation, and many other effects [37].

The most general creep equation relating the creep rate $\dot{\epsilon}_c$, stress σ , time t , and temperature T can be written as

$$\dot{\epsilon}_c = f(\sigma, t, T).$$

This general equation can be simplified by de-coupling into separate functions to account for effects of each parameter

$$\dot{\epsilon}_c = f_1(\sigma) f_2(t) f_3(T).$$

Several stress functions, $f_1(\sigma)$, were used in the literature with the most common functions [35, 37, 38] as follows:

$$f_1(\sigma) = K \sigma^n \quad (\text{Norton 1929, Bailey 1935})$$

$$f_1(\sigma) = B \exp\left(\frac{\sigma}{\sigma_o} - 1\right) \quad (\text{Soderberg 1936})$$

$$f_1(\sigma) = A \sinh\left(\frac{\sigma}{\sigma_o}\right) \quad (\text{McVetty 1943})$$

$$f_1(\sigma) = A \left\{ \sinh\left(\frac{\sigma}{\sigma_o}\right) \right\}^m \quad (\text{Garofalo 1965})$$

Here, the parameters K , B , A , n , m , and σ_o are the material constants derived based on creep experiments.

The power law attributed to Norton and Bailey is most broadly used primarily thanks to its simplicity. The power law fits best the experimental data for low stresses, but the exponential function is more accurate for higher stresses.

An extensive curve-fitting process for experimentally derived creep curves is required to describe the time dependence of high-temperature creep in complex alloys. Some of the time functions, $f_2(t)$, are [35]

$$f_2(t) = (1 + bt^{1/3}) \exp(kt) - 1 \quad (\text{Andrade 1910})$$

$$f_2(t) = Ft^n \quad (\text{Bailey 1935})$$

$$f_2(t) = G(1 - e^{-qt}) + Ht \quad (\text{McVetty 1943})$$

$$f_2(t) = \theta_1(1 - e^{-\theta_2 t}) + \dot{\epsilon}_s t \quad (\text{Garofalo 1965})$$

Here, F , G , H , b , k , n ($\frac{1}{3} \leq n \leq \frac{1}{2}$), q , θ_1 , and θ_2 are the constants that can vary with time.

The temperature has a significant impact on creep; this effect is driven by the changes in the material microstructure with temperature. As the shape of the creep curve changes with temperature, the material constants used in the stress function can also change. The temperature function, $f_3(T)$, is usually expressed in terms of Arrhenius law

$$f_3(T) = \exp\left(-\frac{Q}{RT}\right),$$

where Q is the activation energy, R is the universal gas constant (8.37 J/molK), and T is the absolute temperature.

In real life, the loading is mostly variable so there is a need to account for the changes in stress and temperature with time. Several theories are available for variable loading including time hardening, strain hardening, total strain theory, combined strain and time hardening, Marin theory, Graham and Walles method, etc. In absence of thermal softening and metallurgical changes, test results demonstrate that the strain-hardening theory is more accurate [35, 39]. The time- and strain-hardening theories bound all other theories in the predicted response to the variable load. The both theories are widely used as approximate methods of component analysis including finite-element studies [35].

In addition to the relationships between the creep rate, stress, time, and temperature, the empirical models include extrapolation methods to predict time-dependent deformation and life of structures. Several extrapolation methods are covered in the literature [35, 39–42]. Two of the most widely used approaches are Larson–Miller parameter method and Monkman–Grant law.

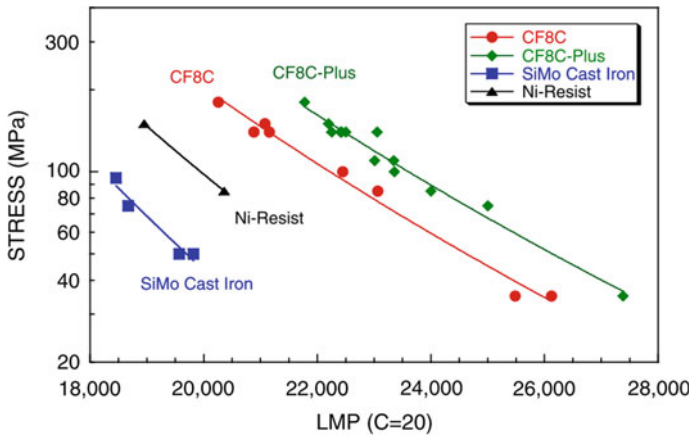


Fig. 11.7 Larson–Miller parameter plot for diesel exhaust alloys [43]

The former method relates temperature with time to failure at a constant stress. The Larson-Miller equation has the following form:

$$P_{LM}(\sigma) = T(\log t + C),$$

where t is the time to failure in hours and C is the material’s constant that can be experimentally found.

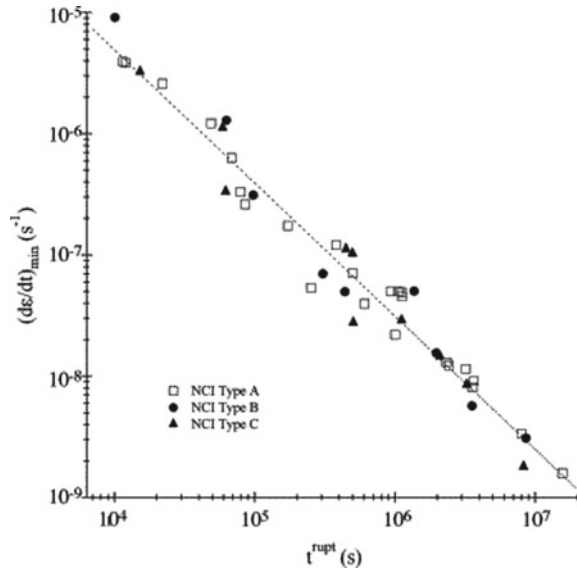
Larson-Miller parameter plots for different materials used in diesel-engine exhausts including SiMo and Ni-Resist cast irons are shown in Fig. 11.7 [43]. These plots also known as *master curves* are built by testing the material to rupture at different stress and temperature levels. The master curve can be used to obtain the time to rupture at any temperature and stress combination on the curve. Another use of Larson-Miller parameter is in comparing and ranking materials as shown in Fig. 11.7 where higher curves represent more heat resistant material.

Another widely used empirical model is the Monkman–Grant relation [44] which relates the minimum creep rate, $\dot{\epsilon}_{mcr}$, and the time to fracture, t_f

$$\dot{\epsilon}_{mcr}^m t_f = C,$$

where m and C are the material constants. The relationship is suitable for a number of materials including aluminium, copper, titanium, iron, and nickel-based alloys, with m ranging between 0.77–0.93 [40]. Figure 11.8 shows the Monkman–Grant graph for three different nodular cast irons reported by Hug et al. [45]. The found parameters were $m = 0.91 \pm 0.04$ and $C = 0.15 \pm 0.06$.

Fig. 11.8 Monkman–Grant graph for three nodular cast irons [45]



11.7.2 Mechanism-Based Models

The mechanism-based models capture the basic mechanisms that contribute to creep in metals such as dislocation creep, diffusional creep, and grain-boundary sliding. It is possible that all the mechanisms may be active at any given time but depending on the stress and temperature levels, one of the creep mechanisms is dominant at any given time.

Dislocation creep involves dislocation glide and climb. The dislocation glide occurs on application of stress, resulting in strain hardening as the density of dislocations increase. The climb is the recovery process at high temperatures, with dislocations able to move or climb to a different slip plane, allowing further dislocation glide. The creep occurs due to sequential glide and climb of dislocations. The dislocation creep is often called *power-law creep* [46], with the steady-state strain rate, $\dot{\epsilon}_{ss}$, given as

$$\dot{\epsilon}_{ss} = A\sigma^n \exp\left(-\frac{Q}{RT}\right),$$

where A is the constant, σ is the stress level, n is the creep exponent, and Q is the activation energy for creep.

Diffusional creep occurs in materials with fine grain size at lower stresses. The mechanism involves diffusion of atoms and vacancies under the influence of stress. Depending on the path of diffusion, diffusional creep can be considered as Nabarro-Herring creep or Coble creep. In Nabarro-Herring creep, which occurs at

higher temperatures, diffusion happens through grain interiors, while Coble creep occurs at relatively lower temperatures through grain boundaries. The steady-state strain rate, $\dot{\epsilon}_{ss}$, in Nabarro-Herring and Coble creep [47] are given as.

$$\dot{\epsilon}_{ss} \approx \frac{7\sigma D_v b^3}{kTd^2} \quad \text{(Nabarro-Herring creep)}$$

$$\dot{\epsilon}_{ss} \approx \frac{50\sigma D_{gb} b^4}{kTd^3} \quad \text{(Coble creep)}$$

where d is the grain diameter, D_v is the volume diffusivity through the grain interior, and D_{gb} is the volume diffusivity through grain boundary, b is the Burgers vector. It is noted that increasing the grain size reduces the strain rate in both cases but more in Coble creep.

Grain-boundary sliding occurs at much higher temperatures and is important in initiating intergranular fracture, which indicates the onset of tertiary creep. The grain-boundary sliding does not contribute to the steady-state creep.

Different creep deformation mechanisms can be illustrated with deformation mechanism maps (Fig. 11.9). Detailed maps for various metals and ceramics are reported in a book by Frost and Ashby [48].

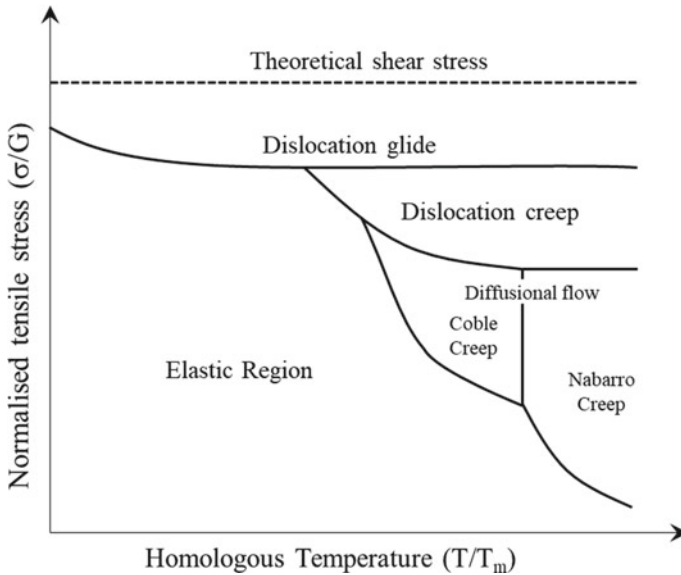


Fig. 11.9 Schematic of deformation mechanism map

11.7.3 *Continuum-Mechanics and Micromechanical Models*

Continuum-mechanics models are useful for investigation of inelastic behaviour in three-dimensional cases by employing constitutive equations, relating the three-dimensional deformation and stress states. State variables and corresponding evolution equations can be used to describe microstructure-related changes such as hardening, recovery, and damage. These approaches were implemented in numerical schemes, including finite-element analysis, to simulate the time-dependent structural behaviour such as creep. Naumenko and Altenbach [37, 38], Betten [49], and Chaboche [50] discussed the continuum-mechanics-based models in great details. Betten et al. [51–54] developed models of creep of materials with tension–compression asymmetry such as cast iron.

Micromechanical models include direct introduction of microstructural features into consideration, often using a representative volume element with geometrically idealized microstructure. The behaviour of constituents and their interactions are captured in such models. In case of cast irons, the graphite particles can be modelled as voids or as inclusions leading to different reposes. Several studies employing micromechanical models of cast irons are reported in the literature [55–59] but there are no micromechanical models specifically dealing with their creep.

11.8 Creep in Cast Irons

As discussed, temperatures in the cylinder heads in modern diesel engines reaches around 400–500 °C, while temperatures in the exhaust manifolds are in the range of 800 °C [45, 60]. So, continuous long-term operation at such elevated temperatures makes these components susceptible to creep.

In cylinder heads, significant thermal gradients related to complex geometries including multiple ports, valves, and attaching components can result in high tensile or compressive stresses at multiple locations. Several investigations of cracking in cast-iron cylinder heads [61–64] found that it mainly occurred in the valve bridge areas. Investigation by Smith et al. [61] found that the valve bridge region experienced compressive stresses at high-temperature condition due to restrained thermal expansion. These stresses can result in permanent deformation due to creep if the temperatures are held for sufficient duration. Conversely, tensile stresses are generated in this region upon cooling, leading to initiation of microcracks, which propagate under repeated start-up–shutdown cycles. Such failures can be considered as thermo-mechanical fatigue (TMF), but they are caused by creep.

Several studies were dedicated to the study of TMF behaviour of cast irons to develop component-level models for life prediction [25, 65–67]. Most studies considered the effects of low- and high-cycle fatigue, plasticity and, to some extent, creep damage in SGI, CGI, and FGI. The material models developed were based on experiments performed within a specific range of stresses and temperatures typical for

real-life conditions. Such analysis is especially useful for understanding of different failure mechanisms and development of models to reflect in-service performance of components. Norton's creep law is widely used in such models to account for creep damage [25, 67] that is added to damage from other mechanisms.

There are not many studies looking specifically into creep of cast irons. A report by Kattus and McPherson [68], focussed on high-temperature mechanical performance of cast irons, included a detailed investigation of creep behaviour in grey cast iron. The study contained microstructural analysis, creep-rupture data, minimum creep rates for different alloys tested and provided a direction for further material improvements. The report also included conclusions about the role of different alloying elements like Mo, Cr, and Si in improving the creep resistance of cast irons. Based on the experiments completed, the study found that pearlite graphitization into ferrite and graphite resulted in lower creep-rupture properties in the pearlitic cast irons compared to standard ferritic grades.

An investigation into the creep properties of cast iron by Wheatley and Pope [69] dealt with compressive creep of cast iron between 325 AND 475 °C at different stress levels. The paper concluded that the materials showed creep behaviour under compression similar to that in tensile creep tests. Only primary creep was observed at 325 °C for stresses up to 200 MPa. Secondary creep was found in tests above 400 °C, creep at 475 °C demonstrating significantly higher strain. The study did not include comparison between tensile and compressive creep.

Creep behaviour of three families of nodular cast irons typically used in exhaust manifolds was analysed by Hug et al. [45]. Two of them were ferritic SiMo nodular cast irons, and the third one was an austenitic nodular cast iron of grade D-5S. The creep test temperature for ferritic irons was between 650 and 800 °C, and the austenitic iron was tested up to 900 °C. The study found that all three materials followed the Monkman–Grant law (Fig. 11.8), indicating similar creep-damage mechanisms. It was found that the austenitic grades were generally more creep-resistant compared to ferritic ones. At high stresses and temperatures, the creep fracture was dominated by plastic straining of the matrix and graphite nodules. At lower stresses and temperatures, it was caused by cavity nucleation and diffusive growth, leading to microcracks and voids without any signs of deformation in the matrix. The damage mechanism in the high-temperature creep tests of ferrite was similar to that reported by Hervas et al. [70] in the tensile tests, with the plastic flow of ferritic grains mainly driven by significant reduced yield strength of ferrite at high temperatures. Plastic strains of graphite nodules reported by Hug et al. [45] were not observed in tensile testing by Hervas et al. [70].

Recent creep studies on ferritic SiMo51 and SiMo1000 and austenitic nodular cast irons D-5S by Öberg et al. [71, 72] employed novel test methods called *sequential tensile tests* (STT), *stress relaxation and thermal cycling* (SRTC) tests, and traditional constant-load creep tests. The STT is a monotonic tensile test carried out at different strain rates, where stress is recorded. It is effectively an inverse of traditional creep test with a constant load and a measured strain rate. The STT was used to evaluate Norton creep parameters for the studied materials. The SRTC test [30] is a relaxation test including isothermal holds in thermal cycles with a specimen fixed in grips. The test

uses compressive stress relaxation at high temperature and tensile stress relaxation at low temperature. The STT and SRTC tests are fast compared to a conventional creep test. The studies found that for all the materials tested, the creep rates matched well both the STT and the SRTC test. A direct comparison of creep rates from STT and SRTC tests with that from traditional creep tests for SiMo51 demonstrated that the latter were an order of magnitude lower. The reason for these differences was not fully identified. The studies provided results for such creep parameters as activation energy and the stress exponent for the different materials that can be helpful for numerical simulations and design of exhaust components. Interestingly, the authors concluded that the creep behaviour was similar in terms of tension and compression and that the data from monotonic tests can be used for cyclic loading conditions. This conclusion may be true for SGI, without pronounced difference in tensile and compressive behaviours, but it is not expected to be the case for FGI or CGI, demonstrating tension–compression asymmetry.

Wu et al. [73] studied the creep behaviour of CGI at stresses between 40 and 150 MPa and temperatures ranging from 350 to 550 °C (Fig. 11.10). Apparently, at 150 MPa, there was no significant creep up to 450 °C but the creep rate rose sharply at 550 °C resulting in specimen's rupture in some 10 h. The study found pearlite transformation at temperatures around 550 °C as in other works [14], which can explain this sharp increase in the creep rate. It was noted that the creep strain-to-failure of about 3% was at the higher end for CGI and might be a result of a higher ferrite content. Cracks originating on the surface of the specimen propagated preferentially through ferrite, the phase weaker than pearlite. The cracks extended further by debonding between graphite and ferrite, with subsequent rupture of the specimen when crack reached a critical length. Grain-boundary sliding was identified as the creep-damage mechanism at 500 °C for 150 MPa. Intragranular deformation was observed at temperatures around 550 °C.

Jing et al. [74] have recently studied creep in CGI at temperatures from 450 to 550 °C and stresses between 100 and 150 MPa; the reported minimum creep rates are shown in Fig. 11.11. Creep performance of CGI significantly deteriorated with an increase in temperature from 450 to 550 °C. Based on a multi-objective optimisation approach for curve fitting, the study found that different creep-damage mechanisms such as grain-boundary sliding, dislocation glide, and dislocation climb were dominant at different combinations of stresses and temperatures.

11.9 Experimental Results for CGI Creep

The literature survey into the creep of cast irons demonstrates that there are a few studies covering tensile creep in CGI [73, 74] but there is no literature available regarding compressive creep in it. As discussed previously, tensile and compressive creep can play a critical role in high-temperature applications such as cylinder heads subjected to multiple start-stop cycles and long operation times. Fundamental understanding of the similarities and differences in creep behaviour under tension

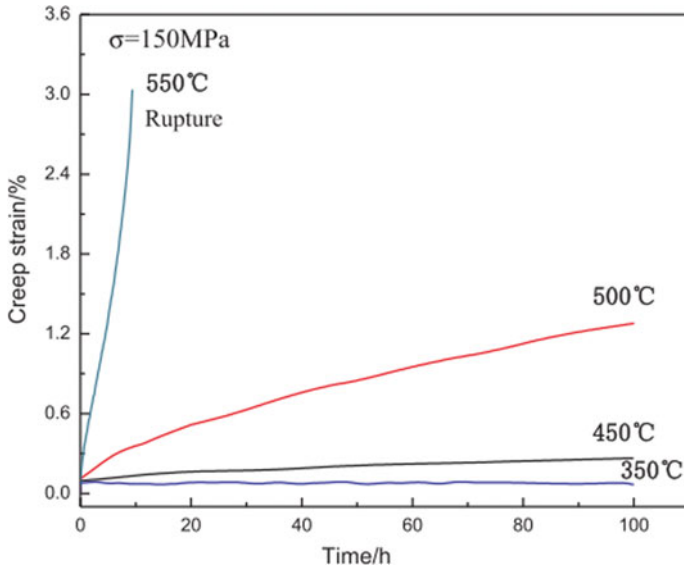


Fig. 11.10 Creep curve of CGI at different temperatures for 150 MPa [73]

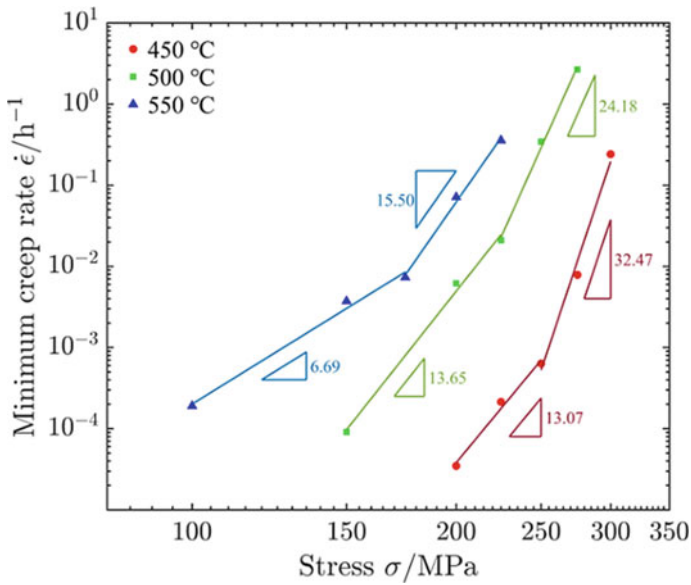


Fig. 11.11 Effect of stress on minimum creep rate in CGI [74]

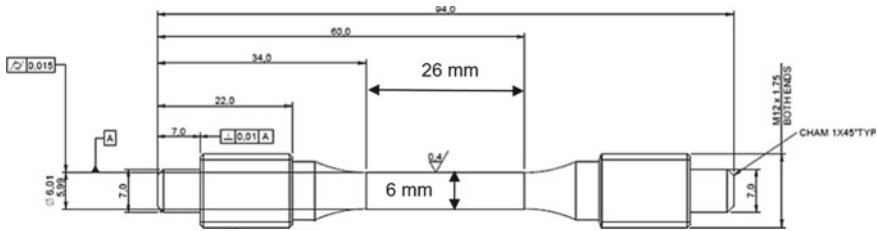


Fig. 11.12 Specimen used in tensile and creep tests

and compression is vital for design of efficient and reliable products. Results from the ongoing research on the tensile and compressive behaviours of CGI are given in this section.

A pearlitic CGI material of EN-GJV-450 grade was procured in the form of cylindrical rods of about 250 mm length and about 25 mm diameter. These rods were machined to produce test specimens with dimensions shown in Fig. 11.12. The specimens had a circular cross section with minimum diameter of 6 mm and a gauge length of 26 mm. The minimum gauge length was 4.33 times the specimen's diameter, meeting the minimum 4xD gauge length requirement in ASTM E8 standard [75].

Instron 5982 electromechanical machine with 100 kN force capacity was used for tensile and compressive creep testing at various level of constant stress. The Instron machine was used together with a 3119–600 series temperature-controlled thermal chamber capable of reaching the maximum temperature of 600 °C. The temperature chamber had temperature stability of ± 2 °C. Epsilon extensometer 7642-0125 M-075 M with a 12.5 mm gauge length was used for testing along with DT6299 controller.

The creep tests were completed in line with ASTM E139-11 standard [76] metallic materials. The specimen was soaked at high temperature for 8 h to ensure that that the specimen, thermal chamber, and all the attaching parts were at the settled temperatures. The temperature soaking was done under a force-control mechanism with a tolerance of ± 250 N (equivalent to ± 9 MPa stress). For the creep experiments, the extensometer filter setting was set to low noise to maximize the resolution of the signal and to minimize the noise in the data. The load was applied at 0.001 mm/mm/min, which was the same in the tensile and compression tests. The load was held steady once the required stress level was achieved. Each test was run for 100 h, which was a sufficient time to capture the strain-rate levels for secondary creep.

The 0.2% proof stress of CGI under tension and compression is shown in Fig. 11.13. At 400 °C, this stress in tension was 300 and 370 MPa for compression. Using this information as a rough guide, the creep tests were conducted at 150 MPa (to test the creep behaviour in the elastic region) and at 300 MPa (to test the creep near the plastic region). Creep tests were conducted at different temperatures—400, 500, and 550 °C.

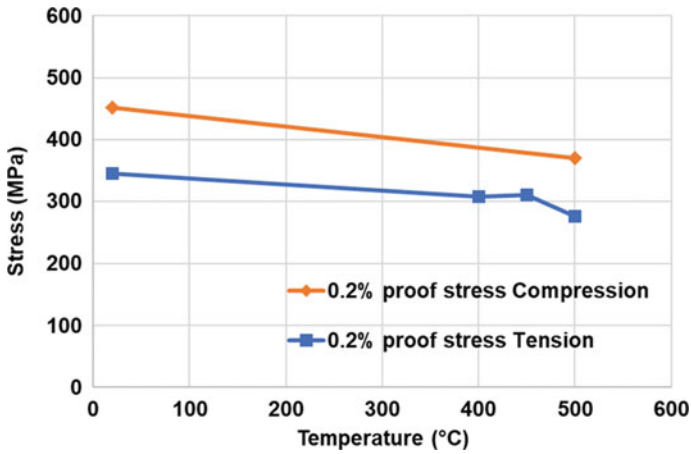


Fig. 11.13 CGI proof stresses under tensile and compressive loading at different temperatures

The strain–time histories for the tensile and compressive creep tests at 300 MPa stress at 400 and 500 °C are shown in Fig. 11.14. The figure vividly demonstrates the significant impact of temperature on tensile and compressive creep behaviours. In tension at 400 °C, there is a short stage of primary creep followed by secondary creep with no rupture when test was stopped at 78 h.

At 500 °C, however, the specimen ruptured within 30 min, most likely driven by the instantaneous plastic strain and the onset of primary creep. The rupture strain of about 1.1% was in line with the strain at fracture in the tensile tests at 500 °C. In compression, some primary creep was evident at 400 °C but there was no sign

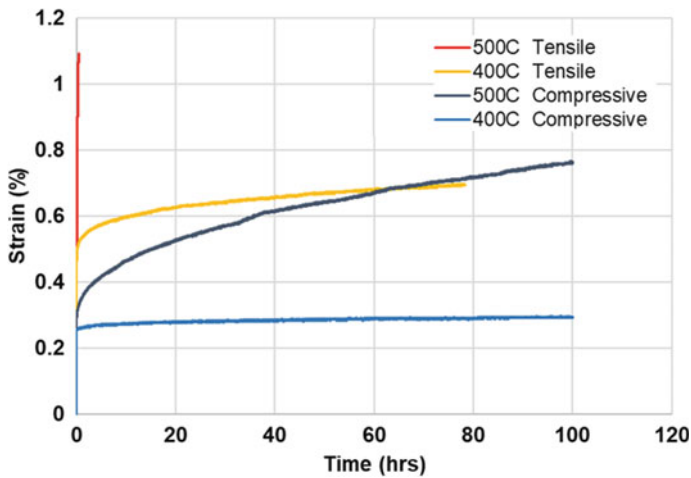


Fig. 11.14 Strain–time histories for tensile and compressive creep at 300 MPa

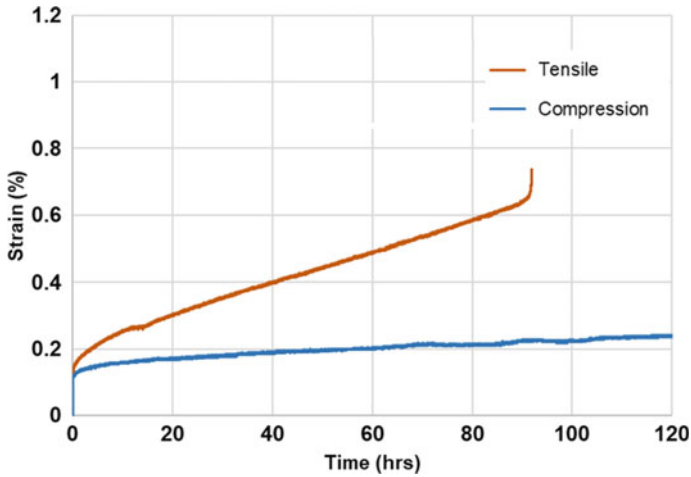


Fig. 11.15 Strain–time histories for tensile and compressive creep at 150 MPa and 550 °C

of secondary creep. However, primary as well as secondary creep were present at 500 °C under compressive load. These results highlighted the level of differences between the tensile and compressive creep regimes in CGI.

Another comparison between these two regimes at 550 °C and 150 MPa stress is presented in Fig. 11.15. For the tensile-creep case, a rapid transition from secondary to tertiary creep and almost instantaneous failure at the onset of tertiary creep were observed. Under compression, however, a short primary-creep stage can be observed followed by the secondary-creep region, demonstrating a gradual progress of creep.

SEM micrographs of the tensile-creep specimen tested at 550 °C and 150 MPa ruptured under tertiary creep demonstrate the presence of voids and grain-boundary sliding (Fig. 11.16).

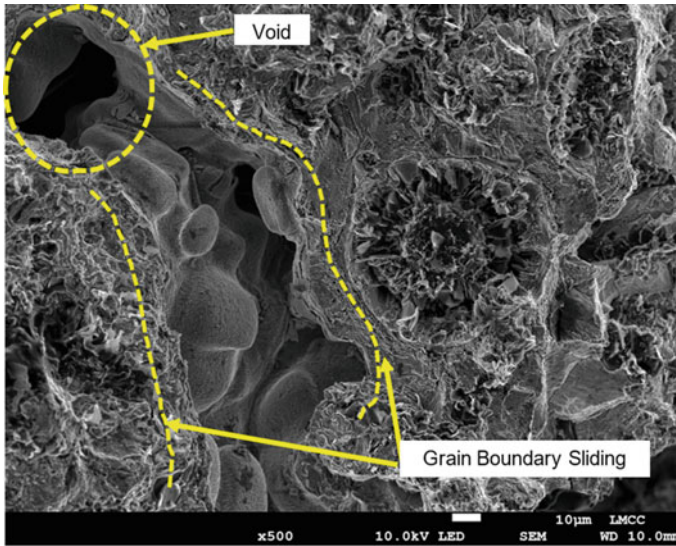


Fig. 11.16 SEM micrograph of fracture surface from the tensile-creep specimen failed under tertiary creep highlighting void and grain-boundary sliding

References

1. Stefanescu, D.M.: The meritocratic ascendance of cast iron: from magic to virtual cast iron. *Int. J. Met.* **13**, 726–752 (2019). <https://doi.org/10.1007/s40962-019-00347-8>
2. Grote, K.-H., Antonsson, E.K. (eds.): *Springer Handbook of Mechanical Engineering*. Springer Berlin Heidelberg, Berlin, Heidelberg (2009). <https://doi.org/10.1007/978-3-540-30738-9>
3. Sjögren, T.: Influences of the Graphite Phase on Elastic and Plastic Deformation Behaviour of Cast Irons (PhD dissertation), LINKÖPING UNIVERSITY, 2007. <http://urn.kb.se/resolve?urn=urn:nbn:se:liu:diva-8776>
4. Dawson, S.: Compacted graphite iron—a material solution for modern engine design. *SAE Tech. Pap. Ser.* (2011). <https://doi.org/10.4271/2011-01-1083>
5. Daeth, J., Robbins, M., Reuter, U., Hollinger, I., Schulz, H., Dawson, S.: The effect of metallurgical variables on the machinability of compacted graphite iron. *SAE Tech. Pap. Ser.* (2001). <https://doi.org/10.4271/2001-01-0409>
6. Chakrabarty, I.: Alloy cast irons and their engineering applications. *Ref. Modul. Mater. Sci. Mater. Eng.*, Elsevier 1–25 (2018). <https://doi.org/10.1016/B978-0-12-803581-8.10092-X>
7. Brown, J.R. (ed.): *Fosco Ferrous Foundryman's Handbook*. Butterworth-Heinemann (2000)
8. BS EN 16079:2011: Founding—Compacted (vermicular) graphite cast irons. <https://bsol.bsigroup.com/> (2011)
9. ASTM International: ASTM A842–11a. *Stand. Specific. Compact. Graph. Iron Cast.* (2018). <https://doi.org/10.1520/A0842-11AR18E01>
10. ISO 16112:2017: Compacted (vermicular) graphite cast irons—Classification (2016). www.iso.org
11. *ASM Handbook: Volume 15: Casting*, ASM International (1998)
12. ASTM A159–83: *Standard Specification for Automotive Gray Iron Castings* (2015). <https://doi.org/10.1520/A0159-83R15>
13. SAE International, SAE J1887, *Automotive Compacted Graphite Iron Castings*. <http://www.sae.org> (2018)

14. Mills, Z.G., Finney, C.E.A., Haynes, J.A., Trofimov, A.A., Wang, H., Pierce, D.T.: Impact of materials properties on higher-temperature engine operation. *SAE Int. J. Adv. Curr. Pract. Mobil.* **4**, 2021–01–1142 (2021). <https://doi.org/10.4271/2021-01-1142>
15. Stefanescu, D.M., Ohio, T.: Classification and basic types of cast iron. In: *Cast Iron Science Technology*, pp. 12–27. ASM International (2017). <https://doi.org/10.31399/asm.hb.v01a.a0006294>
16. Sintercast, Process Control for the Reliable High Volume Production of Compacted Graphite Iron, pp. 1–12. <https://sintercast.com/media/1232/sintercast-process-control-for-the-reliable-high-volume-production-of-compacted-graphite-iron.pdf> (2014)
17. Diaconu, V.L., Sjögren, T., Skoglund, P., Diószegi, A.: Influence of molybdenum alloying on thermomechanical fatigue life of compacted graphite irons. *Int. J. Cast Met. Res.* **25**, 277–286 (2012). <https://doi.org/10.1179/1743133612Y.0000000021>
18. Matteis, P., Scavino, G., Castello, A., Firrao, D.: High-cycle fatigue resistance of Si-Mo ductile cast iron as affected by temperature and strain rate. *Metall. Mater. Trans. A.* **46**, 4086–4094 (2015). <https://doi.org/10.1007/s11661-015-3029-7>
19. Selin, M.: Tensile and thermal properties in compacted graphite irons at elevated temperatures. *Metall. Mater. Trans. A.* **41**, 3100–3109 (2010). <https://doi.org/10.1007/s11661-010-0385-1>
20. Ghodrati, S.: *Thermo-Mechanical Fatigue of Compacted Graphite Iron in Diesel Engine Components*. Delft University of Technology (2013). <https://doi.org/10.4233/uuid:ea8b8910-75f8-4d7d-876d-3801f8445514>
21. Qiu, Y., Pang, J.C., Yang, E.N., Li, S.X., Zhang, Z.F.: Transition of tensile strength and damaging mechanisms of compacted graphite iron with temperature. *Mater. Sci. Eng. A.* **677**, 290–301 (2016). <https://doi.org/10.1016/j.msea.2016.09.035>
22. Zou, C.L., Pang, J.C., Zhang, M.X., Qiu, Y., Li, S.X., Chen, L.J., Li, J.P., Yang, Z., Zhang, Z.F.: The high cycle fatigue, deformation and fracture of compacted graphite iron: influence of temperature. *Mater. Sci. Eng. A.* **724**, 606–615 (2018). <https://doi.org/10.1016/j.msea.2018.01.025>
23. Pevec, M., Oder, G., Potrč, I., Šraml, M.: Elevated temperature low cycle fatigue of grey cast iron used for automotive brake discs. *Eng. Fail. Anal.* **42**, 221–230 (2014). <https://doi.org/10.1016/j.engfailanal.2014.03.021>
24. Wiese, J.W., Dantzig, J.A.: Modeling stress development during the solidification of gray iron castings. *Metall. Trans. A.* **21**, 489–497 (1990). <https://doi.org/10.1007/BF02782429>
25. Seifert, T., Riedel, H.: Mechanism-based thermomechanical fatigue life prediction of cast iron. Part I: Models. *Int. J. Fatigue.* **32**, 1358–1367 (2010). <https://doi.org/10.1016/j.ijfatigue.2010.02.004>
26. Dawson, S., Guesser, W.: Specification, selection, and applications of compacted graphite irons. In: *Cast Iron Science and Technology*, pp. 659–664. ASM International (2017). <https://doi.org/10.31399/asm.hb.v01a.a0006312>
27. Viswanathan, S., Apelian, D., Donahue, R.J., DasGupta, B., Gywn, M., Jorstad, J.L., Monroe, R.W., Sahoo, M., Prucha, T.E., Twarog, D. (eds.): *Compacted graphite iron castings*. In: *Casting*. ASM International, pp. 872–883 (2008). <https://doi.org/10.31399/asm.hb.v15.a0005325>
28. Pierce, D., Haynes, A., Hughes, J., Graves, R., Maziasz, P., Muralidharan, G., Shyam, A., Wang, B., England, R., Daniel, C.: High temperature materials for heavy duty diesel engines: historical and future trends. *Prog. Mater. Sci.* **103**, 109–179 (2019). <https://doi.org/10.1016/j.pmatsci.2018.10.004>
29. Zieher, F., Langmayr, F., Jelatancev, A., Wieser, K.: Thermal mechanical fatigue simulation of cast iron cylinder heads. *SAE Tech. Pap. Ser.* (2005). <https://doi.org/10.4271/2005-01-0796>
30. Öberg, C., Zhu, B.H., Jonsson, S.: Plastic deformation and creep of two ductile cast irons, SiMo51 and SiMo1000, during thermal cycling with large strains. *Mater. Sci. Forum.* **925**, 361–368 (2018). <https://doi.org/10.4028/www.scientific.net/MSF.925.361>
31. Norman, V., Skoglund, P., Leidermark, D., Moverare, J.: Damage mechanisms in silicon-molybdenum cast irons subjected to thermo-mechanical fatigue. *Int. J. Fatigue.* **99**, 258–265 (2017). <https://doi.org/10.1016/j.ijfatigue.2017.01.014>

32. Ekström, M., Jonsson, S.: High-temperature mechanical- and fatigue properties of cast alloys intended for use in exhaust manifolds. *Mater. Sci. Eng. A.* **616**, 78–87 (2014). <https://doi.org/10.1016/j.msea.2014.08.014>
33. Xiang, S., Jonsson, S., Babu, R.P., Zhu, B., Odqvist, J.: Influence of tension and compression dwell on the creep-fatigue properties of the austenitic cast iron Ni-resist D5S. *Mater. Sci. Eng. A.* **814**, 141179 (2021). <https://doi.org/10.1016/j.msea.2021.141179>
34. Andrade, E.N.D.C.: On the viscous flow in metals, and allied phenomena. *Proc. R. Soc. London. Ser. A* **84**, 1–12 (1910). <https://doi.org/10.1098/rspa.1910.0050>
35. Penny, R.K., Marriott, D.L.: *Design for Creep*. Springer Netherlands, Dordrecht (1995). <https://doi.org/10.1007/978-94-011-0561-3>
36. Kassner, M.E.: *Fundamentals of Creep in Metals and Alloys*. Elsevier (2015). <https://doi.org/10.1016/C2012-0-06071-1>
37. Naumenko, K., Altenbach, H.: *Modeling High Temperature Materials Behavior for Structural Analysis*. Springer International Publishing, Cham (2016). <https://doi.org/10.1007/978-3-319-31629-1>
38. Naumenko, K., Altenbach, H.: *Modeling of Creep for Structural Analysis*. Springer Berlin Heidelberg, Berlin, Heidelberg (2007). <https://doi.org/10.1007/978-3-540-70839-1>
39. Dowling, N.E.: *Mechanical Behavior of Materials*, 4th Ed. Pearson Education Limited (2013)
40. Bhaduri, A.: *Mechanical Properties and Working of Metals and Alloys*. Springer Singapore, Singapore (2018). <https://doi.org/10.1007/978-981-10-7209-3>
41. Rösler, J., Harders, H., Bäker, M.: *Mechanical Behaviour of Engineering Materials*. Springer Berlin Heidelberg, Berlin, Heidelberg (2007). <https://doi.org/10.1007/978-3-540-73448-2>
42. Meyers, M.A., Chawla, K.K.: *Mechanical Behavior of Materials*. Cambridge University Press (2009)
43. Shingledecker, J.P., Maziasz, P.J., Evans, N.D., Pollard, M.J.: Creep behavior of a new cast austenitic alloy. *Int. J. Press. Vessel. Pip.* **84**, 21–28 (2007). <https://doi.org/10.1016/j.ijpvp.2006.09.014>
44. Monkman, F.C., Grant, N.J.: *Proc. ASTM* **56**, 593 (1956)
45. Hug, E., Keller, C., Favergeon, J., Dawi, K.: Application of the Monkman-Grant law to the creep fracture of nodular cast irons with various matrix compositions and structures. *Mater. Sci. Eng. A.* **518**, 65–75 (2009). <https://doi.org/10.1016/j.msea.2009.04.020>
46. Ashby, M.M., Jones, D.R.H.: *Engineering Materials 1, An Introduction to their Properties and Applications*, Second edn. Butterworth-Heinemann (n.d.)
47. Hertzberg, R.W., Vinci, R.P., Hertzberg, J.L.: *Deformation and Fracture Mechanics of Engineering Materials*, 5th edn. John Wiley & Sons, Inc. (2012)
48. Frost, H.J., Ashby, M.F.: *Deformation-mechanism maps: the plasticity and creep of metals and ceramics*. Pergamon Press, Oxford, UK (1982)
49. Betten, J.: *Creep Mechanics*. Springer-Verlag, Berlin/Heidelberg (2005). <https://doi.org/10.1007/b138749>
50. Chaboche, J.L.: A review of some plasticity and viscoplasticity constitutive theories. *Int. J. Plast.* **24**, 1642–1693 (2008). <https://doi.org/10.1016/j.ijplas.2008.03.009>
51. Betten, J., Sklepus, S., Zolochovsky, A.: A creep damage model for initially isotropic materials with different properties in tension and compression. *Eng. Fract. Mech.* **59**, 623–641 (1998). [https://doi.org/10.1016/S0013-7944\(97\)00143-4](https://doi.org/10.1016/S0013-7944(97)00143-4)
52. Voyiadjis, G.Z., Zolochovsky, A.: Modeling of secondary creep behavior for anisotropic materials with different properties in tension and compression. *Int. J. Plast.* **14**, 1059–1083 (1998). [https://doi.org/10.1016/S0749-6419\(98\)00045-X](https://doi.org/10.1016/S0749-6419(98)00045-X)
53. Zolochovsky, A., Sklepus, S., Kozmin, Y., Kozmin, A., Zolochovsky, D., Betten, J.: Constitutive equations of creep under changing multiaxial stresses for materials with different behavior in tension and compression. *Forsch. Im Ingenieurwes.* **68**, 182–196 (2004). <https://doi.org/10.1007/s10010-003-0123-6>
54. Zolochovsky, A., Martynenko, A., Kühhorn, A.: Structural benchmark creep and creep damage testing for finite element analysis with material tension–compression asymmetry and symmetry. *Comput. Struct.* **100–101**, 27–38 (2012). <https://doi.org/10.1016/j.compstruc.2012.02.021>

55. Andriollo, T., Thorborg, J., Tiedje, N.S., Hattel, J.: Modeling of damage in ductile cast iron—the effect of including plasticity in the graphite nodules. *IOP Conf. Ser. Mater. Sci. Eng.* **84**, 012027 (2015). <https://doi.org/10.1088/1757-899X/84/1/012027>
56. Andriollo, T., Thorborg, J., Hattel, J.: Modeling the elastic behavior of ductile cast iron including anisotropy in the graphite nodules. *Int. J. Solids Struct.* **100–101**, 523–535 (2016). <https://doi.org/10.1016/j.ijsolstr.2016.09.023>
57. Collini, L., Pirondi, A.: Microstructure-based RVE modeling of the failure behavior and LCF resistance of ductile cast iron. *Procedia Struct. Integr.* **24**, 324–336 (2019). <https://doi.org/10.1016/j.prostr.2020.02.030>
58. Hütter, G., Zybell, L., Kuna, M.: Micromechanisms of fracture in nodular cast iron: from experimental findings towards modeling strategies—A review. *Eng. Fract. Mech.* **144**, 118–141 (2015). <https://doi.org/10.1016/j.engfracmech.2015.06.042>
59. Palkanoglou, E.N., Baxevanakis, K.P., Silberschmidt, V.V.: Thermal debonding of inclusions in compacted graphite iron: effect of matrix phases. *Eng. Fail. Anal.* **139**, 106476 (2022). <https://doi.org/10.1016/j.engfailanal.2022.106476>
60. Trampert, S., Gocmez, T., Pischinger, S.: Thermomechanical fatigue life prediction of cylinder heads in combustion engines. *J. Eng. Gas Turbines Power.* **130**, 012806 (2008). <https://doi.org/10.1115/1.2771251>
61. Smith, L.W.L., Angus, H.T., Lamb, A.D.: Cracking in cast iron diesel engine cylinder heads. *Proc. Inst. Mech. Eng.* **185**, 807–823 (1970). https://doi.org/10.1243/PIME_PROC_1970_185_093_02
62. Wang, Y.J., Xu, Z., Chen, M.: Thermo-mechanical fatigue and life prediction of turbocharged engine cylinder head. In: *SAE Technical Paper*, pp. 1–13 (2020). <https://doi.org/10.4271/2020-01-1163>
63. Zhang, Q., Zuo, Z., Liu, J.: Failure analysis of a diesel engine cylinder head based on finite element method. *Eng. Fail. Anal.* **34**, 51–58 (2013). <https://doi.org/10.1016/j.engfailanal.2013.07.023>
64. Metzger, M., Leidenfrost, M., Werner, E., Riedel, H., Seifert, T.: Lifetime prediction of EN-GJV 450 cast iron cylinder heads under combined thermo-mechanical and high cycle fatigue loading. *SAE Int. J. Eng.* **7**, 2014–01–9047 (2014). <https://doi.org/10.4271/2014-01-9047>
65. Gocmez, T., Awarke, A., Pischinger, S.: A new low cycle fatigue criterion for isothermal and out-of-phase thermomechanical loading. *Int. J. Fatigue.* **32**, 769–779 (2010). <https://doi.org/10.1016/j.ijfatigue.2009.11.003>
66. Hazime, R., Seifert, T., Kessens, J., Ju, F.: Lifetime assessment of cylinder heads for efficient heavy duty engines Part II: component-level application of advanced models for thermomechanical fatigue life prediction of lamellar graphite cast iron GJL250 and vermicular graphite cast iron GJV450 cylinder. *SAE Int. J. Eng.* **10**, 2017–01–0346 (2017). <https://doi.org/10.4271/2017-01-0346>
67. Seifert, T., Maier, G., Uihlein, A., Lang, K.-H., Riedel, H.: Mechanism-based thermomechanical fatigue life prediction of cast iron. Part II: Comparison of model predictions with experiments. *Int. J. Fatigue.* **32**, 1368–1377 (2010). <https://doi.org/10.1016/j.ijfatigue.2010.02.005>
68. Kattus, J., McPherson, B.: Properties of cast iron at elevated temperatures. In: *Report Proposed Cast Iron Elevated Temperatures*. ASTM International, pp. 1–1–90 (1949). <https://doi.org/10.1520/STP48314S>
69. Wheatley, C., Pope, J.A.: An investigation into the creep properties of two cast-irons I. *Int. Shipbuild. Prog.* **7**, 390–402 (1960). <https://doi.org/10.3233/ISP-1960-77302>
70. Hervas, I., Thuault, A., Hug, E.: Damage analysis of a ferritic SiMo ductile cast iron submitted to tension and compression loadings in temperature. *Metals (Basel)*. **5**, 2351–2369 (2015). <https://doi.org/10.3390/met5042351>
71. Öberg, C.: *Creep Behavior of High Temperature Cast Materials for Exhaust Applications*. PhD dissertation, KTH Royal Institute of Technology. <http://urn.kb.se/resolve?urn=urn:nbn:se:kth:diva-286090> (2020)
72. Öberg, C., Rablbauer, R., Zhu, B., Jonsson, S.: Monotonic and cyclic creep of cast materials for exhaust manifolds. *SAE Int. J. Mater. Manuf.* **12**, 05–12–02–0012 (2019). <https://doi.org/10.4271/05-12-02-0012>

73. Wu, Y., Li, J., Yang, Z., Guo, Y., Ma, Z., Liang, M., Yang, T., Tao, D.: Creep behavior accompanying oxidation of compacted graphite cast iron. *Mater. Sci. Eng. A.* **723**, 174–181 (2018). <https://doi.org/10.1016/j.msea.2018.03.039>
74. Jing, G., Li, S., Chen, G., Wei, J., Sun, S., Zhang, J.: Research on creep test of compacted graphite cast iron and parameter identification of constitutive model under wide range of temperature and stress. *Appl. Sci.* **12**, 5032 (2022). <https://doi.org/10.3390/app12105032>
75. ASTM E8/E8M-16a: Standard Test Methods for Tension Testing of Metallic Materials (2016). https://doi.org/10.1520/E0008_E0008M-16A
76. ASTM E139-11: Standard Test Methods for Conducting Creep, Creep-Rupture , and Stress-Rupture Tests of Metallic Materials. <https://www.astm.org/> (2018)

Chapter 12

About the Energy Dissipation Coefficient of Thin-Walled Glass-Plastic Pipes with the Initial Reinforcement Asymmetry with Respect to Axis Subjected to Pulsating Internal Hydrostatic Pressure



Koryun A. Karapetyan and Sona Sh. Valesyan

Abstract Results of study of the influence of possible deviation of the symmetric reinforcement relative to the axis (the disorientation of reinforcement) occurred during the material technological processing into a product on the deformation behavior and dissipative properties thin-walled glass-plastic tubular elements subjected to repeated-static internal hydrostatic pressure are discussed. It is stated that under the conditions of repeated-static internal pressure (low-cycle pulsating), in addition to the main cyclic circumferential deformations for symmetrically reinforced pipes ($\varphi = 0^\circ$), accompanying the main cyclic longitudinal deformations is arising, and for pipes with the initially broken reinforcement symmetry ($\varphi = 6-8^\circ$), accompanying cyclic shear deformations is appearing as well. As is shown, after the stabilization of the deformation process (after 2–3 cycles of loading–unloading), the value of energy dissipation coefficient ψ for glass-plastic pipes with $\varphi = 6-8^\circ$ turns out to be 20% (and more) greater than the value of energy dissipation coefficient ψ defined for glass-plastic pipes with $\varphi = 0^\circ$. The shares of each from the main and accompanying the main deformations into the total energy loss for the glass-plastic pipes with the initially broken reinforcement symmetry ($\varphi = 6-8^\circ$) are shown up. Defined that during the process of low-cycle pulsating internal pressure, the amount of energy loss due to the occurrence of cyclic shear and longitudinal deformations accompanying cyclic main circumferential deformations turns out to be 270% and 12% more than the amount of the energy loss arising from the main deformations, respectively. Practical recommendations by the optimal design of thin-walled

K. A. Karapetyan (✉) · S. Sh. Valesyan
Experimental Investigations Laboratory, Institute of Mechanics of National Academy of Sciences of Armenia, 24B Baghramyan Ave, 0019 Yerevan, Republic of Armenia
e-mail: koryun.a.karapetyan@gmail.com

S. Sh. Valesyan
National University of Architecture and Construction of Armenia, 105 Teryan Str, 0009 Yerevan, Republic of Armenia
e-mail: svalesyan@yahoo.com

tubular structural elements made of reinforced plastics operating under conditions of low-cycle pulsating internal pressure are stated.

Keywords Thin-walled glass-plastic pipes · Disorientation of reinforcement · Intensities of shear stresses and the shear strain · Coefficient of energy dissipation · Pulsating internal hydrostatic pressure

12.1 Introduction

The deviation of the reinforcement angle from its intended value (the reinforcement disorientation is a special case of the violation of the reinforcement symmetry relative to the direction of some geometric parameter of the elements) is one of the most common defects in the macrostructure of reinforced composites, including reinforced plastics [1, 2]. The probability of the reinforcement disorientation occurrence, which is mainly a consequence of the imperfection of the material technological processing into a product, and which is usually of a random nature, is greater in the case of manufacturing spatial structural elements from reinforced composites [3, 4].

Previously, it was found that for thin-walled glass-plastic pipes with initially broken symmetry of reinforcement relative to the axis subjected to static uniaxial force action, in addition to the main deformations (registered in the direction of the force action), deformations accompanying the main ones also occur. In particular, when pipes are loaded by axial tension, shear deformations accompanying the main axial ones arise, and when pipes are loaded by simple torsion, axial deformations accompanying the main shear ones also occur [4]. In the case of internal hydrostatic pressure, for thin-walled glass-plastic pipes with initially broken reinforcement symmetry, in addition to the main circumferential deformations, accompanying both axial and shear deformations arise [5].

As is known, among the main physical and mechanical properties of reinforced plastics are their dissipative properties, the negative influence of which on the reliable operation of construction elements from these materials during the time period can be significant in some cases. The optimal design of such elements subjected to cyclic loading during operation can be largely facilitated by taking into account in the calculations the indicator characterizing the dissipative properties of the material, based on experimentally established reliable data.

According to the results of [6], under the conditions of cyclic loading, in tubular elements made of reinforced plastics with initially broken symmetry of reinforcement relative to the axis, in contrast to pipes reinforced symmetrically, in addition to cyclic main deformations, cyclic deformations also occur that accompany the main ones: shear—with cyclic axial tension and longitudinal—with cyclic torsion of pipes. In this work, as a result of identifying the share of each of the deformations in the loss of the total energy of glass-plastic pipes with an initial reinforcement disorientation, practical recommendations were formulated aiming at the optimal design of such pipes subjected to cyclic loading by the indicated force factors during operation.

The purpose of this work is to identify the share of the main and accompanying main deformations in the loss of the total energy of thin-walled glass-plastic tubular

elements with initially broken symmetry of the reinforcement relative to the axis, subjected to repeated static internal hydrostatic pressure.

12.2 Research Methodology

The phenomenon of the reinforcement disorientation was discovered by us during the manufacture of experimental tubular test pieces based on glass-plastic in laboratory conditions in such a way that the direction of the main knitting fibers of the fabric coincided with the direction of the axis of the pipes (symmetric reinforcement—the value of the reinforcement angle $\varphi = 0^\circ$). However, according to the measurements, for a part of the pipes, which is about 8% of the total, deviations of the reinforcement angle from its zero value were recorded within $6\text{--}8^\circ$ [4]. Based on this, to implement the experimental part of the issues considered here, two batches of glass-plastic thin-walled tubular elements-test pieces with an inner diameter of 38 mm, a wall thickness of 2.25 mm, and a length of 285 mm were manufactured, the dimensions of ones correspond to the requirements of the tested recommendations [7].

The test pieces were made from a glass-plastic prepreg based on a modified epoxy resin by the winding method according to the technology [8]. For one batch of pipes, the value of the above-mentioned reinforcement angle was $\varphi = 0^\circ$, and for the other batch it was $-\varphi = 6\text{--}8^\circ$.

Plain weave fiberglass fabric with the main overlap [9] brand T-23 (TU 6-II -23-76) with a density (the number of fibers per 1 cm^2 of fabric) 36:20 (warp: weft), produced by the Sevan plant “Electrical Glass Insulation” (Republic of Armenia) was used. The value of the fiberglass reinforcement coefficient is $\mu = 0.45$ ($\mu_{\text{warp}} = 0.29$, $\mu_{\text{weft}} = 0.16$).

Part of the manufactured tubular test pieces of both varieties was used to determine the limit of resistance to destruction in the circumferential direction $\sigma_{\theta\theta}^{\text{ult}}$, and the other part was used to test for repeated-static internal hydrostatic pressure. When conducting cyclic tests with an average rate of change in internal pressure of 26.7 atm./min. (corresponds to the rate of stress change in the circumferential direction of the pipes $\sigma_{\theta\theta} = 25.8\text{ MPa/min.}$), the magnitude of the amplitude stress was applied equal to $0.42\sigma_{\theta\theta}^{\text{ult}}$, the choice of which was made on the basis of the preliminary tests. According to these tests, as the internal hydrostatic pressure in the pipes increases, their initial shortening and further elongation are observed. At the same time, if the condition $\sigma_{\theta\theta} \leq 0.45\sigma_{\theta\theta}^{\text{ult}}$ is obeyed, the fiberglass pipes with both $\varphi = 0^\circ$ and $\varphi = 6\text{--}8^\circ$ experience only shortening [10].

The basic number of loading–unloading cycles was used equal to 6 due to the dynamics of changes in the values of amplitude and residual circumferential, shear and longitudinal deformations of the cycle, measured during testing (Fig. 12.1).

To calculate the values of the coefficient ψ of the relative energy dissipation per cycle (dissipation energy) of glass-plastic pipes subjected to cyclic loading–unloading, the following formula was used [4]:

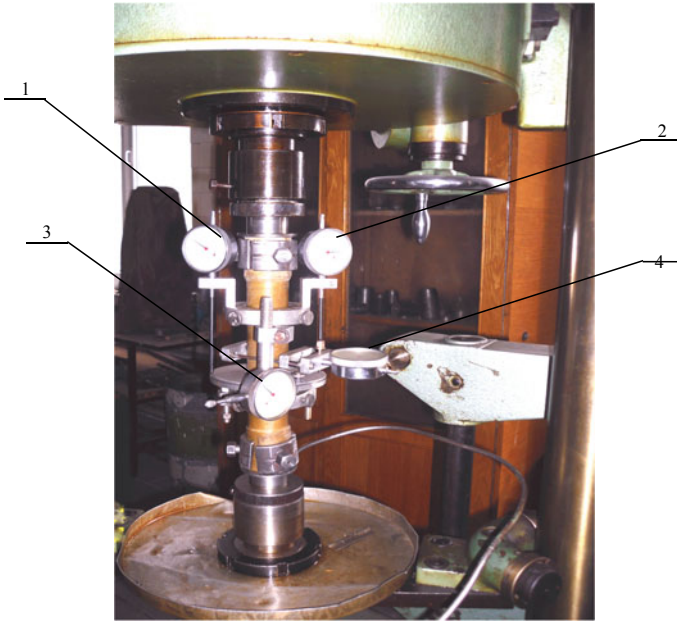


Fig. 12.1 Tubular test piece mounted on a testing machine with meters measuring longitudinal 1 and 2, shear 3, and circumferential 4 deformations

$$\psi = 1 - \frac{\overrightarrow{b} \left[-(\Gamma_{amp} - \Gamma_{res}) - \overleftarrow{X} \ln \left| 1 - \frac{1}{\overleftarrow{X}} (\overleftarrow{\Gamma} - \Gamma_{res}) \right| \right]}{\overleftarrow{b} \left[\Gamma_{amp} - \overrightarrow{X} \ln \left(1 + \frac{1}{\overrightarrow{X}} \Gamma_{amp} \right) \right]} \quad (12.1)$$

Equation (12.1) was obtained on the basis of the well-known dependence [11] $\psi = \Delta W/W$ (where ΔW is the value of the energy dissipated per cycle, and W is the value of the strain energy), using the following linear fractional function (2) applied for analytical description of the experimentally established relationship between the intensities of shear stresses T and the shear strain Γ [12, 13] in the sections of the ascending (\rightarrow) and descending (\leftarrow) branches of the hysteresis loop.

$$\overrightarrow{T} = \frac{T_B}{\overrightarrow{a}} \cdot \frac{\overrightarrow{\Gamma} - \Gamma_{res}}{1 \pm \frac{\overrightarrow{b}}{\overrightarrow{a}} \left(\overrightarrow{\Gamma} - \Gamma_{res} \right)} \quad (12.2)$$

In Eqs. (12.1) and (12.2), Γ_{res} and Γ_{amp} are the values of the intensities of residual and amplitude shear deformations of the cycle, respectively, $\overrightarrow{X} = \overrightarrow{a} / \overrightarrow{b}$, where \overrightarrow{a} and \overrightarrow{b} are the approximation parameters of hysteresis loop curves, and T_{ult} is the limiting value of T , corresponding to the destruction of the test piece.

Let us note that the experimental part of the studies considered here was carried out 30 years after the manufacture of glass-plastic pipes. During this period of time, they were in the laboratory at an ambient temperature of 20 ± 6 °C and a relative humidity of $60 \pm 8\%$.

12.3 Results and Discussions

Before proceeding to the discussion of the problems considered here, we note that the results of studies of the effect of the violation of the symmetry of the reinforcement relative to the axis on the fracture resistance and on the deformation behavior of thin-walled glass-plastic tubular elements subjected to repeated-static internal hydrostatic pressure were considered in detail in paper [5]. Selected data from this work required for their analysis from the standpoint of formulating some practical recommendations on the optimal design of thin-walled structural tubular elements made of reinforced plastics subjected to repeated-static (low-cycle pulsating) internal pressure are brought here.

As the test results showed, and this was noted in the above-mentioned work [5], the difference in the values of resistance to destruction of pipes with initially broken reinforcement symmetry ($\varphi = 6-8^\circ$) and symmetrically reinforced ($\varphi = 0^\circ$) subjected to internal hydrostatic pressure turns out not to be significant. The average value of this characteristic for both mentioned types of glass-plastic tubular elements can be taken equal to 424.9 MPa.

When carrying out studies of deformation behavior in the process of cyclic testing by internal hydrostatic pressure of the above-mentioned both batches of glass-plastic pipes for all cycles of loading–unloading, the data taken from the corresponding indicators (Fig. 12.1) were processed and the approximating curves were constructed according to Eq. (12.2). These results obtained for I, II, III, and VI test cycles are shown in Fig. 12.2.

From the data in Fig. 12.2 pointed out in paper [5], in addition to the main cyclic circumferential deformations, glass-plastic pipes with the reinforcement angle $\varphi = 0^\circ$ subjected to repeated-static internal hydrostatic pressure have experienced cyclic longitudinal deformations accompanying the main ones also (Fig. 12.2a), and pipes with $\varphi = 6-8^\circ$ have experienced accompanying cyclic shear deformations as well (Fig. 12.2b). At the same time, during the entire process of a step-by-step increase of the internal hydrostatic pressure level in pipes with both mentioned reinforcement angles or during the process of a step-by-step decrease of the internal hydrostatic pressure level in pipes with both mentioned reinforcement angles, the branches of the hysteresis loop retain the direction of convexity or concavity, and the discrepancy between the ascending and descending branches of the hysteresis loops of the same deformations is gradually reduced.

Changes of the energy dissipation coefficients ψ depending on the duration of the repeated-static internal hydrostatic pressure of both types of glass-plastic pipes mentioned above can be analyzed from the data presented in Fig. 12.3.

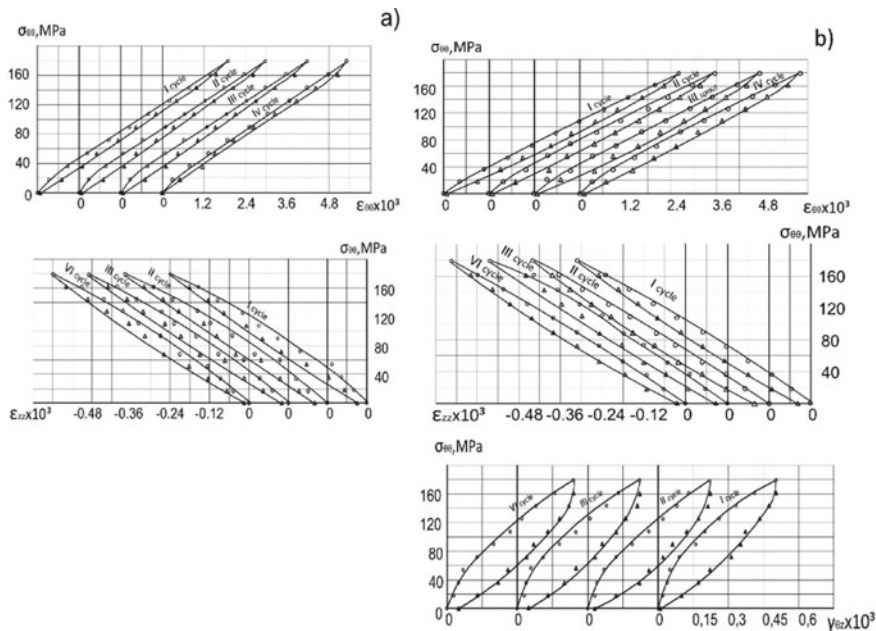


Fig. 12.2 Deformation diagrams of pipes $\varphi = 0^\circ$ (a) and $\varphi = 6-8^\circ$ (b) within the cycle in loading-unloading mode subjected to internal hydrostatic pressure

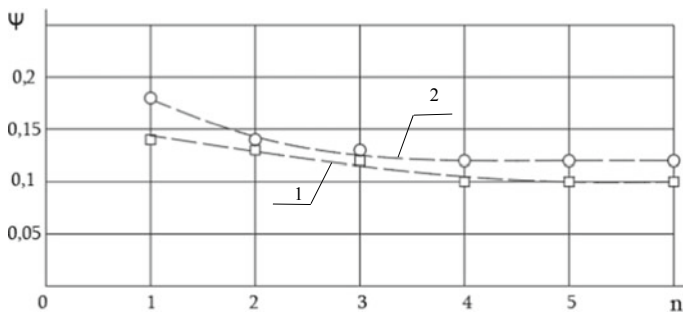


Fig. 12.3 Curves describing changes of the coefficient ψ of glass-plastic pipes with reinforcement angle $\varphi = 0^\circ$ (curve 1) and $\varphi = 6-8^\circ$ (curve 2) depending on the cycle number n of the test for repeated-static internal hydrostatic pressure

From this figure, the marks show the results calculated according to Eq. (12.1), using the experimentally established corresponding data in comparison with the curves approximating these results, we notice that the initial increase in the number of cycles n to 4th leads to a monotonous decrease with decreasing rate of the coefficient ψ defined for both pipes batches with reinforcement angle $\varphi = 0^\circ$ and at angle $\varphi = 6-8^\circ$. With a further increase in the number of cycles n until the end of the cyclic

tests, the change in the value of the coefficient ψ for both batches of mentioned fiberglass pipes is practically not observed (Fig. 12.3). At the same time, it is noted that the ratio of the values of the coefficient ψ determined for I and VI test cycles practically does not depend on the value of the reinforcement angle φ of pipes and equals 1.4–1.5.

The comparisons of the data in Fig. 12.3 show that after 2–3 cycles of loading–unloading by internal pressure, the value of the ratio of the coefficients ψ of pipes with reinforcement angles $\varphi = 6\text{--}8^\circ$ and $\varphi = 0^\circ$ defined for the same cycle number n , practically does not change and is approximately 1.2. That is, for the type of cyclic loading considered here, after the stabilization of the deformation process (after 2–3 cycles of loading–unloading), the amount of energy dissipation in thin-walled glass-plastic pipes with initially broken reinforcement symmetry turns out to be 20% (and more) greater than the value of the same characteristic determined for practically similar pipes, however, reinforced symmetrically relative to the axis.

As already noted, subjected to cyclic loading by internal hydrostatic pressure, for thin-walled glass-plastic pipes with initially broken symmetry of reinforcement relative to the axis ($\varphi = 6\text{--}8^\circ$), in addition to the main cyclic circumferential deformations ($\varepsilon_{\theta\theta}$), cyclic shear deformations ($\gamma_{\theta z}$), as well as, longitudinal (ε_{zz}) deformations accompanying the main circumferential ones are arising. Proceeding from this, we consider to be acceptable the values of the energy dissipation coefficient of the cycle of these pipes, defined according to (1) for all test cycles, and presented in Fig. 12.3 by marks (in the further presentation at the text, they will conventionally be called the total energy dissipation coefficients of the cycle observed during repeated static internal hydrostatic pressure of pipes and will be denoted by $\psi_{H,\text{sum}}$) separate into corresponding summand components and figure in the following form:

$$\psi_{H,\text{sum}} = \psi_{H,\theta\theta} + \psi_{H,\theta z} + \psi_{H,zz} \quad (12.3)$$

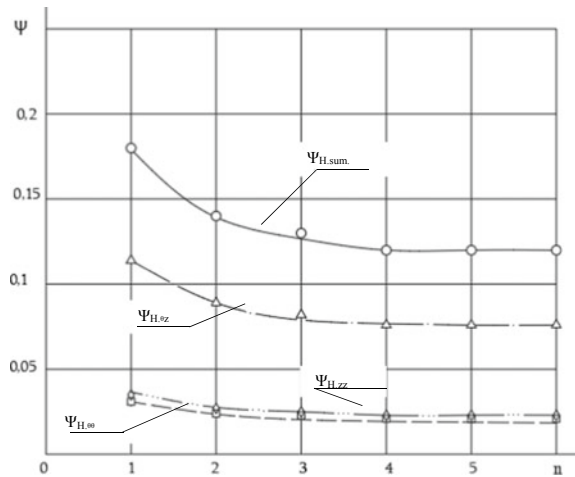
Into Eq. (12.3), $\psi_{H,\theta\theta}$, $\psi_{H,\theta z}$, and $\psi_{H,zz}$ are the values of the energy dissipation coefficients per cycle arising, respectively, from the main circumferential deformations, and from shear and longitudinal deformations accompanying the main deformations.

Approximation curves describing changes of the total energy dissipation coefficient of the cycle and its summand components determined on the basis of experimental data, respectively, according to Eq. (12.1) and using functions of type (1) depending on the cycle number n of loading–unloading by the internal pressure of pipes with $\varphi = 6\text{--}8^\circ$ are shown in Fig. 12.4.

From the data of this figure, it can be noticed that the curves describing the changes in both the total energy dissipation coefficient and the terms of the components of this coefficient, depending on the cycle number n of testing pipes, are practically similar. This indicates that the experimentally established regularity noted above, related to the behavior of the total energy dissipation coefficient $\psi_{H,\text{sum}}$ in the process of cyclic loading by internal pressure, can be considered acceptable for the cases of behavior of the terms of its components $\psi_{H,\theta\theta}$, $\psi_{H,\theta z}$, and $\psi_{H,zz}$.

It should be noted that the phenomenon of similarity of curves describing changes of the total energy dissipation coefficients and summand coefficients depending on

Fig. 12.4 Curves describing the changes of the total energy dissipation coefficient of the cycle and its summand coefficients depending on the cycle number n of testing the pipe with $\varphi = 6-8^\circ$ subjected to repeated-static internal hydrostatic pressure



the number of the loading–unloading cycle was also found in cases of testing for cyclic axial tension and simple torsion of thin-walled glass-plastic pipes with initially broken symmetry of the reinforcement relative to the axis [6].

From the comparison of the data in Fig. 12.4, it follows that the value of the ratios $\psi_{H.\theta z}/\psi_{H.sum}$, $\psi_{H.zz}/\psi_{H.sum}$ and $\psi_{H.zz}/\psi_{H.\theta z}$, determined for the same loading–unloading cycle number of thin-walled glass-plastic pipes with $\varphi = 6-8^\circ$ subjected to internal pressure, practically does not depend on the number of test cycle n and equals approximately to 0.17, 0.63 and 0.19, respectively. That is, in the range of cyclic loading of these pipes by internal pressure considered here, regardless of the number of the loading–unloading cycle, the amount of energy loss due to the occurrence of cyclic shear and longitudinal deformations accompanying cyclic main circumferential deformations turns out to be approximately 270 and 12% more than the amount of the energy loss arising from the main deformations, respectively.

12.4 Conclusions

Thus, a possible violation of the symmetry of the reinforcement relative to the axis occurred during the manufacturing process by winding thin-walled glass-plastic pipes in such a way that the directions of the warp fibers of the fabric and the axis of the pipes coincide, can cause very significant cyclic shear and significant axial deformations that accompany the main cyclic circumferential deformations of the pipes subjected to repeated-static (low-cycle pulsating) internal hydrostatic pressure.

It can be argued with a higher probability that a phenomenon similar to the one mentioned above will also be observed at low-cycle pulsating internal pressure of tubular elements made of reinforced plastics with initially broken symmetry of reinforcement relative to the axis, manufactured by the cross-winding method.

Under the conditions of low-cycle pulsating internal pressure into thin-walled pipes made of reinforced plastics with initially broken reinforcement symmetry relative to the axis, the value of the energy dissipation coefficient arising from shear deformations accompanying the main circumferential deformations significantly exceeds the values of the energy dissipation coefficients arising from both the main deformations themselves and from accompanying main circumferential deformations. In this case, the difference in the values of the mentioned energy dissipation coefficients practically does not depend on the duration of the internal pressure pulsation in the pipes.

The foregoing indicates that at the condition of pulsating internal pressure in pipes made of reinforced composites, the loading of the composite matrix occurred the weak link of the material, is more intense than the loading of the fibers reinforcing the material. As noted in [14], in most cases, it is the destruction of the matrix or the interface between the reinforcing component and the matrix, and not the destruction of the reinforcing fibers, that is the cause of the premature failure of structures made of reinforced composites.

A constructive method for solving the problem can be one of the ways to prevent the influence of defects in the macrostructure of reinforced composites, including the disorientation of reinforcement, on the reliable operation of structural elements made of such materials [15]. In particular, for composite thin-walled tubular elements, it is advisable to provide stiffeners oriented in such a way as to create the maximum obstacle to the deformation of the elements in one direction or another [15].

Given approach mentioned above is quite acceptable for thin-walled composite tubular structural elements with the lowest dissipative characteristics design, operating under conditions of pulsating internal pressure. Namely, it is advisable to orient the direction of the provided stiffeners in such a way as to create maximum resistance to the formation of shear deformations at the stage of these pipes design.

References

1. Tarnopolsky, Yu.M., Rose, A.V., Portnov, G.G.: Negative properties of materials reinforced with fibers. *Mech. Polymers*. **N1**, 140–149 (1963)
2. Ermolenko, S.F., Ermolenko, A.F.: Strength of a layered package with random deviations in reinforcement schemes. *Mech. Compos. Mater*. **N1**, 40–44 (1991)
3. Zhigun, I.G., Polyakov, V.A.: *Properties of Spatially Reinforced Plastics*. Zinatne, Riga (1978)
4. Karapetyan, K.A.: On the strength and deformation properties of fiberglass pipes under repeated static loading depending on the deviation of the reinforcement orientation. *Proc. NAS Armenia. Mech.* **54**(2), 70–79 (2001)
5. Karapetyan, K.A., Valesyan, S.S., Muradyan, N.S.: The dependence of the deformation behavior of fiberglass pipes on the initial disorientation of reinforcement subjected to repeated-static internal hydrostatic pressure and axial tension. *J. Phys.: Conf. Series* **2231**, 012015 (2022) (scopus)
6. Karapetyan, K.A., Valesyan, S.S.: About the coefficient of energy dissipation of fiberglass tubular elements with initially upset the symmetry of the reinforcement with respect to the axis. In: *Proceedings of VII International Conference on Topical Problems of Continuum Mechanics*, pp. 124–128. Armenia, Tzaghkadzor

7. Pagano, N.J., Whitney, J.M.: Geometric design of composite cylindrical characterization specimens. *J Compos. Mater.* 360–378 (1970)
8. Martirosyan, M.M.: Manufacturing pressed thin-walled pipes from fiberglass. *Ind. Armenia* **10**, 56–57 (1971)
9. Martynova, A.A., Yatchenko, O.F., Vasiliev, A.V.: *Fabric Manufacturing Technology*, p. 304p. Academy, Moscow (2007)
10. Karapetyan, K.A., Valesyan, S.S., Muradyan, N.S.: The dependence of the deformability and fracture of glass-plastic pipes on the initial torsion subjected to internal pressure. *Proc. NAS Armenia. Mech.* **72**(1), 49–61 (2019)
11. Davidenkov, N.N.: On the dissipation of energy during vibrations. *J. Tech. Phys. (JTF). T.* **8**(6), 483–499 (1938)
12. Ilyushin, A.A.: *Plasticity*. Gostekhizdat, Moscow-Leningrad (1948)
13. Kachanov, L.M.: *Fundamentals of the theory of plasticity*. M.: Sci. 470p (1969)
14. Hahn, H.T.: Note on determination of the shear stress-strain response of unidirectional composites. *J. Compos. Mater.*, N **7**, 383–386 (1973)
15. Karapetyan, K.A., Valesyan, S.S., Muradyan, N.S.: The influence of the reinforcement disorientation on the deformative behavior and resistance to fracture of the glass-plastic tubes subjected to the axial tension and inner hydrostatic pressure. *Proc. NAS Armenia, Mech.* **71**(N3), 36–43 (2018)

Chapter 13

Contact Problem for Coated Viscoelastic Tube and Rigid Inserts with Complex Profiles



Kirill E. Kazakov

Abstract The article describes the construction of a solution for the problem of the interaction of a viscoelastic aging pipe with an internal thin elastic coating and several different rigid cylindrical inserts, assuming that the profiles of the contacting surfaces are described by rapidly changing functions. The solution method used makes it possible to construct a solution that takes into account both the rheological properties of the pipe and the complex profiles of bodies. Using this method, expressions are obtained for contact pressures in which the features are highlighted by separate terms and multipliers, which allows real calculations to be performed with high accuracy even when holding a small number of members of an infinite series.

Keywords Contact problem · Aging material · Pipe · Coating · Complex profiles · System of integral equations

13.1 Introduction

Pipelines are used in industry to transport various media, such as gas or liquid. Their designs must take into account many different factors: internal and external pressures, temperature effects, possible vibrations, etc. One of the reasons for using multilayer pipes is that some layers are responsible, for example, for the bearing capacity of the pipe, while others protect against aggressive environments. Different sections of pipelines must be connected to each other using various devices. These can be couplings, inserts, etc. Moreover, such devices may be required in other cases, for example, rigid inserts can serve as reinforcing elements of the pipe; the presence of couplings in some areas can reduce vibrations. However, stresses and deformations occur at the attachment points of these elements, which must be calculated, including taking into account both the rheological properties of bodies and their complex shapes

K. E. Kazakov (✉)

Ishlinsky Institute for Problems in Mechanics of the Russian Academy of Sciences, Vernadskogo Ave 101 Bldg 1, Moscow 119526, Russian Federation
e-mail: kazakov@ipmnet.ru

and properties that have arisen, for example, due to the peculiarities of obtaining such bodies (see, for example, [1]).

This article discusses the formulation and construction of an analytical solution for the problem of the interaction of a pipe with a thin inner coating and several rigid inserts. The resulting solution takes into account both the rheological properties of the pipe layers and the complex shapes of the contacting surfaces.

13.2 Problem Formulation and Mathematical Model

Suppose there is a long cylindrical axisymmetric pipe through which a liquid or gas is pumped under relatively low pressure. In order for the pumped substance not to destroy the main bearing layer of the pipe, the pipe is covered from the inside with an additional thin protective layer. Due to the peculiarities of the application of this layer, it can have a variable thickness. Rigid cylindrical inserts are used to strengthen the pipe in a number of places. In order to prevent their horizontal movement, they have a variable diameter. These inserts are placed inside the pipe so that the inserts are completely adjacent to the inner layer of the pipe, and the contact areas coincide with the lengths of the inserts. Schematically, such an interaction is shown in the Fig. 13.1.

It is necessary to determine the levels of contact stresses under the assumption that these stresses significantly exceed the stresses caused by the internal pressure of the medium being transported and/or the external environment. It is also necessary to take into account the possible proximity of the inserts from each other.

First of all, let us formulate the main assumptions:

1. The pipe layers are homogeneous.
2. The pipe layers can be made of viscoelastic aging materials. As a result, stress levels will change over time.
3. The protective layer of the pipe is softer than the main layer.
4. The thickness of the protective layer is much smaller than all other linear dimensions: radii, thickness of the outer layer, lengths of inserts.

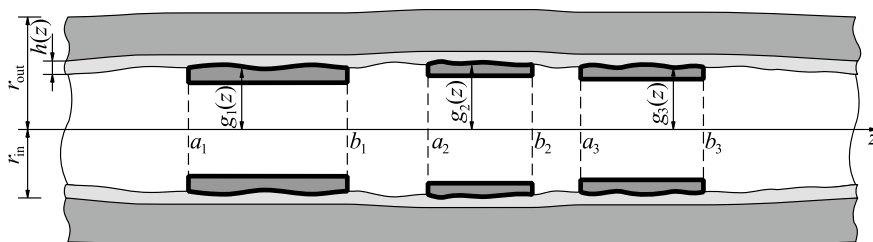


Fig. 13.1 Contact interaction of tube and several rigid inserts

5. Variable insert diameters and coating thickness are described by a relatively smooth function (the tangents of the angles of inclination of the surfaces are much less than 1, see [2]).
6. There is smooth contact between the layers and between the protective layer and the inserts.
7. It is assumed that plastic deformations do not occur as a result of such interaction.

The results of the studies presented in [3, 4] and generalizations to the case of a coating of variable thickness show that unknown contact pressures $q_1(z, t)$, ..., $q_n(z, t)$ in the interaction regions $[a_1, b_1]$, ..., $[a_n, b_n]$ (n is number of inserts) can be found from the following system of equations

$$\left\{ \begin{array}{l}
 h(z)(1 - \nu_{\text{in}}^2) \left[\frac{q_1(z, t)}{E_{\text{in}}(t - \tau_{\text{in}})} - \int_{\tau_0}^t \frac{K_{\text{in}}(t - \tau_{\text{in}}, \tau - \tau_{\text{in}}) q_1(z, \tau)}{E_{\text{in}}(\tau - \tau_{\text{in}})} d\tau \right] \\
 + \frac{2(1 - \nu_{\text{out}}^2)}{\pi} \sum_{j=1}^n \int_{a_j}^{b_j} k_c \left(\frac{z - \zeta}{r_{\text{in}}} \right) \left[\frac{q_j(\zeta, t)}{E_{\text{out}}(t - \tau_{\text{out}})} \right. \\
 \left. - \int_{\tau_0}^t \frac{K_{\text{out}}(t - \tau_{\text{out}}, \tau - \tau_{\text{out}}) q_j(\zeta, \tau)}{E_{\text{out}}(\tau - \tau_{\text{out}})} d\tau \right] d\zeta \\
 = g_1(z) - [r_{\text{in}} - h(z)], \quad a_1 \leq z \leq b_1, \quad t \geq \tau_0, \\
 \dots \\
 h(z)(1 - \nu_{\text{in}}^2) \left[\frac{q_n(z, t)}{E_{\text{in}}(t - \tau_{\text{in}})} - \int_{\tau_0}^t \frac{K_{\text{in}}(t - \tau_{\text{in}}, \tau - \tau_{\text{in}}) q_n(z, \tau)}{E_{\text{in}}(\tau - \tau_{\text{in}})} d\tau \right] \\
 + \frac{2(1 - \nu_{\text{out}}^2)}{\pi} \sum_{j=1}^n \int_{a_j}^{b_j} k_c \left(\frac{z - \zeta}{r_{\text{in}}} \right) \left[\frac{q_j(\zeta, t)}{E_{\text{out}}(t - \tau_{\text{out}})} \right. \\
 \left. - \int_{\tau_0}^t \frac{K_{\text{out}}(t - \tau_{\text{out}}, \tau - \tau_{\text{out}}) q_j(\zeta, \tau)}{E_{\text{out}}(\tau - \tau_{\text{out}})} d\tau \right] d\zeta \\
 = g_n(z) - [r_{\text{in}} - h(z)], \quad a_n \leq z \leq b_n, \quad t \geq \tau_0.
 \end{array} \right. \quad (13.1)$$

The following designations are introduced in this system: r_{in} is inner radius of main layer (or outer radius of protecting layer); $h(z)$ is protecting layer thickness; $g_1(z)$, ..., $g_n(z)$ are outer radii of inserts; a_1 , ..., a_n are left z -coordinates of inserts; b_1 , ..., b_n are right z -coordinates of inserts; τ_{in} and τ_{out} are production times of layers; τ_0 is the time at which the inserts are placed inside the two-layer pipe (the time of the

beginning of the interaction); $\tau_0 \geq \tau_{in}$ and $\tau_0 \geq \tau_{out}$; ν_{in} and ν_{out} are Poisson's ratios of layers (it is assumed that they do not change over time); $E_{in}(t)$ and $E_{out}(t)$ are time-dependent Young's modules; $K_{in}(t, \tau)$ and K_{out} are creep kernels of layers [4, 5]; $k_c(z)$ is kernel of cylindrical contact problem [3, 4]

$$k_c(z) = \int_0^{\infty} L(s)s^{-1} \cos(zs)ds, \quad (13.2)$$

where

$$\begin{aligned} L(s) &= S(s)s^{-1}[c_r^{-1} - c_r s^2 C^2(s) + T(c_r, s)D^2(s)], \\ T(r, s) &= 2r^{-1}(1 - \nu_{out}) + s^2 r, \quad c_r = r_{out}r_{in}^{-1}, \\ S(s) &= c_r^{-1}T(1, s) + T(c_r, s) + c_r s^4 A^2(s) - s^2 T(c_r, s)B^2(s) \\ &\quad - c_r s^2 T(1, s)C^2(s) + T(1, s)T(c_r, s)D^2(s), \\ A(s) &= I_0(s)K_0(c_r s) - I_0(c_r s)K_0(s), \quad B(s) = I_0(s)K_1(c_r s) + I_1(c_r s)K_0(s), \\ C(s) &= I_0(c_r s)K_1(s) + I_1(s)K_0(c_r s), \quad D(s) = I_1(s)K_1(c_r s) - I_1(c_r s)K_1(s). \end{aligned} \quad (13.3)$$

Here r_{out} is outer radius of main layer, $I_0(s)$, $I_1(s)$, $K_0(s)$, $K_1(s)$ are modified Bessel functions of first and second kind.

The system of equations (13.1) can be reduced to the following dimensionless form

$$\left\{ \begin{aligned} &c^*(t^*)(\mathbf{I} - \mathbf{V}_{in}^*)D^{1*}(z^*)q^{1*}(z^*, t^*) + (\mathbf{I} - \mathbf{V}_{out}^*) \sum_{j=1}^n \mathbf{F}^{1j*} q^{j*}(z^*, t^*) \\ &= \delta^{1*}(z^*), \quad -1 \leq z^* \leq 1, \quad t^* \geq 1, \\ &\dots \\ &c^*(t^*)(\mathbf{I} - \mathbf{V}_{in}^*)D^{n*}(z^*)q^{n*}(z^*, t^*) + (\mathbf{I} - \mathbf{V}_{out}^*) \sum_{j=1}^n \mathbf{F}^{nj*} q^{j*}(z^*, t^*) \\ &= \delta^{n*}(z^*), \quad -1 \leq z^* \leq 1, \quad t^* \geq 1, \end{aligned} \right. \quad (13.4)$$

using the following notation

$$\begin{aligned}
z^* &= 2l_i^{-1}(z - m_i), \quad \zeta^* = 2l_j^{-1}(\zeta - m_j), \quad t^* = t\tau_0^{-1}, \quad \tau^* = \tau\tau_0^{-1}, \\
\tau_{in}^* &= \tau_{in}\tau_0^{-1}, \quad \tau_{out}^* = \tau_{out}\tau_0^{-1}, \quad \delta^{i*}(z^*) = 2l_{\min}^{-1}\{g_i(z) - [r_{in} - h(z)]\}, \\
c^*(t^*) &= E_{out}(t - \tau_{out})E_{in}^{-1}(t - \tau_{in}), \\
q^{i*}(z^*, t^*) &= \frac{2l_i(1 - \nu_{out}^2)q_i(z, t)}{l_{\min}E_{out}(t - \tau_{out})}, \quad D^{i*}(z^*) = \frac{1 - \nu_{in}^2}{1 - \nu_{out}^2} \frac{h(z)}{l_i}, \\
\mathbf{V}_{in}^* y(t^*) &= \int_1^{t^*} K_{in}^*(t^*, \tau^*) y(\tau^*) d\tau^*, \quad \mathbf{V}_{out}^* y(t^*) = \int_1^{t^*} K_{out}^*(t^*, \tau^*) y(\tau^*) d\tau^*, \\
K_{in}^*(t^*, \tau^*) &= \frac{E_{in}(t - \tau_{in})E_{out}(\tau - \tau_{out})}{E_{in}(\tau - \tau_{in})E_{out}(t - \tau_{out})} K_{in}(t - \tau_{in}, \tau - \tau_{in})\tau_0, \\
K_{out} &= K_{out}(t - \tau_{out}, \tau - \tau_{out})\tau_0, \\
\mathbf{F}^{ij*} y(z^*) &= \int_{-1}^1 k^{ij*}(z^*, \zeta^*) y(\zeta^*) d\zeta^*, \quad k^{ij*}(z^*, \zeta^*) = \frac{1}{\pi} k_c \left(\frac{z - \zeta}{r_{in}} \right), \\
a_i &\leq z \leq b_i, \quad a_j \leq \zeta \leq b_j, \quad i, j = 1, 2, \dots, n, \quad t \geq \tau_0.
\end{aligned} \tag{13.5}$$

In these equations $l_i = b_i - a_i$ is length of i -th insert, $m_i = \frac{1}{2}(a_i + b_i)$ is its midpoint, $l_{\min} = \min_{i=1,2,\dots,n} l_i$.

If vector-functions, matrix-functions, and matrix operators are introduced into circulation

$$\begin{aligned}
\mathbf{q}^*(z^*, t^*) &= \begin{pmatrix} q^{1*}(z^*, t^*) \\ q^{2*}(z^*, t^*) \\ \vdots \\ q^{n*}(z^*, t^*) \end{pmatrix}, \quad \delta^*(z^*) = \begin{pmatrix} \delta^{1*}(z^*) \\ \delta^{2*}(z^*) \\ \vdots \\ \delta^{n*}(z^*) \end{pmatrix}, \\
\mathbf{D}^*(z^*) &= \begin{pmatrix} D^{1*}(z^*) & 0 & \dots & 0 \\ 0 & D^{2*}(z^*) & \dots & 0 \\ \vdots & \vdots & \ddots & \vdots \\ 0 & 0 & \dots & D^{n*}(z^*) \end{pmatrix} \\
\mathbf{F}^* &= \begin{pmatrix} \mathbf{F}^{11*} & \mathbf{F}^{12*} & \dots & \mathbf{F}^{1n*} \\ \mathbf{F}^{21*} & \mathbf{F}^{22*} & \dots & \mathbf{F}^{2n*} \\ \vdots & \vdots & \ddots & \vdots \\ \mathbf{F}^{n1*} & \mathbf{F}^{n2*} & \dots & \mathbf{F}^{nn*} \end{pmatrix}
\end{aligned} \tag{13.6}$$

then, system (13.4) can be represented in the following compact form

$$\begin{aligned}
c^*(t^*)(\mathbf{I} - \mathbf{V}_{in}^*)\mathbf{D}^*(z^*)\mathbf{q}^*(z^*, t^*) + (\mathbf{I} - \mathbf{V}_{out}^*)\mathbf{F}^*\mathbf{q}^*(z^*, t^*) &= \delta^*(z^*), \\
-1 &\leq z^* \leq 1, \quad t^* \geq 1.
\end{aligned} \tag{13.7}$$

Thus, finding the contact pressure levels reduces to the need to solve the operator equation (13.7) and then transform the solution using (13.5) and (13.6).

13.3 Getting an Analytical Solution

Consider carefully the operator equation (13.7). It has two essential features.

1. The equation includes integral operators of various types:
 - a. Volterra operators with variable integration limits, the presence of which is associated with viscoelasticity and aging of layers;
 - b. Fredholm operator, which arises when solving a boundary value problem for a thick circular cylindrical layer, the results of which are used in constructing a mathematical model of this problem.
2. The equation contains functions describing the profiles of the contacting surfaces. Such a functions can be rapidly changing, which must be taken into account when building a solution.

These features do not allow the use of standard known approaches, as they lead to significant errors when performing real calculations (see [6]), which is due to the limitations of the mantissa in calculations. If standard methods are applied even for the case when all radii are constant (there are no rapidly changing functions), then standard methods lead to the need to solve an infinite system of linear equations, the fully filled matrix of which contains Volterra operators in all cells. Therefore, in the problem under consideration, it is necessary to use a special approach that effectively takes into account “bad” functions, and allows you to build an equation solution with operators of various types.

First of all, let us consider the structure of equation (13.7). Note that when solving the problem of the plane contact of the punch system and the layer with a coating in [7], the system was absolutely the same in appearance [expressions (13.4)]. Despite the fact that the kernel $k_{pl}(x)$ of the Fredholm operator, of course, was different, its properties were similar to those of the Fredholm operator $k_c(z)$ in the problem under consideration:

- functions $L(s)$ has similar asymptotics: $\lim_{s \rightarrow \infty} L(s) = 1$, $\lim_{s \rightarrow 0} L(s) = 0$, $\lim_{s \rightarrow 0} [L(s)s^{-1}] = \text{const}$;
- Fredholm operators are symmetric and positive definite.

These facts allow us to use the solution obtained in [7] to write out the solution of our problem. We will first indicate the main features of the method used in constructing this solution (and described in [7]), and then, we will write out the solution itself.

- Step 1. It is necessary to introduce new unknown vector-function according to the formula

$$\tilde{\mathbf{q}}(z^*, t^*) = -c^\circ(t^*)\mathbf{D}^{-1/2*}(z^*) \cdot \boldsymbol{\delta}^*(z^*) + \mathbf{D}^{1/2*}(z^*) \cdot \mathbf{q}^*(z^*, t^*), \quad (13.8)$$

where $c^\circ(t^*) = (\mathbf{I} - \mathbf{V}_{\text{in}}^*)^{-1}[c^*(t^*)]^{-1}$ and

$$\mathbf{D}^{-1/2*}(z^*) = \begin{pmatrix} \frac{1}{\sqrt{D^{1*}(z^*)}} & 0 & \cdots & 0 \\ 0 & \frac{1}{\sqrt{D^{2*}(z^*)}} & \cdots & 0 \\ \vdots & \vdots & \ddots & \vdots \\ 0 & 0 & \cdots & \frac{1}{\sqrt{D^{n*}(z^*)}} \end{pmatrix}, \quad (13.9)$$

$$\mathbf{D}^{1/2*}(z^*) = \begin{pmatrix} \sqrt{D^{1*}(z^*)} & 0 & \cdots & 0 \\ 0 & \sqrt{D^{2*}(z^*)} & \cdots & 0 \\ \vdots & \vdots & \ddots & \vdots \\ 0 & 0 & \cdots & \sqrt{D^{n*}(z^*)} \end{pmatrix}.$$

Such a replacement will transform the operator equation (13.7) to the form

$$\begin{aligned} c^*(t^*)(\mathbf{I} - \mathbf{V}_{\text{in}}^*)\tilde{\mathbf{q}}(z^*, t^*) + (\mathbf{I} - \mathbf{V}_{\text{out}}^*)\tilde{\mathbf{F}}\tilde{\mathbf{q}}(z^*, t^*) \\ = -(\mathbf{I} - \mathbf{V}_{\text{out}}^*)c^\circ(t^*)\mathbf{D}^{-1/2*}(z^*) \cdot \tilde{\boldsymbol{\delta}}(z^*), \quad -1 \leq z^* \leq 1, \quad t^* \geq 1. \end{aligned} \quad (13.10)$$

Here

$$\begin{aligned} \tilde{\boldsymbol{\delta}}(z^*) &= \mathbf{F}^*(\mathbf{D}^{-1*}(z^*) \cdot \boldsymbol{\delta}^*(z^*)), \\ \tilde{\mathbf{F}}\mathbf{y}(z^*) &= \mathbf{D}^{-1/2*}(z^*) \cdot \mathbf{F}^*(\mathbf{D}^{-1/2*}(z^*) \cdot \mathbf{y}(z^*)), \\ \mathbf{D}^{-1*}(z^*) &= \begin{pmatrix} \frac{1}{D^{1*}(z^*)} & 0 & \cdots & 0 \\ 0 & \frac{1}{D^{2*}(z^*)} & \cdots & 0 \\ \vdots & \vdots & \ddots & \vdots \\ 0 & 0 & \cdots & \frac{1}{D^{n*}(z^*)} \end{pmatrix}. \end{aligned} \quad (13.11)$$

Note that the new Fredholm operator $\tilde{\mathbf{F}}$ is also symmetric and positive definite. Now, unlike the original equation (13.7), the right-hand side of equation (13.11) is “good”, due to the smoothness of the kernels of operator \mathbf{F}^* and hence the smoothness of vector-functions $\tilde{\boldsymbol{\delta}}(z^*)$.

Step 2. The form of the resulting operator equation (13.10) and expressions (13.8) and (13.11) for the function $\tilde{\mathbf{q}}(z^*)$ and the operator $\tilde{\mathbf{F}}$ suggest to us that the solution must be constructed in the Hilbert space $L_2([-1, 1], V)$ in the form of a decomposition according to the basis $\{\mathbf{p}_m^i(z^*)\}_{i=1,2,\dots,n;m=0,1,2,\dots}$ obtained by orthonormalization on $[-1, 1]$ of the following system of linearly independent vector-functions

$$\begin{aligned} & \{\mathbf{D}^{-1/2*}(z^*) \cdot \mathbf{i}^1, z^* \mathbf{D}^{-1/2*}(z^*) \cdot \mathbf{i}^1, (z^*)^2 \mathbf{D}^{-1/2*}(z^*) \cdot \mathbf{i}^1, \dots, \\ & \mathbf{D}^{-1/2*}(z^*) \cdot \mathbf{i}^2, z^* \mathbf{D}^{-1/2*}(z^*) \cdot \mathbf{i}^2, (z^*)^2 \mathbf{D}^{-1/2*}(z^*) \cdot \mathbf{i}^2, \dots, \dots, \quad (13.12) \\ & \mathbf{D}^{-1/2*}(z^*) \cdot \mathbf{i}^n, z^* \mathbf{D}^{-1/2*}(z^*) \cdot \mathbf{i}^n, (z^*)^2 \mathbf{D}^{-1/2*}(z^*) \cdot \mathbf{i}^n, \dots\}. \end{aligned}$$

Here $\mathbf{i}^1, \mathbf{i}^2, \dots, \mathbf{i}^n$ are identity vectors. Thus, it is necessary to construct a special basis $\{\mathbf{p}_m^i(z^*)\}_{i=1,2,\dots,n; m=0,1,2,\dots}$.

Step 3. It is necessary to construct the eigenfunctions of operator $\tilde{\mathbf{F}}$ using obtained basis. This will make it possible to immediately reduce the resulting system of equations for the functional expansion coefficients to a diagonal form. We will give only the final formulas for calculating dimensionless unknown vector-function $\mathbf{q}^*(z^*, t^*)$, since a detailed description of all calculations can be found in [7]

$$\mathbf{q}^*(z^*, t^*) = \mathbf{D}^{-1*}(z^*) \left[c^\circ(t^*) \boldsymbol{\delta}^*(z^*) + \sum_{l=0}^{\infty} z_l(t^*) \sum_{m=0}^{\infty} \sum_{i=1}^n \psi_{lm}^i P_m^{i\circ}(z^*) \mathbf{i}^i \right],$$

$$\begin{aligned} z_k(t^*) &= -(\mathbf{I} + \mathbf{W}_k) \frac{(\mathbf{I} - \mathbf{V}_{\text{out}}^*) c^\circ(t^*)}{c^*(t^*) + \gamma_k} \\ &\times \sum_{i,j=1}^n \sum_{m,l=0}^{\infty} \psi_{km}^i K_{ml}^{ij} \int_{-1}^1 \frac{p_l^{j\circ}(\zeta) \delta^{j*}(\zeta)}{D^{j*}(\zeta)} d\zeta, \end{aligned}$$

$$\mathbf{W}_k y(t^*) = \int_1^{t^*} R_k^*(t^*, \tau^*) y(\tau^*) d\tau^*, \quad d_{k,j} = \begin{vmatrix} J_{0,j} & J_{1,j} & \cdots & J_{k,j} \\ J_{1,j} & J_{2,j} & \cdots & J_{k+1,j} \\ \vdots & \vdots & \ddots & \vdots \\ J_{k,j} & J_{k+1,j} & \cdots & J_{2k,j} \end{vmatrix},$$

$$p_k^{j\circ}(z^*) = \frac{1}{\sqrt{d_{k,j} d_{k-1,j}}} \begin{vmatrix} J_{0,j} & J_{1,j} & \cdots & J_{k,j} \\ J_{1,j} & J_{2,j} & \cdots & J_{k+1,j} \\ \vdots & \vdots & \ddots & \vdots \\ 1 & z^* & \cdots & (z^*)^k \end{vmatrix}, \quad J_{k,j} = \int_{-1}^1 \frac{\zeta^k}{D^{i*}(\zeta)} d\zeta,$$

$$-1 \leq z^* \leq 1, \quad t^* \geq 1, \quad j = 1, 2, \dots, n, \quad k = 0, 1, 2, \dots, \quad (13.13)$$

in which γ_k and ψ_{lm}^i are determined from spectral problem

$$\sum_{j=1}^n \sum_{l=0}^{\infty} K_{ml}^{ij} \psi_{kl}^j = \gamma_k \psi_{km}^i, \quad i = 1, 2, \dots, n \quad k, m = 0, 1, 2, \dots, \quad (13.14)$$

coefficients K_{ml}^{ij} are expansion coefficients of kernel $k^{ij*}(z^*, \zeta^*) [D^{i*}(z^*) D^{j*}(\zeta^*)]^{-1/2}$ in basis $\{\mathbf{p}_m^i(z^*)\}_{i=1,2,\dots,n; m=0,1,2,\dots}$, and $R_k^*(t^*, \tau^*)$ are the resolvents of kernels

$$K_k(t^*, \tau^*) = \frac{c^*(t^*)K_{in}^*(t^*, \tau^*) + \gamma_k K_{out}^*(t^*, \tau^*)}{c^*(t^*) + \gamma_k}. \quad (13.15)$$

Now, using formula (13.13) and change of variables (13.5), it is possible to obtain expressions for contact pressures in the area of interaction of inserts and pipes

$$\begin{aligned} q_i(z, t) &= \frac{g_i(z) - [r_{in} - h(z)] E_{out}(t - \tau_{out})}{h(z)} \frac{E_{out}(t - \tau_{out})}{1 - \nu_{in}^2} (\mathbf{I} - \mathbf{V}_{in}^*)^{-1} \frac{E_{in}(t - \tau_{in})}{E_{out}(t - \tau_{out})} \\ &\quad + \sum_{l=0}^{\infty} f_l(t) \sum_{m=0}^{\infty} \psi_{lm}^i P_m^{i\circ} \left(\frac{2(z - m_i)}{l_i} \right), \quad a_i \leq z \leq b_i, \quad t \geq \tau_0, \\ f_l(t) &= \frac{l_{\min} E_{out}(t - \tau_{out})}{2h(z)(1 - \nu_{in}^2)} z_l \left(\frac{t}{\tau_0} \right), \quad i = 1, 2, \dots, n, \quad l = 0, 1, 2, \dots \end{aligned} \quad (13.16)$$

13.4 Conclusions

The formula for calculating contact pressures in the area of interaction of the pipe with the inner coating is presented in a form in which the functions associated with the thickness of the inner coating, and the profiles of inserts are separated by separate terms and multipliers. This allows calculations to be performed with high accuracy even when these functions are rapidly changing. To achieve sufficiently high accuracy, it is necessary to limit the infinite series to only 20–30 terms, while using other methods of solving this number should differ by more than an order of magnitude, which leads to significant errors due to the limited mantissa of real variables.

It should be noted that the obtained solution allows taking into account both the complex profiles of the contacting surfaces, and the rheological properties of the pipe layers, and the mutual influence of inserts located in close proximity to each other.

Acknowledgements The study was supported by the Government program (contract #AAAA-A20-120011690132-4).

References

1. Technological controlling the contact pressure onto a cylindrical substrate from a coating being formed additionally on its outer surface. AIP Conf. Proc. **2340**, 040005 (2021) <https://doi.org/10.1063/5.0047838>
2. Soldatenkov, I.A.: Wear-Contact Problem with Applications in Engineering Wear Calculations. Fizmatkniga, Moscow (2010) [in Russian]

3. Manzhirrov, A.V., Chernysh, V.A.: Contact problem for a layered inhomogeneous aging cylinder reinforced by a rigid ring. *J. Appl. Mech. Techn. Phys.* **31**(6), 894–900 (1988). <https://doi.org/10.1007/BF00854204>
4. Arutyunyan, NKh., Manzhirrov, A.V.: *Contact Problems in the Theory of Creep*. Izd-vo Inst. Mekhaniki NAN Armenii, Erevan (1999)
5. Arutyunyan, NKh.: *Several Problems of the Theory of Creep*. Gostekhizdat, Moscow, Leningrad (1952) [in Russian]
6. Kazakov, K., Kurdina, S.: Contact problems for bodies with complex coatings. *Math. Meth. Appl. Sci.* **43**(13), 7692–7705 (2020). <https://doi.org/10.1002/mma.6107>
7. Kazakov, K.E., Parshin, D.A.: On the indentation of a system of punches into a layered foundation. *Engng. Lett.* **27**(1), 251–255 (2019)

Chapter 14

Inelastic Behavior of High-Temperature Steel Under Cyclic Loading Conditions



Katharina Knape and Holm Altenbach

Abstract The paper at hand focusses on the constitutive equations to describe the inelastic material behavior of the high-temperature steel X20CrMoV12-1, widely known to be applied for power plant components. Therefore, the purpose is to model its response to a cyclic loading profile under which power plants operate the majority of time. An Armstrong–Frederick type model including a constitutive equation for the inelastic strain rate and an evolution equation for the backstress tensor is considered as basis for the application of the two-time-scale approach. The advantage will be a reduction in computational time while still being able to depict the complete material behavior. The finite element software ABAQUS is used to simulate the creep test as well as the cyclic loading regime of a bar at elevated temperatures.

Keywords Cyclic loading · Frederick–Armstrong model · Two-time-scale approach

14.1 Introduction

Power plants represent one of the most used power generating technologies of today. Their gas turbines are known to have a high performance density so the main purpose is to quickly close the gap between the power generally needed and the power provided through renewable resources. Due to this efficient kind of running, highly frequent start-ups and shut-downs of the system lead to complex mechanical and thermal loading conditions, mechanical loading in the sense of periodic stress and strain states and thermal loading meaning very high surrounding temperatures. Therefore, the high-temperature creep, a slow time-dependent deformation, is the main challenge faced by the material along with the cyclic loading conditions. The combination

K. Knape (✉) · H. Altenbach
Engineering Mechanics, Institute of Mechanics, Otto-von-Guericke-University Magdeburg,
Universitätsplatz 2, 39104 Magdeburg, Germany
e-mail: katharina.knape@ovgu.de

H. Altenbach
e-mail: holm.altenbach@ovgu.de

of both greatly influences the component's life and may lead to failure earlier than expected. To prevent unforeseen events and investment costs, an understanding of the material's behavior and response to certain loading conditions through a reliable simulation is mandatory. In addition, it would be possible to predict the remaining lifetime or adapt the maintenance intervals more precisely.

These computations are very time-consuming. They need time integration procedures with very small time increments in the case of a cycle-by-cycle integration [1]. However, to omit these difficulties, calculation methods including time averaging approaches have been developed within the past years. They can be implemented into the finite element code with the aim of reducing computational time. This work focusses on applying the two-time-scale approach which is already known for the solution of differential equations of dynamical systems [1]. Now, it is also used to simulate inelastic material behavior in a numerically efficient way by differentiating between two time scales, a slow and a fast one, each of them accounting for certain processes [12]. Another technique has for example been suggested in [8], where a wavelet transformation-based multi-time scaling method depicts crystal plasticity. In addition, the cycle jumping method is described in [9] with the intention to model the material's response under periodic loading. Here, internal variables are calculated for as many loading cycles as needed until the integration scheme is stabilized. After that, the rate of change can be estimated for a determined number of cycles avoiding a further cycle-by-cycle integration.

The starting point to achieve the above is a constitutive model as used in [1, 4] which needs to include especially creep, as well as cyclic hardening and softening processes. It can either be a macroscale or microscale model, where for a macroscale-based model, the material parameters are calculated according to experimental data [4] by fitting the curves. With the intention of modeling the inelastic behavior of a realistic gas turbine or shaft, using a microscale model had the advantage of depicting the local deformation better but is numerically much more complex which is why in this paper, a macroscale-model is applied.

The widely known unified constitutive model was firstly used by [7], including an equation to describe the inelastic strain rate tensor and also considering an evolution equation for the backstress tensor. Chaboche picked up the concept and suggested a superposition of several backstress tensors with separate evolution equations [3]. The approach is limited though, since the number of material parameters and hence the complexity of the model is increasing and so is the numerical effort.

The mentioned constitutive models have been successfully applied to predict material behavior under various mechanical and thermal loading conditions, nevertheless, modeling cyclic loading remains challenging [1]. In Sect. 14.2, the equations according to the Armstrong–Frederick model are derived, followed by the explanation of the two-time-scale approach in the third section. The combination of the two is then implemented into the finite element software ABAQUS to model the response of the high-temperature steel X20CrMoV12-1 to small number of loading cycles.

14.2 Two-Time-Scale Technique

The basic idea of the two-time-scale method is the introduction of two different time scales T_0 and T_1 [2, 11, 14] with the aim of reducing the computational time when solving a system of differential equations of the form

$$\frac{d\mathbf{x}}{dt} = \mathbf{X}[t, \mathbf{x}(t)], \quad \mathbf{x}(0) = \mathbf{x}_0 \quad (14.1)$$

where \mathbf{x} represents a set of unknown variables.

The first, slow time scale, is often also called ‘natural time’ or ‘physical time’ and it accounts for quasi-static loading and long-term behavior such as creep, see Eq. (14.2)

$$T_0(t) = t. \quad (14.2)$$

The second, fast or fine time scale, is described using a parameter μ with respect to the total time t_{end}

$$T_1(t) = \tau(t) = \frac{t}{\mu} \quad (14.3)$$

$$\mu = \frac{T}{t_{\text{end}}} \ll 1. \quad (14.4)$$

The total time derivative then yields

$$\frac{d}{dt} = \frac{\delta}{\delta t} + \frac{1}{\mu} \frac{\delta}{\delta \tau}. \quad (14.5)$$

The result of this operation is a system of partial instead of ordinary differential equations which can be solved with an asymptotic series expansion [12] of the set of unknown variables \mathbf{x} with respect to the factor μ

$$\mathbf{x}(t, \tau) = \mathbf{x}^{(0)}(t, \tau) + \mu \mathbf{x}^{(1)}(t, \tau) + \mu^2 \mathbf{x}^{(2)}(t, \tau) + \dots \quad (14.6)$$

Also expanding the right-hand-side of the equation and inserting that into the total time derivative yields a set of differential equations. They can be sorted with respect to the order of μ

$$\mu^{(-1)} : \frac{\delta \mathbf{x}^{(0)}}{\delta \tau} = 0, \quad (14.7)$$

$$\mu^{(0)} : \frac{\delta \mathbf{x}^{(0)}}{\delta t} + \frac{\delta \mathbf{x}^{(1)}}{\delta \tau} = \mathbf{X}(t, \tau, \mathbf{x}^{(0)}), \quad (14.8)$$

$$\mu^{(1)} : \frac{\delta \mathbf{x}^{(1)}}{\delta t} + \frac{\delta \mathbf{x}^{(2)}}{\delta \tau} = \frac{\delta \mathbf{X}(t, \tau, \mathbf{x}^{(0)})}{\delta \mathbf{x}} \mathbf{x}^{(1)}. \quad (14.9)$$

In Eq. (14.7), it can be seen that the mean solution $\mathbf{x}^{(0)}$ is only a function of the slow time scale t .

Now, a time averaging operator has to be applied [1]

$$\langle f(t, \tau) \rangle = \frac{1}{T} \int_0^T f(t, \tau) d\tau \quad (14.10)$$

resulting in the following system of differential equations to calculate the mean solution

$$\frac{d\mathbf{x}^{(0)}}{dt} = \bar{\mathbf{X}}(t, \mathbf{x}^{(0)}). \quad (14.11)$$

The solutions of higher orders of μ may also be calculated according to [14]. Nevertheless, this work focusses only on the mean solution, where the stress tensor takes the following form

$$\boldsymbol{\sigma}(t, \tau) = \boldsymbol{\sigma}^{(0)}(t) + \boldsymbol{\sigma}^{(1)}(\tau) \quad (14.12)$$

with the mean part $\boldsymbol{\sigma}^{(0)}(t)$ and the periodic part $\boldsymbol{\sigma}^{(1)}(\tau)$. The stress deviator and the backstress tensor were also decomposed the same way. The above mentioned method was tested in [1] and now needs to be applied to the material model described in Sect. 14.3.

14.3 Material Model

The material model is supposed to depict elastic and also inelastic behavior. Therefore, the Armstrong–Frederick type constitutive model is applied which includes a constitutive equation for the inelastic strain rate tensor and a nonlinear kinematic hardening rule for the backstress tensor. The material parameters required are already identified in [1, 4] for tempered martensitic steel.

14.3.1 Elastic Behavior

Under the assumption of small strains, the additive decomposition of the strain $\boldsymbol{\varepsilon}$ into an elastic $\boldsymbol{\varepsilon}^{\text{el}}$ and inelastic $\boldsymbol{\varepsilon}^{\text{in}}$ part is considered as the basis

$$\boldsymbol{\varepsilon} = \boldsymbol{\varepsilon}^{\text{el}} + \boldsymbol{\varepsilon}^{\text{in}}. \quad (14.13)$$

In order to define the elastic strain, Hooke's law is applied including the material parameters Young's modulus E , bulk modulus K , shear modulus G , and the Poisson's ratio ν as well as the stress tensor $\boldsymbol{\sigma}$. Here, tr means the trace and \mathbf{I} denotes the unit tensor

$$\boldsymbol{\sigma} = K \text{tr}(\boldsymbol{\varepsilon}^{\text{el}}) \mathbf{I} + 2G\boldsymbol{\varepsilon}^{\text{el}}, \quad (14.14)$$

with

$$K = \frac{E}{3(1-2\nu)}, \quad G = \frac{E}{2(1+\nu)}. \quad (14.15)$$

Taking into account the decomposition of the stress tensor into a spheric σ_m and a deviatoric part $\boldsymbol{\sigma}'$ yields

$$\sigma_m = \frac{1}{3} \text{tr}(\boldsymbol{\sigma}), \quad (14.16)$$

$$\boldsymbol{\sigma}' = \boldsymbol{\sigma} - \sigma_m \mathbf{I}. \quad (14.17)$$

Within this paper, all deviators will be marked with a prime. The equation for the elastic strain can be derived as follows

$$\boldsymbol{\varepsilon}^{\text{el}} = \frac{\sigma_m}{3K} \mathbf{I} + \frac{\boldsymbol{\sigma}'}{2G}. \quad (14.18)$$

14.3.2 Inelastic Behavior

Now, the inelastic strain ε^{in} needs to be determined. It is known that in the case of creep behavior the inelastic strain rate has to be a function of the potential depending on the three invariants J_1 , J_2 , and J_3 of the stress tensor and can therefore be written as

$$\dot{\boldsymbol{\varepsilon}}^{\text{in}} = \frac{\delta\psi(J_1(\boldsymbol{\sigma}'), J_2(\boldsymbol{\sigma}'), J_3(\boldsymbol{\sigma}'))}{\delta\boldsymbol{\sigma}'}. \quad (14.19)$$

Since there is no significant change of volume due to the inelastic deformation, only the stress deviator is considered. The influence of the first and third invariants may be neglected, since for a deviator, the first invariant is equal to zero [4]. The third invariant accounts only for so-called second-order effects in the material belonging to the tensorial-nonlinear behavior [13]. So in the simplest case, the inelastic strain is only dependent on the second invariant of the stress deviator

$$\dot{\boldsymbol{\varepsilon}}^{\text{in}} = \frac{\delta\psi(J_2(\boldsymbol{\sigma}'))}{\delta\boldsymbol{\sigma}'} \quad (14.20)$$

which yields

$$\dot{\boldsymbol{\varepsilon}}^{\text{in}} = \frac{3}{2} \dot{\varepsilon}_{\text{vM}}^{\text{in}} \frac{\boldsymbol{\sigma}'}{\sigma_{\text{vM}}} \quad (14.21)$$

with the von Mises stress σ_{vM}

$$\sigma_{\text{vM}} = \sqrt{\frac{3}{2} \boldsymbol{\sigma}' : \boldsymbol{\sigma}'} \quad (14.22)$$

and the von Mises inelastic strain rate $\dot{\boldsymbol{\varepsilon}}_{\text{vM}}^{\text{in}}$

$$\dot{\boldsymbol{\varepsilon}}_{\text{vM}}^{\text{in}} = \sqrt{\frac{2}{3} \dot{\boldsymbol{\varepsilon}}^{\text{in}} : \dot{\boldsymbol{\varepsilon}}^{\text{in}}}. \quad (14.23)$$

Note that $\boldsymbol{\varepsilon}^{\text{in}}$ is a deviator.

Power plant components are not only subjected to mechanical but also very high thermal loading. To account for the temperature dependency of the inelastic strain rate, a separation ansatz is applied as can be seen in Eq. (14.24). It includes the stress response function f_{σ} and a temperature response function $R(\vartheta)$ depending on the absolute temperature ϑ

$$\dot{\boldsymbol{\varepsilon}}^{\text{in}} = f_{\sigma}(\tilde{\boldsymbol{\sigma}}_{\text{vM}}) R(\vartheta). \quad (14.24)$$

These functions are identified by fitting experimental data of the material under monotonic loading conditions.

Furthermore, the stress deviator is decomposed into an active $\tilde{\boldsymbol{\sigma}}$ and a backstress part $\boldsymbol{\beta}$. The tensor's active part will now be denoted by (...)

$$\boldsymbol{\beta} = \boldsymbol{\sigma}' - \tilde{\boldsymbol{\sigma}}. \quad (14.25)$$

To mathematically describe the backstress tensor, an Armstrong–Frederick type backstress [1] with two material parameters B_i is chosen

$$\dot{\boldsymbol{\beta}} = B_1 \dot{\boldsymbol{\varepsilon}}^{\text{in}} - B_2 \dot{\boldsymbol{\varepsilon}}_{\text{vM}}^{\text{in}} \boldsymbol{\beta}. \quad (14.26)$$

The term containing the von Mises inelastic strain rate is called dynamic recovery term and is known to improve the numerical results [4]. In order to also be able to capture cyclic behavior, the superposition of backstresses according to [3] is used where each of the backstresses has its own evolution equation described in Eq. (14.28)

$$\boldsymbol{\beta} = \sum_{i=1}^n \boldsymbol{\beta}_i, \quad (14.27)$$

$$\dot{\boldsymbol{\beta}}_i = B_1 \dot{\boldsymbol{\varepsilon}}^{\text{in}} - B_2 \dot{\boldsymbol{\varepsilon}}_{\text{vM}}^{\text{in}} \boldsymbol{\beta}_i. \quad (14.28)$$

This approach is limited by the ability of identifying the material parameters needed.

14.3.3 Application of the Two-Time-Scale Approach

The backstress tensor for isothermal loading conditions in particular is shown in [1]

$$\dot{\boldsymbol{\beta}} = \frac{2}{3}R(\vartheta) \left[\dot{\boldsymbol{\epsilon}}^{\text{in}} - \frac{3}{2}\dot{\epsilon}_{\text{vM}} \frac{\boldsymbol{\beta}}{h(\sigma_{\text{vM}}, \vartheta)} \right]. \quad (14.29)$$

Including the before mentioned decomposition (Eq. 14.12) of the variables leads to the set of constitutive equations given in Eqs. (14.30)–(14.33) with $C_h(\vartheta) = 8.84$ [1]

$$\dot{\boldsymbol{\epsilon}}^{\text{in}(0)} = \frac{3}{2}R(\vartheta) \left\langle \frac{f_{\sigma}(\tilde{\sigma}_{\text{vM}})}{\tilde{\sigma}_{\text{vM}}} (\boldsymbol{\sigma}'^{(0)} - \boldsymbol{\beta}^{(0)} + \boldsymbol{\sigma}'^{(1)}) \right\rangle \quad (14.30)$$

$$\dot{\boldsymbol{\beta}}^{(0)} = \frac{2}{3}C_h(\vartheta) \left(\dot{\boldsymbol{\epsilon}}^{\text{in}(0)} - \frac{3}{2}\boldsymbol{\beta}^{(0)} \left\langle \frac{\dot{\epsilon}_{\text{vM}}^{(0)}}{h(\tilde{\sigma}_{\text{vM}}, \vartheta)} \right\rangle \right) \quad (14.31)$$

and

$$\tilde{\sigma}_{\text{vM}} = \sqrt{\frac{3}{2} \text{tr} (\boldsymbol{\sigma}'^{(0)} - \boldsymbol{\beta}^{(0)} + \boldsymbol{\sigma}'^{(1)})^2} \quad (14.32)$$

$$\dot{\epsilon}_{\text{vM}}^{(0)} = \sqrt{\frac{2}{3} \text{tr} (\dot{\boldsymbol{\epsilon}}^{\text{in}(0)})^2}. \quad (14.33)$$

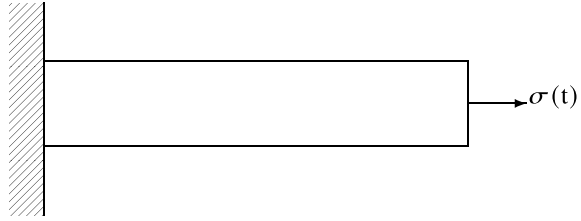
The response functions for high-temperature steel were developed in [10] with the parameters a_0 , α , B , and H_* which should be estimated experimentally

$$R(\vartheta) = a_0 e^{-\frac{\alpha}{\vartheta}}, \quad f(\sigma) = \sinh B\sigma, \quad h(|\sigma|, \vartheta) = H_* |\sigma|. \quad (14.34)$$

14.4 Simulation of the Material Behavior

The simulation of the inelastic material behavior is done using the finite element program ABAQUS. An user-defined subroutine implements the specific material properties of X20CrMoV12-1 [5, 6]. First investigations are done modeling only one single element, now a bar, clamped on one side, is considered as shown in Fig. 14.1.

Fig. 14.1 Schematic model of the bar



14.4.1 Cyclic Loading Condition

Referring to the application of high-temperature steels such as X20CrMoV12-1 in power plants, these components are mostly subjected to cyclic loading. Therefore, a combined uniaxial load of the form described in Eq. (14.12) is considered. In this paper, the stress profile is assumed to be of rectangular shape, as can be seen in Fig. 14.2 with the mean stress $\sigma_m > 0$ and the amplitude $0 < \sigma_a < \sigma_m$. In [10], the material parameters for a surrounding temperature of $\vartheta = 835$ K can be found

$$a_0 = 4.64 \times 10^{23} \frac{1}{\text{h}}, \quad \alpha = 6.12 \times 10^4 \frac{1}{\text{K}}, \quad C_h = 8.84, \quad (14.35)$$

$$B = 7.74 \times 10^{-2} \frac{1}{\text{MPa}}, \quad H_* = 0.46.$$

The loading parameters are chosen as follows

$$\sigma_m = 200 \text{ MPa}, \quad \sigma_a = 10 \text{ MPa} \quad (14.36)$$

for a total simulation time of $t_{\text{end}} = 60$ min.

14.4.2 Results of the Finite Element Simulation

The results of the simulation including the material parameters described before can be seen in Fig. 14.3. The surrounding temperature was set to 873 K which tends to be the operating temperature of a power plant. Additionally, the initial condition of the inelastic and elastic strain being zero was chosen. Figure 14.4 shows the same loading profile but with the mean stress measuring 100 MPa, exactly half of the first simulation. The comparison between both of them can be seen in Fig. 14.5. If the mean stress is increased further from 100 to 200 MPa by steps of 20 MPa, the curve is shifted upward as shown in Fig. 14.6.

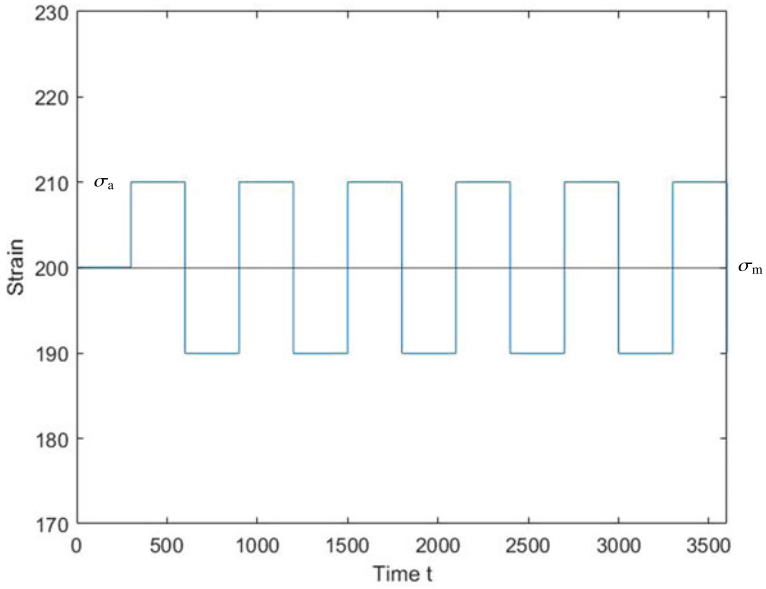


Fig. 14.2 Cyclic loading profile

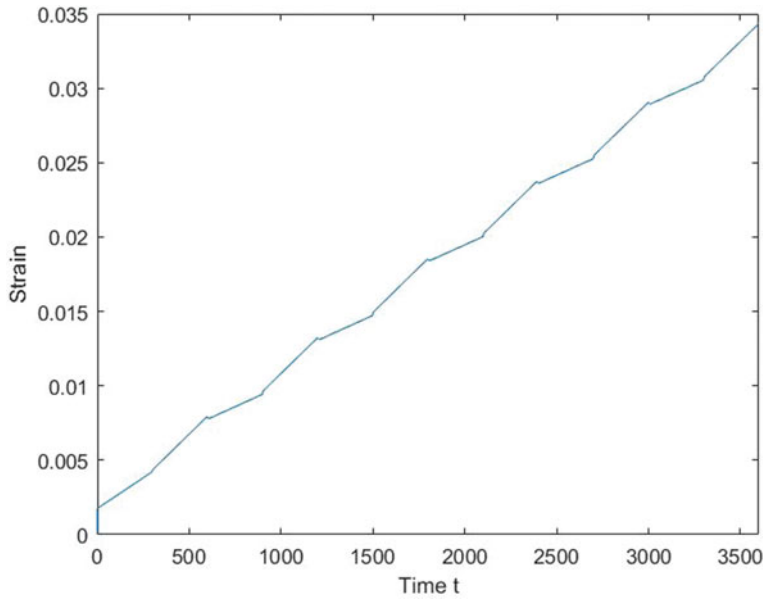


Fig. 14.3 Strain versus time for the given cyclic stress profile

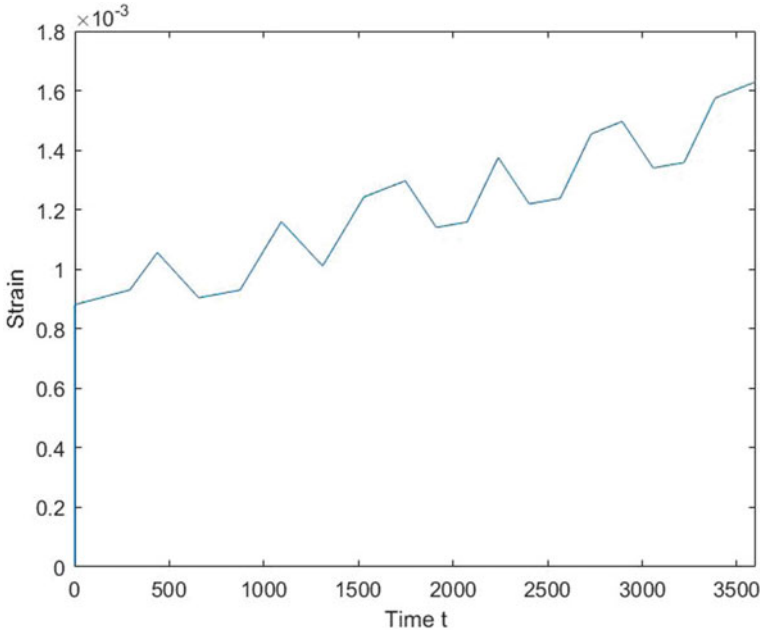


Fig. 14.4 Strain versus time with a mean stress of $\sigma_m = 100$ MPa

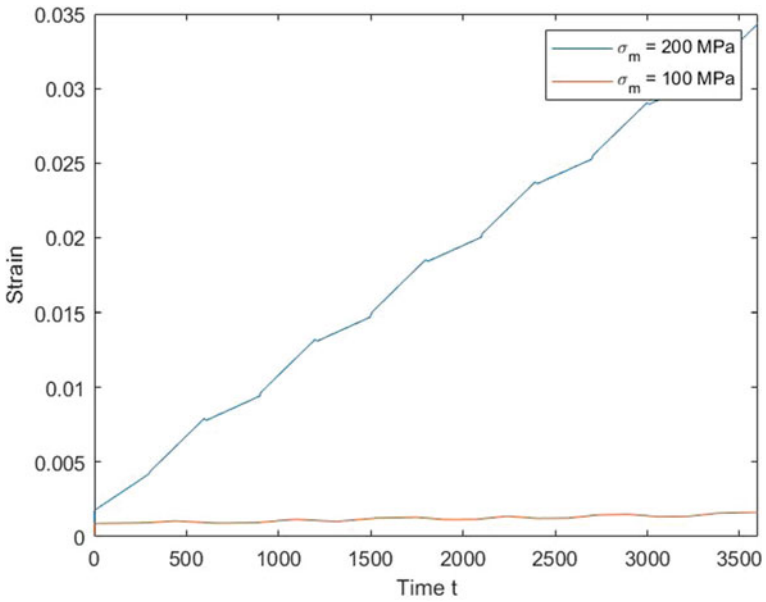


Fig. 14.5 Comparison of the strain versus time curves with the different mean stresses

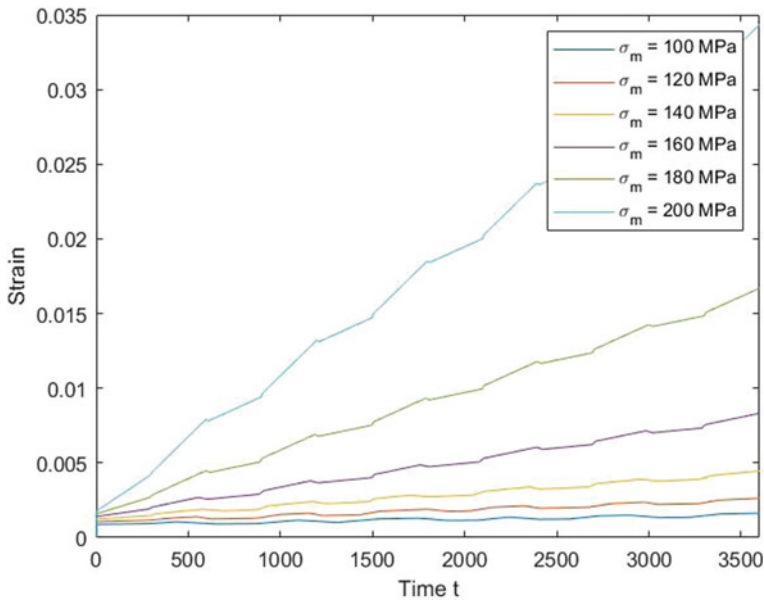


Fig. 14.6 Strain versus time for the given cyclic stress profile

14.5 Conclusion

The aim of this paper was to examine the inelastic material response of high-temperature steel to a cyclic loading profile as it can be found in several real-life applications such as power plants. The widely known Armstrong–Frederick constitutive model was used to model the material behavior. Applying the two-time-scale approach to the derived equations results in a reduction of the computational time needed when the finite element simulation using ABAQUS is carried out.

The applied material model includes the influence of the cyclic loading parameters such as mean stress and stress amplitude depending on the two time scales. The graph showing the strain with respect to time shifts as expected when the magnitude of the load is decreased.

Current and future investigations focus on deriving the constitutive equations and applying the two-time-scale approach also for the inelastic behavior due to thermal cyclic loading conditions or a combination of thermo-mechanical loading.

References

1. Altenbach, H., Breslasky, D., Naumenko, K., Tatarinova, O.: Two-time-scales and time-averaging approaches for the analysis of cyclic creep based on Armstrong-Frederick type constitutive model. *J. Mech. Eng. Sci.* **233**, 1690–1700 (2018)
2. Bensoussan, A., Lions, J.-L., Papanicolaou, G.: *Asymptotic Analysis for Periodic Structures*. North Holland Pub. Co., Amsterdam; American Mathematical Society, New York (1978)
3. Chaboche, J.L.: Constitutive equations for cyclic plasticity and cyclic viscoplasticity. *Int. J. Plast.* **5**, 247–302 (1989)
4. Eisenträger, J.: A framework for modeling the mechanical behavior of tempered martensitic steels at high temperatures. PhD thesis, Otto-von-Guericke-Universität Magdeburg (2018)
5. Eisenträger, J., Naumenko, K., Altenbach, H.: Numerical implementation of a phase mixture model for rate-dependent inelasticity of tempered martensitic steels. *Acta Mech.* **229**, 3051–3068 (2018)
6. Eisenträger, J., Zhang, J., Song, C., Eisenträger, S.: An SBFEM approach for rate-dependent inelasticity with application to image-based analysis. *Int. J. Mech. Sci.* **182**, 105778 (2020)
7. Frederick, C.O., Armstrong, P.J.: A mathematical representation of the multi axial Bauschinger effect. CEGB Report RD/B/N 731, Central Electricity Generating Board. The Report is Reproduced as a Paper: 2007 Materials at High Temperatures, vol. 24, pp. 1–26 (1966)
8. Joseph, D.S., Chakraborty, P., Ghosh, S.: Wavelet transformation based multi-time scaling method for crystal plasticity FE simulations under cyclic loading. *Comput. Methods Appl. Mech. Eng.* **199**, 2177–2194 (2010)
9. Labergere, C., Saanouni, K., Sun, Z.D., Dhifallah, M.H., Li, Y., Duval, Y.L.: Prediction of low cycle fatigue life using cycles jumping integration scheme. *Appl. Mech. Mater.* **784**, 308–316 (2015)
10. Naumenko, K., Altenbach, H., Kutschke, A.: A combined model for hardening, softening, and damage processes in advanced heat resistant steels at elevated temperature. *Int. J. Damage Mech.* **20**, 578–597 (2011)
11. Nayfeh, A.H.: *Introduction to Perturbation Techniques*. Wiley-VCH, New York (1993)
12. Oskay, C., Fish, J.: Fatigue life prediction using 2-scale temporal asymptotic homogenization. *Int. J. Numer. Methods Eng.* **61**, 326–359 (2004)
13. Reiner, M., Abir, D.: *Second Order Effects in Elasticity, Plasticity and Fluid Dynamics*. Pergamon Press, Oxford (1964)
14. Sanders, J.A., Verhulst, F.: *Averaging Methods in Nonlinear Dynamical Systems*. Springer, New York (1985)

Chapter 15

One Case of a Lubrication Problem for a Line Contact of Elastic Solids with Soft Double Coatings



Ilya I. Kudish and Sergei S. Volkov

Abstract The main goal of this paper is to consider formulation and solution of a lubrication problem based on the expressions for elastic surface displacements derived asymptotically from an exact solution for a loaded double coated elastic substrate which are valid within a certain range of the problem input parameters. Based on that, a new relatively simple numerical model of the behavior of lubrication parameters in a line lightly loaded contact of double coated elastic cylinders has been developed. For simplicity materials and coatings of both cylinders are considered identical. The main part of the elastic displacements of the contact surfaces is represented by simple Winkler like contributions. The problem is reduced to a numerical solution of a system of two transcendent equations performed by Newton's method. The formulas for lubrication parameters such as distributions of contact pressure, gap, actual velocity of surface sliding, lubrication film thickness, shear stress, coefficient of friction, and contact energy loss were derived and used for specific calculations. Generally, compared to lubrication parameters in the contact of rigid solids without coatings the effect of the double coating resulted in reduced (up to 40% or more) contact pressure, increased contact area and film thickness as well as some reduction of frictional forces and energy losses. Some specific results for the obtained solutions are provided.

Keywords Line lightly loaded lubricated contacts · Elastic double coatings and substrate · Asymptotic representations for elastic surface displacements

I. I. Kudish (✉)

ILRIMA Consulting, Inc., 19396 Warbler Ln., Millersburg, MI 49759, USA

e-mail: ilyakudish@gmail.com

S. S. Volkov

Laboratory of Functionally Graded and Composite Materials, Research and Education Center Materials, Don State Technical University, 1 Gagrina sq., 344001 Rostov-on-Don, Russian Federation

e-mail: fenix_rsu@mail.ru

15.1 Introduction

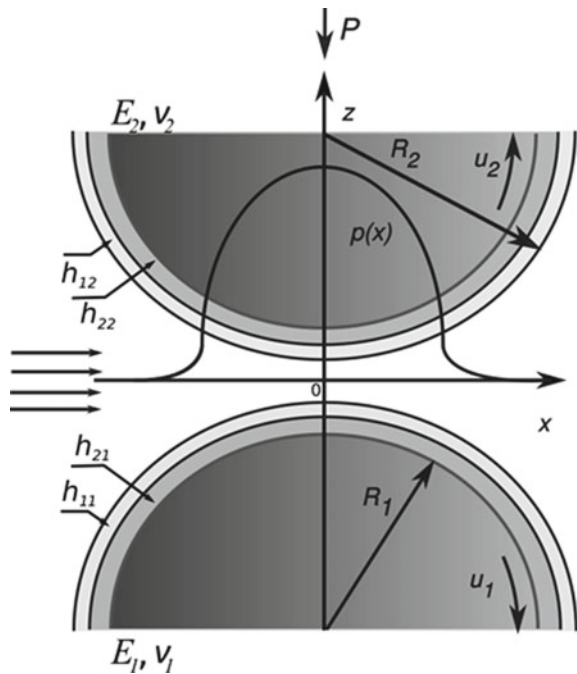
Most machine elements have moving joints. Often, to improve their performance and durability coatings and lubrication are used. For example, different kind of protective coatings are used to improve tribological characteristics of joints, to reduce corrosion and temperature effects in joint contacts. Lubrication usually serves two purposes: decreasing the energy losses and friction as well as reducing contact surface temperatures. Due to continuously increasing requirements to machine performance, there is a need for designs of advanced machinery elements which, in turn, requires development of new advanced mathematical models of machine elements with coatings involved in lubricated contacts. In certain cases, the coatings used may have a complex structure, i.e., besides being just made of a single homogeneous, functionally graded, or porous materials, they may be multi-layered coatings made of different materials, etc. Depending on the coating structure, contact geometry, and applied loads different mathematical models can be used. For example, in [1–13] dry contacts (without lubricant) with and without coatings made of homogeneous and functionally graded materials, multi-layered coatings with and without friction were considered. The surface elasticity approach was used for the analysis of coatings in both static and dynamic loading in [14, 15]. Also, there exist many studies of the behavior of double coatings of different structure subjected to different loads. The interest to double coatings is due to the relative simplicity of their creation (compared to multi-layered and functionally graded coatings) and the fact that they may occur naturally as oxide films and adsorbed lubricant components. The plane contact problem on indentation of bilayer (double-layered elastic coating glued to the non-deformable foundation) was studied in frictionless and frictional formulations in [16, 17], respectively. A problem for an indenter subjected to normal force and torque contacting an elastic half-space with a double coating made of a functionally graded material is considered in [18–20]. A thermomechanical analysis of a double coating made of a functionally graded material is considered in [21]. The wear of a double-layered coating and coating made of a functionally graded material, taking into account heating and friction, is considered in [22, 23]. Consideration of the influence of lubrication on contact mechanical characteristics leads to problems more complex than problems for dry contacts. This is due to the necessity of simultaneous consideration of the rheology equations describing lubricant behavior and the elasticity equations describing solid deformations, linear speeds of contact surfaces, and gap between contact surfaces. Generally, solution of elastohydrodynamic lubrication (EHL) problem is reduced to studying systems of integro-differential equations. The simplest description of lubricants is provided by the Newtonian rheological model [24–27]. In particular, heavily loaded line EHL contacts with Newtonian lubricant rheology [28, 29] with thin adsorbed soft layer are considered in [30] while heavily loaded point EHL contacts for functionally graded coating materials are considered in [31]. The case of lubricant with Ree-Eyring non-Newtonian rheology is considered in [32] for a line contact with a coating. In [33] an EHL model for point contact was investigated numerically. The results showed that hard coatings increase friction

while soft coatings decrease it. A similar problem for contact solids with multiple coatings (including some functionally graded ones) has been considered numerically in [34]. The current paper is the continuation of the investigation of EHL contacts with double coated surfaces [35]. The paper uses the classification of different double coatings and the working regimes they are involved in [36] as well as Newtonian lubricant rheology to simplify the formulation of the EHL problem for a line contact, specifically, the expressions for surface displacements, speeds, and gap between the surfaces. We will consider one classification case from [36] for which the upper coating is significantly softer than the intermediate coating and substrate while the substrate material is harder than the material of the intermediate coating. The results will show how such combination of coatings and work conditions leads to lowering friction force and energy loss and increases lubrication film thickness.

15.2 Main Simplified Relationships Used in the Problem Formulation

Let us consider a plane problem for a lubricated contact of an infinite cylinder with a half-space (see Fig. 15.1). Both the cylinder and the half-space have attached to them relatively thin elastic double coatings. For simplicity we will assume that the lubricant

Fig. 15.1 The general view of a lubricated contact



is a Newtonian incompressible fluid with constant viscosity μ . The coordinate system is introduced in such a way that the x -axis is directed along the lubricant flow and perpendicular to the cylinder axis, the y -axis is directed along the cylinder axis, and the z -axis is directed across the lubricant layer. The cylinder is separated from the surface of the half-space by a continuous lubricant layer. The cylinder steadily rolls and slides in the direction of the x -axis with speed u_2 while the half-space moves in the same direction with speed u_1 . The components of the lubricant velocity are represented by functions $u(x, y, z)$, $v(x, y, z)$, and $w(x, y, z)$, where

$$v(x, y, z) = \frac{\partial v(x, y, z)}{\partial y} = 0$$

due to problem geometry. Due to that the problem parameters are independent of the coordinate y . For a typical line concentrated contact the gap between the contact surfaces is much smaller than the contact length. Therefore, the simplified equations of the motion of such a fluid are as follows [37, 38]

$$-\frac{\partial p}{\partial x} + \frac{\partial \tau_{zx}}{\partial z} = 0, \quad \frac{\partial p}{\partial z} = 0, \quad \tau_{zx} = \mu \frac{\partial u}{\partial z}, \quad (15.1)$$

where p is the contact pressure while τ_{zx} is the tangential stress.

For an incompressible fluid the continuity equation has the form

$$\frac{\partial u}{\partial x} + \frac{\partial w}{\partial z} = 0. \quad (15.2)$$

the no slip boundary conditions on the fluid speed u and no penetration of the fluid on w at the solid boundaries are as follows

$$\begin{aligned} u(x, -h(x)/2) &= u_1, \quad u(x, h(x)/2) = u_2, \\ w(x, -h(x)/2) &= -\frac{1}{2}u_1 \frac{dh(x)}{dx}, \quad w(x, h(x)/2) = \frac{1}{2}u_2 \frac{dh(x)}{dx}, \end{aligned} \quad (15.3)$$

where $h(x)$ is the gap between contact surfaces. The boundary conditions imposed on w are obtained based the fact that in concentrated contacts $dh/dx \ll 1$.

An accurate and precise description of surface normal and tangential displacements for a double-layered elastic solid loaded with a normal and tangential surface loads is provided in [36]. We will assume that the substrate material occupying the lower subspace has Young's modulus E_s and Poisson's ratio ν_s while the materials of the upper and intermediate coatings have Young's modulus E_c and E_i and Poisson's ratios ν_c and ν_i , respectively, while their thicknesses are h_1 and h_2 , respectively. However, the exact expressions for the surface displacements for such elastic solids are very complex. An asymptotic analysis of these expressions in a spectrum of various limiting cases has been conducted in [36] which in some specific limiting cases resulted in a much simpler relationships compared to the original ones. In this paper we will consider couple of such cases of a lightly loaded contact characterized by a

Winkler type relationships for surface displacements U and W called in [36] as Case I or Case II, respectively,

$$E_{33}^{(c)} \ll E_{33}^{(i)} \ll E_{33}^{(s)} \quad \text{or} \quad E_{33}^{(i)} \ll E_{33}^{(c)} \ll E_{33}^{(s)}, \quad (15.4)$$

$$E_{11} = E_{33} = \frac{E}{1 - \nu^2}, \quad E_{13} = \frac{2E}{(1 + \nu)(1 - 2\nu)}, \quad (15.5)$$

where superscripts (i) , (c) , and (s) correspond to the materials of the intermediate and upper coatings as well as the substrate, respectively, E and ν are Young's modulus and Poisson's ratio of the corresponding material.

Specifically, for surface displacements we will consider Case U2U8 for the tangential displacement U_k of the solid k has the form

$$U'_k(x, 0) = \frac{1}{2\pi} \left[B_{11,k}^{(1)} h_{1,k} + B_{11,k}^{(2)} h_{2,k} \right] \tau'_{zx,k}(x) + \dots, \quad (15.6)$$

which is correct if the following relationships are satisfied

$$a_H \ll \frac{E_{13}^{(s)}}{4\pi} \left(B_{13}^{(1)} h_{1,k} + B_{13}^{(2)} h_{2,k} \right), \quad \frac{a_H}{R'} \gg 2 \frac{B_{13,k}^{(1)} h_{1,k} + B_{13,k}^{(2)} h_{2,k}}{B_{11,k}^{(1)} h_{1,k} + B_{11,k}^{(2)} h_{2,k}}, \quad (15.7)$$

and Case W2W7 for the normal displacement W_k of the solid k as follows

$$W'_k(x, 0) = -\frac{1}{2\pi} \left[B_{33,k}^{(1)} h_{1,k} + B_{33,k}^{(2)} h_{2,k} \right] p'(x) + \dots, \quad (15.8)$$

is correct if the following relationships are satisfied

$$a_H \ll E_{33}^{(s)} \left(B_{33}^{(1)} h_{1,k} + B_{33}^{(2)} h_{2,k} \right), \quad \frac{a_H}{R'} \ll 2 \frac{B_{33,k}^{(1)} h_{1,k} + B_{33,k}^{(2)} h_{2,k}}{B_{13,k}^{(1)} h_{1,k} + B_{13,k}^{(2)} h_{2,k}}, \quad (15.9)$$

where subscript k indicates the solid (1 for lower and 2 for upper solid), $h_{1,k}$ and $h_{2,k}$ the thickness of the external and intermediate coatings on solid k , R' is the effective radius of the contact surfaces, a_H is a typical (Hertzian) half-length of a dry contact of elastic solids without coatings,

$$a_H = 2 \sqrt{\frac{R' P}{\pi E_{33}^{(s)}}},$$

P is the load per unit length applied to the cylinder, $p(x)$ and $\tau_{zx,k}(x)$ are the pressure and tangential stress applied to the surface of solid k . Some of the constants involved in the previous formulas are given below [36]

$$\begin{aligned}
 B_{11}^{(1)} &= \frac{4\pi}{(1 - \nu_c)E_{33}^{(c)}}, & B_{11}^{(2)} &= \frac{4\pi}{(1 - \nu_i)E_{33}^{(i)}}, \\
 B_{13}^{(1)} &= \frac{8E_{33}^{(c)}}{E_{13}^{(c)}E_{33}^{(s)}}, & B_{13}^{(2)} &= \frac{4(1 - 2\nu_i)}{(1 - \nu_i)E_{33}^{(s)}}, \\
 B_{33}^{(1)} &= \frac{4\pi}{(1 - \nu_c)E_{13}^{(c)}}, & B_{33}^{(2)} &= \frac{4\pi}{(1 - \nu_i)E_{13}^{(i)}}.
 \end{aligned}
 \tag{15.10}$$

Using (15.7), (15.9), and (15.10) it easy to show that there is a range of problem parameters (material elastic characteristics, contact geometry, coating thicknesses, and applied normal load) for which the above asymptotic estimates for U'_k and W'_k [36] are valid.

For simplicity we will assume that the materials of both contact solids are identical and the coating thicknesses of coatings on both solids are also the same, i.e., $h_{1,1} = h_{1,2} = h_1$ and $h_{2,1} = h_{2,2} = h_2$. Based on the above formulas the actual surface velocities of the solids are

$$v_k(x) = u_k \left[1 + \frac{d}{dx} U_k \left(x, (-1)^k \frac{h(x)}{2} \right) \right], \quad i = 1, 2, \tag{15.11}$$

where $h(x)$ is the gap between the solids in contact. That, finally, allows us to formulate the lubrication problem as follows (see [37, 38])

$$\begin{aligned}
 \frac{d}{dx} \left\{ \frac{v_1(x) + v_2(x)}{2} h(x) - \frac{h^3(x)}{12\mu} \frac{dp(x)}{dx} \right\} &= 0, \quad p(x_i) = p(x_e) = \frac{dp(x_e)}{dx} = 0, \\
 h &= h_e + \frac{x^2 - x_e^2}{2R'} + \frac{1}{\pi} \left(B_{33}^{(1)} h_1 + B_{33}^{(2)} h_2 \right) p(x), \quad \int_{x_i}^{x_e} p(x) dx = P, \\
 \frac{v_1(x) + v_2(x)}{2} &= \frac{u_1 + u_2}{2} + \frac{1}{4\pi} \left[B_{11}^{(1)} h_1 + B_{11}^{(2)} h_2 \right] \left[u_1 \tau'_{zx,1}(x) + u_2 \tau'_{zx,2}(x) \right], \\
 S(x) = v_2(x) - v_1(x) &= u_2 - u_1 + \frac{1}{2\pi} \left[B_{11}^{(1)} h_1 + B_{11}^{(2)} h_2 \right] \left[u_2 \tau'_{zx,2}(x) - u_1 \tau'_{zx,1}(x) \right], \\
 \tau_{zx,1} = \tau_{zx} \left(x, -\frac{h}{2} \right) &= \frac{\mu S}{h} - \frac{h}{2} \frac{dp}{dx}, \quad \tau_{zx,2} = \tau_{zx} \left(x, \frac{h}{2} \right) = -\frac{\mu S}{h} - \frac{h}{2} \frac{dp}{dx},
 \end{aligned}
 \tag{15.12}$$

where x_i and x_e are the contact inlet and exit point coordinates (x_i is considered to be given while x_e needs to be determined from the problem solution), h_e lubrication film thickness at the exit point x_e which is also determined from the problem solution, and R' is the effective curvature radius of the contact solids.

By introducing the following dimensionless variables typical for lightly loaded lubricated contacts [37, 38]

$$\begin{aligned} \{x', a, c\} &= \{x, x_i, x_e\} \frac{\theta}{2R'}, \quad h' = \frac{h}{h_e}, \quad p' = p \frac{\pi R'}{\theta P}, \quad \mu' = \frac{\mu}{\mu_a^4}, \\ \{v'_1, v'_2, S'\} &= \frac{2}{u_1 + u_2} \{v_1, v_2, S\}, \quad F' = \frac{1}{P} F, \quad E' = \frac{1}{\mu_a(u_1 + u_2)^2} E, \\ \gamma &= h_e \frac{\theta^2}{2R'}, \quad S_{00} = 2 \frac{u_2 - u_1}{u_1 + u_2}, \quad \theta^2 = \frac{P}{3\pi \mu_a(u_1 + u_2)}, \end{aligned} \quad (15.13)$$

and omitting in the further considerations primes at the dimensionless variables we obtain the following problem in dimensionless variables

$$\begin{aligned} \frac{d}{dx} \left\{ \frac{v_1(x) + v_2(x)}{2} h - \frac{\gamma^2 h^3}{\mu} \frac{dp}{dx} \right\} &= 0, \\ p(a) = p(c) = \frac{dp(c)}{dx} = \frac{d^2 p(c)}{dx^2} &= 0, \\ \gamma(h - 1) = x^2 - c^2 + \frac{2\sigma_h}{\pi V} p, \quad \int_a^c p(x) dx &= \frac{\pi}{2}, \\ \frac{v_1 + v_2}{2} = 1 - S_{00} \frac{\sigma \delta}{24\pi \gamma} \frac{d}{dx} \left(\frac{\mu S}{h} \right) - \frac{\sigma \delta \gamma}{\pi} \frac{d}{dx} \left(h \frac{dp}{dx} \right), \\ S = S_{00} - \frac{\sigma \delta}{6\pi \gamma} \frac{d}{dx} \left(\frac{\mu S}{h} \right) - S_{00} \frac{\sigma \delta \gamma}{2\pi} \frac{d}{dx} \left(h \frac{dp}{dx} \right), \quad S(x) \rightarrow S_{00}, \quad x \rightarrow \mp \infty, \\ V = \frac{R' E_{33}^{(s)}}{\theta^2 P}, \quad \sigma_h = \theta \left[\frac{h_1/R'}{(1 - \nu_c) E_{13}^{(c)}/E_{33}^{(s)}} + \frac{h_2/R'}{(1 - \nu_i) E_{13}^{(i)}/E_{33}^{(s)}} \right], \\ \sigma = \theta \left[\frac{h_1/R'}{(1 - \nu_c) E_{33}^{(c)}/E_{33}^{(s)}} + \frac{h_2/R'}{(1 - \nu_i) E_{33}^{(i)}/E_{33}^{(s)}} \right], \quad \delta = \frac{P}{R' E_{33}^{(s)}}, \end{aligned} \quad (15.14)$$

where V , S_{00} , θ , σ_h , σ , and δ are given dimensionless parameters. Here in addition to the traditional boundary conditions used in lubrication problems we imposed an additional boundary condition $d^2 p(c)/dx^2 = 0$ at the exit point of the lubricated contact. The dimensionless friction force at the upper surface F (coefficient of friction) and contact energy loss E are expressed by the formulas

$$\begin{aligned} F &= \frac{\mu}{6\pi \theta \gamma} \left\{ \int_a^c \frac{S(x) dx}{h(x)} + \frac{6\gamma^2}{\mu} \int_a^c h(x) \frac{dp(x)}{dx} dx \right\}, \\ E &= \frac{\theta \mu}{\gamma} \left\{ \int_a^c \frac{S^2(x) dx}{h(x)} + \frac{12\gamma^4}{\mu^2} \int_a^c h^3(x) \left(\frac{dp(x)}{dx} \right)^2 dx \right\}. \end{aligned} \quad (15.15)$$

Obviously, the Reynolds differential equation can be analytically integrated one time. After that the problem can be reduced to solution of a system of the equation obtained after one time integration of the Reynolds equation with the boundary condition $dp(c)/dx = 0$ with remaining boundary and integral conditions as well as the initial-value problem for $S(x)$. This system can be solved iteratively in three repeated consequent steps. Suppose the initial approximations are taking the following way: $S(x) = S_{00}$ while $p(x)$, $h(x)$, γ , and c are taken as from the solution of a lubrication problem for rigid solids and Newtonian fluid [37, 38]. The internal iteration process involves **Step 1**: Solving the one time integrated Reynolds equation with boundary conditions $p(a) = d^2p(c)/dx^2 = 0$. Specifically, we satisfy the Reynolds equation at semi-integer nodes $x_{i+1/2}$, $i = 0, \dots, N - 2$, and imposing the boundary conditions $p_0 = 0$ and $p_N - 2p_{N-1} + p_{N-2} = 0$ while the values of pressure $p(x_i) = p_i$ are determined at the integer nodes x_i , $i = 0, \dots, N$. Here N is sufficiently large positive integer. This way we get a system of $N + 1$ nonlinear algebraic equations with $N + 1$ unknowns p_i , $i = 0, \dots, N$. Then on **Step 2** the system of two transcendent equations

$$p(c) = p_N = 0 \quad \text{and} \quad \int_a^c p(x)dx = \sum_{i=0}^{N-1} \frac{p_i + p_{i+1}}{2} (x_{i+1} - x_i) = \frac{\pi}{2}$$

is used to determine the corrections for parameters γ and c . That is done by applying Newton’s method. After that, with the corrected values of γ and c Step 1 is repeated. These calculations are done until the iteration process for $p(x)$, $h(x)$, γ , and c converges. After that with new $p(x)$, $h(x)$, γ , and c is solved the initial-value problem for $S(x)$ from $x = -\infty$ to $x = \infty$ where the equation for S from (15.14) is also satisfied at semi-integer nodes $x_{k+1/2}$, $k = L, \dots, K - 1$ and solved for S_k , $k = L, \dots, K$ where $S_L = S_{00}$, $x_L < 0$, $|x_L| \gg |a|$, and $x_K \gg c$, i.e., $x_K - x_L \gg c - a$. After that the iteration process goes back to Step 1 and so on until all the set of the solution parameters p_i , h_i , S_k , γ and c converges with the desired precision.

The lubrication problem for solids with coatings made of different materials and of different thickness can be set up in a similar way. Moreover, the equations for the case when one of the solids does not have coatings coincides with Eqs. (15.14) in which the dimensionless parameters σ_h and σ have to be replaced by $\sigma_h/2$ and $\sigma/2$, respectively. Therefore, the effect of the coatings is diminished.

It is important to realize that usually the coefficient at the last term in the equations for S and $(v_1 + v_2)/2$ in (15.14) is small compared to the other coefficients. That leads to the presence of a very narrow boundary layer adjacent to the exit point $x = c$. However, the boundary layer is very small and does not change the general behavior of the problem solution. Moreover, numerically the solution of the formulated problem practically coincides with the solution of the problem from (15.14) in which the last terms in the expressions for S and $(v_1 + v_2)/2$ as well as the last boundary condition on $d^2p(c)/dx^2$ are dropped.

On the other hand, the problem described by Eq. (15.14) can be solved using the regular perturbation method for $\sigma_h \sim 1$, $\sigma \sim 1$, $\delta \sim 1$ and $V \gg 1$ presented in [37, 38]. Obviously, for large V as V increases the problem solution approaches the solution of the corresponding lubrication problem for rigid solids [37, 38]. This trend is clear from the numerical data presented below.

15.3 Some Results for the Lubrication Problem

In this section, our goal is to illustrate the developed approach by a specific numerical example. For simplicity we will assume that the geometry and materials of the contact solids are identical. Consider a soft double-layered polymer material lying on an elastic substrate with the following properties: $E_c = 0.1$ GPa, $\nu_c = 0.3$, $E_i = 1$ GPa, $\nu_i = 0.3$, $E_s = 200$ GPa, $\nu_s = 0.48$. Also, it is assumed that the effective radius of contact solids $R' = 0.01$ m, the applied force $P = 2 \cdot 10^3$ N/m, and the coating thicknesses are taken as follows $h_{11} = h_{12} = 10^{-6}$ m and $h_{21} = h_{22} = 10^{-5}$ m. For this set of data all of the conditions (15.7) and (15.9) for the validity of the used approximations for the surface displacements U and W are satisfied. The lubrication regime is lightly loaded and, therefore, the lubricant viscosity μ can be considered independent of pressure and equal to the ambient viscosity $\mu_a = 1 \cdot 10^{-2}$ Ns/m². The following results are obtained for fixed values of parameters $\mu = 1$, $S_{00} = 2$, $\sigma/\theta = 0.675$, $\sigma_h/\theta = 0.193$, and varying values of parameter θ . Just notice, that for the case of rigid solids without coatings the dimensionless film thickness $\gamma_r = 0.157$ and dimensionless coordinate of the exit point $c_r = 0.170$ (see [37, 38]). Here and further the lower index r indicates the corresponding value for the case of rigid solids without coatings.

The graphs of pressure $p(x)$ versus x for different values of θ^{-2} are presented in Fig. 15.2. The graph represented by a solid curve corresponds to the case of rigid solids without coatings. Obviously, as θ increases (which happens when the applied load P increases and/or $\mu_a(u_1 + u_2)$ decreases) the distribution of pressure $p(x)$ decreases and occupies a wider contact area. The decrease in the values of $p(x)$ reaches up to 40% compared to the case of rigid solids.

The graphs of relative lubrication film thickness γ/γ_r and exit coordinate of the contact c/c_r are presented in Figs. 15.3 and 15.4. It is obvious from this graphs that the presence of soft coatings increases the lubrication film thickness and widens the contact region compared to the case of rigid solids without coatings. As θ decreases the contact parameters converge to the ones for the case of rigid solids without coatings. It is worth to notice that the quantitative and qualitative behavior of the relative minimum gap $\gamma h_{\min}/(\gamma_r - c_r^2)$ versus θ^{-2} is very close to the corresponding behavior of γ/γ_r versus θ^{-2} (see Fig. 15.3).

For rigid solids without coatings the dimensionless friction force and loss of energy in the contact are $F_r = 3.084\mu/(6\pi\theta\gamma_r)$ and $E_r = 6.169\theta\mu/\gamma_r$, respectively. The graph of F/F_r (which coincides with the relative friction coefficient) is represented in Fig. 15.5. As θ^{-2} increases the value of F/F_r monotonically increases which

Fig. 15.2 The graphs of the pressure distributions $p(x)$ versus x obtained for different values of θ

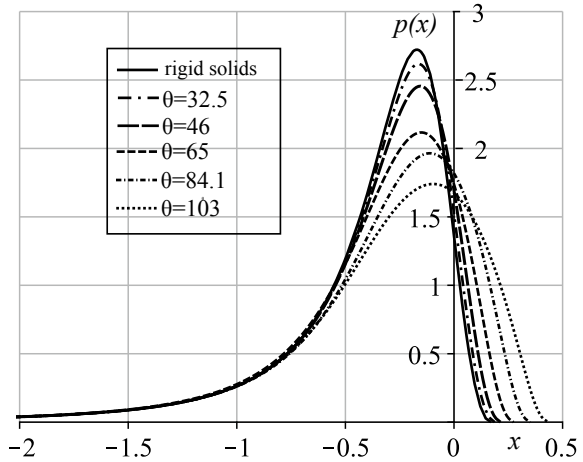
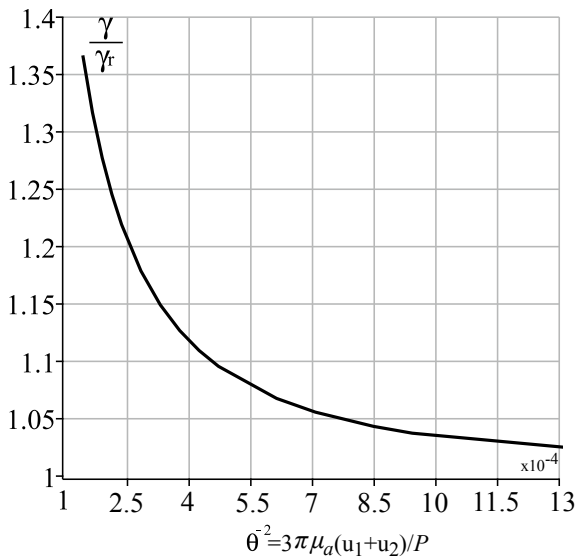


Fig. 15.3 The graph of the relative exit point film thickness γ/γ_r versus θ^{-2}



corresponds to the elastohydrodynamic regime of lubrication on a Stribeck curve. Obviously, the presence of soft coatings decreases the friction and friction coefficient compared to the case of rigid solids without coatings. The graphs of E/E_r coincides with the graph of F/F_r from Fig. 15.5. The actual sliding speed $S(x)$ differs from S_{00} by less than 1% for any x and everywhere it can be taken equal to S_{00} . Obviously, the difference of S from S_{00} practically does not affect the values of F/F_r and E/E_r .

Fig. 15.4 The graph of the relative exit coordinate c/c_r versus θ^{-2}

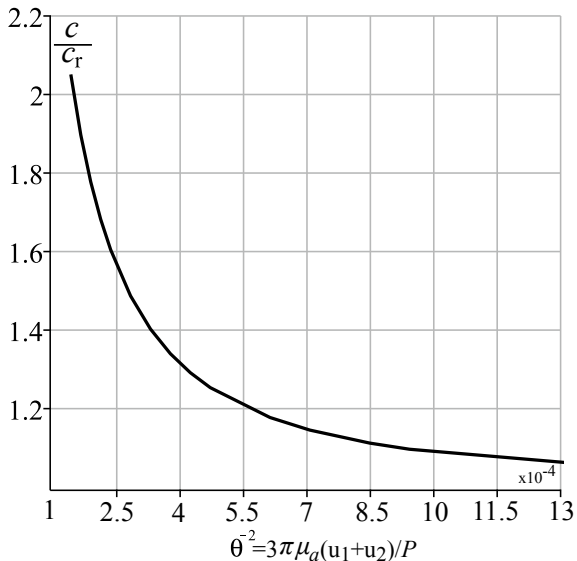
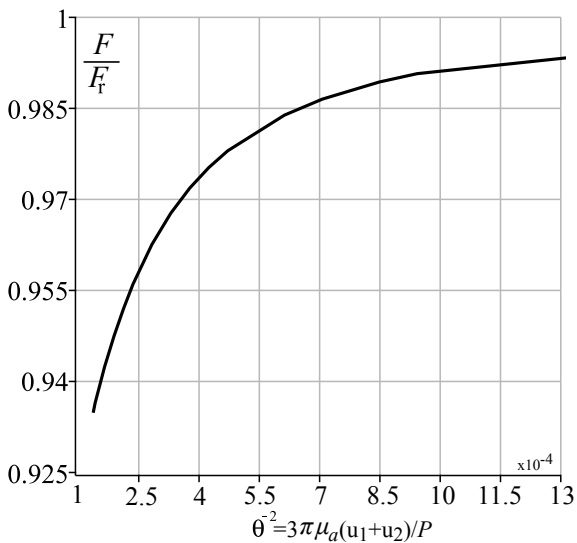


Fig. 15.5 The graph of the friction force F/F_r versus θ^{-2}



15.4 Closure

A relatively simple model of a lubricated contact of elastic solids with soft double coatings was developed. The model is valid within the indicated range of parameters described by (15.7) and (15.9). The development of this simple model made possible by using the obtained by the authors classification [36] based on an asymptotic approach which allowed to significantly simplify the expressions for surface displacements of double coated surfaces. That led to a significant simplification of the Reynolds equation and its solution. The numerical results showed that for low surface speeds and lubricant viscosity and/or high applied force the presence of soft double coatings increases the lubrication film thickness, decreases the level of contact pressure as well as decreases the contact friction and energy losses compared with the case of rigid solids without coatings. For example, for the above indicated input parameters the maximum decrease in friction was 6% while in maximum pressure it was 40%.

Acknowledgements The study was supported by the Russian Science Foundation grant No. 19-19-00444, <https://rscf.ru/project/19-19-00444/>.

References

1. Argatov, I.: A comparison of general solutions to the non-axisymmetric frictionless contact problem with a circular area of contact: when the symmetry does not matter. *Symmetry*. **14**, 1083 (2022). <https://doi.org/10.3390/sym14061083>
2. Kaplunov, J., Prikazchikov, D., Sultanova, L.: Elastic contact of a stiff thin layer and a half-space. *Z. Angew. Math. Phys.* **70**, 22 (2019). <https://doi.org/10.1007/s00033-018-1068-9>
3. Miura, K., Sakamoto, M., Tanabe, Y.: Analytical solution of axisymmetric indentation of multi-layer coating on elastic substrate body. *Acta Mech.* **231**, 4077–4093 (2020). <https://doi.org/10.1007/s00707-020-02752-1>
4. Comez, I.: Continuous and discontinuous contact problem of a functionally graded layer pressed by a rigid cylindrical punch. *Eur. J. Mech. A Solids* **73**, 437–448 (2019). <https://doi.org/10.1016/j.euromechsol.2018.10.009>
5. Liu, T.-J., Ke, L.-L., Wang, Y.-S., Xing, Y.-M.: Stress analysis for an elastic semispace with surface and graded layer coatings under induced torsion. *Mech. Based Des. Struct. Mach.* **43**, 74–94 (2014). <https://doi.org/10.1080/15397734.2014.928222>
6. Zelentsov, V.B., Lapina, P.A., Mitrin, B.I., Eremeyev, V.A.: Characterization of the functionally graded shear modulus of a half-space. *Mathematics*. **8**, 640 (2020). <https://doi.org/10.3390/math8040640>
7. Zelentsov, V.B., Lapina, P.A., Zagrebneva, A.D.: Method for determining the parameters of the exponential shear modulus of a functional-gradient half-space. In: Altenbach, H., Eremeyev, V.A., Galybin, A., Vasiliev, A. (eds.) *Advanced Materials Modelling for Mechanical, Medical and Biological Applications*, pp. 441–466. Springer International Publishing, Cham (2022)
8. Comez, I., Guler, M.A.: The contact problem of a rigid punch sliding over a functionally graded bilayer. *Acta Mech.* **228**, 2237–2249 (2017). <https://doi.org/10.1007/s00707-017-1827-2>
9. Volkov, S., Litvinenko, A., Aizikovich, S., Wang, Y.-C., Vasiliev, A.: Axisymmetric bending of a circular plate with stiff edge on a soft FGM layer. *Struct. Eng. Mech.* **59**, 227–241 (2016). <https://doi.org/10.12989/sem.2016.59.2.227>

10. Liu, T.-J., Wang, Y.-S., Zhang, C.: Axisymmetric frictionless contact of functionally graded materials. *Archive Appl. Mech.* **78**, 267–282 (2008). <https://doi.org/10.1007/s00419-007-0160-y>
11. Yan, J., Wang, C.: Receding contact problem of multi-layered elastic structures involving functionally graded materials. *Crystals*. **12**, 354 (2022). <https://doi.org/10.3390/cryst12030354>
12. Toktas, S.E., Dag, S.: Stresses in multi-layer coatings in Hertzian contact with a moving circular punch (2022). <https://doi.org/10.1016/j.triboint.2022.107565>
13. Zelentsov, V.B., Mitrin, B.I., Lubyagin, I.A.: Wear resistance of coating materials under the frictional heating conditions. *J. Frict. Wear.* **38**, 265–271 (2017). <https://doi.org/10.3103/S1068366617040158>
14. Eremeyev, V.A., Rosi, G., Naili, S.: Surface/interfacial anti-plane waves in solids with surface energy. *Mech. Res. Commun.* **74**, 8–13 (2016). <https://doi.org/10.1016/j.mechrescom.2016.02.018>
15. Eremeyev, V., Rosi, G., Naili, S.: Transverse surface waves on a cylindrical surface with coating. *Int. J. Eng. Sci.* **147**, 103188 (2019). <https://doi.org/10.1016/j.jengsci.2019.103188>
16. Alexandrov, V.M., Klindukhov, V.V.: Contact problems for double-layered elastic base with nonideal mechanical interface between the layers. *Notices Russian Acad. Sci. Mech. Solids (MTT)*. **3**, 84–92 (2000)
17. Ivanochkin, P., Kolesnikov, V., Flek, B., Chebakov, M.: Contact strength of a two-layer covering under friction forces in the contact region. *Mech. Solids*. **42**, 157–165 (2007). <https://doi.org/10.3103/S0025654407010190>
18. Vasiliev, A., Volkov, S., Aizikovich, S.M.: Torsion of an elastic transversely isotropic half-space with a coating reinforced by a functionally graded interlayer. *Shell Struct. Theor. Appl.* **4**, 185–188 (2017). <https://doi.org/10.1201/9781315166605-39>
19. Vasiliev, A., Volkov, S., Aizikovich, S.M.: Approximated analytical solution of contact problem on indentation of elastic half-space with coating reinforced with inhomogeneous interlayer. *Materi. Phys. Mech.* **35**, 175–180 (2018). https://doi.org/10.18720/MPM.3512018_20
20. Vasiliev, A., Volkov, S., Aizikovich, S.M., Litvinenko, A.N.: Indentation of an elastic half-space reinforced with a functionally graded interlayer by a conical punch. *Mater. Phys. Mech.* **40**, 254–260 (2018). https://doi.org/10.18720/MPM.4022018_14
21. Yang, J., Ke, L.-L., Kitipornchai, S.: Thermo-mechanical analysis of an inhomogeneous double-layer coating system under Hertz pressure and tangential traction. *Mech. Adv. Mater. Struct.* **16**, 308–318 (2009). <https://doi.org/10.1080/15376490802666302>
22. Zelentsov, V.B., Mitrin, B.I., Kuznetsova, T.A., Lapitskaya, V.A.: Non-steady wear of a two-layer coating taking into account frictional heating. *J. Appl. Mech. Tech. Phys.* **62**(7), 1088–1096 (2021). <https://doi.org/10.1134/S002189442107021X>
23. Zelentsov, V.B., Lapina, P.A., Mitrin, B.I.: Wear of functionally graded coatings under frictional heating conditions. *Nanomaterials*. **12**, 142 (2022). <https://doi.org/10.3390/nano12010142>
24. Chapkov, A.D., Bair, S., Cann, P., Lubrecht, A.A.: Film thickness in point contacts under generalized Newtonian EHL conditions: numerical and experimental analysis. *Tribology Int.* **40**, 1474–1478 (2007). <https://doi.org/10.1016/j.triboint.2007.01.002>
25. Su, J., Song, H.-X., Ke, L.-L.: Elastohydrodynamic lubrication line contact based on surface Elasticity theory. *J. Appl. Mech.* **87**, (2020). <https://doi.org/10.1115/1.4047088>
26. Katyal, P., Kumar, P.: On the role of second Newtonian viscosity in EHL point contacts using double Newtonian shear-thinning model. *Tribology Int.* **71**, 140–148 (2014). <https://doi.org/10.1016/j.triboint.2013.11.009>
27. Kazama, T.: A comparative Newtonian and thermal EHL analysis using physical lubricant properties. In: *B: Tribology Series*, pp. 435–446. Elsevier (2002)
28. Cherizol, R., Sain, M., Tjong, J.: Review of non-newtonian mathematical models for Rheological characteristics of viscoelastic composites. *Green Sustain. Chem.* **05**, 6–14 (2015). <https://doi.org/10.4236/gsc.2015.51002>
29. Bird, R.B., Curtis, C.F., Armstrong, R.C., Hassager, O.: Dynamics of polymeric liquids. In: *Fluid Mechanics*, vol. 1, 2nd edn. John Wiley & Sons, New York (1987)

30. Kudish, I.I., Pashkovski, E., Volkov, S.S., Vasiliev, A.S., Aizikovich, S.M.: Heavily loaded line EHL contacts with thin adsorbed soft layers. *Math. Mech. Solids*. **25**, 1011–1037 (2020). <https://doi.org/10.1177/1081286519898878>
31. Kudish, I.I., Volkov, S.S., Vasiliev, A.S., Aizikovich, S.M.: Lubricated point heavily loaded contacts of functionally graded materials. Part 2. Lubricated contacts. *Math. Mech. Solids*. **23**, 1081–1103 (2018) <https://doi.org/10.1177/1081286517704690>
32. Su, J., Song, H., Ke, L., Aizikovich, S.M.: The size-dependent elasto-hydrodynamic lubrication contact of a coated half-plane with non-Newtonian fluid. *Appl. Math. Mech.-Engl. Ed.* **42**, 915–930 (2021) <https://doi.org/10.1007/s10483-021-2744-7>
33. Wang, Z., Wang, W., Wang, H., Hu, Y.: Stress analysis on layered materials in point elasto-hydrodynamic-lubricated contacts. *Tribol Lett.* **35**, 229–244 (2009). <https://doi.org/10.1007/s11249-009-9452-4>
34. Wang, Z., Yu, C., Wang, Q.: Model for elasto-hydrodynamic lubrication of multilayered materials. *J. Tribology*. **137**, 011501 (2015). <https://doi.org/10.1115/1.4028408>
35. Kudish I.I., Volkov S.S., Aizikovich S.M., Ke, L.: One simple case of lubricated line contact for double-layered elastic solids. *Probl. Strength Plasticity Disabled*. **84**, 15–24 (2022). <https://doi.org/10.32326/1814-9146-2022-84-1-15-24>
36. Kudish, I.I., Volkov, S.S., Vasiliev, A.S., Aizikovich, S.M.: Characterization of the behavior of different contacts with double coating. *Math. Mech. Compl. Sys.* **9**, 179–202 (2021). <https://doi.org/10.2140/memocs.2021.9.179>
37. Kudish, I.I., Covitch, M.J.: *Introduction to Modeling and Analytical Methods in Tribology*. Chapman & Hall/CRC (2010)
38. Kudish, I.I. *Elastohydrodynamic lubrication for line and point contacts*. In: *Asymptotic and Numerical Approaches*. Chapman & Hall /CRC Press (2013)

Chapter 16

On the Exact Solution of the First Boundary Value Problem for a Plane with a Circular Hole in the Formulation of the Nonlinear Power-Law Theory of Steady Creep Under Antiplane Deformation



Suren M. Mkhitarian

Abstract In the formulation of the nonlinear steady-state creep theory (NSSCT), when there is a power-law dependence between stresses and deformation rates, the first boundary value problem for a deforming plane with a circular hole is considered under antiplane deformation. Using the method of the harmonic function of pseudostresses, the solution to this problem is reduced to the solution of a nonlinear singular integral equation (NSIE) with the Hilbert kernel. The latter, in turn, is reduced to a nonlinear Riemann boundary value problem in the theory of analytic functions. An exact (closed) solution to the Riemann problem is constructed, with the help of which the main characteristics of the problem posed are represented by explicit analytical formulas. A particular case is considered.

Keywords Steady-state creep · Power law · Stresses · Deformation rate · Plane with a circular hole · First boundary value problem · Antiplane deformation

16.1 Introduction

In [1, 2], the formulation of NSSCT with a power-law dependence between stress intensities and deformation rates or in the formulation of the deformation theory of plasticity and with power-law hardening of the material, a physically nonlinear, but geometrically linear, plane contact problem of compression of two bodies was studied. These works proceed from the exact solution of the generalized Flaman problem in displacements depending on normal concentrated forces. To determine the distributed normal force-dependent displacements or deformation rates of the boundary points of deformable half-planes, which replace compressible bodies,

S. M. Mkhitarian (✉)

Institute of Mechanics, National Academy of Sciences of RA, 24/2 Baghramian Ave., 0019 Yerevan, Republic of Armenia

e-mail: smkhitarian39@rambler.ru

according to Hertz's hypotheses, the principle of superposition of generalized displacements (PSGD) or deformation rates is used. Some estimates of this principle were obtained in [3]. In [4, 5] are devoted also to the estimation of PSGD. For the nonlinear power-law contact problem of the interaction between a stamp with a flat base and a half-space under antiplane deformation, a comparative analysis of the exact solution obtained by the hodograph method and an approximate solution by the PSGD was carried out in [5]. The hodograph method applied to crack problems, which leads to a linear differential equation for the potential in the deformation plane, was proposed in [6]. The hodograph method makes it possible to obtain unbounded solutions at the ends of the characteristic interval for the considered mixed power-law nonlinear boundary value problems. Another linearization approach is based on introducing a biharmonic function of pseudostresses in a plane power-law problem and was developed in [7]. This method enables to obtain only solutions to mixed boundary value problems bounded at the ends of the interval. In [8], a harmonic pseudostress function was introduced in nonlinear power-law problems under antiplane deformation, with the help of which an exact (closed) solution of the first boundary value problem of the NSSCT for a half-space under antiplane deformation was constructed. An exact solution of a mixed power-law boundary value problem for a half-space under antiplane deformation, when the boundary conditions on the boundary plane of the half-space are separated by a stripe domain, is also constructed in [9] using the method of harmonic function of pseudostresses in the NSSCT formulation. In the same work, a comparative analysis of the exact and approximate PSGD solutions was carried out. Note that many results of the study of nonlinear contact and mixed problems are summarized in [10, 11].

We also note that the power law between stresses and deformation rates, known as Glenn's law, adequately describes the physical and mechanical behavior of sea ice and covers, glaciers, frozen soils, and other materials. Numerous studies have been devoted to the theoretical and experimental justification of Glen's law. In this direction, we point to [12–14].

In this paper, in the formulation of the NSSCT with a power-law relationship between stresses and deformation rates, we consider a boundary value problem for an infinite space with a circular infinite cylindrical hole, which is under antiplane deformation conditions, when shear stresses are prescribed on the cylindrical surface of the hole. This problem is equivalent to the first boundary value problem for a plane with a circular hole. By the harmonic pseudostress function method, as in [8, 9], the solving this problem is reduced to solving the NSIE with the Hilbert kernel, solving of which, in turn, is reduced to the nonlinear Riemann boundary value problem of the theory of analytic functions. An exact solution of the Riemann problem is constructed based on which the stresses and velocities of the problem under consideration are represented by explicit analytical formulas. A particular case of an external load on the boundary circle of the hole is considered.

16.2 Representation of Stresses and Strain Rates in Terms of the Harmonic Function of Pseudostresses

Let the deformable body be referred to the right rectangular coordinate system $Oxyz$ and be under conditions of antiplanar deformation (longitudinal shear) in the direction of the Oz axis with the reference plane Oxy . Further, let the trace of this body on the Oxy plane be a two-dimensional domain D with a boundary ∂D in the form of a smooth closed Jordan curve. In this coordinate system, as applied to the case of antiplane deformation, we present the basic equations of NSSCT with a power law. They consist [15, 16] of the equilibrium equation

$$\partial\tau_{xz}/\partial x + \partial\tau_{yz}/\partial y = 0 \quad ((x, y) \in D), \quad (16.2.1)$$

where τ_{xz} , τ_{yz} are shear stress components, the equations of continuity of deformation rates

$$\partial\gamma_{xz}/\partial y - \partial\gamma_{yz}/\partial x = 0; \quad \gamma_{xz} = \partial w/\partial x, \quad \gamma_{yz} = \partial w/\partial y \quad ((x, y) \in D), \quad (16.2.2)$$

where γ_{xz} , γ_{yz} are strain rate components, and $w = w(x, y)$ is the only non-zero velocity component in the direction of the Oz axis under antiplanar deformation; from the dependences between stresses and strain rates we have

$$\tau_{xz} = \frac{T(\Gamma)}{\Gamma}\gamma_{xz}, \quad \tau_{yz} = \frac{T(\Gamma)}{\Gamma}\gamma_{yz}; \quad T = T(\Gamma) = K_0\Gamma^m \quad (K_0 > 0; \quad 0 < m \leq 1); \quad (16.2.3)$$

$$T = \sqrt{\tau_{xz}^2 + \tau_{yz}^2}, \quad \Gamma = \sqrt{\gamma_{xz}^2 + \gamma_{yz}^2}. \quad (16.2.4)$$

Here, T is the stress intensity, Γ is the deformation rate intensity, K_0 is the physical constant of the material, and m is the creep index.

In the equilibrium Eq. (16.2.1), we introduce the stress function $\Phi = \Phi(x, y)$ $((x, y) \in D)$ by setting

$$\tau_{xz} = -\frac{\partial\Phi}{\partial y}, \quad \tau_{yz} = \frac{\partial\Phi}{\partial x}. \quad (16.2.5)$$

It is assumed that the function $\Phi(x, y)$, together with its partial derivatives up to the second order, is continuous in the closed domain D . Then, the equilibrium equation is satisfied identically.

Next, we pass to the complex plane z and set

$$z = x + iy, \bar{z} = x - iy \Rightarrow x = \frac{1}{2}(z + \bar{z}), y = -\frac{i}{2}(z - \bar{z})$$

$$\Phi = \Phi(x, y) = \Phi\left(\frac{1}{2}(z + \bar{z}), -\frac{i}{2}(z - \bar{z})\right) = \Phi(z, \bar{z}).$$

From (16.2.5) and the first formula in (16.2.4)

$$\tau_{xz} = -i\left(\frac{\partial\Phi}{\partial z} - \frac{\partial\Phi}{\partial\bar{z}}\right), \tau_{yz} = \frac{\partial\Phi}{\partial z} + \frac{\partial\Phi}{\partial\bar{z}}; \mathbf{T} = 2\left(\frac{\partial\Phi}{\partial z} \frac{\partial\Phi}{\partial\bar{z}}\right)^{1/2}. \quad (16.2.6)$$

For the strain rate components, from (16.2.3)–(16.2.4) using (16.2.6), we obtain

$$\gamma_{xz} = \frac{\Gamma}{\mathbf{T}(\Gamma)}\tau_{xz} = -iK(m)\left(\frac{\partial\Phi}{\partial z} \cdot \frac{\partial\Phi}{\partial\bar{z}}\right)^{\frac{1-m}{2m}}\left(\frac{\partial\Phi}{\partial z} - \frac{\partial\Phi}{\partial\bar{z}}\right),$$

$$\gamma_{yz} = \frac{\Gamma}{\mathbf{T}(\Gamma)}\tau_{yz} = K(m)\left(\frac{\partial\Phi}{\partial z} \cdot \frac{\partial\Phi}{\partial\bar{z}}\right)^{\frac{1-m}{2m}}\left(\frac{\partial\Phi}{\partial z} + \frac{\partial\Phi}{\partial\bar{z}}\right); K(m) = 1/2(2/K_0)^{1/m}. \quad (16.2.7)$$

Then, using the relations

$$\frac{\partial\Lambda}{\partial z} = \left(\frac{\partial\Phi}{\partial z}\right)^{\frac{1+m}{2m}}\left(\frac{\partial\Phi}{\partial\bar{z}}\right)^{\frac{1-m}{2m}}, \frac{\partial\Lambda}{\partial\bar{z}} = \left(\frac{\partial\Phi}{\partial z}\right)^{\frac{1-m}{2m}}\left(\frac{\partial\Phi}{\partial\bar{z}}\right)^{\frac{1+m}{2m}}, \quad (16.2.8)$$

by analogy with [7], we introduce the pseudostress function $\Lambda(x, y) = \Lambda(z, \bar{z})$. In the linear case $m = 1$ and then, $K(1) = 1/K_0 = 1/G$, where G is the shear modulus. It follows from (16.2.8) that for $m = 1$, the pseudostress function $\Lambda(x, y)$ coincides with the stress function $\Phi(x, y)$ up to an additive constant.

We now express the stresses, deformation rates, and velocities in terms of the function $\Lambda(z, \bar{z})$. Namely from (16.2.7) and (16.2.8), it follows that

$$\gamma_{xz} = -iK(m)\left(\frac{\partial\Lambda}{\partial z} - \frac{\partial\Lambda}{\partial\bar{z}}\right), \gamma_{yz} = K(m)\left(\frac{\partial\Lambda}{\partial z} + \frac{\partial\Lambda}{\partial\bar{z}}\right). \quad (16.2.9)$$

Substituting the expressions γ_{xz} and γ_{yz} from (16.2.9) into the deformation rate continuity Eq. (16.2.2), we arrive at the Laplace equation for the function $\Lambda(z, \bar{z})$

$$\Delta\Lambda = \frac{\partial^2\Lambda}{\partial x^2} + \frac{\partial^2\Lambda}{\partial y^2} = \frac{\partial^2\Lambda}{\partial z\partial\bar{z}} = 0 \quad ((x, y) \in D). \quad (16.2.10)$$

To find expressions for stresses and velocities in terms of a function of pseudostresses, we invert relations (16.2.8). To this end, we multiply and divide by each other the left- and right-hand sides of relations (16.2.8). As a result, we will have

$$\frac{\partial \Phi}{\partial z} \frac{\partial \Phi}{\partial \bar{z}} = \left(\frac{\partial \Lambda}{\partial z} \frac{\partial \Lambda}{\partial \bar{z}} \right)^m, \quad \frac{\partial \Phi}{\partial z} / \frac{\partial \Phi}{\partial \bar{z}} = \frac{\partial \Lambda}{\partial z} / \frac{\partial \Lambda}{\partial \bar{z}}$$

and hence

$$\frac{\partial \Phi}{\partial z} = \left(\frac{\partial \Lambda}{\partial z} \right)^{\frac{m+1}{2}} \left(\frac{\partial \Lambda}{\partial \bar{z}} \right)^{\frac{m-1}{2}}, \quad \frac{\partial \Phi}{\partial \bar{z}} = \left(\frac{\partial \Lambda}{\partial z} \right)^{\frac{m-1}{2}} \left(\frac{\partial \Lambda}{\partial \bar{z}} \right)^{\frac{m+1}{2}}. \quad (16.2.11)$$

Then, substituting (16.2.11) into (16.2.6), we get.

$$\tau_{xz} = -i \left(\frac{\partial \Lambda}{\partial z} \frac{\partial \Lambda}{\partial \bar{z}} \right)^{\frac{m-1}{2}} \left(\frac{\partial \Lambda}{\partial z} - \frac{\partial \Lambda}{\partial \bar{z}} \right), \quad \tau_{yz} = \left(\frac{\partial \Lambda}{\partial z} \frac{\partial \Lambda}{\partial \bar{z}} \right)^{\frac{m-1}{2}} \left(\frac{\partial \Lambda}{\partial z} + \frac{\partial \Lambda}{\partial \bar{z}} \right). \quad (16.2.12)$$

Since

$$\frac{\partial \Lambda}{\partial z} = \frac{1}{2} \left(\frac{\partial \Lambda}{\partial x} - i \frac{\partial \Lambda}{\partial y} \right), \quad \frac{\partial \Lambda}{\partial \bar{z}} = \frac{1}{2} \left(\frac{\partial \Lambda}{\partial x} + i \frac{\partial \Lambda}{\partial y} \right),$$

then formulas (16.2.12) can be represented as

$$\begin{aligned} \tau_{xz} &= -\frac{1}{2^{m-1}} \left[\left(\frac{\partial \Lambda}{\partial x} \right)^2 + \left(\frac{\partial \Lambda}{\partial y} \right)^2 \right]^{\frac{m-1}{2}} \frac{\partial \Lambda}{\partial y}, \\ \tau_{yz} &= \frac{1}{2^{m-1}} \left[\left(\frac{\partial \Lambda}{\partial x} \right)^2 + \left(\frac{\partial \Lambda}{\partial y} \right)^2 \right]^{\frac{m-1}{2}} \frac{\partial \Lambda}{\partial x}. \end{aligned} \quad (16.2.13)$$

and formulas (16.2.2) and (16.2.9) in the following form:

$$\gamma_{xz} = \partial w / \partial x = -K(m) \partial \Lambda / \partial y, \quad \gamma_{yz} = \partial w / \partial y = K(m) \partial \Lambda / \partial x. \quad (16.2.14)$$

To express the function $w(x, y)$ in terms of $\Lambda(x, y)$, we introduce the harmonic function $\Omega(x, y)$ ($x, y \in D$) conjugate to $\Lambda(x, y)$. Then, we have up to an arbitrary additive constant

$$w(x, y) = K(m) \Omega(x, y) \quad ((x, y) \in D). \quad (16.2.15)$$

Thus, the velocity component $w(x, y)$ is proportional to the function, harmonic in D , conjugate to the pseudostress function $\Lambda(x, y)$.

Note that the function $\Omega(x, y)$ is expressed in terms of the function $\Lambda(x, y)$ by the well-known formula [17]

$$\Omega(x, y) = \int_{M_0 M} \left(-\frac{\partial \Lambda}{\partial y} dx + \frac{\partial \Lambda}{\partial x} dy \right) + C, \quad (16.2.16)$$

where $M_0 M$ is an arbitrary path connecting an arbitrary fixed point $M_0(x_0, y_0)$ with a variable point $M(x, y)$ and located entirely in the considered area D .

So, the velocity component $w(x, y)$ is expressed through the function of pseudostresses by means of formulas (16.2.15)–(16.2.16).

For further use, it is necessary to write some of the basic equations and relations (16.2.1)–(16.2.16) in the polar coordinate system (r, φ) ($0 \leq r < \infty$; $-\pi < \varphi \leq \pi$). Setting

$$x = r \cos \varphi, \quad y = r \sin \varphi \Rightarrow r = \sqrt{x^2 + y^2}, \quad \varphi = \arctan \left(\frac{y}{x} \right)$$

and omitting intermediate elementary calculations, we obtain that the equilibrium Eq. (16.2.1) takes the form

$$\frac{\partial \tau_{rz}}{\partial r} + \frac{1}{r} \frac{\partial \tau_{\varphi z}}{\partial \varphi} + \frac{\tau_{rz}}{r} = 0 \quad ((r, \varphi) \in D), \quad (16.2.17)$$

deformation rate continuity equation—the form

$$\frac{\partial \gamma_{\varphi z}}{\partial r} + \frac{\gamma_{\varphi z}}{r} - \frac{1}{r} \frac{\partial \gamma_{rz}}{\partial \varphi} = 0 \quad ((r, \varphi) \in D), \quad \gamma_{rz} = \frac{\partial w}{\partial r}, \quad \gamma_{\varphi z} = \frac{1}{r} \frac{\partial w}{\partial \varphi}; \quad (16.2.18)$$

relationship between stresses and deformation rates are represented as

$$\begin{aligned} \tau_{rz} &= \frac{T(\Gamma)}{\Gamma} \gamma_{rz}, \quad \tau_{\varphi z} = \frac{T(\Gamma)}{\Gamma} \gamma_{\varphi z}; \quad T = T(\Gamma) = K_0 \Gamma^m \quad (0 < m \leq 1); \\ T &= \sqrt{\tau_{rz}^2 + \tau_{\varphi z}^2}, \quad \Gamma = \sqrt{\gamma_{rz}^2 + \gamma_{\varphi z}^2}. \end{aligned} \quad (16.2.19)$$

Equations (16.2.17)–(16.2.19) include components of stresses and deformation rates. Their meaning is clear. Now, based on (16.2.17), the stress function is introduced as follows:

$$\tau_{\varphi z} = \frac{\partial \Phi}{\partial r}, \quad \tau_{rz} = -\frac{1}{r} \frac{\partial \Phi}{\partial \varphi} \quad ((r, \varphi) \in D),$$

while the pseudostress function $\Lambda(r, \varphi) = \Lambda(z, \bar{z})$ is represented again by (16.2.8). Further, proceeding similarly to the above, we obtain the following expressions for the stress components:

$$\begin{aligned}\tau_{\varphi z} &= \frac{1}{2^{m-1}} \left[\left(\frac{\partial \Lambda}{\partial r} \right)^2 + \frac{1}{r^2} \left(\frac{\partial \Lambda}{\partial \varphi} \right)^2 \right]^{\frac{m-1}{2}} \frac{\partial \Lambda}{\partial r}, \quad ((r, \varphi) \in D); \\ \tau_{rz} &= -\frac{1}{2^{m-1}} \left[\left(\frac{\partial \Lambda}{\partial r} \right)^2 + \frac{1}{r^2} \left(\frac{\partial \Lambda}{\partial \varphi} \right)^2 \right]^{\frac{m-1}{2}} \frac{1}{r} \frac{\partial \Lambda}{\partial \varphi};\end{aligned}\tag{16.2.20}$$

for the velocity components

$$\gamma_{\varphi z} = K(m) \frac{\partial \Lambda}{\partial r}, \quad \gamma_{rz} = -K(m) \frac{1}{r} \frac{\partial \Lambda}{\partial \varphi} \quad ((r, \varphi) \in D).$$

Formulas (16.2.15)–(16.2.16) in the polar coordinate system will take the form

$$\begin{aligned}w(r, \varphi) &= K(m) \Omega(r, \varphi) \\ &= K(m) \int_{M_0 M} \left(\frac{\partial \Lambda}{\partial r} r d\varphi - \frac{1}{r} \frac{\partial \Lambda}{\partial \varphi} dr \right), \quad K(m) = \frac{1}{2} \left(\frac{2}{K_0} \right)^{1/m}.\end{aligned}\tag{16.2.21}$$

16.3 Formulation of the Problem and Derivation of the Basic Equations

Let an infinite space with a circular cylindrical hole (shaft) $\Omega = \{a \leq r < \infty, -\pi < \varphi \leq \pi, -\infty < z < \infty\}$ of radius a , referred to a cylindrical coordinate system r, φ, z , along its cylindrical surface $r = a$, be uniformly loaded along the axis Oz by tangential forces of intensity $f(\varphi)$, that is

$$\tau_{\varphi z}|_{r=a} = f(\varphi) \quad (-\pi < \varphi \leq \pi),\tag{16.3.1}$$

and

$$\int_{-\pi}^{\pi} f(\varphi) d\varphi = 0.\tag{16.3.2}$$

This condition is satisfied, in particular, when $f(\varphi)$ is an odd function on $(-\pi, \pi)$. It is assumed that under load (16.3.1) and under condition (16.3.2) an infinite space with a cylindrical hole Ω is under conditions of antiplanar deformation (longitudinal shear) in the direction of the Oz axis with a base plane (r, φ) and the power law (16.2.19) is valid for space material. As a result, we arrive at the first boundary value problem for a plane with a circular hole $\omega = \{a \leq r < \infty, -\pi < \varphi \leq \pi\}$ in the NSSCT formulation with a power law of the relationship between stresses and

deformation rates (16.2.19) and with antiplane deformation in the direction of the Oz axis. In this problem, the boundary condition has the form (16.3.1), and condition (16.3.2) must be satisfied, while the tangential stresses $\tau_{\varphi z}$ and τ_{rz} vanish at infinity.

Based on the last conditions, we represent the harmonic function of pseudostresses in ω by the Fourier series

$$\Lambda(r, \varphi) = \sum_{n=1}^{\infty} r^{-n} [A_n \cos(n\varphi) + B_n \sin(n\varphi)] \quad (a < r < \infty; -\pi < \varphi < \pi). \tag{16.3.3}$$

with unknown coefficients A_n and B_n . In exponential form, series (16.3.3) can be written as

$$\Lambda(r, \varphi) = \sum_{\substack{n=-\infty \\ n \neq 0}}^{\infty} C_n r^{-|n|} e^{in\varphi} \quad (a < r < \infty; -\pi < \varphi < \pi)$$

$$C_n = \begin{cases} \frac{1}{2}(A_n - iB_n) & (n = 1, 2, \dots); \\ \frac{1}{2}(A_{-n} + iB_{-n}) & (n = -1, -2, \dots); \end{cases} \quad \overline{C}_{-n} = C_n \quad (n = \pm 1, \pm 2, \dots). \tag{16.3.4}$$

Now, using (16.3.4) and formula (16.2.21), we calculate the function $w(r, \varphi)$. As an integration path M_0M choosing a segment (b, r) ($b > a$) of ray $\varphi = \varphi_0$ ($-\pi < \varphi_0 < \pi$), we obtain up to an additive constant

$$w(r, \varphi) = K(m)\Omega(r, \varphi) = iK(m) \sum_{\substack{n=-\infty \\ n \neq 0}}^{\infty} \text{sign } n C_n r^{-|n|} e^{in\varphi} \quad (r > a, -\pi < \varphi < \pi). \tag{16.3.5}$$

Then, from (16.3.4), we get

$$\omega(\varphi) = \frac{\partial \Lambda}{\partial r} \Big|_{r=a} = - \sum_{\substack{n=-\infty \\ n \neq 0}}^{\infty} |n| C_n a^{-|n|-1} e^{in\varphi} \quad (-\pi < \varphi < \pi), \quad \chi(\varphi) = \frac{1}{r} \frac{\partial \Lambda}{\partial \varphi} \Big|_{r=a}$$

$$= i \sum_{\substack{n=-\infty \\ n \neq 0}}^{\infty} n C_n a^{-|n|-1} e^{in\varphi}. \tag{16.3.6}$$

From the first equality (16.3.6), we determine the Fourier coefficients

$$C_n = -\frac{a^{|n|+1}}{2\pi|n|} \int_{-\pi}^{\pi} \omega(\vartheta) e^{-in\vartheta} d\vartheta \quad (n = \pm 1, \pm 2, \dots) \tag{16.3.7}$$

and substitute them into the second equality (16.3.6). After elementary transformations, we get

$$\chi(\varphi) = \frac{1}{\pi} \int_{-\pi}^{\pi} \left[\sum_{n=1}^{\infty} \sin(n(\varphi - \vartheta)) \right] \omega(\vartheta) d\vartheta,$$

where the convergence of the series is understood in the sense of the theory of generalized functions [17] as weak convergence. To calculate the sum of this series, we use the well-known formula from [18]. We can write

$$\sum_{n=1}^{\infty} \sin(n\varphi) = -\left(\ln \frac{1}{2|\sin \frac{\varphi}{2}|} \right)'_{\varphi} = \left(\ln \left| \sin \frac{\varphi}{2} \right| \right)'_{\varphi} = \frac{1}{2} \text{Cotan} \frac{\varphi}{2}.$$

As a result

$$\chi(\varphi) = \frac{1}{2\pi} \int_{-\pi}^{\pi} \text{Cotan} \left(\frac{\varphi - \vartheta}{2} \right) \omega(\vartheta) d\vartheta \quad (-\pi < \varphi < \pi). \tag{16.3.8}$$

Thus, the partial derivatives of the harmonic pseudostress function $\Lambda(r, \varphi)$ on the circle $r = a$ are interconnected by an integral relation with the Hilbert kernel (16.3.8). This statement also follows from Hilbert’s formula on the relationship between the boundary values of the real and imaginary parts on the boundary unit circle of a function analytic in the unit circle [19].

Now, using the first formula (16.2.20), we implement the boundary condition (16.3.1)

$$\begin{aligned} \tau_{\varphi z}|_{r=a} &= \frac{1}{2^{m-1}} \left[\left(\frac{\partial \Lambda}{\partial r} \Big|_{r=a} \right)^2 + \left(\frac{1}{r} \frac{\partial \Lambda}{\partial r} \Big|_{r=a} \right)^2 \right]^{\frac{m-1}{2}} \frac{\partial \Lambda}{\partial r} \Big|_{r=a} \\ &= f(\varphi) \quad (-\pi < \varphi < \pi). \end{aligned}$$

Taking (16.3.6) into account, we have

$$\left[\omega^2(\varphi) + \chi^2(\varphi) \right]^{\frac{m-1}{2}} \omega(\varphi) = 2^{m-1} f(\varphi) \quad (-\pi < \varphi < \pi) \tag{16.3.9}$$

Next, using the Hilbert inversion formula [20], from (16.3.8), we find

$$\omega(\varphi) = -\frac{1}{2\pi} \int_{-\pi}^{\pi} \operatorname{Cotan}\left(\frac{\varphi - \vartheta}{2}\right) \chi(\vartheta) d\vartheta, \quad (16.3.10)$$

since by the first formula (16.3.6)

$$\int_{-\pi}^{\pi} \omega(\varphi) d\varphi = 0.$$

Substituting this expression of $\omega(\varphi)$ into (16.3.9), we arrive at the following governing NSIE of the problem under consideration for $\chi(\varphi)$:

$$\left\{ \chi^{2^m}(\varphi) + \left[\frac{1}{2\pi} \int_{-\pi}^{\pi} \operatorname{Cotan}\left(\frac{\vartheta - \varphi}{2}\right) \chi(\vartheta) d\vartheta \right]^2 \right\}^{\frac{m-1}{2}} \frac{1}{2\pi} \int_{-\pi}^{\pi} \operatorname{Cotan}\left(\frac{\vartheta - \varphi}{2}\right) \chi(\vartheta) d\vartheta = 2^{m-1} f(\varphi) \quad (-\pi < \varphi < \pi). \quad (16.3.11)$$

After solving the NSIE (16.3.11), the function $\omega(\varphi)$ is determined from (16.3.10), and the Fourier coefficients C_n will be determined from (16.3.7) or from the second equality in (16.3.6).

16.4 Solving Nonlinear Singular Integral Equation

We reduce solving this NSIE to solving the Riemann boundary value problem of the theory of analytic functions. To this end, we introduce into consideration a piecewise holomorphic function—the Cauchy-type integral

$$\Phi(z) = \frac{1}{2\pi i} \oint_C \frac{\chi(t) dt}{t - z},$$

where C is a circle of radius a centered at the origin. From here, according to the Plemelya-Sokhotsky formulas for the boundary values of the function $\Phi(z)$, we will have

$$\begin{aligned} \Phi^+(\zeta) &= \frac{1}{2} \chi(\zeta) + \frac{1}{2\pi i} \oint_C \frac{\chi(t) dt}{t - \zeta}, \\ \Phi^-(\zeta) &= -\frac{1}{2} \chi(\zeta) + \frac{1}{2\pi i} \oint_C \frac{\chi(t) dt}{t - \zeta} \quad (\zeta \in C). \end{aligned} \quad (16.4.1)$$

On the circle C , we put

$$t = ae^{i\vartheta}, \quad \zeta = ae^{i\varphi}; \quad \chi(t) = \chi(ae^{i\vartheta}) = \chi_0(\vartheta), \quad \Phi^\pm(\zeta) = \Phi^\pm(ae^{i\varphi}) = \Phi_0^\pm(\varphi) \\ (-\pi < \vartheta, \varphi \leq \pi)$$

and transform the expression

$$\frac{dt}{t - \zeta} = \frac{aie^{i\vartheta} d\vartheta}{ae^{i\vartheta} - ae^{i\varphi}} = i \frac{e^{i\vartheta} d\vartheta}{e^{i\frac{\vartheta+\varphi}{2}} \left(e^{i\frac{\vartheta-\varphi}{2}} - e^{-i\frac{\vartheta+\varphi}{2}} \right)} = \frac{1}{2} \frac{\cos\left(\frac{\vartheta-\varphi}{2}\right) + i \sin\left(\frac{\vartheta-\varphi}{2}\right)}{\sin \frac{\vartheta-\varphi}{2}} \\ = \frac{1}{2} \left[\operatorname{Cotan}\left(\frac{\vartheta - \varphi}{2}\right) + i \right].$$

Then, relations (16.4.1) can be written in the form

$$\Phi_0^\pm(\varphi) = \pm \frac{1}{2} \chi_0(\varphi) + \frac{1}{4\pi i} \int_{-\pi}^{\pi} \operatorname{Cotan}\left(\frac{\vartheta - \varphi}{2}\right) \chi_0(\vartheta) d\vartheta \quad (-\pi < \varphi < \pi), \quad (16.4.2)$$

since according to the second formula of (16.3.6)

$$\int_{-\pi}^{\pi} \chi_0(\vartheta) d\vartheta = 0.$$

Then, from (16.4.2), we find

$$\Phi_0^+(\varphi) \Phi_0^-(\varphi) = -\frac{1}{4} \left\{ \chi_0^2(\varphi) + \left[\frac{1}{2\pi} \int_{-\pi}^{\pi} \operatorname{Cotan}\left(\frac{\vartheta - \varphi}{2}\right) \chi_0(\vartheta) d\vartheta \right]^2 \right\} \\ (-\pi < \varphi < \pi).$$

As a result, the NSIE (16.3.11) reduces to the following nonlinear Riemann boundary value problem

$$\left[-4\Phi_0^+(\varphi) \Phi_0^-(\varphi) \right]^{\frac{m-1}{2}} \left[\Phi_0^+(\varphi) + \Phi_0^-(\varphi) \right] = -i2^{m-1} f(\varphi) \quad (-\pi < \varphi < \pi). \quad (16.4.3)$$

However, from (16.4.2), it follows that

$$\Phi_0^+(\varphi) = \overline{-\Phi_0^-(\varphi)} \quad \text{or} \quad \Phi_0^-(\varphi) = \overline{-\Phi_0^+(\varphi)} \quad (-\pi < \varphi < \pi). \quad (16.4.4)$$

Taking into account relations (16.4.4), we can write

$$\begin{aligned}
 1) \left[-\Phi_0^+(\varphi)\Phi_0^-(\varphi) \right]^{\frac{m-1}{2}} \Phi_0^+(\varphi) &= \left[\Phi_0^+(\varphi)\overline{\Phi_0^+(\varphi)} \right]^{\frac{m-1}{2}} \Phi_0^+(\varphi) = |\Phi_0^+(\varphi)|^{m-1} \Phi_0^+(\varphi) = \Psi^+(\varphi), \\
 2) \left[-\Phi_0^+(\varphi)\Phi_0^-(\varphi) \right]^{\frac{m-1}{2}} \Phi_0^-(\varphi) &= \left[\Phi_0^-(\varphi)\overline{\Phi_0^-(\varphi)} \right]^{\frac{m-1}{2}} \Phi_0^-(\varphi) = |\Phi_0^-(\varphi)|^{m-1} \Phi_0^-(\varphi) = \Psi^-(\varphi).
 \end{aligned}
 \tag{16.4.5}$$

As a result, of these transformations, the nonlinear boundary value problem (16.4.3) is reduced to the following linear boundary value problem

$$\Psi^+(\zeta) + \Psi^-(\zeta) = -if(\zeta) \quad (\zeta = ae^{i\varphi} \in C). \tag{16.4.6}$$

To solve problem (16.4.6), we introduce the Cauchy-type integral

$$\Omega(z) = -\frac{1}{2\pi i} \oint_C \frac{if(t)dt}{t-z} \tag{16.4.7}$$

and put [20]

$$\Psi(z) = \begin{cases} \Omega(z) & (z \in S^+) \\ -\Omega(z) & (z \in S^-), \end{cases} \tag{16.4.8}$$

where S^+ is a circle of radius a centered at the origin and with a boundary circle C , and S^- is a complex plane with a circular hole of radius a . It is easy to see that

$$\Omega^+(\zeta) - \Omega^-(\zeta) = -if(\zeta) \Rightarrow \Psi^+(\zeta) + \Psi^-(\zeta) = -if(\zeta) \quad (\zeta \in C)$$

and hence, the piecewise holomorphic function $\Psi(z)$ does give a solution to the boundary value problem (16.4.6). Now, by multiplying relations (16.4.5), we obtain

$$\left[-\Phi_0^+(\varphi)\Phi_0^-(\varphi) \right]^m = -\Psi^+(\varphi)\Psi^-(\varphi) \quad (-\pi < \varphi < \pi)$$

and, further, from the same relations, we find

$$\begin{aligned}
 \Phi_0^+(\varphi) &= \left[-\Psi^+(\varphi)\Psi^-(\varphi) \right]^{\frac{1-m}{2m}} \Psi^+(\varphi), \quad \Phi_0^-(\varphi) \\
 &= \left[-\Psi^+(\varphi)\Psi^-(\varphi) \right]^{\frac{1-m}{2m}} \Psi^-(\varphi) \quad (-\pi < \varphi < \pi).
 \end{aligned}
 \tag{16.4.9}$$

Then, the solution of the original NSIE (16.3.11) according to (16.4.2) and (16.4.9) will be expressed by the formula

$$\chi_0(\varphi) = \left[-\Psi^+(\varphi)\Psi^-(\varphi) \right]^{\frac{1-m}{2}} \left[\Psi^+(\varphi) - \Psi^-(\varphi) \right] \quad (-\pi < \varphi < \pi).$$

From here, using (16.4.7) and (16.4.8), after simple transformations, taking into account condition (16.3.2), we finally obtain the solution of the original NSIE (16.3.11)

$$\chi_0(\varphi) = \chi(ae^{i\varphi}) = -2 \frac{m-1}{m} \left\{ f^2(\varphi) + \left[\frac{1}{2\pi} \int_{-\pi}^{\pi} \operatorname{Cotan}\left(\frac{\vartheta - \varphi}{2}\right) f(\vartheta) d\vartheta \right]^2 \right\}^{\frac{m-1}{2m}} \frac{1}{2\pi} \int_{-\pi}^{\pi} \operatorname{Cotan}\left(\frac{\vartheta - \varphi}{2}\right) f(\vartheta) d\vartheta$$

($-\pi < \varphi < \pi$).

(16.4.10)

In the linear case $m = 1$ and we get from (16.4.10)

$$\chi_0(\varphi) = -\frac{1}{2\pi} \int_{-\pi}^{\pi} \operatorname{Cotan}\left(\frac{\vartheta - \varphi}{2}\right) f(\vartheta) d\vartheta.$$

In a particular case, we take

$$f(\varphi) = \sin(n\varphi) \quad (n = 1, 2, \dots, \quad -\pi < \varphi < \pi).$$

Taking into account, the known relations [21]

$$\frac{1}{2\pi} \int_{-\pi}^{\pi} \operatorname{Cotan}\left(\frac{\vartheta - \varphi}{2}\right) \sin(n\vartheta) d\vartheta = \cos(n\varphi) \quad (-\pi < \varphi < \pi, \quad n = 1, 2, \dots),$$

from (16.4.10), we have

$$\chi_0(\varphi) = -2 \frac{m-1}{m} \cos(n\varphi) \quad (-\pi < \varphi < \pi). \quad (16.4.11)$$

We represent it as

$$\chi_0(\varphi) \Rightarrow \chi(\varphi) = \alpha_m (e^{in\varphi} + e^{-in\varphi}), \quad \alpha_m = -\frac{1}{2^{1/m}}$$

and compare it with the expansion in a Fourier series by the second formula in (16.3.6). We get

$$in a^{-n-1} (C_n e^{in\varphi} - C_{-n} e^{-in\varphi}) = \alpha_m (e^{in\varphi} + e^{-in\varphi}) \quad (n = 1, 2, \dots, \quad -\pi < \varphi < \pi).$$

Taking into account the properties of the coefficients C_n from (16.3.4), we have

$$C_n = -\frac{i\alpha_m}{n} a^{n+1} \quad (n = 1, 2, \dots). \quad (16.4.12)$$

Now, using (16.4.12) and formulas (16.2.10), (16.3.4)–(16.3.6), we calculate the corresponding harmonics of stresses $\tau_{\varphi z}$, τ_{rz} and functions $\omega(\varphi)$, $\Lambda(r, \varphi)$, $w(r, \varphi)$. We obtain

$$\begin{aligned}\tau_{\varphi z} &= -2|\alpha_m|^{m-1}\alpha_m\left(\frac{a}{r}\right)^{m(n+1)}\sin(n\varphi); & \tau_{rz} &= -2|\alpha_m|^{m-1}\alpha_m\left(\frac{a}{r}\right)^{m(n+1)}\cos(n\varphi); \\ \omega(\varphi) &= 2\alpha_m\cos(n\varphi); & \Lambda(r, \varphi) &= 2a\frac{\alpha_m}{n}\left(\frac{a}{r}\right)^n\sin(n\varphi); & (\zeta \geq a & -\pi < \varphi \leq \pi) \\ w(r, \varphi) &= 2K(m)\frac{\alpha_m}{n}a^{n+1}\cos(n\varphi). & (n = 1, 2, \dots).\end{aligned}$$

16.5 Conclusion

Further, development of the results presented in this article is connected with the application of the conformal mapping method. Namely, the solution of the first boundary value problem in the NSSCT formulation under a power law and an antiplane deformation for a given domain can be obtained from the solution (16.4.10). The solution constructed here using a conformal mapping of this domain onto a plane with a circular hole or onto a half-plane, for which the solution of the first boundary problem is given in [8]. Consideration of these issues is the subject of a separate study.

References

1. Arutyunyan, N.K.: The plane contact problem of the theory of creep. *J. Appl. Math. Mech.* **23**(5), 1283–1313 (1959)
2. Arutyunyan, N.K.: Plane contact problem of creeping with power-law strengthening of the material. *Sov. J. Contemporary Math. Anal.* **12**(2), 77–105 (1959)
3. Atkinson, C.: A note on crack problems in power-law elastic materials and contact problems in nonlinear creep. *Int. J. Eng. Sci.* **9**(8), 729–739 (1971)
4. Alexandrov, V.M., Sumbatyan, M.A.: On a solution of contact problem of nonlinear steady creep for halfplane. *Mech. Solids.* **1**, 107–113 (1983)
5. Alexandrov, V.M., Brudnyi, S.R.: On the method of generalized superposition in contact problem of antiplane shear. *Mech. Solids.* **4**, 71–78 (1986)
6. Rice, J.R.: Mathematical analysis in the mechanics of fracture. In: Liebowitz, H. (ed.) *Fracture: An Advanced Treatise*, vol. 2, pp. 191–311 (1986)
7. Lee, Y.S., Gong, H.: Application of complex variables and pseudo-stress function to power-law materials and stress analysis of single rigid inclusion in power-law materials subjected to simple tension and pure shear. *Int. J. Mech. Sci.* **29**(10/11), 669–694 (1987)
8. Mkhitarian, S.M.: Solution of the first boundary value problem of nonlinear theory of steady-state creep for a half-space in antiplane deformation. *Mech. Solids.* **47**, 646–653 (2012). <https://doi.org/10.3103/S0025654412060064>
9. Mkhitarian, S.M.: Solution of a mixed boundary value problem of nonlinear creep theory. *Mech. Solids.* **54**, 461–473 (2019). <https://doi.org/10.3103/S0025654419020109>
10. Arutyunyan, N.K., Manzhurov, A.V.: *Contact Problems in the Theory of Creep*. Izd-vo NAN RA, Yerevan. [In Russ.] (1999)
11. Galin, L.A. (ed.): *The Development of Theory of Contact Problems in USSR*. Nauka, Moscow. [in Russ.] (1976)

12. Budd, W.F., Warner, R.C., Jacka, T.H., Li, J., Treverrow, A.: Ice flow relations for stress and strain-rate components from combined shear and compression laboratory experiments. *J. Glaciol.* **59**(214), 374–392 (2013)
13. Graham, F.S., Morlighem, M., Warner, R.C., Treverrow, A.: Implementing an empirical scalar constitutive relation for ice with flow-induced polycrystalline anisotropy in large-scale ice sheet models. *The Cryosphere.* **12**(3), 1047–1067 (2018)
14. Bons, P.D., Kleiner, T., Llorens, M.G., Prior, D.J., Sachau, T., Weikusat, I., Jansen, D.: Greenland ice sheet: Higher nonlinearity of ice flow significantly reduces estimated basal motion. *Geophys. Res. Let.* **45**(13), 6542–6548 (2018)
15. Kachanov, L.M.: *Theory of Creep*. Fizmatgiz, Moscow (1960).[in Russ.]
16. Kachanov, L.M.: *Fundamentals of Fracture Mechanics*. Nauka, Moscow (1974).[in Russ.]
17. Gelfand, I.M., Shilov, G.E.: *Generalized Functions, and Actions upon them*. Dobrosvet, Moscow (2007).[in Russ.]
18. Gradshtein, I.S., Ryzhik, I.M.: *Tables of Integrals, Sums, Series and Products*. Elsevier, New York (2014)
19. Gakhov, F.D.: *Boundary Value Problems*. Elsevier, New York, London (2014)
20. Muskhelishvili, N.I.: *Singular Integral Equations*. Wolters-Noordhoff, Groningen (1958)
21. Tricomi, F.G.: *Integral Equations*. Dover Publ, New York (1985)

Chapter 17

On the Generalised Boundary Conditions in Harutyunyan's Model of Growing Solids



Evgenii V. Murashkin

Abstract The paper deals with the problem of boundary conditions derivation on the propagating growing surface for Harutyunyan's model in case of materials sensitive to mirror reflections and inversions of three-dimensional space. The growing surface positions are specified as the level surface of the pseudoscalar field. The notions of fundamental orienting pseudoscalar and pseudoscalar time of weight W are introduced. The unit normal pseudovector to the propagating growing surface given by the pseudoscalar field are calculated and discussed. The boundary conditions for stresses on the propagating growing surface proposed by G. I. Bykovtsev are generalised to the case of pseudoscalar geometry.

Keywords Surface growth · Differential constraint · Pseudotensor · Pseudoscalar time · Harutyunyan's model

17.1 Introduction

Conventional methods of manufacturing complex shape products imply a variety of technological treating processes, both related to the material removal and based on the synthesis of products by sequentially depositing material to a boundary surface [1–3]. All these stimulates the development of mechanics of growing solids. Additive manufacturing technologies are widely used in modern industrial production of parts with complex shapes and designs. These methods include: laser stereolithography, selective laser sintering, electron beam melting, deposition modelling, multi-jet modelling, lamination, 3D-printing, computer axial lithography, layer-by-layer concreting and production of woven composites.

The mentioned above methods are based on well-known natural processes of surface growth: accretion of space objects, formation of avalanches and glaciers and crystal growth processes. At the same time, the processes of growth of biological

E. V. Murashkin (✉)

Ishlinsky Institute for Problems in Mechanics of the Russian Academy of Sciences, Vernadsky Ave 101 Bldg 1, Moscow 119526, Russian Federation
e-mail: murashkin@ipmnet.ru

tissues and organisms are related to the processes of volumetric growth; nevertheless, processes of surface growth can also be distinguished among them. For example, the growth of atherosclerotic plaques [4–6], growth of the root system and the human bones growth. The growth of an atherosclerotic plaque can be described as the process of initial infiltration of blood plasma components into a thin subsurface layer of the inner wall of an artery. The growth of a crystal nucleus occurs by deposition individual atoms or their groups to its surface.

The main feature of the growing solids is the solids forming simultaneously with the deformation process. This circumstance, of course, significantly complicates the mathematical modelling of such deformation processes in comparison with solids of constant staff. Suffice it to mention the situation that takes place in the dynamics of an absolutely rigid body of variable mass. The mass variability, on the one hand, leads to more complex mathematical problems, and on the other hand, generates qualitatively new effects in the behaviour of bodies. It is natural to expect that generalised model of solids and the initial-boundary value problems will become more complicated, and the influence of the growth parameters on the response of the solids will become more diverse.

The solution of the boundary problem of growing solids is a very laborious problem. An important feature of boundary value problems in mechanics of growing solids is the derivation of boundary conditions at the propagating growing surface between the main solids and the deposited part. We can found the discussions on boundary conditions problems in studies [7, 8]. The present paper deals with the consideration of Harutyunyan’s model of surface growing solids [7] and several variants of constitutive relations on the growing surface, akin to the simplest relations (see the well-known book by G. I. Bykovtsev: [8, pp. 288–292]). Throughout the paper, the terminology and notations adopted in publications [8–13] will be used.

17.2 Governing Equations of Harutyunyan’s Model of Surface Growing Solids

The in-depth study of modelling surface growing solids proposed by N.Kh. Harutyunyan can be found in [7]. Let us revisit the governing equation of this model. The equilibrium equations for Cauchy stress tensor σ^{sr} can be furnished in terms of velocities by

$$\nabla_s(\partial.\sigma^{sr}) = \mathbf{0}, \quad (17.1)$$

where ∇_s is the Hamilton (nabla) operator, $\partial.$ is a time derivative.

Boundary conditions on a non-growing part of the surface (surface of the main solids) are reads by

$$n_s \partial.\sigma^{sr} = \partial.p_0^r \quad (17.2)$$

and (or)

$$v^s = \partial_t u_0^s. \quad (17.3)$$

where p_0^r is the given traction vector, v^s is the velocity vector, u_0^s is the given displacement vectors, n_s is the unit normal covariant vector.

Condition on a growing surface Σ can be obtained from the solution of contact problem between 3D solid and 2D surface in form [14]

$$n_s \partial_t \sigma^{sr} = -c \sigma_{2d}^{kh} L_{hk} n_k, \quad (17.4)$$

where c is the linear velocity of propagating growing surface in the normal direction n_s , σ_{2d}^{kh} is the 2D tensor of the given elastic surface tension, L_{hk} is the 2D tensor of the surface curvature.

Constitutive equations for the strain rates ε_{sr} and velocities are furnished by

$$\varepsilon_{sr} = \frac{1}{2} (\nabla_s v_r + \nabla_r v_s), \quad (17.5)$$

and the general form of constitutive equations for Cauchy stress rate tensor can be assumed in form

$$\partial_t \sigma^{sr} = 2 \mathcal{F}^{sr}(\varepsilon_{sr}, v_s). \quad (17.6)$$

where \mathcal{F}^{sr} is the tensor function defining by experiments.

The equation of the propagating growing surface $\Sigma(t)$ in the implicit form reads by formula

$$t = \tau_*(x^k), \quad (17.7)$$

Governing Eqs. (17.1)–(17.7) must be supplemented by the recovering rules for stress tensor and displacements according to

$$\begin{aligned} \sigma^{sr}(x^k, t) &= \sigma_*^{sr}(x^k) + \int_{\tau_*(x^k)}^t \partial_t \sigma^{sr}(x^k, t') dt', \\ u^s(x^k, t) &= u_*^s(x^k) + \int_{\tau_*(x^k)}^t v^s(x^k, t') dt'. \end{aligned} \quad (17.8)$$

Herein $\sigma_*^{sr} = \sigma^{sr}|_{t=\tau_*(x^k)}$; $u_*^s(x^k) = u^s|_{t=\tau_*(x^k)}$. Equation (17.8) are the simple integrating rule of primitives.

It should be noted that the boundary value problem for a growing solid can be controlled by loads, stresses on the propagating growing surface and velocity of material deposition.

17.3 Differential Constraints on Propagating Growing Surface

Boundary conditions on the propagating growing surface require additional attention and discussion. An attempt to obtain boundary conditions from the equilibrium equations was made by G.I. Bykovtsev (see book [8, pp. 288–292]) and later generalised in [9–13] to the case of micropolar media and predeformed media.

As previously shown (see, for example, [9–13]), the transformation of equations of equilibrium (17.1) using a formula for the actual components of the force stress tensor σ^{ij}

$$\sigma^{ij} = \int_{\tau_*+0}^t [\partial_t \sigma^{ij}(x^s, t')] dt' + \mathcal{S}^{ji} + \sigma_*^{ij}(x^s), \quad (17.9)$$

$$\mathcal{S}^{ij} = \int_{\tau_*-0}^{\tau_*+0} [\partial_t \sigma^{ij}(x^s, t')] dt', \quad (17.10)$$

allows us to derive the equation on the propagating growing surface in the form of the following differential constraints

$$c[\nabla_j \sigma_*^{ji}(x^s) + \nabla_j \mathcal{S}^{ji} + X_*^i(x^s)] - n_j \partial_t \sigma^{ji}(x^s, t) = 0 \quad (t = \tau_* + 0), \quad (17.11)$$

where the unit normal vector n_i on the propagating growing surface Σ directed towards its propagation is related to the spatial gradient (17.7) by the equation

$$n_i = c \partial_i \tau_*, \quad c = |\nabla \tau_*|^{-1} \quad (t = \tau_*). \quad (17.12)$$

In Eqs. (17.9)–(17.11), we use the notation adopted in [9–11]: \mathcal{S}^{ji} is the stress jump related integral, $\sigma_*^{ij}(x^s) = \sigma^{ij}(x^s, t)|_{t=\tau_*(x^s)-0}$ are the stress tensor components, respectively, at the moment $t = \tau_*(x^s) - 0$ right before when the element is included in the main solid, $X_*^i(x^s) = X^i(x^s, t)|_{t=\tau_*(x^s)+0}$. Moment $t = \tau_*(x^s) + 0$ corresponds to the moment right after attaching the element to the growing surface.

In the general case, the forces stresses σ_*^{ij} are to be expressed in terms of the actual stresses and couples on propagating growing surface by a tensor constitutive equations as follows

$$\sigma_*^{ij} = \mathfrak{F}^{ij}(\sigma^{ij}, n_i, \dots). \quad (17.13)$$

Constitutive tensor function \mathfrak{F}_{ij} can be determinate by experiments. The function \mathfrak{F}_{ij} means possible changes in the parameters of the stress-strain state of the growing

material in the time interval from the moment of growing element creation to the moment of its deposition to the main solid, i.e. in the time interval $\tau - 0 \leq t \leq \tau + 0$. In particular, constitutive tensor functions \mathfrak{F}_{ij} in the woven materials producing will depend on the selected directions associated with the propagating growing surface and localisation of composite fibres. An important restriction on constitutive tensor functions \mathfrak{F}_{ij} is the insensitivity of its arguments under rotations of the moving coordinate system around the unit normal vector n_j to the growing surface. In this case, it is necessary to choose a system of joint invariants of tensors σ^{ij} and vectors n_j, ι_j , satisfying the condition of rotational invariance with respect to the vector n_j .

17.4 Pseudoscalar Geometry of Propagating Growing Surface

In some case, it may turn out that the propagating growing surface is the level surface of the pseudoscalar field. For example, in the case of materials (woven composites, chiral materials, metamaterials and biological tissues) exhibiting the properties of sensitivity to mirror reflections and inversions of three-dimensional space. The base object sensitive to mirror reflections and inversions of three-dimensional space is the fundamental orienting pseudoscalar of weight +1 defined as a triple product of covariant base vectors $(\mathbf{t}_1, \mathbf{t}_2, \mathbf{t}_3)$

$$e = [\mathbf{t}_1, \mathbf{t}_2, \mathbf{t}_3] = (\mathbf{t}_1 \times \mathbf{t}_2) \cdot \mathbf{t}_3. \quad (17.14)$$

A number of approaches to the development of pseudotensor formalism can be found out in books on tensor analysis and continuum mechanics [15–20].

Let the propagating surface Σ in three-dimensional space is defined as the level surface of the pseudoscalar field $f(x^i)$ of weight W :

$${}^{[W]}t = f(x^i), \quad (17.15)$$

where ${}^{[W]}t$ is pseudoscalar time, and

$${}^{[W]}t = e^W t. \quad (17.16)$$

Considering the pseudoscalar time differential ${}^{[W]}t$ in virtue of (17.16) we can get

$$d{}^{[W]}t = d(e^W t) = e^W dt + t W e^{W-1} de, \quad (17.17)$$

or

$$d^{[W]}t = e^W (dt + te^{-1} \partial_s e dx^s). \quad (17.18)$$

Let us note the important in applied problems case [21]. We choose a coordinate system subject to the condition:

$$\sqrt{g} = 1, \quad (17.19)$$

and using following equation,

$$e^2 = g \quad (17.20)$$

come to restriction

$$e = \text{sgn } e. \quad (17.21)$$

There are infinitely many such systems in three-dimensional space, for example, Cartesian left-handed and right-handed coordinate systems.

The constraint $\sqrt{g} = 1$ is often used not only in the theory of relativity [21], but also in mechanics of solids [22]. On pages 135–142 of the [21] monograph, the condition $\sqrt{g} = 1$ is used to derive the gravity equation in 4-space-time, which greatly simplifies the equations of relativity theory.

If, in addition to equation (17.21), we assume that the coordinate system is left-handed (i.e. $e < 0$), then the pseudoscalar time differential takes the form

$$d^{[W]}t = \begin{cases} dt, & \text{if } W \text{ is even weight;} \\ -dt, & \text{if } W \text{ is odd weight.} \end{cases} \quad (17.22)$$

The covariant vector of the unit normal n_s to the surface Σ , can be determined up to a multiplier according to the formula

$$Nn_i = \partial_i (e^{-W} f^{[W]}). \quad (17.23)$$

Note that the absolute scalar a satisfies the equation

$$\nabla_i a = \partial_i a. \quad (17.24)$$

Then the Eqs. (17.12), (17.24) are transformed to the form

$$Nn_i = \partial_i (e^{-W} f^{[W]}) = \nabla_i (e^{-W} f^{[W]}) = e^{-W} \nabla_i f^{[W]}. \quad (17.25)$$

Introducing into consideration the normal pseudovector according to the formula

$$n_i^{[W]} = e^W n_i, \quad (17.26)$$

we can get

$$N n_i^{[W]} = \nabla_i^{[W]} f. \quad (17.27)$$

According to equation

$$g^{ij} n_i^{[W]} n_j^{[W]} = e^{2W} \quad (17.28)$$

it is easy to conclude that

$$N^2 e^{2W} = g^{ik} \nabla_i^{[W]} f \nabla_k^{[W]} f, \quad (17.29)$$

hence for the unknown multiplier, N can be calculated by the equation

$$\pm N = e^{-W} \sqrt{g^{ik} \nabla_i^{[W]} f \nabla_k^{[W]} f}, \quad (17.30)$$

Finally, the normal pseudovector to the level surface Σ of the pseudoscalar field $f^{[W]}$ is calculated by the formula

$$n_i^{[W]} = e^W \frac{\nabla_i^{[W]} f}{\sqrt{g^{ik} \nabla_i^{[W]} f \nabla_k^{[W]} f}} \quad (17.31)$$

The linear velocity of the propagating growing surface in the direction of the normal pseudovector $n_s^{[W]}$ is calculated according to

$$c^{[-W]} = \left(\sqrt{g^{ik} \nabla_i^{[W]} f \nabla_k^{[W]} f} \right)^{-1}. \quad (17.32)$$

The absolute vector of the normal to the level surface Σ of the pseudoscalar field $f^{[W]}$ can be calculated by the formula

$$n_i = c^{[-W]} \nabla_i^{[W]} f. \quad (17.33)$$

17.5 Differential Constraints on Propagating Growing Pseudoscalar Surface

Following the discussions in previous sections, we can obtain the differential constraints on propagating growing pseudoscalar surface. In the growth process, the

maximum intensity of shear stresses can be reached at the contact (growing) surface between the main solid and the growing part. Let us define the growing surface as a level surface of a pseudoscalar function, as was indicated in the Sect. 17.3

$$t^{[W]} = \frac{[W]}{\tau_*}(x^i). \tag{17.34}$$

The relations (17.11) in the case of propagating growing pseudoscalar surface are transformed as follows

$$c^{[-W]}[\nabla_j t^{ji}(x^k) + X^i(x^k)] - n_j \partial. t^{ji}(x^k)|_{t^{[W]} = \frac{[W]}{\tau_*}(x^k)} = 0. \tag{17.35}$$

The recovering equation for the stress tensor components takes the form

$$t^{ij} = \int_{\frac{[W]}{\tau_*}}^t [\partial. t^{ij}(x^k, t^{[W]})] d t^{[W]} + t^{ij}(x^k). \tag{17.36}$$

Equations (17.35) and (17.36) are the generalised boundary conditions on the growing surfaces which can be used for wide class of materials including woven composites.

17.6 Conclusions

The paper is devoted to the boundary value problems formulations in the frameworks of Harutyunyan’s model in case of materials sensitive to mirror reflections and inversions of three-dimensional space. The growing surface positions have been specified as the level surface of the pseudoscalar field. The notions of fundamental orienting pseudoscalar and pseudoscalar time of weight W have been introduced. The unit normal pseudovector to the propagating growing surface given by the pseudoscalar field have been calculated and discussed. The boundary conditions for stresses on the propagating growing surface proposed by G. I. Bykovtsev have been generalised to the case of pseudoscalar geometry.

Acknowledgements The present work was partially supported by the Ministry of Science and Higher Education within the framework of the Russian State Assignment under contract No. AAAA-A20-120011690132-4 and partially supported by Russian Foundation for Basic Research (RFBR) Grant No. 20-01-00666.

References

1. Gardan, J.: Additive manufacturing technologies: state of the art and trends. In: *Additive Manufacturing Handbook*, pp. 149–168. CRC Press, Boca Raton (2017)
2. Gibson, I., Rosen, D.W., Stucker, B., Khorasani, M., Rosen, D., Stucker, B., Khorasani, M.: *Additive Manufacturing Technologies*, vol. 17. Springer, Cham (2021)
3. Alammar, A., Kois, J.C., Revilla-León, M., Att, W.: Additive manufacturing technologies: current status and future perspectives. *J. Prosthodontics* **31**(S1), 4–12 (2022). <https://doi.org/10.1111/jopr.13477>
4. Murashkin, E., Dats, E., Stadnik, N.: The simulation of atherosclerosis by the 3-layered growing cylinder. In: *Proceedings of The World Congress on Engineering and Computer Science 2019*, 22–24 October, 2019, San Francisco, USA. *Lecture Notes in Engineering and Computer Science*, pp. 362–365. IAENG, London (2019)
5. Stadnik, N.E., Murashkin, E.V., Dats, E.P.: Residual stresses in blood vessel wall during atherosclerosis. *AIP Conf. Proc.* **2116**, 380013 (2019). <https://doi.org/10.1063/1.5114394>
6. Murashkin, E.V., Dats, E.P., Stadnik, N.E.: Application of surface growth model for a pathological process in a blood vessel's wall. *Math. Meth. Appl. Sci.* **45**(5), 3197–3212 (2022). <https://doi.org/10.1002/mma.7056>
7. Harutyunyan, N.Kh., Drozdov, A.D., Naumov, V.E.: *Mechanics of Growing Viscoelastoplastic Solids*. Nauka, Moscow (1987). (in Russian)
8. Bykovtsev, G. I.: *Selected Problems from Solid Mechanics*. Collection of papers. Vladivostok, Dal'nauka (2002) (in Russian)
9. Murashkin, E.V., Radayev, Yu.N.: On a differential constraint in asymmetric theories of the mechanics of growing solids. *Mech. Sol.* **54**(8), 1157–1164 (2019). <https://doi.org/10.3103/S0025654419080053>
10. Murashkin, E.V., Radayev, Yu.N.: On a differential constraint in the continuum theory of growing solids. *J. Samara State Tech. Univ. Ser. Phys. Math. Sci.* **23**(4), 646–656 (2019). <https://doi.org/10.14498/vsgtu1696>
11. Murashkin, E.V., Radayev, Yu.N.: On a class of constitutive equations on propagating growing surface. *Vestn. Chuvash. Gos. Ped. Univ. I.Ya. Yakovlev. Ser.: Mekh. Pred. Sost.* **3**(41), 11–29 (2019). <https://doi.org/10.26293/chgppu.2019.40.2.012>
12. Murashkin, E.V., Radayev, Yu.N.: On a micropolar theory of growing solids. *J. Samara State Tech. Univ. Ser. Phys. Math. Sci.* **24**(3), 424–444 (2020). <https://doi.org/10.14498/vsgtu1792>
13. Murashkin, E.V.: On a system of independent arguments for constitutive tensor functions on the growing surface in micropolar continuum. *J. Phys.: Conf. Ser.* **2231**(1), 012019 (2022). <https://doi.org/10.1088/1742-6596/2231/1/012019>
14. Manzhirov, A.V., Murashkin, E.V., Parshin, D.A.: Modeling of additive manufacturing and surface growth processes. *AIP Conf. Proc.* **2116**, 380011 (2019). <https://doi.org/10.1063/1.5114392>
15. Veblen, O., Thomas, T.Y.: Extensions of relative tensors. *Trans. Am. Math. Soc.* **26**(3), 373–377 (1924)
16. Synge, J.L., Schild, A.: *Tensor Calculus*. Dover Publication Inc, New York (1951)
17. Schouten, J.A.: *Tensor Analysis for Physicist*. Clarendon Press, Oxford (1951)
18. Truesdell, C., Toupin, R.: The classical field theories. *Encyclopedia of physics*, vol. III/1. In: Flügge, S. (ed.) *Principles of Classical Mechanics and Field Theory*, pp. 226–902. Springer, Heidelberg (1960). https://doi.org/10.1007/978-3-642-45943-6_2
19. Sokolnikoff, I.S.: *Tensor Analysis: Theory and Applications to Geometry and Mechanics of Continua*. Wiley, New York (1964)
20. Gurevich, G.B.: *Foundations of the Theory of Algebraic Invariants*. Noordhoff, Groningen (1964)
21. Kopff, A.: *Mathematical Theory of Relativity*. Dutton Press, Dutton (1921)
22. Radayev, Yu.N.: *The Spatial Problem of the Mathematical Theory of Plasticity*. Samara University, Samara (2006). (in Russian)

Chapter 18

Concerning Identification of Two Thermomechanical Characteristics of Functionally Graded Pipe



Rostislav D. Nedin, Sergei A. Nesterov, and Alexander O. Vatulyan

Abstract We consider an inverse problem on the identification of two thermomechanical characteristics of a functionally graded pipe based on the additional data picked on the outer surface of the pipe over a finite time interval. The pipe's thermomechanical characteristics depend on the radial coordinate. Two direct thermoelasticity problems for different thermal loads on the pipe's outer surface, after applying the Laplace transform, are solved with the help of the shooting method and transform inversion based on the expansion of the actual space in terms of shifted Legendre polynomials. The numerical solution of the inverse problem is built via the iterative process of solving the system of the Fredholm integral equations of the 1st kind. Computational experiments are carried out to restore two thermomechanical characteristics with the known others. It is revealed that monotonic functions are restored with sufficient accuracy; the reconstruction procedure is resistant to 2% input data noise.

Keywords Functionally graded materials · Pipe · Thermoelasticity · Identification · Coefficient inverse problem · Iterative process · Shooting method · System of the Fredholm integral equations · Thermal conductivity coefficient · Specific heat capacity · Thermal stress coefficient

R. D. Nedin (✉) · S. A. Nesterov · A. O. Vatulyan
Institute of Mathematics, Mechanics and Computer Sciences named after I.I. Vorovich, Southern Federal University, 8a Mil'chakova Str., 344090 Rostov-on-Don, Russian Federation
e-mail: rdn90@bk.ru

S. A. Nesterov
e-mail: 1079@list.ru

A. O. Vatulyan
e-mail: aovatulyan@sfedu.ru

Southern Mathematical Institute, Vladikavkaz Scientific Center of Russian Academy of Sciences, 22 Markusa Str., 362027 Vladikavkaz, Russian Federation

18.1 Intro

Cylindrical elements are used to be the parts of many structures subjected to high thermomechanical loads. Calculations related to finding the stress-strain state of such structures are usually carried out for homogeneous materials. However, at present, functionally graded materials (FGM) are increasingly being introduced into various fields of technology, mainly as two-phase composites synthesized from metal and ceramics, providing a continuous change in thermomechanical characteristics [1, 2]. Due to the complex and multi-stage FGM manufacturing technology, deviations from the specified laws may be present in the final product. Therefore, determination of the actual properties after fabrication is of certain importance. However, due to the dependence of thermomechanical characteristics on coordinates, the former can be determined by non-destructive testing methods based on the theoretical foundations of the apparatus of coefficient inverse problems (CIPs) of thermoelasticity [3]. Thermoelasticity CIP is the problem of determining thermomechanical characteristics as coefficients of thermoelasticity differential equations from some additional data on the displacement or temperature fields measured on a part of the body's boundary. From a mathematical point of view, such problems are essentially ill-posed and non-linear. Therefore, building time-saving and stable algorithms for their treatment is an urgent issue.

The most common way of solving CIP is to construct the residual functional and to minimize it by any of the gradient methods [4]. Based on this approach, studies on CIP thermal conductivity [4–9] and elasticity theory [10–12] were carried out. Alternative techniques were also proposed, for example, the quasi-inversion method [13], the inversion of finite-difference schemes [14], the reduction to the Fredholm integral equation of the 1st kind [15]. In these research works, only one material characteristic was restored with the known others. However, in practice, several thermomechanical characteristics are usually unknown at once. In [16], an approach was proposed to identify two thermophysical characteristics, the rod's thermal conductivity coefficient and specific heat capacity, based on conducting two thermophysical experiments with different thermal loads applied to the rod ends. The numerical solution of the inverse problem was constructed on the basis of the iterative process, at each stage of which the system of the Fredholm integral equations of the 1st kind was solved.

However, for a number of material classes, it is necessary to take into account the coupling of elastic and thermal fields and solve inverse thermoelasticity problems; such problems have been solved mainly for weakly inhomogeneous materials [3]. Previously, the authors of [17] proposed an approach to solving the nonlinear thermoelasticity CIP via the iterative process, at each stage of which linear problems were solved. To do this, starting from the weak statement in the Laplace transforms space and using the linearization technique, the operator equations that relate the sought-for and measured within the experiment characteristics were obtained. After applying the transformation to the actual space, the operator equations were obtained for solving one-dimensional thermoelasticity CIP over a finite time interval. Based

on the iterative approach, the identification of thermomechanical characteristics of a rod [18], a pipe [19, 20] and a finite cylinder [21, 22] was carried out. In these cases, only one of the thermomechanical characteristics was restored, while the rest were assumed to be given. At the same time, the thermoelasticity CIP on restoring two characteristics is still relevant.

The present research is aimed at solving the thermoelasticity CIP on the identification of two thermomechanical characteristics of the pipe. Two thermoelasticity problem statements for different types of thermal load on the outer surface of the pipe are considered. For the first problem, a constant heat flux acts on the outer surface of the pipe, and for the second one, a temperature does. The additional data measured on the outer pipe's surface represents the temperature for the first problem considered, and the heat flux for the second one. Direct problems for the pipe after non-dimensionalization and applying the Laplace transform are solved based on the shooting method and transform inversion by expanding the actual space in terms of the shifted Legendre polynomials. A system of two coefficients of thermoelasticity differential operators is restored in two stages. At the first stage, the initial approximation is determined in the class of positive bounded linear functions based on the minimization of the residual functional. At the second stage, the corrections to the reconstructed functions are determined by solving the corresponding system of the Fredholm integral equations of the 1st kind. Computational experiments were carried out to reconstruct two pairs of characteristics: (1) thermal conductivity coefficient and specific heat capacity; (2) thermal conductivity coefficient and thermal stress coefficient.

18.2 Inverse Thermoelasticity Problem Statement

Let us study the thermoelasticity CIP on the reconstruction of two thermomechanical characteristics of functionally graded pipe. To do this, we consider two quasi-static thermoelasticity problems for a radially inhomogeneous pipe with different loads applied to its surfaces. In both problems, a constant temperature is maintained on the inner stress-free surface of the pipe $r = r_1$. On the outer surface of the pipe $r = r_2$, stress-free as well, in the first problem (Problem 1), there is a constant heat flux, and in the second problem (Problem 2), the temperature changing according to the law $t e^{-t}$ is set. The initial conditions are zero.

The Problem 1 statement has form

$$\frac{\partial \sigma_{rr}}{\partial r} + \frac{\sigma_{rr} - \sigma_{\varphi\varphi}}{r} = 0, \quad r_1 \leq r \leq r_2, \quad (18.1)$$

$$\sigma_{rr} = (\lambda + 2\mu) \frac{\partial u}{\partial r} + \lambda \frac{u}{r} - \gamma\theta, \quad \sigma_{\varphi\varphi} = \lambda \frac{\partial u}{\partial r} + (\lambda + 2\mu) \frac{u}{r} - \gamma\theta, \quad (18.2)$$

$$\frac{1}{r} \frac{\partial}{\partial r} \left(k(r)r \frac{\partial \theta}{\partial r} \right) = c_\varepsilon(r) \frac{\partial \theta}{\partial t} + T_0 \gamma(r) \left(\frac{\partial^2 u}{\partial r \partial t} + \frac{1}{r} \frac{\partial u}{\partial t} \right), \quad r_1 \leq r \leq r_2, \quad t \geq 0, \tag{18.3}$$

$$\sigma_{rr}(r_1, t) = \sigma_{rr}(r_2, t) = 0, \tag{18.4}$$

$$\theta(r_1, t) = 0, \quad -k(r_2) \frac{\partial \theta}{\partial r}(r_2, t) = q_0, \tag{18.5}$$

$$\theta(r, 0) = u(r, 0) = \frac{\partial u}{\partial t}(r, 0) = 0. \tag{18.6}$$

Here, r is the radial coordinate, σ_{rr} and $\sigma_{\varphi\varphi}$ are nonzero components of the stress tensor in the cylindrical coordinate system, u is the component of the displacement vector in the radial direction, θ is the temperature increment from the natural state with the temperature T_0 , λ and μ are the Lamé coefficients, k is the thermal conductivity coefficient, c_ε is the specific volumetric heat capacity at a constant strain tensor, γ is the radial component of the thermal stress tensor and q_0 is the heat flux density.

The statement of the Problem 2 coincides with the Problem 1 statement, except for the thermal boundary conditions (18.5), which take the form:

$$\theta(r_1, t) = 0, \quad \theta(r_2, t) = \theta_0 t e^{-t}. \tag{18.7}$$

Let us pass in (18.1)–(18.7) to dimensionless parameters and functions, denoting: $\xi = \frac{r}{r_2}$, $\xi_0 = \frac{r_1}{r_2}$, $U = \frac{u_r}{r_2}$, $W = \frac{\gamma_0 \theta}{\mu_0}$, $\tau = \frac{t}{t_1}$, $t_1 = \frac{r_2 c_0}{k_0}$, $\delta_0 = \frac{\gamma_0^2 T_0}{c_0 \mu_0}$, $\Omega_{rr} = \frac{\sigma_{rr}}{\mu_0}$, $\Omega_{\varphi\varphi} = \frac{\sigma_{\varphi\varphi}}{\mu_0}$, $\bar{\lambda} = \frac{\lambda}{\mu_0}$, $\bar{\mu} = \frac{\mu}{\mu_0}$, $\bar{\gamma} = \frac{\gamma}{\gamma_0}$, $\bar{k} = \frac{k}{k_0}$, $\bar{c} = \frac{c}{c_0}$, $\beta_1 = \frac{q_0 r_2 \gamma_0}{k_0 \mu_0}$, $\beta_2 = \frac{\theta_0 r_2 c_0 \gamma_0}{k_0 \mu_0}$. Here $\lambda_0, \mu_0, \rho_0, \gamma_0, k_0$ and c_0 are characteristic quantities.

Then the statement of the dimensionless Problem 1 takes the form:

$$\frac{\partial \Omega_{rr}^I}{\partial \xi} + \frac{\Omega_{rr}^I - \Omega_{\varphi\varphi}^I}{\xi} = 0, \quad \xi_0 \leq \xi \leq 1, \tag{18.8}$$

$$\Omega_{rr}^I = (\bar{\lambda} + 2\bar{\mu}) \frac{\partial U_I}{\partial \xi} + \bar{\lambda} \frac{U_I}{\xi} - \bar{\gamma} W_I, \quad \Omega_{\varphi\varphi}^I = \bar{\lambda} \frac{\partial U_I}{\partial \xi} + (\bar{\lambda} + 2\bar{\mu}) \frac{U_I}{\xi} - \bar{\gamma} W_I, \tag{18.9}$$

$$\frac{1}{\xi} \frac{\partial}{\partial \xi} \left(\bar{k}(\xi) \xi \frac{\partial W_I}{\partial \xi} \right) = \bar{c}(\xi) \frac{\partial W_I}{\partial \tau} + \delta_0 \bar{\gamma}(\xi) \left(\frac{\partial^2 U_I}{\partial \xi \partial \tau} + \frac{1}{\xi} \frac{\partial U_I}{\partial \tau} \right), \quad \xi_0 \leq \xi \leq 1, \quad \tau \geq 0, \tag{18.10}$$

$$\Omega_{rr}^I(\xi_0, \tau) = 0, \quad \Omega_{rr}^I(1, \tau) = 0, \tag{18.11}$$

$$W_I(\xi_0, \tau) = 0, \quad -\bar{k}(1) \frac{\partial W_I}{\partial \xi}(1, \tau) = \beta_1, \quad \tau \geq 0, \tag{18.12}$$

$$W_I(\xi, 0) = U_I(\xi, 0) = \frac{\partial U_I}{\partial \tau}(\xi, 0) = 0. \tag{18.13}$$

The statement of the dimensionless Problem 2 has the form:

$$\frac{\partial \Omega_{rr}^{II}}{\partial \xi} + \frac{\Omega_{rr}^{II} - \Omega_{\varphi\varphi}^{II}}{\xi} = 0, \quad \xi_0 \leq \xi \leq 1, \quad (18.14)$$

$$\Omega_{rr}^{II} = (\bar{\lambda} + 2\bar{\mu}) \frac{\partial U_{II}}{\partial \xi} + \bar{\lambda} \frac{U_{II}}{\xi} - \bar{\gamma} W_{II}, \quad \Omega_{\varphi\varphi}^{II} = \bar{\lambda} \frac{\partial U_{II}}{\partial \xi} + (\bar{\lambda} + 2\bar{\mu}) \frac{U_{II}}{\xi} - \bar{\gamma} W_{II}, \quad (18.15)$$

$$\frac{1}{\xi} \frac{\partial}{\partial \xi} \left(\bar{k}(\xi) \xi \frac{\partial W_{II}}{\partial \xi} \right) = \bar{c}(\xi) \frac{\partial W_{II}}{\partial \tau} + \delta_0 \bar{\gamma}(\xi) \left(\frac{\partial^2 U_{II}}{\partial \xi \partial \tau} + \frac{1}{\xi} \frac{\partial U_{II}}{\partial \tau} \right), \quad \xi_0 \leq \xi \leq 1, \quad \tau \geq 0, \quad (18.16)$$

$$\Omega_{rr}^{II}(\xi_0, \tau) = 0, \quad \Omega_{rr}^{II}(1, \tau) = 0, \quad (18.17)$$

$$W_{II}(\xi_0, \tau) = 0, \quad W_{II}(1, \tau) = \beta_2 \tau e^{-\tau}, \quad \tau \geq 0, \quad (18.18)$$

$$W_{II}(\xi, 0) = U_{II}(\xi, 0) = \frac{\partial U_{II}}{\partial \tau}(\xi, 0) = 0. \quad (18.19)$$

As the additional data on the pipe's outer surface we consider:

1. Temperature for the Problem 1

$$W_I(1, \tau) = f_I(\tau), \quad \tau \in [a_1, b_1], \quad (18.20)$$

2. Heat flux for the Problem 2

$$Q_{II}(1, \tau) = f_{II}(\tau), \quad \tau \in [a_2, b_2]. \quad (18.21)$$

The direct thermoelasticity problem is to find the stress-strain state of the pipe from (18.8)–(18.13), (18.14)–(18.19) with the known thermomechanical characteristics $\bar{\lambda}$, $\bar{\mu}$, $\bar{\gamma}$, \bar{k} , \bar{c} . In the inverse problem, it is required to restore two thermomechanical characteristics with the rest known from (18.8)–(18.13) and (18.14)–(18.19) using the additional data (18.20), (18.21).

18.3 Solution of the Direct Thermoelasticity Problem

Direct thermoelasticity problem for the pipe (18.8)–(18.13) and (18.14)–(18.19) after applying the Laplace transform in time τ with arbitrary laws of change in thermomechanical characteristics can only be solved numerically, for example, by the shooting method, similarly as in [21, 23]. After applying some standard transformations, we pass to the canonical system of 4 ordinary differential equations of the 1st order with variable coefficients:

$$\frac{d\tilde{W}}{d\xi} = \frac{1}{\bar{k}(\xi)} \tilde{Q}(\xi, p), \tag{18.22}$$

$$\begin{aligned} \frac{d\tilde{Q}}{d\xi} = & -\frac{1}{\xi} \tilde{Q} + p \left(\bar{c} + \delta_0 \frac{\bar{\gamma}^2}{\bar{\lambda} + 2\bar{\mu}} \right) \tilde{W} + \delta_0 p \frac{\bar{\gamma}}{\bar{\lambda} + 2\bar{\mu}} \tilde{\Omega}_{rr} + \\ & + \delta_0 p \frac{\bar{\gamma}}{\xi} \left(1 - \frac{\bar{\lambda}}{\bar{\lambda} + 2\bar{\mu}} \right) \tilde{U}, \end{aligned} \tag{18.23}$$

$$\frac{d\tilde{\Omega}_{rr}}{d\xi} = \frac{1}{\xi} \left(1 - \frac{\bar{\lambda}}{\bar{\lambda} + 2\bar{\mu}} \right) \tilde{\Omega}_{rr} - \frac{1}{\xi^2} \left(\bar{\lambda} + 2\bar{\mu} - \frac{\bar{\lambda}^2}{\bar{\lambda} + 2\bar{\mu}} \right) \tilde{U} + \frac{\bar{\gamma}}{\xi} \left(1 - \frac{\bar{\lambda}}{\bar{\lambda} + 2\bar{\mu}} \right) \tilde{W}, \tag{18.24}$$

$$\frac{d\tilde{U}}{d\xi} = \frac{1}{\bar{\lambda} + 2\bar{\mu}} \tilde{\Omega}_{rr} - \frac{\bar{\lambda}}{(\bar{\lambda} + 2\bar{\mu})\xi} \tilde{U} + \frac{\bar{\gamma}}{\bar{\lambda} + 2\bar{\mu}} \tilde{W}. \tag{18.25}$$

Next, we consider two auxiliary Cauchy problem statements for the canonical system of differential equations (18.22)–(18.25) and two sets of conditions for:

1. $\tilde{W}_1(\xi_0, p) = 0, \tilde{\Omega}_1(\xi_0, p) = 0, \tilde{U}_1(\xi_0, p) = 1, \tilde{Q}_1(\xi_0, p) = 0;$
2. $\tilde{W}_2(\xi_0, p) = 0, \tilde{\Omega}_2(\xi_0, p) = 0, \tilde{U}_2(\xi_0, p) = 0, \tilde{Q}_2(\xi_0, p) = 1.$

For any value of the Laplace transform parameter, the Cauchy problems are solved numerically by the 4th order Runge–Kutta method. Next, two groups of solutions are composed in the form: $\tilde{U}_I = \alpha_1 \tilde{U}_1 + \alpha_2 \tilde{U}_2, \tilde{\Omega}_{rr}^I = \alpha_1 \tilde{\Omega}_1 + \alpha_2 \tilde{\Omega}_2, \tilde{W}_I = \alpha_1 \tilde{W}_1 + \alpha_2 \tilde{W}_2, \tilde{Q}_I = \alpha_1 \tilde{Q}_1 + \alpha_2 \tilde{Q}_2; \tilde{U}_{II} = \alpha_3 \tilde{U}_1 + \alpha_4 \tilde{U}_2, \tilde{\Omega}_{rr}^{II} = \alpha_3 \tilde{\Omega}_1 + \alpha_4 \tilde{\Omega}_2, \tilde{W}_{II} = \alpha_3 \tilde{W}_1 + \alpha_4 \tilde{W}_2, \tilde{Q}_{II} = \alpha_3 \tilde{Q}_1 + \alpha_4 \tilde{Q}_2.$ The unknown constants $\alpha_1, \dots, \alpha_4$ are determined by satisfying 4 conditions in the transforms for $\xi = 1: \tilde{Q}_I(1, p) = \frac{\beta_1}{p}, \tilde{\Omega}_{rr}^I(1, p) = \tilde{\Omega}_{rr}^{II}(1, p) = 0, \tilde{W}_{II}(1, p) = \frac{\beta_2}{(p+1)^2}.$

Since the temperature, displacement and stress transforms are known in the set of values of the Laplace transform parameter, the inversion of the Laplace transform can only be performed numerically. We use the numerical inversion of the Laplace transform based on the technique of expanding the actual space into a series in terms of shifted Legendre polynomials; the latter (P_n^*) differ from the common Legendre polynomials P_n by the fact that their domain of definition is reduced to the segment $[0, 1]$ instead of common $[-1, 1]$, i.e., $P_n^*(x) = P_n(2x - 1).$

The shifted Legendre polynomials have the form:

$$P_n^*(x) = (-1)^n \sum_{s=0}^n (-1)^s \binom{n}{s} \frac{(n+s)!}{n!s!} x^s. \tag{18.26}$$

According to [24], the expansion of the function $F(\tau)$ with respect to the shifted Legendre polynomials takes the form:

$$F(\tau) = \sum_{s=0}^{\infty} (2s + 1)a_s P_s^*(e^{-\tau}). \tag{18.27}$$

In [24], an expression was obtained for the expansion coefficients a_s through the known coefficients $c_i^{(s)}$ of the polynomials P_s^* and the Laplace transform values $\tilde{F}(p)$ at integer points $p = 1, 2, \dots$ in the form $a_s = \sum_{i=0}^s c_i^{(s)} \tilde{F}(i)$. The accuracy of solving the direct problems (18.8)–(18.13) and (18.14)–(18.19) was verified by comparing the approximate solution for a homogeneous cylinder with the finite element method (FEM) solution obtained in the FlexPDE package.

Table 18.1 gives a comparative analysis of the dimensionless temperature values on the pipe’s outer surface, $\xi = 1$, calculated by the FEM and the shooting method when solving the problem (18.8)–(18.13) with the parameters $\delta_0 = 0.05$, $\beta_1 = 1$, $\xi_0 = 0.6$ and different values of the parameter s in the series (18.27).

Table 18.2 gives a comparative analysis of the dimensionless temperature values for $\xi = 0.9$, obtained by the FEM and the shooting method when solving the problem (18.14)–(18.19) with the parameters $\delta_0 = 0.05$, $\beta_2 = 1$, $\xi_0 = 0.6$ and different values of the parameter s in the series (18.27).

From the analysis of Tables 18.1 and 18.2, it follows that in order for the error in calculating the temperature for the time $\tau > 10^{-3}$ to not exceed 1%, it is sufficient to make a restriction to 45 terms in the expansion (18.27).

Table 18.1 Comparison of the results of solving the direct problem (18.8)–(18.13) for $\xi = 1$

Moment of time	FEM	Shooting method	
		$s = 20$	$s = 45$
0.001	0.03619	0.04988	0.03628
0.01	0.11814	0.11901	0.11819
0.1	0.38639	0.385446	0.38643
0.2	0.47512	0.47467	0.475165
0.5	0.50997	0.50828	0.50998

Table 18.2 Comparison of the results of solving the direct problem (18.14)–(18.19) for $\xi = 0.9$

Moment of time	FEM	Shooting method	
		$s = 20$	$s = 45$
0.001	0.02503	0.03649	0.02532
0.01	0.40389	0.40435	0.40393
0.1	0.63451	0.63534	0.63458
0.2	0.75789	0.76035	0.75792
0.5	0.76749	0.76759	0.76750

18.4 Iterative Scheme for Solving the Inverse Thermoelasticity Problem

In this work, we solve the nonlinear thermoelasticity CIP on the identification of two characteristics of the pipe on the basis of the construction of an iterative process, at each stage of which a linear problem is to be solved. The scheme for solving the considered CIP for the pipe is constructed similarly to the scheme for reconstructing two thermophysical characteristics of a rod [16].

The iterative process of identifying two thermomechanical characteristics of the pipe consists of two stages. At the first stage, the initial approximation is determined in the class of positive bounded linear functions $k_1\xi + b_1$, $k_2\xi + b_2$ based on the residual functional minimization:

$$J = \int_{a_1}^{b_1} (f_I(\tau) - W_I^{(n-1)}(1, \tau))^2 d\tau + \int_{a_2}^{b_2} (f_{II}(\tau) - Q_{II}^{(n-1)}(1, \tau))^2 d\tau. \quad (18.28)$$

At the second stage, the corrections of the two reconstructed functions are determined by solving a system of the integral Fredholm equations of the 1st kind, and the current laws of change in thermomechanical characteristics are then corrected. In [21], to find corrections for thermomechanical characteristics, the operator equations were obtained in the Laplace transform space, both for thermal and mechanical loading applied of the outer surface of the cylinder. Using only thermal loading, taking into account two types of thermal load on the outer surface of the pipe, we now obtain a system of the following two operator equations of the 1st kind:

$$\begin{aligned} & p \int_{\xi_0}^1 \delta \bar{k}^{(n-1)} \left(\frac{d\tilde{W}_I^{(n-1)}}{d\xi} \right)^2 \xi d\xi + p^2 \int_{\xi_0}^1 \delta \bar{c}^{(n-1)} (\tilde{W}_I^{(n-1)})^2 \xi d\xi \\ & + \delta_0 p^2 \int_{\xi_0}^1 \delta \bar{\gamma}^{(n-1)} \left(\frac{d\tilde{U}_I^{(n-1)}}{d\xi} + \frac{\tilde{U}_I^{(n-1)}}{\xi} \right) \tilde{W}_I^{(n-1)} \xi d\xi \\ & = \beta_1 (\tilde{f}_I(p) - \tilde{W}_I^{(n-1)}(1, p)), \quad p \in [0, \infty), \end{aligned} \quad (18.29)$$

$$(p+1)^2 \int_{\xi_0}^1 \delta \bar{k}^{(n-1)} \left(\frac{d\tilde{W}_{II}^{(n-1)}}{d\xi} \right)^2 \xi d\xi + p(p+1)^2 \int_{\xi_0}^1 \delta \bar{c}^{(n-1)} (\tilde{W}_{II}^{(n-1)})^2 \xi d\xi$$

$$\begin{aligned}
& + \delta_0 p(p+1)^2 \int_{\xi_0}^1 \delta \bar{\gamma}^{(n-1)} \left(\frac{d\tilde{U}_{II}^{(n-1)}}{d\xi} + \frac{\tilde{U}_{II}^{(n-1)}}{\xi} \right) \tilde{W}_{II}^{(n-1)} \xi d\xi \\
& = \beta_2 (\tilde{f}_{II}(p) - \tilde{Q}_{II}^{(n-1)}(1, p)), \quad p \in [0, \infty). \tag{18.30}
\end{aligned}$$

The system of two Eqs. (18.29), (18.30) is written out to identify three corrections $\bar{k}(\xi)$, $\bar{c}(\xi)$ and $\bar{\gamma}(\xi)$, which is impossible to implement. Therefore, we confine ourselves to identifying two pairs of thermomechanical characteristics: (1) $\bar{k}(\xi)$ and $\bar{c}(\xi)$ when $\bar{\gamma}(\xi)$ is known; (2) $\bar{k}(\xi)$ and $\bar{\gamma}(\xi)$ when $\bar{c}(\xi)$ is known.

1. Assume $\bar{\gamma}(\xi)$ to be known. Required to restore $\bar{k}(\xi)$ and $\bar{c}(\xi)$.

Here, putting $\delta \bar{\gamma}^{(n-1)} = 0$ in (18.29), (18.30), we get:

$$\begin{aligned}
& p \int_{\xi_0}^1 \delta \bar{k}^{(n-1)} \left(\frac{d\tilde{W}_I^{(n-1)}}{d\xi} \right)^2 \xi d\xi + p^2 \int_{\xi_0}^1 \delta \bar{c}^{(n-1)} (\tilde{W}_I^{(n-1)})^2 \xi d\xi \\
& = \beta_1 (\tilde{f}_I(p) - \tilde{W}_I^{(n-1)}(1, p)), \quad p \in [0, \infty), \tag{18.31}
\end{aligned}$$

$$\begin{aligned}
& (p+1)^2 \int_{\xi_0}^1 \delta \bar{k}^{(n-1)} \left(\frac{d\tilde{W}_{II}^{(n-1)}}{d\xi} \right)^2 \xi d\xi + p(p+1)^2 \int_{\xi_0}^1 \delta \bar{c}^{(n-1)} (\tilde{W}_{II}^{(n-1)})^2 \xi d\xi \\
& = \beta_2 (\tilde{f}_{II}(p) - \tilde{Q}_{II}^{(n-1)}(1, p)). \tag{18.32}
\end{aligned}$$

Inverting the Eqs. (18.31), (18.32), we obtain a system of operator equations in the actual space:

$$\int_{\xi_0}^1 \left(\delta \bar{k}^{(n-1)} R_{11}(\xi, \tau) + \delta \bar{c}^{(n-1)} R_{12}(\xi, \tau) \right) \xi d\xi = f_I(\tau) - W_I^{(n-1)}(1, \tau), \quad \tau \in [a_1, b_1], \tag{18.33}$$

$$\int_{\xi_0}^1 \left(\delta \bar{k}^{(n-1)} R_{21}(\xi, \tau) + \delta \bar{c}^{(n-1)} R_{22}(\xi, \tau) \right) \xi d\xi = f_{II}(\tau) - Q_{II}^{(n-1)}(1, \tau), \tag{18.34}$$

$\tau \in [a_2, b_2]$. Here, the kernels of (18.33), (18.34) have the form:

$$R_{11}(\xi, \tau) = \frac{1}{\beta_1} \int_0^\tau \frac{\partial^2 W_I^{(n-1)}(\xi, \tau_1)}{\partial \xi \partial \tau_1} \frac{\partial W_I^{(n-1)}(\xi, \tau - \tau_1)}{\partial \xi} d\tau_1,$$

$$R_{12}(\xi, \tau) = \frac{1}{\beta_1} \int_0^\tau \frac{\partial W_{II}^{(n-1)}(\xi, \tau_1)}{\partial \tau_1} \frac{\partial W_{II}^{(n-1)}(\xi, \tau - \tau_1)}{\partial \tau_1} d\tau_1,$$

$$R_{21}(\xi, \tau) = \frac{1}{\beta_2} \int_0^\tau \left(\frac{\partial^3 W_{II}^{(n-1)}(\xi, \tau_1)}{\partial \xi \partial \tau_1^2} + 2 \frac{\partial^2 W_{II}^{(n-1)}(\xi, \tau_1)}{\partial \xi \partial \tau_1} + \frac{\partial W_{II}^{(n-1)}(\xi, \tau_1)}{\partial \xi} \right) \times \frac{\partial W_{II}^{(n-1)}(\xi, \tau - \tau_1)}{\partial \xi} d\tau_1,$$

$$R_{22}(\xi, \tau) = \frac{1}{\beta_2} \int_0^\tau \left(\frac{\partial^2 W_{II}^{(n-1)}(\xi, \tau_1)}{\partial \tau_1^2} + 2 \frac{\partial W_{II}^{(n-1)}(\xi, \tau_1)}{\partial \tau_1} + W_{II}^{(n-1)}(\xi, \tau_1) \right) \times \frac{\partial W_{II}^{(n-1)}(\xi, \tau - \tau_1)}{\partial \tau_1} d\tau_1.$$

2. Assume $\bar{c}(\xi)$ to be known. Required to restore $\bar{k}(\xi)$ and $\bar{\gamma}(\xi)$. this case, putting in (18.29), (18.30) $\delta \bar{A}^{(n-1)} = 0$, after inversion, we obtain a system of the operator equations in the actual space allowing to find the system of corrections $\delta \bar{k}^{(n-1)}$ and $\delta \bar{\gamma}^{(n-1)}$:

$$\int_{\xi_0}^1 (\delta \bar{k}^{(n-1)} M_{11}(\xi, \tau) + \delta \bar{\gamma}^{(n-1)} M_{12}(\xi, \tau)) \xi d\xi = f_I(\tau) - W_I^{(n-1)}(1, \tau), \tag{18.35}$$

$$\tau \in [a_1, b_1],$$

$$\int_{\xi_0}^1 (\delta \bar{k}^{(n-1)} M_{21}(\xi, \tau) + \delta \bar{\gamma}^{(n-1)} M_{22}(\xi, \tau)) \xi d\xi = f_{II}(\tau) - Q_{II}^{(n-1)}(1, \tau), \tag{18.36}$$

$\tau \in [a_2, b_2]$, where the kernels of the Eqs. (18.35), (18.36) have the form:

$$M_{11}(\xi, \tau) = R_{11}(\xi, \tau), \quad M_{21}(\xi, \tau) = R_{21}(\xi, \tau),$$

$$M_{12}(\xi, \tau) = \frac{\delta_0}{\beta_1} \int_0^\tau \left(\frac{\partial^2 U_{II}^{(n-1)}(\xi, \tau_1)}{\partial \xi \partial \tau_1} + \frac{1}{\xi} \frac{\partial U_{II}^{(n-1)}(\xi, \tau_1)}{\partial \tau_1} \right) \frac{\partial W_I^{(n-1)}(\xi, \tau - \tau_1)}{\partial \tau_1} d\tau_1,$$

$$M_{22}(\xi, \tau) = \frac{\delta_0}{\beta_2} \int_0^\tau A_1(\xi, \tau_1) A_2(\xi, \tau_1) d\tau_1,$$

$$A_1(\xi, \tau_1) = \left(\frac{\partial^2 U_{II}^{(n-1)}(\xi, \tau_1)}{\partial \xi \partial \tau_1} + \frac{1}{\xi} \frac{\partial U_{II}^{(n-1)}(\xi, \tau_1)}{\partial \tau_1} \right),$$

$$A_2(\xi, \tau_1) = \left(\frac{\partial^2 W_{II}^{(n-1)}(\xi, \tau_1)}{\partial \tau_1^2} + 2 \frac{\partial W_{II}^{(n-1)}(\xi, \tau_1)}{\partial \tau_1} + W_{II}^{(n-1)}(\xi, \tau_1) \right).$$

The iterative process is repeated until the stopping condition is fulfilled: reaching the threshold value of the residual functional (18.28), equal to 10^{-4} , or reaching the limit number of iterations equal to 20. Since solving systems of the integral Fredholm equations of the 1st kind (18.33), (18.34) and (18.35), (18.36) represents an ill-posed problem, the method of A.N. Tikhonov [25] was employed.

18.5 Results of Two Thermomechanical Characteristics Reconstruction

Computational experiments were carried out to reconstruct two thermophysical characteristics in the classes of power and exponential functions, which are most often used to model FGM. When carrying out computational experiments, it was accepted: $\beta_1 = \beta_2 = 1$, $\delta_0 = 0.05$, $\xi_0 = 0.8$.

The influence of the inhomogeneity laws for the variable characteristics on the simulated input data values gained in the experiment is analyzed. It is found that the laws of change in the thermal conductivity coefficient and specific heat capacity proportionally affect the boundary physical fields—temperature and heat flux, while the influence of the thermal stress coefficient is proportional to the value of the coupling parameter.

For each inhomogeneity law, the most informative intervals for measuring the input data are determined in which the boundary temperature and heat flux change most rapidly.

During the first series of computational experiments, the thermal conductivity coefficient $\bar{k}(\xi)$ and specific heat capacity $\bar{c}(\xi)$ were restored. The residual functional (18.28) reached the threshold value in no more than 12 iterations. A pair of dimensionless characteristics was reconstructed with sufficient accuracy: the maximum error in the reconstruction of two monotonic functions did not exceed 5%.

The figures below reveal the results of recovering the thermophysical characteristics; the solid line shows the exact law of inhomogeneity, the dots show the reconstructed law. Figure 18.1 presents the results of reconstructing the following decreasing functions: (a) $\bar{k}(\xi) = 4e^{-8(\xi-\xi_0)}$; (b) $\bar{c}(\xi) = 2e^{-6(\xi-\xi_0)}$.

The additional data was collected at 6 equally spaced points inside the selected informative segments $[a_1, b_1] = [0.05, 0.35]$, $[a_2, b_2] = [0.01, 0.18]$. It took 7 iterations to reach the threshold value of the functional (18.28), while the maximum error in the reconstruction of two functions did not exceed 4%.

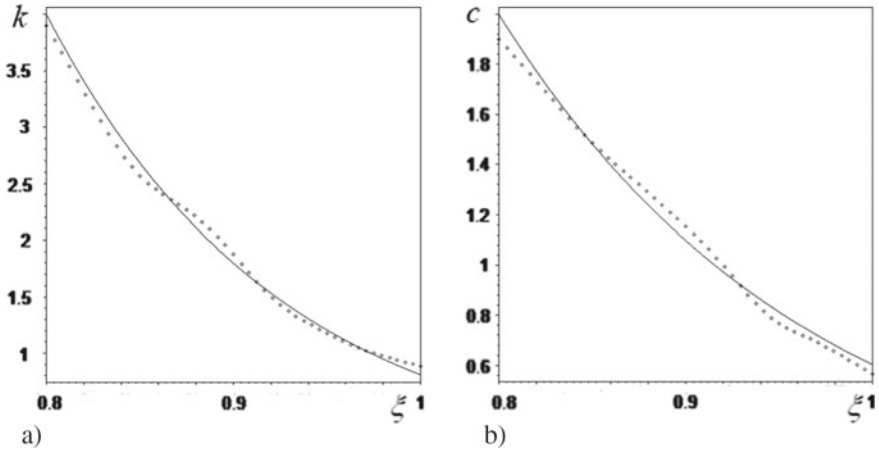


Fig. 18.1 Reconstruction of decreasing functions: **a** $\bar{k}(\xi) = 4e^{-8(\xi-\xi_0)}$; **b** $\bar{c}(\xi) = 2e^{-6(\xi-\xi_0)}$

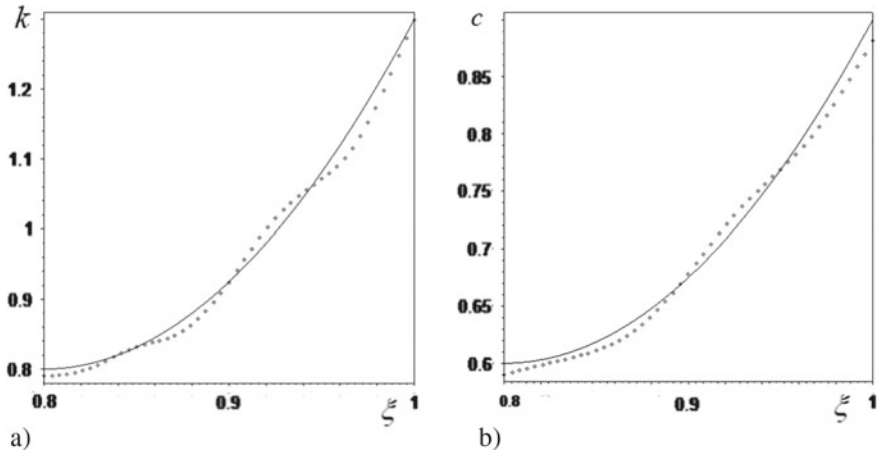


Fig. 18.2 Reconstruction of increasing functions: **a** $\bar{k}(\xi) = 0.8 + 0.5 \left(\frac{\xi-\xi_0}{1-\xi_0}\right)^2$; **b** $\bar{c}(\xi) = 0.6 + 0.3 \left(\frac{\xi-\xi_0}{1-\xi_0}\right)^2$

Figure 18.2 shows the results of reconstructing the increasing functions:

- (a) $\bar{k}(\xi) = 0.8 + 0.5 \left(\frac{\xi-\xi_0}{1-\xi_0}\right)^2$;
- (b) $\bar{c}(\xi) = 0.6 + 0.3 \left(\frac{\xi-\xi_0}{1-\xi_0}\right)^2$.

The input data was measured at 6 equally spaced points inside the selected informative segments $[a_1, b_1] = [0.04, 0.28]$, $[a_2, b_2] = [0.02, 0.14]$. This time it took 6

Table 18.3 Values of residual functional and maximum relative reconstruction error for the functions $\bar{k}(\xi) = 0.8 + 0.5 \left(\frac{\xi - \xi_0}{1 - \xi_0}\right)^2$ and $\bar{c}(\xi) = 0.6 + 0.3 \left(\frac{\xi - \xi_0}{1 - \xi_0}\right)^2$

Iteration #	Functional J	Relative reconstruction error, %
1	0.007123	15.64
2	0.003612	12.32
3	0.000951	10.71
4	0.000711	9.02
5	0.000294	8.43
6	0.000089	6.78

iterations to reach the threshold value of the functional (18.28), and the maximum error in the reconstruction of two functions did not exceed 3%.

The convergence of the iterative process was also investigated. Table 18.3 gives the residual values and the maximum relative reconstruction error depending on the iteration number when restoring functions

$$\bar{k}(\xi) = 0.8 + 0.5 \left(\frac{\xi - \xi_0}{1 - \xi_0}\right)^2 \text{ and}$$

$$\bar{c}(\xi) = 0.6 + 0.3 \left(\frac{\xi - \xi_0}{1 - \xi_0}\right)^2 \tag{18.37}$$

The effect of the input data noise on the reconstruction accuracy was also investigated; the former was modeled by using the relations:

$$f_I^s(\tau) = f_I(\tau)(1 + s\beta), f_{II}^s(\tau) = f_{II}(\tau)(1 + s\beta), \tag{18.38}$$

where s is the noise level and β is random variable with a uniform distribution law on the interval $[-1, 1]$. It was found that in the presence of noise, the reconstruction error increased with the growth of s , but even with 2% noise ($s = 0.02$) it did not exceed 11%.

Table 18.4 gives the values of the function $\bar{k}(\xi) = 0.8 + 0.5 \left(\frac{\xi - \xi_0}{1 - \xi_0}\right)^2$ and its reconstruction in the absence of input data noise and for 2% noise.

From Table 18.4, it follows that the maximum reconstruction error for 2% noise does not exceed 9%.

In the course of the second series of computational experiments, the thermal conductivity coefficient $\bar{k}(\xi)$ and thermal stress coefficient $\bar{\gamma}(\xi)$ were restored. It is found out that the accuracy of the reconstruction of this pair increases with an increase in the value of the coupling parameter δ_0 . In this way, with $\delta_0 = 0.1$ and in the absence of the input noise, the maximum error in the reconstruction of two monotonic functions was 16%, and with $\delta_0 = 0.4$, it did not exceed 5%.

Figure 18.3 presents the reconstruction results for the decreasing functions:

Table 18.4 Reconstruction of the function $\bar{k}(\xi) = 0.8 + 0.5 \left(\frac{\xi - \xi_0}{1 - \xi_0} \right)^2$

Radial coordinate ξ	Exact value $\bar{k}(\xi)$	Recovered value $\bar{k}(\xi)$		Relative reconstruction error	
		$s = 0$	$s = 0.02$	$s = 0$	$s = 0.02$
0.8	0.80	0.792	0.771	1.19	3.63
0.82	0.805	0.801	0.762	0.49	5.34
0.84	0.82	0.822	0.791	0.24	3.54
0.86	0.845	0.841	0.821	0.47	2.84
0.88	0.880	0.861	0.832	2.27	5.46
0.9	0.925	0.927	0.891	0.21	3.68
0.92	0.980	0.994	0.903	1.43	7.86
0.94	1.045	1.051	1.021	0.57	2.30
0.96	1.120	1.098	1.18	1.96	5.36
0.98	1.205	1.192	1.310	1.07	8.71
1	1.30	1.310	1.393	0.77	6.34

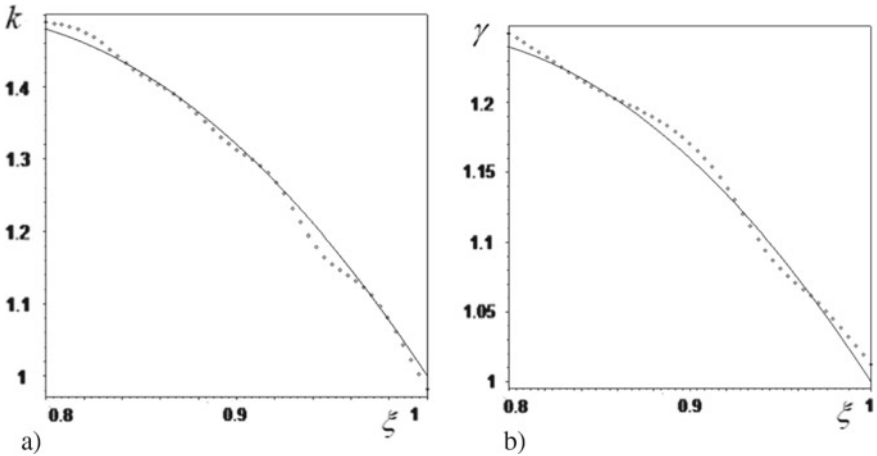


Fig. 18.3 Reconstruction of monotonically decreasing functions: **a** $\bar{k}(\xi) = -8\xi^2 + 12\xi - 3$; **b** $\bar{\gamma}(\xi) = -4\xi^2 + 6\xi - 1$

(a) $\bar{k}(\xi) = -8\xi^2 + 12\xi - 3$;

(b) $\bar{\gamma}(\xi) = -4\xi^2 + 6\xi - 1$

for $\delta_0 = 0.4$. The input data was gained at 8 equally spaced points inside the segments $[a_1, b_1] = [0.01, 0.17]$, $[a_2, b_2] = [0.02, 0.26]$. To reach the threshold value of the functional (18.28), it took 7 iterations, while the maximum error in the reconstruction of two functions did not exceed 4%.

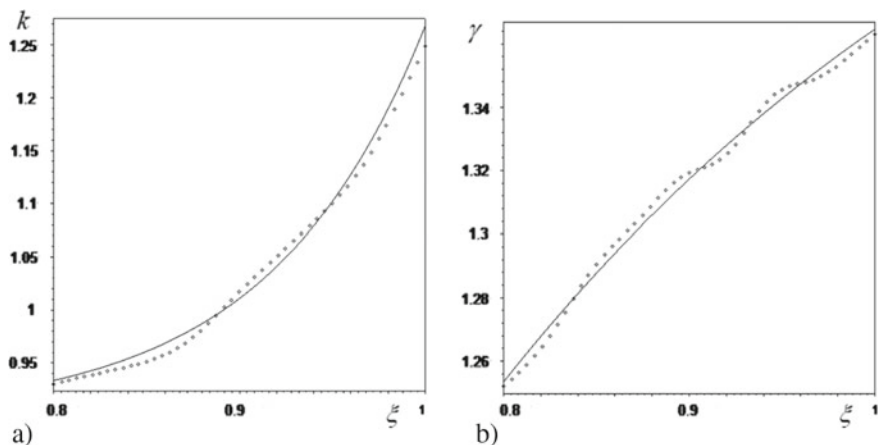


Fig. 18.4 Reconstruction of monotonically increasing functions: **a** $\bar{k}(\xi) = 0.9 + e^{12\xi-13}$; **b** $\bar{\gamma}(\xi) = 1.5 - e^{1-3\xi}$

In the same way, Fig. 18.4 shows the results of the increasing functions reconstruction:

(a) $\bar{k}(\xi) = 0.9 + e^{12\xi-13}$;

(b) $\bar{\gamma}(\xi) = 1.5 - e^{1-3\xi}$

for $\delta_0 = 0.4$.

The additional data was collected at 8 equally spaced points inside the selected informative segments $[a_1, b_1] = [0.03, 0.27]$, $[a_2, b_2] = [0.05, 0.13]$. It took 9 iterations to reach the threshold value of the functional (18.28), and the maximum error in the reconstruction of two functions did not exceed 4%.

18.6 Conclusion

- The inverse coefficient thermoelasticity problem on the identification of thermo-mechanical characteristics of a functionally graded pipe has been studied.
- The solution of the nonlinear inverse problem is built on the basis of the iterative process, at each stage of which the system of the Fredholm integral equations of the 1st kind is solved.
- Computational experiments on reconstructing two pairs of characteristics (“thermal conductivity coefficient + specific heat capacity”, and “thermal conductivity coefficient + thermal stress coefficient”) were conducted.
- Successful reconstruction of the pair “thermal conductivity coefficient + thermal stress coefficient” is possible only with a large coupling parameter. A pair of dimensionless characteristics “thermal conductivity + specific heat capacity” was reconstructed with sufficient accuracy for any coupling parameter.
- The computational reconstruction scheme proposed is resistant to 2% input noise.

Acknowledgements This work was supported by the Southern Mathematical Institute of Vladikavkaz Scientific Center of the Russian Academy of Sciences.

References

1. Birman, V., Byrd, L.W.: Modeling and analysis of functionally graded materials and structures. *Appl. Mech. Rev.* **60**(5), 195–216 (2007). <https://doi.org/10.1115/1.2777164>
2. Wetherhold, R.C., Seelman, S., Wang, S.: The use of functionally graded materials to eliminated or control thermal deformation. *Compos. Sci. Technol.* **56**(9), 1099–1104 (1996). [https://doi.org/10.1016/0266-3538\(96\)00075-9](https://doi.org/10.1016/0266-3538(96)00075-9)
3. Lomazov, V.A.: *Diagnostics Problems for Inhomogeneous Thermoelastic Media*. OrelGTU, Orel (2002) (in Russian)
4. Alifanov, O.M.: *Inverse Heat Transfer Problem*. Springer, New York (1994)
5. Kabanikhin, S.I., Hasanov, A., Penenko, A.V.: A gradient descent method for solving an inverse coefficient heat conduction problem. *Numerical Anal. Appl.* **1**(1), 34–45 (2008). <https://doi.org/10.1134/S1995423908010047>
6. Razzaghi, H., Kowsary, F., Ashjaee, M.: Derivation and application of the adjoint method for estimation of both spatially and temporally varying convective heat transfer coefficient. *Appl. Therm. Eng.* **154**, 63–75 (2019). <https://doi.org/10.1016/j.applthermaleng.2019.03.068>
7. Dulikravich, G.S., Reddy, S.R., Pasqualetta, M.A., Colaco, M.J., Orlande, H.R., Coverston, J.: Inverse determination of spatially varying material coefficients in solid objects. *J. Inverse Ill-Posed Probl.* **24**, 181–194 (2016). <https://doi.org/10.1515/jiip-2015-0057>
8. Cao, K., Lesnic, D.: Determination of space-dependent coefficients from temperature measurements using the conjugate gradient method. *Num. Methods Part. Different. Eq.* **34**(4), 1370–1400 (2018). <https://doi.org/10.1002/num.22262>
9. Chen, W.L., Chou, H.M., Yang, Y.C.: An inverse problem in estimating the space-dependent thermal conductivity of a functionally graded hollow cylinder. *Composites, Part B* **50**, 112–119 (2013)
10. Geymonat, G., Pagano, S.: Identification of mechanical properties by displacement field measurement: a variational approach. *Meccanica* **38**, 535–545 (2003). <https://doi.org/10.1023/A:1024766911435>
11. Grediac, M., Hild, F., Pineau, A.: *Full-Field Measurements and Identification in Solid Mechanics*. Wiley-ISTE, Great Britain (2013)
12. Avril, S., Pierron, F.: General framework for the identification of constitutive parameters from full-field measurements in linear elasticity. *Int. J. Solids Struct.* **44**, 4978–5002 (2007). <https://doi.org/10.1016/j.ijsolstr.2006.12.018>
13. Danilaev, P.G.: *Coefficient Inverse Problems for Parabolic Type Equations and their Applications*. Boston, Koln, VSP, Tokyo, Utrecht (2001)
14. Yeung, W.K., Lam, T.T.: Second-order finite difference approximation for inverse determination of thermal conductivity. *Int. J. Heat Mass Transf.* **39**(17), 3685–3693 (1996). [https://doi.org/10.1016/0017-9310\(96\)00028-2](https://doi.org/10.1016/0017-9310(96)00028-2)
15. Xu, M.H., Cheng, J.C., Chang, S.Y.: Reconstruction theory of the thermal conductivity depth profiles by the modulated photo reflectance technique. *J. Appl. Phys.* **84**(2), 675–682 (2002)
16. Nedin, R., Nesterov, S., Vatulyan, A.: Identification of thermal conductivity coefficient and volumetric heat capacity of functionally graded materials. *Int. J. Heat Mass Transf.* **102**, 213–218 (2016). <https://doi.org/10.1016/j.ijheatmasstransfer.2016.06.027>
17. Vatulyan, A.O., Nesterov, S.A.: *Coefficient Inverse Problems of Thermomechanics*. Publishing House of the Southern Federal University, Rostov-on-Don - Taganrog (2019) (in Russian)
18. Nedin, R., Nesterov, S., Vatulyan, A.: On an inverse problem for inhomogeneous thermoelastic rod. *Int. J. Solids Struct.* **51**(3), 767–773 (2014). <https://doi.org/10.1016/j.ijsolstr.2013.11.003>

19. Nedin, R., Nesterov, S., Vatulyan, A.: On reconstruction of thermalphysic characteristics of functionally graded hollow cylinder. *Appl. Math. Modelling* **40**(4), 2711–2719 (2016). <https://doi.org/10.1016/j.apm.2015.09.078>
20. Vatul'yan, A.O., Nesterov, S.A.: On determination of inhomogeneous thermomechanical characteristics of a pipe. *J. Eng. Phys. Thermophysics* **88**(4), 984–993 (2015). <https://doi.org/10.1007/s10891-015-1274-7>
21. Vatulyan, A.O., Nesterov, S.A.: On the identification problem of the thermomechanical characteristics of the finite functionally graded cylinder. *Izvestiya of Saratov University. New Series. Ser.: Math. Mech. Inf.* **21**(1), 35–47 (2021) (in Russian). <https://doi.org/10.18500/1816-9791-2021-21-1-35-47>
22. Vatulyan, A.O., Nesterov, S.A.: On determination of the thermomechanical characteristics of a functionally graded finite cylinder. *Mech. Solids* **56**(7), 1429–1438 (2021). <https://doi.org/10.3103/S0025654421070256>
23. Dudarev, V.V., Vatulyan, A.O., Mnukhin, R.M., Nedin, R.D.: Concerning an approach to identifying the Lamé parameters of an elastic functionally graded cylinder. *Math. Methods Appl. Sci.* **43**(11), 6861–6870 (2020). <https://doi.org/10.1002/mma.6428>
24. Krylov, V.I., Skoblya, N.S.: *Approximate Fourier Transform and Laplace Transform Inversion Methods*. Nauka, Moscow (1974) (in Russian)
25. Tikhonov, A.N., Goncharskiy, A.V., Stepanov, V.V., Yagola, A.G.: *Numerical Methods for Solving Ill-posed Problems*. Nauka, Moscow (1990) (in Russ.)

Chapter 19

Regularities of Technological Residual Stress Fields Formation in Cylindrical Products Manufactured by Additive Methods



Dmitry A. Parshin

Abstract The regularities of the development of residual stress fields in deformable solids formed in layers of viscoelastic aging materials are investigated by the example of the technological problem on additive manufacturing of a hollow cylindrical product of arbitrary thickness on a rapidly rotating substrate, with arbitrarily varying initial circumferential stress in the added material. Quasi-static processes of deformation of such products during and after their manufacture, which are accompanied by small strains, have been studied. An effective procedure for calculating the distributions of the mentioned stresses is constructed.

Keywords Additive manufacturing · Technological stresses · Residual stresses · Viscoelasticity · Aging · Quasi-static deformation · Prestress · Centrifugal inertia forces · Hollow cylindrical product · Layered product

19.1 Introduction

In this paper, the process of additive manufacturing of a product is considered from the standpoint of mechanics of deformable solids. Classical for mechanics are solids of constant material composition, which have already acquired their final appearance by the beginning of the deformation process. This appearance is represented in the configuration of the solid, which is called *natural* and which the displacements of the solid points, causing its deformation under the action of applied loads, are then referred to. The main difference between any classical solid and an additively manufactured one is that the latter still continues to be replenished with new material elements during the deformation process and, thus, is basically devoid of a natural configuration. This feature is the reason for, among other things, the emergence of *residual stress fields* in additively manufactured solids after their manufacture is

D. A. Parshin (✉)

Institute for Problems in Mechanics RAS, Vernadsky Ave 101 Bldg 1, Moscow 119526, Russian Federation

e-mail: parshin@ipmnet.ru

completed and the loads accompanying the manufacturing process are removed. The presented work is devoted to the analysis of these stresses on the example of one specific technological problem—the problem of additive forming a cylindrical layer of material with mechanical properties of viscoelasticity and aging on the surface of an axisymmetric substrate. The need for such an analysis is dictated by the urgency of solving various engineering problems on contact, wear and destruction of structural elements and machine parts layered with coatings having complex properties [4, 5, 7, 11]. It is obvious that the results of the corresponding calculations should be influenced in a decisive way by the stress distributions in the considered products that have arisen as a result of the technological features of their manufacture.

It is obvious that an adequate mechanical study of additive processes requires correct consideration of kinematic and power features of the manufactured solid replenishment with a new material. Such consideration cannot take place within the scope of classical equations and boundary conditions of solid mechanics, even when they are formulated for the time variable region of space associated with the *growing solid*. This is easy to understand if we pay attention to the fact, native for growing solids, that while some of material elements are only included in the material composition of the solid, others have been already deformed compatibly with it for some time. This foundational fact is expressed in strain incompatibility (in the classical sense of the term) inside any growing solid and generates a *special class of problems* in solid mechanics—the problems of mechanics of growing solids. The mathematical approach to the formulation and research of this class of problems is dynamically developed in the framework of the Russian scientific school founded by Academician N.Kh. Arutyunyan and his disciple Professor A.V. Manzhirov. Some of the results of this school can be found, for instance, by Arutyunyan et al. [3], Manzhirov and Chernysh [10], Manzhirov [8], Arutyunyan and Manzhirov [2], Manzhirov [9], Manzhirov and Mikhin [11], Manzhirov and Parshin [13], Parshin [14], Parshin [15], Kazakov and Parshin [6].

19.2 Basic Relations for the Problem Under Consideration

In Parshin [14], a mathematical model for the process of manufacturing axisymmetric cylindrical products with an arbitrary wall thickness by additive methods using viscoelastic aging isotropic materials [1] was formulated. As mechanical factors causing deformation of the manufactured product, and already in the process of its manufacture, the model takes into account:

1. centrifugal inertia forces caused by the rapid rotation of the (absolutely) rigid substrate used around its axis with an arbitrary (variable) angular velocity $\omega(t)$;
2. arbitrary initial circumferential stresses $\sigma_{\varphi,0}(\rho)$ arising in the (infinitely thin) material layers sequentially deposited onto the (inner) surface of this substrate.

Here t , ρ and φ indicate respectively the time, radial and circumferential coordinates in the rotating frame of reference associated with the substrate.

Let us be interested in two, generally speaking, different programs of the substrate rotation during the manufacture of the product in question: $\omega_1(t)$ and $\omega_2(t)$. For these programs, we shall have the following initial boundary value problem [14].

$$\begin{aligned} \nabla \cdot \mathbf{S}_{1,2} + \mathbf{e}_\rho f_{1,2}(\rho, t) &= \mathbf{0} \quad \text{as } a(t) < \rho < a_0, \quad t > t_0; \\ \mathbf{S}_{1,2} &= 2\mathbf{D}_{1,2} + \phi \mathbf{1} I_1[\mathbf{D}_{1,2}], \quad \mathbf{D}_{1,2} = \frac{1}{2}(\nabla \mathbf{v}_{1,2}^{\text{transp}} + \nabla \mathbf{v}_{1,2}); \\ \mathbf{e}_\rho \cdot \mathbf{S}_{1,2} &= \mathbf{e}_\rho g_{1,2}(t) \quad \text{as } \rho = a(t); \quad \mathbf{v}_{1,2} = \mathbf{0} \quad \text{as } \rho = a_0; \\ \mathbf{T}_{1,2} &= \mathbf{e}_\varphi \mathbf{e}_\varphi \sigma_{\varphi,0}(\rho) \quad \text{as } t = \tau_0(\rho). \end{aligned} \quad (19.1)$$

In this problem, we use the notation consistent with the notation adopted in the paper by Parshin [14], index $i = 1, 2$ for all the variables corresponds to the i -th rotation program:

- $a(t)$ is the current radius of the inner surface of the manufactured product;
- $\tau_0(\rho)$ function inverse to $a(t)$ in all intervals of strict monotony of the latter, $a(\tau_0(\rho)) \equiv \rho$;
- t_0 initial moment of the manufacturing process;
- a_0 initial radius of the inner surface of the manufactured product, $a_0 = a(t_0)$;
- \mathbf{S}_i tensor of operator stress velocities, $\mathbf{S}_i = d\tilde{\mathbf{T}}_i/dt$, where
- $\tilde{\mathbf{T}}_i$ tensor of operator stress, $\tilde{\mathbf{T}}_i = \mathcal{Q}_{\tau_0(\rho)} \mathbf{T}_i$, where
- \mathcal{Q}_{τ_0} viscoelasticity operator,

$$\begin{aligned} \mathcal{Q}_{\tau_0} \psi(t) &= \frac{\psi(t)}{G(t)} - \int_{\tau_0}^t \frac{\psi(\tau)}{G(\tau)} K(t, \tau) d\tau, \\ K(t, \tau) &= G(\tau) \frac{\partial}{\partial \tau} \left[\frac{1}{G(\tau)} + c_{\text{shear}}(t, \tau) \right], \quad \text{where} \end{aligned}$$

- K kernel of creep,
- c_{shear} measure of creep,
- $G(t)$ elastic modulus of pure shear;
- \mathbf{T}_i stress tensor;
- \mathbf{D}_i tensor of strain rates;
- \mathbf{v}_i velocity vector;
- f_i, g_i are the known functions determined by the program of replenishment of the product with additional material and the program of rotation of the substrate during manufacture, and also by the density of the material used and its viscoelastic and aging properties,

$$f_i(\rho, t) = \mu\rho \mathcal{W}_{\tau_0(\rho)} \omega_i^2(t),$$

$$\mathcal{W}_{\tau_0} \psi(t) = \psi(\tau_0) \frac{\partial c_{\text{shear}}(t, \tau_0)}{\partial t} + \frac{1}{G(t)} \frac{d\psi(t)}{dt} + \int_{\tau_0}^t \frac{d\psi(\tau)}{d\tau} \frac{\partial c_{\text{shear}}(t, \tau)}{\partial t} d\tau, \quad (19.2)$$

$$g_i(t) = -\frac{1}{G(t)} \frac{da(t)}{dt} \left[\frac{\sigma_{\varphi,0}(a(t))}{a(t)} - \mu\omega_i^2(t) a(t) \right], \quad \text{where} \quad (19.3)$$

μ is the material density;
 $\mathbf{e}_s(\varphi)$ is the unit vector of a coordinate direction,

$$\mathbf{e}_s = \frac{\partial \mathbf{r}}{\partial s} \bigg/ \left\| \frac{\partial \mathbf{r}}{\partial s} \right\|, \quad s = \rho, \varphi, \quad \text{where}$$

\mathbf{r} radius-vector of an arbitrary point of the manufactured product referred to the rotating frame;
 $\mathbf{1}$ tensor unit;
 ϕ material constant depending only on the Poisson ratio;
 $I_1[\mathbf{A}]$ linear invariant of the tensor \mathbf{A} .

Note that at each point of the additively manufactured solid under consideration, the stress-strain state begins to develop from the moment this point is included in the composition of the solid, that is, from the moment of time $t = \tau_0(\rho)$

$$\mathbf{A} = \mathbf{A}(\mathbf{r}, t), \quad \mathbf{A} = \mathbf{S}_i, \tilde{\mathbf{T}}_i, \mathbf{T}_i, \mathbf{D}_i, \quad \mathbf{v}_i = \mathbf{v}_i(\mathbf{r}, t), \quad t \geq \tau_0(\rho).$$

Remark also that problem (19.1) describes the mechanical behavior of the product in question not only *during* the process (including possible *pauses* in it), but also for an arbitrarily long time *after* the moment $t = t_{\text{fin}}$ of final completion of *additive application* of the material to the inner surface of this product, unless in those time intervals when the product is not replenished with new material, its inner surface is not being loaded [8].

19.3 Calculating Residual Stresses After Stopping Rotation

Suppose now that the first rotation program $\omega_1(t)$ corresponds to the *true change* in angular velocity *during* the manufacture of the product, i.e., for $t \leq t_{\text{fin}}$, and then is arbitrary. In particular, it can be $\omega_1(t) \equiv \omega = \text{const}$ for any $t \in (t_0, +\infty)$ (note that the constancy of ω_1 for all $t > t_0$, including for $t > t_{\text{fin}}$, noticeably simplifies the solution of corresponding problem (19.1)—see formula (19.2)).

Let the second rotation program $\omega_2(t)$ coincide with the first one at $t_0 < t < t_{\text{stop}}$, where $t_{\text{stop}} > t_{\text{fin}}$ is some arbitrarily fixed moment in time. Herewith $\omega_2(t) \neq \omega_1(t)$

at $t \geq t_{\text{stop}}$ and

$$\omega_2(t) \rightarrow 0 \quad \text{as } t \rightarrow +\infty. \quad (19.4)$$

It is clear that in the above assigned case, the *residual technological stresses* in the finished product under consideration, caused by the manufacturing process in itself and acting indefinitely at the points \mathbf{r} of this product after the manufacturing completion and stopping rotation, will be equal to

$$\mathbf{T}_{\text{res}}(\mathbf{r}) = \lim_{t \rightarrow +\infty} \mathbf{T}_2(\mathbf{r}, t). \quad (19.5)$$

We set the task to calculate these residual stresses under the assumptions that

$$\exists \lim_{t \rightarrow +\infty} \omega_1(t) = \omega_\infty \quad (19.6)$$

and we have found the limit values

$$\mathbf{T}_\infty(\mathbf{r}) = \lim_{t \rightarrow +\infty} \mathbf{T}_1(\mathbf{r}, t) \quad (19.7)$$

of the stresses corresponding to the solution of the problem (19.1)₁.

Define the following functions

$$\begin{aligned} \Delta \mathbf{S} &= \mathbf{S}_2 - \mathbf{S}_1, & \Delta \mathbf{D} &= \mathbf{D}_2 - \mathbf{D}_1, & \Delta \mathbf{v} &= \mathbf{v}_2 - \mathbf{v}_1, \\ \Delta \tilde{\mathbf{T}} &= \tilde{\mathbf{T}}_2 - \tilde{\mathbf{T}}_1, & \Delta \mathbf{T} &= \mathbf{T}_2 - \mathbf{T}_1, & \Delta f &= f_2 - f_1, & \Delta g &= g_2 - g_1. \end{aligned}$$

Looking at (19.3), we can see that $\Delta g(t) \equiv 0$ for all $t > t_0$. Indeed, for $t < t_{\text{stop}}$, there is the identical match of the both rotation programs, i.e.,

$$h(t) = \omega_2^2(t) - \omega_1^2(t) \equiv 0 \quad \text{as } t < t_{\text{stop}}, \quad (19.8)$$

and for any $t > t_{\text{fin}}$, there will be $da(t)/dt \equiv 0$. By virtue of (19.2) and (19.8) we can also declare that

$$\Delta f(\rho, t) = \mu \rho \mathcal{W}_{\tau_0(\rho)} h(t) \equiv 0 \quad \text{as } t < t_{\text{stop}}. \quad (19.9)$$

For $t \geq t_{\text{stop}}$, we have obviously to use the general expression

$$\begin{aligned} \mathcal{W}_{\tau_0(\rho)} h(t) &= h(\tau_0(\rho)) \frac{\partial c_{\text{shear}}(t, \tau_0(\rho))}{\partial t} \\ &+ \frac{1}{G(t)} \frac{dh(t)}{dt} + \int_{\tau_0(\rho)}^t \frac{dh(\tau)}{d\tau} \frac{\partial c_{\text{shear}}(t, \tau)}{\partial t} d\tau \end{aligned} \quad (19.10)$$

where the first term on the right-hand side vanishes by virtue of (19.8) because $\tau_0(\rho) \leq t_{\text{fin}} < t_{\text{stop}}$ at any point of the considered solid and consequently $h(\tau_0(\rho)) = 0$.

For further transformations, let us fix an arbitrary time instant $\hat{t} \in (t_{\text{fin}}, t_{\text{stop}})$. Then we can transform (19.10) into

$$\mathcal{W}_{\tau_0(\rho)} h(t) = \frac{1}{G(t)} \frac{dh(t)}{dt} + \int_{\hat{t}}^t \frac{dh(\tau)}{d\tau} \frac{\partial c_{\text{shear}}(t, \tau)}{\partial t} d\tau$$

inasmuch $h(\tau) \equiv 0$ as $\tau \in (\tau_0(\rho), \hat{t}]$. With use of the rule for differentiating an integral with respect to a parameter and of partial integration procedure (considering that $h(\hat{t}) = 0$) we can write

$$\begin{aligned} \mathcal{W}_{\tau_0(\rho)} h(t) &= \frac{dh(t)}{dt} \left[\frac{1}{G(t)} - c_{\text{shear}}(t, t) \right] + \frac{d}{dt} \int_{\hat{t}}^t \frac{dh(\tau)}{d\tau} c_{\text{shear}}(t, \tau) d\tau \\ &= \frac{dh(t)}{dt} \left[\frac{1}{G(t)} - c_{\text{shear}}(t, t) \right] + \frac{d}{dt} \left[h(t) c_{\text{shear}}(t, t) - \int_{\hat{t}}^t h(\tau) \frac{\partial c_{\text{shear}}(t, \tau)}{\partial \tau} d\tau \right]. \end{aligned}$$

Here we have $c_{\text{shear}}(t, t) \equiv 0$ since the creeping strain is equal to zero at the time of load application. And so far as

$$\frac{dh(t)}{dt} \frac{1}{G(t)} = \frac{d}{dt} \frac{h(t)}{G(t)} - h(t) \frac{d}{dt} \frac{1}{G(t)} = \frac{d}{dt} \left[\frac{h(t)}{G(t)} - \int_{\hat{t}}^t h(\tau) \frac{d}{d\tau} \frac{1}{G(\tau)} d\tau \right]$$

we get thereupon

$$\mathcal{W}_{\tau_0(\rho)} h(t) = \frac{d}{dt} \left[\frac{h(t)}{G(t)} - \int_{\hat{t}}^t h(\tau) \frac{\partial}{\partial \tau} \left[\frac{1}{G(\tau)} + c_{\text{shear}}(t, \tau) \right] d\tau \right] = \frac{d\mathcal{Q}_{\hat{t}} h(t)}{dt} \quad (19.11)$$

for any $t > \hat{t}$ (for $t \in (\hat{t}, t_{\text{stop}})$ formula (19.11) remains true because of (19.8)).

Subtract (19.1)₁ from (19.1)₂. For the time interval (t_0, t_{stop}) , we will have the problem

$$\begin{aligned} \nabla \cdot \Delta \mathbf{S} &= \mathbf{0} \quad \text{as } a(t) < \rho < a_0, \quad t_0 < t < t_{\text{stop}}; \\ \Delta \mathbf{S} &= 2\Delta \mathbf{D} + \phi \mathbf{1} I_1[\Delta \mathbf{D}], \quad \Delta \mathbf{D} = \frac{1}{2} (\nabla \Delta \mathbf{v}^{\text{transp}} + \nabla \Delta \mathbf{v}); \\ \mathbf{e}_\rho \cdot \Delta \mathbf{S} &= \mathbf{0} \quad \text{as } \rho = a(t); \quad \Delta \mathbf{v} = \mathbf{0} \quad \text{as } \rho = a_0; \\ \Delta \mathbf{T} &= \mathbf{0} \quad \text{as } t = \tau_0(\rho). \end{aligned}$$

which obviously has the only *trivial solution*. Hereby

$$\Delta \mathbf{T}(\mathbf{r}, t) \equiv \mathbf{0} \quad \text{as } t \in [\tau_0(\rho), t_{\text{stop}}] \quad (19.12)$$

including $t = \hat{t}$. So we can formulate the following initial boundary value problem for the Δ -variables in the time interval $(\hat{t}, +\infty)$

$$\begin{aligned} \nabla \cdot \Delta \mathbf{S} + \mathbf{e}_\rho \Delta f(\rho, t) &= \mathbf{0} \quad \text{as } a_{\text{fin}} < \rho < a_0, \quad t > \hat{t}; \\ \Delta \mathbf{S} &= 2\Delta \mathbf{D} + \phi \mathbf{1} I_1[\Delta \mathbf{D}], \quad \Delta \mathbf{D} = \frac{1}{2}(\nabla \Delta \mathbf{v}^{\text{transp}} + \nabla \Delta \mathbf{v}); \\ \mathbf{e}_\rho \cdot \Delta \mathbf{S} &= \mathbf{0} \quad \text{as } \rho = a_{\text{fin}}; \quad \Delta \mathbf{v} = \mathbf{0} \quad \text{as } \rho = a_0; \\ \Delta \mathbf{T} &= \mathbf{0} \quad \text{as } t = \hat{t}. \end{aligned} \quad (19.13)$$

where $a_{\text{fin}} = a(t_{\text{fin}})$ and (considering (19.9), (19.11), and (19.8))

$$\Delta f(\rho, t) = \mu \rho \frac{d\mathcal{Q}_i h(t)}{dt}, \quad \mathcal{Q}_i h(\hat{t}) = \frac{h(\hat{t})}{G(\hat{t})} = 0. \quad (19.14)$$

Taking into account (19.12) we find for $t > \hat{t}$

$$\begin{aligned} \Delta \tilde{\mathbf{T}}(\mathbf{r}, t) &= \mathcal{Q}_{\tau_0(\rho)} \Delta \mathbf{T}(\mathbf{r}, t) = \frac{\Delta \mathbf{T}(\mathbf{r}, t)}{G(t)} - \int_{\tau_0(\rho)}^t \frac{\Delta \mathbf{T}(\mathbf{r}, \tau)}{G(\tau)} K(t, \tau) d\tau \\ &= \frac{\Delta \mathbf{T}(\mathbf{r}, t)}{G(t)} - \int_{\hat{t}}^t \frac{\Delta \mathbf{T}(\mathbf{r}, \tau)}{G(\tau)} K(t, \tau) d\tau = \mathcal{Q}_i \Delta \mathbf{T}(\mathbf{r}, t), \\ \Delta \tilde{\mathbf{T}}(\mathbf{r}, \hat{t}) &= \frac{\Delta \mathbf{T}(\mathbf{r}, \hat{t})}{G(\hat{t})} = \mathbf{0}. \end{aligned}$$

Therefore,

$$\Delta \tilde{\mathbf{T}}(\mathbf{r}, t) = \int_{\hat{t}}^t \Delta \mathbf{S}(\mathbf{r}, \tau) d\tau, \quad \Delta \mathbf{T}(\mathbf{r}, t) = \mathcal{Q}_i^{-1} \int_{\hat{t}}^t \Delta \mathbf{S}(\mathbf{r}, \tau) d\tau.$$

At the same time, it follows from (19.14) that

$$\mu \rho \mathcal{Q}_i h(t) = \int_{\hat{t}}^t \Delta f(\rho, \tau) d\tau, \quad \mu \rho h(t) = \mathcal{Q}_i^{-1} \int_{\hat{t}}^t \Delta f(\rho, \tau) d\tau.$$

Thus, from the differential equation of problem (19.13), we obtain the equation

$$\nabla \cdot \Delta \mathbf{T} + \mathbf{e}_\rho \mu \rho h(t) = \mathbf{0} \quad \text{as } a_{\text{fin}} < \rho < a_0, \quad t > \hat{t}. \quad (19.15)$$

Let us introduce the following tensor- and vector-function on the entire spatial domain which the finally manufactured cylindrical product under consideration occupies

$$\Delta \mathbf{u}(\mathbf{r}, t) = \int_{\hat{t}}^t \Delta \mathbf{v}(\mathbf{r}, \tau) d\tau, \quad \Delta \mathbf{E}(\mathbf{r}, t) = \int_{\hat{t}}^t \Delta \mathbf{D}(\mathbf{r}, \tau) d\tau.$$

Then we get the relations

$$\Delta \mathbf{T} = \mathcal{Q}_{\hat{t}}^{-1}(2\Delta \mathbf{E} + \phi \mathbf{1} I_1[\Delta \mathbf{E}]), \quad \Delta \mathbf{E} = \frac{1}{2}(\nabla \Delta \mathbf{u}^{\text{transp}} + \nabla \Delta \mathbf{u}) \quad (19.16)$$

from the corresponding relations of problem (19.13). And we do similarly for boundary conditions in (19.13)

$$\mathbf{e}_\rho \cdot \Delta \mathbf{T} = \mathbf{0} \quad \text{as } \rho = a_{\text{fin}}; \quad \Delta \mathbf{u} = \mathbf{0} \quad \text{as } \rho = a_0. \quad (19.17)$$

Boundary value problem (19.15), (19.16), (19.17) represents a classical problem (for the *fixed composition* deformable cylindrical solid of inner radius a_{fin} and outer radius a_0) of the viscoelasticity theory for aging solids, with the stress tensor $\Delta \mathbf{T}$, small strain tensor $\Delta \mathbf{E}$, and displacement vector $\Delta \mathbf{u}$, with homogeneous boundary conditions and with the point- and time-dependent bulk forces. The *correspondence principle* is well known [2] according to which the stresses $\Delta \mathbf{T}(\mathbf{r}, t)$ in this problem coincide with the stresses in the corresponding classical problem of the elasticity theory for the finally manufactured product

$$\begin{aligned} \nabla \cdot \Delta \mathbf{T} + \mathbf{e}_\rho \mu \rho h(t) &= \mathbf{0} \quad \text{as } a_{\text{fin}} < \rho < a_0, \quad t > \hat{t}; \\ \Delta \mathbf{T}/G(t) &= 2\Delta \mathbf{E}_{\text{el}} + \phi \mathbf{1} I_1[\Delta \mathbf{E}_{\text{el}}], \quad \Delta \mathbf{E}_{\text{el}} = \frac{1}{2}(\nabla \Delta \mathbf{u}_{\text{el}}^{\text{transp}} + \nabla \Delta \mathbf{u}_{\text{el}}); \\ \mathbf{e}_\rho \cdot \Delta \mathbf{T} &= \mathbf{0} \quad \text{as } \rho = a_{\text{fin}}; \quad \Delta \mathbf{u}_{\text{el}} = \mathbf{0} \quad \text{as } \rho = a_0. \end{aligned} \quad (19.18)$$

The time variable t in boundary value problem (19.18) is considered as a parameter.

Subject to the definition of $h(t)$ and to conditions (19.4), (19.6), we can pass in (19.18) to the limit when the parameter t tends to $+\infty$

$$\begin{aligned}
\nabla \cdot \Delta \mathbf{T}_\infty &= \mathbf{e}_\rho \mu \rho \omega_\infty^2 \quad \text{as } a_{\text{fin}} < \rho < a_0; \\
\Delta \mathbf{T}_\infty / G_\infty &= 2 \Delta \mathbf{E}_{\text{el}, \infty} + \phi \mathbf{1} I_1 [\Delta \mathbf{E}_{\text{el}, \infty}], \\
\Delta \mathbf{E}_{\text{el}, \infty} &= \frac{1}{2} (\nabla \Delta \mathbf{u}_{\text{el}, \infty}^{\text{transp}} + \nabla \Delta \mathbf{u}_{\text{el}, \infty}); \\
\mathbf{e}_\rho \cdot \Delta \mathbf{T}_\infty &= \mathbf{0} \quad \text{as } \rho = a_{\text{fin}}; \quad \Delta \mathbf{u}_{\text{el}, \infty} = \mathbf{0} \quad \text{as } \rho = a_0.
\end{aligned} \tag{19.19}$$

Here $\Delta \mathbf{T}_\infty(\mathbf{r}) = \lim_{t \rightarrow +\infty} \Delta \mathbf{T}(\mathbf{r}, t)$ and $G_\infty = \lim_{t \rightarrow +\infty} G(t)$.

Now we are ready to formulate the following result (on the basis of formula (19.5), (19.7) and the definition of the tensor $\Delta \mathbf{T}$) the resulting *residual stress field* in the technological problem in question is to be calculated as

$$\mathbf{T}_{\text{res}}(\mathbf{r}) = \mathbf{T}_\infty(\mathbf{r}) + \Delta \mathbf{T}_\infty(\mathbf{r})$$

where the tensor field $\mathbf{T}_\infty(\mathbf{r})$ can be found by formula (19.7) using the solution of *nonclassical* initial boundary value *problem of mechanics of growing solids* (19.1)₁, and the tensor field $\Delta \mathbf{T}_\infty(\mathbf{r})$ is known after solving *classical elasticity problem* (19.19).

19.4 Conclusions

In the additive manufacture of products using rapidly rotating substrates, significant technological stresses develop in these products. After stopping the rotation of a fully manufactured product, these stresses cannot disappear. This is due to the incompatibility of strains in a solid made by additive growth. The resulting technological stresses in the finished product are re-formed into residual stresses. The regularities of the stress occurrence and re-formation under specific conditions of the technological process organization and specific rheological features of the material mechanical behavior considered in this paper are described by the above formulated initial boundary value problems. As a result of the conducted research, an effective procedure has been developed for predicting the distribution of final residual stresses that will persist indefinitely in the finished cylindrical product made of aging viscoelastic material after the termination of rotation, when no external influences are acting on this product.

Acknowledgements The work was carried out on topic No. AAAA-A20-120011690132-4 of the State assignment to IPMech RAS.

References

1. Arutyunyan, N.Kh.: Some Problems in the Theory of Creep. Pergamon Press, Oxford (1966)
2. Arutyunyan, N.Kh., Manzhurov, A.V.: Contact Problems of the Theory of Creep (in Russ.). Izdat. Inst. Mekhaniki NAN RA, Erevan (1999)

3. Arutyunyan, N.Kh., Manzhurov, A.V., Naumov, V.E.: Contact Problems in Mechanics of Growing Solids (in Russ.). Nauka, Moscow (1991)
4. Hakobyan, V.N., Amirjanyan, H.A.: Kazakov K.Ye.: Axisymmetric stressed state of uniformly layered space with periodic systems of internal disc-shaped cracks and inclusions. Herald Bauman Moscow State Technical University: Series Natural Sciences **89**(2), 25–40 (2020)
5. Kazakov, K.E., Kurdina, S.P.: Interaction of viscoelastic tube with inner nonuniform coating of variable thickness and rigid cylindrical insert. Key Eng. Mater. **894**, 67–71 (2021)
6. Kazakov, K.E., Parshin, D.A.: A model of mechanics of growing solids for the stress-strain analysis of wound composites reinforced with thin unidirectional fibers. J. Phys.: Conf. Ser. **2231**(1), 012006 (2022)
7. Kazakov, K.E., Sahakyan, A.A.: On the flat interaction of foundations and punches with complex forms of contacting surfaces. J. Phys.: Conf. Ser. **1474**, 012023 (2020)
8. Manzhurov, A.V.: The general non-inertial initial-boundary value problem for a viscoelastic ageing solid with piecewise-continuous accretion. J. Appl. Math. Mech. **59**(5), 805–816 (1995)
9. Manzhurov, A.V.: Mechanical analysis of an AM fabricated viscoelastic shaft under torsion by rigid disks. Lect. Notes Eng. Comput. Sci. **2230**, 856–860 (2017)
10. Manzhurov, A.V., Chernysh, V.A.: Problem of a buried arch structure reinforcement by the accretion method (in Russ.). Izvestiya Akademii Nauk. Mekhanika Tvyordogo Tela **27**(5):25–37 (1992)
11. Manzhurov, A.V., Kazakov, K.E.: Axisymmetric problem of fretting wear for a foundation with a nonuniform coating and rough punch. AIP Conf. Proc. **1959**, 070023 (2018)
12. Manzhurov, A.V., Mikhin, M.N.: 2D problems of surface growth theory with applications to additive manufacturing. J. Phys.: Conf. Ser. **991**, 012057 (2018)
13. Manzhurov, A.V., Parshin, D.A.: Analytical solution of the mechanical problem on additive thickening of aging viscoelastic tapers under nonstationary longitudinal end forces. Eng. Lett. **26**(2), 267–275 (2018)
14. Parshin, D.A.: Mathematical modelling of the process of internal technological stress fields development in cylindrical solids being layer-by-layer made of ageing viscoelastic materials. J. Phys.: Conf. Ser. **1479**, 012145 (2020)
15. Parshin, D.A.: Technological controlling the contact pressure onto a cylindrical substrate from a coating being formed additively on its outer surface. AIP Conf. Proc. **2340**, 040005 (2021)

Chapter 20

Two-Point Rotations in Geometry of Finite Deformations



Yuri N. Radayev

Abstract The paper is devoted to a study of deformed states of continuous medium. The study is restricted to the case when a deformed state admits a comparison to the referential state. The latter are considered to be immersed in the three-dimensional Euclidean space. A derivation of the two-point tensor of finite rotation and its unconventional orthogonality are discussed. One-point rotation tensors are introduced. Both of the two one-point rotation tensors are orthogonal in the conventional sense thus allowing to determine all geometrical characteristics related to a rotation in a three-dimensional space. Priority in the paper is given to simple algorithmic procedures for obtaining natural components of measures and tensors of finite deformations, as well as transformations of the fundamental equations of continuum mechanics realized by the rotation tensors and corresponding vectors of finite rotations. The two pseudovectors of finite rotations are defined and are to be employed, along with the pseudovectors of the “extra” rotations, as the principal kinematic parameters in mathematical models of micropolar elastic continuum.

Keywords Finite deformation · Distortion · Two-point rotation tensor · Conventional orthogonality · Unconventional orthogonality · Finite rotation pseudovector · Micropolar continuum

20.1 Requisite Notions and Equations

Deformation of continuous media is recognized by the change in the mutual distances between the spatial positions of the material points, chosen for observation, measured in the referential and the actual (deformed) states. The spatial positions of these points are characterized by coordinates (generally speaking, curvilinear): X^α in the reference position and x^s in the actual one. Therefore, the deformation is a differentiable transformation of variables (the Lagrangian referential to the Eulerian spatial):

Y. N. Radayev (✉)

Institute for Problems in Mechanics of RAS, Prosp. Vernadskogo, 101,
Moscow, Russian Federation
e-mail: radayev@ipmnet.ru

$$X^\alpha \longrightarrow x^s. \quad (20.1)$$

Since deformation manifests itself as a change in the metric characteristics of continuum, in the theory of finite deformations, it is then necessary to compare the referential $g_{\alpha\sigma}$ and the convective $g_{\alpha\sigma}$ metrics. The spatial metric is denoted by g_{ks} . We systematically employ Latin indices in order to refer to spatial components of geometrical objects, whereas Greek indices to point on convective components (only a few instances can be found in the present study) or referential components (additionally, root symbol is sometimes supplied by backprime).

In the following, tensors (including two-point tensors, see [1]) will always be considered with respect to one of two tensor bases (or a suitable combination of them in the case of a two-point tensor): referential or spatial.

We proceed to the notion of the reciprocal description of finite deformation. It is now well established that also acceptable to describe the deformation by the inverse with respect to (20.1) transformation:

$$X^\alpha \longleftarrow x^s. \quad (20.2)$$

In such a case, we talk about the inverse description of finite deformation. Both descriptions of deformation are absolutely equivalent although the first of them is given a priority. In order to emphasize the equivalence of the two mathematical descriptions of finite deformation, we write

$$X^\alpha \longleftrightarrow x^s. \quad (20.3)$$

In nonlinear continuum mechanics, the two-point *distortion tensor* is determined by partial differentiations of the Eulerian coordinates by the Lagrangian coordinates. Denoting by ∂_α operators of partial differentiations by variables X^α , we define the components of the distortion tensor according to

$$\partial_\alpha x^s \quad (\alpha, s = 1, 2, 3). \quad (20.4)$$

For the distortion tensor (20.4), we will also employ a more compact notation:

$$x_\alpha^s = \partial_\alpha x^s \quad (\alpha, s = 1, 2, 3).$$

In the inverse description of deformation, operating with the inverse distortion tensor

$$\partial_s X^\alpha \quad (\alpha, s = 1, 2, 3). \quad (20.5)$$

is required. For the inverse distortion tensor, in turn, the notation

$$X_s^\alpha = \partial_s X^\alpha \quad (\alpha, s = 1, 2, 3).$$

is introduced.

The polar Cauchy decomposition of the two-point distortion tensor (20.4) has two reciprocal forms. This fact is of crucial importance for the entire theory of finite deformations since it is based on the principle of reciprocity: any tensor field with referential Lagrangian indices can always be correlated with a reciprocal (dual) tensor field with Eulerian spatial indices. The principle of reciprocity is then applied to the straightforward classification of strain measures and strain tensors.

At first, let us consider the polar decomposition of distortion in the form

$$\partial_\alpha x^s = |x|_{\alpha\sigma} \lambda^{s\sigma}, \quad (20.6)$$

where $|x|_{\alpha\sigma}$ is the distortion modulus, $\lambda^{s\sigma}$ is the tensor of finite rotation (or rotation tensor).

The distortion modulus is a one-point absolute second rank symmetric tensor. It is positive, i.e., the eigenvalues $|x|_{(\alpha)}$ ($\alpha = 1, 2, 3$) are positive.

The rotation tensor is a two-point second rank tensor. It can be characterized by the following equations of “two-point orthogonality”:

$$\lambda^{s\sigma} \lambda_{k\sigma} = \delta_k^s, \quad \lambda^{s\alpha} \lambda_{s\sigma} = \delta_\sigma^\alpha. \quad (20.7)$$

The reciprocal to (20.6) variant of polar decomposition reads

$$\partial_\alpha x^s = |x|^{sk} \lambda_{k\alpha}, \quad (20.8)$$

wherein $|x|^{sk}$ is the reciprocal distortion modulus.

It is not difficult to notice that the reciprocal distortion modulus is obtained from the original one by raising the lower Greek indices by means of finite rotation tensors

$$|x|^{sk} = |x|_{\alpha\sigma} \lambda^{s\alpha} \lambda^{k\sigma}. \quad (20.9)$$

In fact, the rotation tensor $\lambda^{s\sigma}$ acts in nonlinear continuum mechanics as a simple mean for transforming Greek indices into Latin ones. A remarkable Eq. (20.9) just reflects such an opportunity provided by the two-point rotation tensor $\lambda^{s\sigma}$.

20.2 Pairs of Reciprocal Deformation and Strain Tensors

The geometry of finite deformations is thoroughly described in a number of classical monographs (see, for example, [1–5]). Now, we proceed to discussion of the based on the principle of reciprocity classification of measures and tensors known from the theory of finite deformations. All tensors related to measurements of finite deformations are one-point, have the second rank, and are determined by their *natural components* in tensor bases formed by dyadic products of local vectors of referential or spatial coordinate trihedra.

For measures of finite deformation, we have the following three pairs of reciprocal tensors (the algebraic powers of a tensor are situated above the root symbol; conventional symbols and terminology are used):

The 1st pair:

$$\begin{aligned} U_{\alpha\beta} &= |x|_{\alpha\beta} && \text{the right Biot stretch tensor} \\ V^{ik} &= |x|^{ik} && \text{the left Biot stretch tensor} \end{aligned}$$

The 2nd pair:

$$\begin{aligned} C_{\alpha\beta} &= \overset{2}{U}_{\alpha\beta} = g_{\alpha\beta} = x_{\alpha}^i x_{\beta}^k g_{ik} && \text{the right Cauchy–Green deformation tensor} \\ B^{ik} &= \overset{2}{V}^{ik} = x_{\alpha}^i x_{\beta}^k g^{\alpha\beta} && \text{the left Cauchy–Green deformation tensor} \\ &&& \text{or the Finger deformation tensor} \end{aligned}$$

The 3rd pair:

$$\begin{aligned} \overset{-1}{C}^{\alpha\beta} &= g^{ks} X_k^{\alpha} X_s^{\beta} && \text{the Finger deformation tensor} \\ \overset{-1}{B}_{ik} &= c_{ik} = g_{\alpha\beta} X_i^{\alpha} X_k^{\beta} && \text{the Cauchy (Finger, Piola) deformation tensor} \end{aligned}$$

The three most widely used pairs of reciprocal finite strain tensors of continuum mechanics are given below:

The 1st pair:

$$\begin{aligned} \gamma_{\alpha\beta} &= U_{\alpha\beta} - g_{\alpha\beta} && \text{the Biot strain tensor} \\ p^{ik} &= V^{ik} - g^{ik} && \text{the Almansi–Hamel strain tensor} \end{aligned}$$

The 2nd pair:

$$\begin{aligned} \varepsilon_{\alpha\beta} &= \frac{1}{2}(C_{\alpha\beta} - g_{\alpha\beta}) && \text{the Green–Lagrange (Green–St-Venant) strain tensor} \\ b^{ik} &= \frac{1}{2}(B^{ik} - g^{ik}) && \text{no known conventional terminology} \end{aligned}$$

The 3rd pair:

$$\begin{aligned} A^{\alpha\beta} &= \frac{1}{2}(g^{\alpha\beta} - \overset{-1}{C}^{\alpha\beta}) && \text{the Almansi strain tensor} \\ a_{ik} &= \frac{1}{2}(g_{ik} - \overset{-1}{B}_{ik}) && \text{the Euler–Almansi strain tensor} \end{aligned}$$

Note that the components of strain and deformation tensors with Greek indices are invariant under rotations of local spatial coordinate trihedra (and in this sense they are objective); in turn, the components of strain tensors with Latin indices are invariant under rotations of local referential coordinate trihedra. It is clear that the two-point finite rotation tensor $\lambda^{s\sigma}$ does not have any of these properties.

It should be noted that the covariant components of the right Cauchy–Green deformation tensor are the same that the components of the convective metric tensor. Simple reasoning allows us to demonstrate that

$$g_{\alpha\beta} = x_{\alpha}^i x_{\beta}^k g_{ik} = \backslash g^{\gamma\sigma} |x|_{\alpha\gamma} |x|_{\beta\sigma},$$

and to come to the reciprocal equation

$$x_{\alpha}^i x_{\beta}^k \backslash g^{\alpha\beta} = g_{ls} |x|^{il} |x|^{ks}.$$

20.3 Unconventional Orthogonality of the Two-point Rotation Tensor

In view of (20.9) the two-point tensor of the finite rotation $\lambda^{s\sigma}$ determines the rotation of the principal axes of deformation in the referential state to their new spatial orientations. In the referential state, the corresponding trihedron consists of mutually orthogonal eigenvectors of the tensor $|x|_{\alpha\beta}$. The new spatial orientations are determined by mutually orthogonal eigenvectors of the reciprocal distortion modulus $|x|^{ik}$. Translations of the spatial and referential coordinates do not affect the distortion. The same is true for the distortion modulus and reciprocal distortion modulus. However, rotations of the local coordinate frame (referential or spatial) affect the distortion.

We proceed to discussion of the metric properties of the rotation tensor $\lambda^{s\sigma}$. As in the case of transformation (20.9), the rotation tensor $\lambda^{s\sigma}$ allows us to transform Latin indices into Greek ones for components of the referential and spatial metrics. Namely, it is not difficult to see that the following equation is valid

$$g_{ij} \lambda^{i\beta} \lambda^{j\gamma} = \backslash g^{\beta\gamma} \quad (20.10)$$

along with the reciprocal equation

$$\backslash g_{\beta\gamma} \lambda^{i\beta} \lambda^{j\gamma} = g^{ij}. \quad (20.11)$$

The pair of Eqs. (20.10) and (20.11) establishes that an arbitrary referential vector $\backslash p_{\beta}$ is transformed into the spatial vector p^i determined by

$$p^i = \lambda^{i\beta} \backslash p_{\beta} \quad (20.12)$$

and having exactly the same length as $\backslash p_{\beta}$, while the lengths of the corresponding vectors are measured based on the referential and spatial metrics, respectively. The formulated property leads to the following conclusions: The rotation tensor $\lambda^{s\sigma}$ can be called as unconventionally orthogonal; the transformation (20.12) can be interpreted as a rotation in three-dimensional space.

In applications of continuum mechanics to micropolar elasticity, the two-point un conventionally orthogonal tensor of finite rotation $\lambda^{s\sigma}$ is not convenient since the rich arsenal of the linear algebra techniques cannot be directly applied to it. Therefore, there is a need to pass from $\lambda^{s\sigma}$ to a one-point orthogonal rotation tensor.

An orthogonal second rank tensor α^{ij} is conventionally defined by the fundamental relation

$${}^* \alpha^{ij} = \alpha^{-1ij},$$

or the equivalent pair of equations

$$\alpha^{ij} \alpha_{kj} = \delta_k^i, \quad \alpha^{ij} \alpha_{ik} = \delta_k^j.$$

In a three-dimensional space, a proper orthogonal tensor α^{ij} is completely determined by the spatial axis of rotation (directed along the unit vector c_k , $c^s c_s = 1$) and the angle of rotation θ . In geometric terms of c_k and θ , a proper orthogonal tensor can be represented as follows:

$$\alpha^{ij} = \cos \theta g^{ij} + (1 - \cos \theta) c^i c^j - \sin \theta e^{ijk} c_k, \quad (20.13)$$

where e^{ijk} is the discriminant tensor. In (20.13) the first and the second terms give the symmetric part of α^{ij} , whereas the third term—the skewsymmetric part:

$$\alpha^{(ij)} = \cos \theta g^{ij} + (1 - \cos \theta) c^i c^j, \quad \alpha^{[ij]} = -\sin \theta e^{ijk} c_k.$$

The unit spatial director c_k is the eigenvector of α^{ij} corresponding to the real eigenvalue +1:

$$\alpha^{ij} c_j = c^i.$$

It can be obtained in the form

$$c_k = -\frac{1}{2 \sin \theta} e_{kij} \alpha^{[ij]}.$$

The rotation angle θ can be found from the equation

$$2 \cos \theta = g_{ls} \alpha^{(ls)},$$

demonstrating that this angle is determined by the symmetric part of the in general asymmetric conventional orthogonal tensor α^{ij} .

In micropolar theories of continuum mechanics, it is much more convenient to operate with the *modulated* rotation vector

$$C_k = \sin \theta c_k.$$

20.4 Conventionally Orthogonal Finite Rotation Tensors. Finite Rotation Pseudovectors

Taking into consideration the discussion of Sect. 20.3, we now define two conventionally orthogonal tensors determined by the rotation of the principal axes of deformation.

At this aim, it is convenient to start from the two-point g -symbols introduced as the scalar products of the local base vectors \mathbf{l}_σ (or \mathbf{l}_σ^σ) and \mathbf{l}_s (or \mathbf{l}_s^s) of the referential and spatial coordinate frames. As an example, we write down two of them:

$$g_s^{\cdot\alpha} = \mathbf{l}_s \cdot \mathbf{l}_\sigma^\alpha, \quad g_\alpha^{\cdot k} = \mathbf{l}_\sigma^k \cdot \mathbf{l}_s.$$

The g -symbols have a number of remarkable properties. For example, it is easily verified that

$$g^{ks} g_k^{\cdot\alpha} = \mathbf{l}_\sigma^{\alpha\sigma} g_\sigma^{\cdot s}. \quad (20.14)$$

In addition, the following reciprocal relations are valid

$$\mathbf{l}_\sigma^{\alpha\sigma} = g_{js} g_\alpha^{\cdot j} g_\sigma^{\cdot s},$$

$$g_{il} = \mathbf{l}_\sigma g_{\sigma\mu} g_i^{\cdot\sigma} g_l^{\cdot\mu}.$$

The reciprocal one-point rotation tensors can be introduced in continuum mechanics by the aid of g -symbols according to

$$\lambda^{\alpha\sigma} = g_k^{\cdot\alpha} \lambda^{k\sigma}, \quad \lambda^{ij} = g_\alpha^{\cdot j} \lambda^{i\alpha}. \quad (20.15)$$

First of them is called as Lagrangian rotation tensor, while the second—Eulerian.

Both of the one-point tensors (20.15) satisfy the conventional orthogonality conditions. Both are characterized by the same rotation angle since their first principal invariants are the same:

$$\mathbf{l}_\sigma g_{\alpha\beta} \lambda^{\alpha\beta} = \mathbf{l}_\sigma g_{\alpha\beta} g_k^{\cdot\alpha} \lambda^{k\beta} = \mathbf{l}_\sigma g_{\alpha\beta} g_{ks} \mathbf{l}_\sigma^{\alpha\sigma} g_\sigma^{\cdot s} = g_{ks} g_\beta^{\cdot s} \lambda^{k\beta} = g_{ks} \lambda^{ks}.$$

The spatial modulated rotation vector Λ_l can be obtained from the one-point rotation tensor λ^{ks} as

$$\Lambda_l = -\frac{1}{2} \epsilon_{lik} \lambda^{[ik]}. \quad (20.16)$$

The following two new rotation pseudovectors (of weights -1 and $+1$ are derived from the modulated rotation vector (20.16):

$$\Lambda_l^{[-1]} = -\frac{1}{2} \epsilon_{lik} \lambda^{[ik]}, \quad (20.17)$$

$$\Lambda^{[+1]l} = -\frac{1}{2}\epsilon^{lik}\lambda_{[ik]}, \tag{20.18}$$

where $\epsilon_{lik}, \epsilon^{lik}$ are the alternating symbols (the covariant alternating symbol is of weight -1 , the contravariant alternating symbol is of weight $+1$).

Thus, the absolute vector and the two pseudovectors can be associated with a finite instantaneous rotation of the deformation principal axes trihedron:

$${}^{[-1]}\Lambda_l, \quad \Lambda_l(\text{or } \Lambda^l), \quad {}^{[+1]}\Lambda^l.$$

We conclude this section by relations among the rotation vector and pseudovectors. The most remarkable relations are as follows:

$${}^{[-1]}\Lambda_l = \frac{\Lambda_l}{E}, \quad {}^{[+1]}\Lambda^l = E^2 g^{lk} {}^{[-1]}\Lambda_k,$$

where E is the fundamental orienting pseudoscalar, defined as the triple product of the covariant base vectors

$$E = \mathbf{t}_1 \cdot (\mathbf{t}_2 \times \mathbf{t}_3).$$

20.5 Final Remarks and Conclusions

The vector and pseudovectors of rotation and “extra” rotation can be considered as the most important kinematic parameters of mathematical models of micropolar elasticity (see [6]). The micropolar continuum theories are still rapidly developing due to their numerous applications to mechanics of granular media, fibrous materials, and honeycomb structures. Hemitropic micropolar mechanical properties are inherent in biomaterials sensitive to mirror reflections of their physical states.

The equations of the micropolar theory of elasticity are known from numerous previous discussions. A derivation of the covariant linear theory of micropolar elasticity, based on the principle of virtual displacements and virtual microrotations combined with the Lagrange multipliers rule, is given in the paper [7].

In micropolar continuum, rotation of an elementary volume consists of a rotation of principal axes of deformation and an “extra” rotation, which is determined by a kinematically “independent” rotation vector. The “extra” rotation reflects the presence of a microstructure. In simple models of the micropolar elasticity, the microstructure manifests itself by a characteristic microlength and the three other physically dimensionless constitutive constants. In pseudotensor formulations of the micropolar elasticity, the characteristic microlength can be treated as a pseudoscalar of the negative weight -1 .

Introduced in Sect. 20.4 the modulated rotation pseudovectors do not change their components after reflections of the local coordinate frame. They are associated in

the simplest way with skewsymmetric parts of conventionally orthogonal absolute rotation tensor.

The final conclusion we give as the following statement: In developments of micropolar continuum theories, the absolute microrotation vector is conventionally used (see [6] as an example); developments of micropolar continuum models sensitive to mirror reflections of physical states (as for hemitropic elastic continuum) require operating with modulated microrotation pseudovectors: covariant pseudovector of weight -1 or contravariant pseudovector of weight $+1$.

Acknowledgements The present study was partially supported by the Ministry of Science and Higher Education within the framework of the Russian State Assignment under contract No. AAAA-A20-120011690132-4.

References

1. Truesdell, C., Toupin, R.: The classical field theories. Encyclopedia of physics, vol. III/1. In: Flugge S. (ed.) Principles of Classical Mechanics and Field Theory. Springer, Heidelberg (1960)
2. Prager, W.: Introduction to the Mechanics of Continua. Ginn and Company, Boston (1961)
3. Sedov, L.I.: Introduction to the Mechanics of a Continuous Medium. Addison-Wesley Publishing Company, London (1965)
4. Berdichevsky, V.L.: Variational Principles of Continuum Mechanics. I. Fundamentals. Springer, Heidelberg (2009)
5. Lurie, A.I.: Theory of Elasticity. Springer, Heidelberg (2005)
6. Nowacki, W.: Theory of Asymmetric Elasticity. Pergamon Press, Oxford (1986)
7. Radayev, Y.N.: The Lagrange multipliers method in covariant formulations of micropolar continuum mechanics theories. Vestn. Samar. Gos. Tekhn. Univ., Ser. Fiz.-Mat. Nauki [J. Samara State Tech. Univ., Ser. Phys. Math. Sci.] **22**(3), 504–517 (2018) (in Russian)

Chapter 21

Quadrature Formulas for Integrals with a Weak Singularity in the Kernel and a Weight Function of Jacobi Polynomials with Complex Exponents



Avetik V. Sahakyan and Harutyun A. Amirjanyan

Abstract Quadrature formulas are presented for integrals with a logarithmic singularity and with a sign function, containing the weight function of Jacobi orthogonal polynomials, the exponents of which can be complex numbers with a real part greater than minus one. The latter are remarkable in that they have the same structure as the quadrature formulas for singular and regular integrals and can be used to solve singular integral equations that also contain terms with a weak singularity. Formulas for calculating the integral with a logarithm at an arbitrary point of the complex plane are also presented, and by numerical analysis, the area around the interval is outlined, outside of which this integral, with a certain degree of accuracy, can also be calculated using the quadrature formula for smooth functions.

Keywords Quadrature formula · Weight function · Jacobi polynomials · Complex exponents · Logarithmic singularity · Signum function

21.1 Introduction

It is known that many problems of mathematical physics and, in particular, of continuum mechanics are reduced to solving singular integral equations. The most effective methods for solving such equations are direct integration methods, among which the mechanical quadrature method occupies a special place, since it takes into account the behavior of the solution at the ends of the integration interval. There are a huge number of works devoted to the development of methods for calculating singular integrals and solving singular integral equations. Among them, we note only the following monographs [1–10]. Most of the papers refer to the case when the exponents of the weight function are equal to ± 0.5 . The number of papers in which the

A. V. Sahakyan (✉) · H. A. Amirjanyan
Institute of Mechanics, National Academy of Sciences of Armenia, 24B Baghramyan Ave.,
Yerevan 0019, Republic of Armenia
e-mail: avetik.sahakyan@sci.am

H. A. Amirjanyan
e-mail: amirjanyan@gmail.com

exponents of the weight function are real numbers different from ± 0.5 , or they are complex numbers, is significantly smaller. Among such works, the following works [11–21] can be noted. Much less attention has been paid to integrals and integral equations with a weak singularity, for example, a logarithmic one [22–27]. Perhaps this is a consequence of the fact that in plane problems of elasticity theory, equations with a logarithmic singularity, as a rule, are reduced to singular integral equations. However, in axisymmetric problems of the theory of elasticity, there are singular integral equations that also contain integrals with a logarithm and a signum function.

In this paper, we derive quadrature formulas for integrals containing a weak singularity of the type of a logarithmic function or a signum function together with the weight function of Jacobi polynomials.

21.2 Quadrature Formula for an Integral with a Logarithmic Singularity

Let us consider the integral

$$J_L(z) = \int_{-1}^1 \ln \frac{1}{x-z} \varphi(x) \omega(x) dx \tag{21.1.1}$$

Here, $\varphi(x)$ is a function that satisfies the Hölder condition along the interval $[-1, 1]$, and $\omega(x)$ is a weight function describing the behavior of the integrand at the ends of the integration interval and defined by the formula

$$\omega(x) = (1-x)^\alpha (1+x)^\beta (\operatorname{Re} \alpha, \operatorname{Re} \beta > -1)$$

Integral $J_L(z)$ is a single-valued function in the complex plane cut along the ray $(-1, \infty)$. At the points of the specified ray, the integral is assigned a value equal to half the sum of the values above and below, i.e., we have:

$$J_L(z) = \begin{cases} \int_{-1}^1 \ln \frac{1}{x-z} \varphi(x) \omega(x) dx & z \in C, z \notin (-1, \infty) \\ \int_{-1}^1 \ln \frac{1}{|x-y|} \varphi(x) \omega(x) dx = \frac{J_L(y+0i) + J_L(y-0i)}{2} & y \in (-1, \infty) \end{cases} \tag{21.1.2}$$

We replace the function $\varphi(x)$ by the Lagrange interpolation polynomial whose nodes are the roots of the Jacobi polynomial $P_n^{(\alpha, \beta)}(x)$:

$$\varphi_n(x) = \sum_{j=1}^n \frac{\varphi(\xi_j) P_n^{(\alpha, \beta)}(x)}{(x - \xi_j) P_n^{(\alpha, \beta)}(\xi_j)}, \quad P_n^{(\alpha, \beta)}(\xi_j) = 0 \tag{21.1.3}$$

In the case of complex exponents, the polynomial (21.1.3) is not an interpolation polynomial in the classical sense, since the nodes of the polynomial are not in the interval $(-1, 1)$. But, obviously, if $\varphi(x)$ will be a polynomial of order $m < n$, we will have $\varphi_n(x) \equiv \varphi(x)$. Note that the complex nodes ξ_j ($j = \overline{1, n}$) are located on an ellipse-like curve covering the interval $(-1, 1)$ on one side and approach it with n increasing. Since the departure of the roots from the interval $(-1, 1)$ is due to the imaginary parts of the exponents α and β , the larger the imaginary part, the farther the roots are located. A change in the real parts of these exponents leads to a displacement of the roots along the indicated ellipse-like curve.

In the considered integral (21.1.1) function, $\varphi(x)$ can only be defined on the segment $[-1, 1]$ and, therefore, the question may arise about the legitimacy of using the interpolation polynomial (21.1.3). In the case when this integral is a part of an integral equation with respect to a function $\varphi(x)$, such a question cannot arise, since the unknown function is sought in the form of a polynomial with unknown coefficients. And in the case when it is necessary to calculate the integral (21.1.1) for a given function $\varphi(x)$, we can at first replace this function with an interpolation polynomial of the same order with respect to Chebyshev nodes and instead of $\varphi(\xi_j)$ use the values of this polynomial at complex roots ξ_j . Alternatively, if $\varphi(x)$ can be analytically extended to the complex plane, then $\varphi(\xi_j)$ can be the values $\varphi(x)$ in roots ξ_j . However, it should be noted that in this case, the accuracy of the approximation will essentially depend on the magnitude of the imaginary parts of the exponents α and β .

The polynomial $\varphi_n(x)$ in the form (21.1.3) is inconvenient for further actions, so we present it in a different form. To do this, we use the Christoffel–Darboux formula for Jacobi polynomials [28] and some results on Gauss–Jacobi mechanical quadrature [29]. If in the Christoffel–Darboux formula, one of the variables is replaced by the roots $P_n^{(\alpha, \beta)}(\xi_i) = 0$, we will have:

$$\frac{P_n^{(\alpha, \beta)}(x) P_{n+1}^{(\alpha, \beta)}(\xi_i)}{x - \xi_i} = -\frac{k_{n+1} h_n}{k_n} \sum_{m=0}^{n-1} \frac{1}{h_m} P_m^{(\alpha, \beta)}(x) P_m^{(\alpha, \beta)}(\xi_i)$$

where

$$k_m = \frac{\Gamma(2m + \alpha + \beta + 1)}{2^m \Gamma(m + \alpha + \beta + 1) \Gamma(m + 1)},$$

$$h_m = \frac{2^{\alpha + \beta + 1} \Gamma(m + \alpha + 1) \Gamma(m + \beta + 1)}{(2m + \alpha + \beta + 1) \Gamma(m + 1) \Gamma(m + \alpha + \beta + 1)}.$$

Substituting this representation into (21.1.3), we obtain

$$\varphi_n(x) = -\sum_{j=1}^n \varphi(\xi_j) \frac{k_{n+1} h_n}{k_n P_{n+1}^{(\alpha, \beta)}(\xi_j) P_n'^{(\alpha, \beta)}(\xi_j)} \sum_{m=0}^{n-1} \frac{1}{h_m} P_m^{(\alpha, \beta)}(x) P_m^{(\alpha, \beta)}(\xi_j)$$

According to the results of [29] for the Cotes–Christoffel coefficients, we have

$$w_j = -\frac{k_{n+1}h_n}{k_n P_{n+1}^{(\alpha,\beta)}(\xi_j) P_n'^{(\alpha,\beta)}(\xi_j)} \tag{21.1.4}$$

Here, $w_j (j = \overline{1, n})$ are the weight coefficients of the well-known Gauss–Jacobi quadrature formula [29]:

$$\int_{-1}^1 \varphi(x)(1-x)^\alpha(1+x)^\beta dx \approx \sum_{j=1}^n w_j \varphi(\xi_j) \tag{21.1.5}$$

$$w_j = \frac{2^{\alpha+\beta+3} \Gamma(\alpha+n+1)\Gamma(\beta+n+1)}{1-\xi_j^2 \Gamma(n+1)\Gamma(\alpha+\beta+n+1)} \left[\frac{1}{(\alpha+\beta+n+1)P_{n-1}^{(\alpha+1,\beta+1)}(\xi_j)} \right]^2$$

The same weight coefficients are present in quadrature formulas for Cauchy-type integrals and other integrals [26].

As a result, representation (21.1.3) of the interpolation polynomial can be written as

$$\varphi_n(x) = \sum_{j=1}^n w_j \varphi(\xi_j) \sum_{m=0}^{n-1} \frac{1}{h_m} P_m^{(\alpha,\beta)}(\xi_j) P_m^{(\alpha,\beta)}(x) \tag{21.1.6}$$

After substituting (21.1.6) into (21.1.1), we will have

$$J_L(y) \approx \sum_{i=1}^n w_i \varphi(\xi_i) \sum_{m=0}^{n-1} \frac{1}{h_m} P_m^{(\alpha,\beta)}(\xi_i) \int_{-1}^1 \ln \frac{1}{x-y} P_m^{(\alpha,\beta)}(x) \omega(x) dx \tag{21.1.7}$$

Integrating over ζ the known spectral relation [28]

$$\int_{-1}^1 \frac{P_n^{(\alpha,\beta)}(x)\omega(x)}{x-\zeta} dx = -\left(\frac{2}{\zeta-1}\right)^{n+1} 2^{\alpha+\beta} B(n+\alpha+1, n+\beta+1) \times F\left[n+1, n+\alpha+1; 2n+\alpha+\beta+2; \frac{2}{1-\zeta}\right] \tag{21.1.8}$$

we obtain:
for $n = 0$

$$\int_{-1}^1 \ln \frac{1}{x - \zeta} \omega(x) dx = \frac{2^\alpha \pi e^{i\pi\alpha} \operatorname{sign}(\operatorname{Im}\zeta) (1 + \zeta)^{1+\beta}}{(1 + \beta) \sin \pi\alpha} F\left[-\alpha, 1 + \beta; 2 + \beta; \frac{1 + \zeta}{2}\right] + 2^{\alpha+\beta} (1 - \zeta) B(\alpha, 1 + \beta) {}_3F_2\left[1, -\alpha - \beta, 1; 1 - \alpha, 2; \frac{1 - \zeta}{2}\right] - 2^{\alpha+\beta+1} B(1 + \alpha, 1 + \beta) [\pi \operatorname{ctg}\pi\alpha + \ln 2 + \psi(1 + \alpha) - \psi(2 + \alpha + \beta)] \tag{21.1.9}$$

for $n \geq 1$

$$\int_{-1}^1 \ln \frac{1}{x - \zeta} P_n^{(\alpha, \beta)}(x) \omega(x) dx = \left(\frac{2}{\zeta - 1}\right)^n \frac{2^{\alpha+\beta+1}}{n} \times B(n + \alpha + 1, n + \beta + 1) F\left[n + \alpha + 1, n; 2n + \alpha + \beta + 2; \frac{2}{1 - \zeta}\right] \tag{21.1.10}$$

Special functions are used here: hypergeometric series F and ${}_3F_2$, beta function B , and psi function ψ .

After substituting (21.1.9) and (21.1.10) into formula (21.1.7), we will have:

$$J_L(z) \approx \sum_{i=1}^n w_i \varphi(\xi_i) \left[L_0^{(\alpha, \beta)}(z) + \sum_{m=1}^{n-1} P_m^{(\alpha, \beta)}(\xi_i) L_m^{(\alpha, \beta)}(z) \right] \tag{21.1.11}$$

where

$$L_0^{(\alpha, \beta)}(z) = \frac{1 + \alpha + \beta}{\alpha} \frac{1 - z}{2} {}_3F_2\left[1, -\alpha - \beta, 1; 1 - \alpha, 2; \frac{1 - z}{2}\right] + \frac{\pi e^{i\pi\alpha} \operatorname{sign}(\operatorname{Im}z)}{B(1 + \alpha, 1 + \beta)(1 + \beta) \sin \pi\alpha} \left(\frac{1 + z}{2}\right)^{1+\beta} F\left[-\alpha, 1 + \beta; 2 + \beta; \frac{1 + z}{2}\right] - \pi \operatorname{ctg}\pi\alpha - \ln 2 - \psi(1 + \alpha) + \psi(2 + \alpha + \beta) \tag{21.1.12}$$

$$L_m^{(\alpha, \beta)}(z) = \left(\frac{2}{z - 1}\right)^m \frac{2m + \alpha + \beta + 1}{m} \times B(m + 1, m + 1 + \alpha + \beta) F\left[m + \alpha + 1, m; 2m + \alpha + \beta + 2; \frac{2}{1 - z}\right] \tag{21.1.13}$$

It is easy to see that in the case $\alpha = 0$, formula (21.1.12) cannot be used.

However, considering the equivalence of the roles of the exponents α and β in the integral (21.1.1), it is obvious that it is possible to obtain another equivalent representation for $L_0^{(\alpha, \beta)}(z)$ that can be used for $\alpha = 0$, but will be unacceptable for the case $\beta = 0$.

The relationship between these two representations is as follows:

$$L_0^{(\alpha,\beta)}(z) = L_0^{(\beta,\alpha)}(-z) + i\pi \operatorname{sign}(\operatorname{Im}z) \tag{21.1.14}$$

In the case $\alpha = \beta = 0$, we have:

$$L_0^{(0,0)}(z) = -\frac{1+z}{2} \ln(-1-z) - \frac{1-z}{2} \ln(1-z) + 1 \tag{21.1.15}$$

The function $L_m^{(\alpha,\beta)}(z)$ can be calculated for any values of α and β . The quadrature formula (21.1.11) is more important from the point of view of its use for solving integral equations containing an integral of type (21.1.1):

$$I_L(y) = \int_{-1}^1 \ln \frac{1}{|x-y|} \varphi(x) \omega(x) dx \quad (-1 < y < 1) \tag{21.1.16}$$

Since in integral equations the range of variation of parameter z is limited by the integration interval, expressions of functions $L_0^{(\alpha,\beta)}(z)$ and $L_n^{(\alpha,\beta)}(z)$ can be simplified.

Indeed, if instead of the spectral relation (21.1.8), we use the equivalent relation that holds for the points of the interval $(-1, 1)$:

$$\int_{-1}^1 \frac{P_n^{(\alpha,\beta)}(x) \omega(x)}{x-\zeta} dx = \pi \operatorname{ctg} \alpha \pi \omega(\zeta) P_n^{(\alpha,\beta)}(\zeta) - \frac{2^{\alpha+\beta} \pi}{\sin \alpha \pi} P_{n+\alpha+\beta}^{(-\alpha,-\beta)}(\zeta) \quad (|\zeta| < 1)$$

for functions $L_0^{(\alpha,\beta)}(z)$ и $L_n^{(\alpha,\beta)}(z)$, we obtain:

$$L_0^{(\alpha,\beta)}(y) = -\frac{B_{(1-y)/2}(\alpha+1, \beta+1)}{B(\alpha+1, \beta+1)} \pi \operatorname{ctg} \pi \alpha + \psi(\alpha + \beta + 2) - \psi(\alpha + 1) - \ln 2 + \frac{(1-y)(1+\alpha+\beta)}{2\alpha} {}_3F_2\left(1, 1, -\alpha - \beta; 2, 1 - \alpha; \frac{1-y}{2}\right) \tag{21.1.17}$$

$$L_0^{(\alpha,\beta)}(y) = L_0^{(\beta,\alpha)}(-y) \tag{21.1.18}$$

$$L_0^{(0,0)}(y) = -\frac{1+y}{2} \ln(1+y) - \frac{1-y}{2} \ln(1-y) + 1 \tag{21.1.19}$$

$$L_m^{(\alpha \neq 0, \beta)}(y) = -\frac{\pi \operatorname{ctg} \alpha \pi}{2mh_m} \omega(y) (1-y^2) P_{m-1}^{(\alpha+1, \beta+1)}(y) - \frac{2^{\alpha+\beta+1} \pi}{mh_m \sin \alpha \pi} P_{m+\alpha+\beta+1}^{(-1-\alpha, -1-\beta)}(y) \tag{21.1.20}$$

$$\begin{aligned}
 L_m^{(\alpha, \beta \neq 0)}(y) &= (-1)^m \frac{\pi \operatorname{ctg} \pi \beta}{2mh_m} \omega(y)(1 - y^2) P_{m-1}^{(\alpha+1, \beta+1)}(y) \\
 &\quad - \frac{2^{\alpha+\beta+1} \pi}{mh_m \sin \pi \beta} P_{m+\alpha+\beta+1}^{(-1-\beta, -1-\alpha)}(-y)
 \end{aligned}
 \tag{21.1.21}$$

$$\begin{aligned}
 L_m^{(0,0)}(y) &= \left(\frac{2}{y-1} \right)^m \frac{2m+1}{m} B(m+1, m+1) \\
 &\quad \times \operatorname{Re} \left[F \left(m+1, m; 2m+2; \frac{2}{1-y} \right) \right]
 \end{aligned}
 \tag{21.1.22}$$

It should be noted that for arbitrary admissible values of the exponents α and β , «polynomial» $P_{m+\alpha+\beta+1}^{(-1-\alpha, -1-\beta)}(y)$ in (21.1.16), like similar “polynomials” in other formulas, are understood in a generalized sense, i.e., are calculated using the hypergeometric series, which, when $\alpha + \beta$ is equal to an integer, turns into an ordinary Jacobi polynomial.

Thus, we have obtained quadrature formulas of the type (21.1.11) for calculating the integral $J_L(z)$, ($z \in C$) and replacing the integral $I_L(y)$, ($-1 < y < 1$) in the integral equation with a quadrature sum. In the first case, the functions $L_0^{(\alpha, \beta)}(z)$ and $L_n^{(\alpha, \beta)}(z)$ are determined by formulas (21.1.12)–(21.1.15), and in the second case—by formulas (21.1.17)–(21.1.22).

21.3 Numerical Analysis

The quadrature formula (21.1.11), taking into account (21.1.2), allows one to calculate the integral $J_L(z)$ at an arbitrary point of the complex plane. At first glance, it seems obvious that standard software packages can be used to calculate the integral $J_L(z)$, and there is no need for a quadrature formula. However, standard programs cannot cope with this task if at least one of the exponents α and β has a value close to -1 or has a relatively large imaginary part.

Table 21.1 shows the values of the integral

$$J(z) = \int_{-1}^1 \ln \frac{1}{x-z} \cos 6x (1-x)^\alpha (1+x)^\beta dx$$

at the point $z_0 = 0.6 + 0.5i$ for different values of the exponents α and β calculated by the quadrature formula (21.1.11), and, if possible, by the standard program. For the sake of compactness, the table does not give the values of the integral $J(z_0)$ itself, but it’s absolute value $|J(z_0)|$.

The data in the table clearly indicate that the convergence of the quadrature formula to the true value of the integral does not depend on the exponents α and β , while the standard programs essentially depend on them.

Table 21.1 The absolute value $|J(z_0)|$ for different α and β

$z_0 = 0.6 + 0.5i$	$n = 6$	$n = 8$	$n = 10$	Wolf. Math
$\alpha = -0.34 + i; \beta = -0.81 - 0.3i$	4.1019	4.08954	4.08975	4.08976
$\alpha = -0.34 + i; \beta = -0.81 - 5i$	1.37259	1.36349	1.36344	1.34871*)
$\alpha = -0.95; \beta = -0.41$	12.5901	12.6159	12.6153	12.6097*)
$\alpha = -0.999 + i; \beta = -0.81 - 5i$	1.71926	1.70941	1.70935	17.9344*)
$\alpha = -0.999; \beta = -0.999$	1789.35	1789.39	1789.39	190.133*)

*) An error message is issued

On the other hand, if the point z does not belong to the interval of integration, then the logarithmic kernel ceases to have a singularity, and the question arises of how expedient is it to use a special quadrature formula to calculate the integral $J_L(z)$. To study this issue, a numerical analysis of the integral $J_L(z)$ was carried out, calculated by the quadrature formula for smooth functions:

$$J_L(z) \approx Q_L(z) = \sum_{j=1}^M w_j f(\xi_j) \ln \frac{1}{\xi_j - z}, \quad P_M^{(\alpha, \beta)}(\xi_i) = 0. \quad (21.2.1)$$

in the area around the interval $(-1, 1)$. In order to find out the degree of approximation of the logarithmic kernel, we take $f(x) \equiv 1$. It is obvious that the quadrature formula (21.1.11) already for $n = 1$ gives the exact value of the integral $J_L(z)$. To estimate the rate of convergence of formula (21.2.1), we calculate the relative standard deviation of the functions $J_L(z)$ and $Q_L(z)$ on the interval $[1, 3]$, calculated on a uniform grid of 40 points:

$$\delta = \frac{\sqrt{\left| \sum_{i=1}^{40} (Q_L(x_i) - J_L(x_i))^2 \right|}}{\sqrt{\left| \sum_{i=1}^{40} J_L(x_i)^2 \right|}}, \quad x_i = 1 + (i - 1)0.05$$

Figure 21.1 shows graphs of the dependence of quantity δ on the order of approximation M of formula (21.2.1) for different values of the exponents α and β .

Figure 21.2 shows the level lines of the modulus of the difference $\varepsilon(z) = |J_L(z) - Q_L(z)|$ between the exact and approximate value of the integral outside the segment $[-1, 1]$ for two pairs of exponents α and β values. Function $Q_L(z)$ is calculated by the formula (21.2.1) for $M = 10$. Level lines corresponds to values $\varepsilon(z) = 2 \times 10^{-2}, 1.25 \times 10^{-2}, 7.5 \times 10^{-3}$, solid lines corresponds to exponents values $\alpha = -0.5 + 0.04i, \beta = -0.7 - 0.03i$, and dashed lines corresponds to values $\alpha = -0.2 + 0.1i, \beta = -0.4 - 0.03i$.

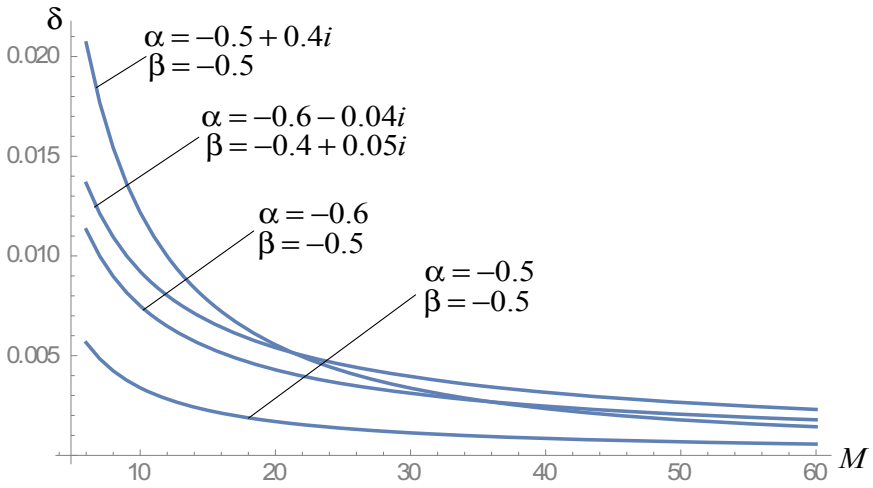


Fig. 21.1 Dependence of a relative standard deviation δ on the order M

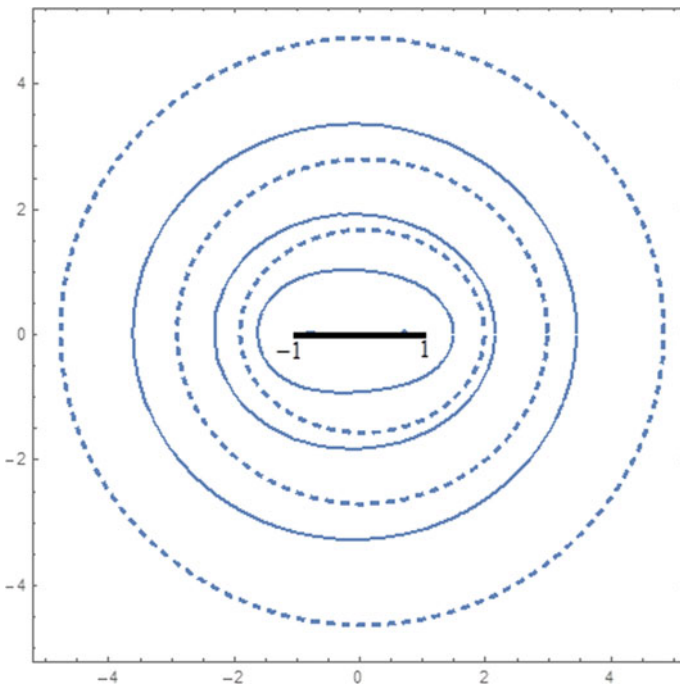


Fig. 21.2 Level lines of in a complex plane

From Fig. 21.2, we notice that the level lines at large values of $\varepsilon(z)$ have the shape of an oval and significantly depend on the values of the exponents α and β , and at small values they tend to circles with different radii.

Obviously, with increasing of level lines will cover a smaller area, i.e., approach the interval $(-1, 1)$. According to the graphs in Fig. 21.1, this approaching is significant only for $M < 30$.

21.4 Quadrature Formula for an Integral with a Signum Function

Let us consider integral

$$J_S(y) = \int_{-1}^1 \text{sign}(x - y)\varphi(x)\omega(x)dx \quad (-1 < y < 1) \tag{21.3.1}$$

where the functions $\varphi(x)$ and $\omega(x)$ are the same as in the previous paragraph.

It is easy to see that the calculation of the integral (21.3.1) reduces to the calculation of an integral with a variable limit of integration. Indeed, by representing the signum function in the form:

$$\text{sign}(x - y) = 1 - 2H(y - x),$$

the considered integral can be represented as the sum of two integrals:

$$J_S(y) = \int_{-1}^1 \varphi(x)\omega(x)dx - 2 \int_{-1}^y \varphi(x)\omega(x)dx. \tag{21.3.2}$$

For the first integral, we have the quadrature formula (21.1.5), but for the second integral, it must be constructed. We substitute representation (21.1.6) into this integral and use the values of the integrals:

$$\int_{-1}^y (1 - x)^\alpha (1 + x)^\beta dx = 2^{1+\alpha+\beta} B_{\frac{1+y}{2}}(1 + \beta, 1 + \alpha)$$

$$\int_{-1}^y (1 - x)^\alpha (1 + x)^\beta P_m^{(\alpha,\beta)}(x)dx = -\frac{1}{2m} P_{m-1}^{(\alpha+1,\beta+1)}(y)(1 - y)^{\alpha+1}(1 + y)^{\beta+1}$$

where $B_z(a, b)$ is an incomplete beta function.

As a result, for an integral with a variable upper limit of integration, we will have the following quadrature formula:

$$\int_{-1}^y \varphi(x)\omega(x)dx \approx \sum_{i=1}^n w_i \varphi(\xi_i) \left[\frac{B_{\frac{1+y}{2}}(\beta + 1, \alpha + 1)}{B(\beta + 1, \alpha + 1)} - (1 - y)^{\alpha+1}(1 + y)^{\beta+1} \sum_{m=1}^{n-1} \frac{P_m^{(\alpha,\beta)}(\xi_i)P_{m-1}^{(\alpha+1,\beta+1)}(y)}{2m h_m} \right] \tag{21.3.3}$$

Combining formulas (21.1.5) and (21.3.2) for the integral with the signum function, we will have:

$$J_S(y) \approx \sum_{i=1}^n w_i \varphi(\xi_i) \left[S_0(y) + \sum_{m=1}^{n-1} P_m^{(\alpha,\beta)}(\xi_i) S_m(y) \right] \quad (-1 < y < 1) \tag{21.3.4}$$

where

$$S_0(y) = 1 - \frac{2}{B(\beta + 1, \alpha + 1)} B_{\frac{1+y}{2}}(\beta + 1, \alpha + 1) \tag{21.3.5}$$

$$S_m(y) = (1 - y^2)\omega(y) \frac{P_{m-1}^{(\alpha+1,\beta+1)}(y)}{m h_m}$$

Thus, we have obtained the quadrature formula (21.3.4) for the integral with the signum function, as well as formula (21.3.3), which is no less useful for applications, for the integral with a variable upper limit.

Note that all obtained quadrature formulas are fulfilled exactly if the function $\varphi(x)$ is a polynomial of order $m < n$. Therefore, the accuracy of the calculation of the integral by the quadrature formula is determined solely by how well the function $\varphi(x)$ is approximated by the polynomial. When solving integral equations, the rate of convergence of an approximate solution to an exact one depends essentially on the regular kernels included in the integral equation. Therefore, when solving a specific equation, a numerical analysis of convergence should be carried out by comparing the results of calculations performed at different orders of approximation n .

21.5 Quadrature Formulas for Particular Values of the Exponents α and β

In contact and mixed boundary value problems of solid mechanics, the most common cases are when the features of the behavior of the desired functions at the ends of the integration interval are described by a root function.

Since for such particular values of the exponents α and β the functions $L_0^{(\alpha,\beta)}(z)$, $L_n^{(\alpha,\beta)}(z)$, $S_0(z)$, and $S_n(z)$ are significantly simplified, it is advisable to write out the quadrature formulas (21.1.11), when the variable y changes within the integration interval $(-1 < y < 1)$ and (21.3.4) for these cases in explicit form.

Let $\alpha = \beta = -0.5$. Then, the roots of the Chebyshev polynomial of the first kind $T_n(x)$ will act as nodes x_i of the quadrature formulas and the corresponding weights w_i will be:

$$x_i = \cos \frac{(2i - 1)\pi}{2n}, \quad w_i = \frac{\pi}{n} \quad (i = \overline{1, n})$$

Formulas (21.1.11) and (21.3.4) themselves take the form:

$$\int_{-1}^1 \ln \frac{1}{|x - y|} \frac{\varphi(x)}{\sqrt{1 - x^2}} dx \approx \frac{\pi}{n} \sum_{i=1}^n \varphi(x_i) \left[\ln 2 + 2 \sum_{m=1}^{n-1} \frac{T_m(x_i)T_m(y)}{m} \right] \quad (21.4.1)$$

$(-1 < y < 1)$

and

$$\int_{-1}^1 \text{sign}(x - y) \frac{\varphi(x)}{\sqrt{1 - x^2}} dx \approx \frac{1}{n} \sum_{i=1}^n \varphi(x_i) \left[-\arcsin y + \sum_{m=1}^{n-1} T_m(x_i)R_m(y) \right] \quad (21.4.2)$$

where

$$R_m(y) = \frac{4\sqrt{1 - y^2}}{m} U_{m-1}(y)$$

Let now $\alpha = \beta = 0.5$. The nodes ξ_i of the quadrature formulas will be the roots of the Chebyshev polynomial of the second kind $U_n(x)$, and the quadrature formulas (21.1.11) and (21.3.4) will be written as:

$$\int_{-1}^1 \ln \frac{1}{|x - y|} \varphi(x) \sqrt{1 - x^2} dx \approx \sum_{i=1}^n w_i \varphi(x_i) \left[L_0^*(y) + \sum_{m=1}^{n-1} U_m(\xi_i)L_m^*(y) \right] \quad (-1 < y < 1) \quad (21.4.3)$$

$$\int_{-1}^1 \text{sign}(x - y) \varphi(x) \sqrt{1 - x^2} dx \approx \sum_{i=1}^n w_i \varphi(x_i) \left[S_0^*(y) + \sum_{m=1}^{n-1} U_m(\xi_i)S_m^*(y) \right] \quad (21.4.4)$$

where

$$w_i = \frac{\pi}{n + 1} (1 - \xi_i^2), \quad \xi_i = \cos \frac{i\pi}{n + 1} \quad (i = 1, \dots, n),$$

$$L_0^*(y) = \ln 2 + \frac{1}{2} - y^2, \quad L_m^*(y) = \frac{T_m(y)}{m} - \frac{T_{m+2}(y)}{m+2}.$$

$$S_0^*(y) = 1 - \pi + \arccos y - y\sqrt{1-y^2}$$

$$S_m^*(y) = \frac{2\sqrt{1-y^2}}{\pi} \left[\frac{U_{m-1}(y)}{m} - \frac{U_{m+1}(y)}{m+2} \right]$$

Formulas (21.4.1)–(21.4.4) have a fairly simple form and are convenient for solving a singular integral equation with kernels with a weak singularity, when its solution at the ends of the integration interval has a root behavior.

21.6 Conclusion

We have obtained quadrature formulas for integrals with a logarithmic singularity and with a sign function, containing the weight function of Jacobi orthogonal polynomials, the exponents of which can be complex numbers with a real part greater than minus one. Formulas are presented for calculating the integral $J_L(z)$ at an arbitrary point of the complex plane, as well as formulas necessary for solving integral equations by the method of mechanical quadrature. The latter are remarkable in that they have the same structure as the quadrature formulas for singular and regular integrals and can be used to solve singular integral equations that also contain terms of the type $I_L(y)$ and $J_S(y)$.

References

1. Belotserkovsky, S.M., Lifanov, I.K.: Method of Discrete Vortices. CRC Press (1992)
2. Gabdulkaev, B.G.: Direct Methods for Solving Singular Integral Equations of the First Kind. Kazan University Press, Kazan (1994). (in Russ.)
3. Ivanov, V.V.: The Theory of Approximate Methods and its Application to the Numerical Solution of Singular Integral Equations. Kyiv, Naukova dumka, (in Russ.) (1968)
4. Lifanov, I.K.: Method of Singular Integral Equations and Numerical Experiment. Janus LLP, Moscow (1995)
5. Prössdorf, S.: Einige Klassen singulärer Gleichungen. Birkhäuser (1974)
6. Pykhteev, G.N.: Exact Methods for Calculating Integrals of the Cauchy Type. Nauka, Siberian Branch, Novosibirsk (1980)
7. Sheshko, M.A.: Singular Integral Equations with Cauchy and Hilbert Kernel and their Approximate Solution. Scientific Society of the Catholic University of Lublin, Lublin (2003)
8. Stroud, A.H., Secrest, D.: Gaussian Quadrature Formulas. Prentice-Hall, N.J. (1966)
9. Boykov, I.V.: Approximate methods for calculating singular and hypersingular integrals. Part 1. Singular integrals. Izd-vo PGU, Penza, 360 (in Russ.) (2005)
10. Boykov, I.V.: Approximate methods for calculating singular and hypersingular integrals. Part 2. Hypersingular integrals. Izd-vo PGU, Penza, 250 (in Russ.) (2009)
11. Karpenko, L.N.: Approximate solution of a singular integral equation by means of Jacobi polynomials. J. Appl. Math. Mech. **30**(3), 668–675 (1966)

12. Erdogan, F., Gupta, G.D., Cook, T.S.: Numerical solution of singular integral equations. In: G.C. Sih (ed.) *Mechanics of Fracture*, vol. 1, pp. 368–425. Noordhoff, Leyden (1973)
13. Krenk, S.: On the use of interpolation polynomial for solutions of singular integral equations. *Quart. Appl. Math.* **32**(4), 479–484 (1975)
14. Lifanov, I.K., Saakian, A.V.: Method of numerical solution of the problem of impressing a moving stamp into an elastic half-plane, taking heat generation into account. *J. Appl. Math. Mech.* **46**(3), 388–394 (1982)
15. Miller, G.R., Keer, L.M.: A numerical technique for the solution of singular integral equations of the second kind. *Quart. Appl. Math.* **42**(4), 455–465 (1985)
16. Junghanns, P., Rathsfeld, A.: On polynomial collocation for Cauchy singular integral equations with fixed singularities. *Integr. Eqn. Oper. Theory* **43**(2), 155–176 (2002)
17. Ma, L.F., Korsunsky, A.M.: An efficient numerical method for the solution of sliding contact problems. *Int. J. Numer. Meth. Engng* **64**, 1236–1255 (2005)
18. Andreev, A.V.: Direct numerical method for solving singular integral equations of the first kind with generalized kernels. *Mech. Solids* **40**(1), 104–119 (2005)
19. Theocaris, P.S., Ioakimidis, N.I.: A method of numerical solution of Cauchy-type singular integral equations with generalized kernels and arbitrary complex singularities. *J. Comp. Phys.* **30**(3), 309–323 (1979)
20. Andreev, A.V.: Method for numerical solution of complete singular integral equations with complex singularities of power type. *Mech. Solids* **41**(1), 76–87 (2006)
21. Saakyan, A.V.: Quadrature formulas of maximum algebraic accuracy for Cauchy type integrals with complex exponents of the Jacobi weight function. *Mech. Solids* **47**(6), 695–699 (2012)
22. Theocaris, P.S., Chrysakis, A.C., Ioakimidis, N.I.: Cauchy type integrals and integral equations with logarithmic singularities. *J. Eng. Math.* **13**(1), 63–74 (1979)
23. Yan, Y., Sloan, I.H.: On integral equations of the first kind with logarithmic kernel. *Numer. Math.* **53**, 499–512 (1988)
24. Saranen, J.: The modified quadrature method for logarithmic-kernel integral equations on closed curves. *J. Integr. Eqn. Appl.* **3**(4), 575–600 (FALL 1991). <https://doi.org/10.1216/jiea/1181075650>
25. Celorrio, R., Dominguezand, V., Sayas, F.-J.: An improved quadrature method for integral equations with logarithmic kernel, *Monografias del Semin. Matem. Garcia de Galdeano* **27**, 185–192 (2003)
26. Sahakyan, A.V., Amirjanyan, H.A.: Method of mechanical quadratures for solving singular integral equations of various types. In: *IOP Conference Series: Journal of Physics: Conference Series* vol. 991, p. 012070 (2018). <https://doi.org/10.1088/1742-6596/991/1/012070>
27. Assari, P., Asadi-Mehregan, F., Cuomo, S.: A numerical scheme for solving a class of logarithmic integral equations arisen from two-dimensional Helmholtz equations using local thin plate splines. *Appl. Math. Comput.* **356**, 157–172 (2019). <https://doi.org/10.1016/j.amc.2019.03.042>
28. Bateman, H., Erdelyi, A.: *Higher Transcendental Functions*, vol. 2. McGraw-Hill (1953)
29. Szegő, G.: *Orthogonal Polynomials*. AMS, NY (1959)

Chapter 22

Bending and Contact Problem for a Graphene Sheet Within the Framework of the Model of Bending Deformation of Elastic Thin Plates Based on Cosserat Theory



Samvel H. Sargsyan

Abstract In this paper, basic system of equations, boundary conditions and Lagrange variational principle of bending deformation of elastic thin plates are presented, constructed on the basis of Cosserat theory, as a continual model of graphene sheet bending. The values of elastic constants of the moment theory of elasticity for graphene material are presented. Based on this continuum model, the problem of bending of a rectangular graphene sheet is considered, when all its sides are hinged supported. Further, a contact problem is studied, when the graphene sheet is bent under the action of a rigid stamp. The contact pressure between the stamp and the graphene sheet, the size of the contact zone and the stamp deposit are determined depending on the magnitude of the applied load.

Keywords Thin plate bending model · Built on the basis of Cosserat theory · Continual model of bending of a graphene sheet · Bending problem and contact problem for a graphene sheet

22.1 Introduction

Methods of mechanics of a deformable solid body are widely used in modeling of nanostructures. The construction of continuous models of deformations of two-dimensional nanomaterials, in particular that of a graphene, is one of the topical problems of applied mechanics of solid deformable bodies. The statement is also substantiated that when studying the deformations of two-dimensional nanomaterials according to the continuous theory (graphene, nanotubes, fullerene), it is necessary to use the three-dimensional moment theory of elasticity with independent fields of displacements and rotations [1–5].

S. H. Sargsyan (✉)
State University of Shirak, Gyumri, Armenia
e-mail: s_argryan@yahoo.com

It should be noted that there have been obtained significant results based on the studies of the construction of the discrete (or discrete–continuous) models of two-dimensional nanomaterials considering non-central force and moment interaction between their atoms [1–5]. However, it should be also noted that the problem of development of an approach, that allows to connect discrete (or discrete–continuous) description of the lattice of a two-dimensional nanomaterial with a continuous theory of elastic thin shells and plates, constructed on the basis of the moment theory of elasticity, is still topical.

In paper [6], first, a continuous one-dimensional beam model of a linear atomic chain is constructed (in the general case of its deformation), when in its discrete model the interaction between atoms is force non-central and momental. Using the constructed continuous-moment beam model, replacing the interaction between the atoms of a two-dimensional nanomaterial with the beam system according to this model, its discrete–continuous model is constructed (in particular, also for graphene). On the example of a graphene, further, two continuous models of its deformation are constructed by passing to the limit: (1) a model of a plane stress state of a graphene sheet and (2) a model of its bending deformation. It has been established that these models of graphene are identical to the corresponding models of elastic thin plates [7–9] constructed on the basis of Cosserat theory. Based on a comparison of the corresponding two similar models, all six elastic constants of the moment theory of elasticity for the graphene material are determined through the physical parameters of the atomic structure of this material.

Summarizing the above-mentioned observations, it can be stated that the models of the plane stress state and bending deformation of elastic thin plates [7–9], built on the basis of Cosserat theory, with already known elastic constants, can be interpreted as continuous models for the corresponding deformations of the graphene sheet. It is clear that this opens up new opportunities for studying various problems of statics, dynamics and stability of a graphene sheet based on these continuous models.

In this paper, the main system of equations, boundary conditions and Lagrange-type variational principle for the bending deformations of elastic plates, built on the basis of Cosserat theory, are introduced, and on the basis of this model, two applied problems of the bending of a graphene sheet are formulated and studied (it is clear that these problems relate specifically to the graphene sheet):

1. static bending of a rectangular graphene sheet, when all its sides are hinged, under the action of a distributed normal load,
2. cylindrical bending of a graphene sheet under the action of a rigid stamp (contact problem).

22.2 Basic System of Equations, Boundary Conditions and Variational Lagrange Principle of Bending Deformation of an Elastic Plate Based on Cosserat Theory

If we consider the equations and boundary conditions of elastic shells [8], constructed on the basis of the Cosserat theory, taken into account, then when passing to the plate, two models will be obtained: (a) a system of equations and boundary conditions for the plane stress state of the plate and (b) a system of equations and boundary conditions for plate bending.

The system of equations and the boundary conditions for the bending of an elastic plate (Fig. 22.1) are considered, based on Cosserat theory:

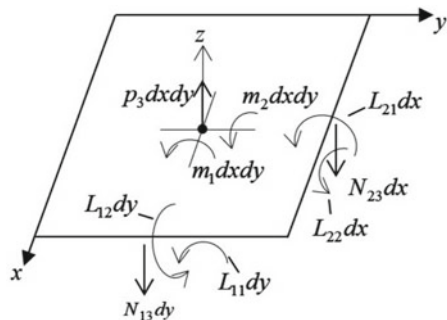
- Equilibrium equations

$$\begin{aligned} \frac{\partial N_{13}}{\partial x} + \frac{\partial N_{23}}{\partial y} &= -(p_3^+ - p_3^-), \\ \frac{\partial L_{11}}{\partial x} + \frac{\partial L_{21}}{\partial y} + N_{23} &= -(m_1^+ - m_1^-), \\ \frac{\partial L_{12}}{\partial x} + \frac{\partial L_{22}}{\partial y} - N_{13} &= -(m_2^+ - m_2^-); \end{aligned} \tag{22.1}$$

- Elasticity relations

$$\begin{aligned} N_{13} &= 2G_*h\Gamma_{13}, \quad N_{23} = 2G_*h\Gamma_{23}, \quad G_* = \frac{4\mu\alpha}{\mu + \alpha}, \\ L_{11} &= 2h(\gamma + \varepsilon) \left[k_{11} + \frac{1}{2}v_m(2k_{11} + k_{22}) \right], \end{aligned}$$

Fig. 22.1 Bending of the plate



$$L_{22} = 2h(\gamma + \varepsilon) \left[k_{22} + \frac{1}{2}v_m(2k_{22} + k_{11}) \right], \quad (22.2)$$

$$L_{12} = 2h(\gamma + \varepsilon) \left[k_{12} + \frac{1}{2}v_mk_{21} \right],$$

$$L_{21} = 2h(\gamma + \varepsilon) \left(k_{21} + \frac{1}{2}v_mk_{12} \right) v_m = 2\frac{\gamma - \varepsilon}{\gamma + \varepsilon};$$

- Geometric relations

$$\Gamma_{13} = \frac{\partial w}{\partial x} + \Omega_2, \quad \Gamma_{23} = \frac{\partial w}{\partial y} - \Omega_1,$$

$$k_{11} = \frac{\partial \Omega_1}{\partial x}, \quad k_{22} = \frac{\partial \Omega_2}{\partial y}, \quad k_{12} = \frac{\partial \Omega_2}{\partial x}, \quad k_{21} = \frac{\partial \Omega_1}{\partial y}; \quad (22.3)$$

- Boundary conditions

$$\begin{aligned} N_{13} &= N_{13}^*, \quad L_{11} = L_{11}^*, \quad L_{12} = L_{12}^*, \quad \text{when } x = \text{const}, \\ \text{or} \\ w &= w^*, \quad \Omega_1 = \Omega_1^*, \quad \Omega_2 = \Omega_2^*, \quad \text{when } x = \text{const}. \end{aligned} \quad (22.4)$$

Here w is the displacement (bending); Ω_1, Ω_2 —free rotations; Γ_{13}, Γ_{23} —shear deformations; $k_{11}, k_{22}, k_{12}, k_{21}$ —bending-torsions; N_{13}, N_{23} —crosscutting forces; $L_{11}, L_{22}, L_{12}, L_{21}$ —torques and bending moments (from moment stresses).

- Variational principle of Lagrange type

$$\delta U_0 = \delta A_0 \quad \text{or} \quad \delta(U_0 - A_0) = 0, \quad (22.5)$$

where

$$U_0 = \iint_S W_0 dx dy, \quad (22.6)$$

$$\begin{aligned} A_0 &= \iint_{(S)} (q_3^+ - q_3^-) w + [(m_1^+ - m_1^-) - h(q_2^+ + q_2^-)] \Omega_1 + \\ &+ [(m_2^+ - m_2^-) + h(q_1^+ + q_1^-)] \Omega_2 \} dx dy + \\ &+ \int_{\Gamma_1'} (\bar{N}_{23} w + \bar{L}_{21} \Omega_1 + \bar{L}_{22} \Omega_2) dx \\ &- \int_{\Gamma_2'} (\bar{N}_{13} w + \bar{L}_{11} \Omega_1 + \bar{L}_{12} \Omega_2) dy; \end{aligned} \quad (22.7)$$

$$W_0 = \frac{1}{2} \left[2G_*h (\Gamma_{13}^2 + \Gamma_{23}^2) + 2h \frac{4\gamma(\beta + \gamma)}{\beta + 2\gamma} (k_{11}^2 + k_{22}^2) + 2h \frac{4\gamma\beta}{\beta + 2\gamma} k_{11}k_{22} + 2h(\gamma + \varepsilon) (k_{12}^2 + k_{21}^2) + 4h(\gamma - \varepsilon)k_{12}k_{21} \right]. \tag{22.8}$$

Here W_0 is the surface density of the potential energy of the deformation of the plate; U_0 —total potential energy of the plate; A_0 —the work of external forces and moments; $(U_0 - A_0)$ —total energy of the system; Γ'_1 and Γ'_2 —external contours of the middle plane of the plate, where external forces and moments are given; region of the median plane of the plate. It is shown in [8] that the total energy of the system takes on a minimum value.

Paying attention to the geometric model (22.3) of the bending of the plate, built on the basis of Cosserat theory, we note that in the aggregate, the deformations (Γ_{13}, Γ_{23}) of the shear type and the type of bending-torsion ($k_{11}, k_{22}, k_{12}, k_{21}$, that are associated with independent rotations Ω_1, Ω_2), from this point of view, we can say that the model (22.3) represents the formation in a continuum form of deformation manifestations of crystalline nanomaterials, which were experimentally detected in [10–12].

22.3 Bending of a Hinged Supported Rectangular Plate Under the Action of a Distributed Normal Load

Let us reduce the initial equations and relations (22.1)–(22.3) of the bending model of the elastic thin plates, constructed on the basis of Cosserat theory, to resolving equations. Substituting (22.3) into (22.2) and then into the equilibrium Eq. (22.1), a system of differential equations for the functions $w(x, y), \Omega_1(x, y), \Omega_2(x, y)$ will be obtained:

$$\begin{aligned} \Delta w + \left(\frac{\partial \Omega_2}{\partial x} - \frac{\partial \Omega_1}{\partial y} \right) &= -\frac{p_3}{D_*}, \\ \Delta \Omega_1 + \nu_m \frac{\partial}{\partial x} \left(\frac{\partial \Omega_1}{\partial x} + \frac{\partial \Omega_2}{\partial y} \right) + \frac{D_*}{D'} \left(\frac{\partial w}{\partial y} - \Omega_1 \right) &= 0, \\ \Delta \Omega_2 + \nu_m \frac{\partial}{\partial y} \left(\frac{\partial \Omega_1}{\partial x} + \frac{\partial \Omega_2}{\partial y} \right) - \frac{D_*}{D'} \left(\frac{\partial w}{\partial x} + \Omega_2 \right) &= 0, \end{aligned} \tag{22.9}$$

where

$$D_* = 2G_*h, \quad D' = 2h(\gamma + \varepsilon), \quad \Delta(\cdot) = \frac{\partial^2(\cdot)}{\partial x^2} + \frac{\partial^2(\cdot)}{\partial y^2}, \quad p_3 = p_3^+ - p_3^-. \tag{22.10}$$

It should be noted that when obtaining the system of resolving equations for the bending model of the elastic thin plates, the formula [6, 9] was considered:

$$\beta = \frac{\gamma - \varepsilon}{\gamma + \varepsilon} 2\gamma. \quad (22.11)$$

It is easy to see that the system of equations for the bending model of the moment–membrane theory of elastic thin plates is identical with the system of equations for the bending deformation of elastic thin plates of Timoshenko type [13].

Sometimes, it is convenient to reduce the system of Eq. (22.9) of the bending model of the elastic thin plates to a system of two equations—to a biharmonic problem and to the Helmholtz equation. For this purpose, the combination $\left(\frac{\partial\Omega_2}{\partial x} - \frac{\partial\Omega_1}{\partial y}\right)$ will be eliminated from the last two equations of system (22.9), for which we will differentiate the second equation from (22.9) by y , and the third by x and subtract the obtained ones:

$$(k\Delta - 1) \left(\frac{\partial\Omega_2}{\partial x} - \frac{\partial\Omega_1}{\partial y}\right) = \Delta w, \quad (22.12)$$

where

$$k = \frac{D'}{D_*}. \quad (22.13)$$

Using the first equation from the system (22.9), as well as Eq. (22.12), the following equation will be obtained for the bending $w(x, y)$

$$\Delta\Delta w = \frac{p_3}{D'} - \frac{1}{D_*} \Delta p_3. \quad (22.14)$$

Following [13], functions ψ and φ will be introduced with the help of the formulas:

$$\Omega_1 = -\frac{\partial\varphi}{\partial y} + \frac{\partial\psi}{\partial x}, \quad \Omega_2 = \frac{\partial\varphi}{\partial x} + \frac{\partial\psi}{\partial y}, \quad (22.15)$$

where the function φ is expressed by w and p_3 :

$$\varphi = -w - \frac{D'}{D_*} \Delta w - \frac{D'}{D_*} p_3. \quad (22.16)$$

The last two equations from (22.9) will be satisfied if the function ψ satisfies the Helmholtz equation:

$$\Delta\psi - \tilde{k}^2\psi = 0, \quad (22.17)$$

where

$$\tilde{k}^2 = \frac{D_*}{(1 + \nu_m) D'}. \quad (22.18)$$

Thus, the system of resolving equations for the model of bending of the elastic thin plates, in this case, graphene sheet bending from its plane, will have the form:

$$D' \Delta \Delta w = p_3 - k \Delta p_3, \quad \Delta \psi - \tilde{k}^2 \psi = 0. \quad (22.19)$$

Forces and moments will be expressed by functions w , ψ , considering (22.2), (22.3) and (22.15), (22.16). It can be shown that if the plate is hinged supported along the entire outer contour, then $\psi \equiv 0$.

22.4 Elastic Constants of the Plane Stress State and Bending Deformation of Plates for the Graphene Material

In [6], after determination of the potential energy of a graphene deformation under a plane stress state and under bending deformation, these expressions are compared with the corresponding expressions of continuous theory of elastic plates, constructed on the basis of Cosserat theory. As a result, the elastic constants of continuous theory of plates, are determined (for the two specified deformations) through the physical parameters of graphene in its discrete model.

Thus, in the plane stress state of theory of elastic plates, for the elastic constants of the graphene material we have [6]:

$$E_* = 2Eh = 287 \frac{\text{N}}{\text{m}}; \quad \mu_* = 2\mu h = 116 \frac{\text{N}}{\text{m}}; \quad \alpha_* = 2\alpha h = 42 \frac{\text{N}}{\text{m}}; \quad \nu = 0.24;$$

$$B_* = 2Bh = 5.05 \cdot 10^{-10} \text{N} \cdot \text{nm}. \quad (22.20)$$

In the case of bending deformation, the elastic constants of the moment–membrane theory of plates for the graphene material are [6]:

$$D_* = 2G_* h = 86 \frac{\text{N}}{\text{m}}, \quad D' = 2h(\gamma + \varepsilon) = \gamma^* + \varepsilon^* = 4, 15 \cdot 10^{-10} \text{N} \cdot \text{nm},$$

$$D'' = 2h(\gamma - \varepsilon) = \gamma^* - \varepsilon^* = -0, 91 \cdot 10^{-10} \text{N} \cdot \text{nm}, \quad (22.21)$$

$$\nu_m = 2 \frac{D''}{D'} = -0, 41, \quad \nu = 0.$$

22.5 An Example of Calculating the Bending of a Graphene Sheet

An example of bending of a graphene sheet, when the sheet occupies the region of a rectangle $0 \leq x \leq a_1$, $0 \leq y \leq a_2$ is considered. It is assumed that the contour of graphene is hinged supported. For the boundary conditions, we have:

$$\begin{aligned} x = 0, a_1 : w = 0, L_{12} = 0, \Omega_1 = 0 \\ y = 0, a_2 : w = 0, L_{21} = 0, \Omega_2 = 0. \end{aligned} \quad (22.22)$$

Let us consider a graphene under a load of:

$$p_3(x, y) = p_0 \sin \frac{\pi x}{a_1} \sin \frac{\pi y}{a_2}. \quad (22.23)$$

The solution of the system of Eq. (22.9) is set as follows:

$$\begin{aligned} w(x, y) &= w_0 \sin \frac{\pi x}{a_1} \cdot \sin \frac{\pi y}{a_2}, \\ \Omega_1 &= \Omega_{10} \sin \frac{\pi x}{a_1} \cdot \cos \frac{\pi y}{a_2}, \\ \Omega_2 &= \Omega_{20} \cos \frac{\pi x}{a_1} \cdot \sin \frac{\pi y}{a_2}. \end{aligned} \quad (22.24)$$

Here, the multipliers w_0 , Ω_{10} , Ω_{20} are to be determined. It should be noted that with the help of (22.24) the set boundary conditions (22.22) will be satisfied.

To determine w_0 , Ω_{10} and Ω_{20} , (22.24) should be substituted into the system of Eq. (22.9). As a result, to determine the indicated factors, we come to the solution of an algebraic linear inhomogeneous system. If $p_0 = 10^6 \frac{\text{N}}{\text{m}^2}$, $a_1 = a_2 = 20 \text{ nm}$, then for the maximum bending of a graphene, we obtain:

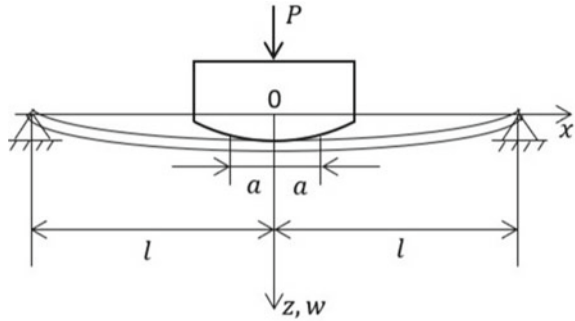
$$w_0 = \frac{p_0 a_1^2}{2\pi^2 \tilde{D}'} \left(1 + \frac{\tilde{D}'}{D_*} \right) = 1, 17 \text{ nm}.$$

In this formula $\tilde{D}' = \frac{D'}{a_1^2} \cdot 2\pi^2$.

22.6 Cylindrical Bending of a Plate (Graphene Sheet) with a Rigid Stamp

Papers [14–20] are devoted to the development of contact problems for thin beams, plates and shells within the framework of the classical theory of elasticity. The

Fig. 22.2 Cylindrical bending of a plate by a rigid stamp



same problems are of direct practical interest for two-dimensional nanomaterials (in particular, for a graphene), and their results can be used in modern engineering computational practice, in this case, in nanotechnology.

A hinged supported plate (under conditions of cylindrical bending) of length $2l$ is considered when a symmetrical smooth rigid stamp acts on it, pressed down by a force P (Fig. 22.2). The stamp base is described by the equation $y = f(x)$, the contact line is assumed equal to $2a$. In the contact zone $(-a \leq x \leq a)$, the plate bending $w(x)$ will be expressed by the formula:

$$w = -[\delta - f(x)], \tag{22.25}$$

where δ is the translational movement of the stamp.

As an initial system of equations for the bending of a hinged supported plate, Eq. (22.9) for the bending of the plate, constructed on the basis of Cosserat theory, is considered in case of cylindrical bending. As a result, we will have:

$$D_* \frac{d^2 w}{dx^2} + D_* \frac{d\Omega_2}{dx} = -p_3, \quad D' \frac{d^2 \Omega_2}{dx^2} - D_* \frac{dw}{dx} - D_* \Omega_2 = 0. \tag{22.26}$$

Here, $p_3(x)$ is the intensity of the external force, normal to the middle plane of the plate, which will represent the contact force stress $q(x)$ between the stamp and the plate under the stamp:

$$p_3(x) = \begin{cases} q(x), & -a \leq x \leq a, \\ 0, & -l \leq x \leq -a, \quad a \leq x \leq l. \end{cases} \tag{22.27}$$

The boundary conditions for hinged support at the edges $x = \pm l$ of the plate will be expressed as follows:

$$w = 0, \quad N_{13} = \frac{P}{2}, \quad L_{12} = 0. \tag{22.28}$$

From the system of Eq. (22.26), for the case when $|x| < a$, differential equation will be obtained to determine the contact pressure

$$\frac{d^2q(x)}{dx^2} - \frac{D_*}{D'}q(x) = -D_* \cdot \frac{d^4w}{dx^4}, \quad (22.29)$$

where w is expressed by formula (22.25).

Further, we will study the case when $f^{IV}(x) \equiv 0$ (with the help of the way described below, similar problems can be solved for the case when $f^{IV}(x) \neq 0$). In that case, to determine the contact stress $q(x)$, we come to the solution of a second-order homogeneous ordinary differential equation with constant coefficients:

$$\frac{d^2q(x)}{dx^2} - \frac{D_*}{D'}q(x) = 0. \quad (22.30)$$

The general solution of this equation can be introduced as follows (we mean that the problem is symmetric by x):

$$q(x) = C \cdot \operatorname{ch} \sqrt{\frac{D_*}{D'}}x, \quad -a \leq x \leq a, \quad (22.31)$$

where C is the integration constant.

To determine the constant C , the stamp equilibrium condition will be used

$$\int_{-a}^a q(x)dx = P. \quad (22.32)$$

Finally, for the contact pressure the following formula will be obtained:

$$q(x) = \frac{1}{2}P \cdot \sqrt{\frac{D_*}{D'}} \cdot \frac{\operatorname{ch} \sqrt{\frac{D_*}{D'}}x}{\operatorname{sh} \sqrt{\frac{D_*}{D'}}a}. \quad (22.33)$$

Outside the contact area $a \leq x \leq l$ (using the symmetry of the problem), we have $p_3(x) \equiv 0$. Therefore, to determine the displacement $w(x)$, we obtain the following differential equation from the system of Eq. (22.26)

$$\frac{d^4w}{dx^4} = 0. \quad (22.34)$$

Its general solution has the form

$$w = \frac{1}{6}c_1x^3 + \frac{1}{2}c_2x^2 + c_3x + c_4, \quad (22.35)$$

where c_1, c_2, c_3, c_4 are integration constants.

For the function $\Omega_2(x)$, we will obtain the following equation from the same system of equations (22.26):

$$\frac{d\Omega_2}{dx} = -\frac{d^2w}{dx^2}. \tag{22.36}$$

If relation (22.35) is used for the function $w(x)$, we will have for Ω_2

$$\Omega_2 = -\frac{c_1}{2}x^2 - c_2x + c_5, \tag{22.37}$$

where c_5 is integration constant.

The total number of unknowns are: $c_1, c_2, c_3, c_4, c_5, a, \delta$, for which we have seven conditions: three conditions of hinged support (22.28) at $x = l$, which can be written as follows

$$w^{II}|_{x=l} = 0, \quad D_* \left(\frac{dw^{II}}{dx} + \Omega_2^{II} \right)_{x=l} = \frac{P}{2}, \quad \frac{d\Omega_2^{II}}{dx} \Big|_{x=l} = 0, \tag{22.38}$$

as well as four conditions for the continuity of quantities, when $x = a$:

$$\begin{aligned} w^I|_{x=a} &= w^{II}|_{x=a}, & \frac{dw^I}{dx} \Big|_{x=a} &= \frac{dw^{II}}{dx} \Big|_{x=a}, \\ \Omega_2^I|_{x=a} &= \Omega_2^{II}|_{x=a}, & \frac{d\Omega_2^I}{dx} \Big|_{x=a} &= \frac{d\Omega_2^{II}}{dx} \Big|_{x=a}. \end{aligned} \tag{22.39}$$

It should be noted that with the help of the three conditions of hinged support (22.38), as well as from the second and third conditions from (22.39), the integration constants c_1, c_2, c_3, c_4, c_5 are completely determined. Based on the last condition from (22.39), we obtain a transcendental equation for determination the contact zone a ; from the first condition of (22.39) we define δ -translational movement of the stamp. As we have seen, when using the model of bending of a plate (graphene sheet), built on the basis of Cosserat theory, the contact pressure is expressed as a continuous function (formula (22.33)).

22.7 Conclusion

A model of bending deformation of a graphene sheet is introduced as a continuous model of bending deformation of an elastic plate, constructed on the basis of Cosserat theory. The values of the elastic constants of this model for the graphene material are given. A specific problem of bending of a graphene sheet is considered on the basis of the indicated continuous model of bending of an elastic plate, and the numerical results of this calculation are presented. Further, on the basis of the same theory,

the problem of cylindrical bending of a plate with a rigid stamp is considered, the contact pressure between the stamp and the plate, the size of the contact zone and the translation of the stamp are determined.

Acknowledgements The work was supported by the Science Committee of RA, in the frames of the research project No. 21T-2C093.

References

1. Krivtsov, A.M.: Deformation and destruction of solids with microstructure. M.: Fizmatlit. (2007)
2. Ivanova, E.A., Krivtsov, A.M., Morozov, N.F.: Derivation of macroscopic relations of the elasticity of complex crystal lattices taking into account the moment interactions at the microlevel. *Appl. Math. Mech.* **71**, 543–561 (2007)
3. Berinskii, I.E., Ivanova, E.A., Krivtsov, A.M., Morozov, N.F.: Application of moment interaction to the construction of a stable model of graphite crystal lattice. *Mech. Solids* **42**, 663–671 (2007)
4. Kuzkin, V.A., Krivtsov, A.M.: Description for mechanical properties of graphene using particles with rotational degrees of freedom. *Dokl. Phys.* **56**, 527–530 (2011)
5. Modern problems of mechanics. Mechanical properties of covalent crystals: Berinsky I.E. [and etc.]; under total ed. Krivtsova A.M., Loboda O.S., St. Petersburg, Publishing house of Politekh. university. (2014)
6. Sargsyan, S.H.: Beam and continual models for deformations of two-dimensional nanomaterials. *Phys. Mesomech.* **25**, 109–121 (2022)
7. Sargsyan, S.H.: A thin shell model within the moment theory of elasticity with the concept of deformation by shear plus rotation. *Phys. Mesomech.* **23**, 309–315 (2020)
8. Sargsyan, S.H.: Variation principles of moment-membrane theory of shells. *Moscow Univ. Mech. Bull.* **77**, 1–11 (2022)
9. Sargsyan, S.H.: Moment-membrane model of a plate as a continual model of graphene deformations and a finite element method for its calculation. In: AIP Conference Proceedings, vol. 2448, Krasnoyarsk, Russia (2021). <https://doi.org/10.1063/5.0073269.P.020020>
10. Physical Mesomechanics and the Computer Design of Materials In 2 volumes: Ed. V.E. Panin. Novosibirsk, Nauka, (1995)
11. Panin, V.E.: Foundations of physical mesomechanics. *Phys. Mesomech.* **1**, 5–20 (1998)
12. Panin, V.E., Grinyayev, Yu.V., Egorushki, V.E.: Foundations of physical mesomechanics of structurally inhomogeneous media. *Mech. Solids.* **45**, 501–518 (2010)
13. Pelekh, B.L.: Theory of shells with finite shear rigidity. Nauka dumka, Kyiv (1987)
14. Aleksandrov, V.M.: Some contact problems for beams, plates and shells. *Eng. J.* **5**, 782–785 (1965)
15. Grigolyuk, E., Tolkachev, V.: Contact Problems of the Theory of Plates and Shells. Mir Publishers, Moscow (1987)
16. Popov, G.Ya: On integral equations of contact problems for thin-walled elements. *Appl. Math. Mech.* **40**, 662–673 (1976)
17. Pelekh, B.L., Sukhorolsky, M.A.: Contact Problems of the Theory of Elastic Anisotropic Shells. Nauka Dumka, Kyiv (1980)
18. Artyukhin, Yu.P., Karasev, S.N.: Theory of Shells with Allowance for Transverse Shear. Publishing house Kazan. University, Kazan (1977)
19. Popov, G.Ya., Tolkachev, V.M.: The problem of contact of rigid bodies with thin-walled elements. *Proc. Acad. Sci. USSR Mech. Solids.* **4**, 192–206 (1980)
20. Sargsyan, S.H.: On cylindrical bending of a plate with rigid dies. *Rep. NAS Armenia SSR* **64**, 216–223 (1977)

Chapter 23

Non-axisymmetric Vibration of Tuned Thin Functionally Graded Planar Structures



Getachew T. Sedebo, Michael Y. Shatalov, and Stephan V. Joubert

Abstract We consider a functionally graded plate (FGP) composed of an arbitrary number of concentric sections of various radii and thicknesses. This structure is supported at the centre by a rigid stem. The FGP is described in terms of the Novozhilov-Goldenveizer theory of thin isotropic linear shells. This system vibrates both in-plane as well as out-of-plane. Hamilton's variational principle is used to derive equations of motion and boundary-continuity conditions. A fixed boundary at the inner edge and a free boundary on the outer edge of the plate are considered. The in-plane and out-of-plane vibrations of the plates are studied in the frame of thin plate models and analytical solutions in terms of Bessel's functions and modified Bessel's functions for the system are determined. To verify our assumptions, we consider an example consisting of two concentric plates, where the inner component is made of an aluminium alloy and the outer component is made of titanium. The eigenvalues and the associated eigenfunctions of the plate are illustrated graphically. For this FGP, both in-plane and out-of-plane vibrations are excited with different circumferential wave numbers, where an elliptical in-plane wave form is considered for in-plane vibrations and a threefold symmetry wave form is considered for out-of-plane vibrations. In order to consider an application of the planar structure as a three-dimensional inertial navigation vibratory gyroscope, it is necessary to tune the eigenvalues of both in-plane and out-of-plane vibrations. The desired tuning between the two modes is achieved by means of a variation of radius and/or thickness of the functionally graded plate.

Keywords Non-axisymmetric vibrations · Tuning · Thin shells · Functionally graded plate · Planar structures · Exact solutions of initial-boundary value problems

G. T. Sedebo (✉) · M. Y. Shatalov · S. V. Joubert
Department of Mathematics and Statistics, Tshwane University of Technology,
Pretoria, South Africa
e-mail: SedeboGT@tut.ac.za

M. Y. Shatalov
e-mail: ShatalovM@tut.ac.za

S. V. Joubert
e-mail: JoubertSV@tut.ac.za

23.1 Introduction

A plate and its vibration properties subject to classical boundaries have been widely studied and are well-documented. Substantial amounts of information on the nature of both in-plane and out-of-plane vibrations can be found in literature. Fundamental methods of solution of elastic problems were developed in [1, 2]. Circular plates are used and applied in widely different areas, amongst others, in nozzle covers, pressure vessels, pump diaphragms, turbine discs, submarines, airplanes, railway wheels, brakes, hard drive discs and as sensors (see [3]). For a thin circular disc with a free edge, the equations of motion as well as an analytical solution were obtained in [4]. The bending of circular plates with various boundary conditions is thoroughly discussed by Timoshenko and Woinowsky-Krieger [5]. Bashmal et al. [3] investigated and analysed the in-plane free vibration of an annular disc with an elastic support at a point. An accurate algorithm for numerically determining eigenvalues for the fundamental and first few overtones in an eigenvalue problem were discussed in [6] where the Rayleigh-Ritz method was used to determine good initial values. Leissa [7] and Leissa and Qatu [8] presented analytical solutions for both solid and annular plates in terms of Bessel functions of the first and second kinds subjected to various boundary conditions. Furthermore, they provided theoretical as well as experimental results for frequencies and ratios of radii for nodal circles were calculated.

Analytical solutions for a rotor consisting of multiple flexible circular plates were obtained in [9]. The authors also investigated the effect of a flexible disc on the coupled longitudinal vibrations that link the disc and shaft. A car brake disc, regarded as an annular plate, was investigated in [10] and its equation of motion was derived using the theory of thin plates. The equations of motion were purely of those of a thin circular plate because the authors intentionally dropped the dynamics of the in-plane vibrations that involve gyroscopic effects. Burdess and Wren [11] investigated a Piezoelectric disc that was used as a gyroscope. The authors proposed a thin piezoelectric disc gyroscope that utilises its in-plane vibration properties to detect the rotation rate. The authors neglected the stresses in the transverse direction of the disc to derive both constitutive and field equations.

Sedebo et al. in [12] detailed the operation principle, investigated Bryan's factor and obtained eigenvalues and eigenfrequencies numerically for a thick-disc and thin-plate which was used as 3D gyroscope. More detailed work with a similar approach can be found in [13]. Rourke et al. [14] assumed that the in-plane and out-of-plane vibrations are independent, and hence, the strain energies of both modes can be separated. It is worth consulting [15, 16] with regard to the theoretical foundations of solid-state vibratory gyroscopes.

The present work deals with the development of a mathematical model that describes the dynamics of a system which consists of arbitrary concentric sections of a *functionally graded plate* (FGP). The FGP consists of a central rigid stem and concentric plates of various radii and thicknesses which are made of the same or different isotropic materials that obey the principles of linear elasticity (see Fig. 23.1).

It is also assumed that all the concentric (coaxial) plates are "thin" and can be described in terms of Novozhilov-Goldenveizer theory of elastic thin shells. The FGP

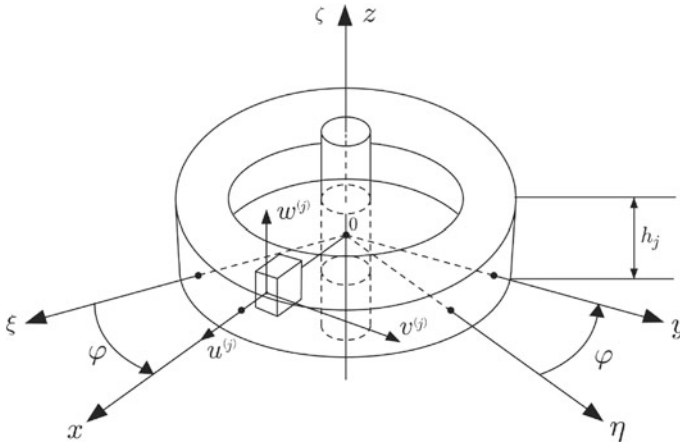


Fig. 23.1 Thick disc and thin plate three-dimensional vibratory plate showing the three orthogonal axes. For simplicity (so that the sketch does not become cluttered with detail), only the central thin vertical stem and the j -th disc are shown, $j = 1, 2, \dots, J$

under consideration is subject to both in-plane and out-of-plane nonaxisymmetric vibrations. We assumed that the circumferential wave number of in-plane vibrations (m) is not equal to the circumferential wave number of out-of-plane vibrations (n). The eigenvalues of both in-plane and out-of-plane vibrations were tuned. We say that the FGP is tuned if one of the eigenvalues of the in-plane vibrations at circumferential wave number m is equal to one of the eigenvalues of the out-of-plane vibrations at circumferential wave number n . For realisation of a 3D rotational rate gyroscope (sensor) on the planar FGP, it is necessary to ensure that $n = m \pm 1$ see [12]. In thin-walled plates, eigenvalues of the in-plane vibrations are normally higher than eigenvalues of the out-of-plane vibrations. Hence, it is reasonable to consider the situation $n = m + 1$, for example, $m = 2, n = 3$.

We present equations of motion for the system in Sect. 23.2 while a derivation (using Hamiltonian variational principle) is provided in Appendix A. Sections 23.3 and 23.5 discuss implicit and explicit boundary-continuity conditions of the system. In Sect. 23.4, we obtained analytical solutions for the system in terms of Bessel's functions by introducing potentials and a change of variables. Numerical results for the eigenvalues and eigenfunctions of both in-plane and out-of-plane vibrations are obtained, and these are graphically presented in Sect. 23.6. Tuning between the two modes was achieved by means of variation of radial and/or axial sizes. Frequency spectra are shown in Figs. 23.3 and 23.7. Conclusions are drawn in Sect. 23.7.

23.2 Equations of Motion

In order to calculate the strain energy (the potential energy), it is assumed that the in-plane displacements u and v and their derivatives do not influence the mid-plane curvatures and torsion. This assumption corresponds to the simplification of

Novozhilov's theory of thin shells to the Novozhilov-Goldenveizer theory of shallow shells as can be seen in Leissa [17], Novozhilov [18] and Goldenveizer [19].

Systems of equations describing the dynamics of a thin plate vibrating in both radial-tangential (in-plane) and out-of-plane direction in the frame of the linear Novozhilov-Goldenveizer theory are given as follows:

$$\frac{\rho_j(1-\eta_j^2)}{E_j} \frac{\partial^2 u^{(j)}}{\partial t^2} = \left[\frac{\frac{\partial^2 u^{(j)}}{\partial r^2} + \frac{\partial u^{(j)}}{r \partial r} + \frac{1-\eta_j}{2r^2} \frac{\partial^2 u^{(j)}}{\partial \varphi^2} - \frac{u^{(j)}}{r^2} + \frac{1+\eta_j}{2r} \frac{\partial^2 v^{(j)}}{\partial \varphi \partial r} - \frac{3-\eta_j}{2r^2} \frac{\partial v^{(j)}}{\partial r} \right]; \quad (23.1)$$

$$\frac{\rho_j(1-\eta_j^2)}{E_j} \frac{\partial^2 v^{(j)}}{\partial t^2} = \left[\frac{1-\eta_j}{2} \left(\frac{\partial^2 v^{(j)}}{\partial r^2} + \frac{\partial v^{(j)}}{r \partial r} - \frac{v^{(j)}}{r^2} \right) + \frac{1}{r^2} \frac{\partial^2 v^{(j)}}{\partial \varphi^2} + \frac{1+\eta_j}{2r} \frac{\partial^2 u^{(j)}}{\partial \varphi \partial r} + \frac{3-\eta_j}{2r^2} \frac{\partial u^{(j)}}{\partial \varphi} \right]; \quad (23.2)$$

$$\left[\frac{12\rho_j(1-\eta_j^2)}{E_j h_j^2} \frac{\partial^2 w^{(j)}}{\partial t^2} + \frac{\partial^4 w^{(j)}}{\partial r^4} + \frac{2\partial^3 w^{(j)}}{r \partial r^3} - \frac{\partial^2 w^{(j)}}{r^2 \partial r^2} + \frac{1}{r^3} \frac{\partial w^{(j)}}{\partial r} + \frac{2\partial^4 w^{(j)}}{r^2 \partial r^2 \partial \varphi^2} - \frac{2\partial^3 w^{(j)}}{r^3 \partial \varphi^2 \partial r} + \frac{4}{r^4} \frac{\partial^2 w^{(j)}}{\partial \varphi^2} + \frac{1}{r^4} \frac{\partial^4 w^{(j)}}{\partial \varphi^4} \right] = 0; \quad (23.3)$$

for $j = 1, 2, \dots, J$ and with $u^{(j)} = u^{(j)}(r, \varphi, t)$, $v^{(j)} = v^{(j)}(r, \varphi, t)$ and $w^{(j)} = w^{(j)}(r, \varphi, t)$, respectively, being the radial, tangential and out-of-plane (axial) displacements. Here t is time, r is the radius of the plate and φ is the polar angle. Furthermore, for the j th component of the plate, ρ_j stands for mass density, E_j for modulus of elasticity, η_j for Poisson's ratio and h_j for thickness. The radius of the junction consisting of a thin stem and the first component of the structure is a_0 . The radius of junction of the j th and $(j+1)$ st components is a_j where, $j = 1, 2, \dots, J-1$. The radius of outer rim of the structure is R .

It follows from Eqs. (23.1), (23.2) and (23.3) that there are $2J$ equations that describe in-plane dynamics of the plate and J -equations of the out-of-plane motion of the plate. According to the Novozhilov-Goldenveizer theory of shells, it is possible to separate in-plane and out-of-plane vibrations. It is further assumed that the inner rim of the first component is fixed to the stem and the outer rim of the plate is free. Intermediate neighbouring components are connected in accordance with conditions of continuity-smoothness, which are derived from the Hamiltonian variational principle (see Appendix A).

23.3 Implicit Boundary Conditions

Given the above assumptions in Sect. 23.2, the following boundary-continuity conditions are derived

For $r = a_0$:

$$u^{(1)}|_{r=a_0} = 0 \quad v^{(1)}|_{r=a_0} = 0; \quad (23.4)$$

$$w^{(1)}|_{r=a_0} = 0, \quad \frac{\partial w^{(1)}}{\partial r} \Big|_{r=a_0} = 0. \quad (23.5)$$

For $r = a_j$:

$$u^{(j)}|_{r=a_j} = u^{(j+1)}|_{r=a_j}, \quad v^{(j)}|_{r=a_j} = v^{(j+1)}|_{r=a_j}; \quad (23.6)$$

$$w^{(j)}|_{r=a_j} = w^{(j+1)}|_{r=a_j}, \quad \frac{\partial w^{(j)}}{\partial r} \Big|_{r=a_j} = \frac{\partial w^{(j+1)}}{\partial r} \Big|_{r=a_j}. \quad (23.7)$$

The radial stresses at $r = a_j$:

$$\left[\begin{array}{l} \frac{E_j h_j}{1 - \eta_j^2} \left[r \frac{\partial u^{(j)}}{\partial r} + \eta_j \left(u^{(j)} + \frac{\partial v^{(j)}}{\partial \varphi} \right) \right] \Big|_{r=a_j} \\ = \frac{E_{j+1} h_{j+1}}{1 - \eta_{j+1}^2} \left[r \frac{\partial u^{(j+1)}}{\partial r} + \eta_{j+1} \left(u^{(j+1)} + \frac{\partial v^{(j+1)}}{\partial \varphi} \right) \right] \Big|_{r=a_j} \end{array} \right]; \quad (23.8)$$

and shear stresses at $r = a_j$:

$$\left[\begin{array}{l} \frac{E_j h_j}{2(1 + \eta_j)} \left[r \frac{\partial v^{(j)}}{\partial r} - v^{(j)} + \frac{\partial u^{(j)}}{\partial \varphi} \right] \Big|_{r=a_j} \\ = \frac{E_{j+1} h_{j+1}}{2(1 + \eta_{j+1})} \left[r \frac{\partial v^{(j+1)}}{\partial r} - v^{(j+1)} + \frac{\partial u^{(j+1)}}{\partial \varphi} \right] \Big|_{r=a_j} \end{array} \right]. \quad (23.9)$$

The boundary-continuity conditions for shear forces of the out-of-plane vibrations of the plate components at $r = a_j$ are as follows

$$\left[\begin{array}{l} \frac{E_j h_j^3}{12(1 - \eta_j^2)} \left(r \frac{\partial^3 w^{(j)}}{\partial r^3} + \frac{\partial^2 w^{(j)}}{\partial r^2} - \frac{1}{r} \frac{\partial w^{(j)}}{\partial r} + \frac{2 - \eta_j}{r} \frac{\partial^3 w^{(j)}}{\partial \varphi^2 \partial r} \right) \Big|_{r=a_j} \\ = \frac{E_{j+1} h_{j+1}^3}{12(1 - \eta_{j+1}^2)} \left(r \frac{\partial^3 w^{(j+1)}}{\partial r^3} + \frac{\partial^2 w^{(j+1)}}{\partial r^2} - \frac{\partial w^{(j+1)}}{r \partial r} + \frac{2 - \eta_{j+1}}{r} \frac{\partial^3 w^{(j+1)}}{\partial \varphi^2 \partial r} \right) \Big|_{r=a_j} \end{array} \right]. \quad (23.10)$$

The boundary-continuity conditions for torques of the out-of-plane vibrations of the plate components at $r = a_j$ are as follows

$$\left[\begin{aligned} & \frac{E_j h_j^3}{12(1-\eta_j^2)} \left[r \frac{\partial^2 w^{(j)}}{\partial r} + \eta_j \left(\frac{\partial w^{(j)}}{\partial r} + \frac{\partial^2 w^{(j)}}{r \partial \varphi^2} \right) \right] \Big|_{r=a_j} \\ & = \frac{E_{j+1} h_{j+1}^3}{12(1-\eta_{j+1}^2)} \left[r \frac{\partial^2 w^{(j+1)}}{\partial r} + \eta_{j+1} \left(\frac{\partial w^{(j+1)}}{\partial r} + \frac{\partial^2 w^{(j+1)}}{r \partial \varphi^2} \right) \right] \Big|_{r=a_j} \end{aligned} \right]; \tag{23.11}$$

where $j = 1, 2, \dots, J - 1$.

The boundary-continuity conditions for the free outer rim at $r = R$ is obtained as follows

$$\frac{E_J h_J}{1-\eta_J^2} \left[r \frac{\partial u^{(J)}}{\partial r} + \eta_J \left(u^{(J)} + \frac{\partial v^{(J)}}{\partial \varphi} \right) \right] \Big|_{r=R} = 0; \tag{23.12}$$

$$\frac{E_J h_J}{2(1+\eta_J)} \left[r \frac{\partial v^{(J)}}{\partial r} - v^{(J)} + \frac{\partial u^{(J)}}{\partial \varphi} \right] \Big|_{r=R} = 0; \tag{23.13}$$

$$\frac{E_J h_J^3}{12(1-\eta_J^2)} \left(\begin{aligned} & r \frac{\partial^3 w^{(J)}}{\partial r^3} + \frac{\partial^2 w^{(J)}}{\partial r^2} - \frac{1}{r} \frac{\partial w^{(J)}}{\partial r} + \frac{2-\eta_J}{r} \frac{\partial^3 w^{(J)}}{\partial \varphi^2 \partial r} \\ & \frac{3-\eta_J}{r^2} \frac{\partial^2 w^{(J)}}{\partial \varphi^2} \end{aligned} \right) \Big|_{r=R} = 0; \tag{23.14}$$

$$\frac{E_J h_J^3}{12(1-\eta_J^2)} \left[r \frac{\partial^2 w^{(J)}}{\partial r} + \eta_J \left(\frac{\partial w^{(J)}}{\partial r} + \frac{\partial^2 w^{(J)}}{r \partial \varphi^2} \right) \right] \Big|_{r=R} = 0. \tag{23.15}$$

It can be seen from the boundary-continuity conditions in (23.4)–(23.15) that there are $8J$ boundary-continuity conditions that can be separated as $4J$ for in-plane vibrations and $4J$ for out-of-plane vibrations.

23.4 Exact Solutions to the Boundary Value Problems

From the boundary-continuity conditions given in Eqs. (23.4)–(23.15), one can see that the boundary value problem can be solved in terms of exact solutions by, as is usual, introducing potential functions $\tilde{\Phi}(\omega, r, \varphi)$ and $\tilde{\Psi}(\omega, r, \varphi)$ and by making a change of variables such that

$$u^{(j)}(t, \omega, r, \varphi) = \left[\frac{\partial \tilde{\Phi}^{(j)}(\omega, r, \varphi)}{\partial r} + \frac{1}{r} \frac{\partial \tilde{\Psi}(\omega, r, \varphi)}{\partial \varphi} \right] e^{i\omega t}; \quad (23.16)$$

$$v^{(j)}(t, \omega, r, \varphi) = \left[\frac{1}{r} \frac{\tilde{\Phi}^{(j)}(\omega, r, \varphi)}{\partial \varphi} - \frac{\partial \tilde{\Psi}(\omega, r, \varphi)}{\partial r} \right] e^{i\omega t}; \quad (23.17)$$

$$w^{(j)}(t, \omega, r, \varphi) = \tilde{W}^{(j)}(\omega, r, \varphi) e^{i\omega t}, \quad (23.18)$$

where $i^2 = -1$ and ω is a parameter which has the physical dimensions of angular frequency. Substitution of Eqs. (23.16), (23.17) and (23.18), respectively, into Eqs. (23.1), (23.2) and (23.3), respectively, yields

$$\frac{\partial^2 \tilde{\Phi}^{(j)}}{\partial r^2} + \frac{1}{r} \frac{\partial \tilde{\Phi}^{(j)}}{\partial r} + \frac{1}{r^2} \frac{\partial^2 \tilde{\Phi}^{(j)}}{\partial \varphi^2} = \frac{\omega^2 \tilde{\Phi}^{(j)}}{c_{1j}}; \quad (23.19)$$

$$\frac{\partial^2 \tilde{\Psi}^{(j)}}{\partial r^2} + \frac{1}{r} \frac{\partial \tilde{\Psi}^{(j)}}{\partial r} + \frac{1}{r^2} \frac{\partial^2 \tilde{\Psi}^{(j)}}{\partial \varphi^2} = \frac{\omega^2 \tilde{\Psi}^{(j)}}{c_{2j}}; \quad (23.20)$$

$$\left[\begin{array}{c} \frac{\partial^4 \tilde{W}^{(j)}}{\partial r^4} + \frac{2\partial^3 \tilde{W}^{(j)}}{r\partial r^3} - \frac{\partial^2 \tilde{W}^{(j)}}{r^2\partial r^2} + \frac{1}{r^3} \frac{\partial \tilde{W}^{(j)}}{\partial r} + \frac{2}{r^2} \frac{\partial^4 \tilde{W}^{(j)}}{\partial r^2\partial \varphi^2} \\ - \frac{2}{r^3} \frac{\partial^3 \tilde{W}^{(j)}}{\partial \varphi^2\partial r} + \frac{4}{r^4} \frac{\partial^2 \tilde{W}^{(j)}}{\partial \varphi^2} + \frac{1}{r^4} \frac{\partial^4 \tilde{W}^{(j)}}{\partial \varphi^4} \end{array} \right] = \beta_j^4(\omega) \tilde{W}^{(j)}; \quad (23.21)$$

where

$$\begin{aligned} \tilde{\Phi}^{(j)} &= \tilde{\Phi}^{(j)}(\omega, r, \varphi), \quad \tilde{\Psi}^{(j)} = \tilde{\Psi}^{(j)}(\omega, r, \varphi), \quad \tilde{W}^{(j)} = \tilde{W}^{(j)}(\omega, r, \varphi), \\ c_{1j} &= \frac{E_j}{\rho_j(1 - \eta_j^2)}, \quad c_{2j} = \frac{E_j}{2\rho_j(1 + \eta_j)}, \quad \beta_j^4(\omega) = \frac{12\rho_j(1 - \eta_j^2)\omega^2}{E_j h_j^2}. \end{aligned}$$

We further investigate particular modes of in-plane and out-of-plane vibrations of the FGP with integer values of circumferential wave numbers m and n such that

$$\tilde{\Phi}^{(j,m)}(\omega, r, \varphi) = \Phi^{(j,m)}(\omega, r) \begin{pmatrix} \cos(m\varphi) \\ \sin(m\varphi) \end{pmatrix}; \quad (23.22)$$

$$\tilde{\Psi}^{(j,m)}(\omega, r, \varphi) = \Psi^{(j,m)}(\omega, r) \begin{pmatrix} \sin(m\varphi) \\ \cos(m\varphi) \end{pmatrix}; \quad (23.23)$$

$$\tilde{W}^{(j,n)}(\omega, r, \varphi) = W^{(j,n)}(\omega, r, \varphi) \begin{pmatrix} \cos(n\varphi) \\ \sin(n\varphi) \end{pmatrix}. \quad (23.24)$$

Note that

$$\begin{pmatrix} \cos(m\varphi) \\ \sin(m\varphi) \end{pmatrix} \text{ and } \begin{pmatrix} \sin(m\varphi) \\ \cos(m\varphi) \end{pmatrix}$$

are orthogonal combinations of $\cos(m\varphi)$ and $\sin(m\varphi)$ and similarly for $\begin{pmatrix} \cos(n\varphi) \\ \sin(n\varphi) \end{pmatrix}$.

Substituting Eqs. (23.22), (23.23) and (23.24), respectively, into Eqs. (23.19), (23.20) and (23.21), respectively, (because of the periodicity of φ for non-trivial cases) yields the following ordinary differential equations

$$\frac{d^2\Phi^{(j,m)}}{dr^2} + \frac{1}{r} \frac{d\Phi^{(j,m)}}{dr} + \left(\frac{\omega^2}{c_{1j}^2} - \frac{m^2}{r^2} \right) \Phi^{(j,m)} = 0; \tag{23.25}$$

$$\frac{d^2\Psi^{(j,m)}}{dr^2} + \frac{1}{r} \frac{d\Psi^{(j,m)}}{dr} + \left(\frac{\omega^2}{c_{2j}^2} - \frac{m^2}{r^2} \right) \Psi^{(j,m)} = 0; \tag{23.26}$$

$$\left[\begin{aligned} &\frac{d^4 W^{(j,n)}}{dr^4} + \frac{2}{r} \frac{d^3 W^{(j,n)}}{dr^3} - \left(\frac{2n^2 + 1}{r^2} \right) \frac{d^2 W^{(j,n)}}{dr^2} + \\ &\left(\frac{2n^2 + 1}{r^3} \right) \frac{dW^{(j,n)}}{dr} - \left[\beta_j^4(\omega) - \frac{n^4 - 4n^2}{r^4} \right] W^{(j,n)} \end{aligned} \right] = 0; \tag{23.27}$$

where $\Phi^{(j,m)} = \Phi^{(j,m)}(\omega, r)$, $\Psi^{(j,m)} = \Psi^{(j,m)}(\omega, r)$ and $W^{(n,j)} = W^{(n,j)}(\omega, r)$. Solving Eqs. (23.25), (23.26) and (23.27), respectively, yields

$$\Phi^{(j,m)}(\omega, r) = C_1^{(j,m)} J_m \left(\frac{\omega}{c_{1j}} r \right) + C_2^{(j,m)} Y_m \left(\frac{\omega}{c_{1j}} r \right); \tag{23.28}$$

$$\Psi^{(j,m)}(\omega, r) = C_3^{(j,m)} J_m \left(\frac{\omega}{c_{2j}} r \right) + C_4^{(j,m)} Y_m \left(\frac{\omega}{c_{2j}} r \right); \tag{23.29}$$

$$\left[\begin{aligned} &W^{(j,n)}(r) = C_5^{(j,n)} J_n(\beta_j(\omega)r) + C_6^{(j,n)} Y_n(\beta_j(\omega)r) + \\ &C_7^{(j,n)} I_n(\beta_j(\omega)r) + C_8^{(j,n)} K_n(\beta_j(\omega)r) \end{aligned} \right], \tag{23.30}$$

where $C_1^{(j,m)}, C_2^{(j,m)}, \dots, C_4^{(j,m)}, C_5^{(j,n)}, C_6^{(j,n)}, \dots, C_8^{(j,n)}$ are arbitrary constants that can be determined from the boundary conditions and which determine the mode shapes. Here $J_m^{(j,m)}$ or $J_n^{(j,n)}$ and $Y_m^{(j,m)}$ or $Y_n^{(j,n)}$ are Bessel functions of the first and second kind, respectively, of order m and n . The functions $I_n^{(j,n)}$ and $K_n^{(j,n)}$ are modified Bessel functions of the first and second kind, respectively, of order n .

Substituting Eqs. (23.28) and (23.29), respectively, into Eqs. (23.16), (23.17), respectively, yields

$$u^{(j)}(t, \omega, r, \varphi) = \left[\begin{aligned} &C_1^{(j,m)} U_1^{(j,m)}(\omega, r) + \\ &C_2^{(j,m)} U_2^{(j,m)}(\omega, r) + \\ &C_3^{(j,m)} U_3^{(j,m)}(\omega, r) + \\ &C_4^{(j,m)} U_4^{(j,m)}(\omega, r) \end{aligned} \right] \begin{pmatrix} \cos(m\varphi) \\ \sin(m\varphi) \end{pmatrix} e^{i\omega t}; \tag{23.31}$$

$$v^{(j)}(t, \omega, r, \varphi) = \begin{bmatrix} C_1^{(j,m)} V_1^{(j,m)}(\omega, r) + \\ C_2^{(j,m)} V_2^{(j,m)}(\omega, r) + \\ C_3^{(j,m)} V_3^{(j,m)}(\omega, r) + \\ C_4^{(j,m)} V_4^{(j,m)}(\omega, r) \end{bmatrix} \begin{pmatrix} \sin(m\varphi) \\ \cos(m\varphi) \end{pmatrix} e^{i\omega t}; \quad (23.32)$$

where

$$\begin{aligned} U_1^{(j,m)}(\omega, r) &= \frac{m}{r} J_m \left(\frac{\omega}{c_{1j}} r \right) - \frac{\omega}{c_{1j}} J_{m+1} \left(\frac{\omega}{c_{1j}} r \right); \\ U_2^{(j,m)}(\omega, r) &= \frac{m}{r} Y_m \left(\frac{\omega}{c_{1j}} r \right) - \frac{\omega}{c_{1j}} Y_{m+1} \left(\frac{\omega}{c_{1j}} r \right); \\ U_3^{(j,m)}(\omega, r) &= \frac{m}{r} J_m \left(\frac{\omega}{c_{2j}} r \right); \quad U_4^{(j,m)}(\omega, r) = \frac{m}{r} Y_m \left(\frac{\omega}{c_{2j}} r \right); \end{aligned}$$

and

$$\begin{aligned} V_1^{(j,m)}(\omega, r) &= -\frac{m}{r} J_m \left(\frac{\omega}{c_{1j}} r \right); \quad V_2^{(j,m)}(\omega, r) = -\frac{m}{r} Y_m \left(\frac{\omega}{c_{2j}} r \right); \\ V_3^{(j,m)}(\omega, r) &= -\frac{m}{r} J_m \left(\frac{\omega}{c_{2j}} r \right) + \frac{\omega}{c_{2j}} J_{m+1} \left(\frac{\omega}{c_{2j}} r \right); \\ V_4^{(j,m)}(\omega, r) &= -\frac{m}{r} Y_m \left(\frac{\omega}{c_{2j}} r \right) + \frac{\omega}{c_{2j}} Y_{m+1} \left(\frac{\omega}{c_{2j}} r \right). \end{aligned}$$

Substituting Eqs. (23.30), into Eqs. (23.18), yields

$$W^{(j,n)}(t, \omega, r, \varphi) = \begin{bmatrix} C_5^{(j,n)} W_1^{(j,n)}(\omega, r) + \\ C_6^{(j,n)} W_2^{(j,n)}(\omega, r) + \\ C_7^{(j,n)} W_3^{(j,n)}(\omega, r) + \\ C_8^{(j,n)} W_4^{(j,n)}(\omega, r) \end{bmatrix} \begin{pmatrix} \cos(n\varphi) \\ \sin(n\varphi) \end{pmatrix} e^{i\omega t}, \quad (23.33)$$

where

$$\begin{aligned} W_1^{(j,n)}(\omega, r) &= J_n(\beta_j(\omega) r); \quad W_2^{(j,n)}(\beta_j(\omega) r) = Y_n(\beta_j(\omega) r); \\ W_3^{(j,n)}(\omega, r) &= I_n(\beta_j(\omega) r); \quad W_4^{(j,n)}(\omega, r) = K_n W_3^{(j,n)}(\omega, r). \end{aligned}$$

23.5 Explicit Boundary Conditions

For boundary-continuity conditions of the out-of-plane vibrations, we need to differentiate the out-of-plane displacement with respect to r . Thus, it follows that

$$\begin{aligned}
 D\tilde{W}^{(j,n)}(t, \omega, r, \varphi) &= \frac{d\tilde{W}^{(j,n)}(t, \omega, r, \varphi)}{dr} \\
 &= \begin{bmatrix} C_5^{(j,n)} DW_1^{(j,n)}(\omega, r) + \\ C_6^{(j,n)} DW_2^{(j,n)}(\omega, r) + \\ C_7^{(j,n)} DW_3^{(j,n)}(\omega, r) + \\ C_8^{(j,n)} W_4^{(j,n)}(\omega, r) \end{bmatrix} \begin{pmatrix} \cos(n\varphi) \\ \sin(n\varphi) \end{pmatrix} e^{i\omega t},
 \end{aligned}
 \tag{23.34}$$

where

$$\begin{aligned}
 DW_1^{(j,n)}(\omega, r) &= \frac{n}{r} J_n(\beta_j(\omega)r) - \beta_j(\omega) J_{n+1}(\beta_j(\omega)r); \\
 DW_2^{(j,n)}(\omega, r) &= \frac{n}{r} Y_n(\beta_j(\omega)r) - \beta_j(\omega) Y_{n+1}(\beta_j(\omega)r); \\
 DW_3^{(j,n)}(\omega, r) &= \frac{n}{r} I_n(\beta_j(\omega)r) + I_{n+1}(\beta_j(\omega)r); \\
 DW_4^{(j,n)}(\omega, r) &= \frac{n}{r} K_n(\beta_j(\omega)r) - \beta_j(\omega) K_{n+1}(\beta_j(\omega)r).
 \end{aligned}$$

For boundary-continuity conditions of in-plane vibrations, radial and shear stresses are obtained by substituting Eqs. (23.31) and (23.32) into Eqs. (23.8) and (23.9) after performing the indicated differentiations. Consequently

$$\begin{aligned}
 \sigma_{rr}^{(j,m)}(t, \omega, r, \varphi) &= \frac{E_j}{1 - \eta_j^2} \begin{bmatrix} C_1^{(j,m)} \sigma_{rr,1}^{(j,m)}(\omega, r) + \\ C_2^{(j,m)} \sigma_{rr,2}^{(j,m)}(\omega, r) + \\ C_3^{(j,m)} \sigma_{rr,3}^{(j,m)}(\omega, r) + \\ C_4^{(j,m)} \sigma_{rr,4}^{(j,m)}(\omega, r) \end{bmatrix} \begin{pmatrix} \cos(m\varphi) \\ \sin(m\varphi) \end{pmatrix} e^{i\omega t}; \\
 \sigma_{r\varphi}^{(j,m)}(t, \omega, r, \varphi) &= \frac{E_j}{2(1 + \eta_j)} \begin{bmatrix} C_1^{(j,m)} \sigma_{r\varphi,1}^{(j,m)}(\omega, r) + \\ C_2^{(j,m)} \sigma_{r\varphi,2}^{(j,m)}(\omega, r) + \\ C_3^{(j,m)} \sigma_{r\varphi,3}^{(j,m)}(\omega, r) + \\ C_4^{(j,m)} \sigma_{r\varphi,4}^{(j,m)}(\omega, r) \end{bmatrix} \begin{pmatrix} \sin(m\varphi) \\ \cos(m\varphi) \end{pmatrix} e^{i\omega t};
 \end{aligned}
 \tag{23.36}$$

where,

$$\begin{aligned}
 \sigma_{rr,1}^{(j,m)}(\omega, r) &= \left[\left(\frac{\omega}{c_{1j}} \right)^2 - \frac{m(m-1)(1-\eta_j)}{r^2} J_m \left(\frac{\omega}{c_{1j}} r \right) - \right. \\
 &\quad \left. \frac{1-\eta_j}{r} \frac{\omega}{c_{1j}} J_{m+1} \left(\frac{\omega}{c_{1j}} r \right); \right. \\
 \sigma_{rr,2}^{(j,m)}(\omega, r) &= \left[\left(\frac{\omega}{c_{1j}} \right)^2 - \frac{m(m-1)(1-\eta_j)}{r^2} Y_m \left(\frac{\omega}{c_{1j}} r \right) - \right. \\
 &\quad \left. \frac{1-\eta_j}{r} \frac{\omega}{c_{1j}} Y_{m+1} \left(\frac{\omega}{c_{1j}} r \right); \right.
 \end{aligned}$$

$$\sigma_{rr,3}^{(j,m)}(\omega, r) = (1 - \eta_j) \left[-\frac{m(m-1)}{r^2} J_m \left(\frac{\omega}{c_{2j}} r \right) + \frac{m}{r} \frac{\omega}{c_{2j}} J_{m+1} \left(\frac{\omega}{c_{2j}} r \right) \right];$$

$$\sigma_{rr,4}^{(j,m)}(\omega, r) = (1 - \eta_j) \left[-\frac{m(m-1)}{r^2} Y_m \left(\frac{\omega}{c_{2j}} r \right) + \frac{m}{r} \frac{\omega}{c_{2j}} Y_{m+1} \left(\frac{\omega}{c_{2j}} r \right) \right];$$

$$\sigma_{r\varphi,1}^{(j,m)}(\omega, r) = \left[\frac{2m(m-1)}{r^2} J_m \left(\frac{\omega}{c_{1j}} r \right) - \frac{2m}{r} \frac{\omega}{c_{1j}} J_{m+1} \left(\frac{\omega}{c_{1j}} r \right) \right];$$

$$\sigma_{r\varphi,2}^{(j,m)}(\omega, r) = \left[\frac{2m(m-1)}{r^2} Y_m \left(\frac{\omega}{c_{1j}} r \right) - \frac{2m}{r} \frac{\omega}{c_{1j}} Y_{m+1} \left(\frac{\omega}{c_{1j}} r \right) \right];$$

$$\sigma_{r\varphi,3}^{(j,m)}(\omega, r) = \left[\begin{array}{c} \left(\frac{2m(m-1)}{r^2} - \left(\frac{\omega}{c_{2j}} \right)^2 \right) J_m \left(\frac{\omega}{c_{2j}} r \right) + \\ \frac{2}{r} \frac{\omega}{c_{2j}} J_{m+1} \left(\frac{\omega}{c_{2j}} r \right) \end{array} \right];$$

$$\sigma_{r\varphi,3}^{(j,m)}(\omega, r) = \left[\begin{array}{c} \left(\frac{2m(m-1)}{r^2} - \left(\frac{\omega}{c_{2j}} \right)^2 \right) Y_m \left(\frac{\omega}{c_{2j}} r \right) + \\ \frac{2}{r} \frac{\omega}{c_{2j}} Y_{m+1} \left(\frac{\omega}{c_{2j}} r \right) \end{array} \right].$$

For boundary-continuity conditions of the out-of-plane vibrations of the plate, we need expressions for shear forces and torques. The shear forces and torques are obtained by substituting Eq. (23.33) into Eqs. (23.10) and (23.11), respectively. After performing the indicated differentiations one obtains

$$\tilde{Q}^{(j,n)}(t, \omega, r, \varphi) = \frac{E_j h_j^3}{12(1 - \eta_j^2)} \left[\begin{array}{c} C_5^{(j,n)} Q_1^{(j,n)}(\omega, r) + \\ C_6^{(j,n)} Q_2^{(j,n)}(\omega, r) + \\ C_7^{(j,n)} Q_3^{(j,n)}(\omega, r) + \\ C_8^{(j,n)} Q_4^{(j,n)}(\omega, r) \end{array} \right] \begin{pmatrix} \cos(n\varphi) \\ \sin(n\varphi) \end{pmatrix} e^{i\omega t}; \quad (23.37)$$

$$\tilde{M}^{(j,n)}(t, \omega, r, \varphi) = \frac{E_j h_j^3}{12(1 - \eta_j^2)} \left[\begin{array}{c} C_5^{(j,n)} M_1^{(j,n)}(\omega, r) + \\ C_6^{(j,n)} M_2^{(j,n)}(\omega, r) + \\ C_7^{(j,n)} M_3^{(j,n)}(\omega, r) + \\ C_8^{(j,n)} M_4^{(j,n)}(\omega, r) \end{array} \right] \begin{pmatrix} \cos(n\varphi) \\ \sin(n\varphi) \end{pmatrix} e^{i\omega t}; \quad (23.38)$$

where

$$Q_1^{(j,n)}(\omega, r) = \begin{bmatrix} -n \left(\beta_j^2(\omega) + \frac{n(n-1)(1-\eta_j)}{r^2} \right) J_n(\beta_j(\omega)r) + \\ \beta_j(\omega) \left(r\beta_j^2(\omega) + \frac{n^2(1-\eta_j)}{r} \right) J_{n+1}(\beta_j(\omega)r) \end{bmatrix};$$

$$Q_2^{(j,n)}(\omega, r) = \begin{bmatrix} -n \left(\beta_j^2(\omega) + \frac{n(n-1)(1-\eta_j)}{r^2} \right) Y_n(\beta_j(\omega)r) + \\ \beta_j(\omega) \left(r\beta_j^2(\omega) + \frac{n^2(1-\eta_j)}{r} \right) Y_{n+1}(\beta_j(\omega)r) \end{bmatrix}$$

$$Q_3^{(j,n)}(\omega, r) = \begin{bmatrix} n \left(\beta_j^2(\omega) - \frac{n(n-1)(1-\eta_j)}{r^2} \right) I_n(\beta_j(\omega)r) + \\ \beta_j(\omega) \left(r\beta_j^2(\omega) - \frac{n^2(1-\eta_j)}{r} \right) I_{n+1}(\beta_j(\omega)r) \end{bmatrix};$$

$$Q_4^{(j,n)}(\omega, r) = \begin{bmatrix} n \left(\beta_j^2(\omega) - \frac{n(n-1)(1-\eta_j)}{r^2} \right) K_n(\beta_j(\omega)r) + \\ \beta_j(\omega) \left(-r\beta_j^2(\omega) + \frac{n^2(1-\eta_j)}{r} \right) K_{n+1}(\beta_j(\omega)r) \end{bmatrix};$$

$$M_1^{(j,n)}(\omega, r) = \begin{bmatrix} \left(r\beta_j^2(\omega) - \frac{n(n-1)(1-\eta_j)}{r} \right) J_n(\beta_j(\omega)r) - \\ \beta_j(\omega)(1-\eta_j) J_{n+1}(\beta_j(\omega)r) \end{bmatrix};$$

$$M_2^{(j,n)}(\omega, r) = \begin{bmatrix} \left(r\beta_j^2(\omega) - \frac{n(n-1)(1-\eta_j)}{r} \right) Y_n(\beta_j(\omega)r) - \\ \beta_j(\omega)(1-\eta_j) Y_{n+1}(\beta_j(\omega)r) \end{bmatrix};$$

$$M_3^{(j,n)}(\omega, r) = \begin{bmatrix} \left(-r\beta_j^2(\omega) - \frac{n(n-1)(1-\eta_j)}{r} \right) I_n(\beta_j(\omega)r) + \\ \beta_j(\omega)(1-\eta_j) I_{n+1}(\beta_j(\omega)r) \end{bmatrix};$$

$$M_4^{(j,n)}(\omega, r) = \begin{bmatrix} \left(-r\beta_j^2(\omega) - \frac{n(n-1)(1-\eta_j)}{r} \right) K_n(\beta_j(\omega)r) - \\ \beta_j(\omega)(1-\eta_j) K_{n+1}(\beta_j(\omega)r) \end{bmatrix}.$$

Consequently, the boundary-continuity conditions in Eqs. (23.4)–(23.15) can now be summarised and rewritten as:

$$U^{(1,m)}(\omega, r)|_{r=a_0} = 0, \quad V^{(1,m)}(\omega, r)|_{r=a_0} = 0; \tag{23.39}$$

$$W^{(1,n)}(\omega, r)|_{r=a_0} = 0, \quad \left. \frac{\partial W^{(1,n)}(\omega, r)}{\partial r} \right|_{r=a_0} = 0; \tag{23.40}$$

$$r [U^{(j,m)}(\omega, r) - U^{(j+1,m)}(\omega, r)]|_{r=a_j} = 0, \tag{23.41}$$

$$[V^{(j,m)}(\omega, r) - V^{(j+1,m)}(\omega, r)]|_{r=a_j} = 0, \tag{23.42}$$

$$[W^{(j,n)}(\omega, r) - W^{(j+1,n)}(\omega, r)]|_{r=a_j} = 0, \tag{23.43}$$

$$\left[\frac{\partial W^{(j,n)}(\omega, r)}{\partial r} - \frac{\partial W^{(j+1,n)}(\omega, r)}{\partial r} \right]|_{r=a_j} = 0; \tag{23.44}$$

$$h_j a_j [\sigma_{rr}^{(j,m)}(\omega, r) - \sigma_{rr}^{(j+1,m)}(\omega, r)]|_{r=a_j} = 0, \tag{23.45}$$

$$h_j a_j [\sigma_{r\varphi}^{(j,m)}(\omega, r) - \sigma_{r\varphi}^{(j+1,m)}(\omega, r)]|_{r=a_j} = 0, \tag{23.46}$$

$$[Q^{(j,n)}(\omega, r) - Q^{(j+1,n)}(\omega, r)]|_{r=a_j} = 0, \tag{23.47}$$

$$[M^{(j,n)}(\omega, r) - M^{(j+1,n)}(\omega, r)]|_{r=a_j} = 0. \tag{23.48}$$

For $r = R$, we have

$$h_j R [\sigma_{rr}^{(j,m)}(\omega, r)]|_{r=R} = 0; \tag{23.49}$$

$$h_j R [\sigma_{r\varphi}^{(j,m)}(\omega, r)]|_{r=R} = 0; \tag{23.50}$$

$$[Q^{(j,n)}(\omega, r)]|_{r=R} = 0; \tag{23.51}$$

$$[M^{(j,n)}(\omega, r)]|_{r=R} = 0. \tag{23.52}$$

Observing the in-plane and out-of-plane boundary-continuity conditions, it can be clearly seen that the spectra of the in-plane and out-of-plane vibrations can be plotted independently. In the next section, we will show that these spectra can be tuned, so that particular eigenvalues may be matched.

23.6 Numerical Results

For a numerical simulation, we take two sections of the functionally graded plate ($J = 2, j = 1, 2$). The inner thin section is made from an aluminium alloy with mass density $\rho_1 = 2.7 \times 10^3 \text{ kg/m}^3$, modulus of elasticity $E_1 = 7 \times 10^4 \text{ MPa}$ and

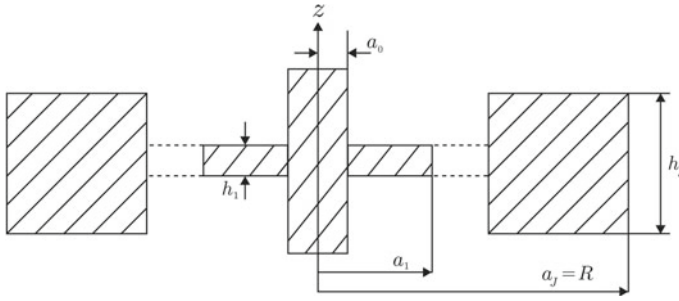


Fig. 23.2 Cross sections of the FGP with two components and the stem at the centre

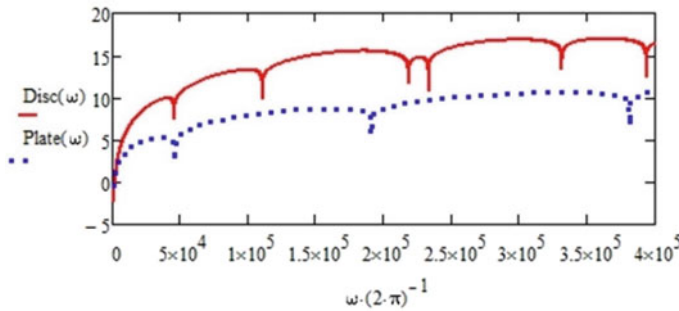


Fig. 23.3 Frequency spectra of in-plane (solid red curve) and out-of-plane (dotted blue curve) vibrations illustrating tuned first eigenvalues

Poisson’s ratio $\eta_1 = 0.33$. Here the geometrical dimensions are $a_0 = 2 \times 10^{-3}\text{m}$, $a_1 = 7 \times 10^{-3}\text{m}$, $h_1 = 1.85 \times 10^{-3}\text{m}$ (see Figs. 23.1 and 23.2).

A relatively thicker outer disc made of a titanium alloy has physical parameters $\rho_2 = 4.5 \times 10^3\text{kg/m}^3$, $E_2 = 1.2 \times 10^6\text{MPa}$ and $\eta_2 = 0.34$. The geometrical dimensions of the outer disc are $a_2 = R = 3.8 \times 10^{-2}\text{m}$ and $h_2 = 5.55 \times 10^{-3}\text{m}$. With these values, a tuning between the first mode of in-plane motion at circumferential wave number $m = 2$ and the first mode of the out-of-plane vibrations of the disc at circumferential wave number $n = 3$ was obtained. This tuning is demonstrated in Fig. 23.3 where the function $\text{Disc}(\omega)$ is the natural logarithm applied to the absolute value of a determinant function (with its roots being the eigenvalues) and similarly for the plate (see [6] Sect. 8.1).

The corresponding eigenfunctions of the in-plane vibrations are shown in Figs. 23.4 and 23.5 (for the radial and tangential motions independently).

In Fig. 23.6 the eigenfunctions of the out-of-plane motion which corresponds to the first eigenvalue is shown.

Numerical simulations show that eigenfrequency of the in-plane vibration for the first mode is approximately 45913.67 Hz and that of out-of-plane vibration is approximately 45967.40 Hz, with an approximate frequency split of $|45913.67 - 45967.40|$

Fig. 23.4 Eigenfunction of the radial mode for the first eigenvalue

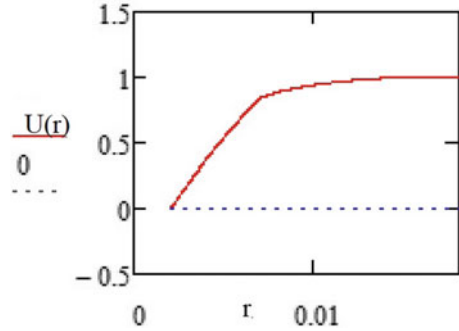


Fig. 23.5 Eigenfunction of the tangential mode for the first eigenvalue

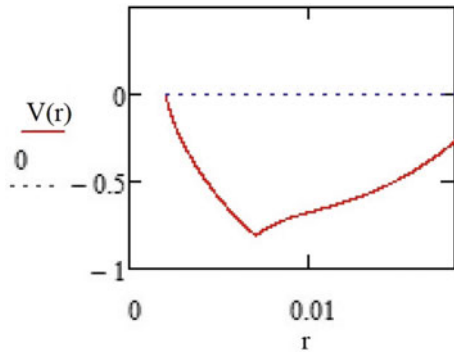
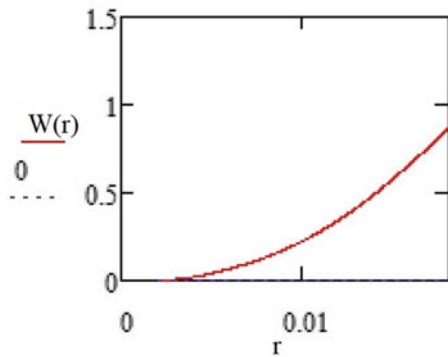


Fig. 23.6 Eigenfunction of the axial mode for the first eigenvalue



≈ 42.73 Hz. Note that the above results were obtained in the frame of the Novozhilov-Goldenveizer theory of shells. In this particular case, the ratio of maximum diameter of the plate to its thickness is $\frac{2R}{h_2} \approx 6.85$ which is not large enough to consider our plate as a thin shell. Consequently, our example for the first mode is provided here merely in order to illustrate that it is possible to tune the frequencies using a theory not necessarily based on the above thin shell theory.

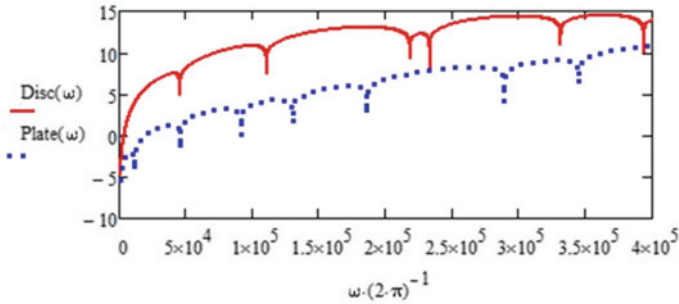


Fig. 23.7 Frequency spectra of in-plane (solid red curve) and out-of-plane (dotted blue curve) vibrations at tuned first and second eigenvalues

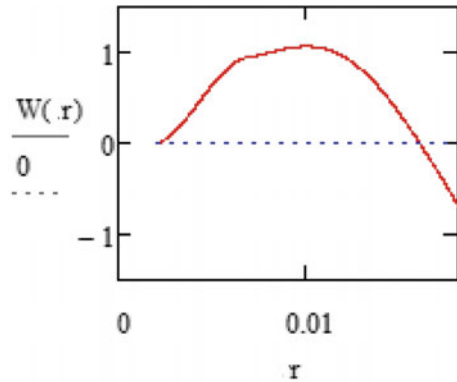
In our second simulation, we tuned the first eigenvalue of the in-plane vibration mode at $m = 2$ and the second eigenvalue of the out-of-plane vibration at $n = 3$. Selection of the physical parameters of the functionally graded plate is exactly the same as before. We also kept the same a_0 and a_1 , but the thicknesses h_1 and h_2 were varied to achieve tuning of both modes. The new values for h_1 and h_2 were respectively, $h_1 = 4.45 \times 10^{-4}$ m and $h_2 = 1.335 \times 10^{-3}$ m. Our new selection of parameters results in the ratio: $\frac{2R}{h_2} \approx 28.46$, which indicates our plate is “thin”. The corresponding frequency spectra are displayed in Fig. 23.7 as sharp negative spikes.

Eigenfrequency of the first mode of the in-plane vibration is approximately 45913.67 Hz and the eigenfrequency of the second mode of out-of-plane vibration is approximately 45903.35 Hz, with a frequency split of $|45913.67 - 45903.35| \approx 10.32$ Hz, which shows that it is possible to tune the first eigenvalue of in-plane vibration with a second eigenvalue of the out-of-plane vibration so that an optimal sensing capability would be achieved by the sensor (see [12]). We have observed that the in-plane eigenfunctions in both examples appear to be similar and consequently we do not repeat the figures here but merely refer the reader to Figs. 23.4 and 23.5. The eigenfunction of the second mode for the out-of-plane vibration is shown in Fig. 23.8.

23.7 Conclusions and Discussions

Exact solutions of vibration of the FGP composed of arbitrary number of concentric sections were derived in the frame of the Novozhilov-Goldenveizer theory of shells. These solutions were obtained in terms of the Bessel, Neumann and modified Bessel functions for both in-plane and out-of-plane vibrations of the FGP. For applications of the considered planar structures as a three-dimensional vibrational gyroscopes (an inertial navigation angular rate sensor), it is necessary to tune the plate so that

Fig. 23.8 Eigenfunction of axial mode for the second eigenvalue



one of the eigenvalues of the in-plane mode with circumferential wave number m is approximately equal to one of eigenvalues of the out-of-plane mode with circumferential wave number $n = m + 1$. Relatively thin plates are normally much stiffer in the radial direction than in the out-of-plane direction. Consequently, this is true with respect to their eigenvalues. Hence, it is necessary to take $m < n$, for instance $n = m + 1$. For numerical simulations, we selected $m = 2$ (an elliptical in-plane wave form for the in-plane vibrations) and $n = 3$ (a three fold symmetry wave form for the out-of-plane vibrations). It can be seen from our numerical experiment that a decrease in the outer radius of the FGP increases the eigenvalues of the in-plane vibrations and vice versa, whereas a decrease in thickness of the FGP decreases the eigenvalues of the out-of-plane vibrations and vice versa.

Initially numerical simulations were performed, and a tuning of the first modes of in-plane and out-of-plane vibrations was done. The result was obtained for a relatively thick plate. This reduces the accuracy of calculations because they were done assuming the theory of thin shells. Nevertheless, it is clear from a qualitative viewpoint that tuning may be achieved in principle. Future work involving a relatively thick plate will involve a more complicated theory such as the Mindlin-Timoshenko plate theory in ([20]). In order to substantially improve calculations, we observed a relatively “thin” plate to perform further numerical simulations. These simulations showed that it is possible to achieve tuning between the first eigenvalue of the in-plane mode and the second eigenvalue of the out-of-plane mode. Tuning between eigenvalues of different modes of in-plane and out-of-plane vibrations can be achieved by the variation of the radial and thickness parameters of the materials of the components of the functionally graded plates. The effectiveness of the tuning has to be investigated further from the viewpoint of the sensitivity of sensors of angular rates and accelerations.

Acknowledgements This material is based upon work supported financially by the Tshwane University of Technology (TUT). Any opinions, findings and conclusions or recommendations expressed in this material are those of the authors, and TUT therefore does not accept any liability in regard thereto.

Appendix A

The *Lagrangian* of the functionally graded plate (see Fig. 23.1) is give by

$$\mathbb{L} = \int_0^{2\pi} \left[\sum_{j=1}^J \int_{a_{j-1}}^{a_j} \left(\Lambda_D^{(j)} + \Lambda_P^{(j)} \right) dr \right] d\varphi, \tag{23.53}$$

where, a_0 is radius of junction of the j^{th} and $(j + 1)^{th}$ sections ($j = 1, 2, \dots, J$), and $a_J = R$. Furthermore $\Lambda_D^{(j)}$ is the Lagrangian density of the j th thin plate vibrations which are characterised by the in-plane displacements $u^{(j)}$ and $v^{(j)}$. The Lagrangian density of the thin plate vibrations that is characterized by the out-of-plane displacements $w^{(j)}$ is designated by $\Lambda_P^{(j)}$. The Lagrangian density of the in-plane vibrations $\Lambda_D^{(j)}$ can be written as

$$\Lambda_D^{(j)} = \left\{ \frac{\rho_j h_j}{2} \dot{u}^{(j)2} + \dot{v}^{(j)2} - \frac{E_j h_j}{2(1 - \eta_j^2)} \left[\left(\varepsilon_1^{(j)} + \varepsilon_2^{(j)} \right)^2 - 2(1 - \eta_j) \left(\varepsilon_1^{(j)} + \varepsilon_2^{(j)} - \frac{\gamma^{(j)2}}{4} \right) \right] \right\} r; \tag{23.54}$$

similarly the Lagrangian density of the out-of-plane vibration $\Lambda_P^{(j)}$ is given by

$$\Lambda_P^{(j)} = \left\{ \frac{\rho_j h_j}{2} \dot{w}^{(j)2} - \frac{E_j h_j^3}{24(1 - \eta^2)} \left[\left(\chi_1^{(j)} + \chi_2^{(j)} \right)^2 - 2(1 - \eta_j) \left(\chi_1^{(j)} \chi_2^{(j)} - \tau_j^{(j)2} \right) \right] \right\} r. \tag{23.55}$$

Take note of the dot and prime notations used for derivatives elsewhere in this chapter. Below we use the following notation

$$\begin{aligned} \dot{u}^{(j)} &= \frac{\partial u^{(j)}}{\partial t}, \quad \dot{v}^{(j)} = \frac{\partial v^{(j)}}{\partial t}, \quad u_r^{(j)'} = \frac{\partial u^{(j)}}{\partial r}, \quad u_\varphi^{(j)'} = \frac{\partial u^{(j)}}{\partial \varphi}, \quad v_r^{(j)'} = \frac{\partial v^{(j)}}{\partial r}, \quad v_\varphi^{(j)'} = \frac{\partial v^{(j)}}{\partial \varphi}; \\ \ddot{u}^{(j)} &= \frac{\partial^2 u^{(j)}}{\partial t^2}, \quad u_{rr}^{(j)''} = \frac{\partial^2 u^{(j)}}{\partial r^2}, \quad u_{\varphi\varphi}^{(j)''} = \frac{\partial^2 u^{(j)}}{\partial \varphi^2}, \quad u_{r\varphi}^{(j)''} = \frac{\partial^2 u^{(j)}}{\partial r \partial \varphi}; \\ \ddot{v}^{(j)} &= \frac{\partial^2 v^{(j)}}{\partial t^2}, \quad v_{rr}^{(j)''} = \frac{\partial^2 v^{(j)}}{\partial r^2}, \quad v_{\varphi\varphi}^{(j)''} = \frac{\partial^2 v^{(j)}}{\partial \varphi^2}; \quad \text{and } v_{r\varphi}^{(j)''} = \frac{\partial^2 v^{(j)}}{\partial r \partial \varphi}. \end{aligned} \tag{23.56}$$

Strains are given as follows (see Soedel [21])

$$\begin{aligned}
 \varepsilon_1^{(j)} &= \frac{\partial u^{(j)}}{\partial r}, \quad \varepsilon_2^{(j)} = \frac{1}{r} \left(u^{(j)} + \frac{\partial v^{(j)}}{\partial \varphi} \right), \quad \Upsilon^{(j)} = \frac{1}{r} \left(\frac{\partial u^{(j)}}{\partial \varphi} - v^{(j)} \right) + \frac{\partial v}{\partial r}; \\
 \chi_1^{(j)} &= -\frac{\partial^2 w^{(j)}}{\partial r^2}, \quad \chi_2^{(j)} = -\frac{1}{r} \left(\frac{\partial w^{(j)}}{\partial r} + \frac{1}{r} \frac{\partial^2 w^{(j)}}{\partial \varphi^2} \right); \\
 \tau^{(j)} &= \frac{1}{r} \left(\frac{1}{r} \frac{\partial w^{(j)}}{\partial \varphi} - \frac{\partial^2 w^{(j)}}{\partial r \partial \varphi} \right).
 \end{aligned} \tag{23.57}$$

The implicit form of the governing equations of motion are obtained from Hamilton’s variational principle see Goldstein et al. [22]. It follows that

$$\frac{\partial}{\partial t} \frac{\partial \Lambda_D^{(j)}}{\partial \dot{u}^{(j)}} + \frac{\partial}{\partial r} \frac{\partial \Lambda_D^{(j)}}{\partial u_r^{(j)'}} + \frac{\partial}{\partial \varphi} \frac{\partial \Lambda_D^{(j)}}{\partial u_\varphi^{(j)'}} - \frac{\partial \Lambda_D^{(j)}}{\partial u^{(j)}} = 0; \tag{23.58a}$$

$$\frac{\partial}{\partial t} \frac{\partial \Lambda_D^{(j)}}{\partial \dot{v}^{(j)}} + \frac{\partial}{\partial r} \frac{\partial \Lambda_D^{(j)}}{\partial v_r^{(j)'}} + \frac{\partial}{\partial \varphi} \frac{\partial \Lambda_D^{(j)}}{\partial v_\varphi^{(j)'}} - \frac{\partial \Lambda_D^{(j)}}{\partial v^{(j)}} = 0; \tag{23.58b}$$

$$\left[\begin{aligned}
 &\frac{\partial}{\partial \tau} \left(\frac{\partial \Lambda_P^{(j)}}{\partial \dot{w}^{(j)}} \right) + \frac{\partial}{\partial r} \left(\frac{\partial \Lambda_P^{(j)}}{\partial w_r^{(j)'}} \right) + \frac{\partial}{\partial \varphi} \left(\frac{\partial \Lambda_P^{(j)}}{\partial w_\varphi^{(j)'}} \right) - \frac{\partial^2}{\partial r^2} \left(\frac{\partial \Lambda_P^{(j)}}{\partial w_{rr}^{(j)''}} \right) - \\
 &\quad \frac{\partial^2}{\partial r \partial \varphi} \left(\frac{\partial \Lambda_P^{(j)}}{\partial w_{r\varphi}^{(j)''}} \right) - \frac{\partial^2}{\partial \varphi^2} \left(\frac{\partial \Lambda_P^{(j)}}{\partial w_{\varphi\varphi}^{(j)''}} \right)
 \end{aligned} \right] = 0. \tag{23.58c}$$

It follows from Eqs. (23.53)–(23.57) that Eqs. (23.58a) and (23.58b) which characterise in-plane motion are separated from the Eq. (23.58c), which characterises the out-of-plane motion. Note that systems of explicit equations of motion are given in Eqs. (23.1), (23.2) and (23.3).

It is possible to derive the boundary-continuity conditions from Hamiltonian Principle, which can be given as follows

$$u^{(1)}|_{r=a_0} = 0 \quad \text{or} \quad \frac{\partial \Lambda_D^{(1)}}{\partial u_r^{(1)'}} \Big|_{r=a_0} = 0; \tag{23.59}$$

$$v^{(1)}|_{r=a_0} = 0, \quad \text{or} \quad \frac{\partial \Lambda_D^{(1)}}{\partial v_r^{(1)'}} \Big|_{r=a_0} = 0; \tag{23.60}$$

The conditions on the left hand side of Eqs. (23.59) and (23.60) are used for fixed inner rim and the derivatives in (23.59) and (23.60) are used for free inner rim. For j th and $(j + 1)$ st component of the plate we have,

$$u^{(j)}|_{r=a_j} - u^{(j+1)}|_{r=a_j} = 0, \quad \frac{\partial \Lambda_D^{(j)}}{\partial u_r^{(j)'}} \Big|_{r=a_j} - \frac{\partial \Lambda_D^{(j+1)}}{\partial u_r^{(j)'}} \Big|_{r=a_j} = 0; \quad (23.61)$$

$$v^{(j)}|_{r=a_j} - v^{(j+1)}|_{r=a_j} = 0, \quad \frac{\partial \Lambda_D^{(j)}}{\partial v_r^{(j)'}} \Big|_{r=a_j} - \frac{\partial \Lambda_D^{(j+1)}}{\partial v_r^{(j)'}} \Big|_{r=a_j} = 0. \quad (23.62)$$

The conditions on the left hand side of Eqs. (23.61) and (23.62) characterise the continuity of the displacements in the radial and tangential directions, while the conditions on the right hand side characterise the equality of action-reaction forces in the radial and tangential directions on junctions of the j^{th} and $(j + 1)^{\text{st}}$ components of the functionally graded plate ($j = 1, 2, \dots, J - 1$).

For the outer rim of the plate, we have

$$u^{(J)}|_{r=R} = 0 \quad \text{or} \quad \frac{\partial \Lambda^{(J)}}{\partial u^{(J)}} \Big|_{r=R} = 0; \quad (23.63)$$

$$v^{(J)}|_{r=R} = 0, \quad \text{or} \quad \frac{\partial \Lambda^{(J)}}{\partial v^{(J)}} \Big|_{r=R} = 0; \quad (23.64)$$

the left hand side of Eqs. (23.63) and (23.64) are used for fixed outer rim of the plate and the right hand side are used for the free outer rim. In our case the inner rim of the first component of the plate is fixed in the stem and the outer rim is free. Hence, we used the following boundary-continuity conditions for inner and outer rims, respectively

$$u^{(1)}|_{r=a_0} = v^{(1)}|_{r=a_0} = 0; \quad (23.65)$$

$$\frac{\partial \Lambda_D^{(J)}}{\partial u_r^{(J)'}} \Big|_{r=R} = \frac{\partial \Lambda_D^{(J)}}{\partial v_r^{(J)'}} \Big|_{r=R} = 0. \quad (23.66)$$

Note that the partial derivatives $\frac{\partial \Lambda_D^{(j)}}{\partial u_r^{(j)'}}$ and $\frac{\partial \Lambda_D^{(j)}}{\partial v_r^{(j)'}}$ used in the boundary-continuity conditions are given by

$$\frac{\partial \Lambda_D^{(j)}}{\partial u_r^{(j)'}} = -\frac{E_j h_j}{1 - \eta_j^2} \left[\frac{\partial u^{(j)}}{\partial r} + \frac{\eta_j}{r} \left(u^{(j)} + \frac{\partial v^{(j)}}{\partial \varphi} \right) \right]; \quad (23.67)$$

$$\frac{\partial \Lambda_D^{(j)}}{\partial v_r^{(j)'}} = -\frac{E_j h_j}{2(1 + \eta_j)} \left[\frac{\partial v^{(j)}}{\partial r} + \frac{1}{r} \left(\frac{\partial u^{(j)}}{\partial \varphi} - v^{(j)} \right) \right]. \quad (23.68)$$

The boundary-continuity conditions for out-of-plane vibration of the functionally graded plate is obtained from Hamilton's variational Principle as follows

$$w^{(1)}|_{r=a_0} = 0 \quad \text{or} \quad Q^{(1)}|_{r=a_0} = 0; \quad (23.69)$$

$$w_r^{(1)'}|_{r=a_0} = 0, \quad \text{or} \quad M^{(1)}|_{r=a_0} = 0. \tag{23.70}$$

The left hand side of Eqs. (23.69) and (23.70) corresponds to the fixed inner rim of the first component of the plate and the right-hand side corresponds to the free rim of the plate.

$$w^{(j)}|_{r=a_j} - w^{(j+1)}|_{r=a_j} = 0 \quad w_r^{(j)'}|_{r=a_j} - w_r^{(j+1)'}|_{r=a_j} = 0; \tag{23.71}$$

$$Q^{(j)}|_{r=a_j} - Q^{(j+1)}|_{r=a_j} = 0 \quad M^{(j)}|_{r=a_j} - M^{(j+1)}|_{r=a_j} = 0. \tag{23.72}$$

Eq. (23.71) corresponds to the continuity of the out-of-plane displacements and continuity of their first derivatives (angles of slopes) at the junctions of the $(j)^{th}$ and $(j + 1)^{st}$ components of the plate. Equation (23.72) shows the equalities between action-reaction of the shear forces (Q) and torques (M) at junctions of the components. Finally at $r = R$

$$w^{(j)}|_{r=R} = 0 \quad \text{or} \quad Q^{(j)}|_{r=R} = 0; \tag{23.73}$$

$$w_r^{(j)'}|_{r=R} = 0, \quad \text{or} \quad M^{(j)}|_{r=R} = 0. \tag{23.74}$$

As above the left hand side of Eqs. (23.69) and (23.70) correspond to the fixed outer rim of the plate and the right hand side corresponds to the free conditions of the outer rim of the plate. Note that the shear forces $Q^{(j)}$ and torques $M^{(j)}$ are given by

$$\begin{aligned}
 Q^{(j)} &= \frac{\partial \Lambda_P^{(j)}}{\partial w_r^{(j)'}} - \frac{\partial}{\partial r} \left(\frac{\partial \Lambda_P^{(j)}}{\partial w_{rr}^{(j)'}} \right) + \frac{\partial}{\partial \varphi} \left(\frac{\partial \Lambda_P^{(j)}}{\partial w_{\varphi r}^{(j)'}} \right); \\
 &= \frac{E_j h_j^3 r_j}{12 (1 - \eta_j^2)} \left(\frac{\partial^3 w^{(j)}}{\partial r^3} + \frac{\partial^2 w^{(j)}}{r \partial r^2} - \frac{1}{r^2} \frac{\partial w^{(j)}}{\partial r} + \frac{2 - \eta_j}{r} \frac{\partial^3 w^{(j)}}{\partial \varphi^2 \partial r} - \frac{3 - \eta_j}{r^3} \frac{\partial^2 w^{(j)}}{\partial \varphi^2} \right); \tag{23.75}
 \end{aligned}$$

$$M^{(j)} = \frac{\partial \Lambda_P^{(j)}}{\partial w_{rr}^{(j)'}} = \frac{E_j h_j^3 r_j}{12 (1 - \eta_j^2)} \left[\frac{\partial^2 w^{(j)}}{\partial r^2} + \frac{\eta_j}{r} \left(\frac{\partial w^{(j)}}{\partial r} + \frac{1}{r} \frac{\partial^2 w^{(j)}}{\partial r^2} \right) \right]. \tag{23.76}$$

References

1. Arutunyan, N.H., Abramiyan, B.L.: Torsion of Elastic Bodies. Fizmatgiz, Moscow (1963).(in Russ.)
2. Arutunyan, N.H., Naumov, V.E., Radaev, Y.N.: Waves in the Growing Elastic Bodies. Institute for Problems in Mechanics of USSR Academy of Science, Moscow (1989).(in Russ.)
3. Bashmal, S., Bhat, R., Rakheja, S.: In-plane free vibration analysis of an annular disk with point elastic support. Shock Vibrat. **18**, 627–640 (2011)

4. Love, A.E.H.: *Treatise on the Mathematical Theory of Elasticity*. Cambridge University Press, London (1893)
5. Timoshenko, S., Woinowsky-Krieger, S.: *Theory of Plates and Shells*. McGraw-Hill Company, New York (1959)
6. Joubert, S.V., Shatalov, M.Y., Fay, T.H.: On numerically solving an eigenvalue problem arising in a resonator gyroscope. *Appl. Math. Comput.* **246**, 561–571 (2014)
7. Leissa, A.W.: *Vibration of Plates-NASA SP-160*. US Government Printing Office, Washington, D.C. (1969)
8. Leissa, A.W., Qatu, M.S.: *Vibrations of Continuous Systems*. McGraw-Hill, New York (2011)
9. Jia, S.H., Chun, S.B., Lee, C.W.: Evaluation of the longitudinal coupled vibrations in rotating flexible disks/spindle systems. *J. Sound Vibrat.* **208**(2), 175–187 (1997)
10. Ouyang, H., Mottershead, J.E., Brookfield, D.J., James, S., Cartmell, M.P.: A methodology for the determination of dynamic instabilities in a car disc brake. *Int. J. Veh. Des.* **23**(3–4), 241–262 (2000)
11. Burdess, J.S., Wren, T.: The theory of a piezoelectric-disc gyroscope. *IEEE Trans. Aerosp. Electron. Syst.* **22**(4), 110–118 (1986)
12. Sedebo, G.T., Joubert, S.V., Shatalov, M.Y.: An analytical theory for a three-dimensional thick-disc, thin-plate vibratory gyroscope. *J. Phys.: Conf. Ser.* **991**(1), 1–8 (2018)
13. Sedebo, G.T.: *The Dynamics of a Tuning-Disc Vibratory Gyroscope*. D. Tech. thesis. Tshwane University of Technology (TUT), Pretoria (2019)
14. Rourke, A.K., McWilliam, S., Fox, C.H.J.: Frequency trimming of a vibrating ring-based multi-axis rate sensor. *J. Sound and Vibrat.* **280**, 495–530 (2005)
15. Zhuravlev, VPh.: Theoretical Foundations of the wave-based solid-state gyroscope (WSG). *Izv. Akad Nauk Mekh Tverd Tela*, No. **3**, 6–19 (1995)
16. Klimov, D.M., Zhuravlev, VPh., Zbanov, Yu.K.: Quartz Hemispherical Resonator (Wave-Based Solid-State Gyroscope). Kim L.A, Moscow (2017).(in Russ.)
17. Leissa, A.W.: *Vibration of Shells*. Acoustical Society of America, New York (1993)
18. Novozhilov, V.V.: *The Theory of Thin Shells*. Wolters-Noordhoff, Groningen, The Netherlands (1970)
19. Gol'denveizer, A.L.: *Theory of Elastic Thin Shells*. Pergamon Press, Oxford, London, New York, Paris (1961)
20. Magrab, E.B.: *Vibrations of Elastic Structural Members*. Sijthoff & Noordhoff, Alphen aan den Rijn, Maryland (1979)
21. Soedel, W.: *Vibrations of Shells and Plates*. Marcel Dekker Inc, New York (2004)
22. Goldstein, H., Poole, C.P., Safko, J.L.: *Classical Mechanics*. Addison-Wesley, New York (2000)

Chapter 24

Adhesive Contact Problems of the Theory of Viscoelasticity



Nugzar Shavlakadze

Abstract The approximate solutions of singular integro-differential equations related to the problems of interaction of an elastic thin finite non-homogeneous patch with a plate are considered, provided that the materials of plate and patch possess the creep property. Using the method of orthogonal polynomials, the problem reduced to the infinite system of Volterra integral equations. The asymptotic analysis is also performed. The quasi-completely regularity of the obtained system is proved.

Keywords Viscoelasticity · Contact problems · Singular integro-differential equation · Method of orthogonal polynomials

24.1 Introduction

The considerable development of the hereditary theory of Bolzano–Volterra mechanics has been defined by various technical applications in the theory of metals, plastics and concrete and in the mining engineering. The fundamentals of the theory of viscoelasticity, the methods for solving linear and nonlinear problems of the theory of creep, the problems of mechanics of inhomogeneous aging viscoelastic materials, some boundary value problems of the theory of growing solids, the contact and mixed problems of the theory of viscoelasticity for composite inhomogeneous aging and nonlinearly aging bodies are considered in [1–4].

The full investigation of various possible forms of viscoelastic relations and some aspects of the general theory of viscoelasticity is studied in [5–8]. Research on the field of creep materials can be found in [9–12].

Contact and mixed boundary value problems on the transfer of the load from elastic thin-walled elements (stringers, inclusions, patches) to massive deformable (including aging viscoelastic) bodies, as well as on the indentation of a rigid stamp on the surface of a viscoelastic body, represent an urgent problem both in theoretical

N. Shavlakadze (✉)
Tbilisi State University A. Razmadze Mathematical Institute,
Georgian Technical University, Tbilisi, Georgia
e-mail: nusha1961@yahoo.com

and applied aspect. Problems of this type are often encountered in engineering applications and lend themselves to rigorous mathematical research due to their applied significance.

Exact and approximate solutions of static contact problems for different domains reinforced with non-homogeneous elastic thin inclusions and patches were obtained, and the behavior of the contact stresses at the ends of the contact line has been investigated [13–16]. One type of analysis assumes continuous interaction and the other the adhesive contact of thin-shared elements (stringers or inclusions) with massive deformable bodies. As is known, stringers, patches and inclusions, such as rigid punch and cuts, are areas of stress concentration. Therefore, the study of the problems of stress concentration and the development of various methods for their reduction is of great importance in engineering practice.

In work [17], we consider integro-differential equations with a variable coefficient relating to interaction of an elastic thin finite inclusion and plate, when the inclusion and plate materials possess the creep property. Here, continuous contact between inclusion and plate is considered. The solutions of the integro-differential equations of first order are obtained on the basis of investigations of different boundary value problems of the theory of analytic functions. The asymptotic behavior of unknown contact stresses is established.

In this paper, contact with a thin layer of glue is studied when the patch, plate and adhesive materials have the property of creep. A two-dimensional singular integro-differential equation was obtained. Here, the asymptotic analysis was also carried out, and the approximate solutions were obtained for various cases.

24.2 Formulation of the Problems and Reduction to the Integral Equations

Let a finite non-homogeneous patch with modulus of elasticity E_1 , thickness $h_1(x)$ and Poisson's coefficient ν_1 be attached to the plate (E_2, ν_2), which occupies the entire complex plane and is in the condition of a plane deformation. It is assumed that the patch, as a thin element, is glued to the plate along the real axis, has no bending rigidity, is in the uniaxial stressed state and is subject only to tension with the tangential stress $q_0(x)H(t - t_0)$ ($H(t)$ is the unit Heaviside function). The one-dimensional contact between the plate and patch is realized by a thin glue layer with thickness h_0 and modulus of shear G_0 .

It is assumed that the plate, patch and glue layer materials have the creep property which is characterized by the non-homogeneity of the aging process and has different creep measures $C_i(t, \tau) = \varphi_i(\tau)[1 - e^{-\gamma(t-\tau)}]$, where $\varphi_i(\tau)$ is the functions that defining the aging process of the plate, patch and glue layer materials; the age of different materials is $\tau_i(x) = \tau_i = \text{const}$, $\gamma = \text{const} > 0$, $i = 1, 2, 3$.

Besides, the plate Poisson's coefficients for elastic-instant deformation $\nu_2(t)$ and creep deformation $\nu_2(t, \tau)$ are the same and constant: $\nu_2(t) = \nu_2(t, \tau) = \nu_2 = \text{const}$.

Assuming that every element of the glue layer is under condition of pure shear, the contact condition has the form [18]

$$u_1(t, x) - u_2(t, x, 0) = k_0(I - L_3)q(t, x), \quad |x| \leq 1 \tag{24.1}$$

where $u_2(t, x, y)$ is displacement of the plate points along the ox -axis and $u_1(t, x)$ is displacement of the patch points along the ox -axis, I is the unit operator, $k_0 := h_0/G_0$.

We have to define the law of distribution of tangential contact stresses $q(t, x)$ on the line of contact and the asymptotic behavior of these stresses at the end of the patch.

To define the unknown contact stresses, we obtain the following integral equation (see [1-4])

$$\begin{aligned} & \frac{2(1 - \nu_2^2)}{\pi E_2} (I - L_2) \int_{-1}^1 \frac{q(t, y) dy}{y - x} \\ &= \frac{1}{E(x)} (I - L_1) \int_{-1}^x [q(t, y) - q_0(y)H(t - t_0)] dy - k_0(I - L_3)q'(t, x), \quad |x| < 1 \\ & \int_{-1}^1 [q(t, y) - q_0(y)H(t - t_0)] dy = 0 \end{aligned} \tag{24.2}$$

where the time operators $L_i, i = 1, 2, 3$ act on an arbitrary function in the following manner

$$\begin{aligned} (I - L_i)\psi(t) &= \psi(t) - \int_{\tau_i^0}^t K_i(t + \rho_i, \tau + \rho_i)\psi(\tau) d\tau, \quad \rho_i = t - \tau_i^0 \quad i = 1, 2, 3 \\ K_i(t, \tau) &= E_i \frac{\partial C_i(t, \tau)}{\partial \tau}, \quad i = 1, 2 \quad K_3(t, \tau) = G_0 \frac{\partial C_3(t, \tau)}{\partial \tau}, \\ E(x) &= \frac{E_1 h_1(x)}{1 - \nu_1^2}, \end{aligned}$$

$\tau_i^0 = t_0$ is the instant of load application.

Introducing the notation

$$\varphi(t, x) = \int_{-1}^x [q(t, y) - q_0(y)H(t - t_0)] dy, \quad \lambda = \frac{2(1 - \nu_2^2)}{E_2},$$

from (24.2), we obtain the following two-dimensional integro-differential equation

$$\begin{aligned} & \frac{\lambda}{\pi}(I - L_2) \int_{-1}^1 \frac{\varphi'(t, y)}{y - x} dy \\ &= \frac{1}{E(x)}(I - L_1)\varphi(t, x) - k_0(I - L_3)\varphi''(t, x) + g(t, x), \quad |x| < 1 \quad (24.3) \\ g(t, x) &= -\frac{\lambda}{\pi} \left((1 - E_2\varphi_2(t))(1 - e^{-\gamma(t-t_0)}) \right) \\ & \int_{-1}^1 \frac{q_0(y)}{y - x} dy - k_0q'_0(x) \left((1 - G_0\varphi_3(t))(1 - e^{-\gamma(t-t_0)}) \right). \end{aligned}$$

with the conditions

$$\varphi(t, 1) = 0, \quad t \geq t_0. \quad (24.4)$$

(In the sequel, the dot means a derivative with respect to the first variable t , and the prime means a derivative with respect to the second variable x).

Thus, the above posed boundary contact problem reduced to the solution of singular integro-differential equation (SIDE) with the condition (24.4). From the symmetry of the problem, we assume, that $E(x)$ and $q_0(x)$ are even and odd functions, respectively. The solution of problem (24.3) under condition (24.4) with respect variable x can be sought in the class of even functions. Moreover, we assume that the function $q_0(x)$ is continuous in the Hölder's sense and is a continuous up to the first-order derivative on an interval $[-1, 1]$, i.e., $q_0 \in C^1([-1, 1])$.

24.3 The Asymptotic Investigation

Under the assumption that

$$\begin{aligned} E(x) &= (1 - x^2)^\omega b_0(x), \quad (24.5) \\ \omega &= \text{const} > 0, \quad b_0(x) = b_0(-x), \quad b_0 \in C([-1, 1]), \quad b_0(x) \geq c_0 = \text{const} > 0, \end{aligned}$$

the solution of problem (24.3) and (24.4) will be sought in the class of even functions whose derivative with respect of variable x can be are represented as follows

$$\varphi'(t, x) = (1 - x^2)^\alpha g_0(t, x), \quad \alpha > -1, \quad (24.6)$$

where $g_0(t, x) = -g_0(t, -x)$, $g_0 \in C^1([-1, 1])$, $g_0(t, x) \neq 0$, $x \in [-1, 1]$. $\varphi'(t, x)$ represents the unknown tangential contact stress.

Introducing the notation

$$\Phi_0(x, t) = \int_{-1}^1 \frac{(1 - s^2)^\alpha g_0(t, s)}{s - x} ds$$

by virtue of the well-known asymptotic formula [19] we have for $-1 < \alpha < 0$

$$\begin{aligned} \Phi_0(x, t) &= \mp \pi \operatorname{ctg} \pi \alpha g_0(t, \mp 1) 2^\alpha (1 \pm x)^\alpha + \Phi_\mp(x, t), \quad x \rightarrow \mp 1; \\ \Phi_\mp(x, t) &= \Phi_\mp^*(x, t) (1 \pm x)^{\alpha_\pm}, \quad \alpha_\pm = \operatorname{const} > \alpha \end{aligned}$$

and for $\alpha = 0$

$$\Phi_0(x, t) = \mp g_0(t, \mp 1) \ln(1 \pm x) + \tilde{\Phi}_\mp(x, t), \quad x \rightarrow \mp 1.$$

The functions $\Phi_\mp^*(x, t)$ and $\tilde{\Phi}_\mp(x, t)$ satisfy (H) condition in a neighborhood of the points $x = \mp 1$ respectively.

In case $\alpha > 0$ the function $\Phi_0(x, t)$ belongs to the (H) class in a neighborhood of the points $x = \pm 1$.

In addition, we have [20]

$$\begin{aligned} \int_{-1}^x (1 - s^2)^\alpha g_0(t, s) ds &= \frac{2^\alpha (1 \pm x)^{\alpha+1}}{\alpha + 1} g_0(t, \mp 1) F(\alpha + 1, -\alpha, 2 + \alpha, (1 \pm x)/2) \\ &+ G_\mp(x, t), \quad x \rightarrow \mp 1, \\ \lim_{x \rightarrow \mp 1} G_\mp(x, t) (1 \pm x)^{-(\alpha+1)} &= 0 \end{aligned}$$

where $F(a, b, c, x)$ is a hypergeometric Gaussian function.

The case $-1 < \alpha < 0$ of interest does not represent, since negative values of the indicator α contradict the physical meaning of the condition (24.1).

Let $0 \leq \alpha \leq 1$, then in a neighborhood of the points $x = -1$ the equation (24.3) can be written in the following form

$$\begin{aligned} (I - L_2)\Psi(x, t) + \frac{2^\alpha (1 + x)^{2+\varepsilon} (I - L_1)g_0(-1, t)}{2^\omega (\alpha + 1) (1 + x)^\omega b_0(-1)} + (I - L_1)G_-(x, t) (1 + x)^{1+\varepsilon-\alpha} \\ - k_0 2^\alpha (1 + x)^\varepsilon (I - L_3)\tilde{g}_0(-1, t) = g(-1, t) (1 + x)^{1+\varepsilon-\alpha} \end{aligned} \tag{24.7}$$

$$\Psi(x, t) = \begin{cases} \lambda g_0(-1, t) (1 + x)^{1+\varepsilon} \ln(1 + x) - \frac{\lambda}{\pi} (1 + x)^{1+\varepsilon} \tilde{\Phi}_-(x, t), & \text{for } \alpha = 0, \\ -\frac{\lambda}{\pi} (1 + x)^{1+\varepsilon-\alpha} \Phi_0(x, t), & \text{for } \alpha \neq 0 \end{cases}$$

where ε is an arbitrarily small positive number. When passing to the limit $x \rightarrow -1$, the analysis of the obtained equations leads to the necessity of satisfying inequality $2 + \varepsilon > \omega$, i.e., $\omega \leq 2$.

In case $\alpha > 1$ from (24.7), it follows that $\alpha = \omega - 1$.

An analogous result is obtained in the neighborhood of the point $x = 1$.

The obtained results can be formulated as follows

Theorem 1 Assume that (24.5) holds, if the problem (24.3), (24.4) has the solution in the form (24.6), then:

- If $\omega > 2$ then $\alpha = \omega - 1$, ($\alpha > 1$)
- If $\omega \leq 2$ then $0 \leq \alpha \leq 1$.

Conclusion. If the patch rigidity varies by the law

$$E(x) = (1 - x^2)^{n+\frac{1}{2}} b_0(x),$$

where $b_0(x) > 0$ for $|x| \leq 1$, $b_0(x) = b_0(-x)$, $n \geq 0$ is integer, then from the above asymptotic analysis, we obtain:

$$\alpha = n - \frac{1}{2}, \quad \text{for } n = 2, 3, \dots$$

and $0 < \alpha < 1$ for $n = 0$ or $n = 1$ (the same result is obtained for $E(x) = b_0(x) > 0$ or $E(x) = \text{const}$, $|x| \leq 1$).

24.4 An Approximate Solution of SIDE (3)

From the relation

$$\begin{aligned} \frac{1}{\pi} \int_{-1}^1 \frac{(1-s)^\alpha (1+s)^\beta P_m^{(\alpha,\beta)}(s)}{s-x} ds &= \text{ctg} \pi \alpha (1-x)^\alpha (1+x)^\beta P_m^{(\alpha,\beta)}(x) \\ &- \frac{2^{\alpha+\beta} \Gamma(\alpha) \Gamma(\beta+m+1)}{\pi \Gamma(\alpha+\beta+m+1)} F(m+1, -\alpha-\beta-m, 1-\alpha, (1-x)/2) \end{aligned}$$

obtained by Tricomi [21] for orthogonal Jacobi polynomials $P_m^{(\alpha,\beta)}(x)$ and from the well-known equality (see [22])

$$m! P_m^{(\alpha,\beta)}(1-2x) = \frac{\Gamma(\alpha+m+1)}{\Gamma(1+\alpha)} F(\alpha+\beta+m+1, -m, 1+\alpha, x)$$

we get the following spectral relation for the Hilbert singular operator

$$\int_{-1}^1 \frac{(1-s^2)^{n-1/2} P_m^{(n-1/2, n-1/2)}(s)}{s-x} ds = (-1)^n 2^{2n-1} \pi P_{m+2n-1}^{(1/2-n, 1/2-n)}(x), \quad (24.8)$$

where $\Gamma(z)$ is the known Gamma function.

1. On the basis of the above asymptotic analysis performed in the cases

$$n = 0; \quad n = 1; \quad E(x) = b_0(x) > 0; \quad E(x) = \text{const}, \quad |x| \leq 1;$$

a solution of equation (24.3) will be sought in the form

$$\varphi'(t, x) = \sqrt{1-x^2} \sum_{k=1}^{\infty} X_k(t) P_k^{(1/2, 1/2)}(x), \quad (24.9)$$

where the function $X_k(t)$ have to be defined, $k = 1, 2, \dots$

Using the relation (24.8) and the Rodrigues formula (see.[23]) for (24.9), we obtain

$$\int_{-1}^1 \frac{\sqrt{1-t^2} P_k^{(1/2, 1/2)}(t) dt}{t-x} = -2\pi P_{k+1}^{(-1/2, -1/2)}(x),$$

$$\varphi(t, x) = -(1-x^2)^{3/2} \sum_{k=1}^{\infty} \frac{X_k(t)}{2k} P_{k-1}^{(3/2, 3/2)}(x),$$

$$\varphi''(t, x) = -2(1-x^2)^{-1/2} \sum_{k=1}^{\infty} k X_k(t) P_{k+1}^{(-1/2, -1/2)}(x). \quad (24.10)$$

Substituting relation (24.9), (24.10) into Eq. (24.3), we have

$$-\frac{(1-x^2)^{3/2}}{E(x)} (I - L_1) \sum_{r=1}^{\infty} \frac{X_k(t)}{2k} P_{k-1}^{(3/2, 3/2)}(x) - 2\lambda_0 (I - L_2) \sum_{k=1}^{\infty} X_k(t) P_{k+1}^{(-1/2, -1/2)}(x) + 2k_0 (1-x^2)^{-1/2} (I - L_3) \sum_{k=1}^{\infty} k X_k(t) P_{k+1}^{(-1/2, -1/2)}(x) = g(t, x), \quad |x| \leq 1. \quad (24.11)$$

Multiplying both part of equality (24.11) by $P_{m+1}^{(-1/2, -1/2)}(x)$ and integrating on the interval $(-1, 1)$, we obtain an infinite system of Volterra's linear integral equations

$$\begin{aligned}
 k_0 m \left(\frac{\Gamma(m+3/2)}{\Gamma(m+2)} \right)^2 (I - L_3) X_m(t) - \sum_{k=1}^{\infty} R_{mk}^{(2)} (I - L_2) X_k(t) \\
 - \sum_{k=1}^{\infty} \frac{R_{mk}^{(1)}}{k} (I - L_1) X_k(t) = g_m(t), \quad m = 1, 2, \dots
 \end{aligned} \tag{24.12}$$

where

$$\begin{aligned}
 R_{mk}^{(1)} &= \frac{1}{2} \int_{-1}^1 \frac{(1-x^2)^{3/2}}{E(x)} P_{k-1}^{(3/2,3/2)}(x) P_{m+1}^{(-1/2,-1/2)}(x) dx, \\
 R_{mk}^{(2)} &= -2\lambda \int_{-1}^1 P_{k+1}^{(-1/2,-1/2)}(x) P_{m+1}^{(-1/2,-1/2)}(x) dx, \\
 g_m(t) &= \int_{-1}^1 g(t, x) P_{m+1}^{(-1/2,-1/2)}(x) dx.
 \end{aligned}$$

Introducing the notation

$$T_m(t) = \omega_m \left[k_0 X_m(t) - \sum_{k=1}^{\infty} \frac{R_{mk}^{(1)}}{k \omega_k} X_k(t) - \sum_{k=1}^{\infty} \frac{R_{mk}^{(2)}}{\omega_k} X_k(t) \right],$$

where $\omega_m = m \left(\frac{\Gamma(m+3/2)}{\Gamma(m+2)} \right)^2 \rightarrow 1, m \rightarrow \infty$, system (24.12) will take the form

$$\begin{aligned}
 T_m(t) - k_0 \int_{t_0}^t K_3(t-\tau) X_k(\tau) d\tau + \sum_{k=1}^{\infty} \frac{R_{mk}^{(1)}}{k \omega_k} \int_{t_0}^t K_1(t-\tau) X_k(\tau) d\tau \\
 + \sum_{k=1}^{\infty} \frac{R_{mk}^{(2)}}{\omega_k} \int_{t_0}^t K_2(t-\tau) X_k(\tau) d\tau = g_m(t) \quad m = 1, 2, \dots
 \end{aligned} \tag{24.13}$$

In condition $G_0 \varphi_3(t) = E_1 \varphi_1(t) = E_2 \varphi_2(t)$ system (24.13) reduces to the following ordinary differential equation of second order

$$\ddot{T}_m(t) + \gamma(1 + G_0 \varphi_3(t)) \dot{T}_m(t) = \ddot{g}_m(t) + \gamma \dot{g}_m(t), \tag{24.14}$$

with the initial conditions:

$$T_m(t_0) = 0, \quad \dot{T}_m(t_0) = \dot{g}_m(t_0).$$

The solving of this differential equation gives an infinite system of linear algebraic equation with respect $X_m(t)$, $m = 1, 2, \dots$

$$k_0 X_m(t) - \sum_{k=1}^{\infty} \frac{R_{mk}^{(1)}}{k\omega_k} X_k(t) - \sum_{k=1}^{\infty} \frac{R_{mk}^{(2)}}{\omega_k} X_k(t) = \frac{T_m(t)}{\omega_m} \tag{24.15}$$

where

$$T_m(t) = \dot{g}_m(t_0) \int_{t_0}^t \frac{d\tau}{\alpha(\tau)} + \int_{t_0}^t \frac{d\tau}{\alpha(\tau)} \int_{t_0}^{\tau} [\ddot{g}_m(s) + \gamma \dot{g}_m(s)] \alpha(s) ds,$$

$$\alpha(t) = \exp \int_{t_0}^t \gamma (1 + G_0 \varphi_3(s)) ds.$$

Let us investigate system (24.15) for regularity in the class of bounded sequences. Using the known relations for the Chebyshev first order polynomials and for the Gamma function [20]

$$P_m^{(-1/2, -1/2)}(x) = \frac{\Gamma(m + 1/2)}{\sqrt{\pi} \Gamma(m + 1)} T_m(x), \quad T_m(\cos \theta) = \cos m\theta$$

$$\lim_{m \rightarrow \infty} m^{b-a} \frac{\Gamma(m + a)}{\Gamma(m + b)} = 1$$

we have

$$R_{mk}^{(2)} = - \frac{2\lambda\alpha(k)\beta(m)}{\pi\sqrt{(k+1)(m+1)}} \int_0^{\pi} \cos(k+1)\theta \cos(m+1)\theta \sin \theta d\theta = - \frac{2\lambda\alpha(k)\beta(k)}{\pi\sqrt{(k+1)(m+1)}}$$

$$\times \begin{cases} 1 - \frac{1}{(2m+3)(2m+1)}, & k = m, \\ -\frac{(-1)^{k+m} + 1}{2} \left[\frac{1}{(k+m+3)(k+m+1)} + \frac{1}{(k-m+1)(k-m-1)} \right], & k \neq m, \end{cases}$$

$$= \begin{cases} O(m^{-1}), & k = m, \quad m \rightarrow \infty, \\ O(m^{-5/2}), \quad O(k^{-5/2}), & k \neq m, \quad m \rightarrow \infty, \quad k \rightarrow \infty, \end{cases}$$

where $\alpha(k), \beta(m) \rightarrow 1$, when $k, m \rightarrow \infty$.

By virtue of the Darboux asymptotic formula (see [23]), we obtain analogous estimates for

$$R_{mk}^{(1)} = \begin{cases} O(m^{-1}), & k = m, \quad m \rightarrow \infty \\ O(m^{-5/2}), \quad O(k^{-1/2}), & k \neq m, \quad m \rightarrow \infty, \quad k \rightarrow \infty \end{cases}$$

and the right-hand side $\frac{T_m(t)}{\omega_m}$ of equation (24.15) satisfies at least the estimate

$$\frac{T_m(t)}{\omega_m} = O(m^{-1/2}), \quad m \rightarrow \infty.$$

2. In case when $n = 2$, the solution of equation (24.3) will be sought in the form

$$\varphi'(t, x) = (1 - x^2)^{3/2} \sum_{k=1}^{\infty} Y_k(t) P_k^{(3/2, 3/2)}(x), \tag{24.16}$$

where the functions $Y_k(t)$ have to be defined, $k = 1, 2, \dots$

Using the relation arising from (24.8) and from the Rodrigues formula (see. [23]) for the orthogonal Jacobi polynomials, we get

$$\begin{aligned} \frac{1}{\pi} \int_{-1}^1 \frac{(1 - x^2)^{3/2} P_k^{(3/2, 3/2)}(t) dt}{t - x} &= -2\pi P_{k+1}^{(-3/2, -3/2)}(x), \\ \varphi(t, x) &= -(1 - x^2)^{5/2} \sum_{k=1}^{\infty} \frac{Y_k(t)}{2k} P_{k-1}^{(5/2, 5/2)}(x), \\ \varphi''(t, x) &= -2(1 - x^2)^{1/2} \sum_{k=1}^{\infty} k Y_k(t) P_{k+1}^{(1/2, 1/2)}(x). \end{aligned} \tag{24.17}$$

Similarly as for system (24.15), we obtain

$$\delta_m Y_m(t) - \sum_{k=1}^{\infty} \left(R_{mk}^{(3)} + \frac{R_{mk}^{(4)}}{k} \right) Y_k(t) = \tilde{T}_m(t), \quad m = 1, 2, \dots, \tag{24.18}$$

where

$$\begin{aligned} R_{mk}^{(3)} &= -2\lambda \int_{-1}^1 P_{k+1}^{(-3/2, -3/2)}(x) P_{m+1}^{(1/2, 1/2)}(x) dx, \\ R_{mk}^{(4)} &= \frac{1}{2} \int_{-1}^1 \frac{1}{b_0(x)} P_{k-1}^{(5/2, 5/2)}(x) P_{m+1}^{(1/2, 1/2)}(x) dx, \\ \tilde{g}_m(t) &= \int_{-1}^1 g(t, x) P_{m+1}^{(1/2, 1/2)}(x) dx, \\ \delta_m &= 4k_0 m \left(\frac{\Gamma(m + 5/2)}{\Gamma(m + 3)} \right)^2 \rightarrow 1, \quad m \rightarrow \infty \\ \tilde{T}_m(t) &= \dot{\tilde{g}}_m(t_0) \int_{t_0}^t \frac{d\tau}{\alpha(\tau)} + \int_{t_0}^t \frac{d\tau}{\alpha(\tau)} \int_{t_0}^{\tau} [\ddot{\tilde{g}}_m(s) + \gamma \dot{\tilde{g}}_m(s)] \alpha(s) ds. \end{aligned}$$

Using again the Darboux formula, and the well-known relation for the Chebyshev second-order polynomials (see [20, 23])

$$P_m^{(1/2,1/2)}(x) = \frac{\Gamma(m+3/2)}{\sqrt{\pi}\Gamma(m+2)}U_m(x), \quad U_m(\cos\theta) = \frac{\sin(n+1)\theta}{\sin\theta}.$$

we obtain the following estimates:

$$R_{mk}^{(3)} = \begin{cases} O(m^{-1}), & k = m, \quad m \rightarrow \infty, \\ O(m^{-5/2}), \quad O(k^{-5/2}) & k \neq m, \quad m \rightarrow \infty, \quad k \rightarrow \infty, \end{cases}$$

$$R_{mk}^{(4)} = \begin{cases} O(m^{-1}), & k = m, \quad m \rightarrow \infty, \\ O(m^{-1/2}), \quad O(k^{-1/2}) & k \neq m, \quad m \rightarrow \infty, \quad k \rightarrow \infty, \end{cases}$$

$$\tilde{g}_m = O(m^{-1/2}), \quad m \rightarrow \infty.$$

Thus, systems (24.15) and (24.18) are quasi-completely regular for any positive values of parameters k_0 and λ in the class of bounded sequences.

On the basis of the Hilbert alternatives [24, 25], if the determinants of the corresponding finite systems of linear algebraic equations are other than zero, then systems (24.15) and (24.18) will have unique solutions in the class of bounded sequences. Therefore, by the equivalence of system (24.15), (or (24.18)) and SIDE (24.3) the latter has a unique solution.

24.5 Discussion and Numerical Results

Asymptotic estimates for the solution of integro-differential equation (24.2) are obtained. A method of reduction for infinite regular systems of linear algebraic equations is justified. For any law of variations of the stiffness of the patch, tangential contact stresses have finite values at the ends of patch.

To obtain numerical results, specific values of the aging functions of the plate, patch and glue materials considered in the form

$$\begin{aligned} \varphi_1(t) &= 0.0098\varphi_3(t), \\ \varphi_2(t) &= 0.00123\varphi_3(t), \\ \varphi_3(t) &= 0.09 \cdot 10^{-10} + \frac{4,82 \cdot 10^{-10}}{t}. \end{aligned}$$

The numerical values of the remaining parameters of the problem are taken as follows:

$$E_1 = 120 \times 10^9 \text{ MPa}, \nu_1 = 0,5, E_2 = 95 \times 10^9 \text{ MPa}, \nu_2 = 0,3, G_0^{(1)} = 0.117 \times 10^9 \text{ MPa}, \\ (G_0^{(2)} = 11.7 \times 10^9 \text{ MPa}), \\ h_0 = 5 \times 10^{-4} \text{ M}, h_1(x) = h_1 = 5 \times 10^{-2} \text{ M}, \gamma = 0.0261/\text{day}, \\ q_0^{(1)}(x) = 10^5 \sqrt{1-x^2} \text{ H}, (q_0^{(2)}(x) = 10^7 \sqrt{1-x^2} \text{ H}), \rho_i = 0, \quad (i = 1, 2, 3), \\ t_0 = 45 \text{ days}, t^{(1)} = 2.5 \times 10^3 \text{ days}, (t^2 = 9 \cdot 10^3 \text{ days}).$$

The shortened finite systems of linear algebraic equations corresponding to the systems (24.15) and (24.18) consisting of ten and twelve equations have been solved. The numerical results show that an increase in the number of equations in systems led to a change only in the seventh decimal place in the solutions.

Increasing of the shear modulus of the glue causes the increase of the sought contact stresses, and the increase of the time value is corresponded a decrease of the values of these stresses. For comparison, the following should be noted: in contrast to a number of works in which a rigid contact between two interacting materials is considered and where unknown contact stresses have singularities at the ends of the contact line (i.e., stress concentrations arise); in this work, the contact between two bodies with viscoelastic (creep) properties is carried out using a thin layer of glue, and therefore the found contact stresses at the ends of the contact line turned out to be limited (finite). Obviously, the absence of stress concentration in the deformable body is extremely important from an engineering point of view.

References

1. Aleksandrov, V.M., Mkhitaryan, S.M.: Contact Problems for Bodies with Thin Coverings and Layers. Nauka, Moscow (1983) (in Russian)
2. Galin, L.A.: Contact Problems of Elasticity Theory and Viscoelasticity. Nauka, Moscow (1980) (in Russian)
3. Rabotnov, Yu.N.: Elements of Continuum Mechanics of Materials with Memory. Nauka, Moscow (1977) (in Russian)
4. Arutyunyan, N.Kh., Kolmanovskii, V.B.: The Creep Theory for Nonhomogeneous Bodies. Nauka, Moscow (1983) (in Russian)
5. Gross, B.: Mathematical Structure of the Theories of Viscoelasticity, No. 1190. Hermann & Cie, Paris (1953)
6. Christensen, R.M.: Theory of Viscoelasticity. Academic, New York (1971)
7. Pipkin, A.C.: Lecture on Viscoelasticity Theory. Springer, New York (1971)
8. Fabrizio, M., Morro, A.: Mathematical problems in linear viscoelasticity. In: SIAM Studies in Applied Mathematics, vol. 12. Society for Industrial and Applied Mathematics (SIAM), Philadelphia, PA (1992)
9. Altenbach, H., Skrzypek, J.J.: Creep and Damade in Materials and Structures. CISM Courses and Lectures, No. 399. Springer, Wien, New York (1999)

10. Altenbach, H.: Creep analysis of thin-walled structures. *ZAMM Z. Angew. Math. Mech.* **82**(8), 507–533 (2002)
11. Altenbach, H., Gorash, Y., Naumenko, K.: Steady-state creep of a pressurized thick cylinder in both the linear and power law ranges. *Acta Mechanica* **195**(1), 263–274 (2008)
12. Lakes, R.: *Viscoelastic Materials*. Cambridge University Press (2009)
13. Shavlakadze, N.N.: The contact problems of the mathematical theory of elasticity for plates with an elastic inclusion. *Acta Appl. Math.* **99**(1), 29–51 (2007)
14. Bantsuri, R., Shavlakadze, N.: The contact problem for piecewise homogeneous orthotropic plane with finite inclusion. *J. Appl. Math. Mech.* **75**(1), 93–97 (2011)
15. Shavlakadze, N., Odishelidze, N., Criado-Aldeanueva, F.: The contact problem for a piecewise-homogeneous orthotropic plate with a finite inclusion of variable cross-section. *Math. Mech. Solids* **22**(6), 1326–1333 (2017)
16. Bantsuri, R., Shavlakadze, N.: Solutions of integro-differential equations related to contact problems of viscoelasticity. *Georgian Math. J.* **21**(4), 393–405 (2014)
17. Shavlakadze, N.: The effective solution of two-dimensional integral-differential equations and their applications in the theory of viscoelasticity. *ZAMM. Z. Angew. Math. Mech.* **95**(12), 1548–1557 (2015)
18. Lubkin, J.I., Lewis, I.C.: Adhesive shear flow for an axially loaded finite stringer bonded to an infinite sheet. *Quart. J. Mech Appl. Math.* **23**(4), 521–533 (1970)
19. Muskhelishvili, N.I.: *Singular Integral Equations. Boundary Problems of Function Theory and Their Application to Mathematical Physics*. Wolters-Noordhoff Publishing, Groningen (1967)
20. Abramowitz, M., Stegun, I. (eds.): *Reference Book on Special Function*. Nauka, Moscow (1979) (in Russian)
21. Tricomi, F.: On the finite Hilbert transformation. *Quart. J. Math. Oxford Ser.* **2**(2), 199–211 (1951)
22. Popov, G.Ya.: Some new relations for Jacobi polynomials. *Sibirsk. Mat. Ž* **8**, 1399–1404 (1967) (in Russian)
23. Szegő, G.: *Orthogonal Polynomials*, 4th edn. American Mathematical Society Colloquium Publications, vol. XXIII. American Mathematical Society, Providence, R.I. (1975)
24. Kantorovich, L., Krilov, V.: *Approximate Methods of Higher Analysis*. Fifth corrected edition Gosudarstv. Izdat. Fiz.-Mat. Lit., Moscow-Leningrad (1962) (in Russian)
25. Kantorovich, L., Akilov, G.: *Functional Analysis*, 2nd edn. Revised. Izdat. Nauka, Moscow (1977)

Chapter 25

An Efficient Treatment of Sound Diffraction by Arbitrary Obstacles with Angles



Mezhlum Sumbatyan and Natalia Musatova

Abstract The problem under consideration arises in ultrasonic evaluation of modern elastic materials, in the case when potential defects may contain sharp corners on their boundary. The paper is concerned with a two-dimensional diffraction of a point source acoustic wave by arbitrary defect containing a finite number of angles. By Boundary Element Method (BEM), the problem is reduced to the integral equation, over the boundary of the obstacle. We apply a numerical approach, with a discretization of the boundary curve. Then the main Boundary Integral Equation (BIE) is converted to the system of linear algebraic equations (SLAE). Two specific approaches are used to improve the precision of the solution. The first one is based on two different meshes—near and outside a small neighbourhood of the corners. The second one is to take into account the angles, which consists of explicit analytical representation for those matrix elements connected with the nodes closest to the angles. This idea based on a small argument asymptotics of the Hankel function, in a combination with the first advanced method, demonstrates good precision, including small vicinity of the angles as well. As an example, we test the proposed algorithm in the case of diffraction by a polygon with straight-line sides.

Keywords Elastic materials · Ultrasonic evaluation · Acoustic waves · Diffraction · Boundary integral equation

25.1 Introduction

The evaluation of strength is a key problem in mechanics of modern solid materials, like composites, solar panels, plastics, fibre-optical materials, and others. One of efficient methods to evaluate the interior structure of such materials is the ultrasonic

M. Sumbatyan (✉) · N. Musatova
Vorovich Institute of Mathematics, Mechanics and Computer Science, Southern Federal University, Milchakova Street 8a, 344090 Rostov-on-Don, Russian Federation
e-mail: masumbatyan@sfnu.ru

N. Musatova
e-mail: musatova.natalia@gmail.com

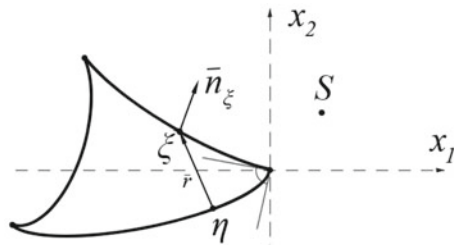
scanning. The latter is based on diffraction of acoustic waves, generated by some sensors, and propagating inside the material or over its surface. The diffraction by defects of regular geometry is a classical problem of wave propagation and scattering [1]. In the case, when the boundary of a defect contains sharp corners, the numerical simulation of the diffraction faces difficulties, due to irregular behaviour of the wave structure around the angles. The main purpose of the present work is to propose some methods which can overcome this difficulty.

In the two-dimensional problem, a particular case of defects with corners, is represented by polygons which may contain both acute and/or obtuse angles. The scattering of sound by a polygon is a classical problem of the diffraction theory. Chronologically, first approaches were based on analytical methods allied with the Geometrical Theory of Diffraction (GTD), see [2, 3]. Being based on the GTD, all methods are efficient only for high frequencies. In the meantime, the formulated problem admits a natural treatment by reducing it to a BIE, where the key trouble is given by a numerical instability of the solution near the corners of the polygon. For diffraction by infinite wedge with single arbitrary angle there are known some efficient solutions, both analytical and numerical (a good survey is presented in [4]). Recently, the present authors with a colleague applied the BIE technique to diffraction by an infinite wedge [5]. The main goal of the present work is to extend some results, obtained in [5], to defects whose boundary line contains a finite number of corners. Regarding diffraction by polygons, the SLAEs arising with a direct discretization of the respective BIE, leads to a specific matrix with irregular elements, corresponding to mesh nodes closest to the corners. This gives, as a rule, a significant error in a vicinity of the corners. To get over this difficulty, we propose an improved approach which modifies the basic matrix and provides numerical stability.

25.2 Formulation of the Problem

Let us consider the two-dimensional diffraction problem about a harmonic sound wave generated by a point source S located near an obstacle with a piecewise-smooth closed boundary contour with the finite number of angles, see Fig. 25.1. Within the frames of the BEM, the diffraction problem can be reduced to the Fredholm BIE of the second kind [6, 7]:

Fig. 25.1 A defect with angles in a solid material



$$p(\eta) - 2 \int_l \frac{\partial G(\xi, \eta)}{\partial n_\xi} p(\xi) dl = 2p^{\text{inc}}(\eta), \quad \eta \in l, \tag{25.1}$$

where $p(\xi)$ is the total acoustic pressure over the boundary contour l , p^{inc} is the acoustic pressure in the incident wave, G is the Green's function, n_ξ is the unit normal to the boundary contour l at point ξ directed towards the acoustic medium, dl is the length of the elementary arc over the boundary curve at point ξ . Both $\langle\langle\text{interior}\rangle\rangle \xi = (\xi_1, \xi_2)$ and $\langle\langle\text{exterior}\rangle\rangle \eta = (\eta_1, \eta_2)$ points are some two-dimensional points on the boundary.

Equation (25.1) is indeed of the Fredholm type since for a piecewise-smooth boundary the kernel is piecewise-continuous, so the integral operator in the equation is compact in the space $C(l)$. Therefore, various efficient theoretical and numerical methods can be applied to this equation. The coefficient in front of $p(\eta)$ in the BIE (25.1) is the unity only in the case when point η does not coincide with any corner. Otherwise this factor depends on the value of respective interior angle β (see [6]):

$$\frac{\beta}{\pi} p(\eta) - 2 \int_l \frac{\partial G(\xi, \eta)}{\partial n_\xi} p(\xi) dl = 2p^{\text{inc}}(\eta), \quad (\eta \in l). \tag{25.2}$$

In [5] an infinite wedge with a sharp angle is considered, and there is approved that the contribution of the small vicinity of the angle in the BIE is small. Therefore, there is no need to put a particular mesh node right at the corner with discretization, to obtain more accurate solution. The same property is also valid for any obstacle with a finite number of angles. This follows from the so-called Meixner condition (see [4]), which claims that the behaviour of solution as $r \rightarrow 0$ in any vicinity of the sharp angle is as follows:

$$p \sim D + O(r^\delta), \quad \delta = \min\left(\frac{\pi}{2(\pi - \alpha)}, 2\right), \tag{25.3}$$

where r is the distance between the current point and the corner, D is a certain constant, and $\alpha = \beta/2$ is the half of the interior angle. As can be seen, there is no singularity whilst $0 \leq \alpha < \pi$. For this reason we consider below the basic BIE only in the form (25.1), implying that both in the continuous and in the discrete form the location of point η is always outside the corners.

The Green's function in the two-dimensional case is the Hankel function of the first kind:

$$G(\xi, \eta) = \frac{i}{4} H_0^{(1)}(kr), \quad \bar{r} = \xi - \eta, \quad r = |\bar{r}|, \tag{25.4}$$

where $k = \omega/c$ is the wave number, and the dependence on time in the harmonic regime is taken with the factor $\exp(-i\omega t)$, which is hidden in all formulas. The derivative of the Green's function is easily calculated in the following form:

$$\frac{\partial G}{\partial n_\xi} = \frac{\partial G}{\partial r} \cdot \frac{\partial r}{\partial n_\xi}, \quad \frac{\partial G}{\partial r} = -\frac{ik}{4} H_1^{(1)}(kr), \quad \frac{\partial r}{\partial n_\xi} = \frac{(\vec{r}, \vec{n}_\xi)}{r}. \quad (25.5)$$

The pressure in the incident field is equal to

$$p^{\text{inc}}(r_0) = \frac{i}{4} H_0^{(1)}(kr_0), \quad (25.6)$$

where r_0 is a distance between the exterior point η and the source $S = (x^0, y^0)$. Any pair of coordinates in the parentheses means the pair of the Cartesian coordinates in the natural coordinate system (x_1, x_2) , see Fig. 25.1.

With so doing, one can rewrite the main BIE (25.1) in the simpler form:

$$p(\eta) + \frac{ik}{2} \int_l H_1^{(1)}(kr) \frac{(\vec{r}, \vec{n}_\xi)}{r} p(\xi) dl = \frac{i}{2} H_0^{(1)}(kr_0), \quad (\eta \in l). \quad (25.7)$$

25.3 An Example of a Specific Geometry

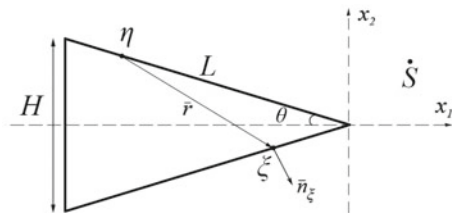
Generally, the approach described below is applicable to any obstacle of arbitrary complex geometry, containing a finite number of angles. In particular, this is applied to arbitrary polygon with curved sides. However, to test numerical efficiency of the proposed method, let us restrict the consideration by the simplest case of the isosceles triangle. Let us assume that the boundary curve consists of two lateral sides and the base. A point source S is located somewhere near the right sharp corner of the interior angle 2θ , see Fig. 25.2. Here L is the length of the lateral sides, H is the length of the base.

For further discretization we rewrite the main BIE (25.7) as follows:

$$p(\eta) + \int_l K(\xi, \eta) p(\xi) dl = 2p^{\text{inc}}, \quad K(\xi, \eta) = \frac{ik}{2} H_1^{(1)}(kr) \frac{(\vec{r}, \vec{n}_\xi)}{r}, \quad (\eta \in l), \quad (25.8)$$

where p^{inc} is given by Eq. (25.6). Let us divide the lateral sides of the isosceles triangle to N equal intervals with the step $h_1 = L/N$ and the base—to M equal intervals with

Fig. 25.2 Diffraction by the isosceles triangle



the step $h_2 = H/M$, and put respective nodes of the mesh at the central points of all elementary intervals. Then the total number of boundary nodes is $K = 2N + M$. Let us operate with the collocation technique, which implies the grids for variables ξ and η to coincide, i.e. $\eta_j = \xi_j, \forall j$. The discretization is performed on the basis of the Simpson quadrature formula. For this aim, let us introduce the three points: the central point t_{0j} coinciding with ξ_j and η_j , the beginning point t_{1j} which is a half-step before and the endpoint t_{2j} which is a half-step after the central point t_{0j} , if passing along the boundary contour anticlockwise.

This implies for the upper lateral side:

$$\begin{aligned}\xi_j &= t_{0j} = (-(j - 0.5)h_1 \cos \theta; (j - 0.5)h_1 \sin \theta), \quad j = 1, \dots, N, \\ t_{1j} &= \xi_j + (h_1 \cos \theta/2; -h_1 \sin \theta/2), \\ t_{2j} &= \xi_j + (-h_1 \cos \theta/2; h_1 \sin \theta/2).\end{aligned}\tag{25.9}$$

Analogous expressions are valid for the left basis:

$$\begin{aligned}\xi_j &= (-L \cos \theta; H/2 - (J - 0.5)h_2), \quad J = j - N, \quad j = N + 1, \dots, N + M, \\ t_{1j} &= \xi_j + (0; h_2/2), \\ t_{2j} &= \xi_j + (0; -h_2/2),\end{aligned}\tag{25.10}$$

and for the lower lateral side:

$$\begin{aligned}\xi_j &= t_{0j} = -((J - 0.5)h_1 \cos \theta; (J - 0.5)h_1 \sin \theta), \\ J &= K - j, \quad j = N + M + 1, \dots, K, \\ t_{1j} &= \xi_j + (-h_1 \cos \theta/2; -h_1 \sin \theta/2), \\ t_{2j} &= \xi_j + (h_1 \cos \theta/2; h_1 \sin \theta/2).\end{aligned}\tag{25.11}$$

The discretization reduces the BIE (25.8) to the SLAE, as follows:

$$Ap = f,\tag{25.12}$$

where A is a matrix of dimension $K \times K$; p, f are vectors of dimension K . The elements of matrix $A = (a_{mj})$ are of the following form:

$$\begin{aligned}a_{mj} &= \delta_{mj} + b_{mj}, \quad b_{mj} = \frac{h_j}{6} [K(t_{1j}, \eta_m) + 4K(t_{0j}, \eta_m) + K(t_{2j}, \eta_m)], \\ p &= (p_j), \quad p_j = p(\xi_j) = p(\eta_j) = p(t_{0j}), \\ f &= (f_m), \quad f_m = \frac{i}{2} H_0^{(1)}(kr_0),\end{aligned}\tag{25.13}$$

where δ_{mj} is Kronecker's delta, h_j is either h_1 or h_2 for respective side of the triangle.

25.4 Qualitative Algebraic Properties of the Basic Matrix

From explicit expressions for the kernel (25.4)–(25.7), one can easily deduce the basic matrix (25.12)–(25.13) to possess some interesting algebraic properties. First of all, the scalar product of the unit normal to the boundary contour and the radius-vector $\bar{r} = \xi - \eta$ in Eq. (25.8) predetermines $b_{mj} = 0$ when boundary points ξ_j and η_m both belong to the same side of the triangle. Therefore, the third part of all elements are simply Kronecker's deltas, which are regular. Unfortunately, the elements of the matrix A become less regular when the grid nodes ξ_j and η_m approach simultaneously any corner, being located over neighbour sides. Since the Hankel function is asymptotically $H_1^{(1)}(z) \sim 2/(\pi iz)$, $z \rightarrow 0$, then with $r \rightarrow 0$ the argument of the Hankel function in (25.8) tends to zero and the kernel $K(\xi, \eta)$ tends to infinity. This results in catastrophic increase of respective matrix elements b_{mj} in (25.9)–(25.11). Obviously, there is the most critical combination in this sense when variable ξ turns into t_{11} which coincides with the right corner whilst variable η turns into the last mesh node η_K closest to the corner, when looking at a vicinity of the right acute angle. The same combination takes place, say for the isosceles triangle in a vicinity of two left corners, and obviously—for any obstacle with angles in small vicinities of every its corner.

If speaking about continuous form of the basic BIE, under the condition that exterior variable η does not coincide with any corner, the integral in the BIE converges in the classical sense. This automatically implies that all elements b_{mj} of respective matrix are finite. However being finite, some of them may become too huge, not guaranteeing stable numerical calculations. In the general theoretical frame, this property requires a different investigation. However, in many concrete examples which were performed for some geometries with angles, we did observe that such specific geometries lead as a rule to irregular behaviour of the solution near the corners. It is surprisingly that in some particular cases the direct treatment, not taking into account the irregularity described above, leads to quite acceptable precision. One of such examples is demonstrated in Fig. 25.3 for the obstacle in the form of regular triangle, where both real and imaginary parts of the boundary function $p(\xi)$ are demonstrated over the boundary contour.

It is obvious that in this case $\theta = \pi/6$ for all three interior angles. One can see from this diagram that both the lines are very smooth over the boundary line, even in the neighbourhood of the corners.

Let us vary the acute angles of the isosceles triangle, to see how the pressure behaves with such a variation. Figures 25.4 and 25.5 demonstrate this property when the half of the right angle, quantity θ , passes through the values $\pi/9$, $\pi/12$ and the sharpest one $\pi/18$. Even a general diagram for real part of the solution shows extremely irregular behaviour in a small vicinity of the first node (recall that the enumeration of the mesh nodes starts from the right acute angle with an anticlockwise traversal along the boundary contour). This feature becomes more clear from the more detailed diagram, see Fig. 25.5, where it is clearly seen that wrong sharp bends

Fig. 25.3 Functions $\text{Re}[p(\xi)]$ (solid line) and $\text{Im}[p(\xi)]$ (dashed line) versus distance z along the boundary contour:
 $\theta = \pi/6, k = 1, H = L = 10, S = (1, 0), M = N = 1000, K = 3000.\text{eps}$

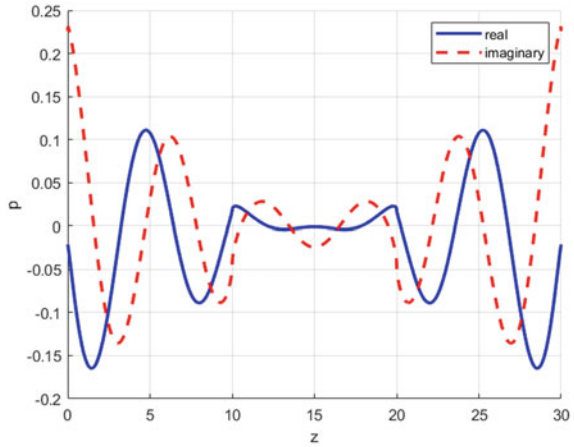
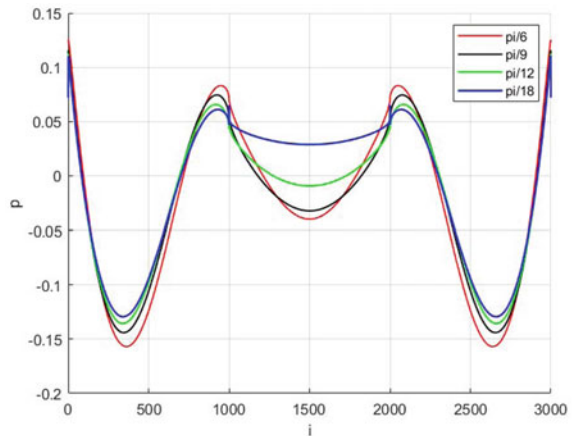


Fig. 25.4 Function $\text{Re}[p(\xi)]$ versus node's number for different isosceles triangles: $k = 0.5, L = 10, S = (1,0), N = M=1000, K = 3000$



take place for all three angles of the triangle. And the amplitude of the jumps in the diagram lines becomes greater with decreasing of the acute angle.

Figure 25.6 shows that simple application of a denser mesh, by increasing its dimension, does not improve significantly the precision of the solution around the acute angles. This feature becomes apparent stronger near the sharpest right angle (Fig. 25.6a). The amplitude of the jump in the diagram exceeds 50%, keeping almost the same value with the increase of the mesh dimension even up to the value $K = 14,000$.

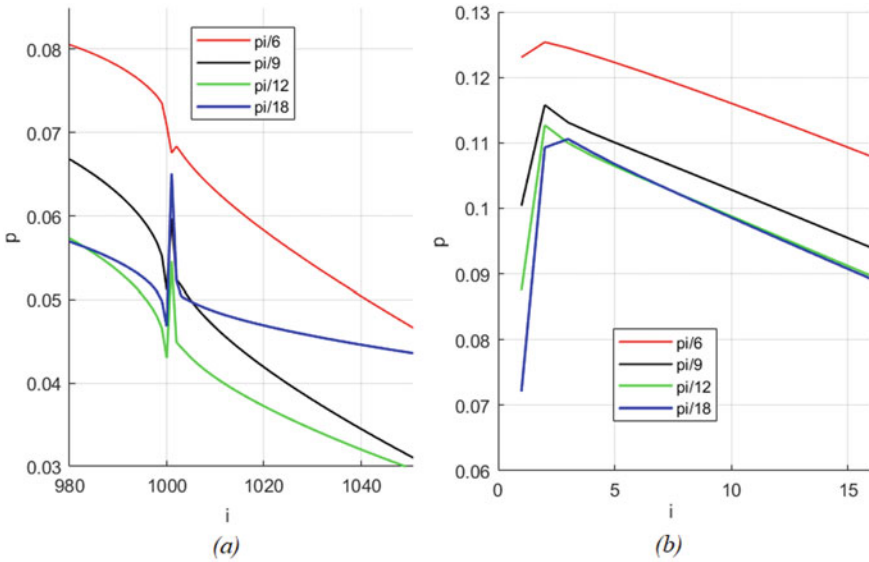


Fig. 25.5 Detailed fragments of Fig. 25.4, near the upper angle (a) and the right angle (b)

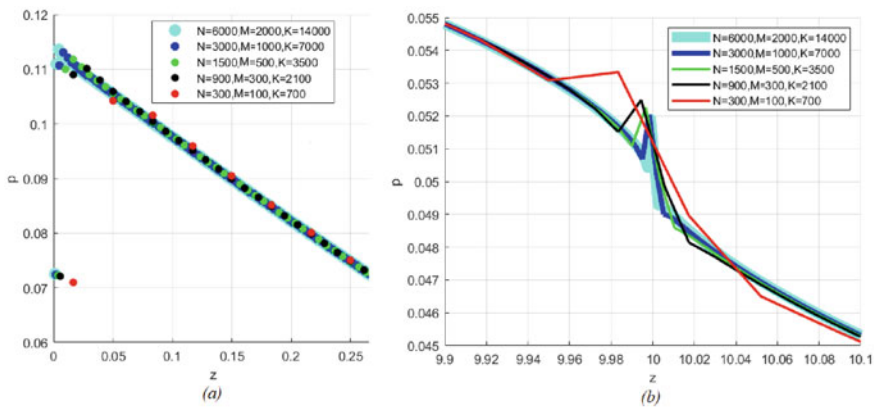


Fig. 25.6 Function $\text{Re}[p(\xi)]$ versus distance z , near the right angle (a) and the upper angle (b): $\theta = \pi/18, k = 0.5, L = 10, S = (1, 0)$. Uniform meshes of different dimensions

25.5 Two Methods to Improve the Structure of the Basic Matrix

It is obvious that the irregularity of the solution, described in the final part of the previous section, is caused by a specific structure of the basic matrix A . Geometrically, this is connected with presence of the sharp angles. Algebraically, this is caused by the influence of elements b_{mj} , for which respective nodes ξ_j and η_m are

located on neighbour sides of the boundary contour, being simultaneously closest to the same sharp angle. For such combinations of nodes kernel $K(\xi, \eta)$ in Eq. (25.8) is extremely large, and so are respective elements of the matrix. These large elements are located outside the principal diagonal, therefore they make worse the qualitative algebraic properties of the matrix and the convergence of any iterative scheme for respective SLAE as well.

The first idea, to overcome this difficulty, is to apply a non-uniform mesh which becomes denser when the nodes approach any corner. Since we apply the Simpson quadrature formula with discretization of the basic integral operator in the BIE at hand, this is problematic because the Simpson rule requires equal steps over two neighbour elementary subintervals. However, this idea in the almost same way can be realized by choosing small but finite vicinities of every corner where significantly denser uniform mesh may be used than the mesh over the remaining smooth parts of the boundary contour. By accepting the abbreviation *nbhd* for the word *neighbourhood*, the indicated small intervals near the corners may be taken, say of length $L_{nbhd}/L = 10^{-q}$ (good values for q are from 1.0 to 4.0), with a special relatively small step $h_{nbhd} = L_{nbhd}/N_{nbhd}$, where the dimension N_{nbhd} may be accepted sufficiently large. With doing so, over the remaining smooth part of the boundary, for every such a smooth boundary intervals, relatively moderate number of respective nodes may be taken—say, N^* nodes with the step $h_1^* = (L - 2L_{nbhd})/N^*$ for the upper and lower lateral sides (if we speak about the isosceles triangle), and M^* nodes with the step $h_2^* = (H - 2L_{nbhd})/M^*$ for the left triangle’s base. Then the total number of nodes for the full mesh is given as $K = 6N_{nbhd} + 2N^* + M^*$. The basic advance of this method is that, by keeping a moderate dimension K of the full mesh, the mesh-step near the corners becomes extremely small,—so that the critical elements corresponding to nodes near the corners, being multiplied with discretization of the basic integral by small values of these steps, are calculated with a higher precision, if compared with the standard *ungraceful* method described above. The scheme of this mesh is shown in Fig. 25.7.

Figure 25.8 shows that typically this first modified method works well, even not removing the irregularity completely. Indeed, the modified method with the mesh dimension $K = 670$ (red points) demonstrates better precision than the standard

Fig. 25.7 A refined discretization scheme with a non-uniform mesh, denser near the corners

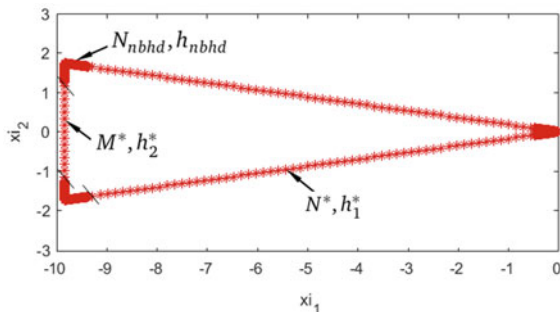
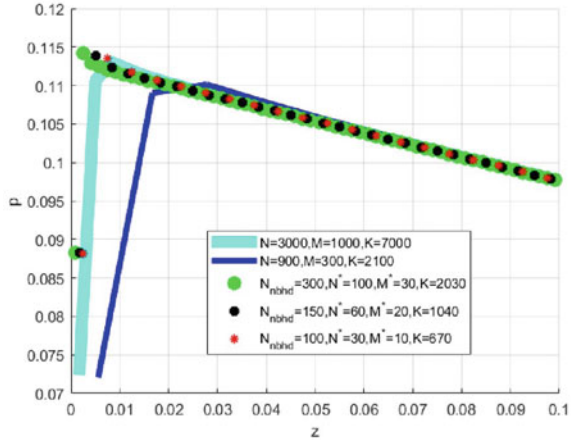


Fig. 25.8 Function $\text{Re}[p(\xi)]$ versus distance z , with a dense mesh near the right corner and a normal mesh on the smooth part: $\theta = \pi/18, k = 0.5, L = 10, S = (1, 0)$



approach with the mesh dimension $K = 2100$ (blue line). For the first (improved) method we put here near the angle $L_{nbhd} = 0.5, N_{nbhd} = 100$, hence the step is $h_{nbhd} = 0.5/100 = 0.005$. For the standard method we put $h \approx 0.01$, uniformly over the entire boundary contour. It is seen that with the same order of the grids' steps the improved method leads to a more regular solution. Nevertheless, as indicated above, this first improved method does not remove absolutely the irregularity in the vicinity of the sharp angle. Below we can see that a combination of this first improved method with the second advanced one described below leads to very stable solution, free of any irregular behaviour.

Let us pass to an alternative improved method which is based on the idea that instead of constructing a quadrature formula near any corner with a certain discretization, it is more preferable to calculate the integral over a small vicinity of the corner analytically. This idea is based on the asymptotic representation of the Hankel function for small argument (see the first paragraph of the previous section), and firstly was applied for diffraction by an infinite wedge in [5]. This idea can directly be extended to any polygon with a finite number of corners. Fortunately, the arising integral, taken over a small subinterval of length h adjoint with a corner, can be calculated analytically indeed. Thus, on example of the right corner of the isosceles triangle, in the case when "exterior" point η turns to the last K -th mesh node: $\eta_K = \{-(h/2) \cos \theta, -(h/2) \sin \theta\}$, and "interior" point ξ passes over the first subinterval S_1 of the grid, one easily derives the following relations: $\xi = \{-t \cos \theta, t \sin \theta\}, t \in (0, h)$, then $\bar{r} = \xi - \eta_K = \{(h/2 - t) \cos \theta, (h/2 + t) \sin \theta\}$, $\bar{n}_\xi = \{\sin \theta, \cos \theta\}, (\bar{r}, \bar{n}_\xi) = (h/2) \sin 2\theta$. Therefore, the integral over subinterval S_1 for the kernel in (25.8) can explicitly be calculated for small h , as follows:

$$\begin{aligned}
 \frac{ik}{2} \int_{S_1} H_1^{(1)}(kr) \frac{(\vec{r}, \vec{n}_\xi)}{r} dl_\xi &\sim \frac{1}{\pi} \int_{S_1} \frac{(\vec{r}, \vec{n}_\xi)}{r^2} dl_\xi \\
 &= \frac{h}{2\pi} \sin 2\theta \int_0^h \frac{dt}{t^2 - h t \cos 2\theta + h^2/4} \\
 &= \frac{1}{\pi} \left(\arctan \frac{2 - \cos 2\theta}{\sin 2\theta} + \arctan \frac{\cos 2\theta}{\sin 2\theta} \right) \\
 &= \frac{1}{\pi} \left[\arctan \frac{2 - \cos 2\theta}{\sin 2\theta} + \frac{\pi}{2} - \operatorname{arccot}(\cot 2\theta) \right] \\
 &= \frac{1}{\pi} \arctan \frac{2 - \cos 2\theta}{\sin 2\theta} + \frac{\pi - 4\theta}{2\pi}
 \end{aligned}
 \tag{25.14}$$

if the interior angle 2θ is acute. For arbitrary angle, respective expression can be found in [5].

Figure 25.9 demonstrates that a combination of these two proposed methods results in an amazing improvement of the solution. There are compared three ways of numerical calculation of acoustic pressure on the boundary contour. The first one (green line) is based on a simple uniform mesh all over the contour, and this leads to the roughest result due to a jump of respective diagram line near the right corner. The blue line is related to the first improved method, with a non-uniform mesh denser near the corners. Here we can see a slight improvement in precision, with significantly less mesh dimension. And the red line is based upon a combination of two advanced methods proposed above: (i) a denser mesh near the corners, and (ii) explicit analytical expressions for certain matrix elements. One can see from Fig. 25.9 that red line is the best amongst three ones, and this requires a mesh of a smaller dimension.

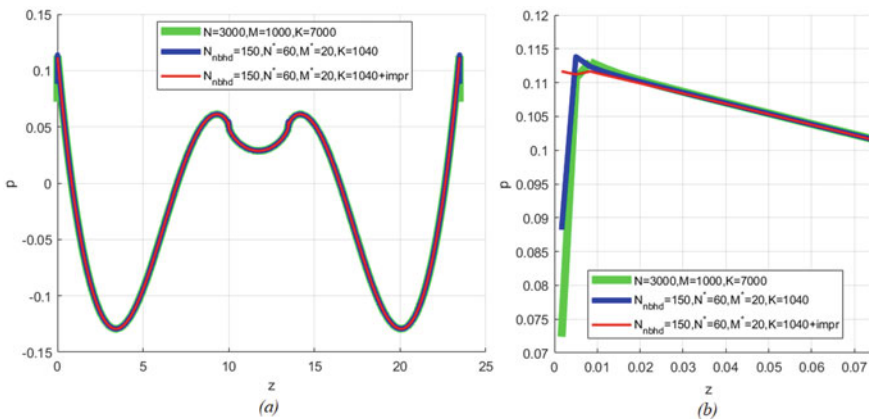


Fig. 25.9 The same as in Fig. 25.8, three different methods: **a** total diagram along the full boundary; **b** a detailed view near the right angle

It should finally be noted that once the boundary value of the acoustic pressure, function $p(\xi)$, $\xi \in l$ is determined, the scattered wave field at arbitrary point in the acoustic medium can directly be calculated by the following formula:

$$p^{sc}(R) = \int_l \frac{\partial G(\xi, R)}{\partial n_\xi} p(\xi) dl = \int_l \frac{(\bar{r}_R, \bar{n}_\xi)}{|\bar{r}_R|} p(\xi) dl. \quad (25.15)$$

A clear way to convert this continuous expression to an algebraic form, after discretization, is obvious.

25.6 Conclusions

1. This paper investigates a two-dimensional diffraction problem applied to defect evaluation in the modern elastic materials by ultrasonic methods, about a point source acoustic wave by arbitrary obstacle containing a finite number of angles. As a test example there is chosen an isosceles triangle. The Boundary Element Method is successfully implemented to this problem. The problem is reduced to the integral equation over the boundary of the obstacle. Then after discretization, the main BIE is converted to the SLAE, which is solved by a built-in Matlab instrument LSQR. The direct approach based on the uniform mesh does not provide the required precision, due to a certain irregularity of the basic matrix.
2. The authors propose an advanced discretization method, which is based on the idea of small intervals around every corner, where the uniform mesh is taken significantly denser, compared to the remaining smooth parts of the boundary curve. Therefore the mesh structure is such that far from the corners its step is moderate, whilst inside the small intervals the step may be chosen extremely small. Some concrete examples show that this first method improves the precision but does not finally remove the irregularity near the angles.
3. For the reason indicated in the previous paragraph, we propose the second method which is based upon an asymptotic behaviour of the Hankel function for small argument. This allows us to write out the most irregular elements of the basic matrix, associated with small intervals closest to the corners, in an explicit analytical form, instead of to treat respective integrals over the small vicinity of the corners by a certain discretization scheme. This idea is taken from the authors' recent work devoted to diffraction by an infinite wedge [5]. Such an approach demonstrates good precision and can be used for any geometry containing finite number of angles.
4. The most impressive results are obtained by a combination of the two proposed methods in the unique algorithm. This demonstrates regular behaviour of the solution with variation of the interior angle, when passing to the very sharp angles, more precisely—for test values of the angle: $\theta = \pi/6, \pi/9, \pi/12, \pi/18$.

Acknowledgements The authors are grateful to the Russian Foundation for Basic Research (RFBR), for the support by Project No. 19-29-06013. The first author dedicates this work to a memory of his scientific adviser Prof. Nagush Arutyunyan during the period of three Ph.D. years.

References

1. Achenbach, J.D.: *Wave Propagation in Elastic Solids*. North-Holland, Amsterdam (1973)
2. Keller, J.B.: Geometrical theory of diffraction. *J. Opt. Soc. Am.* **52**, 116–130 (1962)
3. Borovikov, V.A., Kinber, B.Ye.: *Geometrical theory of diffraction*. IEE Publ, London (1994)
4. Nethercote, M.A., Assier, R.C., Abrahams, I.D.: Analytical methods for perfect wedge diffraction: a review. *Wave Motion* **93**, 102479 (2020)
5. Sumbatyan, M.A., Martynova, T.S., Musatova, N.K.: Boundary element methods in diffraction of a point-source acoustic wave by a rigid infinite wedge. *Eng. Anal. Boundary Elem.* **127**, 157–167 (2021)
6. Brebbia, C.A., Telles, J.C.F., Wrobel, L.: *Boundary Element Techniques: Theory and Applications in Engineering*. Springer, Berlin (1984)
7. Sumbatyan, M.A., Scalia, A.: *Equations of Mathematical Diffraction Theory*. CRC Press, Boca Raton (2005)

Chapter 26

Exact Solution of the Axisymmetric Problem for Poroelastic Finite Cylinder



Natalya Vaysfeld and Zinaida Zhuravlova

Abstract The novelty of this paper is the application of the mathematical apparatus of boundary problems' theory to solve poroelasticity problems. The new analytical method to solve a three-dimensional boundary problem of poroelasticity for a finite circular cylinder in terms of Biot's model was worked out. With the help of this method, the explicit formulae for displacements, stress, and pore pressure inside the cylinder were derived. The construction of the solution required the use of matrix differential calculation apparatus. Derived explicit formulae that describe the cylinder's stress state can be used as etalons while applying various numerical methods to solve analogous problems of poroelasticity for finite circular cylinder and also for the clarification of important qualitative characteristics of the cylinder's stress state regarding the load type and poroelastic parameters. The proposed analytical solving method allows to solve the problems in more complex statements in the presence of defects in the form of rigid inclusions and cracks inside the cylinder.

Keywords Poroelastic cylinder · Integral transform · Matrix differential calculation · Vector boundary problem · Exact solution

26.1 Introduction

Poroelastic materials are widely used in engineering and medicine, which leads to the necessity of the investigation of their properties depending on the parameters of the certain poroelastic medium and different work regimes. For this purpose, various modeling methods are used. As it is known, there are many such models, which

N. Vaysfeld · Z. Zhuravlova
Faculty of Mathematics, Physics and Information Technologies,
Odessa I.I. Mechnikov National University, str. Dvoryanskaya, 2, Odessa 65082, Ukraine
e-mail: z.zhuravlova@onu.edu.ua

N. Vaysfeld (✉)
King's College, London Strand, London WC2R 2LS, UK
e-mail: vaysfeld@onu.edu.ua; natalya.vaysfeld@kcl.ac.uk

were developed in [1–5]. The modeling of poroelastic problems can be based both on the application of pure numeric solving methods and to solve using analytical approaches.

Among the papers dedicated to the numeric analysis of poroelasticity problems, one should indicate different applications of such numerical methods as: finite element method, stochastic methods, and pseudo-transient numerical method. An axisymmetric cylindrical model of fully coupled fluid flow was presented in [6], and elastic deformation solution was derived by a pseudo-transient numerical method. The development of a mechanobiological concept of reparative regeneration of bone tissue, controlled by the law of cell differentiation and the action of an external mechanical load of a periodic nature, was presented in [7]. A mathematical model had been developed there for bone reconstruction in the volume of a porous implant (scaffold) with a regular or chaotic internal structure based on the analysis of the stress–strain state of a poroelastic medium by the finite element method. The dispersion equation for cylindrical poroelastic structures was solved numerically in [8] with the help of an algorithm based on the spectral method which solved the corresponding equations as a generalized eigenvalue problem. The stochastic meshless local Petrov–Galerkin method was employed in [9] for dynamic analysis of cylinders made of fully saturated porous materials while considering uncertainties in the constitutive mechanical properties.

It would be possible to represent a number more researches here, but this is not in the interest of this paper. This is due to the fact that with the help of numerical methods it is impossible to establish important qualitative characteristics of the stress and pore pressure in body, as, for example, in corner points of the body, and also in any areas of essential growth and concentration of stress and pore pressure. With this purpose, the effective analytical methods might be used as will be seen from further review.

But, it should be emphasized that the quantity of papers dedicated to the application of analytical method for solving poroelasticity problems is significantly limited. Some of the papers propose the application of a combined approach based on the mutual use of analytical methods with the following application of various numerical techniques. Among these problems, the problem of a cylinder under plane strain conditions after sudden application of a constant fluid pressure [10] should be mentioned. There the solution was obtained explicitly for the Laplace transform of the various quantities, and the solution showing the dependence of parameters on time was then calculated using a numerical inversion technique. The formulation, based on the Biot model, was approximated by the equivalent elastic solid model in [11], and the problem of long bone-like or borehole sample specimen probed by low frequency sound was solved. The transient response of a poroelastic cylinder to sudden fluid injection was studied in [12]. The analytical solution was derived for a partial case, and numerical solutions were derived for different cases there.

Generalized solutions for the differential equations of three-dimensional consolidation were deduced with the aid of Laplace transformations for strains and stresses in cylindrical bodies in [13]. Acoustic scattering of spherical waves generated by a monopole point source in a perfect compressible fluid by a fluid-saturated

porous cylinder of infinite length was studied theoretically in [14]. The phenomena of mechanical creep and deformation in rock formations, coupled with the hydraulic effects of fluid flow, was studied in [15]. The theory was based on Biot’s poroelasticity, generalized to encompass viscoelastic effects through the correspondence principle. Based on the resultant poroviscoelastic theory, stress and deformation analyses were performed. The axisymmetric non-stationary problem of propagation surface disturbances from the boundary of a semi-plane filled with elasticity-porous medium was solved with the help of Hankel and Laplace transforms in [16].

Among these methods, for example, the method proposed in [17] stands out, where the solution for hollow cylindrical body of arbitrary cross-section with a tunnel crack under conditions of antiplane deformation was proposed. Two elasticity problems for cylinders were solved in [18] with the help of Hankel integral transforms and matrix differential calculations, which allows us to get effective analytical solutions. The axisymmetric elasticity problem for a cylinder with conditions of the first main elasticity problem on the cylinder’s surface was solved in [19]. The methods developed in [20, 21] seem to the authors to be very promising from the point of view of their application for problems in poroelastic formulation.

It is noticeable that the number of analytical methods developed for solving poroelasticity problems is significantly less than solving with purely numerical approaches and requires further development. So, the authors of the paper proposed a new analytical approach [20] resulting in the exact solution of axisymmetric poroelasticity problem for a circular finite cylinder under the conditions of Biot’s model [2]. Accordingly, the initial problem is reduced to a one-dimensional problem with the help of finite Fourier integral transform. The one-dimensional problem is formulated as a vector boundary problem. Its solution is constructed via matrix differential calculation apparatus. The derived formulae allow investigation of the cylinder’s mechanical characteristics and pore pressure depending on the poroelasticity parameters and load types using the explicit formulae for stress, displacements, and pore pressure.

26.2 Statement of the Problem

The poroelastic cylinder, $0 < R < a, -\pi < \varphi < \pi, 0 < h$ (or in dimensionless form $0 < r < 1, -\pi < \varphi < \pi, 0 < z < d, d = h/a$) is considered in the terms of Biot’s model [2] (Fig. 26.1).

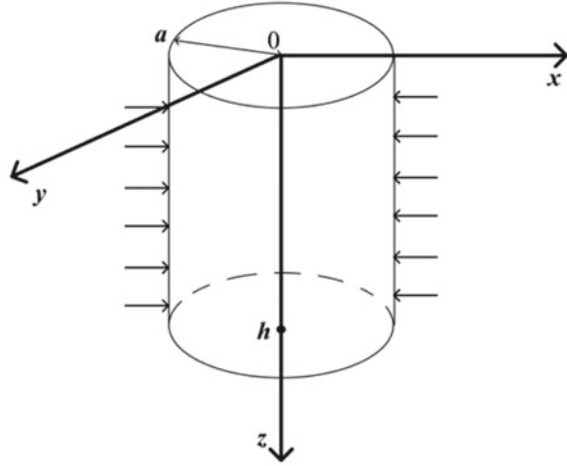
At the boundary $r = 1$ the following conditions are fulfilled

$$\sigma_r^F|_{r=1} = -l(z), \quad \tau_{rz}^F|_{r=1} = 0, \quad p|_{r=1} = P(z), \quad (26.1)$$

where $p(r, z)$ is dimensionless pore pressure, $\sigma_r^F(r, z), \tau_{rz}^F(r, z)$ are dimensionless normal and shear full stress.

$$p(r, z) = \frac{\tilde{p}(r, z)}{G}, \quad \sigma_r^F(r, z) = \frac{\tilde{\sigma}_r^F(r, z)}{G}, \quad \tau_{rz}^F(r, z) = \frac{\tilde{\tau}_{rz}^F(r, z)}{G},$$

Fig. 26.1 Geometry and coordinate system of the poroelastic cylinder



where $\tilde{p}(r, z)$ is pore pressure, $\tilde{\sigma}_r^F(r, z)$, $\tilde{\tau}_{rz}^F(r, z)$ are normal and shear full stress, G is shear modulus.

According to the relation between full and effective stress [4], the conditions (26.1) can be rewritten in the following form

$$\sigma_r|_{r=1} = -l(z) - \alpha P(z), \quad \tau_{rz}|_{r=1} = 0, \quad p|_{r=1} = P(z), \quad (26.2)$$

where $\sigma_r(r, z)$, $\tau_{rz}(r, z)$ are dimensionless normal and shear effective stress.

The conditions of ideal contact with undrained conditions are given at the boundaries $z = 0, z = d$

$$\begin{aligned} w|_{z=0} = 0, \quad \tau_{rz}|_{z=0} = 0, \quad \left. \frac{\partial p}{\partial z} \right|_{z=0} = 0, \\ w|_{z=d} = 0, \quad \tau_{rz}|_{z=d} = 0, \quad \left. \frac{\partial p}{\partial z} \right|_{z=d} = 0, \end{aligned} \quad (26.3)$$

Here, $u(r, z) = \frac{u_r(r,z)}{a}$, $w(r, z) = \frac{u_z(r,z)}{a}$ are dimensionless displacements of the solid skeleton.

The system of equilibrium and storage equations has the following dimensionless form [4, 22]

$$\begin{aligned} \frac{1}{r} \frac{\partial}{\partial r} \left(r \frac{\partial u}{\partial r} \right) - \frac{1}{r^2} u + \frac{\kappa - 1}{\kappa + 1} \frac{\partial^2 u}{\partial z^2} + \frac{2}{\kappa + 1} \frac{\partial^2 w}{\partial r \partial z} - \alpha \frac{\kappa - 1}{\kappa + 1} \frac{\partial p}{\partial r} = 0, \\ \frac{1}{r} \frac{\partial}{\partial r} \left(r \frac{\partial w}{\partial r} \right) + \frac{\kappa + 1}{\kappa - 1} \frac{\partial^2 w}{\partial z^2} + \frac{2}{\kappa - 1} \frac{1}{r} \frac{\partial}{\partial r} \left(r \frac{\partial u}{\partial z} \right) - \alpha \frac{\partial p}{\partial z} = 0, \\ \frac{1}{r} \frac{\partial}{\partial r} \left(r \frac{\partial p}{\partial r} \right) + \frac{\partial^2 p}{\partial z^2} - \frac{\alpha}{K} \left[\frac{1}{r} \frac{\partial}{\partial r} (ru) + \frac{\partial w}{\partial z} \right] - \frac{S_p}{K} p = 0, \end{aligned} \quad (26.4)$$

Here, $\kappa = 3 - 4\mu$ is Muskhelishvili's constant; μ is Poisson ratio; α is Biot's coefficient; S_p is storativity of the pore space; k is permeability. $K = \frac{\alpha^2}{Gk}$, $S_P = S_p G$ are dimensionless values. The stress state of the poroelastic cylinder, which satisfy the correspondences (26.2)–(26.4), should be found.

26.3 Exact Solution of a One-Dimensional Problem in the Transform Domain and Its Analytical Inversion

The boundary-valued problem (26.2)–(26.4) is reduced to a one-dimensional problem with the help of finite sin-, cos-Fourier transform applied regarding variable z

$$\begin{bmatrix} u_\beta(r) \\ w_\beta(r) \\ p_\beta(r) \end{bmatrix} = \int_0^d \begin{bmatrix} u(r, z) \\ w(r, z) \\ p(r, z) \end{bmatrix} \begin{bmatrix} \cos \beta z \\ \sin \beta z \\ \cos \beta z \end{bmatrix} dz, \beta_n = \frac{\pi n}{d}, n = 0, 1, 2, \dots$$

The one-dimensional problem in the transform space is formulated in a vector form [20]

$$\begin{aligned} L_2 \mathbf{y}_\beta(r) &= 0, 0 < r < 1, \\ A_\beta \mathbf{y}'_\beta(1) + B_\beta \mathbf{y}_\beta(1) &= \mathbf{g}_\beta \end{aligned} \tag{26.5}$$

Here, L_2 is differential operator of the second order; $\mathbf{y}_\beta(r)$ is the vector containing displacements and pore pressure transforms; A_β, B_β are known matrices, and \mathbf{g}_β is known vector shown in Appendix A.

The solution of the boundary problem (26.5) is constructed with the help of the matrix differential calculation [23]. According to it, the solution of the corresponding matrix equation should be found $L_2 Y_\beta(r) = 0, 0 < r < 1$. Here, $Y_\beta(r)$ is the matrix 3×3 order. The correspondence $L_2 H(r, \xi) = -H(r, \xi)M(\xi)$ is used, where [19]

$$H(r, \xi) = \begin{bmatrix} J_1(\xi r) & 0 & 0 \\ 0 & J_0(\xi r) & 0 \\ 0 & 0 & J_0(\xi r) \end{bmatrix},$$

$J_0(\xi r), J_1(\xi r)$ are Bessel functions,

$$M(\xi) = \begin{bmatrix} \xi^2 + \frac{\kappa-1}{\kappa+1} \beta^2 & \frac{2\beta}{\kappa+1} \xi & -\alpha \frac{\kappa-1}{\kappa+1} \xi \\ \frac{2\beta}{\kappa-1} \xi & \xi^2 + \frac{\kappa+1}{\kappa-1} \beta^2 & -\alpha \beta \\ \frac{\alpha \xi}{K} & \frac{\alpha \beta}{K} & \xi^2 + \beta^2 + \frac{S_p}{K} \end{bmatrix}.$$

According to [19], the solution of the matrix homogenous equation is constructed by the formula:

$$Y_\beta(r) = \frac{1}{2\pi i} \oint_C H(r, \xi) M^{-1}(\xi) d\xi$$

where $M^{-1}(\xi)$ is the inverse matrix to the matrix $M(\xi)$. The closed contour C covers all singularity points of the matrix $M^{-1}(\xi)$.

The determinant of the matrix $M(\xi)$ has 2 multiple poles of the second order $\xi = i\beta, \xi = -i\beta$ and 2 simple poles

$$\xi = i\sqrt{\frac{\alpha^2(\kappa-1)}{\kappa+1} + S_P} + \beta^2, \quad \xi = -i\sqrt{\frac{\alpha^2(\kappa-1)}{\kappa+1} + S_P} + \beta^2.$$

So, with the help of the residual theorem, the system of four fundamental matrix solutions is derived $Y_i(r), i = \overline{1, 4}$.

The solution of the boundary-valued problem (26.5) for the case when $\beta \neq 0$ has the following form

$$\mathbf{y}_\beta(r) = (Y_1(r) + Y_3(r)) \begin{pmatrix} c_1 \\ c_2 \\ c_3 \end{pmatrix} \tag{26.6}$$

where constants $c_i, i = \overline{1, 3}$ are found from the boundary conditions in (26.5). The case for $\beta = 0$ is considered separately due to the fact that for this case the dimensions of the problem's matrices change and will have a dimension of 2 by 2 (see Appendix B).

So, the solution of the boundary-valued problem in transform space is found, and it can be defined by the formulae (26.6) and (26.9). The solutions (26.6), (26.9) are united, and the following inverse formula is used:

$$\begin{bmatrix} u(r, z) \\ w(r, z) \\ p(r, z) \end{bmatrix} = \frac{1}{d} \begin{bmatrix} u_0(r) \\ w_0(r) \\ p_0(r) \end{bmatrix} + \frac{2}{d} \sum_{n=1}^{\infty} \begin{bmatrix} u_{\beta_n}(r) \\ w_{\beta_n}(r) \\ p_{\beta_n}(r) \end{bmatrix} \begin{bmatrix} \cos \beta_n z \\ \sin \beta_n z \\ \cos \beta_n z \end{bmatrix}, \beta_n = \frac{\pi n}{d} \tag{26.7}$$

Here, $w_0(r) \equiv 0, u_0(r), p_0(r)$ are defined by the formula (26.9), and $u_{\beta_n}(r), w_{\beta_n}(r), p_{\beta_n}(r)$ are defined by the formula (26.6).

The derived formula (26.7) presents the analytical solution of the boundary-valued problem for poroelastic cylinder (26.2)–(26.4). It should be taken into consideration that series in (26.7) are conditionally convergent series. Using an approach based on the summation of the weakly converging parts of the series [24] and the asymptotic representation of the Bessel functions for large values of the argument [25], the final expression is derived for analysis of displacements, stress, and pore pressure.

26.4 Results and Discussion

With the help of exact derived formulae, it is useful to investigate different mechanical characteristics depending on the size of the cylinder, poroelastic material, and applied load. Notice that conditions (26.2) can describe three different load types:

1. when $l(z) \neq 0, P(z) = 0$ the cylinder is loaded with the mechanical load $l(z)$, and perfect drainage conditions are fulfilled.
2. when $l(z) = 0, P(z) \neq 0$ the cylinder is loaded by fluid pressure $P(z)$, and conditions of the first elasticity problem are fulfilled.
3. when $-l(z) = P(z) \neq 0$ the cylinder is in contact with a static fluid under pressure $P(z)$ [3].

The authors conducted a study for 3 different types of load applied at the cylinder:

1. concentrated mechanical load $l(z) = \delta(z - d/2)$ when $P(z) = 0$;
2. distributed mechanical load $l(z) = \sin(\pi z/d)$ when $P(z) = 0$;
3. distributed fluid pressure $P(z) = \sin(\pi z/d)/G$ when $l(z) = 0$.

Three different poroelastic materials [3] were investigated. Characteristics of poroelastic materials are presented in Table 26.1, and were used in the dimensionless form for numerical calculations.

The numerical results corresponded to the case 1 for a concentrated mechanical load are presented at Figs. 26.2 and 26.3. The stress and pore pressure were investigated for the different values of d at Fig. 26.2. As it can be seen from the figures, the maximal absolute values of the normal stress and pore pressure are observed near the place of the point of load's application $z = d/2$, and the highest absolute

Table 26.1 Characteristics of poroelastic materials

Material	$G, N/m^2$	μ	α	$k, m^4/N$	$S_p, m^2/N$
Ruhr sandstone	1.33×10^{10}	0.12	0.637	2×10^{-13}	2.604×10^{-11}
Boise sandstone	4.2×10^9	0.15	0.853	8×10^{-13}	2.075×10^{-13}
Hard sediment	2.61×10^7	0.25	0.999	1×10^{-10}	2.237×10^{-10}

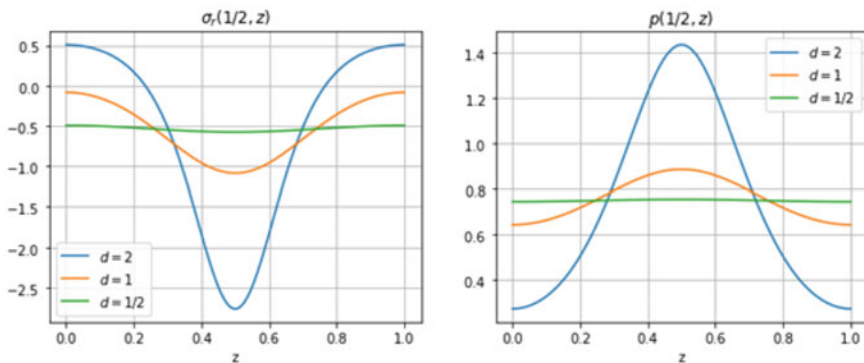


Fig. 26.2 The distributions of dimensionless effective stress $\sigma_r(1/2, z)$ and pore pressure $p(1/2, z)$ during the change of d for the concentrated mechanical load

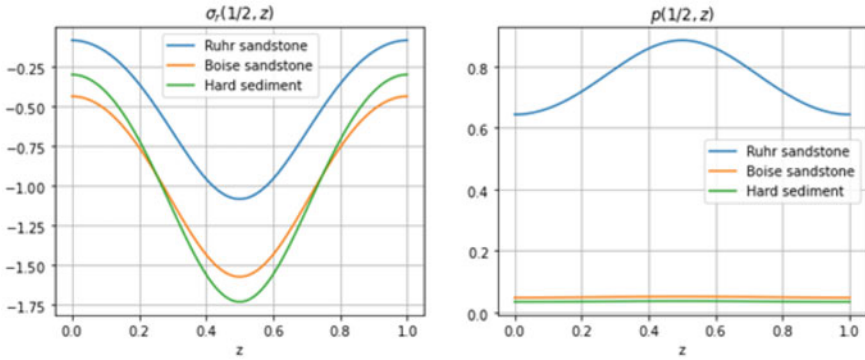


Fig. 26.3 The distributions of dimensionless effective stress $\sigma_r(1/2, z)$ and pore pressure $p(1/2, z)$ during the change of the poroelastic material for the concentrated mechanical load

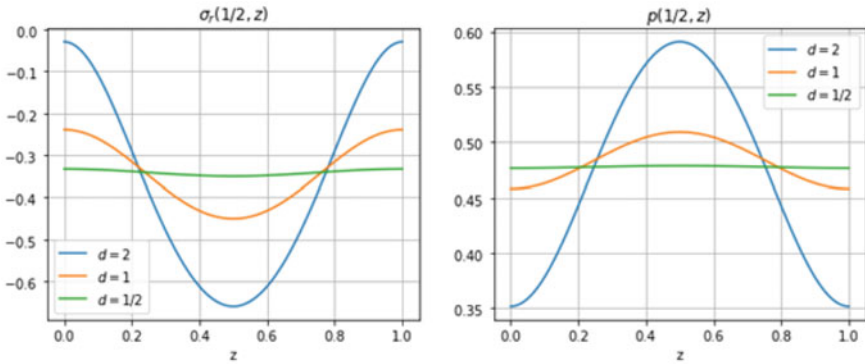


Fig. 26.4 The distributions of dimensionless effective stress $\sigma_r(1/2, z)$ and pore pressure $p(1/2, z)$ during the change of d for the distributed mechanical load

values of the normal stress and pore pressure in this zone are reached when the radius of the cylinder is less than the cylinder’s length $d > 1$. When z is close to the edges 0 or d , the stretching stress is observed. The pore pressure is positive for all values of d . This is caused by the drainage, which starts at the boundary of the cylinder $r = 1$ and which produce a tendency for shrinkage of the cylinder’s boundary. Also, the graphics of normal stress and pore pressure are symmetric regarding the line $z = d/2$ where the concentrated load is applied. The numerical investigation of cylinder’s geometric proportions shown that the stretching stress arises when the cylinder’s radius is essentially smaller than the cylinder’s length for the case of the concentrated load. It means that for such ratios of cylinder’s sizes, the applicability of the proposed method is restricted. The stress and pore pressure were investigated for the different materials when $d = 1$ at Fig. 26.3. As it can be seen, the increasing of Biot’s constant implies the reduction of stress and pore pressure.

Figures 26.4 and 26.5 correspond to the case 2 with distributed mechanical load.

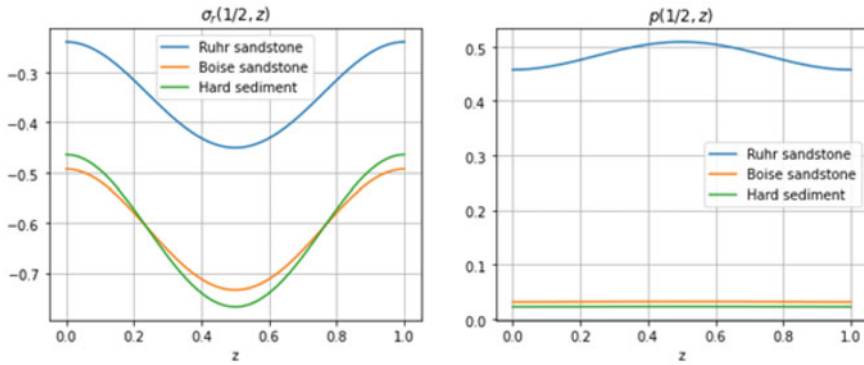


Fig. 26.5 The distributions of dimensionless effective stress $\sigma_r(1/2, z)$ and pore pressure $p(1/2, z)$ during the change of the poroelastic material for the distributed mechanical load

The load is symmetric, so the normal stress and pore pressure are also symmetric regarding the line $z = d/2$. The maximal absolute values of the normal stress and pore pressure are reached when the radius of the cylinder is less than the cylinder's length $d > 1$ (Fig. 26.4). The results are similar to the results derived for the case with the concentrated load, but in this case the stress and pore pressure values are smaller by their absolute values than in the previous case. The change of stress and pore pressure regarding the change of materials when $d = 1$ is shown at Fig. 26.5. The tendency observed for the concentrated load is preserved here. The stresses and pore pressure are greater for the material with the least Biot's constant.

The case 3 with the distributed fluid pressure is shown in Figs. 26.6 and 26.7. The load is symmetric, so the normal stress and pore pressure are also symmetric regarding the line $z = d/2$. Comparing to the case with distributed mechanical load, the absolute values of the normal stress and pore pressure are significantly larger. The largest absolute values of the normal stress and pore pressure are observed when the radius of the cylinder is less than the cylinder's length (Fig. 26.6). In Fig. 26.7 the change of stress and pore pressure regarding the change of materials when $d = 1$ is shown. Here the highest values of pore pressure are derived for the material with the least Biot's constant, and the highest absolute values of the stress are presented for the material with the highest Biot's constant.

With the aim to validate the derived results, the calculations for small values of α were done. The results when $\alpha = 0$ completely coincide with the classical elasticity problem under the same mechanical conditions.

1. As it is seen from the numerical investigation the application of concentrated mechanical load to the poroelastic cylinder in comparison with the distributed mechanical load cause higher stress and pore pressure. The highest stress and pore pressure are reached for the distributed fluid pressure case.

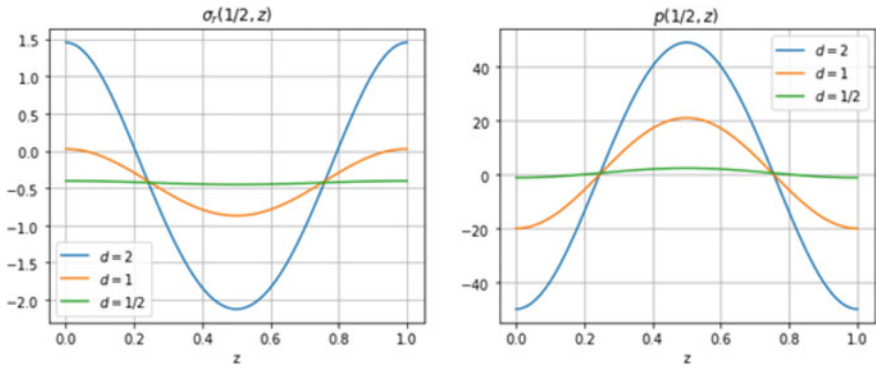


Fig. 26.6 The distributions of dimensionless effective stress $\sigma_r(1/2, z)$ and pore pressure $p(1/2, z)$ during the change of d for the distributed fluid pressure

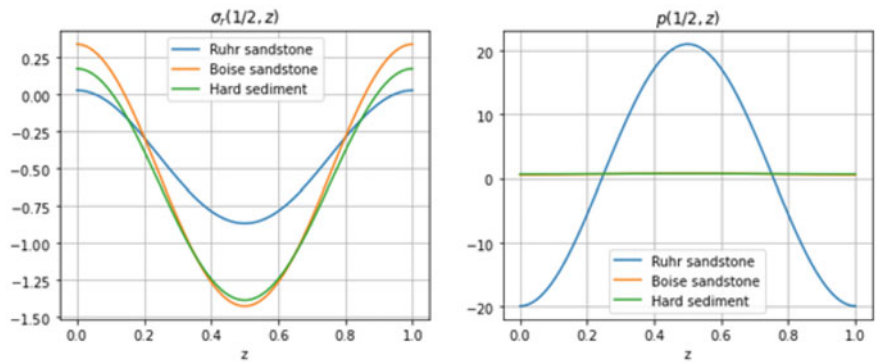


Fig. 26.7 The distributions of dimensionless effective stress $\sigma_r(1/2, z)$ and pore pressure $p(1/2, z)$ during the change of the poroelastic material for the distributed fluid pressure

2. The investigation regarding porous materials characteristics shown that the increasing of Biot's coefficient α implies the decreasing of stress and pore pressure.
3. The numerical calculation shown up the restriction of the proposed model under the ratio of cylinder's sizes for the case of the concentrated load.

26.5 Conclusions

The new analytical method for solving of axisymmetric poroelasticity problem for a finite circular cylinder is proposed by authors. The problem is formulated as three-dimensional boundary problem of poroelasticity in terms of Biot's model. The method is based on the application of integral transforms, reducing the problem in

transform domain, where the exact solution for the vector boundary problem is constructed. It allowed derivation of the explicit formulae for the displacements, stress, and pore pressure for the poroelastic cylinder in the frame of Biot's model. These explicit formulae made it possible to comprehensively investigate the dependence of stress and pressure of the cylinder on its size, the nature of poroelastic material and load. The proposed approach might be expanded to solve poroelasticity problems for bodies of canonic shape with defects in the form of cracks and rigid inclusions.

Appendix A: The Form of Matrices and Vectors at Boundary Vector Problem (5)

The matrices and vectors shown in (26.5) have the following form

$$L_2 = \begin{bmatrix} \frac{1}{r} \frac{d}{dr} \left(r \frac{d}{dr} \right) - \frac{1}{r^2} - \frac{\kappa-1}{\kappa+1} \beta^2 & \frac{2\beta}{\kappa+1} \frac{d}{dr} & -\alpha \frac{\kappa-1}{\kappa+1} \frac{d}{dr} \\ -\frac{2\beta}{\kappa-1} \frac{1}{r} \frac{d}{dr} (r) & \frac{1}{r} \frac{d}{dr} \left(r \frac{d}{dr} \right) - \frac{\kappa+1}{\kappa-1} \beta^2 & \alpha \beta \\ -\frac{\alpha}{K} \frac{1}{r} \frac{d}{dr} (r) & -\frac{\alpha \beta}{K} & \frac{1}{r} \frac{d}{dr} \left(r \frac{d}{dr} \right) - \beta^2 - \frac{S_p}{K} \end{bmatrix},$$

$$\mathbf{y}_\beta(r) = \begin{bmatrix} u_\beta(r) \\ w_\beta(r) \\ p_\beta(r) \end{bmatrix}, \quad \mathbf{g}_\beta = \begin{bmatrix} l_\beta/2 \\ 0 \\ P_\beta \end{bmatrix},$$

$$A_\beta = \begin{bmatrix} \kappa+1 & & \\ 2(\kappa-1) & 0 & 0 \\ 0 & 1 & 0 \\ 0 & 0 & 0 \end{bmatrix}, \quad B_\beta = \begin{bmatrix} 3-\kappa & (3-\kappa)\beta & \\ 2(\kappa-1) & 2(\kappa-1) & 0 \\ -\beta & 0 & 0 \\ 0 & 0 & 1 \end{bmatrix}$$

Appendix B: The Particular Case of the Boundary Vector Problem (5)

In the case when $\beta = 0$ the boundary-valued problem (5) transforms to the following form

$$\begin{aligned} \tilde{L}_2 \mathbf{y}_0(r) &= 0, \quad 0 < r < 1, \\ A_0 \mathbf{y}'_0(1) + B_0 \mathbf{y}_0(1) &= \mathbf{g}_0 \end{aligned} \quad (26.8)$$

Here

$$\tilde{L}_2 = \begin{bmatrix} \frac{1}{r} \frac{d}{dr} \left(r \frac{d}{dr} \right) - \frac{1}{r^2} & -\alpha \frac{\kappa-1}{\kappa+1} \frac{d}{dr} \\ -\frac{\alpha}{K} \frac{1}{r} \frac{d}{dr} (r) & \frac{1}{r} \frac{d}{dr} \left(r \frac{d}{dr} \right) - \frac{S_p}{K} \end{bmatrix},$$

$$\mathbf{y}_0(r) = \begin{bmatrix} u_0(r) \\ p_0(r) \end{bmatrix}, \quad \mathbf{g}_0 = \begin{bmatrix} l_0/2 \\ P_0 \end{bmatrix}, \quad A_0 = \begin{bmatrix} \kappa+1 & \\ 2(\kappa-1) & 0 \\ 0 & 0 \end{bmatrix}, \quad B_0 = \begin{bmatrix} 3-\kappa & \\ 2(\kappa-1) & 0 \\ 0 & 1 \end{bmatrix}.$$

Analogically to the previous the corresponding matrix equation

$$\tilde{L}_2 Y_0(r) = 0, \quad 0 < r < 1$$

is considered. The correspondence $\tilde{L}_2 H_0(r, \xi) = -H_0(r, \xi) M_0(\xi)$ is used, where

$$H_0(r, \xi) = \begin{bmatrix} J_1(\xi r) & 0 \\ 0 & J_0(\xi r) \end{bmatrix}, \quad M_0(\xi) = \begin{bmatrix} \xi^2 & -\alpha \frac{\kappa - 1}{\kappa + 1} \xi \\ \frac{\alpha}{K} \xi & \xi^2 + \frac{S_P}{K} \end{bmatrix}.$$

The solution of the matrix homogenous equation is constructed by a formula

$$Y_0(r) = \frac{1}{2\pi i} \oint_{C_0} H_0(r, \xi) M_0^{-1}(\xi) d\xi$$

where $M_0^{-1}(\xi)$ is the inverse matrix to the matrix $M_0(\xi)$. The closed contour C_0 covers all singularity points of the matrix $M_0^{-1}(\xi)$.

The determinant of the matrix $M_0(\xi)$ has 1 multiple pole of the second order $\xi = 0$ and 2 simple poles

$$\xi = i \sqrt{\frac{\alpha^2(\kappa-1)}{\kappa+1} + S_P} / K, \quad \xi = -i \sqrt{\frac{\alpha^2(\kappa-1)}{\kappa+1} + S_P} / K.$$

So, with the help of the residual theorem, the system of three fundamental matrix solutions is derived $Y_{0,i}(r), i = \overline{1, 3}$.

The solution of the boundary-valued problem (26.8) which corresponds to the case when $\beta = 0$ has the following form

$$\mathbf{y}_0(r) = (Y_{0,1}(r) + Y_{0,3}(r)) \begin{pmatrix} c_{0,1} \\ c_{0,2} \end{pmatrix} \tag{26.9}$$

where constants $c_{0,i}, i = \overline{1, 2}$ are found from the boundary conditions in (26.8).

Acknowledgements The research is supported by Ukrainian Department of Science and Education under Project No. 0121U111664. Gratitude for Simon Dyke for the editing of the article’s text.

References

1. Terzaghi, K.: Erdbaumechanik auf bodenphysikalischer Grundlage. Deuticke, Wien (1925)
2. Biot, M.A.: General theory of three-dimensional consolidation. J. Appl. Phys. **12**, 155–164 (1941)
3. Cheng, A. H.-D.: Poroelasticity. Theory and Applications of Transport in Porous Media, vol. 27. Springer, Heidelberg (2016)
4. Verruijt, A.: An introduction to soil dynamics. In: Theory and Applications of Transport in Porous Media, vol. 24. Springer, Heidelberg (2010)
5. Arutyunyan, N.KH.: Some Problems in the Theory of Creep. Pergamon Press (1966)

6. Ishbulatov, S., Yarushina, V., Podladchikov, Yu.: A numerical simulation of poroelastic cylinder decompression problem on CUDA in an axisymmetric domain. EGU21-1955. <https://doi.org/10.5194/egusphere-egu21-11955>
7. Maslov, L.B.: Biomechanical model and numerical analysis of tissue regeneration in the volume of a porous implant (in Russian). *Appl. Math. Mech.* **83**(5–6), 834–860 (2019)
8. Karpfinger, F., Gurevich, B., Bakulin, A.: Modeling of axisymmetric wave modes in a poroelastic cylinder using spectral method. *J. Acoustical Soc. Am.* **10**(1121/1), 2968303 (2008)
9. Kazemi, H., Shahabian, F., Hosseini, S.M.: Shock-induced stochastic dynamic analysis of cylinders made of saturated porous materials using MLPG method: considering uncertainty in mechanical properties. *Acta Mechanica* **228**, 3961–3975 (2017). <https://doi.org/10.1007/s00707-017-1898-0>
10. Detournay, E., Cheng, A.H.-D.: Fundamentals of poroelasticity. In: Fairhurst, C. (ed.) *Comprehensive Rock Engineering: Principles, Practice and Projects, Analysis and Design Method*, pp. 113–171. Pergamon Press (1993)
11. Fellah, Z., Groby, J.-P., Ogam, E., Scotti, Th., Wirgin, A.: Acoustic Identification of Poroelastic Cylinder. OR 22, HAL Id: hal-00014654 (2005)
12. Auton, L.C., MacMinn, Ch.W.: From arteries to boreholes: transient response of a poroelastic cylinder to fluid injection. *Proc. Royal Soc. A* **474**, 20180284 (2018). <https://doi.org/10.1098/rspa.2018.0284>
13. de Leeuw, E.H.: The theory of three-dimensional consolidation applied to cylindrical bodies. In: *Proceedings of 6th International Conference on Soil Mechanics and Foundation Engineering*, Montreal, vol. 1, 287290 (1965)
14. Hosseini, N., Namazi, N.: Acoustic scattering of spherical waves incident on a long fluid-saturated poroelastic cylinder. *Acta Mechanica* **223**, 2075–2089 (2012). <https://doi.org/10.1007/s00707-012-0697-x>
15. Abousleiman, Y., Cheng, A.H.-D., Jiang, C., Roegiers, J.-C.: Poroviscoelastic analysis of borehole and cylinder problems. *Acta Mechanica* **119**, 199–219 (1996). <https://doi.org/10.1007/BF01274248>
16. Tarlakovsky, D.V., Dang, K.Z.: Propagation of axisymmetric surface disturbances in elastically porous half-space (in Russian). *Electronic J. Proc. MAI* **76**, 22 (2014)
17. Kyrlyova, O. I., Mykhas'kiv, V.V.: Harmonic vibration and resonance effects in the case of longitudinal shear of a hollow cylinder with crack. *Mater. Sci.* **55**(1) (2019). <https://doi.org/10.1007/s11003-019-00258-3>
18. Popov, G.Ya., Protserov, Yu.S., Gonchar, I.A.: Exact solutions for some axisymmetric problems for elasticity cylinders of the finite length with regard to its weight (in Russian). *Appl. Mech.* **51**(4) (2015)
19. Protserov Yu.S.: Axisymmetric problems of elasticity theory for a cylinder of finite length with free cylindrical surface and with tacking into account its own weight. *The Herald of Odessa I.I. Mechnikov National University. Math. Mech.* **18**, 3(19), 69–81 (2013)
20. Vaysfel'd, N.D., Zhuravlova, Z.Yu.: On one new approach to the solving of an elasticity mixed plane problem for the semi-strip. *Acta Mechanica* **226**(12), 4159–4172 (2015). <https://doi.org/10.1007/s00707-015-1452-x>
21. Reut, V., Vaysfeld, N., Zhuravlova, Z.: Non-stationary mixed problem of elasticity for a semi-strip. *Coupled Syst. Mech.* **9**(1), 77–89 (2020). <https://doi.org/10.12989/csm.2020.9.1.077>
22. Sonin, A.A.: A generalization of the PI-theorem and dimensional analysis. *PNAS* (2004). <https://doi.org/10.1073/pnas.0402931101>
23. Grantmakher, F.R.: *Theory of Matrices*. Nauka, Moscow (1967). (in Russian)
24. Popov, G.Ya.: *The Elastic Stress' Concentration Around Dies, Cuts, Thin Inclusions and Reinforcements* (in Russian). Nauka, Moscow (1982)
25. Abramowitz, M., Stegun, I.: *Handbook of Mathematical Functions with Formulas, Graphs and Mathematical Tables*. U.S. Government Printing Office, Washington (1972)
26. Popov, G.Ya.: *Exact Solutions of Some Boundary Problems of Deformable Solid Mechanic* (in Russian). Astroprint, Odessa (2013)